Univerza
v Ljubljani

Fakulteta za
gradbeništvo in
geodezijo

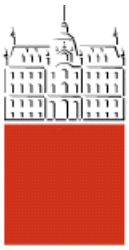

DOKTORSKI ŠTUDIJSKI
PROGRAM III. STOPNJE
GRAJENO OKOLJE

Kandidat:

MIHA JUKIĆ, univ. dipl. inž. grad.

KONČNI ELEMENTI ZA MODELIRANJE LOKALIZIRANIH PORUŠITEV V ARMIRANEM BETONU

Doktorska disertacija št. 5/GO

FINITE ELEMENTS FOR MODELING OF LOCALIZED FAILURE IN REINFORCED CONCRETE

Doctoral thesis No. 5/GO

Temo doktorske disertacije je odobrila Komisija za doktorski študij Univerze v Ljubljani na 20. redni seji, dne 21. septembra 2011.

Za mentorja je bil imenovan izr. prof. dr. Boštjan Brank,
za somentorja prof. dr. Adnan Ibrahimbegović, ENS, Cachan, Francija.

Odobreno je pisanje disertacije v angleškem jeziku.

Ljubljana, 13. december 2013

Univerza
v Ljubljani

Fakulteta za
gradbeništvo in
geodezijo

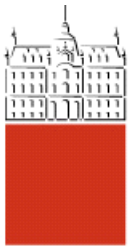

Komisijo za oceno ustreznosti teme doktorske disertacije v sestavi:

- izr. prof. dr. Boštjan Brank,
- prof. dr. Adnan Ibrahimbegović, ENS, Cachan, Francija,
- prof. dr. Miran Saje,
- prof. dr. Jože Korelc

je imenoval Senat Fakultete za gradbeništvo in geodezijo na 19. redni seji, 30. marca 2011.

Poročevalce za oceno doktorske disertacije v sestavi:

- prof. dr. Igor Planinc, UL FGG,
- prof. dr. Gordan Jelenić, Sveučilište u Rijeci, Građevinski fakultet,
- prof. dr. Nenad Bićanić, University of Glasgow, CED

je imenoval Senat Fakultete za gradbeništvo in geodezijo na 4. redni seji, 23. oktobra 2013.

Komisijo za zagovor doktorske disertacije v sestavi:

- doc. dr. Dušan Petrovič, prodekan za razvojno in mednarodno dejavnost UL FGG, predsednik,
- prof. dr. Boštjan Brank, mentor,
- prof. dr. Adnan Ibrahimbegović, ENS, Cachan, Francija, somentor,
- prof. dr. Igor Planinc, UL FGG,
- prof. dr. Gordan Jelenić, Sveučilište u Rijeci, Građevinski fakultet,
- prof. dr. Nenad Bićanić, University of Glasgow, CED

je imenoval Senat Fakultete za gradbeništvo in geodezijo na 5. redni seji, 27. novembra 2013.

IZJAVA O AVTORSTVU

Podpisani Miha Jukić izjavljam, da sem avtor doktorske disertacije z naslovom "Končni elementi za modeliranje lokaliziranih porušitev v armiranem betonu".

Izjavljam, da je elektronska različica disertacije enaka tiskani različici, in dovoljujem njeno objavo v digitalnem repozitoriju UL FGG.

Ljubljana, 9.12.2013

ERRATA

Page	Line	Error	Correction

BIBLIOGRAPHIC-DOCUMENTALISTIC INFORMATION AND ABSTRACT

UDC	**624.012.45:624.042.2:624.042.7(043.3)**
Author:	**Miha Jukić**
Supervisor:	**prof. Boštjan Brank, Ph.D.**
Co-supervisor:	**prof. Adnan Ibrahimbegović, Ph.D.**
Title:	**Finite elements for modeling of localized failure in reinforced concrete**
Document type:	**doctoral dissertation**
Notes:	**200 p., 120 fig., 424 eq.**
Keywords:	**failure analysis, finite element method, reinforced concrete, localized failure, embedded discontinuity, stress-resultant, multi-layer, Euler-Bernoulli beam, Timoshenko beam**

Abstract

In this work, several beam finite element formulations are proposed for failure analysis of planar reinforced concrete beams and frames under monotonic static loading. The localized failure of material is modeled by the embedded strong discontinuity concept, which enhances standard interpolation of displacement (or rotation) with a discontinuous function, associated with an additional kinematic parameter representing jump in displacement (or rotation). The new parameters are local and are condensed on the element level. One stress resultant and two multi-layer beam finite elements are derived. The stress resultant Euler-Bernoulli beam element has embedded discontinuity in rotation. Bending response of the bulk of the element is described by elasto-plastic stress resultant material model. The cohesive relation between the moment and the rotational jump at the softening hinge is described by rigid-plastic model. Axial response is elastic. In the multi-layer beam finite elements, each layer is treated as a bar, made of either concrete or steel. Regular axial strain in a layer is computed according to Euler-Bernoulli or Timoshenko beam theory. Additional axial strain is produced by embedded discontinuity in axial displacement, introduced individually in each layer. Behavior of concrete bars is described by elasto-damage model, while elasto-plasticity model is used for steel bars. The cohesive relation between the stress at the discontinuity and the axial displacement jump is described by rigid-damage softening model in concrete bars and by rigid-plastic softening model in steel bars. Shear response in the Timoshenko element is elastic. The multi-layer Timoshenko beam finite element is upgraded by including viscosity in the softening model. Computer code implementation is presented in detail for the derived elements. An operator split computational procedure is presented for each formulation. The expressions, required for the local computation of inelastic internal variables and for the global computation of the degrees of freedom, are provided. Performance of the derived elements is illustrated on a set of numerical examples, which show that the multi-layer Euler-Bernoulli beam finite element is not reliable, while the stress-resultant Euler-Bernoulli beam and the multi-layer Timoshenko beam finite elements deliver satisfying results.

BIBLIOGRAFSKO-DOKUMENTACIJSKA STRAN IN IZVLEČEK

UDK	**624.012.45:624.042.2:624.042.7(043.3)**
Avtor:	**Miha Jukić**
Mentor:	**prof. dr. Boštjan Brank**
Somentor:	**prof. dr. Adnan Ibrahimbegović**
Naslov:	**Končni elementi za modeliranje lokaliziranih porušitev v armiranem betonu**
Tip dokumenta:	**doktorska disertacija**
Obseg in oprema:	**200 str., 120 sl., 424 en.**
Ključne besede:	**porušna analiza, metoda končnih elementov, armirani beton, lokalizirana porušitev, vgrajena nezveznost, rezultantni model, večslojni model, Euler-Bernoullijev nosilec, Timošenkov nosilec**

Izvleček

V disertaciji predlagamo nekaj formulacij končnih elementov za porušno analizo armiranobetonskih nosilcev in okvirjev pod monotono statično obtežbo. Lokalizirano porušitev materiala modeliramo z metodo vgrajene nezveznosti, pri kateri standardno interpolacijo pomikov (ali zasukov) nadgradimo z nezvezno interpolacijsko funkcijo in z dodatnim kinematičnim parametrom, ki predstavlja velikost nezveznosti v pomikih (ali zasukih). Dodatni parametri so lokalnega značaja in jih kondenziramo na nivoju elementa. Izpeljemo en rezultantni in dva večslojna končna elementa za nosilec. Rezultantni element za Euler-Bernoullijev nosilec ima vgrajeno nezveznost v zasukih. Njegov upogibni odziv opišemo z elasto-plastičnim rezultantnim materialnim modelom. Kohezivni zakon, ki povezuje moment v plastičnem členku s skokom v zasuku, opišemo s togo-plastičnim modelom mehčanja. Osni odziv je elastičen. V večslojnih končnih elementih vsak sloj obravnavamo kot betonsko ali jekleno palico. Standardno osno deformacijo v palici izračunamo v skladu z Euler-Bernoullijevo ali s Timošenkovo teorijo nosilcev. Vgrajena nezveznost v osnem pomiku povzroči dodatno osno deformacijo v posamezni palici. Obnašanje betonskega sloja opišemo z modelom elasto-poškodovanosti, za sloj armature pa uporabimo elasto-plastični model. Kohezivni zakon, ki povezuje napetost v nezveznosti s skokom v osnem pomiku, opišemo z modelom mehčanja v poškodovanosti za beton in s plastičnim modelom mehčanja za jeklo. Strižni odziv Timošenkovega nosilca je elastičen. Večslojni končni element za Timošenkov nosilec nadgradimo z viskoznim modelom mehčanja. Za vsak končni element predstavimo računski algoritem ter vse potrebne izraze za lokalni izračun neelastičnih notranjih spremenljivk in za globalni izračun prostostnih stopenj. Delovanje končnih elementov preizkusimo na več numeričnih primerih. Ugotovimo, da večslojni končni element za Euler-Bernoullijev nosilec ni zanesljiv, medtem ko rezultantni končni element za Euler-Bernoullijev nosilec in večslojni končni element za Timošenkov nosilec dajeta zadovoljive rezultate.

INFORMATION BIBLIOGRAPHIQUE-DOCUMENTAIRE ET RESUME

CDU	**624.012.45:624.042.2:624.042.7(043.3)**
Auteur:	**Miha Jukić**
Directeur de thèse:	**prof. Boštjan Brank, Ph.D.**
Co-directeur de thèse:	**prof. Adnan Ibrahimbegović, Ph.D.**
Titre:	**Éléments finis pour la modélisation de la rupture localisée dans le béton armé**
Type de document:	**mémoire de thèse de doctorat**
Notes:	**200 p., 120 fig., 424 éq.**
Mots-clés:	**rupture, méthode des éléments finis, béton armé, rupture localisée, discontinuité forte, modèle en effort résultant, multicouche, poutre d'Euler Bernoulli, poutre de Timoshenko**

Résumé

Dans ce travail, différentes formulations d'éléments de poutres sont proposées pour l'analyse a rupture de structures de type poutres ou portiques en béton armé soumises a des chargements statiques monotones. La rupture localisée des matériaux est modélisée par la méthode a discontinuité forte, qui consiste a enrichir l'interpolation standard des déplacements (ou rotations) avec des fonctions discontinues associées a un paramètre cinématique supplémentaire interprété comme un saut de déplacement (ou rotation). Ces paramètres additionnels sont locaux et condensés au niveau élémentaire. Un élément fini écrit en efforts résultants et deux éléments finis multicouches sont développés dans ce travail. L'élément de poutre d'Euler Bernouilli écrit en effort résultant présente une discontinuité en rotation. La réponse en flexion du matériau hors discontinuité est décrite par un modèle élastoplastique en effort résultant et la relation cohésive liant moment et saut de rotation sur la rotule plastique est, quant a elle, décrite par un modèle rigide plastique. La réponse axiale est suppposée élastique. Pour ce qui concerne l'approche multi-couche, chaque couche est considérée comme une barre constituée de béton ou d'acier. La partie régulière de la déformation de chaque couche est calculée en s'appuyant sur la cinématique associée a la théorie d'Euler Bernoulli ou de Timoshenko. Une déformation axiale additionnelle est considérée par l'introduction d'une discontinuité du déplacement axial, introduite indépendamment dans chaque couche. Le comportement du béton est pris en compte par un modèle élasto-endommageable alors que celui de l'acier est décrit par un modèle élastoplastique. La relation cohésive entre la traction sur la discontinuité et le saut de déplacement axial est décrit par un modèle rigide endommageable adoucissant pour les barres (couches) en béton et rigide plastique adoucissant pour les barres en acier. La réponse en cisaillement pour l'élement de Timoshenko est supposée élastique. Enfin, l'élément multi-couche de Timoshenko est enrichi en introduisant une partie visqueuse dans la réponse adoucissante. L'implantation numérique des différents éléments développés dans ce travail est présentée en détail. La résolution par une procédure d'operator split est décrite pour chaque type d'élément. Les différentes quantités nécessaires pour le calcul au niveau local des variables internes des modèles non linéaires ainsi que pour la construction du système global fournissant les valeurs des dégrés de liberté sont précisées. Les performances des éléments développés sont illustrées a travers des exemples numériques montrant que la formulation basée sur un élément multicouche d'Euler Bernouilli n'est pas robuste alors les simulations s'appuyant sur des éléments d'Euler Bernouilli en efforts résultants ou sur des éléments multicouche de Timoshenko fournissent des résultats très satisfaisants.

TABLE OF CONTENTS

LIST OF FIGURES

KAZALO SLIK

1 INTRODUCTION

In the introductory chapter, the motivation for research on numerical modeling of localized failure of material, with emphasis on reinforced concrete, is presented. Previous achievements in this field of research are briefly reviewed, and the goals and the outline of the thesis are explained.

1.1 Motivation

Localized failure is a common phenomenon in variety of materials, used in civil engineering. At a certain load level, materials often exhibit highly localized deformations before failing. Typical examples are cracks in brittle materials, such as concrete, stone, brick or ceramic, and shear bands in metals or soils, see [1] and references therein. Growth of localized deformations is accompanied by reduction of stress, a process called softening of material. Adequate description of this phenomenon is essential for a comprehensive material model, which allows for a more accurate numerical modeling of structures and structural elements, made of such material.

In this work, we focus on reinforced concrete beams and frames, which are one of the most widespread structural forms. It has been observed in experimental tests, as well as on actual buildings, damaged in earthquakes, that most of material damage is concentrated at several critical locations in the structure. Localized failure of reinforced concrete comprises cracking and crushing of concrete, yielding of reinforcement and bond slip between the two components. This leads to the concept of plastic hinge in the limit load and push-over analyses, see e.g. [2–4]. In the classical limit load analysis, the limit capacity of each plastic hinge is kept constant, while additional hinges develop with the increasing load. This approach restrains the accuracy, with which the limit load of the structure is determined, and prevents the computation of structure's ductility and post-peak response. In highly statically undetermined structures, failure of a critical element does not jeopardize their integrity. It is therefore essential for an accurate analysis to be able to describe the softening response of the critical element, associated with the localized failure. This leads to the concept of softening plastic hinge, which allows for computation of ductility and post-peak response of the analyzed structure.

There are many different approaches to modeling of softening hinges in numerical analysis, see e.g. [5, 6]. In earthquake engineering, researchers often deal with large scale models of complex structures under rather complicated loads. Effective analysis of such problems can only be performed by using relatively simple finite elements, e.g. finite element with lumped plasticity, see [7, 8], where all plastic deformations are concentrated in the nodes, while the rest of the finite element stays elastic. Plastic hardening and softening of the element are described by the moment-rotation relationship of the nodes. Another way to model a softening hinge is to use a short crack-band finite element, in which localization is smeared over the whole element, see [9–11]. Since the softening is described on strain level, a fixed length of the crack-band element has to be computed, which is then considered a material property. In contrast to these two typical approaches, we decide to use lately established strong discontinuity concept, main characteristic of which is incorporation of discontinuous displacement fields into standard displacement based finite elements. The aim is to develop precise, effective and robust finite elements, capable of accurate description of localized failure in reinforced concrete beams and frames.

1.2 Theoretical background

Past decades have seen significant improvement in modeling of localized failure in numerical analysis, however, many issues still remain unsolved. A brief history and an overview of proposed solutions can be found in [12–14]. In earlier attempts, the structural softening response, associated with localized failure of material, was modeled simply by using elastoplastic constitutive model with softening to describe the local relation between the strain measure and the conjugate stress (or stress resultant), e.g. curvature and bending moment. The moment was computed in the same way as in classical elastoplasticity, except that after the limit load was reached, moment decreased with increasing curvature. This very simple model, called strain softening, is troubled by several problems, which are usually described as mathematical, physical and numerical [12].

In a structural element, discretized with a mesh of finite elements, only the critical element fails. Due to volumetric character of energy dissipation, determined by strain softening, the total energy dissipated in the softening range approaches zero when the mesh is refined. From mathematical point of view, the tangent stiffness matrix in softening ceases to be positive definite due to the negative value of tangent modulus. The boundary value problem becomes ill-posed and the solution of the problem is no longer unique [12, 15, 16]. The limit solution, when finite element size approaches zero, suggests failure of the structure without energy dissipation, which is physically unrealistic. From the aspect of numerical modeling, strain softening model leads to severe mesh dependency [17, 18].

Different approaches have been used to tackle the above mentioned problems. They are often referred to as localization limiters because their purpose is to prevent the strain localization to a vanishing volume. The earlier ones are briefly described in [19]. The simplest way to deal with the problem is to limit the minimum size of finite elements, as in crack band models [20–22], where the fracture is smeared over the whole finite element. The crack is therefore represented by an element-wide crack band. The volume of material, where strain softening takes place, is obviously still mesh dependent, so the strain softening modulus has to be adjusted according to the chosen mesh, in order to preserve the fracture energy. A similar approach is to embed a strain softening band of fixed width into a finite element, with the width of the band a material property [23, 24]. As stated in [12], these approaches do not solve the mathematical issue of an ill-posed boundary value problem and the solution is restricted to certain types of failure.

Nonlocal continuum theories have been proposed as an alternative [19, 25–27]. Here, the stress at a certain point of material domain is considered to be a function of average (nonlocal) strain in a representative volume of material, centered at that point. More generally, nonlocal strain is a weighted value of the entire strain field, and the weighting functions determine the domain of influence of strain on stress. This method enables the finite element analysis to overcome some problems caused by singularities, such as crack-tip problems. According to [12], nonlocal theories are fully regularized from the mathematical point of view.

Several variations of the nonlocal continuum model exist. By expanding the nonlocal variable into Taylor series and neglecting the higher order derivatives, the gradient (also weakly nonlocal) theory is obtained [28, 29]. Here, the stress at a certain point is computed from the values of strain and strain gradient at that point. Alternatively, incorporation of higher order derivatives in the constitutive relation results in higher order gradient theory, e.g. [30] for plasticity.

Apart from the above described localization limiters, several other regularization concepts have been proposed, such as Cosserat (or micropolar) continuum models [31, 32], which include local rotation of points in addition to their translation, or viscoplastic regularization, where the problem is treated as rate dependent [33]. The common aim of all presented approaches is to capture as accurately as possible the material behavior on the micro scale and incorporate it into finite elements for numerical analysis of structures subject to localized failure. The finite elements are devised to automatically develop localization at the critical point of the structure or the structural element (within their limitations). Appropriate behavior of structural elements on the macro scale is therefore

granted by sufficiently accurate material description on the micro scale.

Quite an opposite approach is often used in development of finite elements for numerical analysis in earthquake engineering. Dealing with large and complex structures under rather complicated loading, the analysis can become very time consuming and computationally demanding, so the finite elements are designed in the simplest possible way that still provides appropriate macro scale behavior of the structural element. For instance, columns of multi-story buildings subject to earthquake loading are known to exhibit highly localized inelastic deformations at their ends. Such behavior can be approximated by the lumped plasticity model, see e.g. [34, 35], where all inelastic response is concentrated at the zero-length hinges at the ends of the element, while the bulk of the element remains elastic. Of course, this does not correspond exactly to the actual material state of the beam, but the model captures all essential properties of the column's response.

The discrete approach to modeling of localized failure, used in the lumped plasticity and similar models, is an alternative to the smeared approach, used in previously described concepts. Both have advantages and drawbacks. The main advantage of the smeared fracture concepts is that the finite elements are developed on the micro scale, so they can generally represent any piece of material, regardless of its size and position in the structure, and the localization is positioned automatically. On the downside, many models have been found to suffer from stress locking due to inadequate kinematic description of discontinuous displacements around a macroscopic crack, see [13,36] and references within. Besides that, most techniques require sufficiently fine meshing of the softening zone to achieve mesh objectivity, which can prove computationally too demanding for large structures [12, 36]. In the discrete approach, the issues regarding size and representation of the softening zone are avoided by contracting it to a single point and introducing a localized dissipative mechanism. Another benefit of this method is that the finite elements are capable of kinematically accurate description of strong discontinuities in displacement and rotation. Consequently, a structure can be represented by a relatively coarse finite element mesh. The main drawback is that the localized failures can only occur at the predetermined locations.

A new family of methods, characterized by incorporation of the discontinuity within the finite element, has become very popular recently. Strain (weak) discontinuity models were developed first, by adding new discontinuous modes into the strain field [37, 38]. The displacement field remained continuous, however, which limited their applicability, see [36] and references within. This led to development of the strong discontinuity approach, utilized also in this work.

Numerous variations of strong discontinuity models have been developed, see [39–48] among others. Their application to beam finite elements, as in [49–56], is especially relevant for this work. All the models are based on the same idea. The finite volume of highly localized strain, which represented the fracture energy dissipation zone in smeared crack approaches, is replaced by a displacement (strong) discontinuity and an associated localized dissipative mechanism. This is achieved by upgrading displacement interpolation of standard finite elements with additional discontinuous shape functions. Each interpolation function is associated with an additional parameter, representing the corresponding displacement jump. Introduction of the conjugate traction at the discontinuity, related to the displacement jump by a softening cohesive law, establishes a localized dissipative mechanism. Additional equations for the new parameters are written in the form of local equilibrium between the stress in the bulk of the element and the traction at the discontinuity [1, 14].

Strong discontinuity approach can be described as a hybrid of the smeared and discrete approaches and it combines strong points of both concepts. Since the fracture energy dissipation is associated with the discontinuity, which has zero volume, the issues with the vanishing volume of the localization zone are successfully avoided and the physically unrealistic failure without energy dissipation is prevented. Mesh objectivity is granted as well, because the width of the softening zone and the energy dissipation at the discontinuity do not depend on the finite element size. From the mathematical point of view, the boundary value problem is well posed, which means that the concept efficiently copes with the physical, numerical and mathematical inconsistencies, presented earlier.

The enhanced kinematics provide an accurate description of the discontinuous displacement field around the frac-

ture, allowing for development of non-locking finite elements, namely the additional displacement modes are designed in such manner that they enable the finite elements to capture the stress-free state in case of a fully softened discontinuity [14]. Moreover, incorporation of local kinematics, describing the small-scale response of material (fracture), into the large-scale material model, corresponds well to the multi-scale nature of the considered physical problem [1, 12, 14, 36, 40]. Hence, the discontinuity can be adequately modeled with a relatively coarse mesh. Since each finite element is capable of forming a discontinuity, there is no need to predetermine its location. It occurs automatically and propagates through the structure, without modification of the original finite element mesh. These properties make the strong discontinuity concept convenient for numerical analysis of larger problems.

Implementation of displacement jumps can be performed by different methods, but generally two major families are distinguished – extended finite element methods (X-FEM) [39,40,42,57–59], and embedded discontinuity finite element methods (ED-FEM) [41, 60–63]. They differ in treatment of the additional parameters, associated with enhanced displacement modes. In X-FEM methods, the parameters are connected to the nodes of the finite element mesh and treated as global unknowns. In ED-FEM methods on the other hand, the parameters are associated with the finite elements and treated as local variables. Several studies have been performed, comparing advantages and disadvantages of both approaches [14, 64]. The main advantage of ED-FEM methods is that the additional unknowns can be eliminated from the global equations by static condensation, while in X-FEM each additional discontinuity increases the global system of equations. In this work, we follow the ED-FEM concept, motivated mainly by the previous work and experience in our research group. Illustration of the method on a basic 1D example can be found in [65].

1.3 Goals and outline of the thesis

Failure analysis has received much attention in our research group. Recently, a great part of research has been focused on modeling of localized failure of material with the strong discontinuity approach, more specifically the embedded discontinuity concept (ED-FEM) [46–48, 54, 66, 67]. The original contribution of Ibrahimbegovic and Brancherie [48] with respect to the strong discontinuity approach was to combine two inelastic mechanisms, both hardening in fracture process zone and softening at the discontinuity. This concept has been generalized to different structural models - continuum mechanics, plate and shell models, beam elements etc. The thesis relates particularly to the recent works, dealing with beam models. Dujc et al. [54] have developed a stress-resultant Euler-Bernoulli beam finite element with embedded discontinuities in rotation and axial displacement for failure analysis of steel (metal) beams and frames. Pham et al. [52] have presented a stress-resultant Timoshenko beam finite element with embedded discontinuity in rotation for failure analysis of reinforced concrete beams and frames. The first objective of the thesis is to combine the two concepts, namely to develop a similar finite element that uses Euler-Bernoulli kinematics and material laws for reinforced concrete. The next objective is to extend this concept to a multi-layer finite element in a similar manner as presented in [51]. More specifically, the goals are to:

- develop a straight planar stress-resultant Euler-Bernoulli beam finite element with embedded discontinuity in rotation for simple, robust and efficient failure analysis of reinforced concrete beams and frames,
- develop a straight planar multi-layer Euler-Bernoulli beam finite element with layer-wise embedded discontinuities in axial displacement for precise failure analysis of reinforced concrete beams and frames, and for computation of stress-resultant properties, required in analysis with the stress-resultant finite element,
- develop a straight planar multi-layer Timoshenko beam finite element with layer-wise embedded discontinuities in axial displacement for precise failure analysis of reinforced concrete beams and frames, and for computation of stress-resultant properties, required in analysis with the stress-resultant finite element,
- upgrade the multi-layer Timoshenko beam finite element by applying viscous regularization.

Besides the introduction, where the motivation, the theoretical background and the objectives are presented, the dissertation comprises five other chapters. Their outline is as follows.

In chapter 2, a stress-resultant Euler-Bernoulli beam finite element is developed. Standard kinematics is enhanced by incorporating a strong discontinuity in rotation. Enhanced curvature is defined by an additional parameter (degree of freedom) and a corresponding discontinuous interpolation function. The shape function is determined in such a manner, that the finite element is able to describe a stress-free state in case of a fully softened discontinuity. Equilibrium equations are derived from the virtual work principle, taking into account the contribution of the additional parameter. This produces an additional equation, describing the local equilibrium between the bulk of the element and the discontinuity. Due to the local character, it is solved on the element level and the additional parameter is condensed out of the global system of equations. Constitutive relation between the moment and the curvature of the bulk is defined by an elastoplastic material law with bilinear hardening and the relation between the moment and the rotational jump at the discontinuity is described by a plastic linear softening law. Axial response is assumed linear elastic. An operator split iterative computational procedure is developed, in which the internal variables and the additional degree of freedom are computed on the element level, and the standard displacements (degrees of freedom) are computed globally - on the structure level. The derived finite element is tested on several numerical examples. Finally, concluding remarks are presented.

A multi-layer Euler-Bernoulli beam finite element is considered in chapter 3. A reinforced concrete beam is divided into a desired number of concrete and steel layers. Axial displacements (and deformations) of a layer are computed in accordance with Euler-Bernoulli kinematics. Then, each layer is treated separately as a special "bar" - special in the sense that strain is generally linear in a layer, which can be attributed to interaction between layers. Layer kinematics is enhanced by introduction of a strong discontinuity in axial displacement. The enhanced layer strain is determined by an additional parameter (limited to a single layer) and a corresponding discontinuous shape function. The latter is derived on the layer level in such way, that it does not alter the layer displacements at the nodes. A different discontinuous shape function is derived for interpolation of virtual enhanced strain, so as not to collide with the definition of the traction at the discontinuity. Equilibrium equations are derived from the virtual work principle, taking into account the contributions of the additional parameters. In addition to standard equilibrium equations of the finite element, an extra equation is acquired for each layer. It represents local equilibrium between the bulk of the layer and the discontinuity. On account of their local nature, they are solved on the layer level and the enhanced parameters are condensed out of the global system of equations. Behavior of a concrete layer is controlled by an elasto-damage hardening law in the bulk (stress vs. strain) and a damage softening law at the discontinuity (traction vs. displacement jump). Behavior of a reinforcement layer is controlled by an elastoplastic hardening law in the bulk (stress vs. strain) and a plastic softening law at the discontinuity (traction vs. displacement jump). An operator split iterative computation procedure is presented. The internal variables and the enhanced parameters are calculated locally in each finite element, and the standard degrees of freedom are computed on the global level. Performance of the finite element is tested on several numerical examples. The chapter ends with concluding remarks.

In chapter 4, a multi-layer Timoshenko beam finite element is derived, following the procedure from chapter 3. A reinforced concrete is divided into concrete and steel layers. Axial displacements (and deformations) of a layer are determined according to Timoshenko kinematics. Layers are then treated individually, as bars. Due to Timoshenko beam theory, strain is constant over the length of each layer. Layer kinematics is enhanced by introducing a strong discontinuity in axial displacements. Enhanced strain is defined by an additional parameter and an additional discontinuous interpolation function. Contrary to the Euler-Bernoulli multi-layer beam, virtual enhanced strain is interpolated with the same shape function as the real strain. Equilibrium equations are derived from the virtual work principle, taking into account the contributions of enhanced parameters. This provides an additional equation for each layer, on top of the standard equilibrium equations. The additional equations are strictly local and are solved on the layer level, allowing for condensation of the additional parameters. They describe local equilibrium between the bulk of the layer and the discontinuity. Axial response of layers is controlled by identical material

laws as in chapter 3 - two laws (bulk, discontinuity) are given for a concrete layer, and two for a reinforcement layer. Additionally, a shear constitutive relation has to be defined for a Timoshenko beam. The shear response is assumed linear elastic. Equations of the problem are solved by an operator split iterative procedure. The internal variables and additional degrees of freedom are computed locally in each element. The nodal degrees of freedom are computed globally. The finite element is tested on several numerical examples. At the end of the chapter, concluding remarks are given.

In chapter 5, the multi-layer Timoshenko beam element from chapter 4 is upgraded, so as to include viscous regularization of the softening response. This is done by introducing at each discontinuity a viscous force, depending on the rate of change of the displacement jump and on the additional viscosity parameter. The viscous forces are added into the virtual work equation, derived in chapter 4, resulting in a modified local equilibrium equation, describing the relation between the stress in the bulk of the layer and the traction at the discontinuity. The global equilibrium equations, as well as kinematic and constitutive equations, remain unchanged. New expressions are derived for the softening multiplier, the traction at the discontinuity and the displacement jump. The modified element stiffness matrix is defined. Performance of the altered finite element is tested on basic numerical examples. The chapter is rounded with concluding remarks.

Finally, conclusions of the dissertation are presented in chapter 6.

2 STRESS RESULTANT EULER-BERNOULLI BEAM FINITE ELEMENT WITH EMBEDDED DISCONTINUITY IN ROTATION

2.1 Introduction

In this chapter we derive a planar stress-resultant Euler-Bernoulli beam finite element with embedded strong discontinuity in rotation, intended for analysis of reinforced concrete beams and frames up to complete failure, with automatic generation of softening plastic hinges at critical locations of the structure to describe localized failure in bending. Similar finite elements have been developed by Dujc et al. in [54] and Pham et al. in [52]. Dujc et al. derived a stress resultant Euler-Bernoulli beam element with embedded discontinuity in rotation for analysis of metal beams and frames. Pham et al. derived a stress-resultant Timoshenko beam with embedded discontinuity in rotation for reinforced concrete structures, which can describe only constant moment over the length of the element. Our finite element combines features of both above mentioned elements - constitutive equations suitable for reinforced concrete, and linear description of moment over the element in accordance with the standard Euler-Bernoulli beam element.

The derived element is based on small deformation kinematics. It features a strong discontinuity in rotation (rotational jump) at a location where a softening plastic hinge forms when carrying capacity of the element is reached. Behavior of the bulk is described by an elastoplastic material law with bilinear isotropic hardening. Behavior of the discontinuity is described by a linear softening law.

The chapter is organized as follows: Kinematic, constitutive and equilibrium equations are considered in section 2.2. Finite element discretization and numerical procedure are presented in section 2.3. Performance of the finite element is illustrated by several numerical examples in section 2.4. Concluding remarks of the chapter are given in section 2.5.

2.2 Finite element formulation

2.2.1 Kinematics

Let us consider a planar Euler-Bernoulli beam finite element with two nodes, presented in Fig. 2.1. Each node has three degrees of freedom, two in-plane displacements and rotation about the axis, perpendicular to the plane. If carrying capacity of the beam is reached, a softening plastic hinge forms at a distance x_d from the first node. The hinge is kinematically described by embedded strong discontinuity in rotation α.

Axial displacement $u(x)$ is interpolated between the axial nodal displacements $\mathbf{u}$, using linear interpolation functions $\mathbf{N}^u(x)$, shown in Fig. 2.2 (left).

$$u(x) = \mathbf{N}^u(x)\,\mathbf{u}, \quad \mathbf{N}^u(x) = \left\{1 - \frac{x}{L}, \frac{x}{L}\right\}, \quad \mathbf{u} = \{u_1, u_2\}^T \tag{2.1}$$

Axial strain $\varepsilon(x)$ is computed as the first derivative of axial displacement over coordinate x. Interpolation functions $\mathbf{B}^u$ are the derivatives of $\mathbf{N}^u$ and are constant. They are depicted in Fig. 2.2 (right).

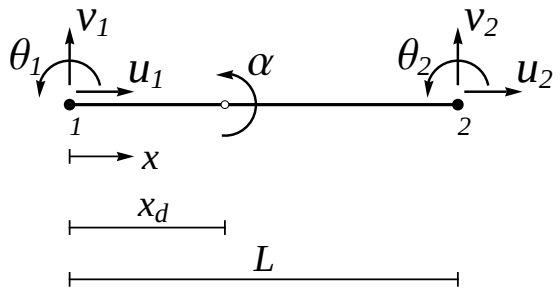

Figure 2.1: Finite element with six nodal degrees of freedom and embedded discontinuity in rotation.
Slika 2.1: Končni element s šestimi prostostnimi stopnjami in vgrajeno nezveznostjo v zasuku.

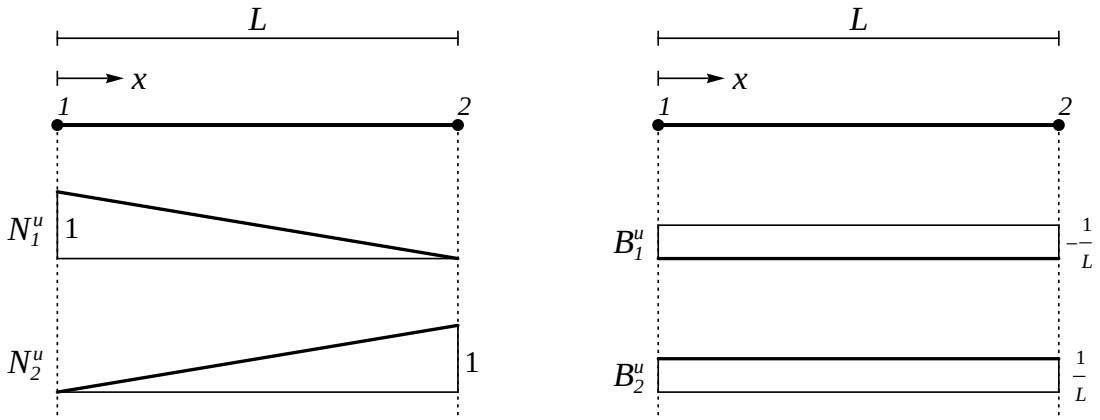

Figure 2.2: Interpolation functions for axial displacement (left) and axial strain (right).
Slika 2.2: Interpolacijske funkcije za osni pomik (levo) in osno deformacijo (desno).

$$\varepsilon(x) = \frac{\partial u}{\partial x} = \mathbf{B}^u(x)\,\mathbf{u}, \quad \mathbf{B}^u(x) = \left\{-\frac{1}{L}, \frac{1}{L}\right\} \tag{2.2}$$

Transversal displacement v_x is described by the following equation.

$$v(x, x_d) = \mathbf{N}^v(x)\,\mathbf{v} + \mathbf{N}^\theta(x)\,\boldsymbol{\theta} + \overbrace{\hat{M}(x, x_d)\,\alpha}^{v^{add}} \tag{2.3}$$

The first two parts of expression (2.3) represent standard transversal displacement, which is interpolated between transversal nodal displacements v and nodal rotations θ with Hermite interpolation functions $\mathbf{N}^v(x)$ and $\mathbf{N}^\theta(x)$, depicted in Fig. 2.3 (left). The last term represents the additional displacement $v^{add}(x, x_d)$, due to rotational jump α. Function $\hat{M}(x, x_d)$ will be considered later. Note that v^{add} is zero until the carrying capacity is reached.

$$\begin{aligned} \mathbf{N}^v(x) &= \left\{2\left(\frac{x}{L}\right)^3 - 3\left(\frac{x}{L}\right)^2 + 1, -2\left(\frac{x}{L}\right)^3 + 3\left(\frac{x}{L}\right)^2\right\}, \qquad \mathbf{v} = \{v_1, v_2\}^T \\ \mathbf{N}^\theta(x) &= L\left\{\left(\frac{x}{L}\right)^3 - 2\left(\frac{x}{L}\right)^2 + \frac{x}{L}, \left(\frac{x}{L}\right)^3 - \left(\frac{x}{L}\right)^2\right\}, \qquad \boldsymbol{\theta} = \{\theta_1, \theta_2\}^T \end{aligned} \tag{2.4}$$

According to Euler-Bernoulli beam theory, the curvature of the beam $\kappa(x, x_d)$ is computed as the second derivative of the transversal displacement.

$$\kappa(x,x_d) = \frac{\partial^2 v}{\partial x^2} = \overbrace{\mathbf{B}^v(x)\,\mathbf{v} + \mathbf{B}^\theta(x)\,\boldsymbol{\theta}}^{\tilde{\tilde{\kappa}}} + \overbrace{G(x,x_d)\,\alpha}^{\kappa^{add}} \tag{2.5}$$

The first two terms in expression (2.5) represent the regular curvature $\tilde{\tilde{\kappa}}$. Linear functions $\mathbf{B}^v$ and $\mathbf{B}^\theta$ are second derivatives of Hermite polynomials $\mathbf{N}^v$ and $\mathbf{N}^\theta$. They are written in equation (2.6), and drawn in Fig. 2.3 (right). The last part of expression (2.5) is the additional curvature, caused by the discontinuity in rotation. Function $G(x, x_d)$ is the second derivative of $\hat{M}(x, x_d)$ and will be discussed in the following section.

$$\mathbf{B}^v(x) = \left\{ -\frac{6}{L^2}\left(1-\frac{2x}{L}\right), \frac{6}{L^2}\left(1-\frac{2x}{L}\right) \right\}, \quad \mathbf{B}^\theta(x) = \left\{ -\frac{2}{L}\left(2-\frac{3x}{L}\right), -\frac{2}{L}\left(1-\frac{3x}{L}\right) \right\} \tag{2.6}$$

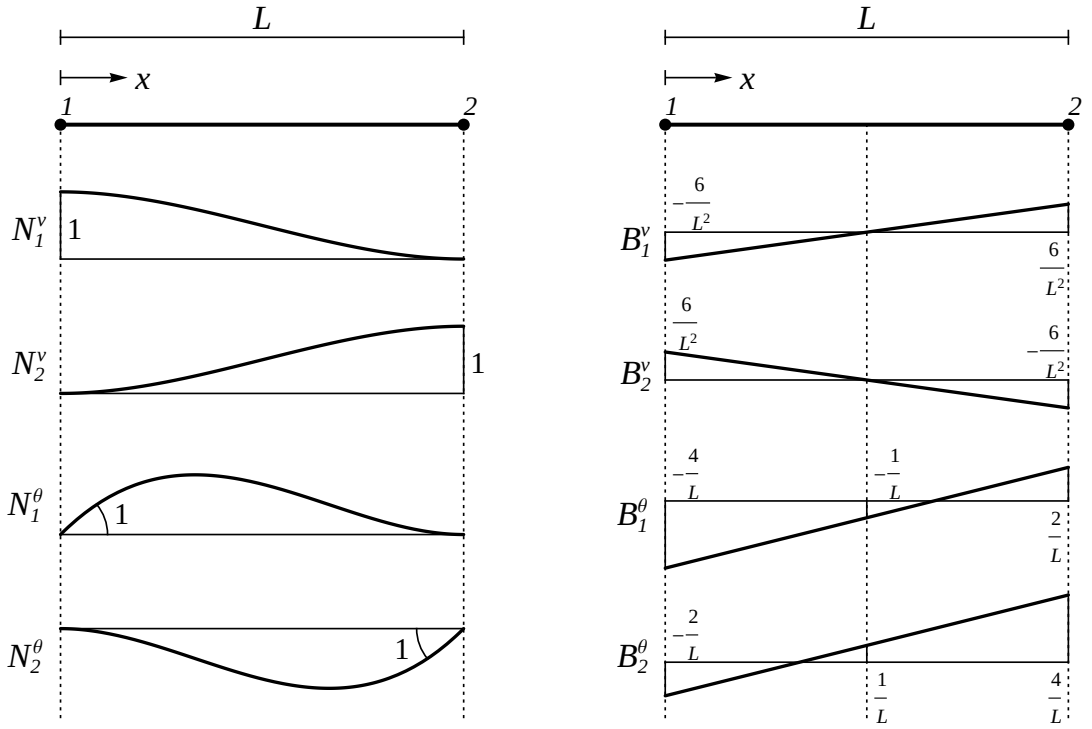

Figure 2.3: Interpolation functions for transversal displacement (left) and curvature (right).
Slika 2.3: Interpolacijske funkcije za prečni pomik (levo) in ukrivljenost (desno).

It is convenient to collect all degrees of freedom of the finite element in a single vector of generalized nodal displacements $\mathbf{d}$ and rewrite expressions for the axial strain ε and the regular part of the curvature $\tilde{\tilde{\kappa}}$, defined in equations (2.2) and (2.5).

$$\varepsilon = \begin{bmatrix} \mathbf{B}^u & \mathbf{0} & \mathbf{0} \end{bmatrix} \mathbf{d} = \breve{\mathbf{B}}^\varepsilon \mathbf{d}, \quad \tilde{\tilde{\kappa}} = \begin{bmatrix} \mathbf{0} & \mathbf{B}^v & \mathbf{B}^\theta \end{bmatrix} \mathbf{d} = \breve{\mathbf{B}}^\kappa \mathbf{d}, \quad \mathbf{d}^T = \left\{ \mathbf{u}^T, \mathbf{v}^T, \boldsymbol{\theta}^T \right\} \tag{2.7}$$

2.2.2 Derivation of operator G

Interpolation function $\hat{M}(x,x_d)$, introduced in equation (2.3), describes the additional transversal displacements of the beam, due to discontinuity in rotation α. Its main feature is a unit jump in the first derivative at the location of the discontinuity x_d. Everywhere else the function is smooth. In order not to affect the nodal displacements and rotations, the values of $\hat{M}$ and its first derivative $\hat{M}'$ must be zero at the nodes, see Fig. 2.4 (left). It is not necessary to know $\hat{M}$ beyond these requirements, as it does not appear in the computation on its own.

The first derivative $\hat{M}'$ can be composed from a Heaviside function H_{x_d} and a smooth continuous function $\varphi(x)$ with nodal values $\varphi(0)=0$ and $\varphi(L)=-1$. The Heaviside function and its derivative, the Dirac-delta function δ_{x_d}, are defined in equation (2.8) and displayed in Fig. 2.4 (right). Just like $\hat{M}$, φ is not required for the computation.

$$\hat{M}' = H_{x_d} + \varphi(x), \quad H_{x_d} = \begin{cases} 0; & x < x_d \\ 1; & x \geq x_d \end{cases}, \quad \frac{\partial H_{x_d}}{\partial x} = \delta_{x_d} = \begin{cases} \infty; & x = x_d \\ 0; & \text{otherwise} \end{cases} \tag{2.8}$$

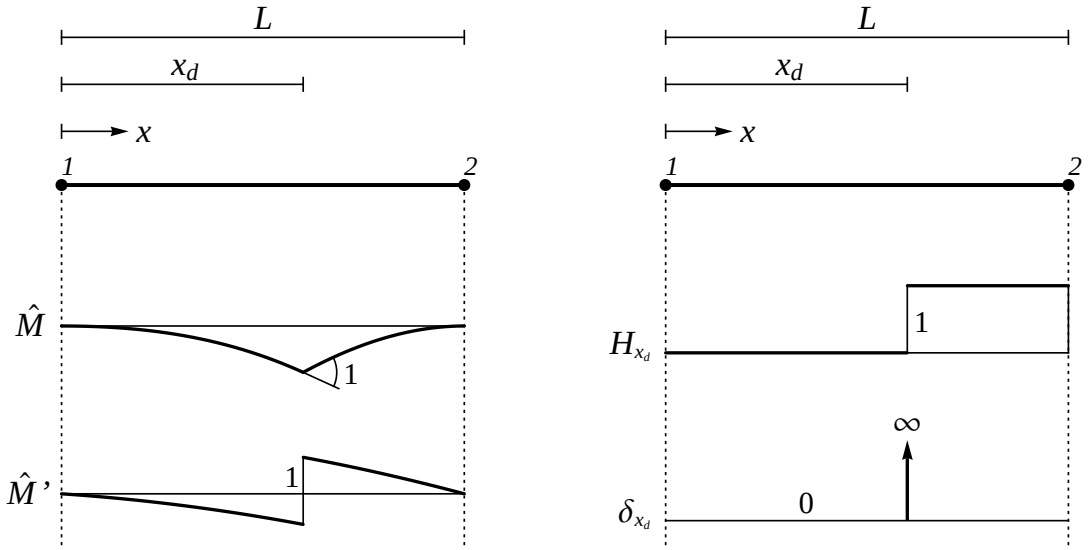

Figure 2.4: Interpolation function $\hat{M}$ and its first derivative $\hat{M}'$ (left). Heaviside and Dirac-delta functions (right).

Slika 2.4: Interpolacijska funkcija $\hat{M}$ in njen prvi odvod $\hat{M}'$ (levo). Heaviside-ova in Dirac-delta funkcija (desno).

Operator G is the second derivative of interpolation function $\hat{M}$ or the first derivative of $\hat{M}'$. According to (2.8), we can write:

$$G = \left(\hat{M}'\right)' = \left(H_{x_d} + \varphi(x)\right)' = \bar{\bar{G}} + \bar{G}, \qquad \bar{\bar{G}} = \delta_{x_d}, \qquad \bar{G} = \varphi'(x) \tag{2.9}$$

We can see that G consists of a discrete part $\bar{\bar{G}}$ and a continuous part $\bar{G}$. While the former is known, the latter still has to be determined. This can be done (without knowing $\hat{M}$ or φ) from requirement that the element must be able to describe a curvature-free state when the moment in the softening plastic hinge drops to zero, see Fig. 2.5. At that

point, the element should behave as two rigid bodies, connected by a rotation hinge, which implies the following relations between the nodal degrees of freedom:

$$v_2 = v_1 + L\theta_1 + (L - x_d)\,\alpha, \qquad \theta_2 = \theta_1 + \alpha \tag{2.10}$$

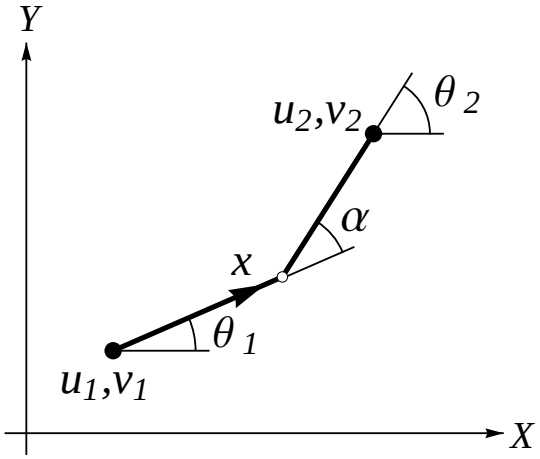

Figure 2.5: Curvature-free deformation of the beam when the moment in the hinge drops to zero.
Slika 2.5: Deformirana lega brez ukrivljenosti, ko moment v plastičnem členku pade na nič.

Let us now rewrite the expression (2.5) for curvature, taking into account the form of G.

$$\kappa(x, x_d) = \overbrace{\mathbf{B}^v(x)\,\mathbf{v} + \mathbf{B}^\theta(x)\,\boldsymbol{\theta} + \bar{G}(x, x_d)\,\alpha}^{\bar{\kappa}} + \overbrace{\bar{\bar{G}}(x, x_d)\,\alpha}^{\bar{\bar{\kappa}}} \tag{2.11}$$

Continuous part of expression (2.11) is designated with $\bar{\kappa}$ and represents the curvature of the bulk of the element. The discrete part $\bar{\bar{\kappa}}$ represents the infinite curvature at location of the discontinuity x_d. In a situation, depicted in Fig. 2.5, the bulk curvature is zero. After applying relations (2.10) and equations (2.6) for $\mathbf{B}^v$ and $\mathbf{B}^\theta$, the expression for $\bar{\kappa}$ is equaled to zero. Solution of obtained equation delivers the expression for $\bar{G}$.

$$\bar{G}(x, x_d) = -\frac{1 + 3\left(1 - \frac{2x_d}{L}\right)\left(1 - \frac{2x}{L}\right)}{L} \tag{2.12}$$

2.2.3 Relations between global and local quantities

2.2.3.1 Real degrees of freedom

A structure is modeled with a mesh of finite elements. A part of such mesh is depicted in Fig. 2.6. The total number of the nodes in the mesh is designated with n_N. Each node has three degrees of freedom - displacement U parallel to the global X axis, displacement V parallel to the global Y axis, and rotation Θ about the axis, perpendicular to the XY plane. The structure has in total $n_{DOF} = 3n_N$ degrees of freedom, which are collected in the vector $\mathbf{d}^{\text{str}}$.

$$\mathbf{d}^{\text{str}} = \left\{U_1, V_1, \Theta_1, U_2, V_2, \Theta_2, \ \ldots\ , U_{n_N}, V_{n_N}, \Theta_{n_N}\right\}^T \tag{2.13}$$

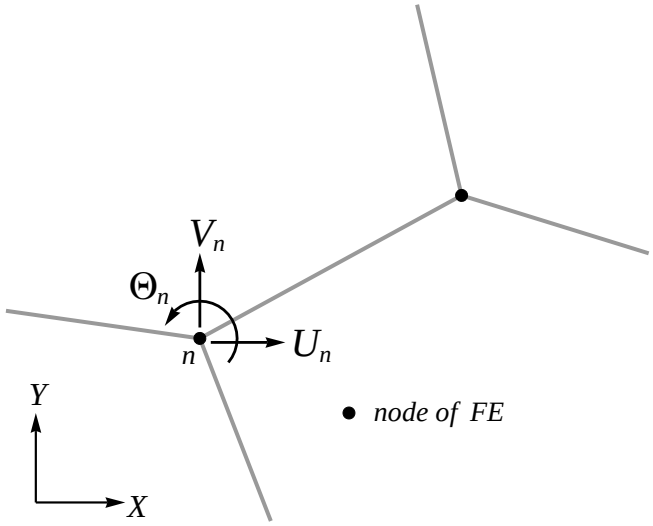

Figure 2.6: Degrees of freedom at a node of the finite element mesh.
Slika 2.6: Prostostne stopnje v posameznem vozlišču mreže končnih elementov.

Let us now consider a finite element (e) with end nodes (n_1) and (n_2). The local x axis is parallel to the axis of the element, with x increasing from node (n_1) towards node (n_2), see Fig. 2.7. The element's degrees of freedom, defined in the local coordinate system, are collected in the vector $\mathbf{d}^{(e)}$. Global degrees of freedom, associated with the nodes of the element are similarly organized into vector $\mathbf{D}^{(e)}$. The two are connected with a transformation matrix $\mathbf{R}^{(e)}$, (2.14). In equation (2.15), zeros are replaced by dots for clarity. $\phi^{(e)}$ is the angle between the global X axis and the local x axis (rotation of the coordinate system around the global Z axis, which is equal to the local z axis), see Fig. 2.7.

$$\mathbf{d}^{(e)} = \mathbf{R}^{(e)}\mathbf{D}^{(e)} \tag{2.14}$$

$$\mathbf{d}^{(e)} = \left\{u_1^{(e)}, u_2^{(e)}, v_1^{(e)}, v_2^{(e)}, \theta_1^{(e)}, \theta_2^{(e)}\right\}^T, \quad \mathbf{D}^{(e)} = \left\{U_{n_1}, U_{n_2}, V_{n_1}, V_{n_2}, \Theta_{n_1}, \Theta_{n_2}\right\}^T$$
$$\mathbf{R}^{(e)} = \begin{bmatrix} \cos\phi^{(e)} & \cdot & \sin\phi^{(e)} & \cdot & \cdot & \cdot \\ \cdot & \cos\phi^{(e)} & \cdot & \sin\phi^{(e)} & \cdot & \cdot \\ -\sin\phi^{(e)} & \cdot & \cos\phi^{(e)} & \cdot & \cdot & \cdot \\ \cdot & -\sin\phi^{(e)} & \cdot & \cos\phi^{(e)} & \cdot & \cdot \\ \cdot & \cdot & \cdot & \cdot & 1 & \cdot \\ \cdot & \cdot & \cdot & \cdot & \cdot & 1 \end{bmatrix} \tag{2.15}$$

Vector $\mathbf{D}^{(e)}$ contains those components of vector $\mathbf{d}^{\text{str}}$ that correspond to the nodes of the finite element. The selection of appropriate components is done by matrix $\mathbf{P}^{(e)}$ of size $6 \times n_{DOF}$ with only six non-zero entries.

$$\begin{aligned} &\mathbf{D}^{(e)} = \mathbf{P}^{(e)}\mathbf{d}^{\text{str}} \\ &P^{(e)}_{1,\,3n_1-2} = P^{(e)}_{2,\,3n_2-2} = P^{(e)}_{3,\,3n_1-1} = P^{(e)}_{4,\,3n_2-1} = P^{(e)}_{5,\,3n_1} = P^{(e)}_{6,\,3n_2} = 1, \quad \text{other } P^{(e)}_{i,j} = 0 \end{aligned} \tag{2.16}$$

Obeying equations (2.14) and (2.16), we can write the relation between the local degrees of freedom of the finite element (e) and the global degrees of freedom of the mesh.

$$\mathbf{d}^{(e)} = \mathbf{R}^{(e)}\mathbf{P}^{(e)}\mathbf{d}^{\text{str}} \tag{2.17}$$

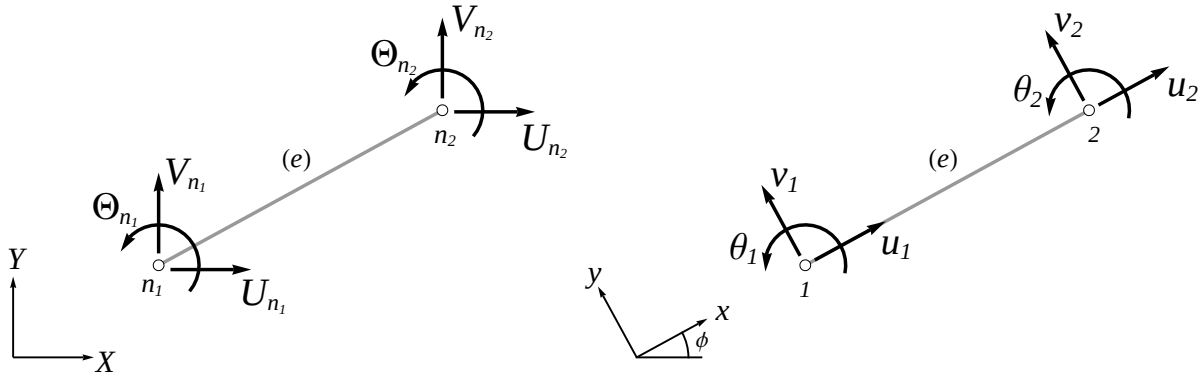

Figure 2.7: Global (left) and local (right) degrees of freedom, associated with a finite element.
Slika 2.7: Globalne (levo) in lokalne (desno) prostostne stopnje, povezane s končnim elementom.

2.2.3.2 Virtual degrees of freedom

Virtual displacements are a kinematically admissible variation of real displacements. As with the real displacements, they are interpolated between the nodal values with appropriate interpolation functions. The virtual deformation of the mesh is therefore defined by the virtual displacements of its nodes.

The global virtual degrees of freedom (virtual nodal displacements of the structure) $\hat{\mathbf{d}}^{\text{str}}$, the virtual displacements of the element $\hat{\mathbf{d}}^{(e)}$ and the selection $\hat{\mathbf{D}}^{(e)}$ of the global virtual displacements, associated with the element (e), are defined analogously to the real quantities $\mathbf{d}^{\text{str}}$, $\mathbf{d}^{(e)}$ and $\mathbf{D}^{(e)}$, defined in equations (2.13) and (2.15).

$$\begin{aligned}
&\hat{\mathbf{d}}^{\text{str}} = \left\{\hat{U}_1, \hat{V}_1, \hat{\Theta}_1, \hat{U}_2, \hat{V}_2, \hat{\Theta}_2, \ \ldots\ , \hat{U}_{n_N}, \hat{V}_{n_N}, \hat{\Theta}_{n_N}\right\}^T \\
&\hat{\mathbf{d}}^{(e)} = \left\{\hat{u}_1^{(e)}, \hat{u}_2^{(e)}, \hat{v}_1^{(e)}, \hat{v}_2^{(e)}, \hat{\theta}_1^{(e)}, \hat{\theta}_2^{(e)}\right\}^T, \quad \hat{\mathbf{D}}^{(e)} = \left\{\hat{U}_{n_1}, \hat{U}_{n_2}, \hat{V}_{n_1}, \hat{V}_{n_2}, \hat{\Theta}_{n_1}, \hat{\Theta}_{n_2}\right\}^T
\end{aligned} \tag{2.18}$$

Relations between them are equivalent to equations (2.14)-(2.17), matrices $\mathbf{R}^{(e)}$ and $\mathbf{P}^{(e)}$ remain the same.

$$\hat{\mathbf{d}}^{(e)} = \mathbf{R}^{(e)}\hat{\mathbf{D}}^{(e)}, \quad \hat{\mathbf{D}}^{(e)} = \mathbf{P}^{(e)}\hat{\mathbf{d}}^{\text{str}}, \quad \hat{\mathbf{d}}^{(e)} = \mathbf{R}^{(e)}\mathbf{P}^{(e)}\hat{\mathbf{d}}^{\text{str}} \tag{2.19}$$

2.2.3.3 Internal forces

Internal forces can be organized in the same way as the generalized displacements. Each degree of freedom from the vector $\mathbf{d}^{\text{str}}$ is accompanied by a corresponding internal force. Analogously to equation (2.13) we can write:

$$\mathbf{f}^{\text{int,str}} = \left\{f_{U_1}^{\text{int}}, f_{V_1}^{\text{int}}, f_{\Theta_1}^{\text{int}}, f_{U_2}^{\text{int}}, f_{V_2}^{\text{int}}, f_{\Theta_2}^{\text{int}}, \ \ldots\ , f_{U_{n_N}}^{\text{int}}, f_{V_{n_N}}^{\text{int}}, f_{\Theta_{n_N}}^{\text{int}}\right\}^T \tag{2.20}$$

Vector $\mathbf{f}^{\text{int,str}}$ has $n_{DOF} = 3n_N$ components - for each node a force parallel to global X axis, a force parallel to Y axis, and a moment around the axis, perpendicular to the XY plane. They are labeled with f_U^{int}, f_V^{int} and f_Θ^{int}, respectively, and depicted in Fig. 2.8.

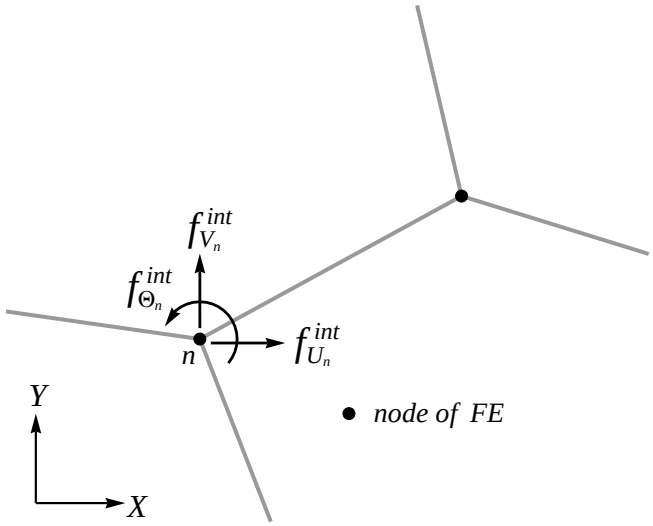

Figure 2.8: Internal forces, corresponding to degrees of freedom at a node of the finite element mesh.
Slika 2.8: Notranje sile, ki ustrezajo prostostnim stopnjam v vozlišču mreže končnih elementov.

Internal forces at a certain node of the structure are composed of contributions from all the elements, meeting in that node. Let us now take a closer look at a finite element (e). The internal forces of the element are defined in the local coordinate system and correspond to the local degrees of freedom $\mathbf{d}^{(e)}$, see Fig. 2.9 (right). They are collected in the vector $\mathbf{f}^{\text{int},(e)}$. The forces can be transformed by matrix $\mathbf{R}^{(e)}$ so as to match the directions of the global internal forces $\mathbf{f}^{\text{int,str}}$. The new, transformed vector is designated with $\mathbf{F}^{\text{int},(e)}$, Fig. 2.9 (left). The transformation matrix $\mathbf{R}^{(e)}$ is the same as in equation (2.15).

$$\mathbf{f}^{\text{int},(e)} = \mathbf{R}^{(e)}\mathbf{F}^{\text{int},(e)} \quad \Leftrightarrow \quad \mathbf{F}^{\text{int},(e)} = \mathbf{R}^{(e)^{-1}}\mathbf{f}^{\text{int},(e)} \tag{2.21}$$

$$\begin{aligned} \mathbf{f}^{\text{int},(e)} &= \left\{ f_{u_1}^{\text{int},(e)}, f_{u_2}^{\text{int},(e)}, f_{v_1}^{\text{int},(e)}, f_{v_2}^{\text{int},(e)}, f_{\theta_1}^{\text{int},(e)}, f_{\theta_2}^{\text{int},(e)} \right\}^T \\ \mathbf{F}^{\text{int},(e)} &= \left\{ f_{U_{n_1}}^{\text{int},(e)}, f_{U_{n_2}}^{\text{int},(e)}, f_{V_{n_1}}^{\text{int},(e)}, f_{V_{n_2}}^{\text{int},(e)}, f_{\Theta_{n_1}}^{\text{int},(e)}, f_{\Theta_{n_2}}^{\text{int},(e)} \right\}^T \end{aligned} \tag{2.22}$$

The components of the global vector $\mathbf{f}^{\text{int,str}}$ are computed by summing the contributions $\mathbf{F}^{\text{int},(e)}$ of individual finite elements. Matrix $\mathbf{P}^{(e)}$ is defined in (2.16).

$$\mathbf{f}^{\text{int,str}} = \sum_{e=1}^{n_{FE}} \mathbf{P}^{(e)^T}\mathbf{F}^{\text{int},(e)} \tag{2.23}$$

Transformation (2.21) and summation (2.23) can be joined in a simplified notation A. Operator A represents the assembly of the internal forces $\mathbf{f}^{\text{int},(e)}$ and n_{FE} is the total number of finite elements.

$$\mathbf{f}^{\text{int,str}} = \sum_{e=1}^{n_{FE}} \mathbf{P}^{(e)^T}\mathbf{R}^{(e)^{-1}}\mathbf{f}^{\text{int},(e)} = \mathop{\mathsf{A}}_{e=1}^{n_{FE}} \left[\mathbf{f}^{\text{int},(e)} \right] \tag{2.24}$$

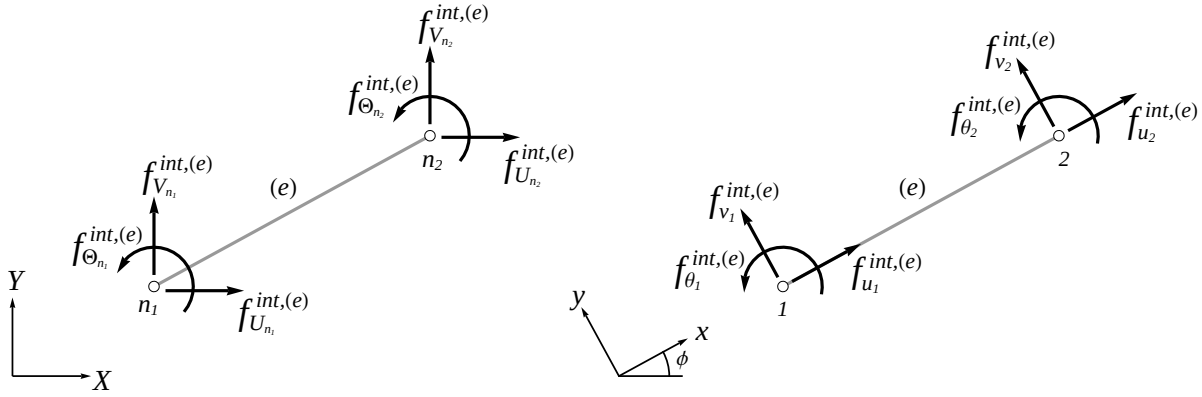

Figure 2.9: Contribution of a finite element to internal forces of the structure in global (left) and local (right) coordinate system.

Slika 2.9: Prispevek končnega elementa k notranjim silam konstrukcije v globalnem (levo) in lokalnem (desno) koordinatnem sistemu.

Another useful relation can be observed. For rotation matrix $\mathbf{R}^{(e)}$ it holds $\mathbf{R}^T = \mathbf{R}^{-1}$ or $\mathbf{R}^T\mathbf{R} = \mathbf{I}$, where $\mathbf{I}$ is the identity matrix. By using this property as well as equations (2.19) and (2.21), we can conclude that the scalar product of virtual displacements and internal forces is equal in local and global coordinate system.

$$\hat{\mathbf{d}}^{(e)^T}\mathbf{f}^{\text{int},(e)} = \hat{\mathbf{D}}^{(e)^T}\mathbf{R}^{(e)^T}\mathbf{R}^{(e)}\mathbf{F}^{\text{int},(e)} = \hat{\mathbf{D}}^{(e)^T}\mathbf{F}^{\text{int},(e)} \tag{2.25}$$

2.2.4 Virtual work equation

Equilibrium of a structure can be described in a weak from, by the virtual work principle, which states that the virtual work of internal forces G^{int} on any kinematically admissible perturbation of displacements - virtual displacements - must be equal to the work of external forces G^{ext} on the same displacements.

$$G^{\text{int}} - G^{\text{ext}} = 0 \tag{2.26}$$

Since we are dealing with a discretized model, the external loads are defined at the nodes of the mesh. Distributed loads have to be transferred to the nodes appropriately. The virtual work of external forces is therefore computed simply as a scalar product of the vector of virtual nodal displacements of the mesh $\hat{\mathbf{d}}^{\text{str}}$ and the corresponding vector of generalized external forces $\mathbf{f}^{\text{ext,str}}$. Virtual displacements are defined in equation (2.18) and the external forces are defined analogously to the internal forces in equation (2.20).

$$G^{\text{ext}} = \hat{\mathbf{d}}^{\text{str}^T}\mathbf{f}^{\text{ext,str}} = \sum_{j=1}^{n_{DOF}} \hat{d}_j^{\text{str}} f_j^{\text{ext,str}} \tag{2.27}$$

Here n_{DOF} is the number of the structure's degrees of freedom. Many components of the sum (2.27) may be zero. The virtual work of internal forces is composed of contributions from individual finite elements. The total number of finite elements in the mesh is n_{FE}.

$$G^{\text{int}} = \sum_{e=1}^{n_{FE}} G^{\text{int},(e)}, \quad G^{\text{int},(e)} = \int_{L^{(e)}} (\hat{\varepsilon} N + \hat{\kappa} M)\, dx \tag{2.28}$$

For each element, $G^{\text{int},(e)}$ is computed by multiplying the virtual axial deformation and virtual curvature with the axial force and moment, respectively, and integrating the products over the length of the element. The virtual quantities $\hat{\varepsilon}$ and $\hat{\kappa}$ are interpolated between the virtual nodal displacements in the same way as the real quantities in equations (2.2) and (2.5). The additional part of virtual curvature $\hat{\kappa}^{add}$ is only defined in the finite elements that have already developed a softening plastic hinge.

$$\hat{\varepsilon} = \mathbf{B}^u \hat{\mathbf{u}}, \quad \hat{\kappa} = \mathbf{B}^v \hat{\mathbf{v}} + \mathbf{B}^\theta \hat{\boldsymbol{\theta}} + \overbrace{G\hat{\alpha}}^{\hat{\kappa}^{add}} \tag{2.29}$$

Expressions (2.29) are inserted into integral (2.28), which is then rearranged to produce the internal forces, corresponding to the virtual degrees of freedom of the finite element $\hat{\mathbf{d}}^{(e)}$, as defined in (2.18). Index (e) is omitted until the last line in equation (2.30).

$$\begin{aligned} G^{\text{int},(e)} &= \int_L (\hat{\varepsilon} N + \hat{\kappa} M)\, dx = \\ &= \int_L \mathbf{B}^u \hat{\mathbf{u}} N dx + \int_L \left(\mathbf{B}^v \hat{\mathbf{v}} + \mathbf{B}^\theta \hat{\boldsymbol{\theta}} + G\hat{\alpha}\right) M dx = \\ &= \hat{\mathbf{u}}^T \int_L \mathbf{B}^{u^T} N dx + \hat{\mathbf{v}}^T \int_L \mathbf{B}^{v^T} M dx + \hat{\boldsymbol{\theta}}^T \int_L \mathbf{B}^{\theta^T} M dx + \hat{\alpha} \int_L G M dx = \\ &= \underbrace{\hat{\mathbf{d}}^{(e)^T} \mathbf{f}^{\text{int},(e)}}_{G^{\text{int},reg}} + \underbrace{\hat{\alpha}^{(e)} h^{(e)}}_{G^{\text{int},add}} \end{aligned} \tag{2.30}$$

The second term of the last line $G^{\text{int},add}$ is the additional virtual work due to enhanced kinematics. It only exists in the n_α finite elements that have reached the carrying capacity and formed a softening hinge. Virtual work of the remaining finite elements consists solely of the regular part $G^{\text{int},reg}$. Virtual nodal displacements of the element and the internal forces have been defined in (2.18) and (2.22).

$$\hat{\mathbf{d}}^{(e)^T} = \left\{\hat{\mathbf{u}}^T, \hat{\mathbf{v}}^T, \hat{\boldsymbol{\theta}}^T\right\}, \quad \mathbf{f}^{\text{int},(e)^T} = \left\{\mathbf{f}^{u,\text{int},(e)^T}, \mathbf{f}^{v,\text{int},(e)^T}, \mathbf{f}^{\theta,\text{int},(e)^T}\right\} \tag{2.31}$$

Components of $\mathbf{f}^{\text{int},(e)}$ are computed as follows:

$$\mathbf{f}^{u,\text{int},(e)} = \int_L \mathbf{B}^{u^T} N dx, \quad \mathbf{f}^{v,\text{int},(e)} = \int_L \mathbf{B}^{v^T} M dx, \quad \mathbf{f}^{\theta,\text{int},(e)} = \int_L \mathbf{B}^{\theta^T} M dx \tag{2.32}$$

A shorter notation (2.33) will also be used.

$$\mathbf{f}^{\text{int},(e)} = \int_L \begin{bmatrix} \mathbf{B}^u \\ \mathbf{0} \\ \mathbf{0} \end{bmatrix} N dx + \int_L \begin{bmatrix} \mathbf{0} \\ \mathbf{B}^v \\ \mathbf{B}^\theta \end{bmatrix} M dx = \int_L \breve{\mathbf{B}}^{\varepsilon^T} N dx + \int_L \breve{\mathbf{B}}^{\kappa^T} M dx \tag{2.33}$$

Quantity $h^{(e)}$ corresponds to the virtual rotational jump $\hat{\alpha}^{(e)}$.

$$h^{(e)} = \int_L GM dx = \int_L \left(\bar{G} + \delta_{x_d}\right) M dx = \int_L \bar{G} M dx + M|_{x_d} = \int_L \bar{G} M dx + t \tag{2.34}$$

In (2.34), we have used equation (2.9) for G and rule (2.35) for integration of the Dirac-delta function. Quantity $M|_{x_d}$ is the value of function $M(x)$ at coordinate x_d. We assign to it a new symbol t and assume it as the moment at the discontinuity (the moment in the softening hinge).

$$\int_L g(x)\,\delta_{x_d} dx = g(x_d) \tag{2.35}$$

The virtual work of external and internal forces in the equilibrium equation (2.26) is replaced by expressions (2.27) and (2.28), applying also (2.30) and (2.25). Remember, that the additional virtual work $G^{\text{int},add}$ is only included for the n_α finite elements, already in the softening phase. For the sake of simplicity, it is assumed that they are labeled with consecutive numbers from 1 to n_α. Finally, the second of equations (2.19) allows us to express the weak equilibrium in the manner of global virtual displacement vector $\hat{\mathbf{d}}^{\text{str}}$ and virtual rotational jumps $\hat{\alpha}^{(e)}$.

$$\begin{aligned}
0 &= \sum_{e=1}^{n_{FE}} G^{\text{int},(e)} - G^{\text{ext}} = \\
&= \sum_{e=1}^{n_{FE}} \hat{\mathbf{D}}^{(e)^T} \mathbf{F}^{\text{int},(e)} + \sum_{e=1}^{n_\alpha} \hat{\alpha}^{(e)} h^{(e)} - \hat{\mathbf{d}}^{\text{str}^T} \mathbf{f}^{\text{ext,str}} = \\
&= \hat{\mathbf{d}}^{\text{str}^T} \sum_{e=1}^{n_{FE}} \mathbf{P}^{(e)^T} \mathbf{F}^{\text{int},(e)} + \sum_{e=1}^{n_\alpha} \hat{\alpha}^{(e)} h^{(e)} - \hat{\mathbf{d}}^{\text{str}^T} \mathbf{f}^{\text{ext,str}} = \\
&= \hat{\mathbf{d}}^{\text{str}^T} \left(\mathbf{f}^{\text{int,str}} - \mathbf{f}^{\text{ext,str}}\right) + \sum_{e=1}^{n_\alpha} \hat{\alpha}^{(e)} h^{(e)}
\end{aligned} \tag{2.36}$$

Equilibrium (2.36) must hold for any kinematically admissible virtual displacements $\hat{\mathbf{d}}^{\text{str}}$ and virtual rotational jumps $\hat{\alpha}^{(e)}$. From this requirement we can conclude:

$$\begin{aligned}
&\mathbf{f}^{\text{int,str}} - \mathbf{f}^{\text{ext,str}} = \mathbf{0} \\
&\forall e \in \{1, 2, \ldots, n_\alpha\}: \quad h^{(e)} = 0
\end{aligned} \tag{2.37}$$

The first of equations (2.37) represents equilibrium of every individual node of the mesh, or the global equilibrium. Here $\mathbf{f}^{\text{int,str}}$ and $\mathbf{f}^{\text{ext,str}}$ are vectors of internal and external forces on the structural level. They correspond in position and direction to the degrees of freedom of the structure. Their length is equal to the total number of degrees of freedom n_{DOF}. The second of equations (2.37) can be better interpreted after inserting expression (2.34) for $h^{(e)}$. Equation (2.38) represents a weak form (integral form) of Cauchy equilibrium between the moment t at the discontinuity and the moment M in the bulk of the element.

$$h^{(e)} = 0 \quad \Leftrightarrow \quad t = -\int_L \bar{G} M dx \tag{2.38}$$

Another verification is required at this place. The principle of embedded discontinuity can be regarded as a method of incompatible modes. In that view, the additional virtual work $G^{\text{int},add}$, performed on the virtual rotational jump $\hat{\alpha}$, should be zero at least for the case of constant moment in the element.

$$\hat{\alpha}\int_L GM\,dx = \underbrace{\hat{\alpha}M}_{\neq 0}\int_L G\,dx = 0 \quad \Rightarrow \quad \int_L G\,dx = 0 \tag{2.39}$$

Taking into account the rule (2.35) for integration of the Dirac-delta function, requirement (2.39) can be reformulated.

$$\int_L G\,dx = \int_L \left(\bar{G}+\delta_{x_d}\right)dx = \int_L \bar{G}\,dx + \overbrace{\int_L \delta_{x_d}\,dx}^{=1} = 0 \quad \Rightarrow \quad \int_L \bar{G}\,dx = -1 \tag{2.40}$$

Operator $\bar{G}$, as defined in equation (2.12) satisfies this condition, regardless of the location of the discontinuity x_d.

2.2.5 Constitutive models

In this section we describe selected constitutive models. Bending is controlled by two separate laws, one for the bulk of the element and the other for the softening hinge at the location of the discontinuity.

2.2.5.1 Axial response

The axial response is presumed linear elastic. In equation (2.41), N is the axial force, E is the elastic modulus, A is the cross-section and ε is the axial strain, computed according to equation (2.2).

$$N = EA\varepsilon, \quad \frac{\partial N}{\partial \varepsilon} = EA \tag{2.41}$$

2.2.5.2 Bending response for the bulk of the element

Behavior of the bulk of the element is described by elasto-plastic model with bilinear isotropic hardening. A typical moment-curvature diagram is shown in Fig. 2.10 (left). Response is linear elastic up to moment M_c, at which the first cracks in concrete appear, reducing the bending stiffness of the beam. Another drop in stiffness occurs at moment M_y, when the reinforcement starts to yield. Unloading lines are parallel to the initial elastic line. This also holds for the part of the diagram between M_c and M_y. Although a combined damage-plasticity model would be more accurate, this simple plasticity model performs well enough for typical reinforced concrete cross-sections, where the largest part of inelastic deformations comes from tensile reinforcement. The diagrams in Fig. 2.10 depend on the axial force N. In this chapter, we limit ourselves to beams with symmetrical cross-section, which implies a symmetrical response for positive and negative bending moment. The bulk material model is mathematically described by the following equations, which can be derived from the principle of maximum plastic dissipation, see e.g. [54].

Remark. *For beams with a non-symmetrical cross-section, the material parameters, which determine the diagrams in Fig. 2.10, would be different for positive and negative moments.*

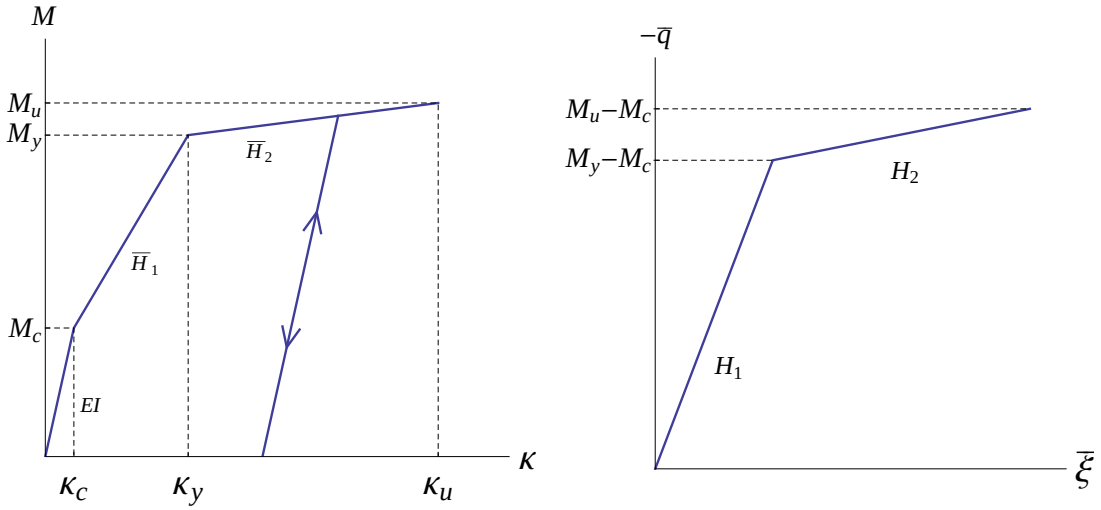

Figure 2.10: *Moment - curvature* diagram (left). Bilinear hardening law (right). Only positive parts of the diagrams are shown. They are valid for constant value of axial force.
Slika 2.10: Diagram *moment - ukrivljenost* (levo). Bilinearno utrjevanje (desno). Prikazana sta samo pozitivna dela diagramov. Veljata za konstantno osno silo.

Moment M is related to curvature $\bar{\kappa}$ by equation (2.42), which represents the elastic loading path and elastic unloading/reloading path of the $M-\bar{\kappa}$ diagram.

$$M = EI\,(\bar{\kappa} - \bar{\kappa}_p)\,, \quad \bar{\kappa} = \mathbf{B}^v\mathbf{v} + \mathbf{B}^\theta\boldsymbol{\theta} + \bar{G}\alpha \tag{2.42}$$

Here E is the elastic modulus, I is the moment of inertia, $\bar{\kappa}_p$ plastic curvature, and $\bar{\kappa}$ the bulk curvature, as defined in equation (2.11). Before the formation of the softening hinge, the rotational jump α is zero. The plastic loading path of the $M-\bar{\kappa}$ diagram is determined indirectly by the remaining equations in this section.

$$\bar{\phi}\,(M, \bar{q}) = |M| - (M_c - \bar{q}) \tag{2.43}$$

Yield function $\bar{\phi}$ prescribes the admissible moments. Elasticity limit M_c is the absolute value of the moment, at which the first plastic deformation occurs. Moment-like hardening variable $\bar{q}$ controls the yield threshold evolution.

$$\bar{q} = \begin{cases} -H_1\bar{\xi}; & \bar{\xi} \le \bar{\xi}_{\Delta H} \\ -(M_y - M_c) - H_2\left(\bar{\xi} - \bar{\xi}_{\Delta H}\right); & \bar{\xi} > \bar{\xi}_{\Delta H} \end{cases} \qquad \bar{\xi}_{\Delta H} = \frac{M_y - M_c}{H_1} \tag{2.44}$$

Equation (2.44) describes the bilinear isotropic hardening of the material, presented in Fig. 2.10 (right). Here $H_1 > 0$ and $H_2 > 0$ are constant hardening moduli, $\bar{\xi}$ is a curvature-like hardening variable with the initial value zero, and $\bar{\xi}_{\Delta H}$ is the value of $\bar{\xi}$, at which the slope in the $\bar{q} - \bar{\xi}$ diagram changes from H_1 to H_2. Evolution in pseudo-time of internal hardening variables for plasticity, $\bar{\kappa}_p$ and $\bar{\xi}$, is prescribed by evolution equations (2.45).

$$\dot{\bar{\kappa}}_p = \dot{\bar{\gamma}}\, sign\,(M)\,, \quad \dot{\bar{\xi}} = \dot{\bar{\gamma}} \tag{2.45}$$

The dot designates the derivative with respect to pseudo-time and $\dot{\bar{\gamma}} > 0$ is plastic multiplier. The loading/unloading conditions and consistency condition (2.46) apply as well.

$$\dot{\bar{\gamma}} \geq 0, \quad \bar{\phi} \leq 0, \quad \dot{\bar{\gamma}}\,\bar{\phi} = 0, \quad \dot{\bar{\gamma}}\,\dot{\bar{\phi}} = 0 \tag{2.46}$$

Tangent moduli of the $M - \bar{\kappa}$ diagram are determined by the above equations. In elastic response, the plastic multiplier is equal to zero. As a consequence, internal variables are constant and the tangent modulus is simply computed by differentiating the expression (2.42) for M with respect to $\bar{\kappa}$.

$$\dot{\bar{\gamma}} = 0 \quad \Rightarrow \quad \bar{\kappa}_p = \text{const.}, \quad \frac{\partial M}{\partial \bar{\kappa}} = EI \tag{2.47}$$

In plastic loading, the plastic curvature $\bar{\kappa}_p$ is not constant. It depends on the plastic multiplier $\dot{\bar{\gamma}}$ which depends on the curvature $\bar{\kappa}$. The tangent modulus can be computed from pseudo-time derivatives of moment and curvature. It follows from the last two equations in (2.46) that $\bar{\phi} = 0$ and $\dot{\bar{\phi}} = 0$. We can express M from equation (2.43) and differentiate it over pseudo-time. Both options for $\bar{q}$ from equation (2.44) have to be considered. In both cases, M is expressed as a function of $\bar{\xi}$, which is differentiated according to the second of evolution equations (2.45).

$$M = (M_c - \bar{q})\, sign\,(M), \quad \dot{M} = \begin{cases} H_1 \dot{\bar{\gamma}}\, sign\,(M); & \bar{\xi} \leq \bar{\xi}_{\Delta H} \\ H_2 \dot{\bar{\gamma}}\, sign\,(M); & \bar{\xi} > \bar{\xi}_{\Delta H} \end{cases} \tag{2.48}$$

Now we differentiate equation (2.42) over pseudo-time, exploiting expressions (2.48) for $\dot{M}$. The first of evolution equations (2.45) is utilized in the procedure.

$$\begin{aligned} \dot{M} &= EI\,(\dot{\bar{\kappa}} - \dot{\bar{\kappa}}_p) \\ H_i \dot{\bar{\gamma}}\, sign\,(M) &= EI\,(\dot{\bar{\kappa}} - \dot{\bar{\gamma}}\, sign\,(M)) \\ EI\dot{\bar{\kappa}} &= (EI + H_i)\,\dot{\bar{\gamma}}\, sign\,(M) \\ \dot{\bar{\kappa}} &= \frac{EI + H_i}{EI}\,\dot{\bar{\gamma}}\, sign\,(M) \end{aligned} \qquad H_i = \begin{cases} H_1; & \bar{\xi} \leq \bar{\xi}_{\Delta H} \\ H_2; & \bar{\xi} > \bar{\xi}_{\Delta H} \end{cases} \tag{2.49}$$

Pseudo-time derivatives $\dot{M}$ and $\dot{\bar{\kappa}}$, defined in (2.48) and (2.49), are divided to produce the plastic tangent modulus.

$$\frac{\partial M}{\partial \bar{\kappa}} = \frac{\dot{M}}{\dot{\bar{\kappa}}} = \frac{EI\,H_i}{EI + H_i} \qquad H_i = \begin{cases} H_1; & \bar{\xi} \leq \bar{\xi}_{\Delta H} \\ H_2; & \bar{\xi} > \bar{\xi}_{\Delta H} \end{cases} \tag{2.50}$$

The elastic and plastic tangent moduli are gathered below. The first expression represents the slope of the elastic loading and unloading path, while the second one represents the slopes $\bar{H}_1$ and $\bar{H}_2$ of the plastic loading path in the $M - \kappa$ diagram in Fig. 2.10.

$$\frac{\partial M}{\partial \bar{\kappa}} = \begin{cases} EI; & \dot{\bar{\gamma}} = 0 \\ \dfrac{EI\,H_i}{EI + H_i}; & \dot{\bar{\gamma}} > 0 \end{cases} \qquad H_i = \begin{cases} H_1; & \bar{\xi} \leq \bar{\xi}_{\Delta H} \\ H_2; & \bar{\xi} > \bar{\xi}_{\Delta H} \end{cases} \tag{2.51}$$

2.2.5.3 Softening plastic hinge in bending

Behavior of the softening plastic hinge is described by a plastic softening law, presented in Fig. 2.11. It associates the moment in the hinge t to the jump in rotation α. When the hinge forms, the rotational jump is zero and the moment is equal to the ultimate moment M_u of the cross-section. If the imposed nodal displacements of the finite element are increased, the carrying capacity of the hinge reduces. The moment t decreases, while the rotational jump α increases. This is referred to as plastic softening. If the imposed nodal displacements of the finite element are reduced, the rotational jump remains the same, representing plastic deformation. The moment in the hinge decreases in such a way to remain in equilibrium with the moment in the bulk, as demanded by equation (2.38). This process is called elastic unloading. When t reaches the admissible value again (in absolute value), the plastic softening continues and α changes accordingly to the sign of the moment. The diagram in Fig. 2.11 depends on the present axial force N, and may be different for positive and negative bending moment, if the cross-section is not symmetric. In this chapter, we limit ourselves to symmetrical behavior for both load signs. Mathematical representation of the described behavior is condensed in the following equations, which can be derived by the principle of maximum plastic dissipation, see e.g. [54].

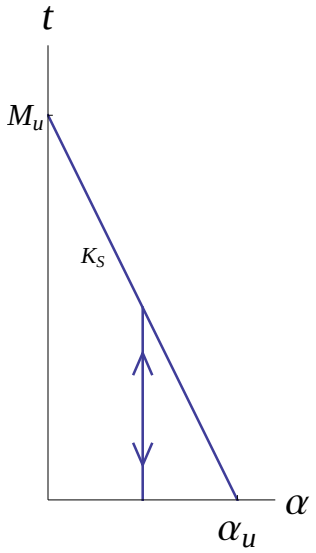

Figure 2.11: *Moment at the hinge - rotational jump* diagram.
Slika 2.11: Diagram *moment v členku - skok v zasuku*.

$$\bar{\bar{\phi}}(t,\bar{\bar{q}}) = |t| - (M_u - \bar{\bar{q}}) \tag{2.52}$$

Failure function $\bar{\bar{\phi}}$ defines the admissible values of moment t in the hinge. The ultimate moment of the cross-section M_u is the absolute value of the moment, at which the softening plastic hinge forms. The moment-like softening variable $\bar{\bar{q}}$ manages the softening threshold evolution.

$$\bar{\bar{q}} = \min\left\{-K\bar{\bar{\xi}}, M_u\right\} \tag{2.53}$$

The linear softening law is described by equation (2.53), where $\bar{\bar{\xi}}$ is a rotation-like softening variable with initial value zero, and $K \leq 0$ is a constant softening modulus with units kNm/rad. Evolution in pseudo-time of internal softening variables α and $\bar{\bar{\xi}}$ is defined by evolution equations (2.54).

$$\dot{\alpha} = \dot{\bar{\gamma}}\, sign\,(t), \quad \dot{\bar{\xi}} = \dot{\bar{\gamma}} \tag{2.54}$$

The dot designates the derivative with respect to pseudo-time and $\dot{\bar{\gamma}} > 0$ is plastic softening multiplier. The loading/unloading conditions and consistency condition (2.55) also apply.

$$\dot{\bar{\gamma}} \geq 0, \quad \bar{\phi} \leq 0, \quad \dot{\bar{\gamma}}\,\bar{\phi} = 0, \quad \dot{\bar{\gamma}}\,\dot{\bar{\phi}} = 0 \tag{2.55}$$

The equation of the plastic softening loading path of $t-\alpha$ diagram is not unique. It depends on the loading history. If the softening process alternates between both load signs, the loading path is translated sideways (left or right). The slope, however, is not affected and can be determined from the pseudo-time derivatives of t and α. In softening process, when $\dot{\bar{\gamma}} > 0$, the failure function $\bar{\phi} = 0$. Expression for t is then determined from (2.52) and (2.53). The derivative is obtained in accordance with evolution equation (2.54) for $\bar{\xi}$.

$$t = (M_u - \bar{q})\, sign\,(t) = \begin{cases} \left(M_u + K\bar{\xi}\right) sign\,(t); & \bar{q} < M_u \\ 0; & \bar{q} = M_u \end{cases} \quad \dot{t} = \begin{cases} K\dot{\bar{\gamma}}\, sign\,(t); & \bar{q} < M_u \\ 0; & \bar{q} = M_u \end{cases} \tag{2.56}$$

The slope of the plastic softening path, defined as the derivative of t over α, is computed by dividing the pseudo-time derivatives (2.56) and (2.54) of both quantities.

$$\frac{\partial t}{\partial \alpha} = \frac{\dot{t}}{\dot{\alpha}} = \begin{cases} \text{not defined}; & \dot{\bar{\gamma}} = 0 \\ K; & \dot{\bar{\gamma}} > 0,\ \bar{q} < M_u \\ 0; & \dot{\bar{\gamma}} > 0,\ \bar{q} = M_u \end{cases} \tag{2.57}$$

A third option was added in equation (2.57). It corresponds to elastic unloading path with $\dot{\bar{\gamma}} = 0$. It follows from evolution equations (2.54) that $\dot{\alpha} = 0$ in that case. And since the failure function $\bar{\phi}$ is no longer required to be zero, the traction t cannot be computed as in (2.56). It changes in accordance with equation (2.38) which represents the equilibrium between the bulk and the discontinuity. The derivative $\partial t/\partial \alpha$ cannot be defined in this case, because α is constant.

2.3 Computational procedure

Response of a structure, discretized by a mesh of n_{FE} above derived finite elements, is computed at discrete pseudo-time points $\tau_0,\ \tau_1,\ \ldots\ ,\ \tau_n,\ \tau_{n+1},\ \ldots\ ,\ T$ by solving at each pseudo-time point nonlinear equations (2.58) for current values of nodal displacements/rotations.

$$\begin{aligned} &\mathbf{f}^{\text{int,str}} - \mathbf{f}^{\text{ext,str}} = \mathbf{0} \\ &\forall e \in \{1,\ 2,\ \ldots\ ,\ n_\alpha\}: \quad h^{(e)} = 0 \end{aligned} \tag{2.58}$$

Here, n_α is the number of elements that have reached the carrying capacity and formed a softening plastic hinge. At a particular pseudo-time point τ_{n+1}, the solution is searched iteratively by the Newton-Raphson method. Each iteration, denoted by k, consists of two subsequent phases: (A) computation of internal variables, corresponding

to the current iterative values of nodal displacements/rotations, in order to compute the moments in the bulk and in the softening plastic hinge according to the chosen material laws; (B) solution of linearized equations (2.58) in order to update the iterative values of nodal displacements/rotations. When one phase of the computation is completed, the results are used immediately in the next one.

For a pseudo-time point τ_{n+1}, the computational problem related to a generic finite element (e) can be stated as:

$$\text{given } \left\{\mathbf{d}_n^{(e)};\quad \bar{\kappa}_{p,n}^{(e)},\, \bar{\xi}_n^{(e)},\, \alpha_n^{(e)},\, \bar{\bar{\xi}}_n^{(e)}\right\} \quad \text{find } \left\{\mathbf{d}_{n+1}^{(e)};\quad \bar{\kappa}_{p,n+1}^{(e)},\, \bar{\xi}_{n+1}^{(e)},\, \alpha_{n+1}^{(e)},\, \bar{\bar{\xi}}_{n+1}^{(e)}\right\}$$

Note that superscript (e) was omitted in section 2.2.5 for the above internal variables. The subscript n and $n+1$ denote the values at pseudo-times τ_n and τ_{n+1}, respectively.

2.3.1 Computation of internal variables

In this section we will present computations of phase (A). The internal variables for element (e) at pseudo-time point τ_{n+1} will be computed for the k-th iteration, while the nodal displacements/rotations are fixed at the values from the previous iteration $\mathbf{d}_{n+1}^{(e),(k-1)}$. Since every internal variable is connected to a single finite element, the computations are local, i.e. they are performed independently for each element. The condition of the discontinuity is known by the following flag.

$$crack^{(e)} = \begin{cases} false & \ldots \quad \text{no discontinuity in element } (e) \\ true & \ldots \quad \text{discontinuity in element } (e) \end{cases} \tag{2.59}$$

The algorithm in Fig. 2.12 is applied. If there was no discontinuity in the previous pseudo-time step, we begin with equations for the hardening phase of material, described in section 2.3.1.2. We must do so even if the previous iteration of the current step indicated occurrence of the discontinuity, because that was not a converged result. We check if the carrying capacity is reached. If not, we keep the obtained results, otherwise we discard them and use equations for the softening phase of material, described in section 2.3.1.3. If the discontinuity already existed in the previous pseudo-time step, it must also exist in the current step, therefore we follow the procedure from section 2.3.1.3.

The integrals that appear in expressions (2.32), (2.34) and (2.38) for $\mathbf{f}^{\text{int},(e)}$, $h^{(e)}$ and t, are evaluated with numerical integration. A three-point Gauss-Lobatto integration scheme is used with integration points at both ends and at the center of the finite element. Curvature, moment and hardening internal variables are therefore computed only at those three locations. Softening internal variables are defined at the location of the discontinuity, which coincides with one of the integration points (although the two are not connected).

For the sake of clarity we will omit in the rest of this section the superscript (e), denoting the finite element.

2.3.1.1 Axial response

Computation of the axial response is straightforward. Axial strain is computed according to equation (2.7) with the current values of the nodal displacements. Axial force is calculated from (2.41).

$$\varepsilon_{n+1}^{(k)} = \breve{\mathbf{B}}^{\varepsilon}\mathbf{d}_{n+1}^{(k-1)}, \quad N_{n+1}^{(k)} = EA\varepsilon_{n+1}^{(k)}, \quad \left.\frac{\partial N}{\partial \varepsilon}\right|_{n+1}^{(k)} = EA \tag{2.60}$$

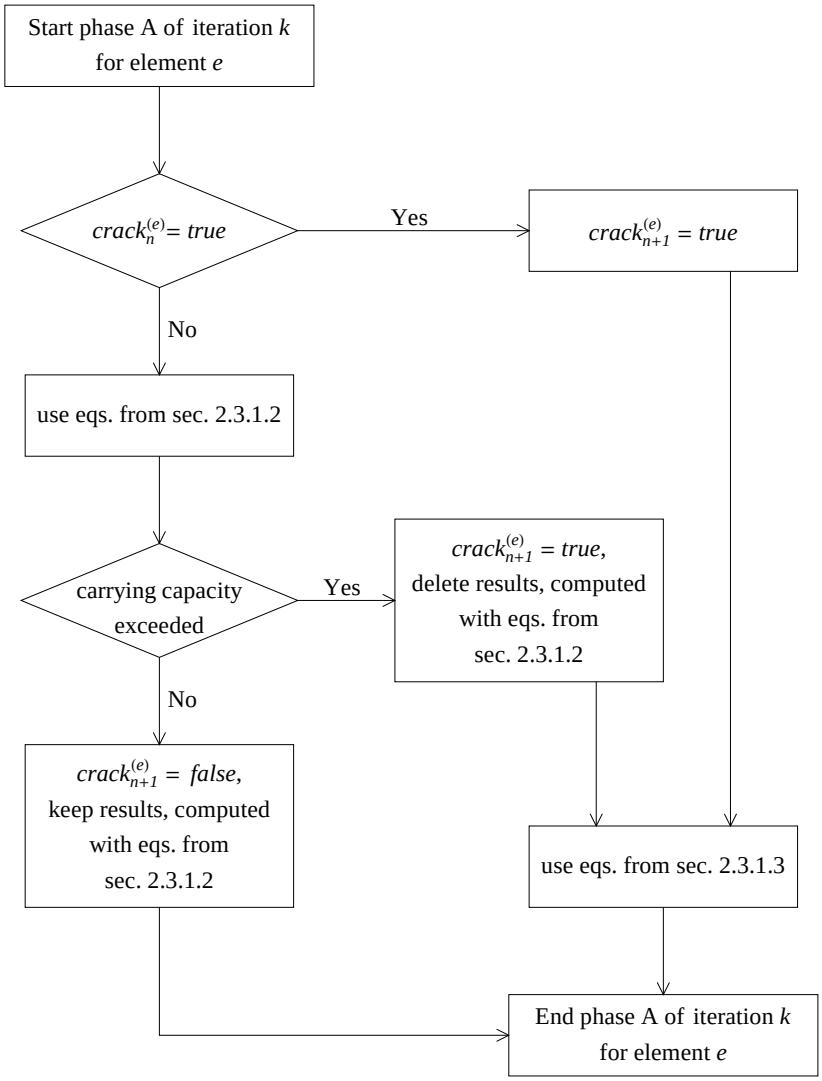

Figure 2.12: Algorithm for phase (A) of k-th iteration for finite element (e).
Slika 2.12: Algoritem za fazo (A) k-te iteracije za končni element (e).

2.3.1.2 Bending response in the hardening phase

The computational procedure for the hardening phase is described next. There is no discontinuity (hinge) in the element and the rotation jump is zero. First, we assume elastic behavior, which means that the hardening internal variables keep the values from the previous step. Moment is computed in accordance with equation (2.42), where $\alpha_{n+1}^{(k)} = 0$.

$$\bar{\kappa}_{p,n+1}^{(k),trial} = \bar{\kappa}_{p,n}, \quad \bar{\xi}_{n+1}^{(k),trial} = \bar{\xi}_n, \quad M_{n+1}^{(k),trial} = EI\left(\bar{\kappa}\left(\mathbf{d}_{n+1}^{(k-1)}, \alpha_{n+1}^{(k)}\right) - \bar{\kappa}_{p,n+1}^{(k),trial}\right) \tag{2.61}$$

Trial yield function $\bar{\phi}_{n+1}^{(k),trial}$ is computed, as defined in (2.43) and (2.44).

$$\begin{aligned}
\bar{\phi}_{n+1}^{(k),trial} &= \left|M_{n+1}^{(k),trial}\right| - \left(M_c - \bar{q}_{n+1}^{(k),trial}\right) \\
\bar{q}_{n+1}^{(k),trial} &= \begin{cases} -H_1\bar{\xi}_n; & \bar{\xi}_n \leq \bar{\xi}_{\Delta H} \\ -(M_y - M_c) - H_2\left(\bar{\xi}_n - \bar{\xi}_{\Delta H}\right); & \bar{\xi}_n > \bar{\xi}_{\Delta H} \end{cases}
\end{aligned} \tag{2.62}$$

The trial solution is accepted if the trial yield function is negative or zero.

$$\bar{\phi}_{n+1}^{(k),trial} \leq 0 \quad \Rightarrow \quad \bar{\kappa}_{p,n+1}^{(k)} = \bar{\kappa}_{p,n+1}^{(k),trial}, \quad \bar{\xi}_{n+1}^{(k)} = \bar{\xi}_{n+1}^{(k),trial}, \quad M_{n+1}^{(k)} = M_{n+1}^{(k),trial} \tag{2.63}$$

If the trial yield function is positive, the internal variables must be corrected, according to incremental form of evolution equations (2.45), where $\bar{\gamma}_{n+1}^{(k)} = \dot{\bar{\gamma}}_{n+1}^{(k)}\left(\tau_{n+1} - \tau_n\right) > 0$. It is shown in appendix A that $sign\left(M_{n+1}^{(k)}\right) = sign\left(M_{n+1}^{(k),trial}\right)$.

$$\bar{\phi}_{n+1}^{(k),trial} > 0 \quad \Rightarrow \quad \bar{\kappa}_{p,n+1}^{(k)} = \bar{\kappa}_{p,n} + \bar{\gamma}_{n+1}^{(k)} sign\left(M_{n+1}^{(k),trial}\right), \quad \bar{\xi}_{n+1}^{(k)} = \bar{\xi}_n + \bar{\gamma}_{n+1}^{(k)} \tag{2.64}$$

By exploiting equations (2.64), the moment $M_{n+1}^{(k)}$ can be expressed with the trial moment and the plastic multiplier $\bar{\gamma}_{n+1}^{(k)}$.

$$M_{n+1}^{(k)} = M_{n+1}^{(k),trial} - EI\,\bar{\gamma}_{n+1}^{(k)} sign\left(M_{n+1}^{(k),trial}\right) \tag{2.65}$$

We do the same for the moment-like hardening variable $\bar{q}_{n+1}^{(k)}$. Since the expression for $\bar{q}$ depends on the value of $\bar{\xi}$, we have to consider three options. The values form previous and current step, $\bar{\xi}_n$ and $\bar{\xi}_{n+1}$, can be either both smaller than $\bar{\xi}_{\Delta H}$, both greater, or one smaller and one greater. Note that $\bar{\xi}_{n+1}$ is the greater of the two values, because $\bar{\gamma}_{n+1}^{(k)}$ is positive.

$$\bar{q}_{n+1}^{(k)} = \begin{cases} \bar{q}_{n+1}^{(k),trial} - H_1\bar{\gamma}_{n+1}^{(k)}; & \bar{\xi}_n < \bar{\xi}_{n+1} \leq \bar{\xi}_{\Delta H} \\ \bar{q}_{n+1}^{(k),trial} - (H_1 - H_2)\left(\bar{\xi}_{\Delta H} - \bar{\xi}_n\right) - H_2\bar{\gamma}_{n+1}^{(k)}; & \bar{\xi}_n \leq \bar{\xi}_{\Delta H},\ \bar{\xi}_{n+1} > \bar{\xi}_{\Delta H} \\ \bar{q}_{n+1}^{(k),trial} - H_2\bar{\gamma}_{n+1}^{(k)}; & \bar{\xi}_{n+1} > \bar{\xi}_n > \bar{\xi}_{\Delta H} \end{cases} \tag{2.66}$$

Yield function $\bar{\phi}_{n+1}^{(k)}$ is expressed as a function of plastic multiplier $\bar{\gamma}_{n+1}^{(k)}$ by employing equations (2.65) and (2.66). Value of the plastic multiplier is computed from requirement $\bar{\phi}_{n+1}^{(k)} = 0$, coming from the loading/unloading conditions.

$$\bar{\phi}_{n+1}^{(k)} = \left|M_{n+1}^{(k)}\right| - \left(M_u - \bar{q}_{n+1}^{(k)}\right) = \bar{\phi}_{n+1}^{(k)}\left(\bar{\gamma}_{n+1}^{(k)}\right) = 0 \tag{2.67}$$

Considering the different values of $\bar{q}_{n+1}^{(k)}$, we obtain three expressions for $\bar{\gamma}_{n+1}^{(k)}$.

$$\bar{\gamma}_{n+1}^{(k)} = \begin{cases} \dfrac{\bar{\phi}_{n+1}^{(k),trial}}{EI+H_1}; & \bar{\xi}_n < \bar{\xi}_{n+1} \leq \bar{\xi}_{\Delta H} \\ \dfrac{\bar{\phi}_{n+1}^{(k),trial} - (H_1-H_2)\left(\bar{\xi}_{\Delta H} - \bar{\xi}_n\right)}{EI+H_2}; & \bar{\xi}_n \leq \bar{\xi}_{\Delta H},\ \bar{\xi}_{n+1} > \bar{\xi}_{\Delta H} \\ \dfrac{\bar{\phi}_{n+1}^{(k),trial}}{EI+H_2}; & \bar{\xi}_{n+1} > \bar{\xi}_n > \bar{\xi}_{\Delta H} \end{cases} \tag{2.68}$$

Consistent tangent modulus is computed as the derivative of moment over curvature. Moment takes the trial value from equation (2.61) if plastic multiplier $\bar{\gamma}_{n+1}^{(k)}$ is zero, and the value from (2.65) if $\bar{\gamma}_{n+1}^{(k)}$ is positive. In the second case, equations (2.64), (2.68), (2.62) and (2.61) are used to express the moment as a function of curvature.

$$\left.\frac{\partial M}{\partial \bar{\kappa}}\right|_{n+1}^{(k)} = \begin{cases} EI; & \bar{\gamma}_{n+1}^{(k)} = 0 \\ \dfrac{EI\,H_i}{EI+H_i}; & \bar{\gamma}_{n+1}^{(k)} > 0 \end{cases} \qquad H_i = \begin{cases} H_1; & \bar{\xi} \leq \bar{\xi}_{\Delta H} \\ H_2; & \bar{\xi} > \bar{\xi}_{\Delta H} \end{cases} \tag{2.69}$$

The hardening internal variables, the moment and the tangent modulus have been calculated under assumption that the ultimate moment is not exceeded. This still requires verification. If the assumption is confirmed, the above results are accepted. Otherwise, they are discarded and recomputed with the presence of the discontinuity.

The first step in the verification is to determine the location of the potential discontinuity x_d. Since we have restricted ourselves to symmetric cross-sections, the hinge is simply placed at the location of maximal moment in absolute value. This can occur at either end of the element because of the linear form of moment. If the moment is constant, the discontinuity is placed in the middle of the element.

$$\begin{array}{lcll} M_1 = M_2 = M_3 & \Rightarrow & x_d = L/2 & \\ |M_1| > |M_2| & \Rightarrow & x_d = 0 & \text{where} \quad M_1 = M|_{x=0} \\ |M_1| < |M_2| & \Rightarrow & x_d = L & \qquad\quad M_2 = M|_{x=L} \\ & & & \qquad\quad M_3 = M|_{x=L/2} \end{array} \tag{2.70}$$

Remark. *For beams with a non-symmetrical cross-section, the positioning of the discontinuity would be less simple because of the different values of ultimate moment M_u for positive and negative moments. Location of the discontinuity would be determined in a similar way as in a concrete layer of a multi-layer element in section 3.3.1.1 of the next chapter.*

With the location of the potential discontinuity determined, we can calculate the potential value of moment at the discontinuity $t_{n+1}^{(k),pot}$ by equation (2.38). The integral is evaluated numerically with the three-point Gauss-Lobatto integration scheme.

$$t_{n+1}^{(k),pot} = -\int_L \bar{G} M_{n+1}^{(k)} dx \tag{2.71}$$

Failure function $\bar{\bar{\phi}}_{n+1}^{(k),pot}$ is evaluated with the moment-like softening variable $\bar{\bar{q}}$ equal to zero, as there has been no reduction of carrying capacity in previous steps.

$$\bar{\bar{\phi}}_{n+1}^{(k),pot} = \left| t_{n+1}^{(k),pot} \right| - \left(M_u - \bar{\bar{q}}_{n+1}^{(k),pot} \right), \quad \bar{\bar{q}}_{n+1}^{(k),pot} = 0 \tag{2.72}$$

We set the value of the discontinuity flag to $true$ if the failure function is positive, and to $false$ otherwise. The value is not final, however, until the converged state is reached. It can change in following iterations.

$$\begin{aligned} \bar{\bar{\phi}}_{n+1}^{(k),pot} \leq 0 \quad &\Rightarrow \quad crack_{n+1}^{(e)} = false \\ \bar{\bar{\phi}}_{n+1}^{(k),pot} > 0 \quad &\Rightarrow \quad crack_{n+1}^{(e)} = true \end{aligned} \tag{2.73}$$

If the carrying capacity is exceeded, the above computed values of internal hardening variables and moment in the bulk of the element are discarded and computed again, as explained in the following section.

2.3.1.3 Bending response in the softening phase

This section describes the computational procedure for an element in the softening phase. It is applied if the current value of the discontinuity flag $crack_{n+1}^{(e)} = true$, which happens if the discontinuity already existed in the previous step, or if the carrying capacity of the element was exceeded in this iteration, see equation (2.73). In any case, the hardening internal variables take the values from the previous step, which are the last converged results.

$$\bar{\kappa}_{p,n+1}^{(k)} = \bar{\kappa}_{p,n}, \quad \bar{\bar{\xi}}_{n+1}^{(k)} = \bar{\bar{\xi}}_n \tag{2.74}$$

We start by assuming a trial solution, keeping the softening internal variables at the values from the previous step. The moment in the bulk and the moment at the discontinuity are computed according to equations (2.42) and (2.38), respectively.

$$\begin{aligned} &\alpha_{n+1}^{(k),trial} = \alpha_n, \quad \bar{\bar{\xi}}_{n+1}^{(k),trial} = \bar{\bar{\xi}}_n, \\ &M_{n+1}^{(k),trial} = EI\left(\bar{\kappa}\left(d_{n+1}^{(k-1)}, \alpha_{n+1}^{(k),trial}\right) - \bar{\kappa}_{p,n}\right), \quad t_{n+1}^{(k),trial} = -\int_L \bar{G} M_{n+1}^{(k),trial} dx \end{aligned} \tag{2.75}$$

The integral is computed numerically with the three-point Gauss-Lobatto integration scheme and evaluates to $t_{n+1}^{(k),trial} = M_{n+1}^{(k),trial}\Big|_{x_d}$ for the linear distribution of moment over the bulk of the element.

The trial value of failure function $\bar{\bar{\phi}}_{n+1}^{(k),trial}$ is calculated, respecting equations (2.52) and (2.53).

$$\bar{\bar{\phi}}_{n+1}^{(k),trial} = \left|t_{n+1}^{(k),trial}\right| - \left(M_u - \bar{\bar{q}}_{n+1}^{(k),trial}\right), \quad \bar{\bar{q}}_{n+1}^{(k),trial} = \min\left\{-K\bar{\bar{\xi}}_{n+1}^{(k),trial}, M_u\right\} = \bar{\bar{q}}_n \tag{2.76}$$

If $\bar{\bar{\phi}}_{n+1}^{(k),trial} \leq 0$, the trial solution is accepted.

$$\alpha_{n+1}^{(k)} = \alpha_{n+1}^{(k),trial}, \quad \bar{\bar{\xi}}_{n+1}^{(k)} = \bar{\bar{\xi}}_{n+1}^{(k),trial}, \quad M_{n+1}^{(k)} = M_{n+1}^{(k),trial}, \quad t_{n+1}^{(k)} = t_{n+1}^{(k),trial} \tag{2.77}$$

If $\bar{\bar{\phi}}_{n+1}^{(k),trial} > 0$, the assumed solution is not admissible. The softening internal variables are updated according to the incremental form of evolution equations (2.54), where $\bar{\bar{\gamma}}_{n+1}^{(k)} = \dot{\bar{\bar{\gamma}}}_{n+1}^{(k)}(\tau_{n+1} - \tau_n) > 0$. It is shown in appendix A that $sign\left(t_{n+1}^{(k)}\right) = sign\left(t_{n+1}^{(k),trial}\right)$.

$$\alpha_{n+1}^{(k)} = \alpha_n + \bar{\bar{\gamma}}_{n+1}^{(k)} sign\left(t_{n+1}^{(k),trial}\right), \quad \bar{\bar{\xi}}_{n+1}^{(k)} = \bar{\bar{\xi}}_n + \bar{\bar{\gamma}}_{n+1}^{(k)} \tag{2.78}$$

By using equations (2.78), the moment at the discontinuity $t_{n+1}^{(k)}$ and the moment-like softening variable $\bar{\bar{q}}_{n+1}^{(k)}$ are expressed with their trial values and the softening multiplier $\bar{\bar{\gamma}}_{n+1}^{(k)}$.

$$\begin{aligned} t_{n+1}^{(k)} &= M_{n+1}^{(k)}\Big|_{x_d} = \left[EI\left(\breve{\mathbf{B}}^{\kappa}\mathbf{d}_{n+1}^{(k-1)} + \bar{G}\alpha_{n+1}^{(k)} - \bar{\kappa}_{p,n}\right)\right]_{x=x_d} = \\ &= \left[EI\left(\breve{\mathbf{B}}^{\kappa}\mathbf{d}_{n+1}^{(k-1)} + \bar{G}\alpha_{n} - \bar{\kappa}_{p,n}\right)\right]_{x=x_d} + \left[EI\,\bar{G}\bar{\bar{\gamma}}_{n+1}^{(k)} sign\left(t_{n+1}^{(k),trial}\right)\right]_{x=x_d} = \\ &= t_{n+1}^{(k),trial} + EI\,\bar{G}\big|_{x_d}\bar{\bar{\gamma}}_{n+1}^{(k)} sign\left(t_{n+1}^{(k),trial}\right) \end{aligned} \tag{2.79}$$

$$\bar{\bar{q}}_{n+1}^{(k)} = \begin{cases} \bar{\bar{q}}_{n+1}^{A} = \bar{\bar{q}}_{n+1}^{(k),trial} - K\bar{\bar{\gamma}}_{n+1}^{(k)}; & -K\left(\bar{\bar{\xi}}_n + \bar{\bar{\gamma}}_{n+1}^{A}\right) < M_u \\ \bar{\bar{q}}_{n+1}^{B} = M_u; & -K\left(\bar{\bar{\xi}}_n + \bar{\bar{\gamma}}_{n+1}^{A}\right) > M_u \end{cases} \tag{2.80}$$

Linear operator $\bar{G}$ in expression for $t_{n+1}^{(k)}$ is evaluated at x_d. Obtained expressions are inserted in equation $\bar{\bar{\phi}}_{n+1}^{(k)} = 0$, coming from loading/unloading conditions (2.55).

$$\bar{\bar{\phi}}_{n+1}^{(k)} = \left|t_{n+1}^{(k)}\right| - \left(M_u - \bar{\bar{q}}_{n+1}^{(k)}\right) = 0 \quad \Leftrightarrow \quad t_{n+1}^{(k)} = \left(M_u - \bar{\bar{q}}_{n+1}^{(k)}\right) sign\left(t_{n+1}^{(k),trial}\right) \tag{2.81}$$

After a short derivation we get two expressions for $\bar{\bar{\gamma}}_{n+1}^{(k)}$, depending on the expression, used for $\bar{\bar{q}}_{n+1}^{(k)}$.

$$\bar{\bar{\gamma}}_{n+1}^{(k)} = \begin{cases} \bar{\bar{\gamma}}_{n+1}^{A} = \dfrac{\bar{\bar{\phi}}_{n+1}^{(k),trial}}{-\bar{G}\big|_{x_d} EI + K}; & -K\left(\bar{\bar{\xi}}_n + \bar{\bar{\gamma}}_{n+1}^{A}\right) < M_u \\ \bar{\bar{\gamma}}_{n+1}^{B} = \dfrac{\left|t_{n+1}^{(k),trial}\right|}{-\bar{G}\big|_{x_d} EI}; & -K\left(\bar{\bar{\xi}}_n + \bar{\bar{\gamma}}_{n+1}^{A}\right) > M_u \end{cases} \tag{2.82}$$

The tangent modulus is computed as the derivative of moment at the discontinuity $t_{n+1}^{(k)}$ over the rotation jump $\alpha_{n+1}^{(k)}$. If $\bar{\bar{\gamma}}_{n+1}^{(k)} > 0$, the moment takes the value from (2.81). Equations (2.80) and (2.78) are used to express $t_{n+1}^{(k)}$ as a function of $\alpha_{n+1}^{(k)}$. If $\bar{\bar{\gamma}}_{n+1}^{(k)} = 0$, the rotation jump remains constant, while the moment at the discontinuity changes to satisfy the local equilibrium (2.38). The tangent modulus cannot be determined, but it is not required for further computation.

$$\left.\frac{\partial t}{\partial \alpha}\right|_{n+1}^{(k)} = \begin{cases} \text{not defined}; & \bar{\bar{\gamma}}_{n+1}^{(k)} = 0 \\ K; & \bar{\bar{\gamma}}_{n+1}^{(k)} > 0,\ \bar{\bar{q}}_{n+1}^{(k)} < M_u \\ 0; & \bar{\bar{\gamma}}_{n+1}^{(k)} > 0,\ \bar{\bar{q}}_{n+1}^{(k)} = M_u \end{cases} \tag{2.83}$$

The discontinuity flag is set to $crack_{n+1}^{(e)} = true$.

2.3.2 Computation of nodal degrees of freedom

In this section we will describe the computations of phase (B) of k-th iteration, mentioned in the introduction of section 2.3. In this phase, a linearized form of equilibrium equations (2.58) is solved to provide the k-th update of

the nodal displacements/rotations at pseudo-time point τ_{n+1}. The computation is performed with known values of internal variables $\bar{\kappa}_{p,n+1}^{(e),(k)}$, $\bar{\xi}_{n+1}^{(e),(k)}$, $\alpha_{n+1}^{(e),(k)}$ and $\bar{\bar{\xi}}_{n+1}^{(e),(k)}$ for each finite element, freshly updated in preceding phase (A) of the same iteration. Since the nodal degrees of freedom are generally common to several finite elements, the equations of phase (B) must be handled on structural (global) level. Hence, they are also referred to as global equations.

The first of equations (2.58) would be sufficient for calculating the new values of generalized displacements $\mathbf{d}_{n+1}^{(e),(k)}$, if all rotational jumps $\alpha_{n+1}^{(e),(k)}$ were fixed at the values, computed in phase (A). To improve convergence, however, it is useful to update the rotational jumps as well. For that purpose, the second of equations (2.58) are engaged. Actually, they have once already been satisfied by using expression (2.38) for the moment at the discontinuity, but that equality held for the displacements from the previous iteration $\mathbf{d}_{n+1}^{(e),(k-1)}$. Updating the displacements would disrupt the equilibrium between the moment at the discontinuity and the moment in the bulk of the element, unless the rotational jumps are updated as well. Solving the whole system of equations (2.58) therefore promises a more accurate solution.

2.3.2.1 Linearization of equilibrium equations

The first of equations (2.58) ensures the equilibrium of the structure, i.e. of its each and every node. It is linearized around the current values of nodal degrees of freedom of the structure $\mathbf{d}_{n+1}^{\text{str},(k-1)}$.

$$\underbrace{\frac{\partial \mathbf{f}_{n+1}^{\text{int,str},(k)}}{\partial \mathbf{d}_{n+1}^{\text{str},(k-1)}}}_{\mathbf{K}_{n+1}^{\text{str},(k)}} \Delta\mathbf{d}_{n+1}^{\text{str},(k)} = \mathbf{f}_{n+1}^{\text{ext,str}} - \mathbf{f}_{n+1}^{\text{int,str},(k)}, \qquad \frac{\partial \mathbf{f}_{n+1}^{\text{ext,str}}}{\partial \mathbf{d}_{n+1}^{\text{str},(k-1)}} = \mathbf{0} \tag{2.84}$$

The derivative on the left side of the equation is designated with $\mathbf{K}_{n+1}^{\text{str},(k)}$ and named the tangent stiffness matrix of the structure. $\Delta\mathbf{d}_{n+1}^{\text{str},(k)}$ is the sought update of the nodal displacements in this iteration. The vector of external forces $\mathbf{f}_{n+1}^{\text{ext,str}}$ represents the loading, which is defined in advance for each pseudo-time point τ_{n+1} and is independent of the nodal displacements. The vector of internal forces $\mathbf{f}_{n+1}^{\text{int,str},(k)}$ is computed from contributions of individual finite elements, according to equation (2.24). Matrices $\mathbf{P}^{(e)}$ and $\mathbf{R}^{(e)}$ are constant.

$$\begin{aligned}
\mathbf{f}_{n+1}^{\text{int,str},(k)} &= \sum_{e=1}^{n_{FE}} {\mathbf{P}^{(e)}}^T {\mathbf{R}^{(e)}}^{-1} \mathbf{f}_{n+1}^{\text{int},(e),(k)} \\
\mathbf{K}_{n+1}^{\text{str},(k)} &= \frac{\partial \mathbf{f}_{n+1}^{\text{int,str},(k)}}{\partial \mathbf{d}_{n+1}^{\text{str},(k-1)}} = \sum_{e=1}^{n_{FE}} {\mathbf{P}^{(e)}}^T {\mathbf{R}^{(e)}}^{-1} \frac{\partial \mathbf{f}_{n+1}^{\text{int},(e),(k)}}{\partial \mathbf{d}_{n+1}^{\text{str},(k-1)}}
\end{aligned} \tag{2.85}$$

Let us recall the relation (2.17) between the vector of nodal displacements of a finite element $\mathbf{d}_{n+1}^{(e),(k-1)}$ and the vector of nodal displacements of the structure $\mathbf{d}_{n+1}^{\text{str},(k-1)}$. The derivative of one over the other will prove useful.

$$\mathbf{d}_{n+1}^{(e),(k-1)} = \mathbf{R}^{(e)}\mathbf{P}^{(e)}\mathbf{d}_{n+1}^{\text{str},(k-1)} \quad \Rightarrow \quad \frac{\partial \mathbf{d}_{n+1}^{(e),(k-1)}}{\partial \mathbf{d}_{n+1}^{\text{str},(k-1)}} = \mathbf{R}^{(e)}\mathbf{P}^{(e)} \tag{2.86}$$

Internal forces $\mathbf{f}_{n+1}^{\text{int},(e),(k)}$ of finite element (e) are defined in equation (2.33). In n_α elements, that have developed a hinge, internal forces are functions of nodal displacements $\mathbf{d}_{n+1}^{(e),(k-1)}$ and rotational jumps $\alpha_{n+1}^{(e),(k)}$, while in the

remaining elements (without discontinuity) they depend solely on the nodal displacements. For the sake of clarity it is assumed that the elements with a softening hinge are numbered with consecutive numbers from 1 to n_α.

$$\begin{aligned} &e \in \{1,2,\ldots,n_\alpha\}: && \mathbf{f}_{n+1}^{\text{int},(e),(k)} = \mathbf{f}_{n+1}^{\text{int},(e),(k)}\left(\mathbf{d}_{n+1}^{(e),(k-1)}, \alpha_{n+1}^{(e),(k)}\right) \\ &e \in \{n_\alpha+1,\ldots,n_{FE}\}: && \mathbf{f}_{n+1}^{\text{int},(e),(k)} = \mathbf{f}_{n+1}^{\text{int},(e),(k)}\left(\mathbf{d}_{n+1}^{(e),(k-1)}\right) \end{aligned} \tag{2.87}$$

The derivative $\partial \mathbf{f}_{n+1}^{\text{int},(e),(k)} / \partial \mathbf{d}_{n+1}^{\text{str},(k-1)}$, which appears in expression (2.85), is examined next. For the finite elements without discontinuity, the expression is simple.

$$e \in \{n_\alpha+1,\ldots,n_{FE}\}: \quad \frac{\partial \mathbf{f}_{n+1}^{\text{int},(e),(k)}}{\partial \mathbf{d}_{n+1}^{\text{str},(k-1)}} = \underbrace{\frac{\partial \mathbf{f}_{n+1}^{\text{int},(e),(k)}}{\partial \mathbf{d}_{n+1}^{(e),(k-1)}}}_{\mathbf{K}_{n+1}^{fd,(e),(k)}} \underbrace{\frac{\partial \mathbf{d}_{n+1}^{(e),(k-1)}}{\partial \mathbf{d}_{n+1}^{\text{str},(k-1)}}}_{\mathbf{R}^{(e)}\mathbf{P}^{(e)}} \tag{2.88}$$

The derivative $\mathbf{K}_{n+1}^{fd,(e),(k)}$ can be easily computed and the last term has been defined in (2.86). For the n_α elements, that have already entered the softening phase, the expression is more complicated.

$$e \in \{1,2,\ldots,n_\alpha\}: \quad \frac{\partial \mathbf{f}_{n+1}^{\text{int},(e),(k)}}{\partial \mathbf{d}_{n+1}^{\text{str},(k-1)}} = \left(\underbrace{\frac{\partial \mathbf{f}_{n+1}^{\text{int},(e),(k)}}{\partial \mathbf{d}_{n+1}^{(e),(k-1)}}}_{\mathbf{K}_{n+1}^{fd,(e),(k)}} + \underbrace{\frac{\partial \mathbf{f}_{n+1}^{\text{int},(e),(k)}}{\partial \alpha_{n+1}^{(e),(k)}}}_{\mathbf{K}_{n+1}^{f\alpha,(e),(k)}} \frac{\partial \alpha_{n+1}^{(e),(k)}}{\partial \mathbf{d}_{n+1}^{(e),(k-1)}} \right) \underbrace{\frac{\partial \mathbf{d}_{n+1}^{(e),(k-1)}}{\partial \mathbf{d}_{n+1}^{\text{str},(k-1)}}}_{\mathbf{R}^{(e)}\mathbf{P}^{(e)}} \tag{2.89}$$

The derivatives, marked with $\mathbf{K}_{n+1}^{fd,(e),(k)}$ and $\mathbf{K}_{n+1}^{f\alpha,(e),(k)}$, can be easily computed and the last term has been defined in (2.86). The term $\partial \alpha_{n+1}^{(e),(k)} / \partial \mathbf{d}_{n+1}^{(e),(k-1)}$ depends on the type of the loading step. Let us denote the number of finite elements in plastic softening step ($\bar{\bar{\gamma}}_{n+1}^{(e),(k)} > 0$) with $n_{P\alpha}$. For the sake of simplicity we assume that they are numbered with consecutive numbers from 1 to $n_{P\alpha}$. The number of finite elements in elastic step of the softening phase ($\bar{\bar{\gamma}}_{n+1}^{(e),(k)} = 0$) is marked with $n_{E\alpha} = n_\alpha - n_{P\alpha}$.

For the $n_{E\alpha}$ elements in elastic step of the softening phase, α is constant and the term $\partial \alpha_{n+1}^{(e),(k)} / \partial \mathbf{d}_{n+1}^{(e),(k-1)}$ is zero. For the $n_{P\alpha}$ elements in the plastic softening step, the term is not zero and it is determined from the second of equilibrium equations (2.58), which is linearized and solved locally, i.e. independently for each finite element. This can be done because $h_{n+1}^{(e),(k)}$ depends on the nodal displacements and rotational jump of a single element.

$$\begin{aligned} &\underbrace{\frac{\partial h_{n+1}^{(e),(k)}}{\partial \mathbf{d}_{n+1}^{(e),(k-1)}}}_{\mathbf{K}_{n+1}^{hd,(e),(k)}} \Delta \mathbf{d}_{n+1}^{(e),(k)} + \underbrace{\frac{\partial h_{n+1}^{(e),(k)}}{\partial \alpha_{n+1}^{(e),(k)}}}_{K_{n+1}^{h\alpha,(e),(k)}} \Delta \alpha_{n+1}^{(e),(k)} = -h_{n+1}^{(e),(k)} = 0 \quad \Rightarrow \\ &\Rightarrow \quad \Delta \alpha_{n+1}^{(e),(k)} = \underbrace{-\left(K_{n+1}^{h\alpha,(e),(k)}\right)^{-1} \mathbf{K}_{n+1}^{hd,(e),(k)}}_{\partial \alpha_{n+1}^{(e),(k)} / \partial \mathbf{d}_{n+1}^{(e),(k-1)}} \Delta \mathbf{d}_{n+1}^{(e),(k)} \end{aligned} \tag{2.90}$$

Note that each $h_{n+1}^{(e),(k)}$, computed by (2.34), evaluates to zero because the moment at the discontinuity $t_{n+1}^{(e),(k)}$ has been computed by expression (2.38). The derivatives, designated with $\mathbf{K}_{n+1}^{hd,(e),(k)}$ and $K_{n+1}^{h\alpha,(e),(k)}$ can be

easily calculated. Equation (2.90) defines the relation between the increment of nodal displacements $\Delta\mathbf{d}_{n+1}^{(e),(k)}$ and the increment of rotational jump $\Delta\alpha_{n+1}^{(e),(k)}$. Since we are dealing with linearized equations, the derivative $\partial\alpha_{n+1}^{(e),(k)}/\partial\mathbf{d}_{n+1}^{(e),(k-1)}$ is equal to the ratio of the increments.

$$\begin{aligned} &e\in\{1,2,\ldots,n_{P\alpha}\}: \qquad \bar{\bar{\gamma}}_{n+1}^{(e),(k)}>0, \quad \frac{\partial\alpha_{n+1}^{(e),(k)}}{\partial\mathbf{d}_{n+1}^{(e),(k-1)}}=-\left(K_{n+1}^{h\alpha,(e),(k)}\right)^{-1}\mathbf{K}_{n+1}^{hd,(e),(k)} \\ &e\in\{n_{P\alpha}+1,\ldots,n_{\alpha}\}: \quad \bar{\bar{\gamma}}_{n+1}^{(e),(k)}=0, \quad \frac{\partial\alpha_{n+1}^{(e),(k)}}{\partial\mathbf{d}_{n+1}^{(e),(k-1)}}=\mathbf{0} \end{aligned} \tag{2.91}$$

We gather expressions (2.88) and (2.89) for all n_{FE} elements in the structure, applying relations (2.91) to the latter.

$$\begin{aligned} &e\in\{1,\ldots,n_{P\alpha}\}: \quad \frac{\partial\mathbf{f}_{n+1}^{\text{int},(e),(k)}}{\partial\mathbf{d}_{n+1}^{\text{str},(k-1)}}=\overbrace{\left(\mathbf{K}_{n+1}^{fd,(e),(k)}-\mathbf{K}_{n+1}^{f\alpha,(e),(k)}\left(K_{n+1}^{h\alpha,(e),(k)}\right)^{-1}\mathbf{K}_{n+1}^{hd,(e),(k)}\right)}^{\hat{\mathbf{K}}_{n+1}^{(e),(k)}}\mathbf{R}^{(e)}\mathbf{P}^{(e)} \\ &e\in\{n_{P\alpha}+1,\ldots,n_{FE}\}: \quad \frac{\partial\mathbf{f}_{n+1}^{\text{int},(e),(k)}}{\partial\mathbf{d}_{n+1}^{\text{str},(k-1)}}=\mathbf{K}_{n+1}^{fd,(e),(k)}\mathbf{R}^{(e)}\mathbf{P}^{(e)} \end{aligned} \tag{2.92}$$

Here $\mathbf{K}_{n+1}^{fd,(e),(k)}$ is the standard stiffness matrix of finite element (e). We observe that it is computed in the same way for the $n_{FE}-n_{\alpha}$ elements in the hardening phase and for the $n_{E\alpha}$ elements in elastic step of the softening phase. Stiffness matrix of the $n_{P\alpha}$ finite elements in plastic softening step is designated with $\hat{\mathbf{K}}_{n+1}^{(e),(k)}$. Finally, we can assemble the tangent stiffness matrix of the structure by inserting (2.92) into (2.85).

$$\mathbf{K}_{n+1}^{\text{str},(k)}=\sum_{e=1}^{n_{P\alpha}}\mathbf{P}^{(e)^T}\mathbf{R}^{(e)^{-1}}\hat{\mathbf{K}}_{n+1}^{(e),(k)}\mathbf{R}^{(e)}\mathbf{P}^{(e)}+\sum_{e=n_{P\alpha}+1}^{n_{FE}}\mathbf{P}^{(e)^T}\mathbf{R}^{(e)^{-1}}\mathbf{K}_{n+1}^{fd,(e),(k)}\mathbf{R}^{(e)}\mathbf{P}^{(e)} \tag{2.93}$$

2.3.2.2 Components of internal forces and stiffness matrix

Internal forces $\mathbf{f}_{n+1}^{\text{int},(e),(k)}$ of element (e) are computed according to equations (2.33), where bending moment and axial force take the values computed in phase (A) of this iteration. In order to determine the components of the stiffness matrix, $h_{n+1}^{(e),(k)}$ must be written as well. It is computed in accordance with (2.34).

$$\mathbf{f}_{n+1}^{\text{int},(e),(k)}=\int_L\breve{\mathbf{B}}^{\varepsilon^T}N_{n+1}^{(e),(k)}dx+\int_L\breve{\mathbf{B}}^{\kappa^T}M_{n+1}^{(e),(k)}dx, \quad h_{n+1}^{(e),(k)}=\int_L\bar{G}M_{n+1}^{(e),(k)}dx+t_{n+1}^{(e),(k)} \tag{2.94}$$

To obtain the components of the element stiffness matrix, expressions (2.94) are differentiated over nodal degrees of freedom and over rotational jump.

$$
\begin{aligned}
\mathbf{K}_{n+1}^{fd,(e),(k)} &= \frac{\partial \mathbf{f}_{n+1}^{\text{int},(e),(k)}}{\partial \mathbf{d}_{n+1}^{(e),(k-1)}} = \int_L \check{\mathbf{B}}^{\varepsilon T} \left.\frac{\partial N}{\partial \varepsilon}\right|_{n+1}^{(e),(k)} \underbrace{\check{\mathbf{B}}^{\varepsilon}}_{\partial\varepsilon/\partial\mathbf{d}}\, dx + \int_L \check{\mathbf{B}}^{\kappa T} \left.\frac{\partial M}{\partial \bar{\kappa}}\right|_{n+1}^{(e),(k)} \underbrace{\check{\mathbf{B}}^{\kappa}}_{\partial\bar{\kappa}/\partial\mathbf{d}}\, dx \\
\mathbf{K}_{n+1}^{f\alpha,(e),(k)} &= \frac{\partial \mathbf{f}_{n+1}^{\text{int},(e),(k)}}{\partial \alpha_{n+1}^{(e),(k)}} = \int_L \check{\mathbf{B}}^{\kappa T} \left.\frac{\partial M}{\partial \bar{\kappa}}\right|_{n+1}^{(e),(k)} \underbrace{\bar{G}}_{\partial\bar{\kappa}/\partial\alpha}\, dx \\
\mathbf{K}_{n+1}^{hd,(e),(k)} &= \frac{\partial h_{n+1}^{(e),(k)}}{\partial \mathbf{d}_{n+1}^{(e),(k-1)}} = \int_L \bar{G} \left.\frac{\partial M}{\partial \bar{\kappa}}\right|_{n+1}^{(e),(k)} \underbrace{\check{\mathbf{B}}^{\kappa}}_{\partial\bar{\kappa}/\partial\mathbf{d}}\, dx \\
K_{n+1}^{h\alpha,(e),(k)} &= \frac{\partial h_{n+1}^{(e),(k)}}{\partial \alpha_{n+1}^{(e),(k)}} = \int_L \bar{G} \left.\frac{\partial M}{\partial \bar{\kappa}}\right|_{n+1}^{(e),(k)} \underbrace{\bar{G}}_{\partial\bar{\kappa}/\partial\alpha}\, dx + \left.\frac{\partial t}{\partial \alpha}\right|_{n+1}^{(e),(k)}
\end{aligned}
\tag{2.95}
$$

The tangent moduli $(\partial M/\partial\bar{\kappa}\,)_{n+1}^{(e),(k)}$ and $(\partial t/\partial\alpha\,)_{n+1}^{(e),(k)}$ are defined by equations (2.69) and (2.83). The latter is not defined for $\bar{\bar{\gamma}}_{n+1}^{(k)} = 0$, but we have shown above that $K_{n+1}^{h\alpha,(e),(k)}$ is not required in that case. The tangent stiffness matrix is symmetrical.

2.3.2.3 Solution of global equations

The system of global equilibrium equations (2.84) is rewritten in a clearer form.

$$
\mathbf{K}_{n+1}^{\text{str},(k)} \Delta\mathbf{d}_{n+1}^{\text{str},(k)} = \Delta\mathbf{f}_{n+1}^{\text{str},(k)}, \qquad \Delta\mathbf{f}_{n+1}^{\text{str},(k)} = \mathbf{f}_{n+1}^{\text{ext,str}} - \mathbf{f}_{n+1}^{\text{int,str},(k)} \tag{2.96}
$$

The external forces are an input to the analysis, internal forces are defined by equations (2.85) and (2.94), and the tangent stiffness matrix of the structure is defined by (2.93), (2.92) and (2.95). Finally, we can compute the increments and update the nodal displacements of the structure.

$$
\Delta\mathbf{d}_{n+1}^{\text{str},(k)} = \left(\mathbf{K}_{n+1}^{\text{str},(k)}\right)^{-1} \Delta\mathbf{f}_{n+1}^{\text{str},(k)}, \qquad \mathbf{d}_{n+1}^{\text{str},(k)} = \mathbf{d}_{n+1}^{\text{str},(k-1)} + \Delta\mathbf{d}_{n+1}^{\text{str},(k)} \tag{2.97}
$$

The updates of the rotational jumps could be computed from (2.90), but there is no benefit from that because they will be recomputed anyway in phase (A) of the next iteration.

The iterations at pseudo-time τ_{n+1} are repeated until the tolerance requirements are met.

$$
\left\|\Delta\mathbf{f}_{n+1}^{\text{str},(k)}\right\| < tol, \quad \left\|\Delta\mathbf{d}_{n+1}^{\text{str},(k)}\right\| < tol \tag{2.98}
$$

When the converged solution is found, we proceed to the next pseudo-time step.

2.4 Numerical examples

The computer code for the above described finite element was generated by the AceGen program [68] that combines manipulation of symbolic expressions, automatic differentiation and code generation. The obtained code was introduced into the finite element program AceFEM [69], in which the presented numerical examples were performed. Both programs have been developed by prof. J. Korelc from University of Ljubljana.

Before performing analysis with the derived stress-resultant beam finite element, the material parameters have to be obtained. For the axial response, only axial stiffness is required because the behavior is assumed to be linear elastic. For the bending response, the three-linear moment-curvature relation from Fig. 2.10 (left) is needed for each integration point of each finite element. Also, the linear moment versus rotational jump relation from Fig. 2.11 is needed for each element. The curves depend on the material properties of concrete and reinforcement, geometry of the cross-section and the level of the axial force.

The moment-curvature diagram of the cross-section can be obtained in a standard way from the uniaxial stress-strain concrete and reinforcement diagrams by enforcing cross-sectional equilibrium. From those diagrams, the needed stress resultant material parameters can be estimated. Another way to compute the above stress resultant material parameters is to use a multilayer beam finite element with layer-wise embedded axial discontinuities, where the response of a material of each layer (including softening) is described either by 1D damage model (for concrete) or 1D elastoplastic model (for reinforcement). Of course, the required material parameters can also be obtained directly from experiments.

2.4.1 Failure of a cantilever beam

We consider a cantilever beam of rectangular cross-section for three different load cases, presented in Fig. 2.13. In the first load case, the beam is loaded with moment at the free end. In order to perform the analysis up to the total collapse, the load is controlled with imposed rotation of the free end. The following geometrical and material properties are chosen: length of the beam $L = 2.5$m, elastic bending stiffness $EI = 77650\text{kNm}^2$, elastic axial stiffness $EA = 3727200$kN, moment at elasticity limit $M_c = 37.9$kNm, yield moment $M_y = 268$kNm, ultimate moment $M_u = 274$kNm, hardening moduli $H_1 = 29400\text{kNm}^2$ and $H_2 = 272\text{kNm}^2$, and softening modulus $K = -18000$kNm. Response of the structure is computed for meshes of 1, 2, 5 and 10 finite elements.

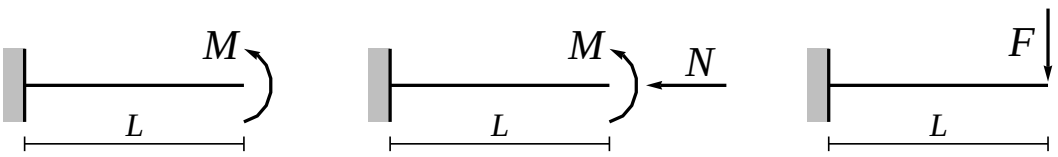

Figure 2.13: Cantilever beam under different loads.
Slika 2.13: Konzola pod različnimi obtežbami.

Results for the load case from Fig. 2.13 (left) are presented in Fig. 2.14 (left), which shows the moment versus imposed rotation diagrams for different meshes. We can see that they are not unique. The elastoplastic parts of the curves are the same, but the slopes of the softening lines decrease with the increasing number of finite elements in the mesh. The reason for such behavior is that, due to homogeneous stress state along the cantilever, each finite element develops its own softening hinge. In finer meshes, multiple discontinuities with smaller values of the rotational jump occur, as opposed to a single discontinuity with a greater value of the rotational jump in a single element mesh. Since the moment at the hinge drops with the growing value of the rotational jump, it is understandable that finer meshes produce a greater moment at the same value of imposed end rotation.

The described problem can be avoided by introducing one weaker element. This is done by slightly raising the ultimate moment M_u for all but one finite element. Thus, when the weakest element enters the softening phase, the moment in that element begins to drop and the remaining elements have to unload to satisfy equilibrium. As a consequence, only one softening hinge appears in the beam and the response is identical for all meshes, see Fig. 2.14 (right).

Next we consider the same cantilever, loaded by end moment and axial force, see the middle image in Fig. 2.13.

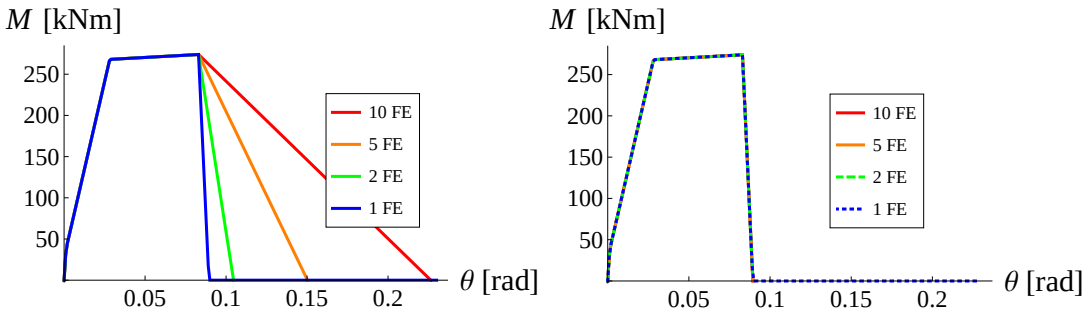

Figure 2.14: *Moment - rotation* diagrams for cantilever beam under end moment: all finite elements are the same (left), one element is slightly weaker (right).

Slika 2.14: Diagram *moment - zasuk* za konzolo, obteženo z momentom: vsi končni elementi so enaki (levo), en element je malce šibkejši (desno).

The axial force is applied first and it is kept constant for the rest of the analysis. The bending load is applied by gradually increasing the imposed rotation of the free end of the beam. Due to the presence of axial force, the parameters that define the moment-curvature diagram are altered. We choose the following data: $N = 100$kN, $M_c = 55$kNm, $M_y = 395$kNm, $M_u = 401$kNm, $H_1 = 35000$kNm^2, $H_2 = 352$kNm^2, $K = -26000$kNm. Bending responses of the beam, with and without the presence of axial force, are shown in Fig. 2.15. They were computed with a mesh with one finite element.

Remark. *In order to determine the influence of axial force on the material parameters for bending, the geometry of the cross-section and the material properties of concrete and reinforcement are required. In the load case without axial force, we defined only the resultant material-geometrical properties of the cross-section, so the modified parameters cannot be computed. Their values are altered (chosen) in a similar way as computed in [51].*

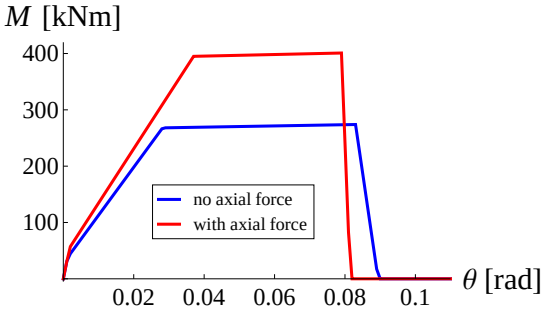

Figure 2.15: *Moment - rotation* diagram for cantilever beam under end moment: with and without axial force.

Slika 2.15: Diagram *moment - zasuk* za konzolo, obremenjeno z momentom: ob prisotnosti in brez prisotnosti osne sile.

The third load case is shown in Fig. 2.13 (right). To obtain the response up to the total failure, the loading is controlled with imposed vertical displacement at the location of the force. The following geometrical and material properties are chosen: $L = 2.5$m, $EI = 77650$kNm^2, $EA = 3727200$kN, $M_c = 37.9$kNm, $M_y = 268$kNm, $M_u = 374$kNm, $H_1 = 29400$kNm^2, $H_2 = 272$kNm^2, $K = -18000$kNm. The beam is modeled with meshes, consisting of 1, 2, 5 and 10 finite elements. The diagrams, showing the relation of moment at the support versus imposed

vertical displacement for different meshes, are presented in Fig. 2.16. We can see that a single finite element cannot adequately describe the beam response. The error arises in hardening plasticity, because three integration points over the whole structure are not enough to properly describe the propagation of plastic deformations. The error diminishes rapidly for finer meshes. Contrary to the previous load cases, the stress state along the beam is not homogeneous, so there is no need for a weakened element to prevent the occurrence of multiple discontinuities. The only softening hinge forms at the support where the moment is the largest.

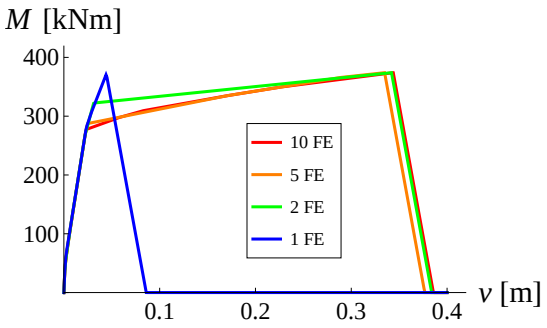

Figure 2.16: *Moment at support - transversal displacement* diagram for cantilever beam under end transversal force: all finite elements are the same.

Slika 2.16: Diagram *moment ob podpori - prečni pomik* za konzolo, obremenjeno s prečno silo: vsi končni elementi so enaki.

2.4.2 Failure of simply supported and clamped beams

We consider the three point bending test of a simply supported reinforced concrete beam of length $L = 5$m, shown in Fig. 2.17. The width and the height of the cross-section are $b = 0.2$m and $h = 0.5$m. The following material properties are used: elastic modulus $E = 37272$MPa, moment at elasticity limit $M_c = 37.9$kNm, yield moment $M_y = 282$kNm, ultimate moment $M_u = 304$kNm, hardening moduli $H_1 = 47314$kNm^2 and $H_2 = 171.6$kNm^2, and softening modulus $K = -85000$kNm. Symmetry allows us to model only one half of the beam, which is divided into 16 identical finite elements. The load is applied by imposing displacement v at the location and in the direction of force F.

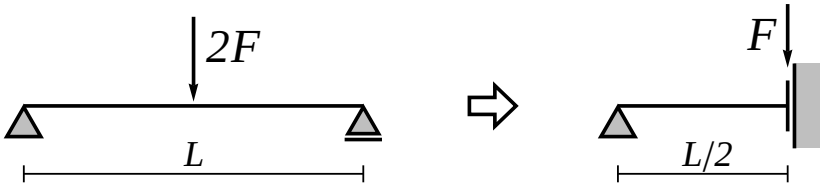

Figure 2.17: Simply supported beam: use of symmetry in computational model.

Slika 2.17: Prostoležeči nosilec: uporaba simetrije v računskem modelu.

Since this is a statically determined structure, we expect the $F - v$ diagram to be similar to the input moment-curvature diagram, which is confirmed by the results, presented in Fig. 2.19 (left). Rounded transition into the plastic part of the curve is a consequence of gradual spreading of plasticity from the middle of the beam toward the supports.

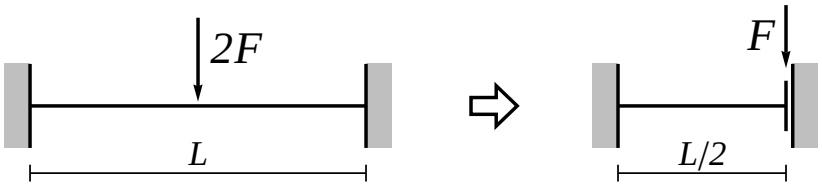

Figure 2.18: Clamped beam: use of symmetry in computational model.
Slika 2.18: Togo podprti nosilec: uporaba simetrije v računskem modelu.

Next, we analyze the same beam with fixed supports, see Fig. 2.18. The geometrical and material properties are the same as before, as well as the mesh and the loading procedure. The force versus imposed displacement diagram is presented in Fig. 2.19 (left). In comparison to the simply supported beam, the clamped beam exhibits greater stiffness and ultimate load, but the yielding of reinforcement and collapse of the structure happen at significantly smaller displacements.

The fact, that the ultimate moment is reached at a smaller imposed displacement in the clamped beam is not surprising, because the fixed support prevents the rotation of the beam at that point. But when the softening plastic hinge forms near the support and begins to soften, the clamped beam behaves more and more like the simply supported beam. In a fully softened state (when the moment in the softening plastic hinge drops to zero), one would expect the imposed displacement to be equal in both beams. This is not so, due to plastic deformations of the bulk of the element. In the simply supported beam, the plastic curvature was caused only by positive bending moment, so the half of the beam takes a *C* shape in the fully softened state. In the clamped beam, however, the plastic curvature was caused by positive moment in the field and by negative moment near the support, so the half of the beam takes an *S* shape.

We verify this by repeating the analysis with an elastic beam. We set the values of the elasticity limit M_c and the yield moment M_y to be greater than M_u. The remaining data is the same as before. Results of the analysis are presented in Fig. 2.19 (right). Just like in the left figure, the ultimate moment is reached at a smaller displacement v in the clamped beam, but the diagrams drop to zero at the same value of v.

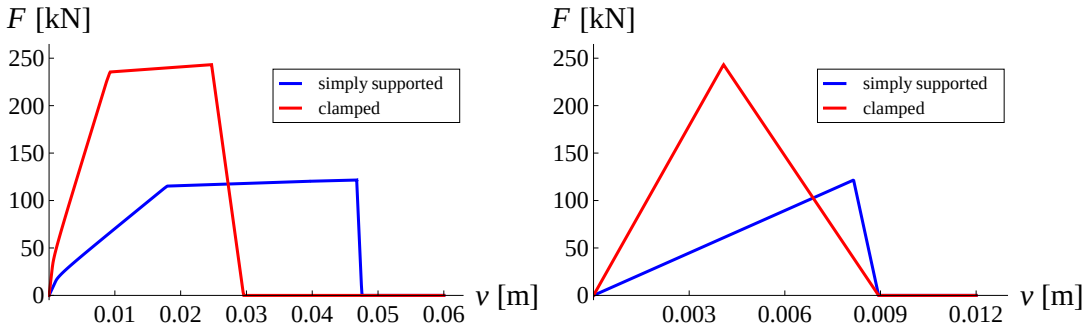

Figure 2.19: *Force - displacement under the force* diagrams for simply supported and clamped beams. Elasto-plastic (left) and elastic (right) behavior in the hardening phase.
Slika 2.19: Diagram *sila - pomik pod silo* za prostoležeči in togo podprti nosilec. Elasto-plastično (levo) in elastično (desno) obnašanje v utrjevanju.

2.4.3 Four point bending test of a simply supported beam

In this example, we examine a four point bending test of a symmetrical, simply supported, reinforced concrete beam with different positions of the loading force. Experiments on such beams were performed by Lane [70], as stated in [49]. The beam of length $L = 3.82$m is loaded with two vertical forces F at distance L_a from each support. Making use of the symmetry, we only model one half of the structure, as shown in Fig. 2.20. The values of L_a are 0.96m, 1.30m and 1.60m, while the corresponding values of L_b are 0.95m, 0.61m and 0.31m. The remaining geometrical and material properties are: elastic bending stiffness $EI = 20400\text{kNm}^2$, yield moment $M_y = 210$kNm, ultimate moment $M_u = 270$kNm, hardening modulus $H_2 = 1543\text{kNm}^2$ and softening modulus $K = -2823$kNm. Since the hardening model in [49] is linear, we take $M_c = M_y$ and the first hardening modulus H_1 is not required. Parameters EI, M_y and M_u were taken directly from [49]. The hardening modulus was computed as $H_2 = \mathscr{H} {M_y}^2$, where $\mathscr{H}$ is the linear hardening modulus in [49]. The transformation is caused by different formulations of the yield function and evolution equations. The softening modulus K was chosen to fit the results, presented in [49].

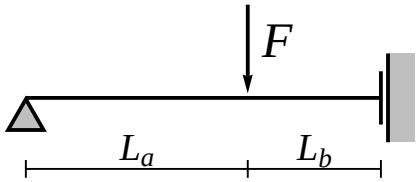

Figure 2.20: Four point bending test of simply supported beam: computational model.
Slika 2.20: Štiritočkovni upogibni preizkus prostoležečega nosilca: računski model.

Responses of the structure for all three load positions are presented in Fig. 2.21. They are compared with experimental results [70] and with computations by Armero and Ehrlich [49], who used the same parameters for elasticity and hardening plasticity, but modeled the softening hinge response with quadratic function. Our results capture well the experimental limit load and the corresponding displacement. The softening parts of the diagrams differ from those in [49], due to a different material law in the softening plastic hinge. The experimental results were taken from [49].

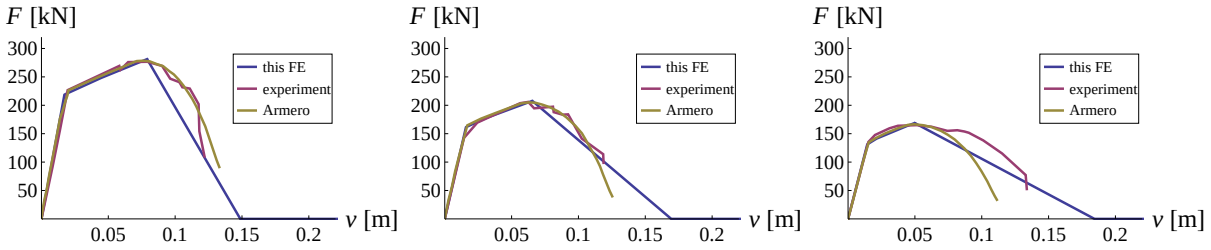

Figure 2.21: *Force - displacement at the middle of the beam* diagrams for different positions of the force: $L_a = 0.96$m (left), $L_a = 1.30$m (middle), $L_a = 1.60$m (right).
Slika 2.21: Diagrami *sila - pomik na sredini nosilca* za različne pozicije sile: $L_a = 0.96$m (levo), $L_a = 1.30$m (sredina), $L_a = 1.60$m (desno).

2.4.4 Two story reinforced concrete frame

In this example we consider a two story reinforced concrete frame in Fig. 2.22. The frame was experimentally tested in [71] and numerically analyzed in [51]. Story height is $H = 2$m and span is $L = 3.5$m. The columns and the beams have the same concrete cross-section $b \times h = 0.3 \times 0.4$m, but different reinforcement. Details can be found in [71]. The stress-resultant material properties, required for analysis with our finite element, were estimated from moment-curvature diagrams, presented by Pham [51]. Material parameters of the beams are: $M_c = 30$kNm, $M_y = 150$kNm, $M_u = 170$kNm, $H_1 = 11190$kNm^2, $H_2 = 137$kNm^2, $K = -1310$kNm. Material parameters of the columns are: $M_c = 100$kNm, $M_y = 245$kNm, $M_u = 265$kNm, $H_1 = 12450$kNm^2, $H_2 = 195$kNm^2, $K = -2410$kNm. Elastic bending stiffness of both columns and beams is $EI = 45760$kNm^2 and elastic axial stiffness is $EA = 3432000$kN.

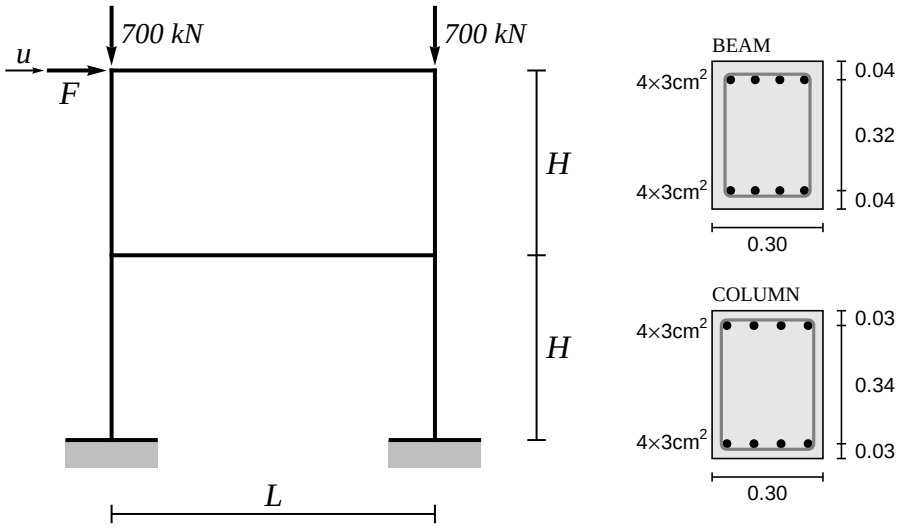

Figure 2.22: Two story frame: geometry, loading pattern and cross-sections.
Slika 2.22: Dvoetažni okvir: geometrija, obtežba in prečni prerezi.

The properties of beams and columns were verified in the following way. For each of the two cross-sections in Fig. 2.22, a cantilever beam of length 1m was modeled with a single finite element and loaded with end moment. The load was applied by imposing rotation θ at the free end of the beam. The diagrams in Fig. 2.23 show the moment versus the end rotation, divided by the length of the finite element (length of the cantilever beam) for a beam and a column of the RC frame. Due to the constant moment, the ratio θ/L is identical to curvature κ up to the ultimate moment, when the softening hinge occurs. The material properties of both structural elements were chosen in such manner, that the diagrams in Fig. 2.23 match the moment-curvature diagrams, presented in [51].

The columns were divided into 16 finite elements from the ground to the top of the frame, and the beams were divided into 14 finite elements. At the beginning of the analysis, vertical forces $N = 700$kN were applied at the top of each column, and remained constant throughout the computation. Next, the horizontal displacement u at the top of the frame was gradually increased and reaction F at location and in direction of the imposed displacement was computed.

Results are presented in Fig. 2.24 (left). First nonlinear behavior occurs at $u = 0.002$m due to cracking of concrete in the beams near the columns. Next, the concrete cracking appears in the columns as well, first at the bottom, then at the top and in the middle. Yielding of the reinforcement first appears at the end of the beams at $u = 0.035$m. At $u = 0.045$m the column reinforcement begins to yield at the supports. Maximal value of force F is reached at $u = 0.073$m, when softening hinges appear at the bottom of both columns. Although the resistance of the structure

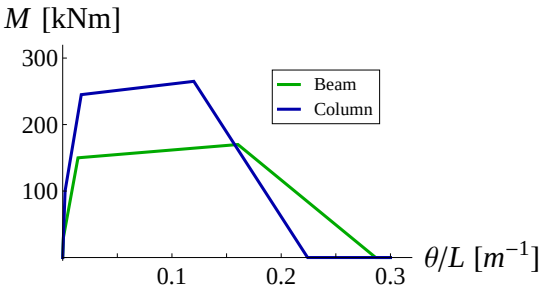

Figure 2.23: *Moment - rotation divided by length of FE* diagrams for beam and column.
Slika 2.23: Diagram *moment - zasuk, deljen z dolžino KE* za prečko in steber.

begins to drop, the moments in the beams still increase, which improves structure ductility. The softening in the beams begins at $u = 0.1$m. Hereafter, internal forces in all structural elements decrease. Total collapse of the structure happens at $u = 0.6$m, see the diagram "data Pham" in Fig. 2.25 (left).

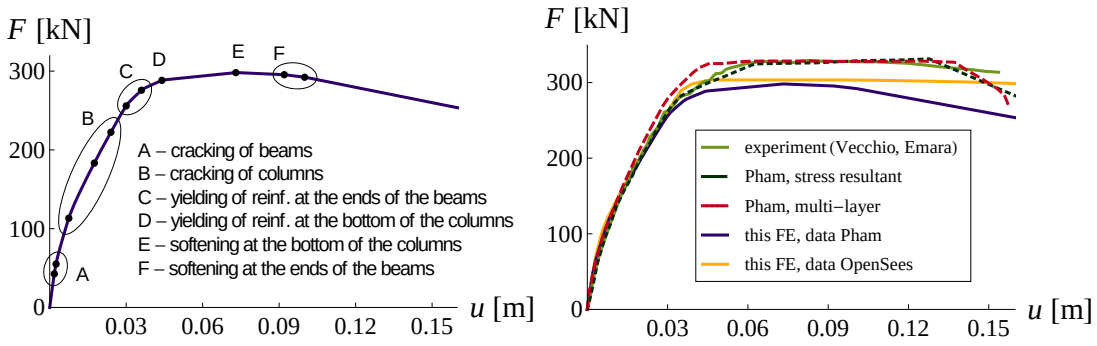

Figure 2.24: Response of two story frame and material state at different stages of analysis (left). Comparison with experiment and results of Pham et al. (right).
Slika 2.24: Odziv dvoetažnega okvirja in stanje materiala v posameznih fazah analize (levo). Primerjava z eksperimentom in z rezultati Pham et al. (desno).

Fig. 2.24 (right) shows the comparison with the experiment [71] and with results, reported in [51]. Our results are very similar in the shape of the curve to the experimental results, but do not reach the measured ultimate capacity. For an additional test, the stress-resultant properties of beams and columns were computed from cross-section geometry and stress-strain diagrams of steel and concrete, presented in [71], using the computer program OpenSees [72]. The following data was obtained for columns: $M_c = 99$kNm, $M_y = 251$kNm, $M_u = 259$kNm, $H_1 = 14800$kNm^2, $H_2 = 85$kNm^2. The following data was computed for the beams: $M_c = 32$kNm, $M_y = 168$kNm, $M_u = 223$kNm, $H_1 = 11100$kNm^2, $H_2 = 248$kNm^2. The values of softening moduli K were preserved from before. Results of the analysis with the new data are included in Fig. 2.24 (right).

Another set of material parameters was obtained by multi-layer Timoshenko beam element, presented in chapter 4 of this work. To obtain material properties of a beam of the frame, a cantilever beam of length 0.25m, which corresponds to the length of finite elements in the RC frame analysis, was modeled with a single multi-layer element. Rotation θ of the free end of the beam was imposed and the corresponding moment M in the beam was computed. Stress-resultant properties were determined in such way, that the $M - \theta$ diagram, obtained with a stress-resultant finite element, matches the diagram, obtained with multi-layer element. To obtain material properties of a column, an identical multi-layer cantilever beam of length 0.25m was analyzed with the presence of a constant axial

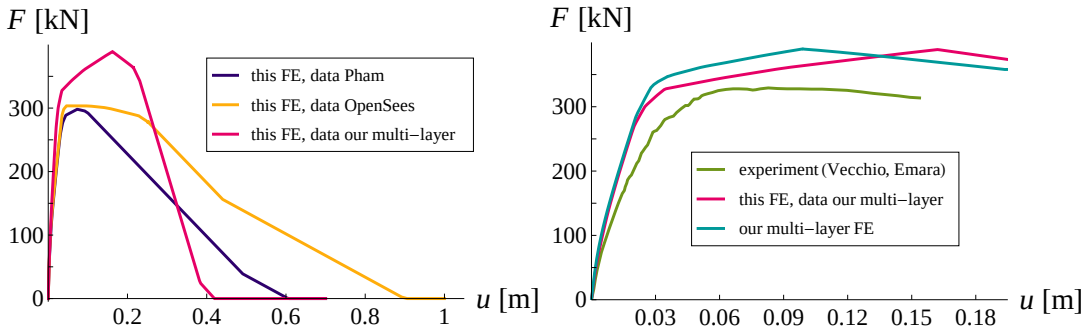

Figure 2.25: Response of two story frame up to total collapse for different material data (left). Comparison with results of analysis with multi-layer finite element (right).
Slika 2.25: Odziv dvoetažnega okvirja do popolne porušitve za različne materialne podatke (levo). Primerjava z rezultati analize z večslojnim končnim elementom (desno).

force $N = 700$kN. The following material properties were calculated for beams: $M_c = 31$kNm, $M_y = 165$kNm, $M_u = 236$kNm, $H_1 = 25800$kNm^2, $H_2 = 349$kNm^2, $K = -5250$kNm. The computed properties of columns: $M_c = 100$kNm, $M_y = 281$kNm, $M_u = 333$kNm, $H_1 = 33800$kNm^2, $H_2 = 216$kNm^2, $K = -4750$kNm. Response of the two-story frame, analyzed with this data, is shown in Fig. 2.25 (left), along with responses, obtained for the data from OpenSees and data estimated from [51]. We observe that the data, computed with our multi-layer element, produces a significantly higher ultimate load and a steeper softening line.

Fig. 2.25 (right) shows the response of the frame, computed by the multi-layer finite element from chapter 4. It is compared to the results of analysis with stress-resultant element, developed in this chapter, and material data, provided by the former multi-layer element. Both curves reach the same ultimate value of force F, but not at the same value of imposed displacement u. In comparison to other results, the curves match pretty well.

2.5 Concluding remarks

We have presented a planar stress-resultant Euler-Bernoulli beam finite element with embedded discontinuity in rotation, which can be used for analysis of reinforced concrete beams and frames up to complete failure. The formulation is based on small deformation kinematics. Stress resultant elastoplasticity with bilinear isotropic hardening is used to model the bending of the bulk of the element, and rigid plasticity is used for the softening bending hinge. The element is able to describe the major characteristics of the reinforced concrete beam behavior up to complete failure. The finite element provides a mesh independent softening response of the modeled structure. The obtained results compare reasonably well to other results available in the literature and to experimental results.

The geometrical and material properties have to be determined individually for each cross-section and for each level of the axial force. The moment-curvature and moment-rotational jump diagrams, required as an input for the analysis, can be determined experimentally or computed with a more complex finite element, such as the multi-layer beam finite elements, presented in the following chapters.

3 MULTI-LAYER EULER-BERNOULLI BEAM FINITE ELEMENT WITH LAYER-WISE EMBEDDED DISCONTINUITIES IN AXIAL DISPLACEMENT

3.1 Introduction

In this chapter we derive a multi-layer Euler-Bernoulli beam finite element with layer-wise embedded discontinuities in axial displacement. The element is intended for precise analysis of reinforced concrete beams and structures up to complete failure, as well as for computation of stress-resultant properties of cross-sections, which are required as input data in analysis with stress-resultant finite element, presented in previous chapter.

The element is composed of several layers of concrete and reinforcement, each with embedded discontinuity in axial displacement. Axial response of concrete layer is determined by elasto-damage hardening law in the bulk and damage softening law at the discontinuity. Axial response of reinforcement layer is controlled by elastoplasticity hardening law in the bulk and plastic softening at the discontinuity. Small deformation kinematics is employed.

The outline of the chapter is the following: Kinematic, constitutive and equilibrium equations are developed in section 3.2. Finite element discretization and computational procedure are presented in section 3.3. Several numerical examples are shown in section 3.4. Finally, concluding remarks are given in section 3.5.

3.2 Finite element formulation

3.2.1 Kinematics

We consider a planar Euler-Bernoulli beam finite element with three nodes, shown in Fig. 3.1. The two end nodes have regular degrees of freedom, two in-plane displacements and rotation about the axis, perpendicular to the plane. The third node is located in the middle of the element and has one degree of freedom, the axial displacement. Its purpose is to raise the interpolation order of axial displacements, which ensures compatibility of the axial strain contributions by bending and axial deformation.

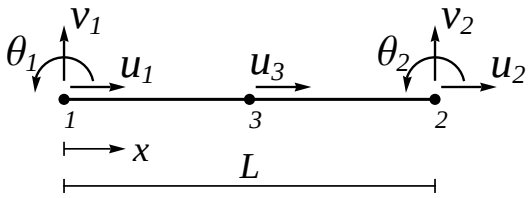

Figure 3.1: Finite element with seven nodal degrees of freedom.
Slika 3.1: Končni element s sedmimi prostostnimi stopnjami.

$$\tilde{u}(x) = \mathbf{N}^u(x)\,\mathbf{u}, \quad \mathbf{N}^u(x) = \left\{1 - \frac{3x}{L} + \frac{2x^2}{L^2}, -\frac{x}{L} + \frac{2x^2}{L^2}, \frac{4x}{L} - \frac{4x^2}{L^2}\right\}, \quad \mathbf{u} = \{u_1, u_2, u_3\}^T \tag{3.1}$$

Axial displacement $\tilde{u}(x)$ of the middle axis of the beam is interpolated between the three nodal displacements $\mathbf{u}$, using quadratic shape functions $\mathbf{N}^u(x)$ shown in Fig. 3.2 (left). Lateral displacement $\tilde{v}(x)$ is interpolated as follows.

$$\tilde{v}(x) = \mathbf{N}^v(x)\,\mathbf{v} + \mathbf{N}^\theta(x)\,\boldsymbol{\theta} \tag{3.2}$$

Here $\mathbf{v}$ and $\boldsymbol{\theta}$ are lateral displacements and rotations of the end nodes, respectively. $\mathbf{N}^v(x)$ and $\mathbf{N}^\theta(x)$ are cubic Hermite polynomials shown in Fig. 3.2 (right).

$$\begin{aligned}
&\mathbf{N}^v(x) = \left\{2\left(\frac{x}{L}\right)^3 - 3\left(\frac{x}{L}\right)^2 + 1, -2\left(\frac{x}{L}\right)^3 + 3\left(\frac{x}{L}\right)^2\right\}, \quad \mathbf{v} = \{v_1, v_2\}^T \\
&\mathbf{N}^\theta(x) = L\left\{\left(\frac{x}{L}\right)^3 - 2\left(\frac{x}{L}\right)^2 + \frac{x}{L}, \left(\frac{x}{L}\right)^3 - \left(\frac{x}{L}\right)^2\right\}, \quad \boldsymbol{\theta} = \{\theta_1, \theta_2\}^T
\end{aligned} \tag{3.3}$$

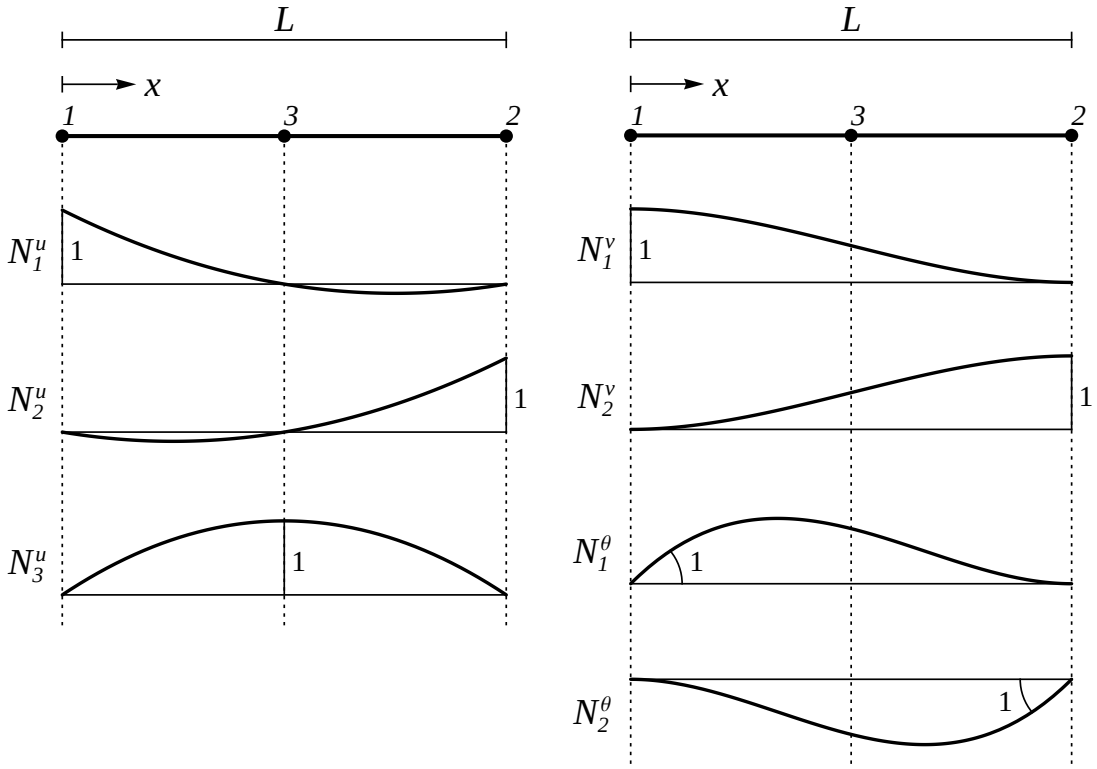

Figure 3.2: Interpolation functions for axial (left) and transversal displacement (right).
Slika 3.2: Interpolacijske funkcije za osni (levo) in prečni pomik (desno).

In Euler-Bernoulli beam theory, a cross-section is always perpendicular to the beam's axis and its rotation is therefore equal to the first derivative of the lateral displacement.

$$\tilde{\theta}(x) = \frac{\partial \tilde{v}}{\partial x} = \frac{\partial \mathbf{N}^v}{\partial x}\mathbf{v} + \frac{\partial \mathbf{N}^\theta}{\partial x}\boldsymbol{\theta} \tag{3.4}$$

The beam is divided into a desired number n_L of layers by height. For a fine enough division, a constant state can be assumed through the thickness of the layer. The axial displacement $u^i(x)$ of the i-th layer is computed in its middle axis.

$$u^i\left(x, x_d^i\right) = \overbrace{\tilde{u}(x) - y^i\tilde{\theta}(x)}^{\tilde{u}^i} + \overbrace{M^i\left(x, x_d^i\right)\alpha^i}^{u^{i,add}} \tag{3.5}$$

The regular part $\tilde{u}^i(x)$ is composed of the axial displacement in the neutral axis of the beam and of displacement due to rotation of the cross-section, depending on the distance y^i from the neutral axis. If the carrying capacity is exceeded, a discontinuity is introduced into the layer (see Fig. 3.3), which results in an additional axial displacement $u^{i,add}\left(x, x_d^i\right)$, described by the jump in displacements α^i at coordinate x_d^i and the shape function $M^i\left(x, x_d^i\right)$.

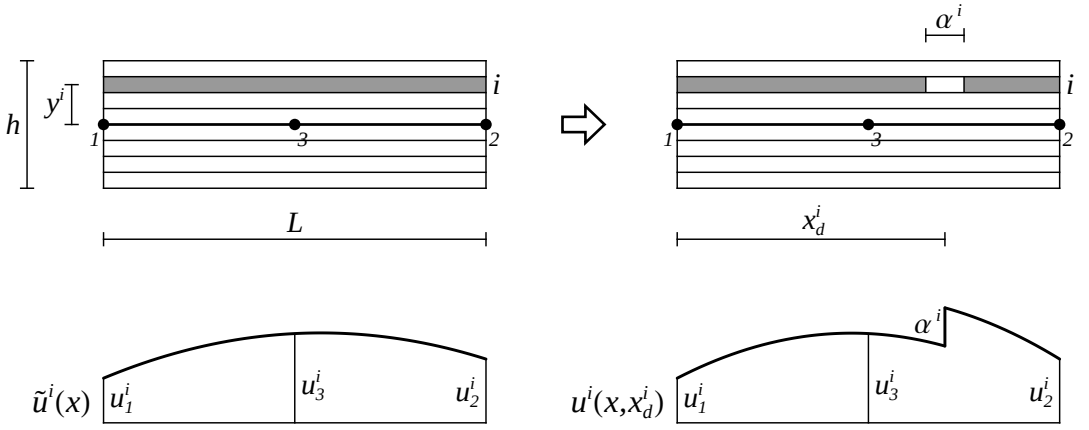

Figure 3.3: Finite element divided into layers, before and after occurrence of discontinuity in i-th layer, with corresponding axial displacement in the layer.

Slika 3.3: Na sloje razdeljen končni element pred in po nastanku nezveznosti v i-tem sloju ter pripadajoči osni pomik v sloju.

A layer is then treated as a bar, namely the strain $\varepsilon^i\left(x, x_d^i\right)$ is computed as the first derivative of the displacement $u^i\left(x, x_d^i\right)$ over the coordinate x.

$$\varepsilon^i\left(x, x_d^i\right) = \frac{\partial u^i}{\partial x} = \overbrace{\mathbf{B}^u(x)\,\mathbf{u} - y^i\left(\mathbf{B}^v(x)\,\mathbf{v} + \mathbf{B}^\theta(x)\,\boldsymbol{\theta}\right)}^{\tilde{\varepsilon}^i} + \overbrace{G_R^i\left(x, x_d^i\right)\alpha^i}^{\varepsilon^{i,add}} \tag{3.6}$$

The first three parts of the expression (3.6) represent the regular axial strain $\tilde{\varepsilon}^i$, while the last part represents the enhanced strain due to embedded discontinuity. The strain interpolation functions for the regular part are shown in equation (3.7). Since we chose quadratic functions $\mathbf{N}^u$ and cubic functions $\mathbf{N}^v$ and $\mathbf{N}^\theta$, their derivatives $\mathbf{B}^u$, $\mathbf{B}^v$ and $\mathbf{B}^\theta$ are all linear (see Fig. 3.4). The additional strain $\varepsilon^{i,add}$ only appears in the layers that have exceeded their carrying capacity. Operator G_R^i is the first derivative of the shape function M^i, but we will discuss it more precisely later on.

$$\begin{aligned}
\mathbf{B}^u(x) &= \frac{\partial \mathbf{N}^u(x)}{\partial x} = \left\{-\frac{1}{L}\left(3 - \frac{4x}{L}\right), -\frac{1}{L}\left(1 - \frac{4x}{L}\right), \frac{4}{L}\left(1 - \frac{2x}{L}\right)\right\} \\
\mathbf{B}^v(x) &= \frac{\partial^2 \mathbf{N}^v(x)}{\partial x^2} = \left\{-\frac{6}{L^2}\left(1 - \frac{2x}{L}\right), \frac{6}{L^2}\left(1 - \frac{2x}{L}\right)\right\} \\
\mathbf{B}^\theta(x) &= \frac{\partial^2 \mathbf{N}^\theta(x)}{\partial x^2} = \left\{-\frac{2}{L}\left(2 - \frac{3x}{L}\right), -\frac{2}{L}\left(1 - \frac{3x}{L}\right)\right\}
\end{aligned} \tag{3.7}$$

We will also use a shorter notation for the regular strain, where all degrees of freedom of the finite element are collected in the vector of generalized nodal displacements $\mathbf{d}$. Interpolation matrix $\check{\mathbf{B}}^i$ is composed accordingly to the arrangement of displacements in $\mathbf{d}$.

$$\tilde{\varepsilon}^i = \begin{bmatrix} \mathbf{B}^u & -y^i\mathbf{B}^v & -y^i\mathbf{B}^\theta \end{bmatrix} \mathbf{d} = \breve{\mathbf{B}}^i\mathbf{d}, \quad \mathbf{d}^T = \left\{\mathbf{u}^T, \mathbf{v}^T, \boldsymbol{\theta}^T\right\} \tag{3.8}$$

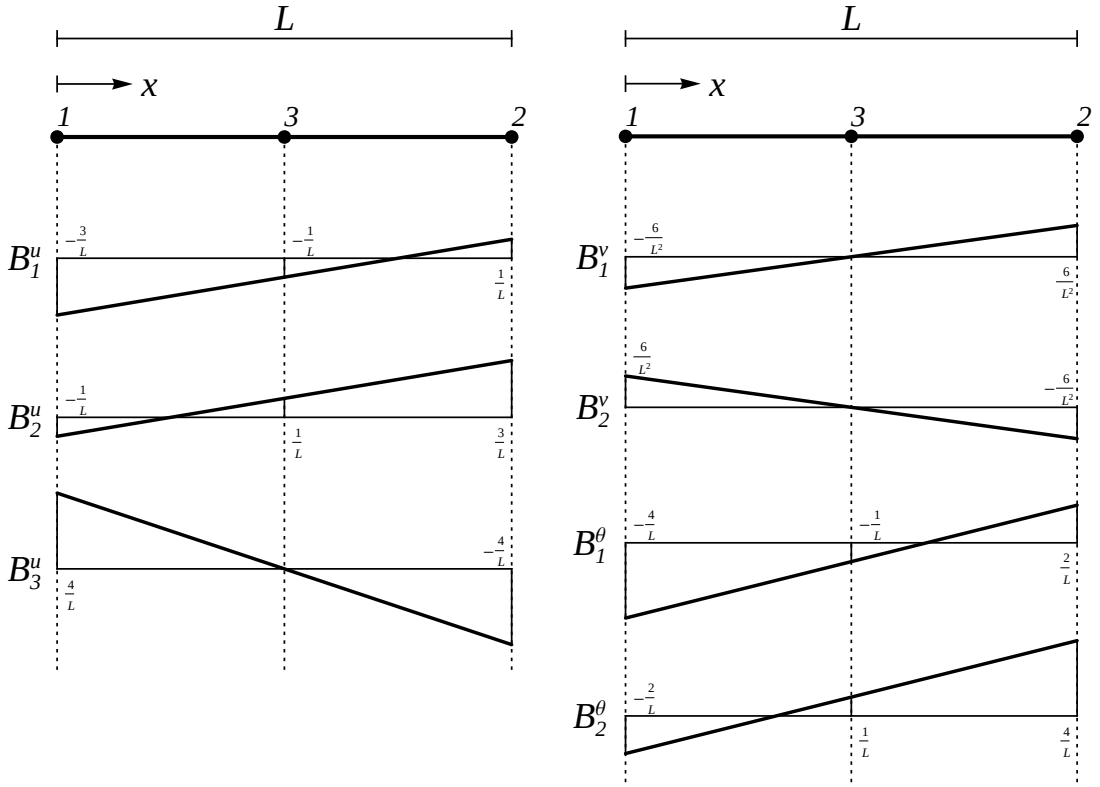

Figure 3.4: Interpolation functions for axial strain due to axial (left) and transversal displacement (right).

Slika 3.4: Interpolacijske funkcije za osno deformacijo zaradi osnega (levo) in prečnega pomika (desno).

3.2.2 Relations between global and local quantities

3.2.2.1 Real degrees of freedom

A structure is modeled with a mesh of finite elements. A part of such mesh is depicted in Fig. 3.5. The finite elements are connected only with their end nodes, while the middle node is strictly local. After the meshing procedure the model has n_{EN} "end nodes" and n_{MN} "middle nodes". The latter number is equal to the number of finite elements. Let us label the end nodes with numbers from 1 to n_{EN} and the middle nodes with numbers from $n_{EN}+1$ to $n_{EN}+n_{MN}$.

Each of the end nodes has three degrees of freedom - displacement U parallel to the global X axis, displacement V parallel to the global Y axis, and rotation Θ about the axis, perpendicular to the XY plane. The middle nodes have only one degree of freedom - displacement W parallel to the axis of the finite element, see Fig. 3.5. The structure has in total $n_{DOF} = 3n_{EN} + n_{MN}$ degrees of freedom, which are collected in the vector $\mathbf{d}^{\text{str}}$.

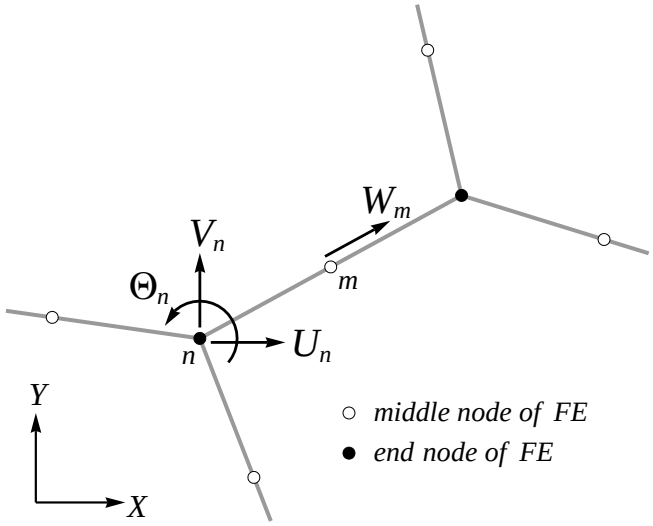

Figure 3.5: Degrees of freedom at nodes of the finite element mesh.
Slika 3.5: Prostostne stopnje v vozliščih mreže končnih elementov.

$$\begin{aligned}&\mathbf{d}^{\text{str}} = \left\{\mathbf{d}_{EN}^T, \mathbf{d}_{MN}^T\right\}^T, \quad \mathbf{d}_{EN} = \left\{U_1, V_1, \Theta_1, U_2, V_2, \Theta_2, \ \ldots\ , U_{n_{EN}}, V_{n_{EN}}, \Theta_{n_{EN}}\right\}^T, \\ &\mathbf{d}_{MN} = \left\{W_{n_{EN}+1}, W_{n_{EN}+2}, \ \ldots\ , W_{n_{EN}+n_{MN}}\right\}^T\end{aligned} \tag{3.9}$$

Let us now consider a finite element (e) with end nodes (n_1), (n_2) and a middle node (n_3). The local x axis is parallel to the axis of the element, with x increasing from node (n_1) towards node (n_2), see Fig. 3.6. The element's degrees of freedom, defined in the local coordinate system, are collected in the vector $\mathbf{d}^{(e)}$, in accordance with equation (3.8). Global degrees of freedom, associated with the nodes of the element can be similarly organized into vector $\mathbf{D}^{(e)}$. The two are connected with a transformation matrix $\mathbf{R}^{(e)}$. Zeros are replaced by dots for clarity. $\phi^{(e)}$ is the angle between the global X axis and the local x axis (rotation of the local coordinate system).

$$\mathbf{d}^{(e)} = \mathbf{R}^{(e)}\mathbf{D}^{(e)} \tag{3.10}$$

$$\mathbf{d}^{(e)} = \left\{u_1^{(e)}, u_2^{(e)}, u_3^{(e)}, v_1^{(e)}, v_2^{(e)}, \theta_1^{(e)}, \theta_2^{(e)}\right\}^T, \ \mathbf{D}^{(e)} = \left\{U_{n_1}, U_{n_2}, W_{n_3}, V_{n_1}, V_{n_2}, \Theta_{n_1}, \Theta_{n_2}\right\}^T$$

$$\mathbf{R}^{(e)} = \begin{bmatrix} \cos\phi^{(e)} & \cdot & \cdot & \sin\phi^{(e)} & \cdot & \cdot & \cdot \\ \cdot & \cos\phi^{(e)} & \cdot & \cdot & \sin\phi^{(e)} & \cdot & \cdot \\ \cdot & \cdot & 1 & \cdot & \cdot & \cdot & \cdot \\ -\sin\phi^{(e)} & \cdot & \cdot & \cos\phi^{(e)} & \cdot & \cdot & \cdot \\ \cdot & -\sin\phi^{(e)} & \cdot & \cdot & \cos\phi^{(e)} & \cdot & \cdot \\ \cdot & \cdot & \cdot & \cdot & \cdot & 1 & \cdot \\ \cdot & \cdot & \cdot & \cdot & \cdot & \cdot & 1 \end{bmatrix} \tag{3.11}$$

Vector $\mathbf{D}^{(e)}$ contains those components of vector $\mathbf{d}^{\text{str}}$ that correspond to the nodes of the finite element. The selection of appropriate components is done by matrix $\mathbf{P}^{(e)}$ of size $7 \times n_{DOF}$ with only seven non-zero components.

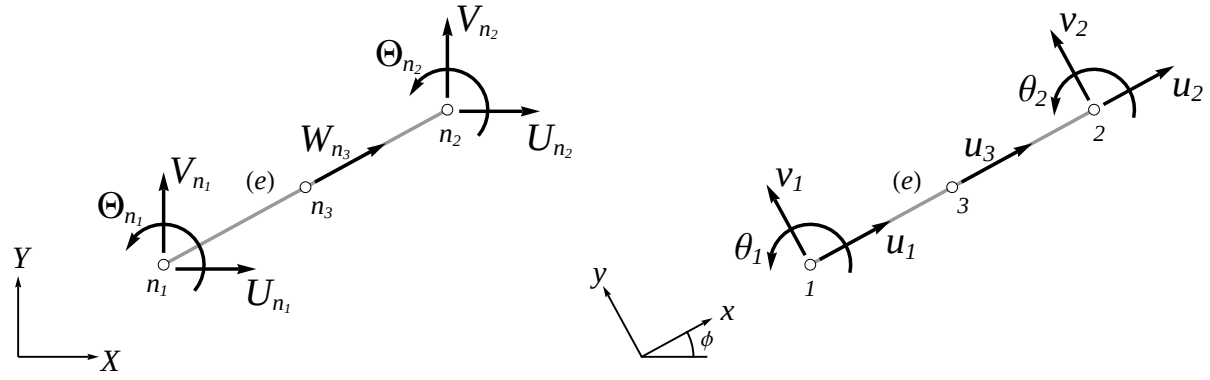

Figure 3.6: Global (left) and local (right) degrees of freedom, associated with a finite element.
Slika 3.6: Globalne (levo) in lokalne (desno) prostostne stopnje, povezane s končnim elementom.

$$\begin{aligned}&\mathbf{D}^{(e)} = \mathbf{P}^{(e)}\mathbf{d}^{\text{str}}\\ &P^{(e)}_{1,\,3n_1-2} = P^{(e)}_{2,\,3n_2-2} = P^{(e)}_{3,\,3n_{EN}+(n_3-n_{EN})} = P^{(e)}_{4,\,3n_1-1} = P^{(e)}_{5,\,3n_2-1} = P^{(e)}_{6,\,3n_1} = P^{(e)}_{7,\,3n_2} = 1\end{aligned} \tag{3.12}$$

Obeying equations (3.10) and (3.12), we can finally write the relation between the local degrees of freedom of the finite element (e) and the global degrees of freedom of the structure.

$$\mathbf{d}^{(e)} = \mathbf{R}^{(e)}\mathbf{P}^{(e)}\mathbf{d}^{\text{str}} \tag{3.13}$$

3.2.2.2 Virtual degrees of freedom

Virtual displacements are a kinematically admissible variation of real displacements. As with the real displacements, they are interpolated between the nodal values with appropriate interpolation functions. The virtual deformation of the structure is therefore defined by the virtual displacements of its nodes.

The global virtual degrees of freedom (virtual displacements of the structure) $\hat{\mathbf{d}}^{\text{str}}$, the virtual displacements of the element $\hat{\mathbf{d}}^{(e)}$ and the selection $\hat{\mathbf{D}}^{(e)}$ of global virtual displacements, associated with the element (e), are defined analogously to the real quantities $\mathbf{d}^{\text{str}}$, $\mathbf{d}^{(e)}$ and $\mathbf{D}^{(e)}$, defined in equations (3.9) and (3.11).

$$\begin{aligned}&\hat{\mathbf{d}}^{\text{str}} = \left\{\hat{\mathbf{d}}^T_{EN}, \hat{\mathbf{d}}^T_{MN}\right\}^T,\\ &\hat{\mathbf{d}}_{EN} = \left\{\hat{U}_1, \hat{V}_1, \hat{\Theta}_1, \ \ldots\ , \hat{U}_{n_{EN}}, \hat{V}_{n_{EN}}, \hat{\Theta}_{n_{EN}}\right\}^T,\ \ \hat{\mathbf{d}}_{MN} = \left\{\hat{W}_{n_{EN}+1}, \ \ldots\ , \hat{W}_{n_{EN}+n_{MN}}\right\}^T\\ &\hat{\mathbf{d}}^{(e)} = \left\{\hat{u}^{(e)}_1, \hat{u}^{(e)}_2, \hat{u}^{(e)}_3, \hat{v}^{(e)}_1, \hat{v}^{(e)}_2, \hat{\theta}^{(e)}_1, \hat{\theta}^{(e)}_2\right\}^T,\ \ \hat{\mathbf{D}}^{(e)} = \left\{\hat{U}_{n_1}, \hat{U}_{n_2}, \hat{W}_{n_3}, \hat{V}_{n_1}, \hat{V}_{n_2}, \hat{\Theta}_{n_1}, \hat{\Theta}_{n_2}\right\}^T\end{aligned} \tag{3.14}$$

Relations between them are equivalent to equations (3.10)-(3.13), matrices $\mathbf{R}^{(e)}$ and $\mathbf{P}^{(e)}$ remain the same.

$$\hat{\mathbf{d}}^{(e)} = \mathbf{R}^{(e)}\hat{\mathbf{D}}^{(e)}, \quad \hat{\mathbf{D}}^{(e)} = \mathbf{P}^{(e)}\hat{\mathbf{d}}^{\text{str}}, \quad \hat{\mathbf{d}}^{(e)} = \mathbf{R}^{(e)}\mathbf{P}^{(e)}\hat{\mathbf{d}}^{\text{str}} \tag{3.15}$$

3.2.2.3 Internal forces

Internal forces can be organized in the same way as the generalized displacements. Each degree of freedom from the vector $\mathbf{d}^{\text{str}}$ is accompanied by a corresponding internal force. Analogously to equation (3.9) we can write:

$$\begin{aligned}\mathbf{f}^{\text{int,str}} &= \left\{ \mathbf{f}_{EN}^{\text{int}T}, \mathbf{f}_{MN}^{\text{int}T} \right\}^T, \quad \mathbf{f}_{EN}^{\text{int}} = \left\{ f_{U_1}^{\text{int}}, f_{V_1}^{\text{int}}, f_{\Theta_1}^{\text{int}}, f_{U_2}^{\text{int}}, f_{V_2}^{\text{int}}, f_{\Theta_2}^{\text{int}}, \ \cdots, f_{U_{n_{EN}}}^{\text{int}}, f_{V_{n_{EN}}}^{\text{int}}, f_{\Theta_{n_{EN}}}^{\text{int}} \right\}^T \\ \mathbf{f}_{MN}^{\text{int}} &= \left\{ f_{W_{n_{EN}+1}}^{\text{int}}, f_{W_{n_{EN}+2}}^{\text{int}}, \ \cdots, f_{W_{n_{EN}+n_{MN}}}^{\text{int}} \right\}^T\end{aligned} \tag{3.16}$$

Vector $\mathbf{f}_{EN}^{\text{int}}$ contains the internal forces of the "end nodes" - for each node a pair of forces, parallel to global X and Y axis, and a moment around the axis, perpendicular to the XY plane. They are labeled with f_U^{int}, f_V^{int} and f_Θ^{int}, respectively. Vector $\mathbf{f}_{MN}^{\text{int}}$ contains the internal forces of the "middle nodes", which are parallel to the local x axis, and labeled with f_W^{int}, see Fig. 3.7.

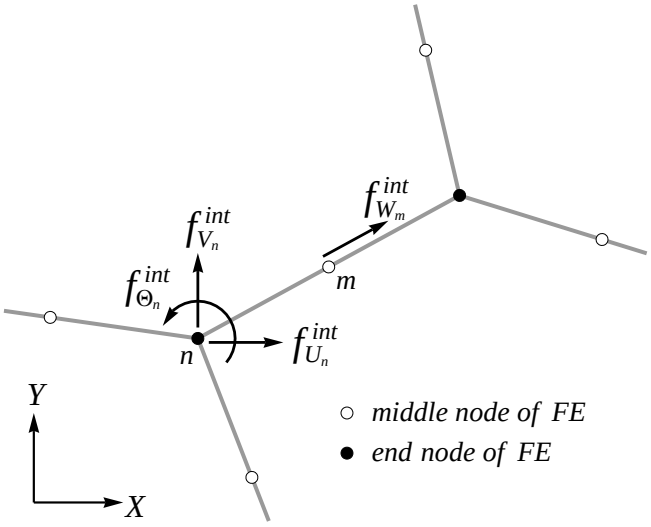

Figure 3.7: Internal forces, corresponding to degrees of freedom at nodes of the finite element mesh.
Slika 3.7: Notranje sile, ki ustrezajo prostostnim stopnjam v vozliščih mreže končnih elementov.

Internal forces at a certain node of the structure are composed of contributions from all the elements, joined in that node. Let us now take a closer look at a finite element (e). The internal forces of the element are defined in the local coordinate system and correspond to the local degrees of freedom $\mathbf{d}^{(e)}$, see Fig. 3.8 (right). They are collected in the vector $\mathbf{f}^{\text{int},(e)}$. The forces can be transformed by matrix $\mathbf{R}^{(e)}$ so as to match the directions of the global internal forces $\mathbf{f}^{\text{int,str}}$. The new, transformed vector is designated with $\mathbf{F}^{\text{int},(e)}$, Fig. 3.8 (left). The transformation matrix $\mathbf{R}^{(e)}$ is the same as in equation (3.11).

$$\mathbf{f}^{\text{int},(e)} = \mathbf{R}^{(e)} \mathbf{F}^{\text{int},(e)} \quad \Leftrightarrow \quad \mathbf{F}^{\text{int},(e)} = \mathbf{R}^{(e)^{-1}} \mathbf{f}^{\text{int},(e)} \tag{3.17}$$

$$\begin{aligned}\mathbf{f}^{\text{int},(e)} &= \left\{ f_{u_1}^{\text{int},(e)}, f_{u_2}^{\text{int},(e)}, f_{u_3}^{\text{int},(e)}, f_{v_1}^{\text{int},(e)}, f_{v_2}^{\text{int},(e)}, f_{\theta_1}^{\text{int},(e)}, f_{\theta_2}^{\text{int},(e)} \right\}^T \\ \mathbf{F}^{\text{int},(e)} &= \left\{ f_{U_{n_1}}^{\text{int},(e)}, f_{U_{n_2}}^{\text{int},(e)}, f_{W_{n_3}}^{\text{int},(e)}, f_{V_{n_1}}^{\text{int},(e)}, f_{V_{n_2}}^{\text{int},(e)}, f_{\Theta_{n_1}}^{\text{int},(e)}, f_{\Theta_{n_2}}^{\text{int},(e)} \right\}^T\end{aligned} \tag{3.18}$$

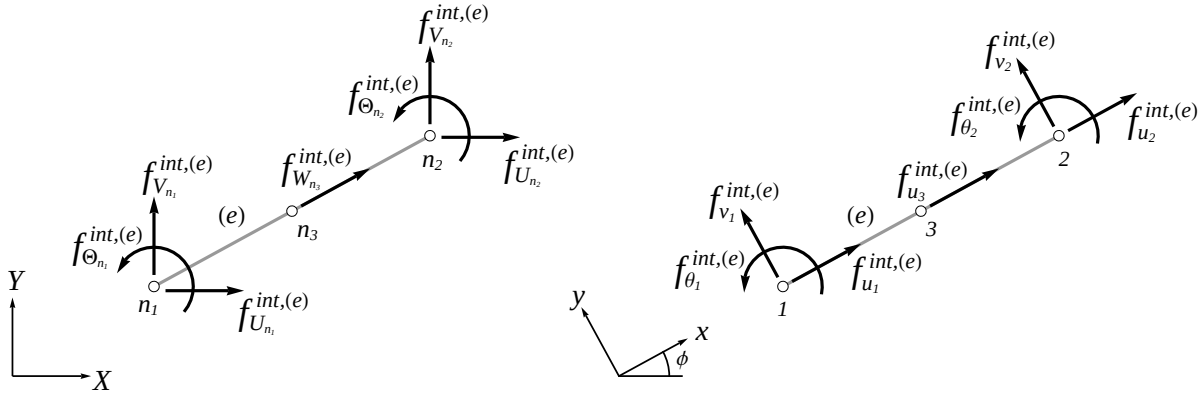

Figure 3.8: Contribution of a finite element to internal forces of the structure in global (left) and local (right) coordinate system.

Slika 3.8: Prispevek končnega elementa k notranjim silam konstrukcije v globalnem (levo) in lokalnem (desno) koordinatnem sistemu.

The components of the global vector $\mathbf{f}^{\text{int,str}}$ are computed by summing the contributions of individual finite elements, written in $\mathbf{F}^{\text{int},(e)}$. Matrix $\mathbf{P}^{(e)}$ is defined in (3.12).

$$\mathbf{f}^{\text{int,str}} = \sum_{e=1}^{n_{FE}} \mathbf{P}^{(e)^T} \mathbf{F}^{\text{int},(e)} \tag{3.19}$$

Transformation (3.17) and summation (3.19) can be joined in a simplified notation. Operator A represents the assembly of the internal forces and n_{FE} is the total number of finite elements.

$$\mathbf{f}^{\text{int,str}} = \sum_{e=1}^{n_{FE}} \mathbf{P}^{(e)^T} \mathbf{R}^{(e)^{-1}} \mathbf{f}^{\text{int},(e)} = \mathop{\mathsf{A}}_{e=1}^{n_{FE}} \left[\mathbf{f}^{\text{int},(e)} \right] \tag{3.20}$$

Another useful relation can be observed. For rotation matrix $\mathbf{R}^{(e)}$ it holds $\mathbf{R}^T = \mathbf{R}^{-1}$ or $\mathbf{R}^T\mathbf{R} = \mathbf{I}$, where $\mathbf{I}$ is the identity matrix. By using this property as well as equations (3.15) and (3.17) we can conclude that the scalar product of virtual displacements and internal forces is equal in local and global coordinate system.

$$\hat{\mathbf{d}}^{(e)^T} \mathbf{f}^{\text{int},(e)} = \hat{\mathbf{D}}^{(e)^T} \mathbf{R}^{(e)^T} \mathbf{R}^{(e)} \mathbf{F}^{\text{int},(e)} = \hat{\mathbf{D}}^{(e)^T} \mathbf{F}^{\text{int},(e)} \tag{3.21}$$

3.2.3 Virtual work equation

Equilibrium of a structure can be described in a weak from, by the virtual work principle, which states that the virtual work of internal forces G^{int} on any kinematically admissible perturbation of displacements - virtual displacements - must be equal to the work of external forces G^{ext} on the same displacements.

$$G^{\text{int}} - G^{\text{ext}} = 0 \tag{3.22}$$

Since we are dealing with a discretized model, the external loads are defined at the nodes of the structure. Linear loads have to be transferred to the nodes appropriately. The virtual work of external forces is therefore computed simply as a scalar product of the vector of virtual nodal displacements of the structure $\hat{\mathbf{d}}^{\text{str}}$ and the corresponding vector of generalized external forces $\mathbf{f}^{\text{ext,str}}$. Virtual displacements are defined analogously to the real displacements in equation (3.9) and the external forces analogously to the internal forces in equation (3.16).

$$G^{\text{ext}} = \hat{\mathbf{d}}^{\text{str}^T} \mathbf{f}^{\text{ext,str}} = \sum_{j=1}^{n_{DOF}} \hat{d}_j^{\text{str}} f_j^{\text{ext,str}} \tag{3.23}$$

Here n_{DOF} is the number of the structure's degrees of freedom. Many components of the sum (3.23) may be zero. The virtual work of internal forces is composed of contributions from individual finite elements.

$$G^{\text{int}} = \sum_{e=1}^{n_{FE}} G^{\text{int},(e)}, \quad G^{\text{int},(e)} = \int_{V^{(e)}} \hat{\varepsilon} \sigma dV \tag{3.24}$$

For each element $G^{\text{int},(e)}$ is computed by multiplying the stress field with the virtual strain field and integrating the product over the volume of the element. The virtual strain is defined individually for each layer of the beam which enables virtual discontinuities $\hat{\alpha}^i$ to be introduced in each layer. The interpolation is done in the same manner as for the real strain in equation (3.6), except that operator G_R^i is replaced by G_V^i. Differentiation between the two operators gives us more freedom to define them according to our needs. The issue will be addressed in the next section. Note that the additional part of the virtual strain $\hat{\varepsilon}^{i,add}$ only exists in the layers that have already developed a discontinuity (cracked layers). In non-cracked layers, the virtual strain consists only of the regular part $\hat{\bar{\varepsilon}}^i$.

$$\hat{\varepsilon}^i\left(x, x_d^i\right) = \overbrace{\mathbf{B}^u(x)\hat{\mathbf{u}} - y^i\left(\mathbf{B}^v(x)\hat{\mathbf{v}} + \mathbf{B}^\theta(x)\hat{\boldsymbol{\theta}}\right)}^{\hat{\bar{\varepsilon}}^i} + \overbrace{G_V^i\left(x, x_d^i\right)\hat{\alpha}^i}^{\hat{\varepsilon}^{i,add}} = \breve{\mathbf{B}}^i\hat{\mathbf{d}} + G_V^i\hat{\alpha}^i \tag{3.25}$$

The volume integral in equation (3.24) is divided into an integral over the length and an integral over the cross-section of the element. The latter can be replaced by a sum over the layers, since everything is assumed to be constant over the cross-section of a layer. The virtual strain is replaced by the whole expression (3.25) for $n_{CL}^{(e)}$ cracked layers and by its regular part $\hat{\bar{\varepsilon}}^i$ for $\left(n_L - n_{CL}^{(e)}\right)$ non-cracked layers, where n_L is the total number of layers in the finite element. Obtained expression is rearranged to produce internal forces, corresponding to the virtual degrees of freedom of the finite element $\hat{\mathbf{d}}^{(e)}$, as defined in (3.14). Index (e) is omitted until the last line. For the sake of simplicity it is assumed that the cracked layers are numbered with 1, 2, …, $n_{CL}^{(e)}$.

$$\begin{aligned}
G^{\text{int},(e)} &= \int_V \hat{\varepsilon}\sigma dV = \iint_{L\,A} \hat{\varepsilon}\sigma dA dx = \int_L \sum_i \hat{\varepsilon}^i \sigma^i A^i dx = \\
&= \int_L \mathbf{B}^u \hat{\mathbf{u}} \sum_{i=1}^{n_L} \sigma^i A^i dx + \int_L \left(\mathbf{B}^v\hat{\mathbf{v}} + \mathbf{B}^\theta\hat{\boldsymbol{\theta}}\right) \sum_{i=1}^{n_L} \left(-y^i\sigma^i A^i\right) dx + \int_L \sum_{i=1}^{n_{CL}} G_V^i \hat{\alpha}^i \sigma^i A^i dx = \\
&= \hat{\mathbf{u}}^T \int_L \mathbf{B}^{u^T} \sum_{i=1}^{n_L} \sigma^i A^i dx + \hat{\mathbf{v}}^T \int_L \mathbf{B}^{v^T} \sum_{i=1}^{n_L} \left(-y^i\sigma^i A^i\right) dx + \hat{\boldsymbol{\theta}}^T \int_L \mathbf{B}^{\theta^T} \sum_{i=1}^{n_L} \left(-y^i\sigma^i A^i\right) dx + \\
&+ \sum_{i=1}^{n_{CL}} \hat{\alpha}^i \int_L G_V^i \sigma^i A^i dx = \hat{\mathbf{d}}^{(e)^T} \mathbf{f}^{\text{int},(e)} + \sum_{i=1}^{n_{CL}^{(e)}} \hat{\alpha}^{(e),i} h^{(e),i}
\end{aligned} \tag{3.26}$$

A condensed form of expressions (3.14) and (3.18) for $\hat{\mathbf{d}}^{(e)}$ and $\mathbf{f}^{\text{int},(e)}$ can be used.

$$\hat{\mathbf{d}}^{(e)^T} = \left\{\hat{\mathbf{u}}^T, \hat{\mathbf{v}}^T, \hat{\boldsymbol{\theta}}^T\right\}, \quad \mathbf{f}^{\text{int},(e)^T} = \left\{\mathbf{f}^{u,\text{int},(e)^T}, \mathbf{f}^{v,\text{int},(e)^T}, \mathbf{f}^{\theta,\text{int},(e)^T}\right\} \tag{3.27}$$

Components of $\mathbf{f}^{\text{int},(e)}$ are defined in (3.28). The order of integration and summation can be reversed. Therefore we can compute the internal forces as a sum of contributions of individual layers, which proves to be very helpful in the computational procedure. Here n_L is the total number of layers in the finite element.

$$\begin{aligned}
\mathbf{f}^{u,\text{int},(e)} &= \int_L \mathbf{B}^{u^T} \sum_{i=1}^{n_L} \sigma^i A^i dx = \sum_{i=1}^{n_L} \int_L \mathbf{B}^{u^T} \sigma^i A^i dx \\
\mathbf{f}^{v,\text{int},(e)} &= \int_L \mathbf{B}^{v^T} \sum_{i=1}^{n_L} \left(-y^i \sigma^i A^i\right) dx = \sum_{i=1}^{n_L} \left(- \int_L \mathbf{B}^{v^T} y^i \sigma^i A^i dx \right) \\
\mathbf{f}^{\theta,\text{int},(e)} &= \int_L \mathbf{B}^{\theta^T} \sum_{i=1}^{n_L} \left(-y^i \sigma^i A^i\right) dx = \sum_{i=1}^{n_L} \left(- \int_L \mathbf{B}^{\theta^T} y^i \sigma^i A^i dx \right)
\end{aligned} \tag{3.28}$$

A shorter notation (3.29) will also be used, where $\mathbf{f}^{\text{int},(e),i}$ is contribution of the i-th layer to the vector of internal forces of the finite element.

$$\mathbf{f}^{\text{int},(e)} = \sum_{i=1}^{n_L} A^i \int_L \begin{bmatrix} \mathbf{B}^{u^T} \\ -y^i \mathbf{B}^{v^T} \\ -y^i \mathbf{B}^{\theta^T} \end{bmatrix} \sigma^i dx = \sum_{i=1}^{n_L} \underbrace{A^i \int_L \check{\mathbf{B}}^{i^T} \sigma^i dx}_{\mathbf{f}^{\text{int},(e),i}} \tag{3.29}$$

The last term of the last line in (3.26) is the additional virtual work due to enhanced kinematics. The sum has $n_{CL}^{(e)}$ summands, one for each cracked layer. Quantity $h^{(e),i}$ is an equivalent of internal force, corresponding to the virtual displacement jump $\hat{\alpha}^{(e),i}$, and is defined as follows.

$$h^{(e),i} = \int_L G_V^i \sigma^i A^i dx, \quad i = 1, 2, \ldots, n_{CL}^{(e)} \tag{3.30}$$

The virtual work of external and internal forces in the equilibrium equation (3.22) is replaced by expressions (3.23) and (3.24), respecting (3.26) and (3.21). Finally, the second of equations (3.15) allows us to express the weak equilibrium in the manner of global virtual displacement vector $\hat{\mathbf{d}}^{\text{str}}$ and virtual displacement jumps $\hat{\alpha}^{(e),i}$.

$$
\begin{aligned}
0 &= \sum_{e=1}^{n_{FE}} G^{\text{int},(e)} - G^{\text{ext}} = \\
&= \sum_{e=1}^{n_{FE}} \left(\hat{\mathbf{D}}^{(e)^T} \mathbf{F}^{\text{int},(e)} + \sum_{i=1}^{n_{CL}^{(e)}} \hat{\alpha}^{(e),i} h^{(e),i} \right) - \hat{\mathbf{d}}^{\text{str}^T} \mathbf{f}^{\text{ext,str}} = \\
&= \sum_{e=1}^{n_{FE}} \hat{\mathbf{d}}^{\text{str}^T} \mathbf{P}^{(e)^T} \mathbf{F}^{\text{int},(e)} + \sum_{e=1}^{n_{FE}} \sum_{i=1}^{n_{CL}^{(e)}} \hat{\alpha}^{(e),i} h^{(e),i} - \hat{\mathbf{d}}^{\text{str}^T} \mathbf{f}^{\text{ext,str}} = \\
&= \hat{\mathbf{d}}^{\text{str}^T} \sum_{e=1}^{n_{FE}} \mathbf{P}^{(e)^T} \mathbf{F}^{\text{int},(e)} + \sum_{e=1}^{n_{FE}} \sum_{i=1}^{n_{CL}^{(e)}} \hat{\alpha}^{(e),i} h^{(e),i} - \hat{\mathbf{d}}^{\text{str}^T} \mathbf{f}^{\text{ext,str}} = \\
&= \hat{\mathbf{d}}^{\text{str}^T} \left(\mathbf{f}^{\text{int,str}} - \mathbf{f}^{\text{ext,str}} \right) + \sum_{e=1}^{n_{FE}} \sum_{i=1}^{n_{CL}^{(e)}} \hat{\alpha}^{(e),i} h^{(e),i}
\end{aligned}
\tag{3.31}
$$

Equilibrium (3.31) must hold for any kinematically admissible virtual displacements $\hat{\mathbf{d}}^{\text{str}}$ and virtual displacement jumps $\hat{\alpha}^{(e),i}$. From this requirement we can conclude:

$$
\begin{aligned}
&\mathbf{f}^{\text{int,str}} - \mathbf{f}^{\text{ext,str}} = \mathbf{0} \\
&\forall e \in \{1,2,\ldots,n_{FE}\},\ \forall i \in \left\{1,2,\ldots,n_{CL}^{(e)}\right\}: \quad h^{(e),i} = 0
\end{aligned}
\tag{3.32}
$$

The first equation in (3.32) represents the global equilibrium or equilibrium of every individual node of the structure. Here $\mathbf{f}^{\text{int,str}}$ and $\mathbf{f}^{\text{ext,str}}$ are vectors of internal and external forces on the structural level. They correspond in position and direction to the degrees of freedom of the structure. Their length is equal to the total number of degrees of freedom n_{DOF}. The second equation in (3.32) is an additional constraint for the stress in cracked layers. The number of cracked layers $n_{CL}^{(e)}$ is generally different for each element, and can also be zero. It has been assumed in equation (3.32) that the cracked layers are numbered with consecutive numbers from 1 to $n_{CL}^{(e)}$.

Let us now examine $h^{(e),i}$, defined in expression (3.30). It will be shown in the next section that the operator G_V^i consists of a continuous part $\bar{G}_V^i$ and a discrete part $\delta_{x_d^i}$, which is a Dirac delta function. Integration of the latter is performed by the following rule.

$$
G_V^i = \bar{G}_V^i + \delta_{x_d^i}, \quad \int_L g(x)\, \delta_{x_d^i} dx = g\left(x_d^i\right) \tag{3.33}
$$

Implementation of (3.33) allows a further development of expression (3.30). Here $\sigma^i\big|_{x_d^i}$ is the value of stress function $\sigma^i(x)$, evaluated at local coordinate x_d^i. We assign to it a new symbol t^i and define it as the traction at the discontinuity.

$$
h^{(e),i} = \int_L \left(\bar{G}_V^i + \delta_{x_d^i} \right) \sigma^i A^i dx = A^i \int_L \bar{G}_V^i \sigma^i dx + A^i \sigma^i\big|_{x_d^i} = A^i \left(\int_L \bar{G}_V^i \sigma^i dx + t^i \right) \tag{3.34}
$$

Inserting (3.34) into the second of equilibrium equations (3.32) provides a new aspect to its meaning. Equation (3.35) can be interpreted as a weak form (integral form) of equilibrium between the traction at the discontinuity t^i and the stress in the bulk σ^i. Being confined to a single finite element, we can refer to it as local equilibrium.

$$h^{(e),i} = 0 \quad \Leftrightarrow \quad t^i = -\int_L \bar{G}_V^i \sigma^i dx \tag{3.35}$$

3.2.4 Derivation of operators G_R and G_V

3.2.4.1 Derivation of operator G_R for real strain

Interpolation of the axial displacement field $u^i(x)$ in the i-th layer is defined in equation (3.5). The regular part $\tilde{u}^i(x)$ is computed from the axial displacement of the middle axis $\tilde{u}(x)$ and rotation $\tilde{\theta}(x)$ of the cross-section. Since they are both quadratic functions of x, $\tilde{u}^i(x)$ is quadratic as well. By the definition it is interpolated between the nodal displacements **u**, **v** and $\boldsymbol{\theta}$ of the finite element. However, if we regard the layer as a special type of a bar with quadratic axial displacement field, then $\tilde{u}^i(x)$ can be interpolated between the nodal displacements $\mathbf{u}^i$ of this bar, see Fig. 3.9. If they are positioned at the ends and in the middle of the layer, the interpolation can be performed with the original interpolation functions $\mathbf{N}^u(x)$ for axial displacements, defined in (3.1).

$$\tilde{u}^i(x) = \tilde{u}(x) - y^i\tilde{\theta}(x) = \mathbf{N}^u(x)\,\mathbf{u}^i, \quad \mathbf{u}^i = \left\{u_1^i, u_2^i, u_3^i\right\}^T \tag{3.36}$$

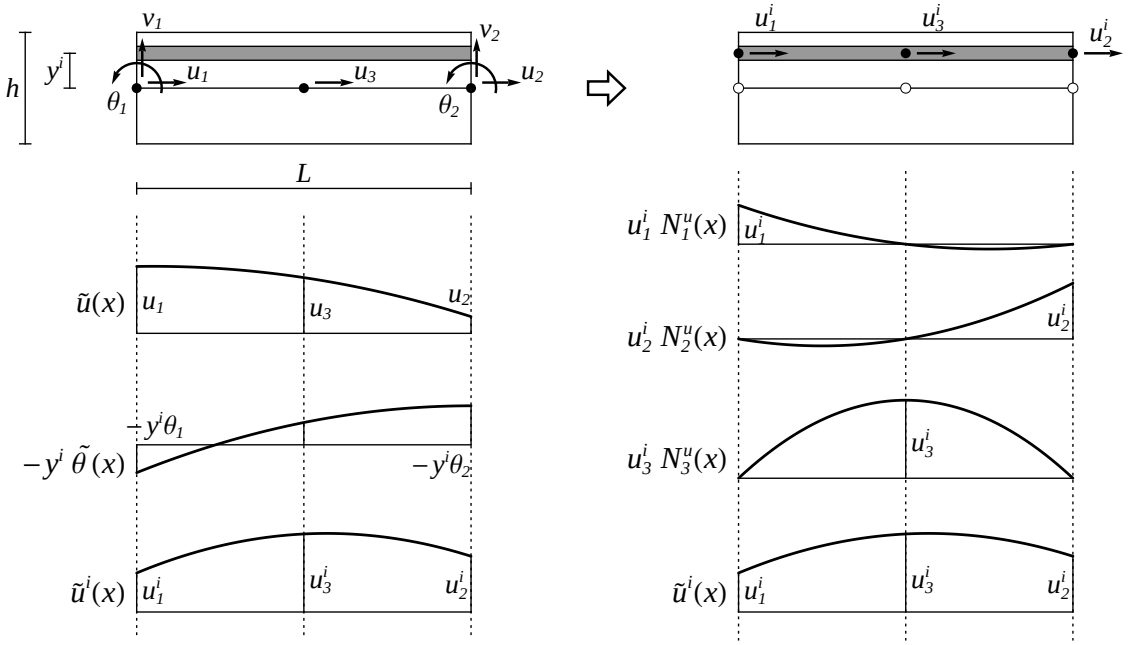

Figure 3.9: Interpolation of standard axial displacement in i-th layer between nodal displacements of the finite element (left) and between nodal axial displacements of the layer (right).

Slika 3.9: Interpolacija standardnega osnega pomika v i-tem sloju med prostostne stopnje končnega elementa (levo) in med vozliščne osne pomike sloja (desno).

The "nodal" displacements $\mathbf{u}^i$ of the i-th layer can be calculated from $\tilde{u}^i(x)$ by inserting for x the coordinates of the layer's "nodes", which are 0, L and $L/2$.

$$\begin{aligned}\mathbf{u}^i &= \left\{ \tilde{u}^i\big|_{x=0}, \tilde{u}^i\big|_{x=L}, \tilde{u}^i\big|_{x=L/2} \right\}^T = \\ &= \left\{ u_1 - y^i\theta_1, u_2 - y^i\theta_2, u_3 - y^i\left(-\frac{3\left(v_1-v_2\right)}{2L} - \frac{\theta_1+\theta_2}{4}\right) \right\}^T\end{aligned} \tag{3.37}$$

The regular axial displacement $\tilde{u}^i(x)$ is enriched with the additional part $u^{i,add}(x,x_d)$, which represents the additional axial displacement due to occurrence of a discontinuity in the layer. It is determined by the interpolation function $M^i\left(x,x_d^i\right)$ and the displacement jump α^i at the discontinuity of the layer.

$$u^i\left(x,x_d^i\right) = \tilde{u}^i(x) + M^i\left(x,x_d^i\right)\alpha^i \tag{3.38}$$

The interpolation function M^i must not influence the nodal displacements $\mathbf{u}^i$ of the layer, which means that it must have zero values at all nodes of the layer, and it must have a unit jump at the location of the discontinuity x_d^i. The easiest way to meet the requirements is to use a combination of the Heaviside function and the suitable choice of shape functions $\mathbf{N}^u$.

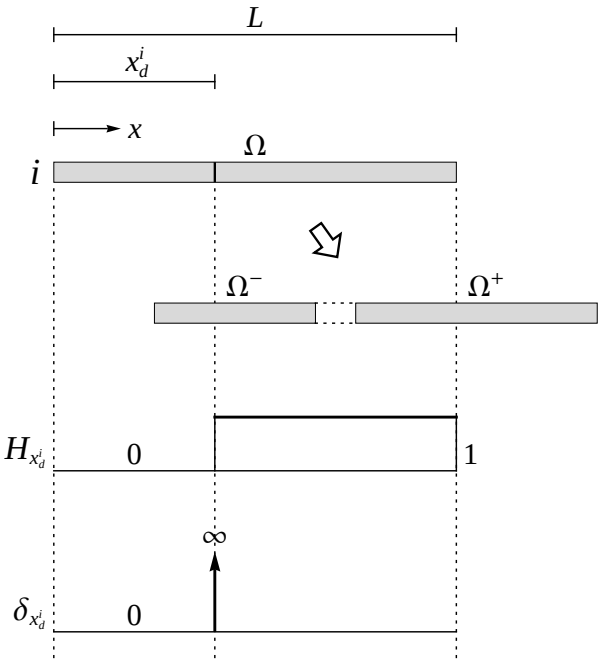

Figure 3.10: Domain and sub-domains of a cracked layer. Heaviside and Dirac-delta functions.
Slika 3.10: Domena in poddomeni razpokanega sloja. Heaviside-ova in Dirac-delta funkcija.

Domain Ω of the cracked layer is divided by the discontinuity into two parts. Ω^- is the part before the discontinuity, with $x < x_d^i$, and Ω^+ is the part after the discontinuity, with $x \geq x_d^i$, see Fig. 3.10. The value of the Heaviside function is 0 on Ω^- and 1 on Ω^+. Its derivative is the Dirac delta function $\delta_{x_d^i}$, which has an infinite value at x_d^i and zero value elsewhere.

$$H_{x_d^i} = \begin{cases} 0; & x < x_d^i \\ 1; & x \geq x_d^i \end{cases} \qquad \frac{\partial H_{x_d^i}}{\partial x} = \delta_{x_d^i} = \begin{cases} \infty; & x = x_d^i \\ 0; & \text{otherwise} \end{cases} \tag{3.39}$$

Heaviside function $H_{x_d^i}$ satisfies the requirement of a unit jump at the discontinuity. Its value, however, is only zero on Ω^-, and not at all nodes of the layer. This can be fixed by subtracting from it those shape functions $N_j^u \in \mathbf{N}^u$, that correspond to the nodes j, included in Ω^+. Since N_j^u are continuous and have zero values at all nodes except j, they will not affect previously fulfilled demands.

$$M^i = H_{x_d^i} - \sum_{j \in \Omega^+} N_j^u \tag{3.40}$$

To avoid complications, let us decide that the discontinuity can occur infinitesimally close to a node, but not at the node itself. Two options remain for the function M^i. If the discontinuity appears in the left half of the layer, Ω^+ contains nodes 2 and 3, and if it appears in the right half, Ω^+ contains only node 2, see Fig. 3.11.

$$M^i = \begin{cases} H_{x_d^i} - (N_2^u + N_3^u); & 0 < x_d^i < L/2 \\ H_{x_d^i} - N_2^u; & L/2 < x_d^i < L \end{cases} \tag{3.41}$$

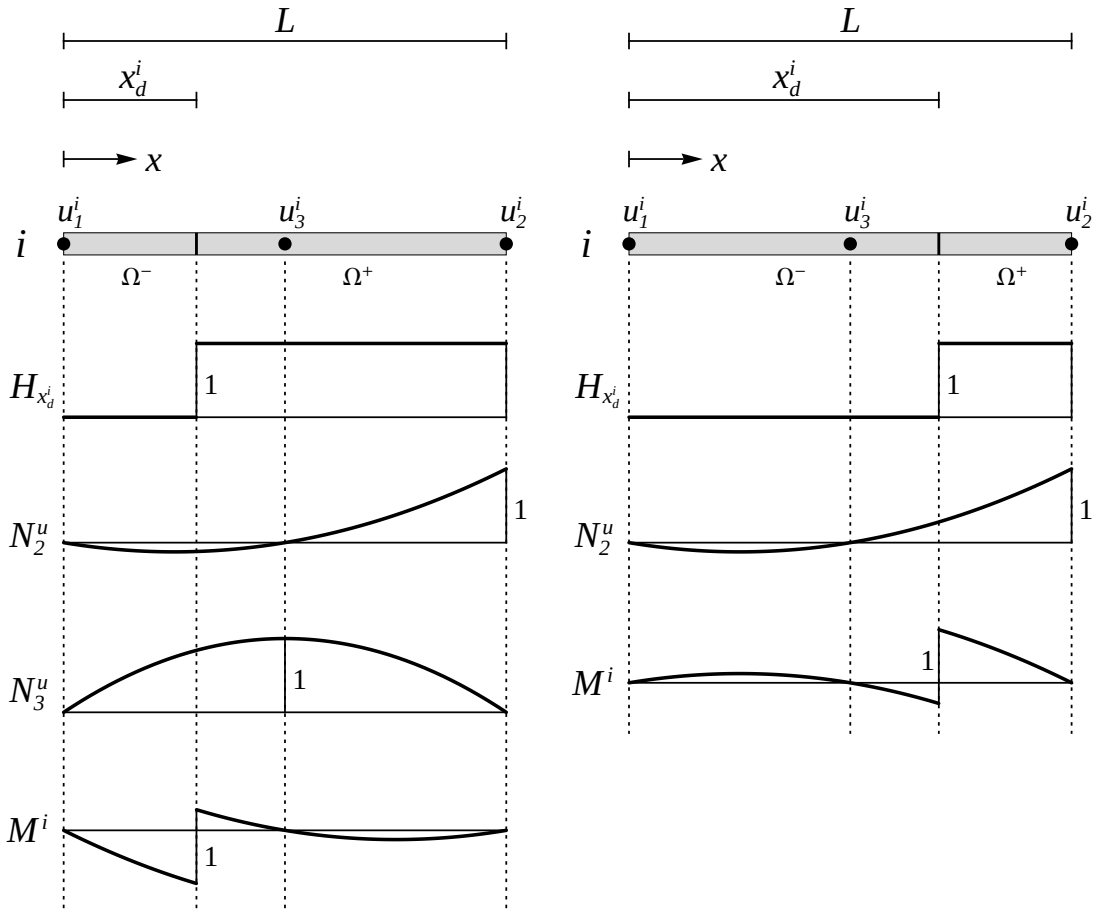

Figure 3.11: Construction of interpolation function M_i in case of discontinuity between nodes 1 and 3 (left) and in case of discontinuity between nodes 3 and 2 (right).

Slika 3.11: Konstruiranje interpolacijske funkcije M_i v primeru nezveznosti med vozliščema 1 in 3 (levo) in v primeru nezveznosti med vozliščema 3 in 2 (desno).

The first derivative of M^i over x is designated with G_R^i. Index R refers to the real strain, for interpolation of which the operator G_R^i is used. The derivatives of N_j^u and $H_{x_d^i}$ have been defined in (3.7) and (3.39).

$$G_R^i\left(x, x_d^i\right) = \frac{\partial}{\partial x} M^i\left(x, x_d^i\right) = \begin{cases} \delta_{x_d^i} - \left(B_2^u + B_3^u\right); & 0 < x_d^i < L/2 \\ \delta_{x_d^i} - B_2^u; & L/2 < x_d^i < L \end{cases} \tag{3.42}$$

It is convenient to divide G_R^i into a continuous part $\bar{G}_R^i$ and a discrete part $\bar{\bar{G}}_R^i$.

$$G_R^i\left(x, x_d^i\right) = \bar{G}_R^i + \bar{\bar{G}}_R^i, \quad \bar{\bar{G}}_R^i = \delta_{x_d^i}, \quad \bar{G}_R^i = \begin{cases} -\left(B_2^u + B_3^u\right); & 0 < x_d^i < L/2 \\ -B_2^u; & L/2 < x_d^i < L \end{cases} \tag{3.43}$$

Location of the discontinuity is determined by the stress state in the layer at the moment when ultimate stress is reached. At that moment the strain still consists solely of the regular part $\bar{\bar{\varepsilon}}^i$, defined in equation (3.8). Since this is a linear function of x, it has extreme values at the ends of the layer. For any monotonically increasing material law, the extreme values of stress coincide with those of the strain. The discontinuity is placed at one of the extreme value positions. The choice depends also on the material properties.

The special case of constant layer strain, which arises in pure axial loading or pure bending of a finite element, requires additional consideration. Linear operator $\bar{G}_R^i$ from (3.43) is not appropriate on such occasion, as the sum of a constant regular strain $\bar{\bar{\varepsilon}}^i$ and a linear additional continuous strain $\bar{G}_R^i \alpha^i$ would be linear. As a consequence, the finite element would not be in equilibrium. For example, in pure tension of a finite element we would compute different internal axial forces at the two end nodes. Another argument against the linear $\bar{G}_R^i$ operator in a constant strain case is that it has two possible values, depending on the location of the discontinuity. A crack just to the left of the middle node would produce completely different strain/stress state than a crack just to the right of the middle node.

Intuitively, one would choose for the case of constant layer strain a constant operator $\bar{G}_R^i$. Such choice is supported by the following reasoning. In case of constant strain in a layer, which corresponds to linear axial displacements, the axial displacements of the layer could be interpolated between two "nodal" displacements of the layer, instead of three, using linear interpolation functions $\mathbf{N}^{u*}$. They are presented in Fig. 3.12.

$$\tilde{u}^i(x) = \mathbf{N}^{u*}(x)\,\mathbf{u}^{i*}, \quad \mathbf{N}^{u*}(x) = \{N_1^{u*}, N_2^{u*}\} = \left\{1 - \frac{x}{L}, \frac{x}{L}\right\}, \quad \mathbf{u}^{i*} = \left\{u_1^i, u_2^i\right\}^T \tag{3.44}$$

Function M^i is determined by the same procedure as before. The difference is that the subdomain Ω^+ only contains node 2, regardless of x_d^i. The first derivative is computed accordingly.

$$M^i = H_{x_d^i} - \sum_{j \in \Omega^+} N_j^{u*} = H_{x_d^i} - N_2^{u*} = H_{x_d^i} - \frac{x}{L}, \quad G_R^i\left(x, x_d^i\right) = \frac{\partial M^i}{\partial x} = \delta_{x_d^i} - \frac{1}{L} \tag{3.45}$$

In a constant strain state, the discontinuity can appear anywhere between the end nodes. Without affecting subsequent computation, we can position it at $x_d^i = L/2$.

Equation (3.46) collects the three possible appearances of the discontinuity in a layer. In case of a constant strain, the discontinuity is set in the middle of the layer and the operator $\bar{G}_R^i$ is constant. In case of a linear strain, the

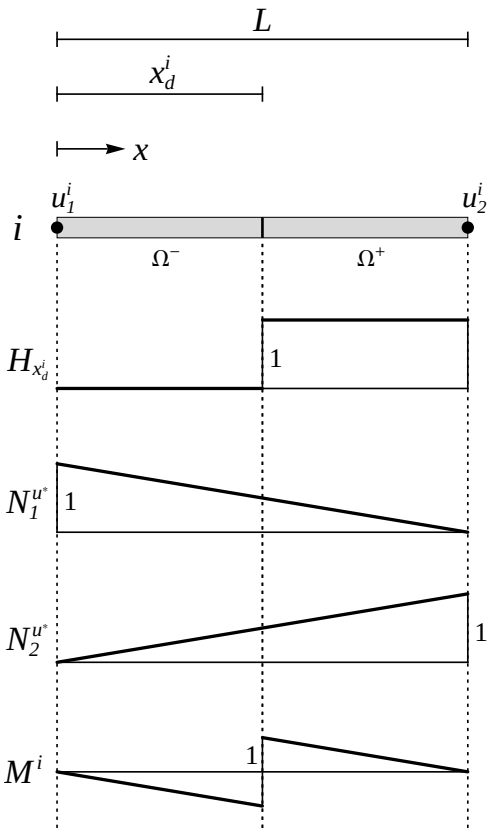

Figure 3.12: Construction of interpolation function M_i in case of constant strain.
Slika 3.12: Konstruiranje interpolacijske funkcije M_i v primeru konstantnih deformacij.

discontinuity is located at either of the two end nodes, accompanied with an appropriate operator $\bar{G}_R^i$ of linear form. Interpolation functions B_j^u are evaluated according to (3.7). Obtained functions are shown in Fig. 3.13.

$$G_R^i\left(x, x_d^i\right) = \bar{G}_R^i + \bar{\bar{G}}_R^i, \quad \bar{\bar{G}}_R^i = \delta_{x_d^i}, \quad \bar{G}_R^i = \begin{cases} -\dfrac{1}{L}; & x_d^i = L/2 \\ -\dfrac{1}{L}\left(3 - \dfrac{4x}{L}\right); & x_d^i = 0 \\ \dfrac{1}{L}\left(1 - \dfrac{4x}{L}\right); & x_d^i = L \end{cases} \tag{3.46}$$

3.2.4.2 Derivation of operator G_V for virtual strain

Operator G_V^i is a function that describes the influence of the virtual displacement jump $\hat{\alpha}^i$ on the virtual strain $\hat{\varepsilon}^i$ of the i-th layer. It is commonly taken to be equal to G_R^i but this is not compulsory. Any function, that appropriately describes a kinematically admissible variation of displacements, can be used. Let us first examine the natural choice $G_V^i = G_R^i$.

We have determined in previous sections that strain is linear in a layer of a finite element. For a piecewise linear material law, such as a combination of linear elasticity and plasticity with linear hardening, stress in the layer is also linear. The only exception is a partially plastified layer - in that case the stress is bilinear. For a fine enough mesh, however, stress in such layer does not reach the ultimate values, as indicated in Fig. 3.14. We can therefore assume a linear form of the stress in the layer at the moment when a discontinuity appears.

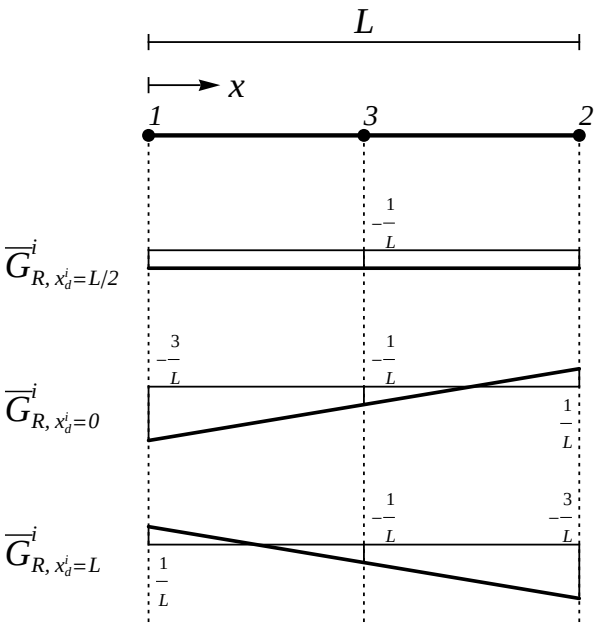

Figure 3.13: Operator $\bar{G}_R$ for interpolation of additional real strain.
Slika 3.13: Operator $\bar{G}_R$ za interpolacijo dodatnih pravih deformacij.

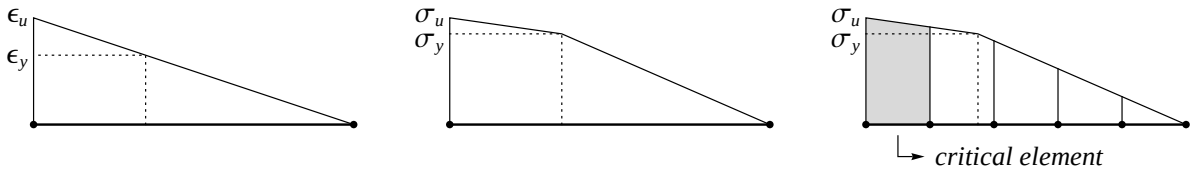

Figure 3.14: Linear strain and bilinear stress in a structural element, modeled with five finite elements.
Slika 3.14: Linearne deformacije in bilinearne napetosti v konstrukcijskem elementu, modeliranem s petimi končnimi elementi.

$$\sigma^i = C_1 x + C_2 \tag{3.47}$$

Expressions (3.46) for $\bar{G}^i_R$ and (3.47) for σ^i are inserted into equation (3.35). The traction at the discontinuity t^i_R is marked with the index R to note the use of $\bar{G}^i_R$. In case of a constant strain, constant C_1 is zero.

$$x^i_d = L/2: \quad C_1 = 0, \quad \sigma^i = C_2, \quad t^i_R = -\int_0^L \bar{G}^i_R \sigma^i dx = -\int_0^L -\frac{1}{L} C_2 \, dx = C_2 \tag{3.48}$$

We can see that the traction at the discontinuity t^i_R is equal to the stress in the bulk σ^i, which is consistent with the definition of t^i_R as the value of $\sigma^i(x)$ at $x = x^i_d$. Next, we consider the linear strain cases with $x^i_d = 0$ and $x^i_d = L$.

$$
\begin{aligned}
x_d^i = 0: \quad & t_R^i = -\int_0^L -\frac{1}{L}\left(3-\frac{4x}{L}\right)(C_1 x + C_2)\,dx = C_1\frac{L}{6} + C_2, \quad \sigma^i\big|_{x_d^i=0} = C_2 \neq t_R^i \\
x_d^i = L: \quad & t_R^i = -\int_0^L \frac{1}{L}\left(1-\frac{4x}{L}\right)(C_1 x + C_2)\,dx = C_1\frac{5L}{6} + C_2, \quad \sigma^i\big|_{x_d^i=L} = C_1 L + C_2 \neq t_R^i
\end{aligned}
\tag{3.49}
$$

The traction at the discontinuity, computed in (3.49), is incompatible with the definition $t_R^i = \sigma^i\left(x_d^i\right)$, which suggests inadequacy of the choice $G_V^i = G_R^i$. An alternative function has to be found for G_V^i, preferably similar to the original proposal. A slight modification of the continuous part $\bar{G}_V^i$ leads to expressions (3.50). The discrete part $\bar{\bar{G}}_V^i$ remains unchanged.

$$
G_V^i\left(x, x_d^i\right) = \bar{G}_V^i + \bar{\bar{G}}_V^i, \quad \bar{\bar{G}}_V^i = \delta_{x_d^i}, \quad \bar{G}_V^i = \begin{cases} -\dfrac{1}{L}; & x_d^i = L/2 \\ -\dfrac{2}{L}\left(2-\dfrac{3x}{L}\right); & x_d^i = 0 \\ \dfrac{2}{L}\left(1-\dfrac{3x}{L}\right); & x_d^i = L \end{cases}
\tag{3.50}
$$

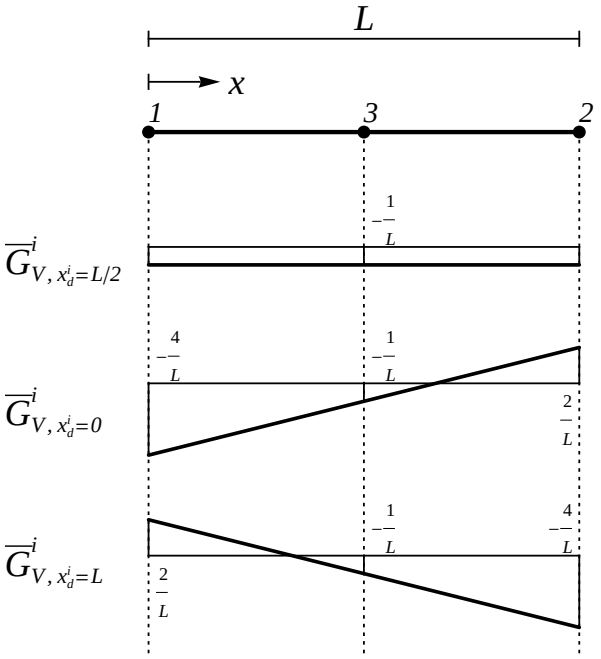

Figure 3.15: Operator $\bar{G}_V$ for interpolation of additional virtual strain.
Slika 3.15: Operator $\bar{G}_V$ za interpolacijo dodatnih virtualnih deformacij.

It turns out that function G_V^i, as defined in (3.50) and shown in Fig. 3.15, solves the compatibility issues encountered before.

$$
\begin{aligned}
x_d^i = 0: \quad & t^i = -\int_0^L -\frac{2}{L}\left(2-\frac{3x}{L}\right)(C_1 x + C_2)\,dx = C_2, \quad \sigma^i\big|_{x_d^i=0} = C_2 = t^i \\
x_d^i = L: \quad & t^i = -\int_0^L \frac{2}{L}\left(1-\frac{3x}{L}\right)(C_1 x + C_2)\,dx = C_1 L + C_2, \quad \sigma^i\big|_{x_d^i=L} = C_1 L + C_2 = t^i
\end{aligned}
\tag{3.51}
$$

Operator G_V^i should also satisfy the patch test which requires the additional virtual work (performed on the virtual displacement jumps $\hat{\alpha}^i$) to be zero in case of constant stress σ^i. Thus, the introduction of $\hat{\alpha}^i$ does not affect the energy dissipation at least for the constant stress state. Such state is approached by refining the finite element mesh.

$$
\hat{\alpha}^i \int_L G_V^i \sigma^i A^i dx \overset{\sigma^i=\text{const.}}{=} \underbrace{\hat{\alpha}^i \sigma^i A^i}_{\neq 0} \int_L G_V^i\,dx = 0 \quad \Rightarrow \quad \int_L G_V^i\,dx = 0 \tag{3.52}
$$

Taking into account the rule (3.33) for integration of G_V^i, requirement (3.52) can be reformulated.

$$
\int_L G_V^i\,dx = \int_L \left(\bar{G}_V^i + \delta_{x_d^i}\right) dx = \int_L \bar{G}_V^i\,dx + \overbrace{\int_L \delta_{x_d^i} dx}^{=1} = 0 \quad \Rightarrow \quad \int_L \bar{G}_V^i\,dx = -1 \tag{3.53}
$$

It can be easily verified that each of expressions (3.50) for $\bar{G}_V^i$ satisfies (3.53).

3.2.5 Constitutive models

In this section we describe constitutive models which control the behavior of concrete and reinforcement layers. For each material, there are two separate models, one for the bulk of the layer and one for the discontinuity.

3.2.5.1 Bulk of concrete layer

Behavior of the bulk of the concrete layer is described by 1D elasto-damage model. Response of the material is linear elastic up to the elasticity limit. Further increase of stress produces micro damage (micro cracking in tension and micro crushing in compression) continuously over the layer, which results in reduction of the elasticity modulus. Unloading is linear elastic with the current value of the elasticity modulus, and leads to the origin of the stress-strain diagram (see Fig. 3.16). These properties of concrete are collected in the following equations, which can be derived through the principle of maximum damage dissipation, see [73].

Equation (3.54) shows the linear elastic relation between stress and strain. It represents the loading curve/path up to elasticity limit and the unloading/reloading curve in the $\sigma^i - \bar{\varepsilon}^i$ diagram.

$$
\sigma^i = \bar{D}^{i^{-1}} \bar{\varepsilon}^i, \quad \bar{D}^i \in \left[E_c^{-1}, \infty\right), \quad \varepsilon^i = \check{\mathbf{B}}^i \mathbf{d} + G_R^i \alpha^i = \overbrace{\check{\mathbf{B}}^i \mathbf{d} + \bar{G}_R^i \alpha^i}^{\bar{\varepsilon}^i} + \bar{\bar{G}}_R^i \alpha^i \tag{3.54}
$$

Here $\bar{D}^i$ is compliance of the bulk material, E_c elastic modulus of intact concrete, and $\bar{\varepsilon}^i$ the continuous part of axial strain in the i-th layer, composed of the regular strain and the continuous part of the additional strain. The

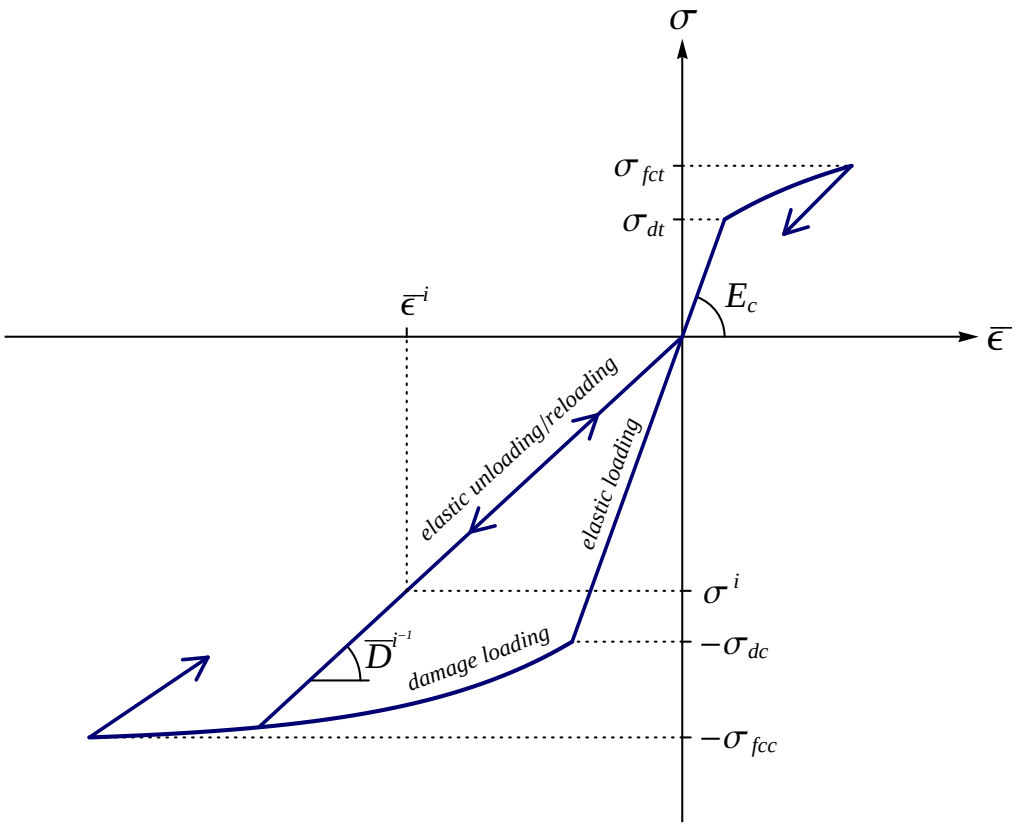

Figure 3.16: *Stress - strain* diagram for bulk of concrete layer.
Slika 3.16: Diagram *napetost - deformacija* za sloj betona.

latter is zero until the discontinuity is formed. The non-elastic part of the loading curve in the $\sigma^i - \bar{\varepsilon}^i$ diagram is defined indirectly by the remaining equations in this section.

$$\bar{\phi}^i\left(\sigma^i, \bar{q}^i\right) = \left|\sigma^i\right| - \left(\sigma_d - \bar{q}^i\right), \quad \sigma_d = \begin{cases} \sigma_{dc} & \text{for compression} \\ \sigma_{dt} & \text{for tension} \end{cases} \tag{3.55}$$

Damage function $\bar{\phi}^i$ prescribes the admissible values of axial stress σ^i in the i-th layer. Elasticity limit $\sigma_d > 0$ marks the beginning of micro damage and is defined separately for tension and compression. Stress-like hardening variable $\bar{q}^i$ handles the damage threshold evolution.

$$\bar{q}^i = -H_c \bar{\xi}^i, \quad H_c = \begin{cases} H_{cc} & \text{for compression} \\ H_{ct} & \text{for tension} \end{cases} \tag{3.56}$$

Linear hardening of the material is described by equation (3.56), where $\bar{\xi}^i$ is a strain-like hardening variable with initial value equal to zero, and $H_c > 0$ is a constant hardening modulus of concrete with separate values for tension and compression. Evolution in pseudo-time of internal hardening variables $\bar{D}^i$ and $\bar{\xi}^i$ is defined by evolution equations (3.57).

$$\dot{\bar{D}}^i = \frac{\dot{\bar{\gamma}}^i sign\left(\sigma^i\right)}{\sigma^i}, \quad \dot{\bar{\xi}}^i = \dot{\bar{\gamma}}^i \tag{3.57}$$

The dot designates the derivative with respect to pseudo-time and $\dot{\bar{\gamma}}^i$ is damage multiplier. The loading/unloading conditions and consistency condition (3.58) also apply.

$$\dot{\bar{\gamma}}^i \geq 0, \quad \bar{\phi}^i \leq 0, \quad \dot{\bar{\gamma}}^i \bar{\phi}^i = 0, \quad \dot{\bar{\gamma}}^i \dot{\bar{\phi}}^i = 0 \tag{3.58}$$

Tangent moduli of the $\sigma^i - \bar{\varepsilon}^i$ diagram can be determined from the above equations. The elastic loading/unloading path corresponds to condition $\dot{\bar{\gamma}}^i = 0$. It follows from evolution equations (3.57), that compliance $\bar{D}^i$ is constant. The tangent modulus is obtained if expression (3.54) for σ^i is differentiated with respect to $\bar{\varepsilon}^i$.

$$\dot{\bar{\gamma}}^i = 0 \quad \Rightarrow \quad \bar{D}^i = \text{const.}, \quad \frac{\partial \sigma^i}{\partial \bar{\varepsilon}^i} = \bar{D}^{i-1} \tag{3.59}$$

In case of damage loading, when $\dot{\bar{\gamma}}^i > 0$, the procedure is more complex. From the third and the fourth of conditions (3.58) we can conclude that $\bar{\phi}^i = 0$ and $\dot{\bar{\phi}}^i = 0$. From (3.55) we can write the expression for σ^i and differentiate it over pseudo-time. We use the appropriate evolution equation to differentiate $\bar{\xi}^i$.

$$\sigma^i = \left(\sigma_d - \bar{q}^i\right) sign\left(\sigma^i\right) = \left(\sigma_d + H_c \bar{\xi}^i\right) sign\left(\sigma^i\right), \quad \dot{\sigma}^i = H_c \dot{\bar{\gamma}}^i sign\left(\sigma^i\right) \tag{3.60}$$

The stress can be replaced by expression (3.54). The obtained equation is again differentiated over pseudo-time. Note that compliance $\bar{D}^i$ is not constant any more.

$$\begin{aligned}
\bar{D}^{i-1} \bar{\varepsilon}^i &= \left(\sigma_d + H_c \bar{\xi}^i\right) sign\left(\sigma^i\right) \\
-\bar{D}^{i-2} \dot{\bar{D}}^i \bar{\varepsilon}^i + \bar{D}^{i-1} \dot{\bar{\varepsilon}}^i &= H_c \dot{\bar{\xi}}^i sign\left(\sigma^i\right) && \Big/ \dot{\bar{D}}^i = \frac{\dot{\bar{\gamma}}^i sign\left(\sigma^i\right)}{\sigma^i},\ \dot{\bar{\xi}}^i = \dot{\bar{\gamma}}^i \\
-\bar{D}^{i-2} \frac{\dot{\bar{\gamma}}^i sign\left(\sigma^i\right)}{\sigma^i} \bar{\varepsilon}^i + \bar{D}^{i-1} \dot{\bar{\varepsilon}}^i &= H_c \dot{\bar{\gamma}}^i sign\left(\sigma^i\right) && \Big/ \frac{\bar{\varepsilon}^i}{\sigma^i} = \bar{D}^i \\
-\bar{D}^{i-1} \dot{\bar{\gamma}}^i sign\left(\sigma^i\right) + \bar{D}^{i-1} \dot{\bar{\varepsilon}}^i &= H_c \dot{\bar{\gamma}}^i sign\left(\sigma^i\right) \\
\dot{\bar{\varepsilon}}^i &= \frac{\bar{D}^{i-1} + H_c}{\bar{D}^{i-1}} \dot{\bar{\gamma}}^i sign\left(\sigma^i\right)
\end{aligned} \tag{3.61}$$

The tangent modulus is computed by dividing the pseudo-time derivatives $\dot{\sigma}^i$ and $\dot{\bar{\varepsilon}}^i$ from (3.60) and (3.61).

$$\frac{\partial \sigma^i}{\partial \bar{\varepsilon}^i} = \frac{\dot{\sigma}^i}{\dot{\bar{\varepsilon}}^i} = \frac{\bar{D}^{i-1} H_c}{\bar{D}^{i-1} + H_c} \tag{3.62}$$

To sum up, the tangent modulus is described by two expressions. The first one covers the elastic behavior - unloading and reloading, including the first elastic loading with the initial value of compliance $\bar{D}^i = E_c^{-1}$. The second expression represents the slope of the damage loading curve.

$$\frac{\partial \sigma^i}{\partial \bar{\varepsilon}^i} = \begin{cases} \bar{D}^{i-1}; & \dot{\bar{\gamma}}^i = 0 \\ \dfrac{\bar{D}^{i-1} H_c}{\bar{D}^{i-1} + H_c}; & \dot{\bar{\gamma}}^i > 0 \end{cases} \tag{3.63}$$

3.2.5.2 Discontinuity in concrete layer

Energy dissipation at the discontinuity of a concrete layer is described by a softening damage law, which connects the traction at the discontinuity to the displacement jump. When the discontinuity is introduced, the displacement jump is zero and the traction is equal to the failure stress of concrete. An increase of the displacement jump (in absolute value) reduces the carrying capacity and thus produces a lower traction. A subsequent decrease of the displacement jump (in absolute value) reduces the traction as well, but the carrying capacity remains the same. Obviously, the problem needs to be controlled by imposed displacements to provide a unique solution. The term "loading" therefore refers to the increase of displacement jump (in absolute value) and "unloading" refers to the decrease of displacement jump. The unloading is always linear elastic, but there are two possibilities for loading. Elastic (re)loading follows the unloading curve, increases the traction, and leaves the internal variables unchanged. When carrying capacity is reached, damage loading continues. It decreases the traction and changes the internal variables (see Fig. 3.17). This material law is mathematically described by the following equations, which can be derived by using the principle of maximum damage dissipation, see [73].

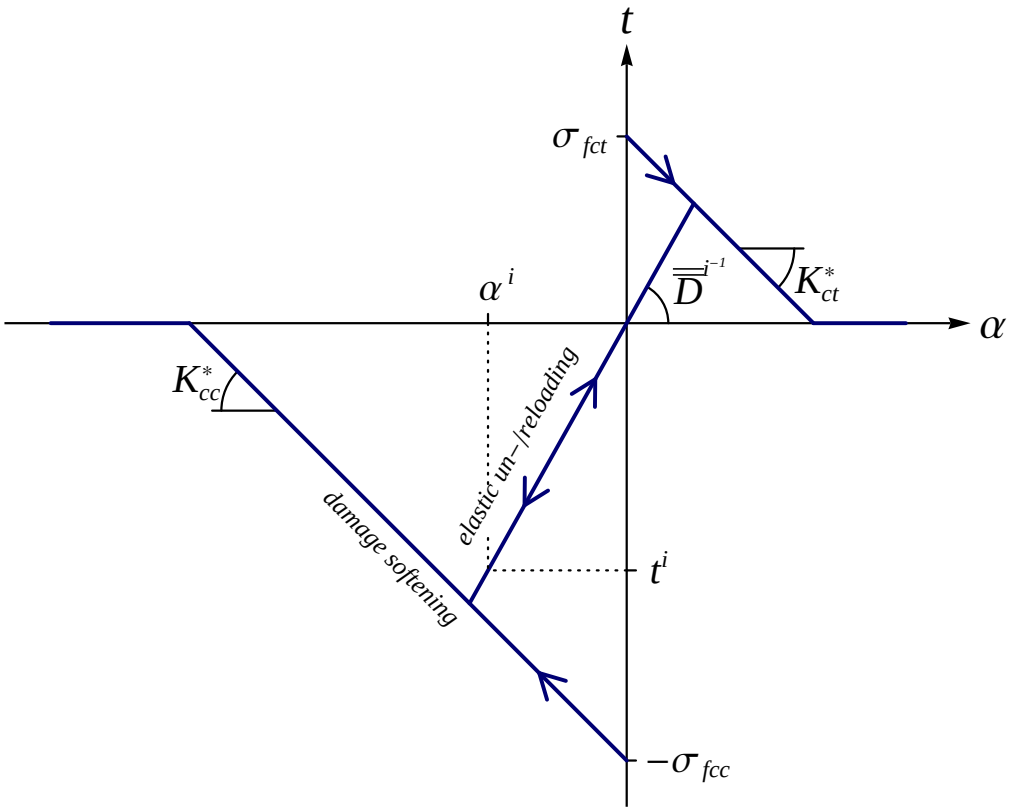

Figure 3.17: *Traction - displacement jump* diagram for discontinuity in concrete layer.
Slika 3.17: Diagram *napetost - skok v pomiku* za nezveznost v sloju betona.

Equation (3.64) describes the linear elastic relation between the traction at the discontinuity t^i and the displacement jump α^i. It represents the unloading/reloading path in the $t^i - \alpha^i$ diagram.

$$t^i = \bar{\bar{D}}^{i^{-1}} \alpha^i, \quad \bar{\bar{D}}^i \in [0, \infty) \tag{3.64}$$

Here $\bar{\bar{D}}^i$ is compliance of the discontinuity which increases with progression of the localized failure. The loading curve of the $t^i - \alpha^i$ diagram is defined indirectly by the remaining equations in this section.

$$\bar{\bar{\phi}}^i\left(t^i,\bar{\bar{q}}^i\right)=\left|t^i\right|-\left(\sigma_{fc}-\bar{\bar{q}}^i\right),\quad \sigma_{fc}=\begin{cases}\sigma_{fcc} & \text{for compression}\\ \sigma_{fct} & \text{for tension}\end{cases} \tag{3.65}$$

Failure function $\bar{\bar{\phi}}^i$ prescribes the admissible values of traction t^i at the discontinuity of a concrete layer. Failure stress of concrete $\sigma_{fc}>0$ indicates the occurrence of the discontinuity and is defined separately for tension and compression. Stress-like softening variable $\bar{\bar{q}}^i$ handles the damage threshold evolution and is described by an exponential function.

$$\bar{\bar{q}}^i=\sigma_{fc}\left(1-e^{K_c\bar{\bar{\xi}}^i}\right),\quad K_c=\begin{cases}K_{cc}=-\dfrac{\sigma_{fcc}}{2G_{fcc}} & \text{for compression}\\ K_{ct}=-\dfrac{\sigma_{fct}}{2G_{fct}} & \text{for tension}\end{cases} \tag{3.66}$$

Here $\bar{\bar{\xi}}^i$ is a displacement-like softening variable with initial value set to zero, and $K_c<0$ is a constant softening modulus of concrete with units m^{-1} and separate values for compression and tension. These are determined by the fracture energies per cross-section unit G_{fcc} and G_{fct} for concrete in compression and tension, respectively. The fracture energy has units kJm^{-2} and is measured in a uniaxial compression/tension test. Fracture energies G_{fcc} and G_{fct} represent the areas between the horizontal axis, and the compressive and tensile softening lines of the $t-\alpha$ diagram in Fig. 3.17, respectively. Evolution in pseudo-time of internal softening variables $\bar{\bar{D}}^i$ and $\bar{\bar{\xi}}^i$ is defined by evolution equations (3.67).

$$\dot{\bar{\bar{D}}}^i=\frac{\dot{\bar{\bar{\gamma}}}^i\ sign\left(t^i\right)}{t^i},\quad \dot{\bar{\bar{\xi}}}^i=\dot{\bar{\bar{\gamma}}}^i \tag{3.67}$$

The dot designates the derivative with respect to pseudo-time and $\dot{\bar{\bar{\gamma}}}^i$ is damage multiplier. The loading/unloading conditions and consistency condition (3.68) also apply.

$$\dot{\bar{\bar{\gamma}}}^i\geq 0,\quad \bar{\bar{\phi}}^i\leq 0,\quad \dot{\bar{\bar{\gamma}}}^i\bar{\bar{\phi}}^i=0,\quad \dot{\bar{\bar{\gamma}}}^i\dot{\bar{\bar{\phi}}}^i=0 \tag{3.68}$$

A closer inspection of equations (3.64)-(3.68) reveals that the damage loading path of $t^i-\alpha^i$ diagram, corresponding to condition $\bar{\bar{\phi}}^i=0$, is a straight line, see appendix B. The discovery suggests a possibility of simplification, but more insight is required.

Each point of the damage loading path is determined by its ordinate t^i and the slope $\bar{\bar{D}}^{i^{-1}}$ of the unloading line, which connects the point to the origin. Abscissa α^i is computed from equation (3.64). Evolution equations (3.67) dictate the change of $\bar{\bar{D}}^i$ and $\bar{\bar{\xi}}^i$, the latter defining t^i through equations (3.65), (3.66) and (3.68). Both $\bar{\bar{D}}^i$ and t^i change non-linearly with respect to $\bar{\bar{\gamma}}^i=\dot{\bar{\bar{\gamma}}}^i\Delta\tau$ ($\Delta\tau$ being pseudo-time step), the first one because of non-linear evolution equation (3.67), and the second due to exponential softening law (3.66). However, the two non-linearities neutralize each other, yielding a linear relation between t^i and α^i.

The same damage loading path can be constructed by defining coordinates α^i and t^i. If they both change linearly with respect to some new variable, the diagram will be a straight line. We introduce a new displacement-like variable $\bar{\bar{\xi}}^{i*}$ and the softening law takes a linear form.

$$\bar{\bar{\xi}}^{i*}=-\frac{1}{K_c}\left(1-e^{K_c\bar{\bar{\xi}}^i}\right),\quad \bar{\bar{q}}^i=\sigma_{fc}\left(1-e^{K_c\bar{\bar{\xi}}^i}\right)=-K_c\sigma_{fc}\bar{\bar{\xi}}^{i*}=-K_c^*\bar{\bar{\xi}}^{i*} \tag{3.69}$$

The expression for $\bar{\bar{q}}^i$ in (3.69) holds for $\bar{\bar{\xi}}^i < \infty$, or equivalently $\bar{\bar{\xi}}^{i*} < -1/K_c$. After that $\bar{\bar{q}}^i$ would become greater than the failure stress of concrete σ_{fc}, which is not acceptable. Physically, it means that the carrying capacity cannot drop below zero.

$$\bar{\bar{q}}^i = \min\left\{-K_c^* \bar{\bar{\xi}}^{i*}, \sigma_{fc}\right\}, \quad K_c^* = K_c\,\sigma_{fc} \tag{3.70}$$

Then, the introduction of a new damage multiplier $\bar{\bar{\gamma}}^{i*}$ allows us to write a new set of linear evolution equations for α^i and $\bar{\bar{\xi}}^{i*}$. See appendix B for details.

$$\bar{\bar{\gamma}}^{i*} = -\frac{1}{K_c}\left(1 - e^{K_c \bar{\bar{\gamma}}^i}\right), \quad \dot{\alpha}^i = \dot{\bar{\bar{\gamma}}}^{i*} sign\left(t^i\right), \quad \dot{\bar{\bar{\xi}}}^{i*} = \dot{\bar{\bar{\gamma}}}^{i*} \tag{3.71}$$

The new softening law (3.70) and evolution equations (3.71), due to their linear form, simplify the computational procedure significantly. But there is another advantage over the original equations. As the original damage multiplier $\bar{\bar{\gamma}}^i$ approaches infinity, the traction t^i approaches zero and the displacement jump α^i approaches $-sign\left(t^i\right)/K_c$. No matter how much we increase the multiplier, α^i cannot pass that value. For an individual bar, such limitation is logical, as the complete loss of carrying capacity implies singularity of the problem and a further increase of the discontinuity is meaningless. However, if a layer of a beam loses all carrying capacity, the beam as a whole still possesses stiffness. The broken layer just follows the rest of the beam without resistance. It is therefore necessary to allow α^i to grow past the point of failure. When the new damage multiplier $\bar{\bar{\gamma}}^{i*}$ reaches the value $-1/K_c$, the original multiplier is pushed to infinity and the old evolution equations (3.67) get out of scope. The new evolution equations (3.71), however, withstand further increase of $\bar{\bar{\gamma}}^{i*}$. As the latter approaches infinity, so does α^i (in absolute value). Once past the failure point the traction t^i remains zero. The constitutive law at the discontinuity is summed up below.

$$t^i = \begin{cases} \bar{\bar{D}}^{i^{-1}} \alpha^i; & \dot{\bar{\bar{\gamma}}}^{i*} = 0 \\ \sigma_{fc}\, sign\left(\alpha^i\right) + \sigma_{fc} K_c \alpha^i; & \dot{\bar{\bar{\gamma}}}^{i*} > 0,\ \bar{\bar{q}}^i < \sigma_{fc} \\ 0; & \dot{\bar{\bar{\gamma}}}^{i*} > 0,\ \bar{\bar{q}}^i = \sigma_{fc} \end{cases} \tag{3.72}$$

The first expression represents the elastic unloading path, the second one the damage loading path until the traction drops to zero, and the third one the damage loading path further on. The tangent moduli are obtained by a simple differentiation of (3.72).

$$\frac{\partial t^i}{\partial \alpha^i} = \begin{cases} \bar{\bar{D}}^{i^{-1}}; & \dot{\bar{\bar{\gamma}}}^{i*} = 0 \\ K_c^* = \sigma_{fc} K_c; & \dot{\bar{\bar{\gamma}}}^{i*} > 0,\ \bar{\bar{q}}^i < \sigma_{fc} \\ 0; & \dot{\bar{\bar{\gamma}}}^{i*} > 0,\ \bar{\bar{q}}^i = \sigma_{fc} \end{cases} \tag{3.73}$$

3.2.5.3 Bulk of reinforcement layer

Behavior of the bulk of a layer of reinforcement is described by 1D elasto-plasticity model with isotropic hardening. It is symmetrical in tension and compression. Response of the material is linear elastic until yield stress is reached. If loading increases, plastic deformations occur and grow continuously over the layer. Elasticity limit is raised as well. Unloading is elastic and follows a line, parallel to the first loading path. When the stress drops to zero,

plastic deformations remain in the layer (Fig. 3.18). Behavior of steel is mathematically described by the following equations, which can be derived by using the principle of maximum plastic dissipation [73].

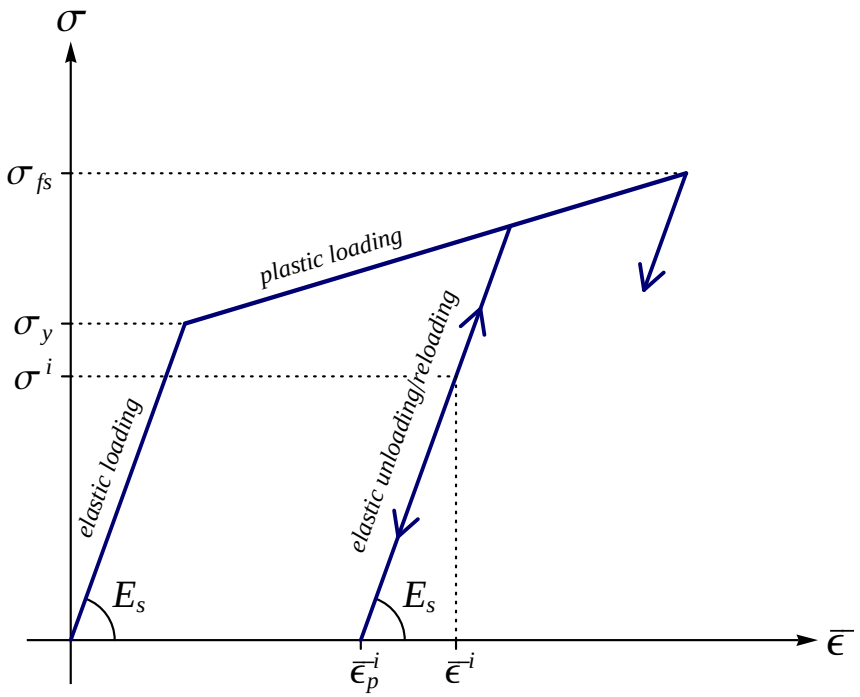

Figure 3.18: *Stress - strain* diagram for bulk of reinforcement layer.
Slika 3.18: Diagram *napetost - deformacija* za sloj armature.

Stress σ^i is computed from equation (3.74), which represents the elastic loading path and elastic unloading or reloading path of the $\sigma^i - \bar{\varepsilon}^i$ diagram.

$$\sigma^i = E_s\left(\bar{\varepsilon}^i - \bar{\varepsilon}^i_p\right), \quad \varepsilon^i = \breve{\mathbf{B}}^i\mathbf{d} + G^i_R\alpha^i = \overbrace{\breve{\mathbf{B}}^i\mathbf{d} + \bar{G}^i_R\alpha^i}^{\bar{\varepsilon}^i} + \bar{\bar{G}}^i_R\alpha^i \tag{3.74}$$

Here E_s is the elastic modulus of steel, $\bar{\varepsilon}^i_p$ plastic strain, and $\bar{\varepsilon}^i$ the continuous part of axial strain in the i-th layer, composed of the regular strain and the continuous part of the additional strain. Before the appearance of the discontinuity the additional strain is zero. The plastic loading path of the $\sigma^i - \bar{\varepsilon}^i$ diagram is determined indirectly by the rest of the equations in this section.

$$\bar{\phi}^i\left(\sigma^i, \bar{q}^i\right) = \left|\sigma^i\right| - \left(\sigma_y - \bar{q}^i\right) \tag{3.75}$$

Yield function $\bar{\phi}^i$ prescribes the admissible axial stress in the layer. Yield stress $\sigma_y > 0$ is the absolute value of the stress, at which the first plastic deformations occur. Stress-like hardening variable $\bar{q}^i$ controls yield threshold evolution.

$$\bar{q}^i = -H_s\bar{\xi}^i \tag{3.76}$$

Equation (3.76) describes the linear isotropic hardening of the material. Here $H_s > 0$ is a constant hardening

modulus of steel and $\bar{\xi}^i$ is a strain-like hardening variable with the initial value zero. Evolution in pseudo-time of internal hardening variables for plasticity, $\bar{\varepsilon}_p^i$ and $\bar{\xi}^i$, is prescribed by evolution equations (3.77).

$$\dot{\bar{\varepsilon}}_p^i = \dot{\bar{\gamma}}^i sign\left(\sigma^i\right), \quad \dot{\bar{\xi}}^i = \dot{\bar{\gamma}}^i \tag{3.77}$$

The dot designates the derivative with respect to pseudo-time and $\dot{\bar{\gamma}}^i$ is plastic multiplier. The loading/unloading conditions and consistency condition (3.78) apply as well.

$$\dot{\bar{\gamma}}^i \geq 0, \quad \bar{\phi}^i \leq 0, \quad \dot{\bar{\gamma}}^i \bar{\phi}^i = 0, \quad \dot{\bar{\gamma}}^i \dot{\bar{\phi}}^i = 0 \tag{3.78}$$

Tangent moduli of the $\sigma^i - \bar{\varepsilon}^i$ diagram are determined by the described equations. In elastic response, the plastic multiplier is equal to zero. As a consequence, internal variables are constant and the tangent modulus is simply computed by differentiating the expression (3.74) for σ^i with respect to $\bar{\varepsilon}^i$.

$$\dot{\bar{\gamma}}^i = 0 \quad \Rightarrow \quad \bar{\varepsilon}_p^i = \text{const.}, \quad \frac{\partial \sigma^i}{\partial \bar{\varepsilon}^i} = E_s \tag{3.79}$$

In plastic loading, the plastic strain $\bar{\varepsilon}_p^i$ is not constant. It depends on the plastic multiplier $\dot{\bar{\gamma}}^i > 0$ and consequently on the strain $\bar{\varepsilon}^i$. The tangent modulus can be computed from pseudo-time derivatives of stress and strain. It follows from the last two equations in (3.78) that $\bar{\phi}^i = 0$ and $\dot{\bar{\phi}}^i = 0$. We can express σ^i from equation (3.75) and differentiate it over pseudo-time.

$$\sigma^i = \left(\sigma_y - \bar{q}^i\right) sign\left(\sigma^i\right) = \left(\sigma_y + H_s \bar{\xi}^i\right) sign\left(\sigma^i\right), \quad \dot{\sigma}^i = H_s \dot{\bar{\gamma}}^i sign\left(\sigma^i\right) \tag{3.80}$$

We can replace the stress σ^i with expression (3.74) and differentiate the modified equation over pseudo-time again. Evolution equations (3.77) are utilized in the procedure.

$$\begin{aligned}
E_s\left(\bar{\varepsilon}^i - \bar{\varepsilon}_p^i\right) &= \left(\sigma_y + H_s \bar{\xi}^i\right) sign\left(\sigma^i\right) \\
E_s\left(\dot{\bar{\varepsilon}}^i - \dot{\bar{\varepsilon}}_p^i\right) &= H_s \dot{\bar{\xi}}^i sign\left(\sigma^i\right) \qquad / \dot{\bar{\varepsilon}}_p^i = \dot{\bar{\gamma}}^i sign\left(\sigma^i\right), \; \dot{\bar{\xi}}^i = \dot{\bar{\gamma}}^i \\
E_s \dot{\bar{\varepsilon}}^i - E_s \dot{\bar{\gamma}}^i sign\left(\sigma^i\right) &= H_s \dot{\bar{\gamma}}^i sign\left(\sigma^i\right) \\
\dot{\bar{\varepsilon}}^i &= \frac{E_s + H_s}{E_s} \dot{\bar{\gamma}}^i sign\left(\sigma^i\right)
\end{aligned} \tag{3.81}$$

Pseudo-time derivatives $\dot{\sigma}^i$ and $\dot{\bar{\varepsilon}}^i$, defined in (3.80) and (3.81), are divided to produce the plastic tangent modulus.

$$\frac{\partial \sigma^i}{\partial \bar{\varepsilon}^i} = \frac{\dot{\sigma}^i}{\dot{\bar{\varepsilon}}^i} = \frac{E_s H_s}{E_s + H_s} \tag{3.82}$$

The elastic and plastic tangent moduli are gathered below. The first expression represents the slope of the elastic loading and unloading path, while the second one represents the slope of the plastic loading path in the $\sigma^i - \bar{\varepsilon}^i$ diagram.

$$\frac{\partial \sigma^i}{\partial \bar{\varepsilon}^i} = \begin{cases} E_s; & \dot{\bar{\gamma}}^i = 0 \\ \dfrac{E_s H_s}{E_s + H_s}; & \dot{\bar{\gamma}}^i > 0 \end{cases} \tag{3.83}$$

3.2.5.4 Discontinuity in reinforcement layer

Behavior of the discontinuity in a layer of reinforcement is described by a plastic softening law, which connects the traction at the discontinuity to the displacement jump (Fig. 3.19). At introduction of the discontinuity the displacement jump is zero and the traction is equal to the failure stress of steel. A further increase of the imposed displacements of the layer reduces the carrying capacity. The traction at the discontinuity decreases and the displacement jump increases. This is referred to as plastic softening. The displacement jump behaves analogously to plastic strain in the continuous model, i.e. it stays the same if the loading is decreased. The traction at the discontinuity in the unloading phase changes in accordance with the stress in the bulk, so that the equilibrium (3.35) is satisfied. When traction (in absolute value) reaches the carrying capacity again, the plastic loading continues and the displacement jump changes accordingly to the sign of traction. It decreases in compression and increases in tension, regardless of its own size and sign. The mathematical description of such behavior is condensed in the following equations, which can be derived by the principle of maximum plastic dissipation, see [73].

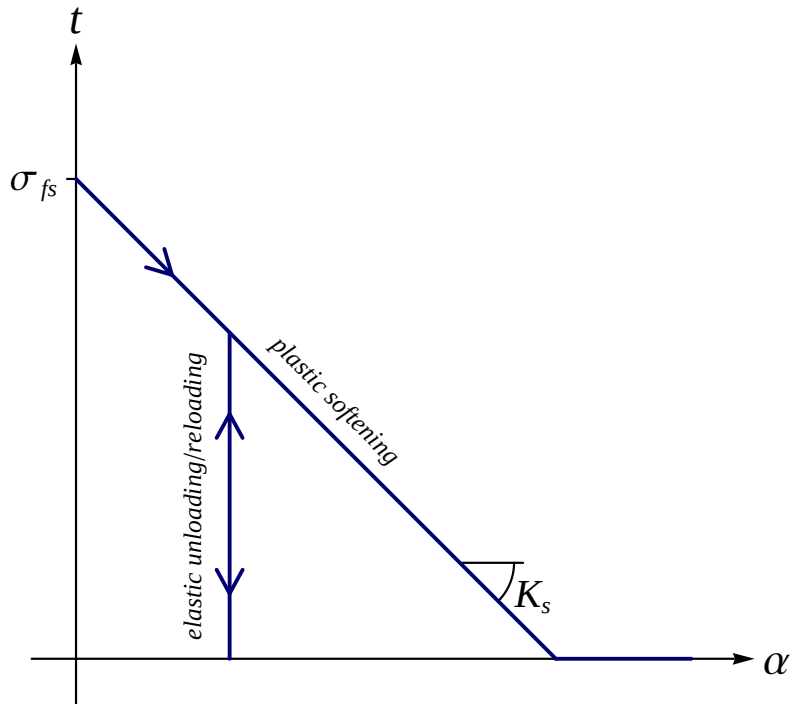

Figure 3.19: *Traction - displacement jump* diagram for discontinuity in reinforcement layer.
Slika 3.19: Diagram *napetost - skok v pomiku* za nezveznost v sloju armature.

$$\bar{\bar{\phi}}^i\left(t^i,\bar{\bar{q}}^i\right)=\left|t^i\right|-\left(\sigma_{fs}-\bar{\bar{q}}^i\right) \tag{3.84}$$

Failure function $\bar{\bar{\phi}}^i$ defines the admissible values of traction t^i at the discontinuity of a reinforcement layer. Failure stress of steel $\sigma_{fs}>0$ is the absolute value of the stress, at which the discontinuity first appears. The stress-like softening variable $\bar{\bar{q}}^i$ manages the softening threshold evolution.

$$\bar{\bar{q}}^i=\min\left\{-K_s\bar{\bar{\xi}}^i,\sigma_{fs}\right\},\quad K_s=-\frac{\sigma_{fs}^2}{2G_{fs}} \tag{3.85}$$

The linear softening law is described by equation (3.85), where $\bar{\bar{\xi}}^i$ is a displacement-like softening variable with initial value zero, and $K_s > 0$ is a constant softening modulus of concrete with units kNm^{-3}. Fracture energy per cross-section unit of steel has units kJm^{-2} and is determined in a uniaxial tension test. Evolution in pseudo-time of internal softening variables α^i and $\bar{\bar{\xi}}^i$ is defined by evolution equations (3.86).

$$\dot{\alpha}^i = \dot{\bar{\bar{\gamma}}}^i sign\left(t^i\right), \quad \dot{\bar{\bar{\xi}}}^i = \dot{\bar{\bar{\gamma}}}^i \tag{3.86}$$

The dot designates the derivative with respect to pseudo-time and $\dot{\bar{\bar{\gamma}}}^i$ is plastic softening multiplier. The loading/unloading conditions and consistency condition (3.87) also apply.

$$\dot{\bar{\bar{\gamma}}}^i \geq 0, \quad \bar{\bar{\phi}}^i \leq 0, \quad \dot{\bar{\bar{\gamma}}}^i \bar{\bar{\phi}}^i = 0, \quad \dot{\bar{\bar{\gamma}}}^i \dot{\bar{\bar{\phi}}}^i = 0 \tag{3.87}$$

The equation of the plastic softening loading path of $t^i - \alpha^i$ diagram is not unique. It depends on the loading history. If the softening process alternates between both load signs, the loading path is translated sideways (left or right). The slope, however, is not affected and can be determined from the pseudo-time derivatives of t^i and α^i. In softening process, when $\dot{\bar{\bar{\gamma}}}^i > 0$, the failure function $\bar{\bar{\phi}}^i = 0$. Expression for t^i is then determined by (3.84) and (3.85).

$$t^i = \left(\sigma_{fs} - \bar{\bar{q}}^i\right) sign\left(t^i\right) = \begin{cases} \left(\sigma_{fs} + K_s \bar{\bar{\xi}}^i\right) sign\left(t^i\right); & \bar{\bar{q}}^i < \sigma_{fs} \\ 0; & \bar{\bar{q}}^i = \sigma_{fs} \end{cases} \tag{3.88}$$

The derivative is obtained in accordance with evolution equation (3.86) for $\bar{\bar{\xi}}^i$.

$$\dot{t}^i = \begin{cases} K_s \dot{\bar{\bar{\xi}}}^i sign\left(t^i\right) = K_s \dot{\bar{\bar{\gamma}}}^i sign\left(t^i\right); & \bar{\bar{q}}^i < \sigma_{fs} \\ 0; & \bar{\bar{q}}^i = \sigma_{fs} \end{cases} \tag{3.89}$$

The slope of the plastic softening loading path, defined as the derivative of t^i over α^i, is computed by dividing the pseudo-time derivatives (3.89) and (3.86) of both quantities.

$$\frac{\partial t^i}{\partial \alpha^i} = \frac{\dot{t}^i}{\dot{\alpha}^i} = \begin{cases} \text{not defined}; & \dot{\bar{\bar{\gamma}}}^i = 0 \\ K_s; & \dot{\bar{\bar{\gamma}}}^i > 0,\ \bar{\bar{q}}^i < \sigma_{fs} \\ 0; & \dot{\bar{\bar{\gamma}}}^i > 0,\ \bar{\bar{q}}^i = \sigma_{fs} \end{cases} \tag{3.90}$$

A third option was added in equation (3.90). It corresponds to elastic unloading path with $\dot{\bar{\bar{\gamma}}}^i = 0$. It follows from evolution equations (3.86) that $\dot{\alpha}^i = 0$. And since the failure function $\bar{\bar{\phi}}^i$ is no longer required to be zero, the traction t^i cannot be computed as in (3.88). It changes in accordance with equation (3.35) which represents the equilibrium between the bulk and the discontinuity. The fraction in (3.90) is not defined, but it is not required in the computational procedure anyway.

3.3 Computational procedure

Response of a structure, discretized by a mesh of n_{FE} above derived finite elements, is computed at discrete pseudo-time points $\tau_0,\ \tau_1,\ \ldots,\ \tau_n,\ \tau_{n+1},\ \ldots,\ T$ by solving at each pseudo-time point nonlinear equations (3.91)

for current values of nodal displacements/rotations.

$$\begin{aligned} &\mathbf{f}^{\text{int,str}} - \mathbf{f}^{\text{ext,str}} = \mathbf{0} \\ &\forall e \in \{1,2,\ldots,n_{FE}\},\ \forall i \in \left\{1,2,\ldots,n_{CL}^{(e)}\right\}: \quad h^{(e),i} = 0 \end{aligned} \tag{3.91}$$

Here, $n_{CL}^{(e)}$ is the number of cracked layers in element (e). At a particular pseudo-time point τ_{n+1}, the solution is searched iteratively by the Newton-Raphson method. Each iteration, denoted by k, consists of two subsequent phases: (A) computation of internal variables, corresponding to the current iterative values of nodal displacements/rotations, in order to compute the stress in accordance with given material laws; (B) solution of linearized equations (3.91) in order to update the iterative values of nodal displacements/rotations. When one phase of the computation is completed, the results are used immediately in the next one.

For a pseudo-time point τ_{n+1}, the computational problem related to a generic element (e) and material layer i can be stated as:

$$\text{given} \quad \mathbf{d}_n^{(e)} \quad \text{and} \quad \begin{cases} \bar{D}_n^{(e),i}, \bar{\xi}_n^{(e),i}, \bar{\bar{D}}_n^{(e),i}, \bar{\bar{\xi}}_n^{(e),i} \\ \bar{\varepsilon}_{p,n}^{(e),i}, \bar{\xi}_n^{(e),i}, \alpha_n^{(e),i}, \bar{\bar{\xi}}_n^{(e),i} \end{cases} \quad \text{find} \quad \mathbf{d}_{n+1}^{(e)} \quad \text{and} \quad \begin{cases} \bar{D}_{n+1}^{(e),i}, \bar{\xi}_{n+1}^{(e),i}, \bar{\bar{D}}_{n+1}^{(e),i}, \bar{\bar{\xi}}_{n+1}^{(e),i} \\ \bar{\varepsilon}_{p,n+1}^{(e),i}, \bar{\xi}_{n+1}^{(e),i}, \alpha_{n+1}^{(e),i}, \bar{\bar{\xi}}_{n+1}^{(e),i} \end{cases}$$

Note that superscript (e) was omitted in section 3.2.5 for the above internal variables. The subscript n and $n+1$ denote the values at pseudo-times τ_n and τ_{n+1}, respectively.

3.3.1 Computation of internal variables

In this section we will present computations of phase (A). The internal variables for i-th layer of element (e) at pseudo-time point τ_{n+1} will be computed for the k-th iteration, while the nodal displacements/rotations are fixed at the values from the previous iteration $\mathbf{d}_{n+1}^{(e),(k-1)}$. Since every internal variable is connected to a single layer of a single finite element, the computations are local, i.e. they are performed independently for each element and each layer. The condition of the discontinuity is known by the following flag.

$$crack^{(e),i} = \begin{cases} false & \ldots \quad \text{no discontinuity in layer } i \\ true & \ldots \quad \text{discontinuity in layer } i \end{cases} \tag{3.92}$$

The algorithm in Fig. 3.20 is applied. If there was no discontinuity in the layer in the previous pseudo-time step, we begin with equations for the hardening phase of material, described in sections 3.3.1.1 for concrete and 3.3.1.3 for steel. We must do so even if the previous iteration of the current step indicated occurrence of the discontinuity, because that was not a converged result. We check if the carrying capacity of the layer is exceeded. If not, we keep the obtained results, otherwise we discard them and use equations for the softening phase of material, described in sections 3.3.1.2 for concrete and 3.3.1.4 for steel. If the discontinuity already existed in the previous pseudo-time step, it must also exist in the current step, therefore we follow the procedure from sections 3.3.1.2 or 3.3.1.4.

The integrals, that appear in expressions (3.29), (3.30) and (3.35) for $\mathbf{f}^{\text{int},(e)}$, $h^{(e),i}$ and t^i, are evaluated with numerical integration. A three-point Gauss-Lobatto integration scheme is used with integration points at both ends and at the center of the finite element. Strain, stress and hardening internal variables are therefore computed only at those three locations. Softening internal variables are defined at the location of the discontinuity, which coincides with one of the integration points (although the two are not connected).

For the sake of clarity we will omit in the rest of this section the superscript (e), denoting the finite element, and the superscript i, denoting the layer.

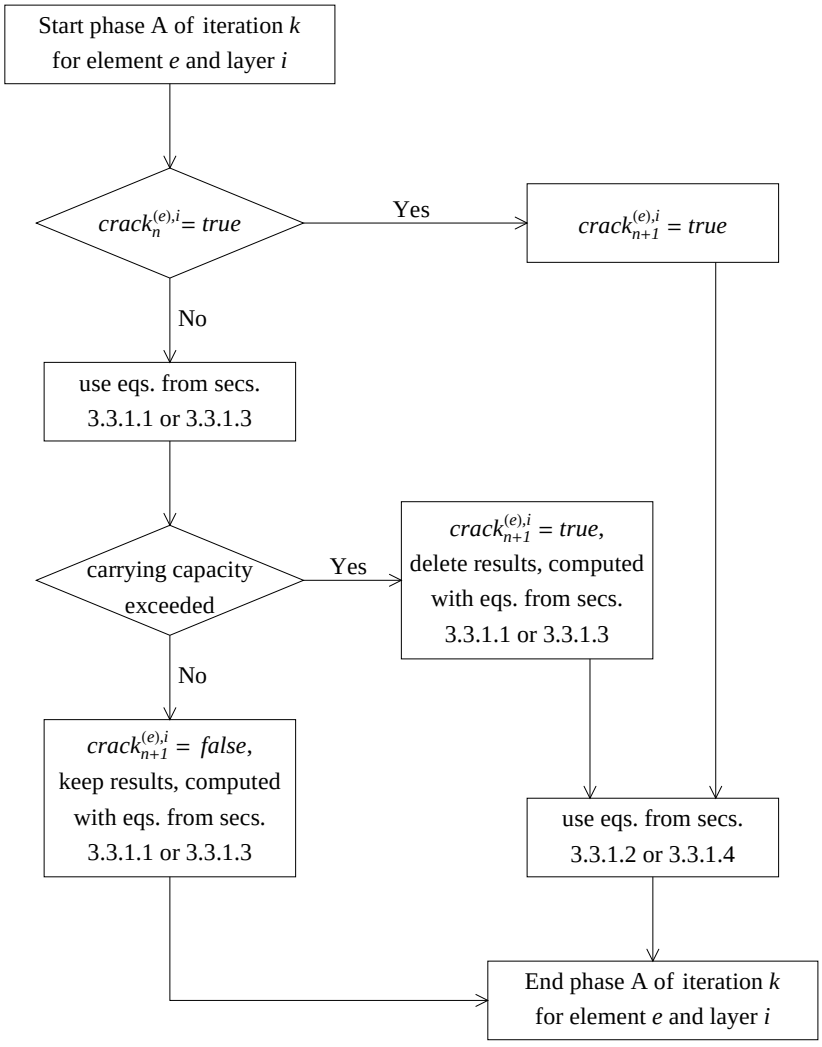

Figure 3.20: Algorithm for phase (A) of k-th iteration for i-th layer of finite element (e).
Slika 3.20: Algoritem za fazo (A) k-te iteracije za i-ti sloj končnega elementa (e).

3.3.1.1 Bulk of concrete layer

This section describes the computational procedure for the hardening phase of a concrete layer. The discontinuity has not yet occurred and the displacement jump is zero. The computation is started by assuming an elastic step, which means that hardening internal variables do not change, but keep the values from the previous step. Trial value of stress is computed according to (3.54), with $\alpha_{n+1}^{(k)} = 0$.

$$\bar{D}_{n+1}^{(k),trial} = \bar{D}_n, \quad \bar{\xi}_{n+1}^{(k),trial} = \bar{\xi}_n, \quad \sigma_{n+1}^{(k),trial} = \bar{D}_{n+1}^{(k),trial^{-1}}\,\bar{\varepsilon}\left(\mathbf{d}_{n+1}^{(k-1)}, \alpha_{n+1}^{(k)}\right) \tag{3.93}$$

The trial damage function $\bar{\phi}_{n+1}^{(k),trial}$ is computed in accordance with equations (3.55) and (3.56).

$$\bar{\phi}_{n+1}^{(k),trial} = \left|\sigma_{n+1}^{(k),trial}\right| - \left(\sigma_d - \bar{q}_{n+1}^{(k),trial}\right), \quad \bar{q}_{n+1}^{(k),trial} = -H_c\bar{\xi}_{n+1}^{(k),trial} = -H_c\bar{\xi}_n \tag{3.94}$$

The trial solution is accepted if the trial damage function is not positive.

$$\bar{\phi}_{n+1}^{(k),trial} \leq 0 \quad \Rightarrow \quad \bar{D}_{n+1}^{(k)} = \bar{D}_{n+1}^{(k),trial}, \quad \bar{\xi}_{n+1}^{(k)} = \bar{\xi}_{n+1}^{(k),trial}, \quad \sigma_{n+1}^{(k)} = \sigma_{n+1}^{(k),trial} \tag{3.95}$$

Otherwise, the internal variables have to be corrected and the stress recomputed. Incremental form of evolution equations (3.57) is applied, where $\bar{\gamma}_{n+1}^{(k)} = \dot{\bar{\gamma}}_{n+1}^{(k)} (\tau_{n+1} - \tau_n) > 0$. The use of $sign\left(\sigma_{n+1}^{(k)}\right) = sign\left(\sigma_{n+1}^{(k),trial}\right)$ is justified in appendix A.

$$\bar{\phi}_{n+1}^{(k),trial} > 0 \quad \Rightarrow \quad \bar{D}_{n+1}^{(k)} = \bar{D}_n + \bar{\gamma}_{n+1}^{(k)} \frac{sign\left(\sigma_{n+1}^{(k),trial}\right)}{\sigma_{n+1}^{(k)}}, \quad \bar{\xi}_{n+1}^{(k)} = \bar{\xi}_n + \bar{\gamma}_{n+1}^{(k)} \tag{3.96}$$

By using equations (3.96), the stress $\sigma_{n+1}^{(k)}$ and the stress-like hardening variable $\bar{q}_{n+1}^{(k)}$ can be expressed with their trial values and the damage multiplier $\bar{\gamma}_{n+1}^{(k)}$.

$$\begin{aligned}
\sigma_{n+1}^{(k)} &= \bar{D}_{n+1}^{(k)^{-1}} \bar{\varepsilon}\left(\mathbf{d}_{n+1}^{(k-1)}, \alpha_{n+1}^{(k)}\right) \\
\bar{D}_{n+1}^{(k)} \sigma_{n+1}^{(k)} &= \bar{\varepsilon}\left(\mathbf{d}_{n+1}^{(k-1)}, \alpha_{n+1}^{(k)}\right) = \bar{D}_{n+1}^{(k),trial} \sigma_{n+1}^{(k),trial} \\
\left(\bar{D}_n + \bar{\gamma}_{n+1}^{(k)} \frac{sign\left(\sigma_{n+1}^{(k),trial}\right)}{\sigma_{n+1}^{(k)}}\right) \sigma_{n+1}^{(k)} &= \bar{D}_n \sigma_{n+1}^{(k),trial} \\
\bar{D}_n \sigma_{n+1}^{(k)} + \bar{\gamma}_{n+1}^{(k)} sign\left(\sigma_{n+1}^{(k),trial}\right) &= \bar{D}_n \sigma_{n+1}^{(k),trial} \\
\sigma_{n+1}^{(k)} &= \sigma_{n+1}^{(k),trial} - \bar{D}_n^{-1} \bar{\gamma}_{n+1}^{(k)} sign\left(\sigma_{n+1}^{(k),trial}\right)
\end{aligned} \tag{3.97}$$

$$\bar{q}_{n+1}^{(k)} = -H_c \bar{\xi}_{n+1}^{(k)} = -H_c \left(\bar{\xi}_n + \bar{\gamma}_{n+1}^{(k)}\right) = \bar{q}_{n+1}^{(k),trial} - H_c \bar{\gamma}_{n+1}^{(k)} \tag{3.98}$$

Equations (3.97) and (3.98) are used to express the damage function $\bar{\phi}_{n+1}^{(k)}$ as a function of damage multiplier $\bar{\gamma}_{n+1}^{(k)}$, which is then computed from requirement $\bar{\phi}_{n+1}^{(k)} = 0$, coming from loading/unloading conditions (3.58).

$$\begin{aligned}
\bar{\phi}_{n+1}^{(k)} &= \left|\sigma_{n+1}^{(k)}\right| - \left(\sigma_d - \bar{q}_{n+1}^{(k)}\right) = \left|\sigma_{n+1}^{(k),trial}\right| - \bar{D}_n^{-1} \bar{\gamma}_{n+1}^{(k)} - \left(\sigma_d - \bar{q}_{n+1}^{(k),trial}\right) - H_c \bar{\gamma}_{n+1}^{(k)} = \\
&= \bar{\phi}_{n+1}^{(k),trial} - \left(\bar{D}_n^{-1} + H_c\right) \bar{\gamma}_{n+1}^{(k)}
\end{aligned} \tag{3.99}$$

$$\bar{\phi}_{n+1}^{(k)} = 0 \quad \Rightarrow \quad \bar{\gamma}_{n+1}^{(k)} = \frac{\bar{\phi}_{n+1}^{(k),trial}}{\bar{D}_n^{-1} + H_c}$$

Consistent tangent modulus is computed as the derivative of stress over strain. Stress takes the trial value from (3.93) if damage multiplier $\bar{\gamma}_{n+1}^{(k)}$ is zero, and the value from (3.97) if $\bar{\gamma}_{n+1}^{(k)}$ is positive. In the second case, equations (3.99), (3.94) and (3.93) are used to express the stress as a function of strain.

$$\left.\frac{\partial \sigma}{\partial \bar{\varepsilon}}\right|_{n+1}^{(k)} = \begin{cases} \bar{D}_n^{-1}; & \bar{\gamma}_{n+1}^{(k)} = 0 \\ \dfrac{\bar{D}_n^{-1} H_c}{\bar{D}_n^{-1} + H_c}; & \bar{\gamma}_{n+1}^{(k)} > 0 \end{cases} \tag{3.100}$$

The hardening internal variables, stress and tangent modulus have been determined under assumption, that carrying capacity is not exceeded. A control is required to verify that assumption. If indeed the carrying capacity is not reached, the results are accepted. In the opposite case, the results are discarded and computed again, taking into account the newly appeared discontinuity.

To perform the control, the location x_d of the potential discontinuity must first be determined. It is positioned according to the stress state in the layer. In case of constant stress, it is placed in the middle of the layer. In case of a linear stress distribution, the positioning is not so trivial because of different failure stresses of concrete in tension and compression. Let us consider the situation, when the highest value of stress is at node 1, $\sigma_1 > \sigma_2$. The seven possible linear stress states are shown in Fig. 3.21. Criterion $\sigma_3 \geq 0$ covers the cases a, b, c and d, where the greatest tensile stress is greater than or equal to the absolute value of the biggest compressive stress. Since the ultimate stress is much higher in compression, the failure is only possible in tension and the discontinuity is placed at the left node. In cases f and g, where $\sigma_1 \leq 0$, the whole layer is in compression and the failure can only occur at node 2. In case e, the location of the discontinuity is determined from the ratio of maximum compressive stress to maximum tensile stress in the layer, compared to the ratio of ultimate stresses in compression and tension. Situation $\sigma_1 < \sigma_2$ would be treated in the same way. Here $\sigma_1 = \sigma|_{x=0}$, $\sigma_2 = \sigma|_{x=L}$ and $\sigma_3 = \sigma|_{x=L/2}$.

$$
\begin{aligned}
&\sigma_1 = \sigma_2 = \sigma_3 \;\Rightarrow\; x_d^i = L/2 \\
&\sigma_1 > \sigma_2 \;\Rightarrow\; \begin{cases} \sigma_3 \geq 0 \;\Rightarrow\; x_d^i = 0 \\ \sigma_3 < 0 \;\Rightarrow\; \begin{cases} \sigma_1 \leq 0 \;\Rightarrow\; x_d^i = L \\ \sigma_1 > 0 \;\Rightarrow\; \begin{cases} |\sigma_2/\sigma_1| \leq (\sigma_{fcc}/\sigma_{fct}) \;\Rightarrow\; x_d^i = 0 \\ |\sigma_2/\sigma_1| > (\sigma_{fcc}/\sigma_{fct}) \;\Rightarrow\; x_d^i = L \end{cases} \end{cases} \end{cases} \\
&\sigma_1 < \sigma_2 \;\Rightarrow\; \text{analogously to } \sigma_1 > \sigma_2
\end{aligned}
\tag{3.101}
$$

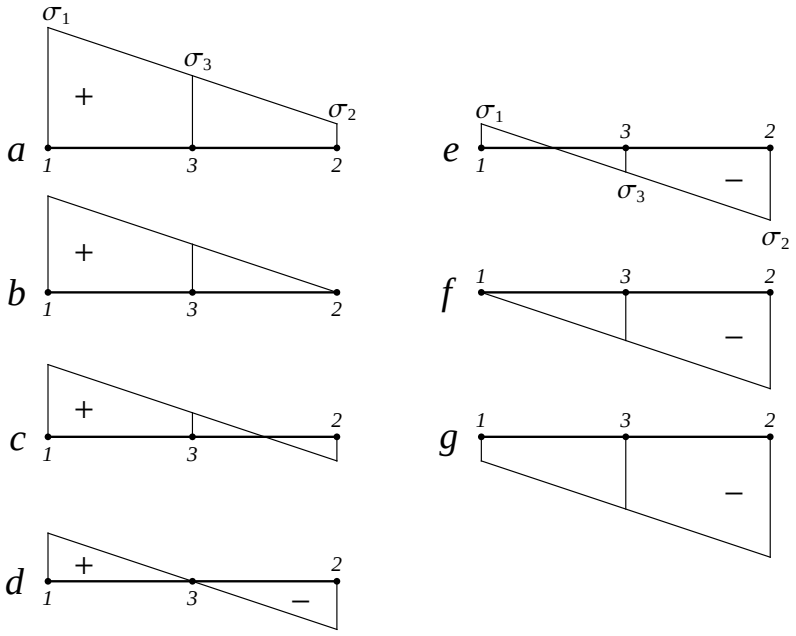

Figure 3.21: Seven possible linear stress states in a layer.
Slika 3.21: Sedem možnih linearnih razporedov napetosti v sloju.

When location of the potential discontinuity is known, we can compute the potential value of traction at the discontinuity $t_{n+1}^{(k),pot}$ according to equation (3.35). Appropriate operator $\bar{G}_V$ is chosen from (3.50), depending on

x_d. The integral is evaluated numerically with the three-point Gauss-Lobatto integration scheme.

$$t_{n+1}^{(k),pot} = -\int_L \bar{G}_V \sigma_{n+1}^{(k)} dx \tag{3.102}$$

As we have shown in section 3.2.4.2, the value of $t_{n+1}^{(k),pot}$ is equal to $\sigma_{n+1}^{(k)}\Big|_{x_d}$ for a linear stress distribution. Failure function $\bar{\bar{\phi}}_{n+1}^{(k),pot}$ is then evaluated with the stress-like softening variable $\bar{\bar{q}}_{n+1}^{(k),pot}$ equal to zero, because there has been no reduction of carrying capacity in previous steps.

$$\bar{\bar{\phi}}_{n+1}^{(k),pot} = \left|t_{n+1}^{(k),pot}\right| - \left(\sigma_{fc} - \bar{\bar{q}}_{n+1}^{(k),pot}\right), \quad \bar{\bar{q}}_{n+1}^{(k),pot} = 0 \tag{3.103}$$

The discontinuity flag is set to $true$ if the failure function is positive, and to $false$ otherwise. Note that the value of the flag is not final, until the converged state is reached. It can change in following iterations.

$$\begin{aligned} \bar{\bar{\phi}}_{n+1}^{(k),pot} \leq 0 \quad &\Rightarrow \quad crack_{n+1}^{(e),i} = false \\ \bar{\bar{\phi}}_{n+1}^{(k),pot} > 0 \quad &\Rightarrow \quad crack_{n+1}^{(e),i} = true \end{aligned} \tag{3.104}$$

If the carrying capacity is exceeded ($\bar{\bar{\phi}}_{n+1}^{(k),pot} > 0$), the above computed values of internal variables, stress and tangent modulus are discarded for this iteration and computed anew as described in section 3.3.1.2.

3.3.1.2 Discontinuity in concrete layer

In this section we describe the computational procedure for the softening phase of the concrete layer. The procedure is used if the current value of discontinuity flag $crack_{n+1}^{(e),i} = true$. This is a consequence of either an existing discontinuity in the previous step ($crack_n^{(e),i} = true$), or exceeded ultimate stress in this iteration, as written in equation (3.104). In both cases, the hardening internal variables take the last converged values, i.e. the values from the last step. The error of such choice is negligible for small enough pseudo-time step.

$$\bar{D}_{n+1}^{(k)} = \bar{D}_n, \quad \bar{\xi}_{n+1}^{(k)} = \bar{\xi}_n \tag{3.105}$$

The computation is started by assuming an elastic step, which implies no change in the softening internal variables in this iteration. We use the displacement-like softening variable $\bar{\bar{\xi}}^*$, introduced in equation (3.69).

$$\bar{\bar{D}}_{n+1}^{(k),trial} = \bar{\bar{D}}_n, \quad \bar{\bar{\xi}}_{n+1}^{*(k),trial} = \bar{\bar{\xi}}_n^* \tag{3.106}$$

The trial value of traction at the discontinuity is defined by equation (3.107), where operator $\bar{G}_R$ is chosen from expressions (3.46), accordingly to the position of the discontinuity x_d, which is known either from the previous step or from equation (3.101). Linear functions $\breve{\mathbf{B}}$ and $\bar{G}_R$ are evaluated at x_d and the bulk compliance $\bar{D}_n$ at x_d is used. Derivation of the expression is shown in appendix C.

$$t_{n+1}^{(k),trial} = \left[\frac{\breve{\mathbf{B}}\mathbf{d}_{n+1}^{(k-1)}}{\bar{D}_n - \bar{G}_R \bar{\bar{D}}_n}\right]_{x=x_d} \tag{3.107}$$

The trial stress in the layer is computed according to expression (3.54), where the trial value of displacement jump $\alpha_{n+1}^{(k),trial}$ is calculated from equation (3.64).

$$\sigma_{n+1}^{(k),trial} = \bar{D}_n\,\bar{\varepsilon}\left(\mathbf{d}_{n+1}^{(k-1)}, \alpha_{n+1}^{(k),trial}\right), \quad \alpha_{n+1}^{(k),trial} = \bar{\bar{D}}_n t_{n+1}^{(k),trial} \tag{3.108}$$

Next, the trial value of failure function $\bar{\bar{\phi}}_{n+1}^{(k),trial}$ is computed, using expression (3.70) for computation of the stress-like softening variable $\bar{\bar{q}}_{n+1}^{(k),trial}$.

$$\bar{\bar{\phi}}_{n+1}^{(k),trial} = \left|t_{n+1}^{(k),trial}\right| - \left(\sigma_{fc} - \bar{\bar{q}}_{n+1}^{(k),trial}\right), \quad \bar{\bar{q}}_{n+1}^{(k),trial} = \min\left\{-K_c^*\bar{\bar{\xi}}_{n+1}^{*(k),trial}, \sigma_{fc}\right\} = \bar{\bar{q}}_n \tag{3.109}$$

If $\bar{\bar{\phi}}_{n+1}^{(k),trial} \leq 0$, the trial solution is accepted.

$$\begin{aligned} &\bar{\bar{D}}_{n+1}^{(k)} = \bar{\bar{D}}_{n+1}^{(k),trial}, \quad \bar{\bar{\xi}}_{n+1}^{*(k)} = \bar{\bar{\xi}}_{n+1}^{*(k),trial}, \quad \alpha_{n+1}^{(k)} = \alpha_{n+1}^{(k),trial} \\ &t_{n+1}^{(k)} = t_{n+1}^{(k),trial}, \quad \sigma_{n+1}^{(k)} = \sigma_{n+1}^{(k),trial} \end{aligned} \tag{3.110}$$

If $\bar{\bar{\phi}}_{n+1}^{(k),trial} > 0$, the assumed trial values are not admissible. We have to compute the softening damage multiplier $\bar{\bar{\gamma}}_{n+1}^{*(k)} = \dot{\bar{\bar{\gamma}}}_{n+1}^{*(k)}(\tau_{n+1} - \tau_n) > 0$ from equation $\bar{\bar{\phi}}_{n+1}^{(k)} = 0$ in order to compute new values of internal softening variables, see appendix C. Linear operator $\bar{G}_R$ is evaluated at x_d and the bulk compliance $\bar{D}_n$ at x_d is used.

$$\bar{\bar{\gamma}}_{n+1}^{*(k)} = \left[\frac{\bar{\bar{\phi}}_{n+1}^{(k),trial}\left(\bar{D}_n - \bar{G}_R\bar{\bar{D}}_n\right)}{K_c^*\bar{D}_n - \bar{G}_R}\right]_{x=x_d} \tag{3.111}$$

If $\bar{\bar{q}}_{n+1}^{(k)} = -K_c^*\left(\bar{\bar{\xi}}_n^* + \bar{\bar{\gamma}}_{n+1}^{*(k)}\right) < \sigma_{fc}$, the softening internal variables are updated, following the incremental form of evolution equations (3.71).

$$\alpha_{n+1}^{(k)} = \left(\alpha_n^{\max} + \bar{\bar{\gamma}}_{n+1}^{*(k)}\right) sign\left(t_{n+1}^{(k),trial}\right), \;\; \bar{\bar{\xi}}_{n+1}^{*(k)} = \bar{\bar{\xi}}_n^* + \bar{\bar{\gamma}}_{n+1}^{*(k)}, \;\; \bar{\bar{D}}_{n+1}^{(k)} = \frac{\alpha_{n+1}^{(k)}}{t_{n+1}^{(k)}} = \frac{\alpha_n^{\max} + \bar{\bar{\gamma}}_{n+1}^{*(k)}}{\sigma_{fc} + K_c^*\bar{\bar{\xi}}_{n+1}^{*(k)}} \tag{3.112}$$

Here, $\alpha_n^{\max} = \bar{\bar{D}}_n t_n^{\max} = \bar{\bar{D}}_n\left(\sigma_{fc} + K_c^*\bar{\bar{\xi}}_n^*\right)$ is the maximal elastic value of α for the given carrying capacity that was reached in the last softening step. Traction at the discontinuity and stress in the layer are computed as follows.

$$t_{n+1}^{(k)} = \left(\sigma_{fc} - \bar{\bar{q}}_{n+1}^{(k)}\right) sign\left(t_{n+1}^{(k),trial}\right), \quad \sigma_{n+1}^{(k)} = \bar{D}_n\,\bar{\varepsilon}\left(\mathbf{d}_{n+1}^{(k-1)}, \alpha_{n+1}^{(k)}\right) \tag{3.113}$$

If $-K_c^*\left(\bar{\bar{\xi}}_n^* + \bar{\bar{\gamma}}_{n+1}^{*(k)}\right) > \sigma_{fc} = \bar{\bar{q}}_{n+1}^{(k)}$, material has lost all carrying capacity and traction at the discontinuity becomes zero.

$$t_{n+1}^{(k)} = \sigma_{n+1}^{(k)}\Big|_{x_d} = \left[\bar{D}_n\left(\check{\mathbf{B}}\mathbf{d}_{n+1}^{(k-1)} + \bar{G}_R\,\alpha_{n+1}^{(k)}\right)\right]_{x=x_d} = 0 \tag{3.114}$$

From above equation we can compute the displacement jump and the compliance at the discontinuity. Note that the linear functions $\breve{\mathbf{B}}$ and $\bar{G}_R$ are evaluated at x_d.

$$\alpha_{n+1}^{(k)} = \left[-\frac{\breve{\mathbf{B}}\mathbf{d}_{n+1}^{(k-1)}}{\bar{G}_R} \right]_{x=x_d}, \quad \bar{\bar{D}}_{n+1}^{(k)} = \frac{\alpha_{n+1}^{(k)}}{t_{n+1}^{(k)}} = \infty \tag{3.115}$$

The tangent modulus is computed as the derivative of traction at the discontinuity over the displacement jump. If $\bar{\bar{\gamma}}_{n+1}^{*(k)} = 0$, their relation is described by equation (3.108). If $\bar{\bar{\gamma}}_{n+1}^{*(k)} > 0$ and $\bar{\bar{q}}_{n+1}^{(k)} = -K_c^* \left(\bar{\bar{\xi}}_n^* + \bar{\bar{\gamma}}_{n+1}^{*(k)} \right) < \sigma_{fc}$, traction takes the value from (3.113). The first of equations (3.112) is used to express the traction as a function of displacement jump. If $\bar{\bar{\gamma}}_{n+1}^{*(k)} > 0$ and $\bar{\bar{q}}_{n+1}^{(k)} = \sigma_{fc}$, traction is constantly zero.

$$\left. \frac{\partial t}{\partial \alpha} \right|_{n+1}^{(k)} = \begin{cases} \bar{\bar{D}}_n^{-1}; & \bar{\bar{\gamma}}_{n+1}^{*(k)} = 0 \\ K_c^* = \sigma_{fc} K_c; & \bar{\bar{\gamma}}_{n+1}^{*(k)} > 0,\ \bar{\bar{q}}_{n+1}^{(k)} < \sigma_{fc} \\ 0; & \bar{\bar{\gamma}}_{n+1}^{*(k)} > 0,\ \bar{\bar{q}}_{n+1}^{(k)} = \sigma_{fc} \end{cases} \tag{3.116}$$

The discontinuity flag is set to $crack_{n+1}^{(e),i} = true$.

3.3.1.3 Bulk of reinforcement layer

The computational procedure for the hardening phase of the reinforcement layer is described next. There is no discontinuity in the layer and the displacement jump is zero. First, we assume elastic behavior, meaning that hardening internal variables keep the values from the previous step. Stress is computed in accordance with equation (3.74), where $\alpha_{n+1}^{(k)} = 0$.

$$\bar{\varepsilon}_{p,n+1}^{(k),trial} = \bar{\varepsilon}_{p,n},\ \bar{\xi}_{n+1}^{(k),trial} = \bar{\xi}_n, \quad \sigma_{n+1}^{(k),trial} = E_s \left(\bar{\varepsilon} \left(\mathbf{d}_{n+1}^{(k-1)}, \alpha_{n+1}^{(k)} \right) - \bar{\varepsilon}_{p,n+1}^{(k),trial} \right) \tag{3.117}$$

Trial yield function $\bar{\phi}_{n+1}^{(k),trial}$ is computed, as defined in (3.75) and (3.76).

$$\bar{\phi}_{n+1}^{(k),trial} = \left| \sigma_{n+1}^{(k),trial} \right| - \left(\sigma_y - \bar{q}_{n+1}^{(k),trial} \right), \quad \bar{q}_{n+1}^{(k),trial} = -H_s \bar{\xi}_{n+1}^{(k),trial} = -H_s \bar{\xi}_n \tag{3.118}$$

The trial solution is accepted if the trial yield function is negative or zero.

$$\bar{\phi}_{n+1}^{(k),trial} \leq 0 \quad \Rightarrow \quad \bar{\varepsilon}_{p,n+1}^{(k)} = \bar{\varepsilon}_{p,n+1}^{(k),trial}, \quad \bar{\xi}_{n+1}^{(k)} = \bar{\xi}_{n+1}^{(k),trial}, \quad \sigma_{n+1}^{(k)} = \sigma_{n+1}^{(k),trial} \tag{3.119}$$

If the trial yield function is positive, the internal variables must be corrected, according to incremental form of evolution equations (3.77), where $\bar{\gamma}_{n+1}^{(k)} = \dot{\bar{\gamma}}_{n+1}^{(k)} \left(\tau_{n+1} - \tau_n \right) > 0$. It is shown in appendix A that $sign \left(\sigma_{n+1}^{(k)} \right) = sign \left(\sigma_{n+1}^{(k),trial} \right)$.

$$\bar{\phi}_{n+1}^{(k),trial} > 0 \quad \Rightarrow \quad \bar{\varepsilon}_{p,n+1}^{(k)} = \bar{\varepsilon}_{p,n} + \bar{\gamma}_{n+1}^{(k)} sign \left(\sigma_{n+1}^{(k),trial} \right), \quad \bar{\xi}_{n+1}^{(k)} = \bar{\xi}_n + \bar{\gamma}_{n+1}^{(k)} \tag{3.120}$$

By exploiting equations (3.120), the stress $\sigma_{n+1}^{(k)}$ and the stress-like hardening variable $\bar{q}_{n+1}^{(k)}$ can be expressed with their trial values and the damage multiplier $\bar{\gamma}_{n+1}^{(k)}$.

$$\begin{aligned}\sigma_{n+1}^{(k)} &= E_s\left(\bar{\varepsilon}\left(\mathbf{d}_{n+1}^{(k-1)},\alpha_{n+1}^{(k)}\right)-\bar{\varepsilon}_{p,n+1}^{(k)}\right)= \\ &= E_s\left(\bar{\varepsilon}\left(\mathbf{d}_{n+1}^{(k-1)},\alpha_{n+1}^{(k)}\right)-\bar{\varepsilon}_{p,n}\right)-E_s\bar{\gamma}_{n+1}^{(k)}sign\left(\sigma_{n+1}^{(k),trial}\right)= \\ &= \sigma_{n+1}^{(k),trial}-E_s\bar{\gamma}_{n+1}^{(k)}sign\left(\sigma_{n+1}^{(k),trial}\right)\end{aligned} \tag{3.121}$$

$$\bar{q}_{n+1}^{(k)} = -H_s\bar{\xi}_{n+1}^{(k)} = -H_s\left(\bar{\xi}_n+\bar{\gamma}_{n+1}^{(k)}\right) = \bar{q}_{n+1}^{(k),trial}-H_s\bar{\gamma}_{n+1}^{(k)} \tag{3.122}$$

Yield function $\bar{\phi}_{n+1}^{(k)}$ is expressed as a function of plastic multiplier $\bar{\gamma}_{n+1}^{(k)}$ by employing equations (3.121) and (3.122). Value of the plastic multiplier is computed from requirement $\bar{\phi}_{n+1}^{(k)}=0$.

$$\begin{aligned}\bar{\phi}_{n+1}^{(k)} &= \left|\sigma_{n+1}^{(k)}\right|-\left(\sigma_y-\bar{q}_{n+1}^{(k)}\right)=\left|\sigma_{n+1}^{(k),trial}\right|-E_s\bar{\gamma}_{n+1}^{(k)}-\left(\sigma_y-\bar{q}_{n+1}^{(k),trial}\right)-H_s\bar{\gamma}_{n+1}^{(k)}= \\ &= \bar{\phi}_{n+1}^{(k),trial}-\left(E_s+H_s\right)\bar{\gamma}_{n+1}^{(k)} \\ \bar{\phi}_{n+1}^{(k)}=0 \quad &\Rightarrow \quad \bar{\gamma}_{n+1}^{(k)}=\frac{\bar{\phi}_{n+1}^{(k),trial}}{E_s+H_s}\end{aligned} \tag{3.123}$$

Consistent tangent modulus is computed as the derivative of stress over strain. Stress takes the trial value from equation (3.117) if plastic multiplier $\bar{\gamma}_{n+1}^{(k)}$ is zero, and the value from (3.121) if $\bar{\gamma}_{n+1}^{(k)}$ is positive. In the second case, equations (3.123), (3.118) and (3.117) are used to express the stress as a function of strain.

$$\left.\frac{\partial\sigma}{\partial\bar{\varepsilon}}\right|_{n+1}^{(k)} = \begin{cases} E_s; & \bar{\gamma}_{n+1}^{(k)}=0 \\ \dfrac{E_sH_s}{E_s+H_s}; & \bar{\gamma}_{n+1}^{(k)}>0 \end{cases} \tag{3.124}$$

The hardening internal variables, stress in the layer and the tangent modulus have been calculated under assumption that the ultimate stress is not exceeded. This still requires verification. If the assumption is confirmed, the above results are accepted. Otherwise, they are discarded and recomputed with the presence of the discontinuity.

The first step is to determine the location of the potential discontinuity x_d. Since the behavior of steel is symmetric in tension and compression, the discontinuity is simply placed at the location of maximal stress in absolute value. This can occur at either end of the layer because of the linear form of stress. If the stress is constant, the discontinuity is placed in the middle of the layer.

$$\begin{array}{lcll} \sigma_1=\sigma_2=\sigma_3 & \Rightarrow & x_d^i=L/2 & \\ |\sigma_1|>|\sigma_2| & \Rightarrow & x_d^i=0 & \text{where} \quad \sigma_2=\sigma|_{x=L} \\ |\sigma_1|<|\sigma_2| & \Rightarrow & x_d^i=L & \sigma_3=\sigma|_{x=L/2} \end{array} \qquad \sigma_1=\sigma|_{x=0} \tag{3.125}$$

With the location of the potential discontinuity determined, we can calculate the potential value of traction at the discontinuity $t_{n+1}^{(k),pot}$ by equation (3.35). Correct operator $\bar{G}_V$ is chosen from (3.50), depending on x_d. The integral is evaluated numerically with the three-point Gauss-Lobatto integration scheme.

$$t_{n+1}^{(k),pot} = -\int_L \bar{G}_V\sigma_{n+1}^{(k)}dx \tag{3.126}$$

As shown in section 3.2.4.2, the traction $t_{n+1}^{(k),pot}$ equals $\sigma_{n+1}^{(k)}\Big|_{x_d}$ for a linear stress distribution. Failure function $\bar{\bar{\phi}}_{n+1}^{(k),pot}$ is evaluated with the stress-like softening variable equal to zero, as there has been no reduction of carrying capacity in previous steps.

$$\bar{\bar{\phi}}_{n+1}^{(k),pot} = \left|t_{n+1}^{(k),pot}\right| - \left(\sigma_{fs} - \bar{\bar{q}}_{n+1}^{(k),pot}\right), \quad \bar{\bar{q}}_{n+1}^{(k),pot} = 0 \tag{3.127}$$

We set the value of the discontinuity flag to $true$ if the failure function is positive, and to $false$ otherwise. The value is not final, however, until the converged state is reached. It can change in following iterations.

$$\begin{aligned} \bar{\bar{\phi}}_{n+1}^{(k),pot} \leq 0 \quad &\Rightarrow \quad crack_{n+1}^{(e),i} = false \\ \bar{\bar{\phi}}_{n+1}^{(k),pot} > 0 \quad &\Rightarrow \quad crack_{n+1}^{(e),i} = true \end{aligned} \tag{3.128}$$

If the carrying capacity is exceeded, the above computed values of internal hardening variables, stress in the layer and traction at the discontinuity are discarded and computed again, as explained in the following section.

3.3.1.4 Discontinuity in reinforcement layer

This section describes the computational procedure for the softening phase of the reinforcement layer. It is applied if the current value of the discontinuity flag $crack_{n+1}^{(e),i} = true$, which happens if the discontinuity already existed in the previous step, or if the carrying capacity of the layer was exceeded in this iteration, see equation (3.128). In any case, the hardening internal variables take the values from the previous step, which are the last converged results. The error of such choice is negligible for small pseudo-time step.

$$\bar{\varepsilon}_{p,n+1}^{(k)} = \bar{\varepsilon}_{p,n}, \quad \bar{\xi}_{n+1}^{(k)} = \bar{\xi}_n \tag{3.129}$$

We start by assuming a trial solution, keeping the softening internal variables at the values from the previous step. Stress in the layer and traction at the discontinuity are computed according to equations (3.74) and (3.35), respectively.

$$\begin{aligned} &\alpha_{n+1}^{(k),trial} = \alpha_n, \quad \bar{\bar{\xi}}_{n+1}^{(k),trial} = \bar{\bar{\xi}}_n \\ &\sigma_{n+1}^{(k),trial} = E_s\left(\bar{\varepsilon}\left(\mathbf{d}_{n+1}^{(k-1)}, \alpha_{n+1}^{(k),trial}\right) - \bar{\varepsilon}_{p,n}\right), \quad t_{n+1}^{(k),trial} = -\int_L \bar{G}_V \sigma_{n+1}^{(k),trial} dx \end{aligned} \tag{3.130}$$

The integral is computed numerically with the three-point Gauss-Lobatto integration scheme and evaluates to $t_{n+1}^{(k),trial} = \sigma_{n+1}^{(k),trial}\Big|_{x_d}$ for the linear distribution of stress over the layer.

The trial value of failure function $\bar{\bar{\phi}}_{n+1}^{(k),trial}$ is calculated, respecting equations (3.84) and (3.85).

$$\bar{\bar{\phi}}_{n+1}^{(k),trial} = \left|t_{n+1}^{(k),trial}\right| - \left(\sigma_{fs} - \bar{\bar{q}}_{n+1}^{(k),trial}\right), \quad \bar{\bar{q}}_{n+1}^{(k),trial} = \min\left\{-K_s \bar{\bar{\xi}}_{n+1}^{(k),trial}, \sigma_{fs}\right\} = \bar{\bar{q}}_n \tag{3.131}$$

If $\bar{\bar{\phi}}_{n+1}^{(k),trial} \leq 0$, the trial solution is accepted.

$$\alpha_{n+1}^{(k)} = \alpha_{n+1}^{(k),trial}, \quad \bar{\bar{\xi}}_{n+1}^{(k)} = \bar{\bar{\xi}}_{n+1}^{(k),trial}, \quad \sigma_{n+1}^{(k)} = \sigma_{n+1}^{(k),trial}, \quad t_{n+1}^{(k)} = t_{n+1}^{(k),trial} \tag{3.132}$$

If $\bar{\bar{\phi}}_{n+1}^{(k),trial} > 0$, the assumed solution is not admissible. The softening internal variables are updated according to the incremental form of evolution equations (3.86), where $\bar{\bar{\gamma}}_{n+1}^{(k)} = \dot{\bar{\bar{\gamma}}}_{n+1}^{(k)} (\tau_{n+1} - \tau_n) > 0$. It is shown in appendix A that $sign\left(t_{n+1}^{(k)}\right) = sign\left(t_{n+1}^{(k),trial}\right)$.

$$\alpha_{n+1}^{(k)} = \alpha_n + \bar{\bar{\gamma}}_{n+1}^{(k)} sign\left(t_{n+1}^{(k),trial}\right), \quad \bar{\bar{\xi}}_{n+1}^{(k)} = \bar{\bar{\xi}}_n + \bar{\bar{\gamma}}_{n+1}^{(k)} \tag{3.133}$$

By using equations (3.133), the traction at the discontinuity $t_{n+1}^{(k)}$ and the stress-like softening variable $\bar{\bar{q}}_{n+1}^{(k)}$ are expressed with their trial values and the softening multiplier $\bar{\bar{\gamma}}_{n+1}^{(k)}$.

$$\begin{aligned} t_{n+1}^{(k)} &= \sigma_{n+1}^{(k)}\Big|_{x_d} = \left[E_s\left(\check{\mathbf{B}}\mathbf{d}_{n+1}^{(k-1)} + \bar{G}_R \alpha_{n+1}^{(k)} - \bar{\varepsilon}_{p,n}\right)\right]_{x=x_d} = \\ &= \left[E_s\left(\check{\mathbf{B}}\mathbf{d}_{n+1}^{(k-1)} + \bar{G}_R \alpha_n - \bar{\varepsilon}_{p,n}\right)\right]_{x=x_d} + \left[E_s \bar{G}_R \bar{\bar{\gamma}}_{n+1}^{(k)} sign\left(t_{n+1}^{(k),trial}\right)\right]_{x=x_d} = \\ &= t_{n+1}^{(k),trial} + E_s \bar{G}_R\big|_{x_d} \bar{\bar{\gamma}}_{n+1}^{(k)} sign\left(t_{n+1}^{(k),trial}\right) \end{aligned} \tag{3.134}$$

$$\bar{\bar{q}}_{n+1}^{(k)} = \begin{cases} \bar{\bar{q}}_{n+1}^{A} = \bar{\bar{q}}_{n+1}^{(k),trial} - K_s \bar{\bar{\gamma}}_{n+1}^{(k)}; & -K_s\left(\bar{\bar{\xi}}_n + \bar{\bar{\gamma}}_{n+1}^{A}\right) < \sigma_{fs} \\ \bar{\bar{q}}_{n+1}^{B} = \sigma_{fs}; & -K_s\left(\bar{\bar{\xi}}_n + \bar{\bar{\gamma}}_{n+1}^{A}\right) > \sigma_{fs} \end{cases} \tag{3.135}$$

Linear operator $\bar{G}_R$ in expression for $t_{n+1}^{(k)}$ is evaluated at x_d. Obtained expressions are inserted in equation $\bar{\bar{\phi}}_{n+1}^{(k)} = 0$, coming from loading/unloading conditions (3.87).

$$\bar{\bar{\phi}}_{n+1}^{(k)} = \left|t_{n+1}^{(k)}\right| - \left(\sigma_{fs} - \bar{\bar{q}}_{n+1}^{(k)}\right) = 0 \quad \Leftrightarrow \quad t_{n+1}^{(k)} = \left(\sigma_{fs} - \bar{\bar{q}}_{n+1}^{(k)}\right) sign\left(t_{n+1}^{(k),trial}\right) \tag{3.136}$$

After a short derivation we get two expressions for $\bar{\bar{\gamma}}_{n+1}^{(k)}$, depending on the expression, used for $\bar{\bar{q}}_{n+1}^{(k)}$.

$$\bar{\bar{\gamma}}_{n+1}^{(k)} = \begin{cases} \bar{\bar{\gamma}}_{n+1}^{A} = \dfrac{\bar{\bar{\phi}}_{n+1}^{(k),trial}}{-\bar{G}_R\big|_{x_d} E_s + K_s}; & -K_s\left(\bar{\bar{\xi}}_n + \bar{\bar{\gamma}}_{n+1}^{A}\right) < \sigma_{fs} \\ \bar{\bar{\gamma}}_{n+1}^{B} = \dfrac{\left|t_{n+1}^{(k),trial}\right|}{-\bar{G}_R\big|_{x_d} E_s}; & -K_s\left(\bar{\bar{\xi}}_n + \bar{\bar{\gamma}}_{n+1}^{A}\right) > \sigma_{fs} \end{cases} \tag{3.137}$$

The tangent modulus is computed as the derivative of traction at the discontinuity over the displacement jump. If $\bar{\bar{\gamma}}_{n+1}^{(k)} > 0$, traction takes the value from (3.136). Equations (3.135) and (3.133) are used to express the traction as a function of displacement jump. If $\bar{\bar{\gamma}}_{n+1}^{(k)} = 0$, the displacement jump remains constant, while the traction changes to satisfy the local equilibrium with stress in the layer. The tangent modulus cannot be determined, but it is not required for further computation.

$$\left.\frac{\partial t}{\partial \alpha}\right|_{n+1}^{(k)} = \begin{cases} \text{not defined}; & \bar{\bar{\gamma}}_{n+1}^{(k)} = 0 \\ K_s; & \bar{\bar{\gamma}}_{n+1}^{(k)} > 0,\ \bar{\bar{q}}_{n+1}^{(k)} < \sigma_{fs} \\ 0; & \bar{\bar{\gamma}}_{n+1}^{(k)} > 0,\ \bar{\bar{q}}_{n+1}^{(k)} = \sigma_{fs} \end{cases} \tag{3.138}$$

The discontinuity flag is set to $crack_{n+1}^{(e),i} = true$.

3.3.2 Computation of nodal degrees of freedom

In this section we will describe the computations of phase (B) of k-th iteration, mentioned in the introduction of section 3.3. In this phase, a linearized form of equilibrium equations (3.91) is solved to provide the k-th update of the nodal displacements/rotations at pseudo-time point τ_{n+1}. The computation is performed with known values of internal variables for each layer of each finite element - $\bar{D}_{n+1}^{(e),i,(k)}$, $\bar{\xi}_{n+1}^{(e),i,(k)}$, $\bar{\bar{D}}_{n+1}^{(e),i,(k)}$, $\bar{\bar{\xi}}_{n+1}^{(e),i,(k)}$ for a concrete layer, and $\bar{\varepsilon}_{p,n+1}^{(e),i,(k)}$, $\bar{\xi}_{n+1}^{(e),i,(k)}$, $\alpha_{n+1}^{(e),i,(k)}$, $\bar{\bar{\xi}}_{n+1}^{(e),i,(k)}$ for a layer of reinforcement - freshly updated in preceding phase (A) of the same iteration. Since the nodal degrees of freedom are generally common to several finite elements, the equations of phase (B) must be handled on structural (global) level. Hence, they are also referred to as global equations.

The first of equations (3.91) would be sufficient for calculating the new values of generalized displacements $\mathbf{d}_{n+1}^{(e),(k)}$, if all displacement jumps $\alpha_{n+1}^{(e),i,(k)}$ were fixed at the values, computed in phase (A). To improve convergence, however, it is useful to update the displacement jumps as well. For that purpose, the second of equations (3.91) are engaged. Actually, they have once already been satisfied by using expression (3.35) for the traction at the discontinuity, but that equality held for the displacements from the previous iteration $\mathbf{d}_{n+1}^{(e),(k-1)}$. Updating the displacements would disrupt the equilibrium between the traction at the discontinuity and the stress in the layer, unless the displacement jumps are updated as well. Solving the whole system of equations (3.91) therefore promises a more accurate solution.

3.3.2.1 Linearization of equilibrium equations

The first of equations (3.91) ensures the equilibrium of the structure, i.e. of its each and every node. It is linearized around the current values of nodal degrees of freedom of the structure $\mathbf{d}_{n+1}^{\text{str},(k-1)}$.

$$\underbrace{\frac{\partial \mathbf{f}_{n+1}^{\text{int,str},(k)}}{\partial \mathbf{d}_{n+1}^{\text{str},(k-1)}}}_{\mathbf{K}_{n+1}^{\text{str},(k)}} \Delta\mathbf{d}_{n+1}^{\text{str},(k)} = \mathbf{f}_{n+1}^{\text{ext,str}} - \mathbf{f}_{n+1}^{\text{int,str},(k)}, \qquad \frac{\partial \mathbf{f}_{n+1}^{\text{ext,str}}}{\partial \mathbf{d}_{n+1}^{\text{str},(k-1)}} = \mathbf{0} \tag{3.139}$$

The derivative on the left side of the equation is designated with $\mathbf{K}_{n+1}^{\text{str},(k)}$ and named the tangent stiffness matrix of the structure. $\Delta\mathbf{d}_{n+1}^{\text{str},(k)}$ is the sought update of the nodal displacements in this iteration. The vector of external forces $\mathbf{f}_{n+1}^{\text{ext,str}}$ represents the loading, which is defined in advance for each pseudo-time point τ_{n+1} and is independent of the nodal displacements. The vector of internal forces $\mathbf{f}_{n+1}^{\text{int,str},(k)}$ is computed from contributions of individual finite elements, according to equation (3.20). Matrices $\mathbf{P}^{(e)}$ and $\mathbf{R}^{(e)}$ are constant.

$$\begin{aligned}
\mathbf{f}_{n+1}^{\text{int,str},(k)} &= \sum_{e=1}^{n_{FE}} {\mathbf{P}^{(e)}}^T {\mathbf{R}^{(e)}}^{-1} \mathbf{f}_{n+1}^{\text{int},(e),(k)} \\
\mathbf{K}_{n+1}^{\text{str},(k)} &= \frac{\partial \mathbf{f}_{n+1}^{\text{int,str},(k)}}{\partial \mathbf{d}_{n+1}^{\text{str},(k-1)}} = \sum_{e=1}^{n_{FE}} {\mathbf{P}^{(e)}}^T {\mathbf{R}^{(e)}}^{-1} \frac{\partial \mathbf{f}_{n+1}^{\text{int},(e),(k)}}{\partial \mathbf{d}_{n+1}^{\text{str},(k-1)}}
\end{aligned} \tag{3.140}$$

Let us recall the relation (3.13) between the vector of nodal displacements of a finite element $\mathbf{d}_{n+1}^{(e),(k-1)}$ and the vector of nodal displacements of the structure $\mathbf{d}_{n+1}^{\text{str},(k-1)}$. The derivative of one over the other will prove useful.

$$\mathbf{d}_{n+1}^{(e),(k-1)} = \mathbf{R}^{(e)}\mathbf{P}^{(e)}\mathbf{d}_{n+1}^{\text{str},(k-1)} \quad \Rightarrow \quad \frac{\partial \mathbf{d}_{n+1}^{(e),(k-1)}}{\partial \mathbf{d}_{n+1}^{\text{str},(k-1)}} = \mathbf{R}^{(e)}\mathbf{P}^{(e)} \tag{3.141}$$

Internal forces $\mathbf{f}_{n+1}^{\text{int},(e),(k)}$ of finite element (e) are defined in equation (3.29) as a sum of contributions of n_L layers. Contributions $\mathbf{f}_{n+1}^{\text{int},(e),i,(k)}$ of the $n_{CL}^{(e)}$ cracked layers are functions of nodal displacements $\mathbf{d}_{n+1}^{(e),(k-1)}$ and displacement jumps $\alpha_{n+1}^{(e),i,(k)}$, while the contributions of the remaining (non-cracked) layers depend solely on the nodal displacements. For the sake of clarity it is assumed that the cracked layers are numbered with consecutive numbers from 1 to $n_{CL}^{(e)}$.

$$\mathbf{f}_{n+1}^{\text{int},(e),(k)} = \sum_{i=1}^{n_L} \mathbf{f}_{n+1}^{\text{int},(e),i,(k)} = \sum_{i=1}^{n_{CL}^{(e)}} \mathbf{f}_{n+1}^{\text{int},(e),i,(k)}\left(\mathbf{d}_{n+1}^{(e),(k-1)}, \alpha_{n+1}^{(e),i,(k)}\right) + \sum_{i=n_{CL}^{(e)}+1}^{n_L} \mathbf{f}_{n+1}^{\text{int},(e),i,(k)}\left(\mathbf{d}_{n+1}^{(e),(k-1)}\right) \tag{3.142}$$

The derivative of $\mathbf{f}_{n+1}^{\text{int},(e),(k)}$ over $\mathbf{d}_{n+1}^{\text{str},(k-1)}$, which appears in expression (3.140), can be developed as follows.

$$\frac{\partial \mathbf{f}_{n+1}^{\text{int},(e),(k)}}{\partial \mathbf{d}_{n+1}^{\text{str},(k-1)}} = \sum_{i=1}^{n_{CL}^{(e)}} \left(\underbrace{\frac{\partial \mathbf{f}_{n+1}^{\text{int},(e),i,(k)}}{\partial \mathbf{d}_{n+1}^{(e),(k-1)}}}_{\mathbf{K}_{n+1}^{fd,(e),i,(k)}} + \underbrace{\frac{\partial \mathbf{f}_{n+1}^{\text{int},(e),i,(k)}}{\partial \alpha_{n+1}^{(e),i,(k)}}}_{\mathbf{K}_{n+1}^{f\alpha,(e),i,(k)}} \frac{\partial \alpha_{n+1}^{(e),i,(k)}}{\partial \mathbf{d}_{n+1}^{(e),(k-1)}} \right) \overbrace{\frac{\partial \mathbf{d}_{n+1}^{(e),(k-1)}}{\partial \mathbf{d}_{n+1}^{\text{str},(k-1)}}}^{\mathbf{R}^{(e)}\mathbf{P}^{(e)}} + \sum_{i=n_{CL}^{(e)}+1}^{n_L} \overbrace{\frac{\partial \mathbf{f}_{n+1}^{\text{int},(e),i,(k)}}{\partial \mathbf{d}_{n+1}^{(e),(k-1)}}}^{\mathbf{K}_{n+1}^{fd,(e),i,(k)}} \overbrace{\frac{\partial \mathbf{d}_{n+1}^{(e),(k-1)}}{\partial \mathbf{d}_{n+1}^{\text{str},(k-1)}}}^{\mathbf{R}^{(e)}\mathbf{P}^{(e)}} \tag{3.143}$$

The derivatives of $\mathbf{f}_{n+1}^{\text{int},(e),i,(k)}$, marked with $\mathbf{K}_{n+1}^{fd,(e),i,(k)}$ and $\mathbf{K}_{n+1}^{f\alpha,(e),i,(k)}$, can be computed and the last term of both sums has been defined in (3.141). The only unknown term $\partial \alpha_{n+1}^{(e),i,(k)} / \partial \mathbf{d}_{n+1}^{(e),(k-1)}$ is determined by the second of equilibrium equations (3.91), which is linearized and solved locally, i.e. independently for each finite element and layer. This can be done because $h_{n+1}^{(e),i,(k)}$ depends on the nodal displacements of a single finite element and on the displacement jump of a single layer.

$$\begin{aligned} &\underbrace{\frac{\partial h_{n+1}^{(e),i,(k)}}{\partial \mathbf{d}_{n+1}^{(e),(k-1)}}}_{\mathbf{K}_{n+1}^{hd,(e),i,(k)}} \Delta \mathbf{d}_{n+1}^{(e),(k)} + \underbrace{\frac{\partial h_{n+1}^{(e),i,(k)}}{\partial \alpha_{n+1}^{(e),i,(k)}}}_{K_{n+1}^{h\alpha,(e),i,(k)}} \Delta \alpha_{n+1}^{(e),i,(k)} = -h_{n+1}^{(e),i,(k)} = 0 \quad \Rightarrow \\ &\Rightarrow \quad \Delta \alpha_{n+1}^{(e),i,(k)} = \underbrace{-\left(K_{n+1}^{h\alpha,(e),i,(k)}\right)^{-1} \mathbf{K}_{n+1}^{hd,(e),i,(k)}}_{\partial \alpha_{n+1}^{(e),i,(k)} / \partial \mathbf{d}_{n+1}^{(e),(k-1)}} \Delta \mathbf{d}_{n+1}^{(e),(k)} \end{aligned} \tag{3.144}$$

Note that each $h_{n+1}^{(e),i,(k)}$, computed by (3.34), evaluates to zero because the traction at the discontinuity $t_{n+1}^{(e),i,(k)}$ has been computed by expression (3.35). The derivatives, designated with $\mathbf{K}_{n+1}^{hd,(e),i,(k)}$ and $K_{n+1}^{h\alpha,(e),i,(k)}$ can be easily calculated. Equation (3.144) defines the relation between the increment of nodal displacements $\Delta \mathbf{d}_{n+1}^{(e),(k)}$ and the increment of displacement jump $\Delta \alpha_{n+1}^{(e),i,(k)}$ in the i-th layer of the finite element. Since we are dealing with linearized equations, the derivative $\partial \alpha_{n+1}^{(e),i,(k)} / \partial \mathbf{d}_{n+1}^{(e),(k-1)}$ must be equal to the ratio of the increments.

$$\frac{\partial \alpha_{n+1}^{(e),i,(k)}}{\partial \mathbf{d}_{n+1}^{(e),(k-1)}} = -\left(K_{n+1}^{h\alpha,(e),i,(k)}\right)^{-1} \mathbf{K}_{n+1}^{hd,(e),i,(k)} \tag{3.145}$$

We can rewrite expression (3.143), now being able to compute all its components.

$$\frac{\partial \mathbf{f}^{\text{int},(e),(k)}_{n+1}}{\partial \mathbf{d}^{\text{str},(k-1)}_{n+1}} = \sum_{i=1}^{n^{(e)}_{CL}} \underbrace{\left(\mathbf{K}^{fd,(e),i,(k)}_{n+1} - \mathbf{K}^{f\alpha,(e),i,(k)}_{n+1} \left(K^{h\alpha,(e),i,(k)}_{n+1} \right)^{-1} \mathbf{K}^{hd,(e),i,(k)}_{n+1} \right)}_{\hat{\mathbf{K}}^{(e),i,(k)}_{n+1}} \mathbf{R}^{(e)} \mathbf{P}^{(e)} + \\ + \sum_{i=n^{(e)}_{CL}+1}^{n_L} \mathbf{K}^{fd,(e),i,(k)}_{n+1} \mathbf{R}^{(e)} \mathbf{P}^{(e)} \tag{3.146}$$

The expression in parenthesis, marked with $\hat{\mathbf{K}}^{(e),i,(k)}_{n+1}$, is the contribution of a cracked layer to the tangent stiffness matrix of finite element (e), and $\mathbf{K}^{fd,(e),i,(k)}_{n+1}$ is the contribution of an non-cracked layer. Finally, we can assemble the tangent stiffness matrix of the structure by inserting (3.146) into (3.140).

$$\mathbf{K}^{\text{str},(k)}_{n+1} = \sum_{e=1}^{n_{FE}} \mathbf{P}^{(e)^T} \mathbf{R}^{(e)^{-1}} \underbrace{\left(\sum_{i=1}^{n^{(e)}_{CL}} \hat{\mathbf{K}}^{(e),i,(k)}_{n+1} + \sum_{i=n^{(e)}_{CL}+1}^{n_L} \mathbf{K}^{fd,(e),i,(k)}_{n+1} \right)}_{\mathbf{K}^{(e),(k)}_{n+1}} \mathbf{R}^{(e)} \mathbf{P}^{(e)} \tag{3.147}$$

Here $\mathbf{K}^{(e),(k)}_{n+1}$ is the tangent stiffness matrix of finite element (e).

3.3.2.2 Components of internal forces and stiffness matrix

Contribution $\mathbf{f}^{\text{int},(e),i,(k)}_{n+1}$ of i-th layer to internal forces of element (e) is computed according to equation (3.29), where stress takes the values computed in phase (A) of this iteration. In order to determine the components of the stiffness matrix, $h^{(e),i,(k)}_{n+1}$ must be written as well. It is computed in accordance with (3.34).

$$\mathbf{f}^{\text{int},(e),i,(k)}_{n+1} = A^i \int_L \breve{\mathbf{B}}^{i^T} \sigma^{(e),i,(k)}_{n+1} dx, \quad h^{(e),i,(k)}_{n+1} = A^i \left(\int_L \bar{G}^i_V \sigma^{(e),i,(k)}_{n+1} dx + t^{(e),i,(k)}_{n+1} \right) \tag{3.148}$$

To obtain layer components of the element stiffness matrix, expressions (3.148) are differentiated over nodal degrees of freedom and over displacement jumps.

$$\begin{aligned}
\mathbf{K}^{fd,(e),i,(k)}_{n+1} &= \frac{\partial \mathbf{f}^{\text{int},(e),i,(k)}_{n+1}}{\partial \mathbf{d}^{(e),(k-1)}_{n+1}} = A^i \int_L \breve{\mathbf{B}}^{i^T} \left. \frac{\partial \sigma}{\partial \bar{\varepsilon}} \right|^{(e),i,(k)}_{n+1} \underbrace{\breve{B}^i}_{\partial \bar{\varepsilon}/\partial \mathbf{d}} dx \\
\mathbf{K}^{f\alpha,(e),i,(k)}_{n+1} &= \frac{\partial \mathbf{f}^{\text{int},(e),i,(k)}_{n+1}}{\partial \alpha^{(e),i,(k)}_{n+1}} = A^i \int_L \breve{\mathbf{B}}^{i^T} \left. \frac{\partial \sigma}{\partial \bar{\varepsilon}} \right|^{(e),i,(k)}_{n+1} \underbrace{\bar{G}^i_R}_{\partial \bar{\varepsilon}/\partial \alpha} dx \\
\mathbf{K}^{hd,(e),i,(k)}_{n+1} &= \frac{\partial h^{(e),i,(k)}_{n+1}}{\partial \mathbf{d}^{(e),(k-1)}_{n+1}} = A^i \left(\int_L \bar{G}^i_V \left. \frac{\partial \sigma}{\partial \bar{\varepsilon}} \right|^{(e),i,(k)}_{n+1} \underbrace{\breve{\mathbf{B}}^i}_{\partial \bar{\varepsilon}/\partial \mathbf{d}} dx \right) \\
K^{h\alpha,(e),i,(k)}_{n+1} &= \frac{\partial h^{(e),i,(k)}_{n+1}}{\partial \alpha^{(e),i,(k)}_{n+1}} = A^i \left(\int_L \bar{G}^i_V \left. \frac{\partial \sigma}{\partial \bar{\varepsilon}} \right|^{(e),i,(k)}_{n+1} \underbrace{\bar{G}^i_R}_{\partial \bar{\varepsilon}/\partial \alpha} dx + \left. \frac{\partial t}{\partial \alpha} \right|^{(e),i,(k)}_{n+1} \right)
\end{aligned} \tag{3.149}$$

The tangent moduli $(\partial\sigma/\partial\bar{\varepsilon}\,)_{n+1}^{(e),i,(k)}$ and $(\partial t/\partial\alpha\,)_{n+1}^{(e),i,(k)}$ are defined by equations (3.100) and (3.116) for concrete, and by equations (3.124) and (3.138) for reinforcement. Note that in case of an elastic step in a cracked layer of reinforcement, when $\bar{\bar{\gamma}}_{n+1}^{(k)} = 0$, the second expression is infinite.

$$\left.\frac{\partial t}{\partial\alpha}\right|_{n+1}^{(e),i,(k)} = \infty \quad \Rightarrow \quad K_{n+1}^{h\alpha,(e),i,(k)} = \infty, \quad \left(K_{n+1}^{h\alpha,(e),i,(k)}\right)^{-1} = 0 \tag{3.150}$$

Since the inverse value of component $K_{n+1}^{h\alpha,(e),i,(k)}$ is consequently zero, the contribution of the i-th layer to the element tangent stiffness matrix is computed in the same way as for the non-cracked layer.

$$\hat{\mathbf{K}}_{n+1}^{(e),i,(k)} = \mathbf{K}_{n+1}^{fd,(e),i,(k)} - \mathbf{K}_{n+1}^{f\alpha,(e),i,(k)}\left(K_{n+1}^{h\alpha,(e),i,(k)}\right)^{-1}\mathbf{K}_{n+1}^{hd,(e),i,(k)} = \mathbf{K}_{n+1}^{fd,(e),i,(k)} \tag{3.151}$$

3.3.2.3 Solution of global equations

The system of global equilibrium equations (3.139) is rewritten in a clearer form.

$$\mathbf{K}_{n+1}^{\text{str},(k)}\Delta\mathbf{d}_{n+1}^{\text{str},(k)} = \Delta\mathbf{f}_{n+1}^{\text{str},(k)}, \qquad \Delta\mathbf{f}_{n+1}^{\text{str},(k)} = \mathbf{f}_{n+1}^{\text{ext,str}} - \mathbf{f}_{n+1}^{\text{int,str},(k)} \tag{3.152}$$

The external forces are an input to the analysis, internal forces are defined by equations (3.140), (3.142) and (3.148), and the tangent stiffness matrix of the structure is defined by (3.147) and (3.149). Finally, we can compute the increments and update the nodal displacements of the structure.

$$\Delta\mathbf{d}_{n+1}^{\text{str},(k)} = \left(\mathbf{K}_{n+1}^{\text{str},(k)}\right)^{-1}\Delta\mathbf{f}_{n+1}^{\text{str},(k)}, \qquad \mathbf{d}_{n+1}^{\text{str},(k)} = \mathbf{d}_{n+1}^{\text{str},(k-1)} + \Delta\mathbf{d}_{n+1}^{\text{str},(k)} \tag{3.153}$$

The updates of the displacement jumps could be computed from (3.144), but there is no benefit from that because they will be recomputed anyway in phase (A) of the next iteration.

The iterations at pseudo-time τ_{n+1} are repeated until the tolerance requirements are met.

$$\left\|\Delta\mathbf{f}_{n+1}^{\text{str},(k)}\right\| < tol, \quad \left\|\Delta\mathbf{d}_{n+1}^{\text{str},(k)}\right\| < tol \tag{3.154}$$

When the converged solution is found, we proceed to the next pseudo-time step.

3.4 Numerical examples

In this section we show some numerical examples to examine the performance of the derived finite element. The element is tested on several beam and frame examples, carried out in the finite element program AceFEM [69].

3.4.1 One element tension and compression tests

We analyze a beam in Fig. 3.22, clamped at one end. At the other end, axial displacement u is imposed and corresponding reaction F is computed. The test is performed for concrete, steel and reinforced concrete beams, in order to verify the correct implementation of material models for tension and compression.

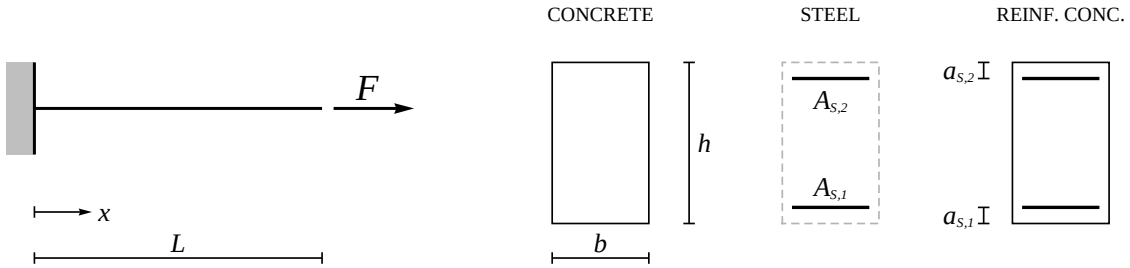

Figure 3.22: Beam in pure tension/compression: geometry.
Slika 3.22: Nosilec v čistem nategu/tlaku: geometrija.

3.4.1.1 Concrete beam

Concrete beam of rectangular cross-section is modeled with one element with two layers. The imposed axial displacement produces either tension or compression. In unloading we do not switch from tension to compression or vice versa. The geometry and the material data are: beam length is $L = 2.5$m, cross-section width is $b = 0.2$m, cross-section height is $h = 0.5$m, elastic modulus is $E_c = 4 \times 10^7 \text{kNm}^{-2}$, elasticity limit in compression is $\sigma_{dc} = 40820 \text{kNm}^{-2}$, limit strength in compression is $\sigma_{fcc} = 44902 \text{kNm}^{-2}$, hardening modulus in compression is $H_{cc} = 2 \times 10^6 \text{kNm}^{-2}$, softening modulus in compression is $K^*_{cc} = -5.2 \times 10^6 \text{kNm}^{-3}$, limit strength in tension is $\sigma_{fct} = 4000 \text{kNm}^{-2}$, and softening modulus in tension is $K^*_{ct} = -8 \times 10^6 \text{kNm}^{-3}$. By setting $\sigma_{dt} > \sigma_{fct}$ we assume no damage of the bulk in tension before crack formation. The diagrams in Fig. 3.23 show computed elasto-damage relations between the end force F and the end displacement u and suggest that the implementation of the elasto-damage model of concrete was correct.

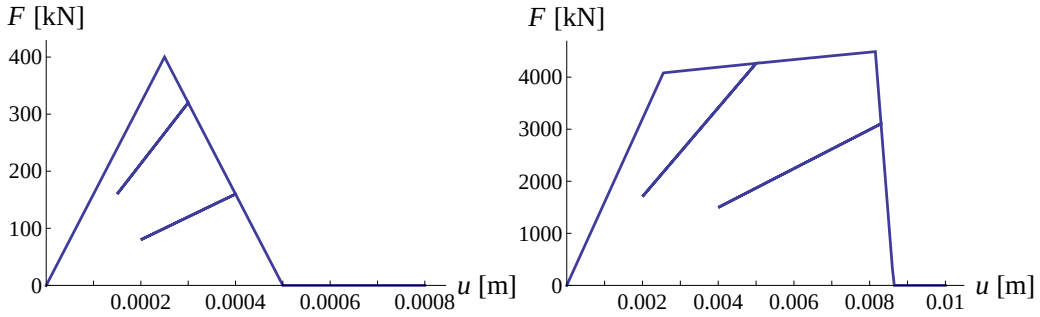

Figure 3.23: *Axial force - displacement* diagrams for concrete beam in pure tension (left) and pure compression (right).
Slika 3.23: Diagram *osna sila - pomik* za betonski nosilec v čistem nategu (levo) in čistem tlaku (desno).

3.4.1.2 Steel beam

Steel beam is modeled with one element with two layers. The following data is used: beam length is $L = 2.5$m, cross-sections of both layers are $A_{s,1} = A_{s,2} = 0.001\text{m}^2$, distances of layer axes from the beam axis are $h/2 - a_{s,1} = h/2 - a_{s,2} = 0.21$m ($a_{s,1} = a_{s,2} = 0.04$m), elastic modulus is $E_s = 2 \times 10^8 \text{kNm}^{-2}$, elasticity limit is $\sigma_y = 4 \times 10^5 \text{kNm}^{-2}$, failure strength is $\sigma_{fs} = 5 \times 10^5 \text{kNm}^{-2}$, hardening modulus is $H_s = 10^7 \text{kNm}^{-2}$, and softening modulus is $K_s = -5 \times 10^7 \text{kNm}^{-3}$. Diagram in Fig. 3.24 shows elasto-plastic relation between the end force F and the end displacement u in tension. Response of the beam in compression is identical. The diagram in Fig. 3.24 suggests that the implementation of the elasto-plastic model of steel was correct.

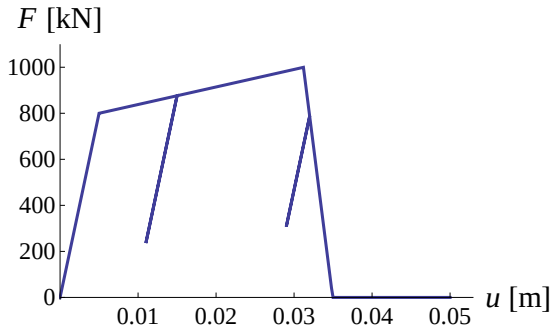

Figure 3.24: *Axial force - displacement* diagram for steel beam (layer) in pure tension.
Slika 3.24: Diagram *osna sila - pomik* za jekleni nosilec (sloj) v čistem nategu.

3.4.1.3 Reinforced concrete beam

Reinforced concrete beam is composed from the two previously presented beams, see Fig. 3.22. Geometry and material properties are listed in sections 3.4.1.1 and 3.4.1.2. The beam is modeled with one finite element with ten concrete layers and two layers of reinforcement. Diagrams in Fig. 3.25 display the responses of the beam under tensile and compressive load. In tension (left image), the first peak represents the point where concrete starts cracking and the force F begins to drop. When it starts rising again, the concrete is completely broken and the whole load is taken by the two reinforcement layers. Hereafter, the response should be equal to the response of the steel beam, modeled in section 3.4.1.2, because in our model there is no shear interaction between concrete and steel layers. However, a comparison of Fig. 3.24 and Fig. 3.25 (left) shows a different situation. Although the yielding and the softening of the material begin at the same values of force F, both processes start at significantly smaller displacements u in the reinforced concrete beam. There is no yield plateau, typical for steel, and the softening slope is not as steep.

The diagram in Fig. 3.25 (right) shows the response of the beam in compression. After the initial elastic part, the stiffness of the beam drops twice, due to micro-cracking of concrete and yielding of reinforcement, respectively. The peak of the diagram marks the moment when concrete begins to soften. Afterwards, the response is different from the expectations. The stress in concrete layers should drop to zero at $u \approx 0.0086$m and then the curve should match the diagram in Fig. 3.24. Up to $u \approx 0.03$m, the beam should offer significant resistance, but F becomes zero at one third of that displacement. Obviously, the finite element is not working properly in this case.

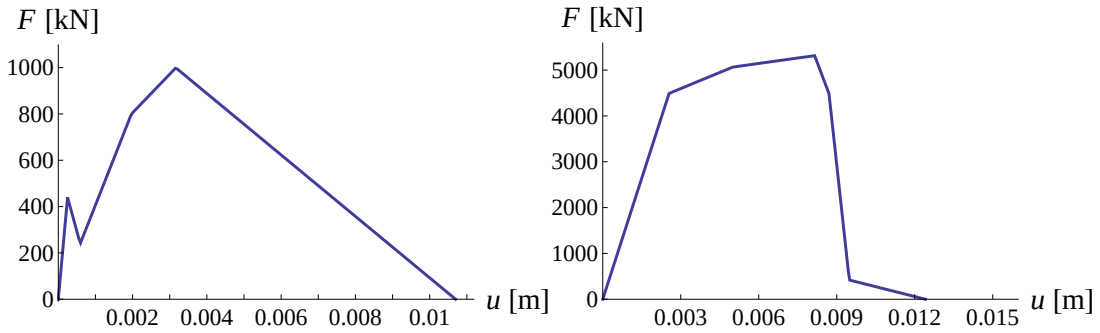

Figure 3.25: *Axial force - displacement* diagrams for reinforced concrete beam in pure tension (left) and pure compression (right).
Slika 3.25: Diagram *osna sila - pomik* za armiranobetonski nosilec v čistem nategu (levo) in čistem tlaku (desno).

It turns out that the incorrect responses, presented in Fig. 3.25, are a consequence of the linear form of operator $\bar{G}_R$, defined in equation (3.46). Although the stress is constant over each layer when the failure stress is reached, the discontinuity is placed at one of the end nodes, rather than in the middle of the element, due to numerical error. Consequently, a linear operator $\bar{G}_R$ is chosen instead of the constant one. While such choice still gives correct results for an element, composed of equal layers (such as in sections 3.4.1.1 and 3.4.1.2), it cannot work for a composition of layers with different material properties. Explanation is given in appendix D. In short, the stress is linear over the length of each layer, which means that the contributions of the layer to the internal forces in the two end nodes are not equal $f_{u_1}^{\text{int},(e),i} \neq -f_{u_2}^{\text{int},(e),i}$, see Fig. 3.26. Each layer by itself is not in balance, but the equilibrium of the finite element as a whole is satisfied by finding the exact value of u_3, at which the imbalance of internal forces in steel and the imbalance of the internal forces in concrete neutralize each other, see Fig. 3.27, where $f_{u_1}^{\text{int},(e)} = -f_{u_2}^{\text{int},(e)}$.

Remark. *Fig. 3.26 and Fig. 3.27 only show the contributions of the i-th layer to the axial internal forces at the end nodes. Contributions to the axial internal force at the middle node and contributions to transversal forces and moments exist also, but their resultants are zero on the element level.*

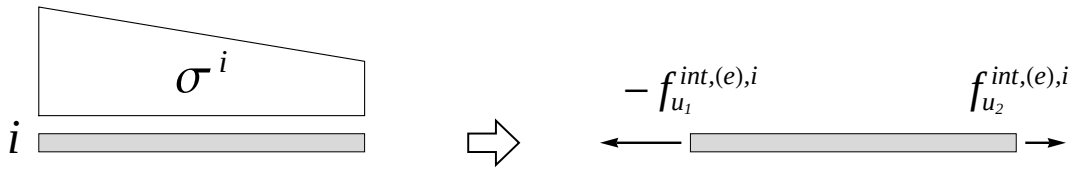

Figure 3.26: Linear stress in i-th layer (left) and resulting unequal contributions of the layer to axial internal forces of the finite element at the two nodes (right).
Slika 3.26: Linearen potek napetosti v i-tem sloju (levo) in rezultirajoča različna prispevka k osnim notranjim silam končnega elementa v obeh vozliščih (desno).

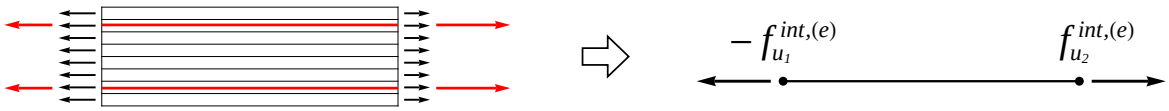

Figure 3.27: Individual layers out of balance (left) and finite element in balance (right).
Slika 3.27: Neuravnoteženi posamezni sloji (levo) in končni element v ravnotežju (desno).

3.4.1.4 Reinforced concrete beam, imposed location of discontinuity at $L/2$

The concrete, steel and reinforced concrete beams from the previous sections are analyzed again, now with the location of the discontinuity manually imposed at the middle of the finite element. Responses of the single-material beams are an exact match to those from sections 3.4.1.1 and 3.4.1.2, so they are not discussed any further. Responses of the reinforced concrete beam in tension and compression are shown in Fig. 3.28. They are a simple superposition of the diagram in Fig. 3.24 for steel and the appropriate of the diagrams in Fig. 3.23 for concrete. The curves from the previous section are included for comparison.

The tensile response in Fig. 3.28 (left) is linear elastic at first. After the first peak the concrete cracks rapidly and only the reinforcement contributes to carrying capacity. The unloading line is parallel to the loading line,

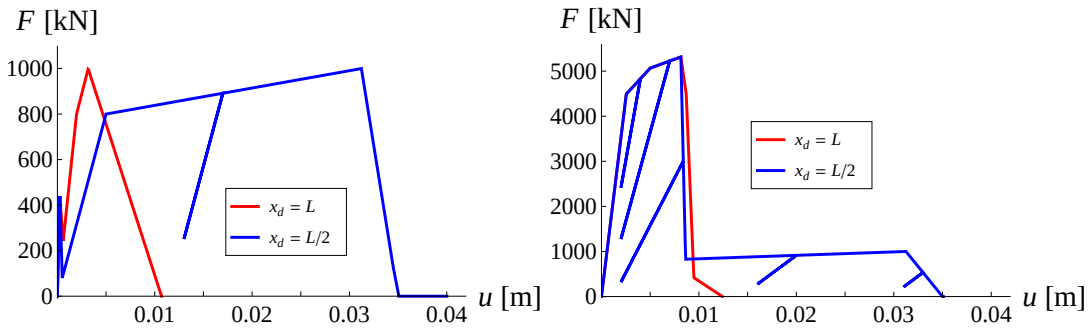

Figure 3.28: *Axial force - displacement* diagrams for reinforced concrete beam in pure tension (left) and pure compression (right) with imposed location of discontinuity at $L/2$.
Slika 3.28: Diagram *osna sila - pomik* za armiranobetonski nosilec v čistem nategu (levo) in čistem tlaku (desno) ob vsiljeni nezveznosti pri $L/2$.

immediately after the concrete is gone. In compression, Fig. 3.28 (right), the elastic part is followed by two subsequent drops in stiffness of the element, as concrete and steel enter the hardening phase. At $u \approx 0.0086$m the concrete layers crush very quickly and only the reinforcement remains. The slope of the unloading curve decreases up to that point. Later on it stays the same and only the plastic deformations still increase. In the last part of the diagram steel begins to soften as well, and the force in the beam drops to zero.

Remark. *Although the plateau from* $u \approx 0.01$m *to* $u \approx 0.03$m *in Fig. 3.28 (right) is computationally correct, it is not very realistic. With the concrete completely crushed, the reinforcement layers would encounter buckling problems. The resistance would probably drop to zero instantly, but that is out of scope of our work.*

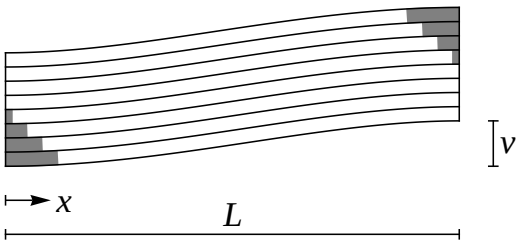

Figure 3.29: Locations and sizes of discontinuities in layers of the beam in pure tension, when transversal displacement of the free end of the beam v_2 is non-zero.
Slika 3.29: Lokacije in velikosti nezveznosti po slojih pri nosilcu v čistem nategu, ko je prečni pomik prostega konca nosilca v_2 različen od nič.

3.4.1.5 Reinforced concrete beam, non-zero transversal displacement

Another problem may arise in case of automatic determination of the location of the discontinuity. Surprisingly, equilibrium is possible in pure tension or pure compression, even if transversal displacement at the free end of the beam is not zero. This happens in a beam with symmetrical cross-section, if the bottom half of the layers (with $y^i < 0$) have a discontinuity at $x = 0$, and the other half (with $y^i > 0$) at $x = L$, or vice versa, see Fig. 3.29. The sizes of the discontinuities grow proportionally with the distance of the layer from the middle axis. For a non-zero transversal displacement v and zero rotation θ at the free end of the beam, the contributions of individual

layers to the nodal shear forces and to the nodal moments neutralize each other, see Fig. 3.31 and Fig. 3.32. The axial force F is the only remaining internal force. Such phenomenon is possible because the equilibrium is only required on the finite element level, and not for each individual layer. A detailed explanation is given in appendix D. As a result, the response of the beam is wrong from the appearance of the first discontinuity, see Fig. 3.30. The transversal displacement affects the computation of the axial force, which even starts growing instead of dropping to zero in softening.

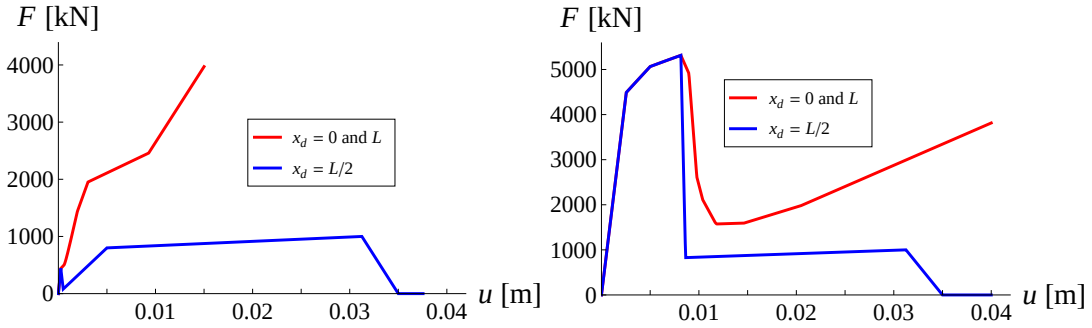

Figure 3.30: *Axial force - displacement* diagrams for reinforced concrete beam in pure tension (left) and pure compression (right): the case of non-zero transversal displacement.
Slika 3.30: Diagram *osna sila - pomik* za armiranobetonski nosilec v čistem nategu (levo) in čistem tlaku (desno): primer, ko je prečni pomik različen od nič.

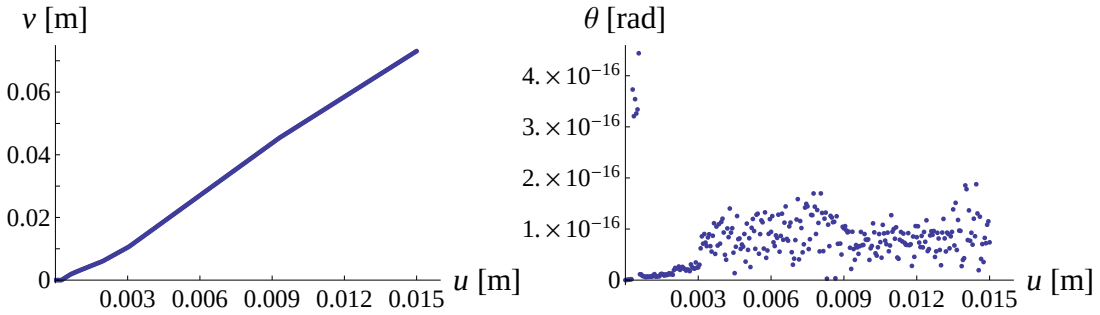

Figure 3.31: Transversal displacement (left) and rotation (right) at the free end of RC beam in tension.
Slika 3.31: Prečni pomik (levo) in zasuk (desno) na prostem koncu AB nosilca v nategu.

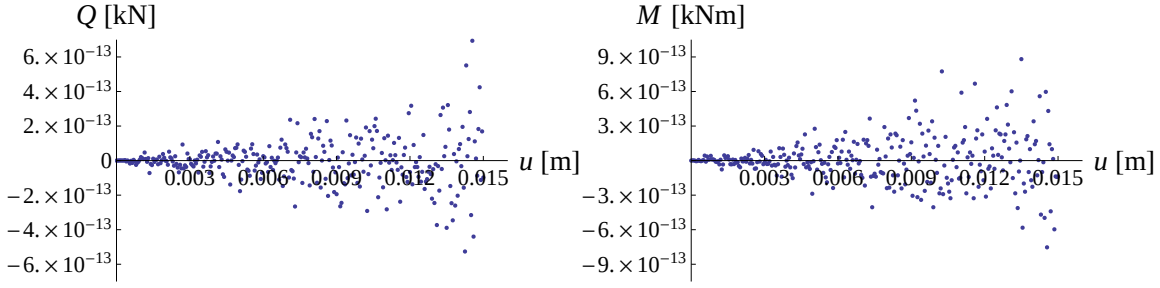

Figure 3.32: Shear force (left) and moment (right) at the support of RC beam in tension.
Slika 3.32: Prečna sila (levo) in moment (desno) ob podpori AB nosilca v nategu.

3.4.2 Cantilever beam under end moment

We analyze a reinforced concrete cantilever beam with rectangular cross-section under end moment, shown in Fig. 3.33. The load is applied by imposing the rotation at the free end of the beam. The length of the beam is $L = 1\text{m}$, the width and height of the cross-section are $b = 0.3\text{m}$ and $h = 0.4\text{m}$. Bottom and top reinforcements are $A_{s,1} = A_{s,2} = 0.001256\text{m}^2$ and they are positioned at $a_1 = a_2 = 0.05\text{m}$ from the edges of the concrete cross-section. Material properties of concrete are: elasticity modulus $E_c = 3.3 \times 10^7\text{kNm}^{-2}$, elasticity limit $\sigma_{dc} = 15200\text{kNm}^{-2}$, ultimate stress in compression $\sigma_{fcc} = 38000\text{kNm}^{-2}$, ultimate stress in tension $\sigma_{fct} = 1815\text{kNm}^{-2}$, hardening modulus in compression $H_{cc} = 3.32 \times 10^7\text{kNm}^{-2}$, softening modulus in compression $K^*_{cc} = -5 \times 10^6\text{kNm}^{-3}$ and softening modulus in tension $K^*_{ct} = -10^6\text{kNm}^{-3}$. Material properties of steel are: elasticity modulus $E_s = 2 \times 10^8\text{kNm}^{-2}$, yield stress $\sigma_y = 4 \times 10^5\text{kNm}^{-2}$, ultimate stress $\sigma_{fs} = 5 \times 10^5\text{kNm}^{-2}$, hardening modulus $H_s = 2.665 \times 10^6\text{kNm}^{-2}$ and softening modulus $K_s = -5 \times 10^7\text{kNm}^{-3}$.

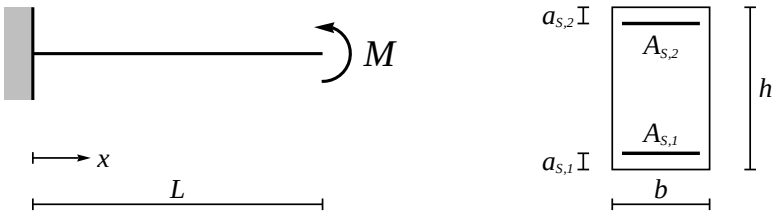

Figure 3.33: Cantilever beam under end moment: geometry.
Slika 3.33: Konzola, obremenjena z momentom: geometrija.

3.4.2.1 Mesh of equal finite elements

The beam is modeled with a mesh of identical finite elements, each consisting of 10 concrete layers and 2 layers of reinforcement. Location of the discontinuity is determined automatically, like in section 3.4.1.3. Fig. 3.34 (left) displays the moment M versus rotation θ at the end of the beam for meshes of 1, 2, 5 and 10 finite elements. The results are different from expectations. After the initial steep part of the curve, the response should exhibit a plateau, caused by yielding of the reinforcement. Instead, the moment begins to drop immediately. This behavior is caused by automatic positioning of the discontinuities. Explanation is given in appendix D.

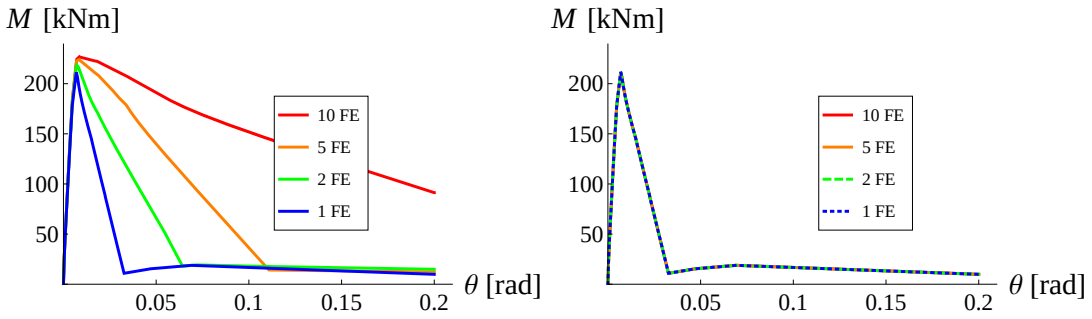

Figure 3.34: *Moment - rotation* diagrams for cantilever beam under end moment: original softening moduli (left), softening moduli modified according to length of FE (right).
Slika 3.34: Diagram *moment - zasuk* za konzolo, obteženo z momentom: originalni moduli mehčanja (levo), moduli mehčanja prirejeni glede na dolžino KE (desno).

We observe that response of the beam depends on the mesh. The slope of the softening part of the curve decreases with increasing number of finite elements. This is caused by simultaneous appearance of multiple smaller discontinuities in finer meshes, as opposed to one big discontinuity in a single FE mesh. The traction at the discontinuity decreases with the increase of its size. It is therefore understandable that, at the same value of imposed end rotation θ, a coarser mesh produces a lower moment M. If the softening moduli of steel and concrete are modified according to the length of FE (i.e. multiplied with the number of FE in the mesh), the results are no longer mesh dependent, Fig. 3.34 (right). However, this is not a proper solution of the problem because it changes the constitutive law at the discontinuity, which is a material property and should not be affected by the choice of a mesh.

3.4.2.2 Weaker reinforcement in one of the finite elements

The correct approach to the aforementioned problem is to prevent the multiple cracks from occurring. This is achieved by slightly weakening one of the finite elements in the mesh, thus simulating a material imperfection. Since the softening of the beam as a whole happens due to softening of the tensile reinforcement layer, it is sufficient to weaken the reinforcement. Rather than decreasing the ultimate stress σ_{fs} in the weak finite element, we slightly increase it in the remaining elements. When the ultimate moment is reached, the reinforcement in the weak element begins to soften and the moment decreases. The moment in the other elements must follow to ensure equilibrium. We can see in Fig. 3.35 that results for different meshes match well. Mesh dependency is avoided, but the results are still wrong due to the erroneous automatic positioning of the discontinuities, see appendix D for a detailed explanation.

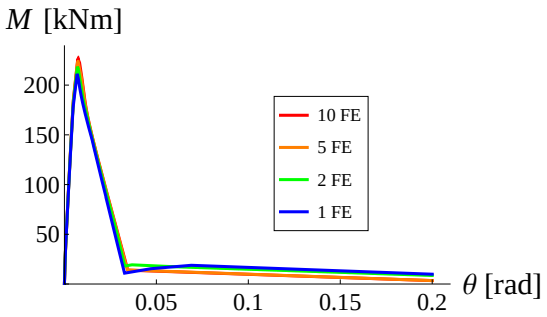

Figure 3.35: *Moment - rotation* diagram for cantilever beam under end moment: weaker reinforcement in one of the finite elements.

Slika 3.35: Diagram *moment - zasuk* za konzolo, obteženo z momentom: malce šibkejša armatura v enem od končnih elementov.

3.4.2.3 Mesh of equal finite elements, imposed location of discontinuity at $L/2$

Analysis from section 3.4.2.1 is repeated, with the only difference that the discontinuity is manually placed in the middle of the finite element $x_d = L/2$ and the constant operator $\bar{G}_R$ is employed. The moment-rotation diagram in Fig. 3.36 takes the expected form. In the first part of the curve the beam is elastic, except for some layers of concrete which soften in tension. When the tensile reinforcement yields, the stiffness of the beam drops substantially. The moment in the beam keeps growing until the tensile reinforcement enters the softening phase. After that point, carrying capacity of the cross-section decreases. Comparison of the curves for $x_d = L/2$ and $x_d = L$ from Fig. 3.36 and Fig. 3.34 is very similar to comparison in Fig. 3.28 (left) for a beam in pure tension.

As in section 3.4.2.1, the moment drops slower for finer meshes, due to formation of multiple discontinuities.

Again, modified softening moduli provide mesh-independent response, see Fig. 3.36 (right), but this is not the proper solution.

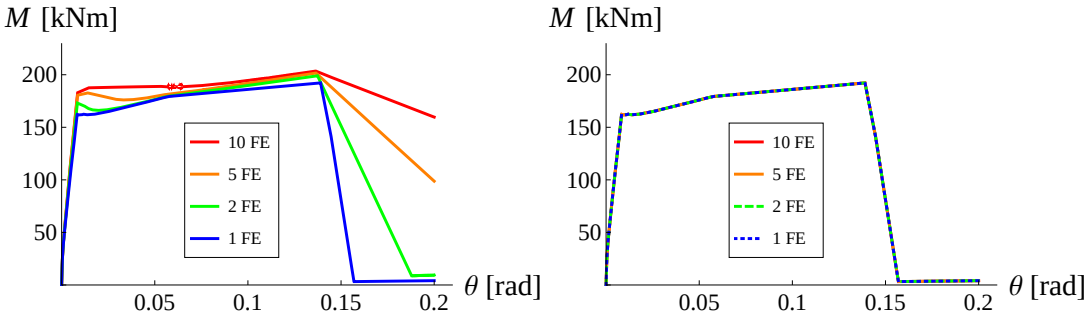

Figure 3.36: *Moment - rotation* diagrams for cantilever beam under end moment: imposed location of discontinuity at $L/2$. Original softening moduli (left), modified softening moduli (right).
Slika 3.36: Diagram *moment - zasuk* za konzolo, obteženo z momentom: vsiljena nezveznost pri $L/2$. Originalni moduli mehčanja (levo), moduli mehčanja prirejeni glede na dolžino KE (desno).

3.4.2.4 Weaker reinforcement in one of the elements, imposed location of discontinuity at $L/2$

The beam is analyzed once more, with ultimate stress of reinforcement σ_{fs} slightly raised in all but one finite element, simulating a material imperfection. The discontinuity is manually positioned at the middle of the element. When the weak element reaches the carrying capacity, the moment in the beam begins to decrease and reinforcement in other elements cannot enter the softening phase. This eliminates mesh dependency in the last part of the response, in which the softening of the tensile reinforcement causes the beam to lose carrying capacity, see Fig. 3.37. The difference between the diagrams in the plateau remains, however. It is caused by simultaneous cracking of concrete in tension in all finite elements. A greater number of finite elements causes a slower growth of each individual discontinuity and a slightly higher value of the rotation, at which the tensile reinforcement yields. Since the major part of the cross-section is still elastic, the yield moment increases considerably. Unlike in reinforcement, this problem cannot be solved by weakening one of the elements, because the cross-section as a whole is still gaining strength after the concrete breaks in tension.

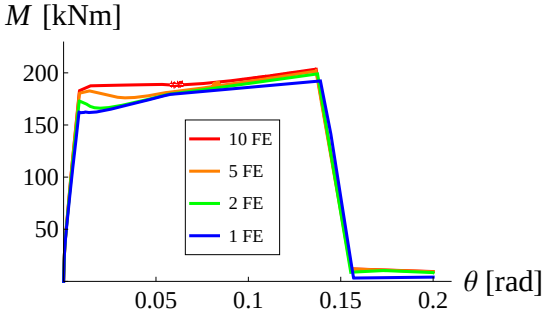

Figure 3.37: *Moment - rotation* diagram for cantilever beam under end moment: imposed location of discontinuity at $L/2$. Weaker reinforcement in one of the finite elements.
Slika 3.37: Diagram *moment - zasuk* za konzolo, obteženo z momentom: vsiljena nezveznost pri $L/2$. Malce šibkejša armatura v enem od končnih elementov.

3.4.3 Cantilever beam under end transversal force

A cantilever beam is subjected to prescribed lateral displacement at the free end, see Fig. 3.38. The length of the beam is $L = 2.5$m, the width and the height of the cross-section $b = 0.2$m and $h = 0.5$m. The tensile and compressive reinforcement are $A_{s,1} = A_{s,2} = 0.001\text{m}^2$ and the distances from the center of the reinforcement layers to the edges of the concrete cross-section are $a_1 = a_2 = 0.04$m. Material properties of concrete are: elasticity modulus $E_c = 4 \times 10^7\text{kNm}^{-2}$, elasticity limit $\sigma_{dc} = 40820\text{kNm}^{-2}$, ultimate stress in compression $\sigma_{fcc} = 44902\text{kNm}^{-2}$, ultimate stress in tension $\sigma_{fct} = 4000\text{kNm}^{-2}$, hardening modulus in compression $H_{cc} = 2 \times 10^6\text{kNm}^{-2}$, softening modulus in compression $K^*_{cc} = -5.2 \times 10^5\text{kNm}^{-3}$ and softening modulus in tension $K^*_{ct} = -8 \times 10^5\text{kNm}^{-3}$. Material properties of steel are: elasticity modulus $E_s = 2 \times 10^8\text{kNm}^{-2}$, yield stress $\sigma_y = 4 \times 10^5\text{kNm}^{-2}$, ultimate stress $\sigma_{fs} = 5 \times 10^5\text{kNm}^{-2}$, hardening modulus $H_s = 10^7\text{kNm}^{-2}$ and softening modulus $K_s = -3 \times 10^7\text{kNm}^{-3}$.

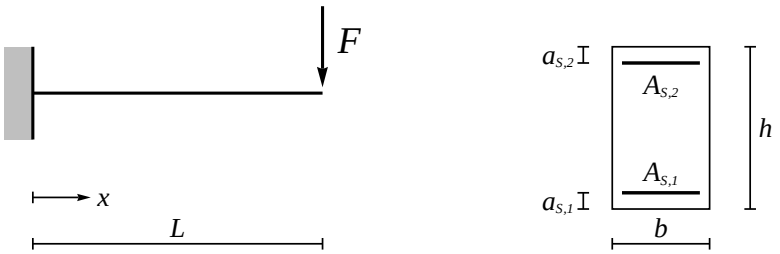

Figure 3.38: Cantilever beam under end transversal force: geometry.
Slika 3.38: Konzola, obremenjena s prečno silo: geometrija.

Moment at the support versus imposed lateral displacement diagrams are presented in Fig. 3.39. The curves match pretty well. There are no great deviations in the softening part because the moment is linear over the length of the beam and only the finite element at the support can reach the ultimate moment. There is no need for artificially created material imperfection. The influence of the mesh on the softening of concrete in tension cannot be avoided because the cross-section is still gaining strength when the concrete breaks, like in section 3.4.2.4.

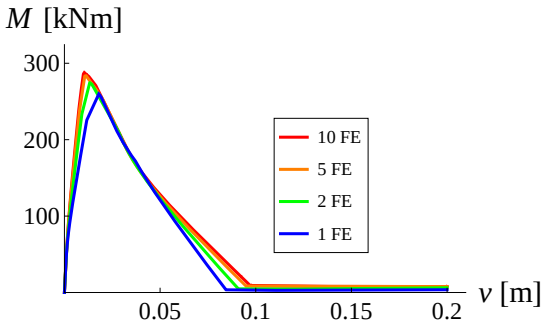

Figure 3.39: *Moment at support - transversal displacement* diagram for cantilever beam under end transversal force: all finite elements are the same.
Slika 3.39: Diagram *moment ob podpori - prečni pomik* za konzolo, obremenjeno s prečno silo: vsi končni elementi so enaki.

It is difficult to assess the results solely from the diagrams in Fig. 3.39, but inspection of the stress state reveals an error. Let us examine the beam, modeled with a single FE, just before the occurrence of the first discontinuity, when all layers are still elastic. The values of stress are anti-symmetric in the cross-section (negative below and positive above the middle axis), their absolute values grow from the middle axis toward the edges. In each layer, they reduce

linearly from the support toward the free end, where they are zero. Such distribution of stress is also assumed in the trial state of the first iteration of the next increment. However, the tensile strength is exceeded at the supported end of the topmost layer. The trial value of stress $\sigma^{i,trial} = \bar{D}^{i^{-1}}\check{\mathbf{B}}^i\mathbf{d}$ is replaced by $\sigma^i = \bar{D}^{i^{-1}}\left(\check{\mathbf{B}}^i\mathbf{d} + \bar{G}_R^i\alpha^i\right)$. The additional part $\bar{D}^{i^{-1}}\bar{G}_R^i(x)\,\alpha^i$ has a negative value at the supported end, where the discontinuity is located, and a positive value at the free end. Thus, after the first iteration, the stress in the top layer is no longer zero at the free end of the beam. Of course, this is not the equilibrium state, but even in the following iterations the stress at the free end does not vanish. Instead, it becomes non-zero also in the remaining layers. Only the resultant axial force and moment at the free end are zero, as required by the equilibrium equations.

This issue arises from completely independent consideration of discontinuities in separate layers. In the stress resultant finite element, the operator $\bar{G}$ is defined for the whole finite element and it contains information, how the cracked element should deform, in order to preserve equilibrium. It imposes an imbalance that is annulled by appropriate nodal displacements. In a multi-layer element, the operator $\bar{G}_R^i$ is defined for a single layer and contains information, how the cracked layer should deform to preserve "equilibrium of the layer". However, the layer cannot deform freely. Modification of the nodal displacements also affects the remaining layers. The imbalance, introduced by $\bar{G}_R^i$ into the cracked layer (and through summation into the finite element), is balanced out by (additional) deformation of all layers in the element, so the final strain/stress in the cracked layer is not the same, as if it would stand alone. The operator $\bar{G}_R^i$, as defined here, cannot perform its original function, which is to provide physically appropriate strain/stress in the cracked layer.

Since the occurrence of a discontinuity in one of the layers actually affects the whole finite element, the operator $\bar{G}_R^i$ should be defined on the element level. This is not easily done, though. The influence of the discontinuity would depend on the type of the load (e.g. pure tension or pure bending), which prevents unique definition of $\bar{G}_R^i$.

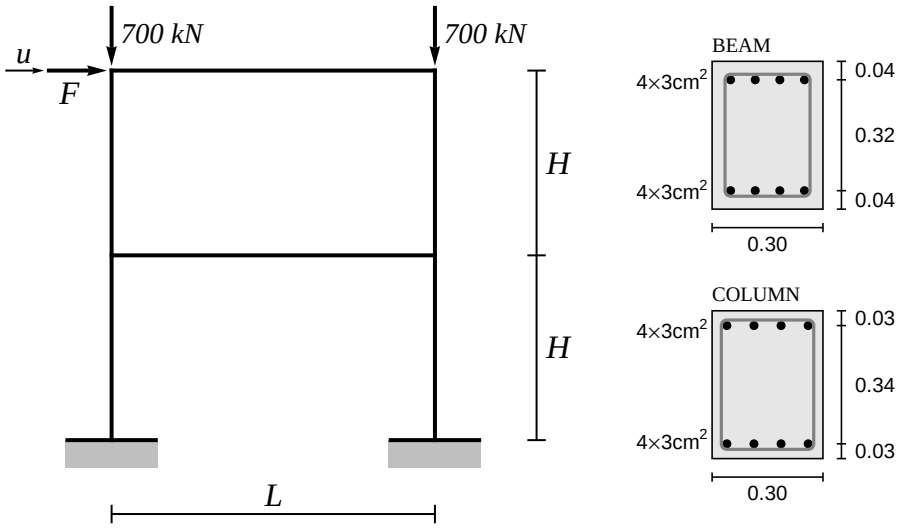

Figure 3.40: Two story frame: geometry, loading pattern and cross-sections.
Slika 3.40: Dvoetažni okvir: geometrija, obtežba in prečni prerezi.

3.4.4 Two story reinforced concrete frame

Two-story reinforced concrete frame has been experimentally tested in [71] and numerically analyzed in [51, 74] with stress-resultant Timoshenko and Euler-Bernoulli finite elements with embedded strong discontinuity in rotation. Analysis with multi-layer Timoshenko element with layer-wise embedded discontinuities in axial displacement and elasto-plastic models for concrete and reinforcement has been done in [51, 52]. Story height of the

frame is $H = 2$m, span is $L = 3.5$m, see Fig. 3.40. Beam cross-section data is: width is $b = 0.3$m, height is $h = 0.4$m, bottom and top reinforcements are $A_{s,1} = A_{s,2} = 0.0012\text{m}^2$, distances of reinforcement axes from the edges are $a_1 = a_2 = 0.04$m. Column cross-section data is the same, except for $a_1 = a_2 = 0.03$m. The steel data is accommodated from data reported in [71], see Fig. 3.41 (left): elasticity modulus $E_s = 192500$MPa, yield stress $\sigma_y = 418$MPa, ultimate stress $\sigma_{fs} = 596$MPa, hardening modulus $H_s = 2790$MPa, softening modulus $K_s = -4 \times 10^7\text{kNm}^{-3}$. The concrete data in compression is also accommodated from data reported in [71], see Fig. 3.41 (right): elasticity modulus $E_c = 28600$MPa, elasticity limit $\sigma_{dc} = 8.5$MPa, ultimate stress $\sigma_{fcc} = 30$MPa, hardening modulus $H_{cc} = 49000$MPa, softening modulus $K^*_{cc} = -2 \times 10^6\text{kNm}^{-3}$. The concrete data in tension is [71]: ultimate stress $\sigma_{fct} = 1.8$MPa, softening modulus $K^*_{ct} = -10^7\text{kNm}^{-3}$.

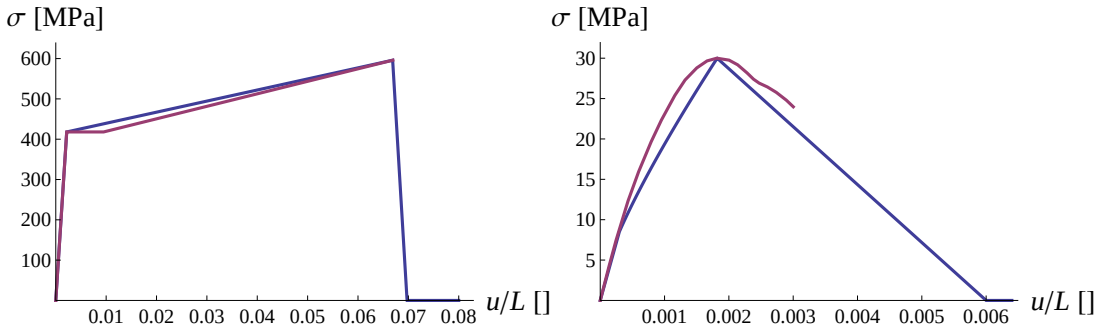

Figure 3.41: Constitutive diagrams for steel (left) and concrete in compression (right): comparison with experimental curves.

Slika 3.41: Konstitutivna zakona za jeklo (levo) in beton v tlaku (desno): primerjava z eksperimentalnimi krivuljami.

Comparison of experimental results and results of our analysis are shown in Fig. 3.42. The relation between the two curves resembles the comparison in Fig. 3.28 (left) or comparison of Fig. 3.35 and Fig. 3.37. The response of the structure is too stiff, the carrying capacity too high, and there is virtually no yield plateau. The problems, encountered in the previous numerical examples are transferred to the more complex structure. Since the issues have been discussed on simpler and clearer cases, there is no need to get into details here.

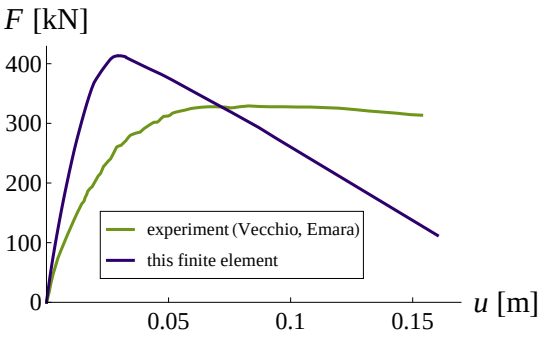

Figure 3.42: Response of two story frame: comparison with experiment.

Slika 3.42: Odziv dvoetažnega okvirja: primerjava z eksperimentom.

3.5 Concluding remarks

We have presented a planar multi-layer Euler-Bernoulli beam finite element with layer-wise embedded discontinuities in axial displacement. Small displacement kinematics is applied on the element level and translated to individual layers by obeying the perpendicularity of cross-section to the beam axis. A jump in axial displacements is introduced separately for each layer. The stress state of the layer is determined by two constitutive relations, one for the bulk of the layer and the other for the discontinuity. In concrete layer, the bulk is controlled by a damage-elasticity hardening law and the discontinuity by damage softening law. In reinforcement layer, the bulk is controlled by elastoplasticity hardening law and the discontinuity by plastic softening law. Internal forces of the element are computed as a sum of contributions of individual layers.

The finite element was intended for precise analysis of reinforced concrete beams and frames up to complete failure, with a detailed description of material state over the cross-section, as well as for computation of stress-resultant properties of different cross-sections, which are required as an input data in analysis with the stress-resultant beam finite element, presented in previous chapter. However, the multi-layer element does not perform as expected. Several issues have been identified.

Operator $\bar{G}_R^i$ has been derived on an isolated layer of the multi-layer element. It contains information, how the cracked layer should deform due to occurrence of the discontinuity. The proper deformation should be enforced by the imbalance, produced by the additional strain. However, the layer cannot deform freely because it is bound to other layers through common nodal displacements and the additional stress in the layer does not redistribute correctly. The stress σ^i is controlled only at the location of the discontinuity, where it has to be equal to the traction t^i and has to drop with increasing displacement jump. Elsewhere in the layer, the stress may grow even above the ultimate stress. Additional discontinuities cannot occur beacuse each layer is allowed to develop only one discontinuity.

Another problem is that equilibrium is only required on the element level, and not for each independent layer. We have seen the example of a finite element in pure tension, where the stress over the length of each layer was linear. If we computed the internal forces only for one layer, they would not be in equilibrium, but for the finite element as a whole the imbalances of individual layers neutralize each other.

Also, the displacement jumps α^i of individual layers are independent of each other. In a specific case of a cantilever beam in pure tension, the layers below the middle axis developed a discontinuity at one end of the beam, while the layers above the middle axis developed a discontinuity at the other end. The displacement jumps in all layers were proportional with the distance of the layer from the middle axis, resulting in a non-zero lateral displacement of the free end of the beam, without disrupting the equilibrium (the internal shear forces and internal moments of the finite element were zero). One way to look at the unconnected α^i is that there is no shear connection between the neighboring layers.

Another issue in kinematics is that there is no discontinuity on the element level. Deformation of the beam axis is always interpolated in the same way as for a regular Euler-Bernoulli beam. Even when the element is completely broken (carrying capacity of each layer has dropped to zero), the middle axis is a smooth curve. The bulk of each layer slides along a path, parallel to the middle axis. This may not be problematic if we use a fine mesh. Since the stiffness of the critical (broken) finite element is considerably reduced in comparison to neighboring (not broken) elements, the broken element exhibits a greater curvature, which can be interpreted as a discontinuity in rotation, smeared over the whole finite element. Still, the global kinematics is not completely accurate.

Finally, we have to mention the mesh dependency problem, which is most obvious in the case of cantilever beam under end moment. Due to constant stress state over the length of the beam, discontinuities appear simultaneously in all finite elements of the mesh. At the same value of imposed rotation of the free end of the beam, fine meshes produce great number of small discontinuities and coarse meshes produce small number of great discontinuities.

According to the softening material law, the traction at the discontinuity drops with its increasing size. Therefore, different meshes lead to different values of moment in the beam. The greatest deviations appear in the last part of the response when the beam as a whole enters the softening phase, which usually happens due to softening of tensile reinforcement. This can be cured by slightly weakening reinforcement in one of the finite elements. When the weak element begins to soften, the remaining elements unload and cannot develop a discontinuity in reinforcement. If softening of the element happens due to crushing of concrete in compression, the problem cannot be solved so effectively because there are multiple critical layers, as opposed to a single critical layer in case of tensile reinforcement. Also, the mesh dependency due to cracking of concrete in tension, when moment in the beam is increasing, cannot be avoided. Even if one of the elements is weaker, the concrete in the remaining elements will crack sooner or later, because the moment is still rising.

Considering all the deficiencies, the above derived multi-layer Euler-Bernoulli beam finite element cannot be recommended for general use. The only viable application is in case of constant strain/stress state over the length of the beam, which can occur either in pure tension/compression or in pure bending. In case of bending, the mesh dependency cannot be completely avoided.

4 MULTI-LAYER TIMOSHENKO BEAM FINITE ELEMENT WITH LAYER-WISE EMBEDDED DISCONTINUITIES IN AXIAL DISPLACEMENT

4.1 Introduction

In this chapter, a multi-layer Timoshenko beam finite element with layer-wise embedded discontinuities in axial displacement is derived. It is intended for detailed failure analysis of reinforced concrete beams and frames, and for computation of stress resultant material properties of reinforced concrete beams, modeled with stress resultant finite elements like the one described in chapter 2. Due to layer-wise constant stress state along its length, this finite element is expected to overcome some of the issues, encountered in the previous chapter when deriving the multi-layer Euler-Bernoulli beam finite element.

The element is composed of several layers of concrete and reinforcement, each with embedded discontinuity in axial displacement. Axial response of concrete layer is described by elasto-damage model with hardening for the bulk and rigid damage softening model for the discontinuity. Axial response of reinforcement layer is governed by elastoplastic model with hardening for the bulk and rigid plastic softening model for the discontinuity. Small deformation kinematics is used.

The chapter is organized as follows: Kinematics, constitutive and equilibrium equations are developed in section 4.2. Finite element discretization and computational procedure are presented in section 4.3. Performance of the finite element is tested on several numerical examples in section 4.4. Concluding remarks are given in section 4.5.

4.2 Finite element formulation

4.2.1 Kinematics

We consider a planar Timoshenko beam finite element with two nodes, shown in Fig. 4.1. Each node has three degrees of freedom, two in-plane displacements and rotation about the axis, perpendicular to the plane.

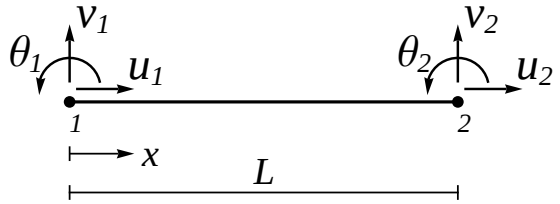

Figure 4.1: Finite element with six nodal degrees of freedom.
Slika 4.1: Končni element s šestimi prostostnimi stopnjami.

Axial displacement $\tilde{u}(x)$ and rotation of the cross-section $\tilde{\theta}(x)$ in the middle axis of the beam are interpolated linearly between the nodal displacements $\mathbf{u}$ and the nodal rotations $\boldsymbol{\theta}$, respectively. The linear interpolation functions $\mathbf{N}(x)$ are shown in Fig. 4.2 (left).

$$\tilde{u}(x) = \mathbf{N}(x)\,\mathbf{u}, \quad \mathbf{N}(x) = \{N_1, N_2\} = \left\{1 - \frac{x}{L}, \frac{x}{L}\right\}, \quad \mathbf{u} = \{u_1, u_2\}^T \tag{4.1}$$

$$\tilde{\theta}(x) = \mathbf{N}(x)\,\boldsymbol{\theta}, \quad \boldsymbol{\theta} = \{\theta_1, \theta_2\}^T \tag{4.2}$$

Linear interpolation of transversal displacement $\tilde{v}(x)$ of the middle axis would result in shear locking of the finite element. The problem is avoided by raising the order of interpolation of $\tilde{v}(x)$ with a quadratic bubble function $N_3(x)$, see Fig. 4.2 (left). Parameter v_3 is determined so as to allow the finite element to describe a shear-free stress state in case of constant moment.

$$\tilde{v}(x) = \mathbf{N}(x)\,\mathbf{v} + N_3(x)\,v_3, \quad \mathbf{v} = \{v_1, v_2\}^T, \quad N_3(x) = \frac{4(L-x)\,x}{L^2}, \quad v_3 = \frac{L}{8}(\theta_1 - \theta_2) \tag{4.3}$$

In Timoshenko beam theory, the cross-section is not necessarily perpendicular to the beam axis and the shear strain $\gamma(x)$ is computed as the difference between the derivative of the transversal displacement and the rotation of the cross-section.

$$\gamma = \frac{\partial \tilde{v}}{\partial x} - \tilde{\theta} = \mathbf{B}\mathbf{v} + \mathbf{B}^*\boldsymbol{\theta}, \quad \mathbf{B} = \{B_1, B_2\} = \left\{-\frac{1}{L}, \frac{1}{L}\right\}, \quad \mathbf{B}^* = \{B^*, B^*\} = \left\{-\frac{1}{2}, -\frac{1}{2}\right\} \tag{4.4}$$

For the interpolations of transversal displacement and rotation, chosen in equations (4.2) and (4.3), the shear strain is constant. Components of the strain interpolation functions $\mathbf{B}$ and $\mathbf{B}^*$ are shown in Fig. 4.2 (right). A simple verification confirms that the shear strain is zero in case of constant moment/curvature ($v_1 = v_2$, $\theta_1 = -\theta_2$).

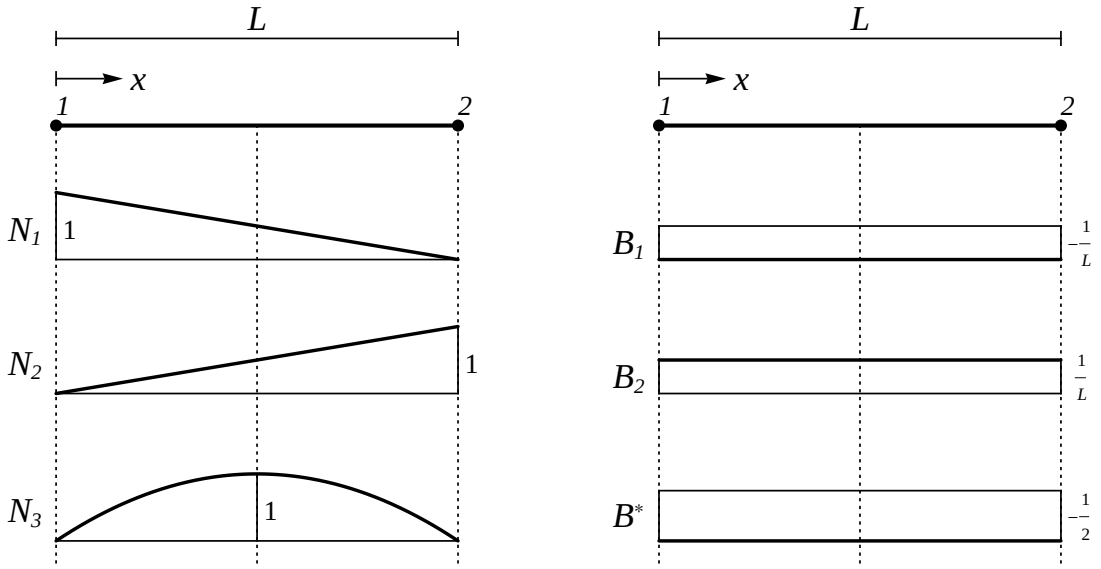

Figure 4.2: Interpolation functions for displacements (left) and strain (right).
Slika 4.2: Interpolacijske funkcije za pomike (levo) in deformacije (desno).

The beam is treated as a composition of n_L layers of concrete and steel. Constant state is assumed over the thickness of each layer and its displacements $u^i(x)$ are computed in its middle axis. Embedded discontinuity concept is used to model the material failure of each layer.

$$u^i\left(x, x_d^i\right) = \overbrace{\tilde{u}(x) - y^i\tilde{\theta}(x)}^{\tilde{u}^i} + \overbrace{M^i\left(x, x_d^i\right)\alpha^i}^{u^{i,add}} \tag{4.5}$$

The standard part of axial displacement $\tilde{u}^i(x)$ is composed of the axial displacement of the middle axis of the beam and of displacement due to rotation of the cross-section, depending on the distance y^i from the middle axis. When the carrying capacity is exceeded, a strong discontinuity in axial displacement is introduced into the layer (see Fig. 4.3), which results in an additional axial displacement $u^{i,add}\left(x, x_d^i\right)$, described by the jump in displacements α^i at coordinate x_d^i and the shape function $M^i\left(x, x_d^i\right)$.

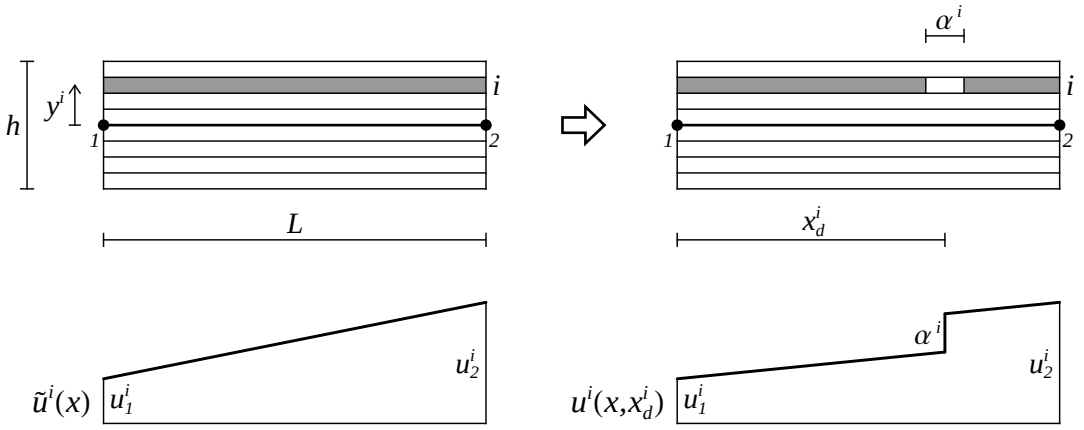

Figure 4.3: Finite element divided into layers, before and after occurrence of discontinuity in i-th layer, with corresponding axial displacement in the layer.

Slika 4.3: Na sloje razdeljen končni element pred in po nastanku nezveznosti v i-tem sloju ter pripadajoči osni pomik v sloju.

Equations (4.1) and (4.2) are inserted into (4.5). Then, the displacement $u^i\left(x, x_d^i\right)$ is differentiated over the coordinate x to obtain the axial strain $\varepsilon^i\left(x, x_d^i\right)$ in the layer.

$$\varepsilon^i\left(x, x_d^i\right) = \frac{\partial u^i}{\partial x} = \overbrace{\mathbf{Bu} - y^i \mathbf{B}\boldsymbol{\theta}}^{\tilde{\varepsilon}^i} + \overbrace{G^i\left(x, x_d^i\right)\alpha^i}^{\varepsilon^{i,add}} \tag{4.6}$$

The first two parts of expression (4.6) represent the standard axial strain $\tilde{\varepsilon}^i$, while the last part represents the enhanced strain due to embedded discontinuity. Derivatives $\mathbf{B}$ of the interpolation functions $\mathbf{N}(x)$ are written in equation (4.4) and depicted in Fig. 4.2 (right). The additional strain $\varepsilon^{i,add}$ only appears in the layers that have exceeded their carrying capacity. Operator G^i is the first derivative of the shape function M^i, which will be examined in the following section.

All degrees of freedom of the finite element are collected in the vector of generalized nodal displacements $\mathbf{d}$, which allows for a shorter notation for the regular axial strain $\tilde{\varepsilon}^i$ and shear strain γ. Interpolation matrices $\tilde{\mathbf{B}}^i$ and $\tilde{\mathbf{B}}^*$ are composed accordingly to the arrangement of displacements in $\mathbf{d}$. The first matrix is different for each layer, while the second one is constant for the whole element.

$$\tilde{\varepsilon}^i = \begin{bmatrix} \mathbf{B} & \mathbf{0} & -y^i\mathbf{B} \end{bmatrix} \mathbf{d} = \check{\mathbf{B}}^i \mathbf{d}, \quad \gamma = \begin{bmatrix} \mathbf{0} & \mathbf{B} & \mathbf{B}^* \end{bmatrix} \mathbf{d} = \check{\mathbf{B}}^* \mathbf{d}, \quad \mathbf{d}^T = \left\{\mathbf{u}^T, \mathbf{v}^T, \boldsymbol{\theta}^T\right\} \tag{4.7}$$

4.2.2 Derivation of operator *G*

Interpolation of the axial displacement field $u^i(x)$ in the i-th layer is defined in equation (4.5). The regular part $\tilde{u}^i(x)$ is computed from the axial displacement of the middle axis $\tilde{u}(x)$ and rotation $\tilde{\theta}(x)$ of the cross-section.

Since they are both linear functions of x, $\tilde{u}^i(x)$ is linear as well. This allows us to interpolate it between the axial displacements of the end points of the layer, designated with $\mathbf{u}^i$, using the linear interpolation functions $\mathbf{N}(x)$ from equation (4.1), see Fig. 4.4.

$$\tilde{u}^i(x) = \tilde{u}(x) - y^i\tilde{\theta}(x) = \mathbf{N}(x)\,\mathbf{u}^i, \quad \mathbf{u}^i = \left\{u_1^i, u_2^i\right\}^T \tag{4.8}$$

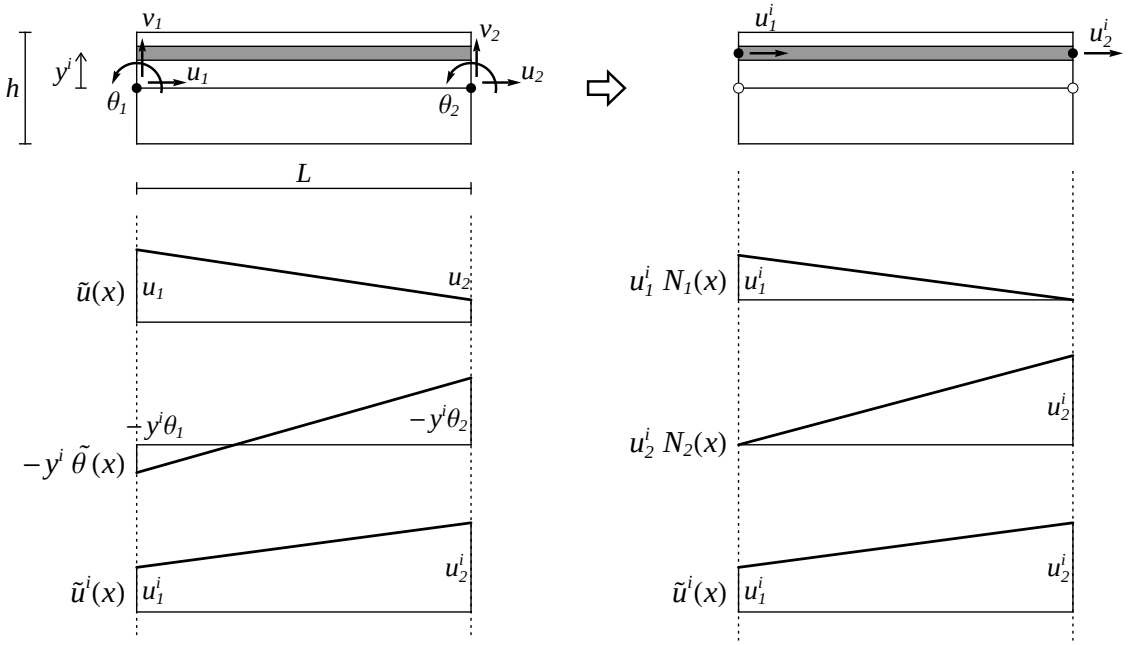

Figure 4.4: Interpolation of standard axial displacement in i-th layer between nodal displacements of the finite element (left) and between nodal axial displacements of the layer (right).
Slika 4.4: Interpolacija standardnega osnega pomika v i-tem sloju med prostostne stopnje končnega elementa (levo) in med vozliščne osne pomike sloja (desno).

The "nodal" displacements $\mathbf{u}^i$ of the i-th layer can be calculated from $\tilde{u}^i(x)$ by inserting for x the coordinates of the layer's "nodes".

$$\mathbf{u}^i = \left\{\tilde{u}^i\big|_{x=0}, \tilde{u}^i\big|_{x=L}\right\}^T = \left\{u_1 - y^i\theta_1, u_2 - y^i\theta_2\right\}^T \tag{4.9}$$

The standard axial displacement $\tilde{u}^i(x)$ is enriched with the additional part $u^{i,add}(x, x_d)$, which represents the additional axial displacement due to occurrence of a discontinuity in the layer. It is determined by the interpolation function $M^i\left(x, x_d^i\right)$ and the displacement jump α^i at the discontinuity of the layer.

$$u^i\left(x, x_d^i\right) = \tilde{u}^i(x) + M^i\left(x, x_d^i\right)\alpha^i \tag{4.10}$$

The interpolation function M^i must not affect the nodal displacements $\mathbf{u}^i$ of the layer, which means that it must have zero values at the nodes, and it must have a unit jump at the location of the discontinuity x_d^i. The easiest way to meet these requirements is to use a combination of the Heaviside function and the appropriate of the shape functions $\mathbf{N}$.

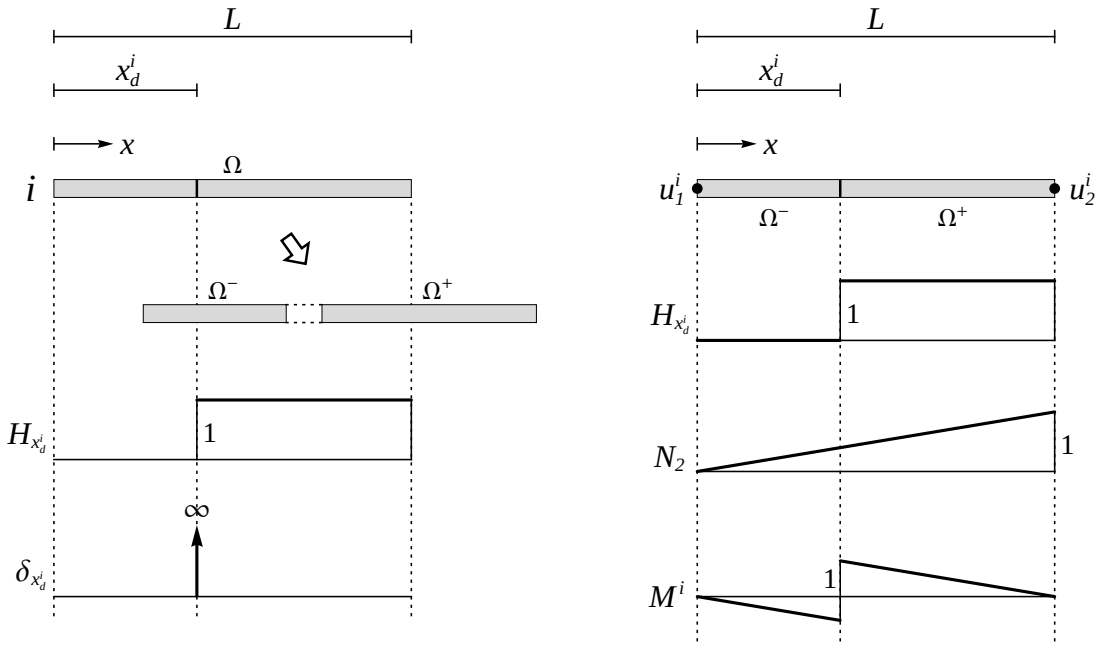

Figure 4.5: Domain and sub-domains of a cracked layer, Heaviside and Dirac-delta functions (left). Construction of interpolation function M_i (right).
Slika 4.5: Domena in poddomeni razpokanega sloja, Heaviside-ova in Dirac-delta funkcija (levo). Konstruiranje interpolacijske funkcije M_i (desno).

Domain Ω of the cracked layer is divided by the discontinuity into two parts. Ω^- is the part before the discontinuity, with $x < x_d^i$, and Ω^+ is the part after the discontinuity, with $x \geq x_d^i$, see Fig. 4.5 (left). The value of the Heaviside function is 0 on Ω^- and 1 on Ω^+. Its derivative is the Dirac delta function $\delta_{x_d^i}$, which has an infinite value at x_d^i and zero value elsewhere.

$$H_{x_d^i} = \begin{cases} 0; & x < x_d^i \\ 1; & x \geq x_d^i \end{cases} \qquad \frac{\partial H_{x_d^i}}{\partial x} = \delta_{x_d^i} = \begin{cases} \infty; & x = x_d^i \\ 0; & \text{otherwise} \end{cases} \tag{4.11}$$

Heaviside function $H_{x_d^i}$ satisfies the requirement of a unit jump at the discontinuity. Its value, however, is only zero on Ω^-, and not at all nodes of the layer. This can be fixed by subtracting from it those shape functions $N_j \in \mathbf{N}$, that correspond to the nodes j, included in Ω^+. Since N_j are continuous and have zero values at all nodes except j, they will not affect previously fulfilled demands. As we are dealing with a simple two-node finite element, we have to subtract the shape function N_2, regardless of the location of the discontinuity, see Fig. 4.5 (right).

$$M^i\left(x, x_d^i\right)\alpha^i = H_{x_d^i}\left(x, x_d^i\right) - N_2\left(x\right) \tag{4.12}$$

The first derivative of M^i over x is designated with G^i and is composed of a continuous part $\bar{G}^i$ and a discrete part $\bar{\bar{G}}^i$. The derivative of N_2 is B_2, defined in (4.4), and the derivative of $H_{x_d^i}$ is defined in (4.11).

$$G^i\left(x, x_d^i\right) = \frac{\partial}{\partial x} M^i\left(x, x_d^i\right) = \bar{G}^i + \bar{\bar{G}}^i, \quad \bar{\bar{G}}^i = \delta_{x_d^i}, \quad \bar{G}^i = -B_2 = -\frac{1}{L} \tag{4.13}$$

Considering the constant strain state in a layer, see equation (4.7), the discontinuity could appear anywhere between the end nodes. Without loss of generality, we can place it at $x_d^i = L/2$.

4.2.3 Relations between global and local quantities

4.2.3.1 Real degrees of freedom

A structure is modeled with a mesh of finite elements. A part of such mesh is depicted in Fig. 4.6. The total number of the nodes in the structure is designated with n_N. Each node has three degrees of freedom - displacement U parallel to the global X axis, displacement V parallel to the global Y axis, and rotation Θ about the axis, perpendicular to the XY plane. The structure has in total $n_{DOF} = 3n_N$ degrees of freedom, which are collected in the vector $\mathbf{d}^{str}$.

$$\mathbf{d}^{\text{str}} = \left\{U_1, V_1, \Theta_1, U_2, V_2, \Theta_2, \ldots, U_{n_N}, V_{n_N}, \Theta_{n_N}\right\}^T \tag{4.14}$$

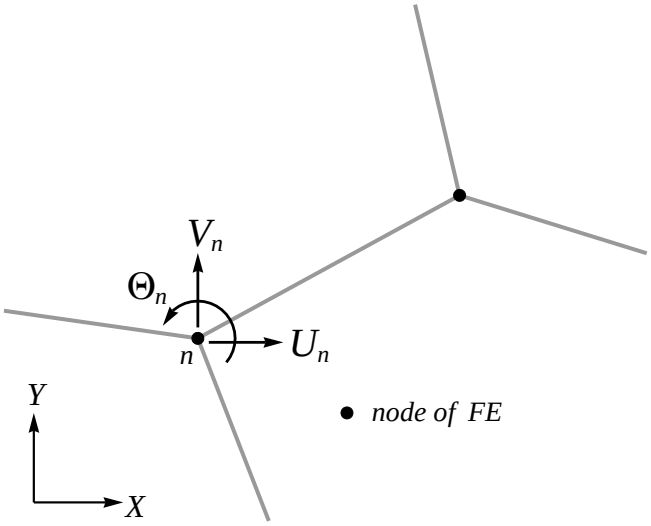

Figure 4.6: Degrees of freedom at a node of the finite element mesh.
Slika 4.6: Prostostne stopnje v posameznem vozlišču mreže končnih elementov.

Let us now consider a finite element (e) with end nodes (n_1) and (n_2). The local x axis is parallel to the axis of the element, with x increasing from (n_1) towards (n_2), see Fig. 4.7. The element's degrees of freedom, defined in the local coordinate system, are collected in the vector $\mathbf{d}^{(e)}$, in accordance with equation (4.7). Global degrees of freedom, associated with the nodes of the element can be similarly organized into vector $\mathbf{D}^{(e)}$. The two are connected with a transformation matrix $\mathbf{R}^{(e)}$. Zeros are replaced by dots for clarity. $\phi^{(e)}$ is the angle between the global X axis and the local x axis (rotation of the local coordinate system).

$$\mathbf{d}^{(e)} = \mathbf{R}^{(e)}\mathbf{D}^{(e)} \tag{4.15}$$

$$\mathbf{d}^{(e)} = \left\{ u_1^{(e)}, u_2^{(e)}, v_1^{(e)}, v_2^{(e)}, \theta_1^{(e)}, \theta_2^{(e)} \right\}^T, \quad \mathbf{D}^{(e)} = \left\{ U_{n_1}, U_{n_2}, V_{n_1}, V_{n_2}, \Theta_{n_1}, \Theta_{n_2} \right\}^T$$

$$\mathbf{R}^{(e)} = \begin{bmatrix} \cos\phi^{(e)} & \cdot & \sin\phi^{(e)} & \cdot & \cdot & \cdot \\ \cdot & \cos\phi^{(e)} & \cdot & \sin\phi^{(e)} & \cdot & \cdot \\ -\sin\phi^{(e)} & \cdot & \cos\phi^{(e)} & \cdot & \cdot & \cdot \\ \cdot & -\sin\phi^{(e)} & \cdot & \cos\phi^{(e)} & \cdot & \cdot \\ \cdot & \cdot & \cdot & \cdot & 1 & \cdot \\ \cdot & \cdot & \cdot & \cdot & \cdot & 1 \end{bmatrix} \tag{4.16}$$

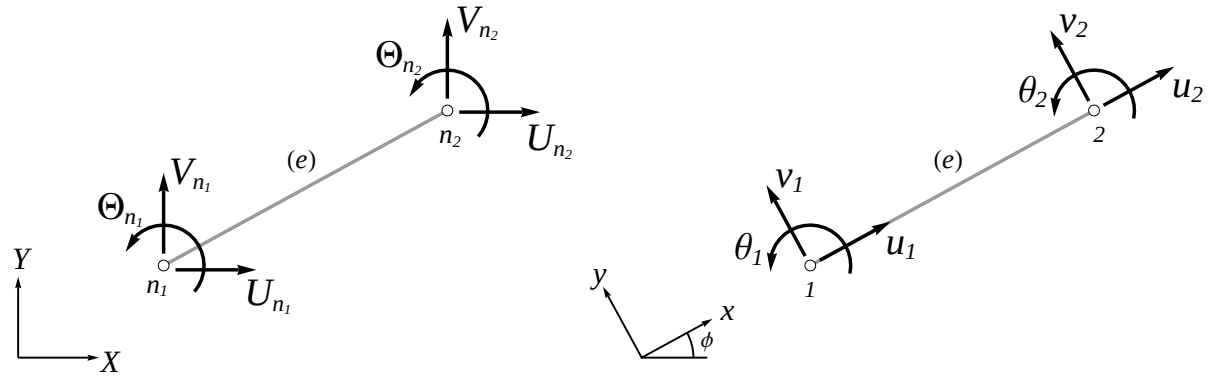

Figure 4.7: Global (left) and local (right) degrees of freedom, associated with a finite element.
Slika 4.7: Globalne (levo) in lokalne (desno) prostostne stopnje, povezane s končnim elementom.

Vector $\mathbf{D}^{(e)}$ contains those components of vector $\mathbf{d}^{str}$ that correspond to the nodes of the finite element. The selection of appropriate components is done by matrix $\mathbf{P}^{(e)}$ of size $6 \times n_{DOF}$ with only six non-zero components.

$$\begin{aligned} &\mathbf{D}^{(e)} = \mathbf{P}^{(e)} \mathbf{d}^{\text{str}} \\ &P^{(e)}_{1,\,3n_1-2} = P^{(e)}_{2,\,3n_2-2} = P^{(e)}_{3,\,3n_1-1} = P^{(e)}_{4,\,3n_2-1} = P^{(e)}_{5,\,3n_1} = P^{(e)}_{6,\,3n_2} = 1, \quad \text{other } P^{(e)}_{i,j} = 0 \end{aligned} \tag{4.17}$$

Obeying equations (4.15) and (4.17), we can write the relation between the local degrees of freedom of the finite element (e) and the global degrees of freedom of the structure.

$$\mathbf{d}^{(e)} = \mathbf{R}^{(e)} \mathbf{P}^{(e)} \mathbf{d}^{\text{str}} \tag{4.18}$$

4.2.3.2 Virtual degrees of freedom

Virtual displacements are a kinematically admissible variation of real generalized displacements. As with the real displacements, they are interpolated between the nodal values with appropriate interpolation functions. The virtual deformation of the mesh is therefore defined by the virtual displacements of its nodes.

The global virtual degrees of freedom (virtual nodal displacements of the mesh) $\hat{\mathbf{d}}^{str}$, the virtual nodal displacements of the element $\hat{\mathbf{d}}^{(e)}$ and the selection $\hat{\mathbf{D}}^{(e)}$ of global virtual displacements, associated with the element (e),

are defined analogously to the real quantities $\mathbf{d}^{str}$, $\mathbf{d}^{(e)}$ and $\mathbf{D}^{(e)}$, defined in equations (4.14) and (4.16).

$$\begin{aligned}\hat{\mathbf{d}}^{\text{str}} &= \left\{\hat{U}_1, \hat{V}_1, \hat{\Theta}_1, \hat{U}_2, \hat{V}_2, \hat{\Theta}_2, \ldots, \hat{U}_{n_N}, \hat{V}_{n_N}, \hat{\Theta}_{n_N}\right\}^T \\ \hat{\mathbf{d}}^{(e)} &= \left\{\hat{u}_1^{(e)}, \hat{u}_2^{(e)}, \hat{v}_1^{(e)}, \hat{v}_2^{(e)}, \hat{\theta}_1^{(e)}, \hat{\theta}_2^{(e)}\right\}^T, \quad \hat{\mathbf{D}}^{(e)} = \left\{\hat{U}_{n_1}, \hat{U}_{n_2}, \hat{V}_{n_1}, \hat{V}_{n_2}, \hat{\Theta}_{n_1}, \hat{\Theta}_{n_2}\right\}^T\end{aligned} \tag{4.19}$$

Relations between them are equivalent to equations (4.15)-(4.18), matrices $\mathbf{R}^{(e)}$ and $\mathbf{P}^{(e)}$ remain the same.

$$\hat{\mathbf{d}}^{(e)} = \mathbf{R}^{(e)}\hat{\mathbf{D}}^{(e)}, \quad \hat{\mathbf{D}}^{(e)} = \mathbf{P}^{(e)}\hat{\mathbf{d}}^{\text{str}}, \quad \hat{\mathbf{d}}^{(e)} = \mathbf{R}^{(e)}\mathbf{P}^{(e)}\hat{\mathbf{d}}^{\text{str}} \tag{4.20}$$

4.2.3.3 Internal forces

Internal forces can be organized in the same way as the generalized displacements. Each degree of freedom from the vector $\mathbf{d}^{str}$ is accompanied by a corresponding internal force. Analogously to equation (4.14) we can write:

$$\mathbf{f}^{\text{int,str}} = \left\{f_{U_1}^{\text{int}}, f_{V_1}^{\text{int}}, f_{\Theta_1}^{\text{int}}, f_{U_2}^{\text{int}}, f_{V_2}^{\text{int}}, f_{\Theta_2}^{\text{int}}, \ldots, f_{U_{n_N}}^{\text{int}}, f_{V_{n_N}}^{\text{int}}, f_{\Theta_{n_N}}^{\text{int}}\right\}^T \tag{4.21}$$

Vector $\mathbf{f}^{\text{int,str}}$ has $n_{DOF} = 3n_N$ components - for each node a force parallel to global X axis, a force parallel to Y axis, and a moment around the axis, perpendicular to the XY plane. They are labeled with f_U^{int}, f_V^{int} and f_Θ^{int}, respectively, and depicted in Fig. 4.8.

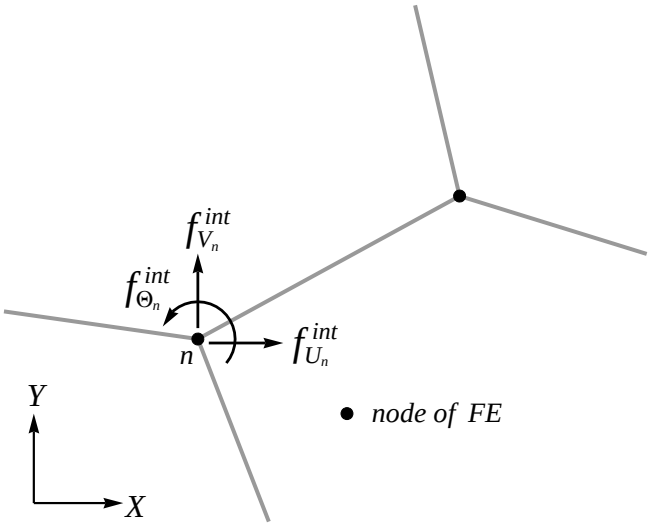

Figure 4.8: Internal forces, corresponding to degrees of freedom at a node of the finite element mesh.
Slika 4.8: Notranje sile, ki ustrezajo prostostnim stopnjam v vozlišču mreže končnih elementov.

Internal forces at a certain node of the structure are composed of contributions from all the elements, joined in that node. Let us now take a closer look at a finite element (e). The internal nodal forces of the element are defined in the local coordinate system and correspond to the local degrees of freedom $\mathbf{d}^{(e)}$, see Fig. 4.9 (right). They are collected in the vector $\mathbf{f}^{\text{int},(e)}$. The forces can be transformed by matrix $\mathbf{R}^{(e)}$ so as to match the directions

of the global internal forces $\mathbf{f}^{\text{int,str}}$. The new, transformed vector is designated with $\mathbf{F}^{\text{int},(e)}$, Fig. 4.9 (left). The transformation matrix $\mathbf{R}^{(e)}$ is the same as in equation (4.16).

$$\mathbf{f}^{\text{int},(e)} = \mathbf{R}^{(e)}\mathbf{F}^{\text{int},(e)} \quad \Leftrightarrow \quad \mathbf{F}^{\text{int},(e)} = \mathbf{R}^{(e)^{-1}}\mathbf{f}^{\text{int},(e)} \tag{4.22}$$

$$\begin{aligned}\mathbf{f}^{\text{int},(e)} &= \left\{ f_{u_1}^{\text{int},(e)}, f_{u_2}^{\text{int},(e)}, f_{v_1}^{\text{int},(e)}, f_{v_2}^{\text{int},(e)}, f_{\theta_1}^{\text{int},(e)}, f_{\theta_2}^{\text{int},(e)} \right\}^T \\ \mathbf{F}^{\text{int},(e)} &= \left\{ f_{U_{n_1}}^{\text{int},(e)}, f_{U_{n_2}}^{\text{int},(e)}, f_{V_{n_1}}^{\text{int},(e)}, f_{V_{n_2}}^{\text{int},(e)}, f_{\Theta_{n_1}}^{\text{int},(e)}, f_{\Theta_{n_2}}^{\text{int},(e)} \right\}^T\end{aligned} \tag{4.23}$$

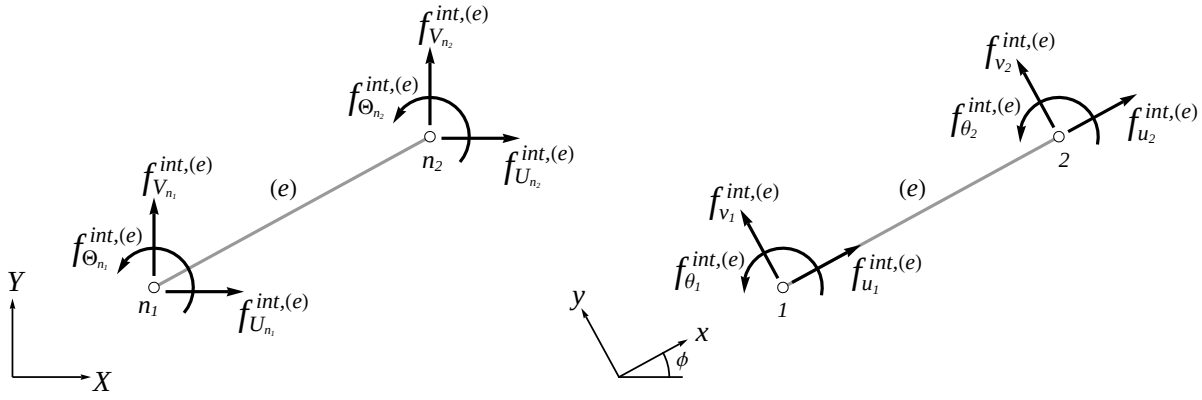

Figure 4.9: Contribution of a finite element to internal forces of the structure in global (left) and local (right) coordinate system.

Slika 4.9: Prispevek končnega elementa k notranjim silam konstrukcije v globalnem (levo) in lokalnem (desno) koordinatnem sistemu.

The components of the global vector $\mathbf{f}^{\text{int,str}}$ are computed by summing the contributions $\mathbf{F}^{\text{int},(e)}$ of individual finite elements. Matrix $\mathbf{P}^{(e)}$ is defined in (4.17).

$$\mathbf{f}^{\text{int,str}} = \sum_{e=1}^{n_{FE}} \mathbf{P}^{(e)^T}\mathbf{F}^{\text{int},(e)} \tag{4.24}$$

Transformation (4.22) and summation (4.24) can be joined in a simplified notation. Operator A represents the assembly of the internal forces and n_{FE} is the total number of finite elements.

$$\mathbf{f}^{\text{int,str}} = \sum_{e=1}^{n_{FE}} \mathbf{P}^{(e)^T}\mathbf{R}^{(e)^{-1}}\mathbf{f}^{\text{int},(e)} = \mathop{\mathsf{A}}_{e=1}^{n_{FE}} \left[\mathbf{f}^{\text{int},(e)}\right] \tag{4.25}$$

Another useful relation can be observed. For rotation matrix $\mathbf{R}^{(e)}$ it holds $\mathbf{R}^T = \mathbf{R}^{-1}$ or $\mathbf{R}^T\mathbf{R} = \mathbf{I}$, where $\mathbf{I}$ is the identity matrix. By using this property as well as equations (4.20) and (4.22) we can conclude that the scalar product of virtual displacements and internal forces is equal in local and global coordinate system.

$$\hat{\mathbf{d}}^{(e)^T}\mathbf{f}^{\text{int},(e)} = \hat{\mathbf{D}}^{(e)^T}\mathbf{R}^{(e)^T}\mathbf{R}^{(e)}\mathbf{F}^{\text{int},(e)} = \hat{\mathbf{D}}^{(e)^T}\mathbf{F}^{\text{int},(e)} \tag{4.26}$$

4.2.4 Virtual work equation

Equilibrium of a structure can be described in a weak from, by the virtual work principle, which states that the virtual work of internal forces G^{int} on any kinematically admissible perturbation of generalized displacements - virtual displacements - must be equal to the work of external forces G^{ext} on the same virtual displacements.

$$G^{\text{int}} - G^{\text{ext}} = 0 \tag{4.27}$$

Since we are dealing with a discretized model, the external loads are defined at the nodes of the structure. Linear loads have to be transferred to the nodes appropriately. The virtual work of external forces is therefore computed simply as a scalar product of the vector of virtual nodal displacements of the structure $\hat{\mathbf{d}}^{\text{str}}$ and the corresponding vector of generalized external forces $\mathbf{f}^{\text{ext,str}}$. Virtual displacements are defined in equation (4.19) and the external forces analogously to the internal forces in equation (4.21).

$$G^{\text{ext}} = \hat{\mathbf{d}}^{\text{str}^T} \mathbf{f}^{\text{ext,str}} = \sum_{j=1}^{n_{DOF}} \hat{d}_j^{\text{str}} f_j^{\text{ext,str}} \tag{4.28}$$

Here n_{DOF} is the number of the structure's degrees of freedom. Many components of the sum (4.28) may be zero. The virtual work of internal forces is composed of contributions from individual finite elements.

$$G^{\text{int}} = \sum_{e=1}^{n_{FE}} G^{\text{int},(e)}, \quad G^{\text{int},(e)} = \int_{V^{(e)}} (\hat{\varepsilon}\sigma + \hat{\gamma}\tau)\, dV \tag{4.29}$$

For each element, $G^{\text{int},(e)}$ is computed by multiplying the corresponding components of the stress field and the virtual strain field and integrating the product over the volume of the element. Virtual shear strain $\hat{\gamma}$ is interpolated between the virtual nodal displacements in the same way as the real strain in equation (4.4) and is constant all over the finite element. Virtual axial strain $\hat{\varepsilon}$ is defined individually for each layer and interpolated in the same manner as the real strain in equation (4.6). Note that the additional part of the virtual strain $\hat{\varepsilon}^{i,add}$ only exists in the cracked layers. In non-cracked layers, the virtual strain consists only of the regular part $\hat{\bar{\varepsilon}}^i$.

$$\hat{\gamma} = \mathbf{B}\hat{\mathbf{v}} + \mathbf{B}^*\hat{\boldsymbol{\theta}} = \breve{\mathbf{B}}^*\hat{\mathbf{d}}, \quad \hat{\varepsilon}^i = \overbrace{\mathbf{B}\hat{\mathbf{u}} - y^i\mathbf{B}\hat{\boldsymbol{\theta}}}^{\hat{\bar{\varepsilon}}^i} + \overbrace{G^i\hat{\alpha}^i}^{\hat{\varepsilon}^{i,add}} = \breve{\mathbf{B}}^i\hat{\mathbf{d}} + G^i\hat{\alpha}^i \tag{4.30}$$

The volume integral in equation (4.29) is divided into an integral over the length and an integral over the cross-section of the element. The latter can be replaced by a sum over the layers, since everything is assumed to be constant over the cross-section A^i of a layer. The virtual axial strain is replaced by the whole expression (4.30) for $n_{CL}^{(e)}$ cracked layers and by its regular part $\hat{\bar{\varepsilon}}^i$ for $\left(n_L - n_{CL}^{(e)}\right)$ non-cracked layers, where n_L is the total number of layers in the finite element. Shear strain $\hat{\gamma}$ is constant over the whole element and is replaced by (4.30) for all n_L layers. Shear stress τ^i depends on the material law and is different for concrete and steel. Obtained expression is rearranged to produce internal forces, corresponding to the virtual degrees of freedom of the finite element $\hat{\mathbf{d}}^{(e)}$, defined in (4.19). Index (e) is omitted until the last line. For the sake of simplicity it is assumed that the cracked layers are numbered with 1, 2, ..., $n_{CL}^{(e)}$.

$$
\begin{aligned}
G^{\text{int},(e)} &= \int_V (\hat{\varepsilon}\sigma + \hat{\gamma}\tau)\, dV = \int_L \int_A (\hat{\varepsilon}\sigma + \hat{\gamma}\tau)\, dA dx = \int_L \sum_i \left(\hat{\varepsilon}^i \sigma^i + \hat{\gamma}\tau^i\right) A^i dx = \\
&= \int_L \sum_{i=1}^{n_L} \mathbf{B}\hat{\mathbf{u}}\, \sigma^i A^i dx + \int_L \sum_{i=1}^{n_L} \mathbf{B}\hat{\boldsymbol{\theta}} \left(-y^i \sigma^i A^i\right) dx + \int_L \sum_{i=1}^{n_{CL}} G^i \hat{\alpha}^i \sigma^i A^i dx + \\
&+ \int_L \sum_{i=1}^{n_L} \mathbf{B}\hat{\mathbf{v}}\, \tau^i A^i dx + \int_L \sum_{i=1}^{n_L} \mathbf{B}^* \hat{\boldsymbol{\theta}}\, \tau^i A^i dx = \\
&= \hat{\mathbf{u}}^T \int_L \sum_{i=1}^{n_L} \mathbf{B}^T \sigma^i A^i dx + \hat{\mathbf{v}}^T \int_L \sum_{i=1}^{n_L} \mathbf{B}^T \tau^i A^i dx + \hat{\boldsymbol{\theta}}^T \int_L \sum_{i=1}^{n_L} \left(-y^i \mathbf{B}^T \sigma^i + \mathbf{B}^{*T} \tau^i\right) A^i dx + \\
&+ \sum_{i=1}^{n_{CL}} \hat{\alpha}^i \int_L G^i \sigma^i A^i dx = \hat{\mathbf{d}}^{(e)^T} \mathbf{f}^{\text{int},(e)} + \sum_{i=1}^{n_{CL}^{(e)}} \hat{\alpha}^{(e),i} h^{(e),i}
\end{aligned}
\tag{4.31}
$$

A condensed form of expressions (4.19) and (4.23) for $\hat{\mathbf{d}}^{(e)}$ and $\mathbf{f}^{\text{int},(e)}$ is used.

$$
\hat{\mathbf{d}}^{(e)^T} = \left\{\hat{\mathbf{u}}^T, \hat{\mathbf{v}}^T, \hat{\boldsymbol{\theta}}^T\right\}, \quad \mathbf{f}^{\text{int},(e)^T} = \left\{\mathbf{f}^{u,\text{int},(e)^T}, \mathbf{f}^{v,\text{int},(e)^T}, \mathbf{f}^{\theta,\text{int},(e)^T}\right\} \tag{4.32}
$$

Components of $\mathbf{f}^{\text{int},(e)}$ are defined in (4.33). Since all present quantities are constant over the length of the finite element, the integrals are easily evaluated. The internal forces are calculated as a sum of contributions of individual layers, which proves to be helpful in the computational procedure.

$$
\begin{aligned}
\mathbf{f}^{u,\text{int},(e)} &= \int_L \sum_{i=1}^{n_L} \mathbf{B}^T \sigma^i A^i dx = \sum_{i=1}^{n_L} \mathbf{B}^T \sigma^i A^i L \\
\mathbf{f}^{v,\text{int},(e)} &= \int_L \sum_{i=1}^{n_L} \mathbf{B}^T \tau^i A^i dx = \sum_{i=1}^{n_L} \mathbf{B}^T \tau^i A^i L \\
\mathbf{f}^{\theta,\text{int},(e)} &= \int_L \sum_{i=1}^{n_L} \left(-y^i \mathbf{B}^T \sigma^i + \mathbf{B}^{*T} \tau^i\right) A^i dx = \sum_{i=1}^{n_L} \left(-y^i \mathbf{B}^T \sigma^i + \mathbf{B}^{*T} \tau^i\right) A^i L
\end{aligned}
\tag{4.33}
$$

A shorter notation (4.34) will also be used. Here, $\mathbf{f}^{\text{int},(e),i}$ is contribution of the i-th layer to the vector of nodal internal forces of the finite element.

$$
\mathbf{f}^{\text{int},(e)} = \sum_{i=1}^{n_L} \left(\begin{bmatrix} \mathbf{B}^T \\ \mathbf{0} \\ -y^i \mathbf{B}^T \end{bmatrix} \sigma^i A^i L + \begin{bmatrix} \mathbf{0} \\ \mathbf{B}^T \\ \mathbf{B}^{*T} \end{bmatrix} \tau^i A^i L \right) = \sum_{i=1}^{n_L} \underbrace{\left(\breve{\mathbf{B}}^{iT} \sigma^i + \breve{\mathbf{B}}^{*T} \tau^i\right) A^i L}_{\mathbf{f}^{\text{int},(e),i}} \tag{4.34}
$$

The second term of the last line in (4.31) is the additional virtual work due to enhanced kinematics. The sum has $n_{CL}^{(e)}$ summands, one for each cracked layer. Quantity $h^{(e),i}$ corresponds to the virtual displacement jump $\hat{\alpha}^{(e),i}$, and is defined as follows:

$$
h^{(e),i} = \int_L G^i \sigma^i A^i dx, \quad i = 1, 2, \ldots, n_{CL}^{(e)} \tag{4.35}
$$

The virtual work of external and internal forces in the equilibrium equation (4.27) is replaced by expressions (4.28) and (4.29), respecting (4.31) and (4.26). Finally, the second of equations (4.20) allows us to express the weak equilibrium in the manner of global virtual displacement vector $\hat{\mathbf{d}}^{\text{str}}$ and virtual displacement jumps $\hat{\alpha}^{(e),i}$.

$$\begin{aligned}
0 &= \sum_{e=1}^{n_{FE}} G^{\text{int},(e)} - G^{\text{ext}} = \\
&= \sum_{e=1}^{n_{FE}} \left(\hat{\mathbf{D}}^{(e)^T} \mathbf{F}^{\text{int},(e)} + \sum_{i=1}^{n_{CL}^{(e)}} \hat{\alpha}^{(e),i} h^{(e),i} \right) - \hat{\mathbf{d}}^{\text{str}^T} \mathbf{f}^{\text{ext,str}} = \\
&= \sum_{e=1}^{n_{FE}} \hat{\mathbf{d}}^{\text{str}^T} \mathbf{P}^{(e)^T} \mathbf{F}^{\text{int},(e)} + \sum_{e=1}^{n_{FE}} \sum_{i=1}^{n_{CL}^{(e)}} \hat{\alpha}^{(e),i} h^{(e),i} - \hat{\mathbf{d}}^{\text{str}^T} \mathbf{f}^{\text{ext,str}} = \\
&= \hat{\mathbf{d}}^{\text{str}^T} \sum_{e=1}^{n_{FE}} \mathbf{P}^{(e)^T} \mathbf{F}^{\text{int},(e)} + \sum_{e=1}^{n_{FE}} \sum_{i=1}^{n_{CL}^{(e)}} \hat{\alpha}^{(e),i} h^{(e),i} - \hat{\mathbf{d}}^{\text{str}^T} \mathbf{f}^{\text{ext,str}} = \\
&= \hat{\mathbf{d}}^{\text{str}^T} \left(\mathbf{f}^{\text{int,str}} - \mathbf{f}^{\text{ext,str}} \right) + \sum_{e=1}^{n_{FE}} \sum_{i=1}^{n_{CL}^{(e)}} \hat{\alpha}^{(e),i} h^{(e),i}
\end{aligned} \tag{4.36}$$

Equilibrium (4.36) must hold for any kinematically admissible virtual displacements $\hat{\mathbf{d}}^{\text{str}}$ and virtual displacement jumps $\hat{\alpha}^{(e),i}$. From this requirement we can conclude:

$$\begin{aligned}
&\mathbf{f}^{\text{int,str}} - \mathbf{f}^{\text{ext,str}} = \mathbf{0} \\
&\forall e \in \{1,2,\ldots,n_{FE}\},\ \forall i \in \left\{1,2,\ldots,n_{CL}^{(e)}\right\}: \quad h^{(e),i} = 0
\end{aligned} \tag{4.37}$$

The first equation in (4.37) represents the global equilibrium of every individual node of the mesh. Here $\mathbf{f}^{\text{int,str}}$ and $\mathbf{f}^{\text{ext,str}}$ are vectors of internal and external nodal forces on the structural mesh. They correspond in position and direction to the degrees of freedom of the mesh. Their length is equal to the total number of degrees of freedom n_{DOF}. The second equation in (4.37) is an additional constraint for the stress in cracked layers. The number of cracked layers $n_{CL}^{(e)}$ is generally different for each element, and can also be zero. It has been assumed in equation (4.37) that the cracked layers are numbered with consecutive numbers from 1 to $n_{CL}^{(e)}$.

Let us now examine $h^{(e),i}$, defined in expression (4.35). Operator G^i, defined by equation (4.13), consists of a continuous part $\bar{G}^i$ and the Dirac delta function $\delta_{x_d^i}$. Integration of the latter is performed by the following rule:

$$G^i = \bar{G}^i + \delta_{x_d^i}, \quad \int_L g(x)\, \delta_{x_d^i} dx = g\left(x_d^i\right) \tag{4.38}$$

Implementation of (4.38) allows a further development of expression (4.35). We introduce $\sigma^i\big|_{x_d^i}$ as the value of stress function $\sigma^i(x)$, evaluated at local coordinate x_d^i. We assign to it a new symbol t^i and define it as the traction at the discontinuity.

$$h^{(e),i} = \int_L \left(\bar{G}^i + \delta_{x_d^i} \right) \sigma^i A^i dx = A^i \int_L \bar{G}^i \sigma^i dx + A^i \sigma^i\big|_{x_d^i} = A^i \left(\int_L \bar{G}^i \sigma^i dx + t^i \right) \tag{4.39}$$

Inserting (4.39) into the second of equilibrium equations (4.37) provides a new aspect to its meaning. Equation (4.40) represents equilibrium between the traction at the discontinuity t^i and the stress in the bulk σ^i. Being

confined to a single finite element, we can refer to it as local equilibrium. Relation $\bar{G}^i = -1/L$ from equation (4.13) is used as well.

$$h^{(e),i} = 0 \quad \Leftrightarrow \quad t^i = -\int_L \bar{G}^i \sigma^i dx = \sigma^i \tag{4.40}$$

In the spirit of the method of incompatible modes, the operator G^i should also meet the requirement, that the additional virtual work (performed on the virtual displacement jumps $\hat{\alpha}^i$) be zero in case of constant stress σ^i. Thus, the introduction of $\hat{\alpha}^i$ does not affect the internal virtual work. Since the stress is always constant in our finite element, this test is trivial (fulfilled already by equilibrium equation (4.40)).

$$\hat{\alpha}^i \int_L G^i \sigma^i A^i dx = \underbrace{\hat{\alpha}^i \sigma^i A^i}_{\neq 0} \int_L G^i \, dx = 0 \quad \Rightarrow \quad \int_L G^i \, dx = 0 \tag{4.41}$$

Taking into account the rule (4.38) for integration of G^i, requirement (4.41) can be reformulated.

$$\int_L G^i \, dx = \int_L \left(\bar{G}^i + \delta_{x_d^i} \right) dx = \int_L \bar{G}^i \, dx + \overbrace{\int_L \delta_{x_d^i} dx}^{=1} = 0 \quad \Rightarrow \quad \int_L \bar{G}^i \, dx = -1 \tag{4.42}$$

Equality $\bar{G}^i = -1/L$ satisfies the condition (4.42).

4.2.5 Constitutive models

In this section we describe constitutive models which control the axial and shear response of concrete and steel-reinforcement layers. Axial response of each material is described by two models, one for the bulk of the layer and one for the discontinuity. Shear model is only required for the bulk of the layer, as there are no discontinuities involved.

4.2.5.1 Shear stress model

The transverse response is assumed to be elastic. While the shear strain is constant all over the finite element, the shear stress is different in concrete and steel layers, due to different material parameters. In equation (4.43), μ_c and μ_s are the shear moduli of concrete and steel, respectively, and c is the shear correction factor for rectangular cross-section. Shear strain γ is computed according to equation (4.4).

$$\tau^i = c\mu^i \gamma, \qquad c = 5/6, \qquad \mu^i = \begin{cases} \mu_c & \text{for concrete} \\ \mu_s & \text{for steel} \end{cases}, \qquad \frac{\partial \tau^i}{\partial \gamma} = c\mu^i \tag{4.43}$$

The shear moduli μ_c and μ_s are computed from the elastic moduli E_c and E_s, and Poisson's ratios ν_c and ν_s of concrete and steel. The usual values are used for ν_c and ν_s.

$$\mu_c = \frac{E_c}{2(1+\nu_c)}, \qquad \mu_s = \frac{E_s}{2(1+\nu_s)}, \qquad \nu_c = 0.2, \qquad \nu_s = 0.3 \tag{4.44}$$

4.2.5.2 Bulk of concrete layer

Behavior of the bulk of the concrete layer is described by 1D elasto-damage model. Response of the material is linear elastic up to the elasticity limit. Further increase of stress produces micro damage (micro cracking in tension and micro crushing in compression) continuously over the layer, which results in reduction of the elasticity modulus. Unloading is linear elastic with the current value of the elasticity modulus, and leads to the origin of the stress-strain diagram (see Fig. 4.10). These properties of concrete are collected in the following equations, which can be derived through the principle of maximum damage dissipation [73].

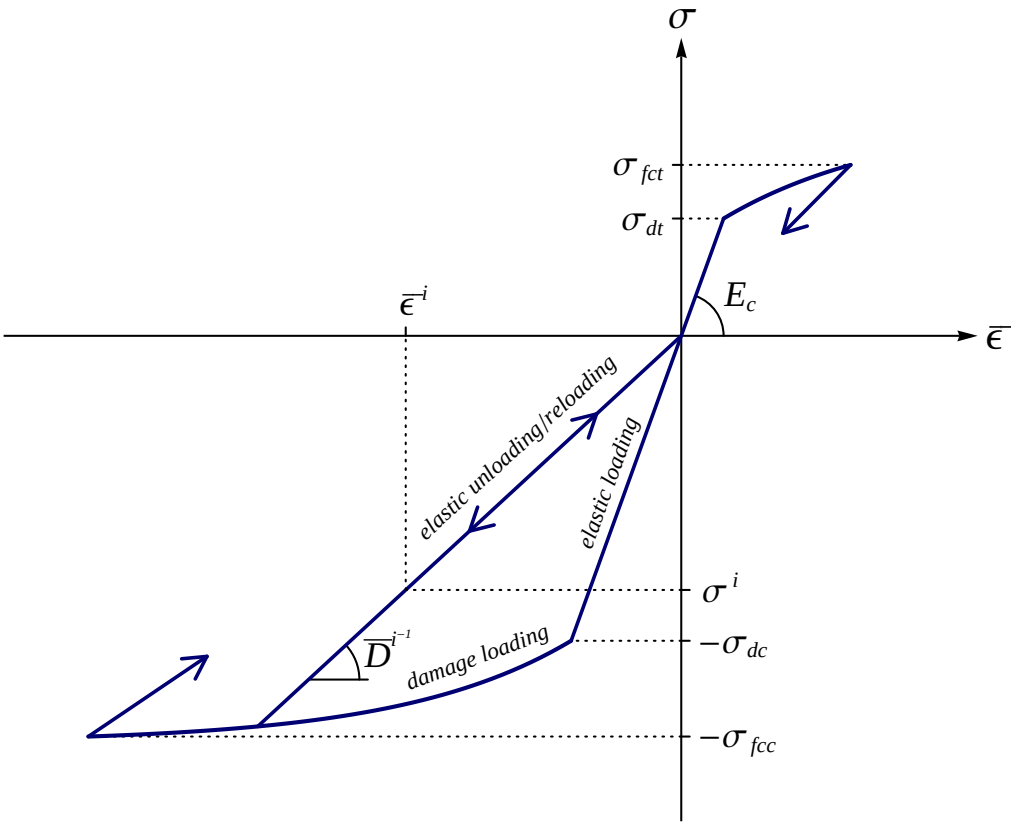

Figure 4.10: *Stress - strain* diagram for bulk of concrete layer.
Slika 4.10: Diagram *napetost - deformacija* za sloj betona.

Equation (4.45) shows the linear elastic relation between the stress and the strain. It represents the loading curve/path up to elasticity limit and the unloading/reloading curve in the $\sigma^i - \bar{\varepsilon}^i$ diagram.

$$\sigma^i = \bar{D}^{i^{-1}}\bar{\varepsilon}^i, \quad \bar{D}^i \in \left[E_c^{-1}, \infty\right), \quad \varepsilon^i = \breve{\mathbf{B}}^i\mathbf{d} + G^i\alpha^i = \overbrace{\breve{\mathbf{B}}^i\mathbf{d} + \bar{G}^i\alpha^i}^{\bar{\varepsilon}^i} + \tilde{\bar{G}}^i\alpha^i \tag{4.45}$$

Here $\bar{D}^i$ is the compliance of the bulk material, E_c the elastic modulus of intact concrete, and $\bar{\varepsilon}^i$ the continuous part of axial strain in the i-th layer, composed of the regular strain and the continuous part of the additional strain. The latter is zero until the discontinuity is formed. The non-elastic part of the loading curve in the $\sigma^i - \bar{\varepsilon}^i$ diagram is defined indirectly by the remaining equations in this section.

$$\bar{\phi}^i\left(\sigma^i,\bar{q}^i\right)=\left|\sigma^i\right|-\left(\sigma_d-\bar{q}^i\right),\quad \sigma_d=\begin{cases}\sigma_{dc} & \text{for compression}\\ \sigma_{dt} & \text{for tension}\end{cases} \tag{4.46}$$

Damage function $\bar{\phi}^i$ prescribes the admissible values of axial stress σ^i in the i-th layer. Elasticity limit $\sigma_d>0$ marks the beginning of micro damage and is defined separately for tension and compression. Stress-like hardening variable $\bar{q}^i$ handles the damage threshold evolution.

$$\bar{q}^i=-H_c\bar{\xi}^i,\quad H_c=\begin{cases}H_{cc} & \text{for compression}\\ H_{ct} & \text{for tension}\end{cases} \tag{4.47}$$

Linear hardening of the material is described by equation (4.47), where $\bar{\xi}^i$ is a strain-like hardening variable with initial value equal to zero, and $H_c>0$ is a constant hardening modulus of concrete with separate values for tension and compression. Evolution in pseudo-time of internal hardening variables $\bar{D}^i$ and $\bar{\xi}^i$ is defined by evolution equations (4.48).

$$\dot{\bar{D}}^i=\frac{\dot{\bar{\gamma}}^i sign\left(\sigma^i\right)}{\sigma^i},\quad \dot{\bar{\xi}}^i=\dot{\bar{\gamma}}^i \tag{4.48}$$

The dot designates the derivative with respect to pseudo-time and $\dot{\bar{\gamma}}^i$ is damage multiplier. The loading/unloading conditions and consistency condition (4.49) also apply.

$$\dot{\bar{\gamma}}^i\geq 0,\quad \bar{\phi}^i\leq 0,\quad \dot{\bar{\gamma}}^i\bar{\phi}^i=0,\quad \dot{\bar{\gamma}}^i\dot{\bar{\phi}}^i=0 \tag{4.49}$$

Tangent moduli of the $\sigma^i-\bar{\varepsilon}^i$ diagram can be determined from the above equations. The elastic loading/unloading path corresponds to condition $\dot{\bar{\gamma}}^i=0$. It follows from evolution equations (4.48), that compliance $\bar{D}^i$ is constant. The tangent modulus is obtained if expression (4.45) for σ^i is differentiated with respect to $\bar{\varepsilon}^i$.

$$\dot{\bar{\gamma}}^i=0\quad\Rightarrow\quad \bar{D}^i=\text{const.},\quad \frac{\partial\sigma^i}{\partial\bar{\varepsilon}^i}=\bar{D}^{i^{-1}} \tag{4.50}$$

In case of damage loading, when $\dot{\bar{\gamma}}^i>0$, the procedure is more complex. From the third and the fourth of conditions (4.49) we can conclude that $\bar{\phi}^i=0$ and $\dot{\bar{\phi}}^i=0$. From (4.46) we can write the expression for σ^i and differentiate it over pseudo-time. We use the appropriate evolution equation to differentiate $\bar{\xi}^i$ within.

$$\sigma^i=\left(\sigma_d-\bar{q}^i\right)sign\left(\sigma^i\right)=\left(\sigma_d+H_c\bar{\xi}^i\right)sign\left(\sigma^i\right),\quad \dot{\sigma}^i=H_c\dot{\bar{\gamma}}^i sign\left(\sigma^i\right) \tag{4.51}$$

The stress can be replaced by expression (4.45). The obtained equation is again differentiated over pseudo-time. Note that compliance $\bar{D}^i$ is not constant any more.

$$
\begin{aligned}
\bar{D}^{i^{-1}}\bar{\varepsilon}^i &= \left(\sigma_d + H_c\bar{\xi}^i\right) sign\left(\sigma^i\right) \\
-\bar{D}^{i^{-2}}\dot{\bar{D}}^i\bar{\varepsilon}^i + \bar{D}^{i^{-1}}\dot{\bar{\varepsilon}}^i &= H_c\dot{\bar{\xi}}^i sign\left(\sigma^i\right) \qquad \Big/ \dot{\bar{D}}^i = \frac{\dot{\bar{\gamma}}^i sign\left(\sigma^i\right)}{\sigma^i},\ \dot{\bar{\xi}}^i = \dot{\bar{\gamma}}^i \\
-\bar{D}^{i^{-2}}\frac{\dot{\bar{\gamma}}^i sign\left(\sigma^i\right)}{\sigma^i}\bar{\varepsilon}^i + \bar{D}^{i^{-1}}\dot{\bar{\varepsilon}}^i &= H_c\dot{\bar{\gamma}}^i sign\left(\sigma^i\right) \qquad \Big/ \frac{\bar{\varepsilon}^i}{\sigma^i} = \bar{D}^i \\
-\bar{D}^{i^{-1}}\dot{\bar{\gamma}}^i sign\left(\sigma^i\right) + \bar{D}^{i^{-1}}\dot{\bar{\varepsilon}}^i &= H_c\dot{\bar{\gamma}}^i sign\left(\sigma^i\right) \\
\dot{\bar{\varepsilon}}^i &= \frac{\bar{D}^{i^{-1}} + H_c}{\bar{D}^{i^{-1}}}\dot{\bar{\gamma}}^i sign\left(\sigma^i\right)
\end{aligned}
\tag{4.52}
$$

The tangent modulus is computed by dividing the pseudo-time derivatives $\dot{\sigma}^i$ and $\dot{\bar{\varepsilon}}^i$ from (4.51) and (4.52).

$$
\frac{\partial\sigma^i}{\partial\bar{\varepsilon}^i} = \frac{\dot{\sigma}^i}{\dot{\bar{\varepsilon}}^i} = \frac{\bar{D}^{i^{-1}}H_c}{\bar{D}^{i^{-1}} + H_c} \tag{4.53}
$$

To sum up, the tangent modulus is described by two expressions. The first one covers the elastic behavior - unloading and reloading, including the first elastic loading with the initial value of compliance $\bar{D}^i = E_c^{-1}$. The second expression represents the slope of the damage loading curve.

$$
\frac{\partial\sigma^i}{\partial\bar{\varepsilon}^i} = \begin{cases} \bar{D}^{i^{-1}}; & \dot{\bar{\gamma}}^i = 0 \\ \dfrac{\bar{D}^{i^{-1}}H_c}{\bar{D}^{i^{-1}} + H_c}; & \dot{\bar{\gamma}}^i > 0 \end{cases} \tag{4.54}
$$

4.2.5.3 Discontinuity in concrete layer

Energy dissipation at the discontinuity of a concrete layer is described by a softening damage law, which connects the traction at the discontinuity to the displacement jump. When the discontinuity is introduced, the displacement jump is zero and the traction is equal to the failure stress of concrete. An increase of the displacement jump (in absolute value) reduces the carrying capacity and thus produces a lower traction. A subsequent decrease of the displacement jump (in absolute value) reduces the traction as well, but the carrying capacity remains the same. Obviously, the problem needs to be controlled by imposed displacements to provide a unique solution. The term "loading" therefore refers to the increase of displacement jump (in absolute value) and "unloading" refers to the decrease of displacement jump. The unloading is always linear elastic, but there are two possibilities for loading. Elastic (re)loading follows the unloading curve, increases the traction, and leaves the internal variables unchanged. When carrying capacity is reached, damage loading continues. It decreases the traction and changes the internal variables (see Fig. 4.11). This material law is mathematically described by the following equations, which can be derived by using the principle of maximum damage dissipation [73].

Equation (4.55) describes the linear elastic relation between the traction at the discontinuity t^i and the displacement jump α^i. It represents the unloading/reloading path in the $t^i - \alpha^i$ diagram.

$$
t^i = \bar{\bar{D}}^{i^{-1}}\alpha^i, \quad \bar{\bar{D}}^i \in [0,\infty) \tag{4.55}
$$

Here $\bar{\bar{D}}^i$ is compliance of the discontinuity which increases with progression of the localized failure. The loading curve of the $t^i - \alpha^i$ diagram is defined indirectly by the remaining equations in this section.

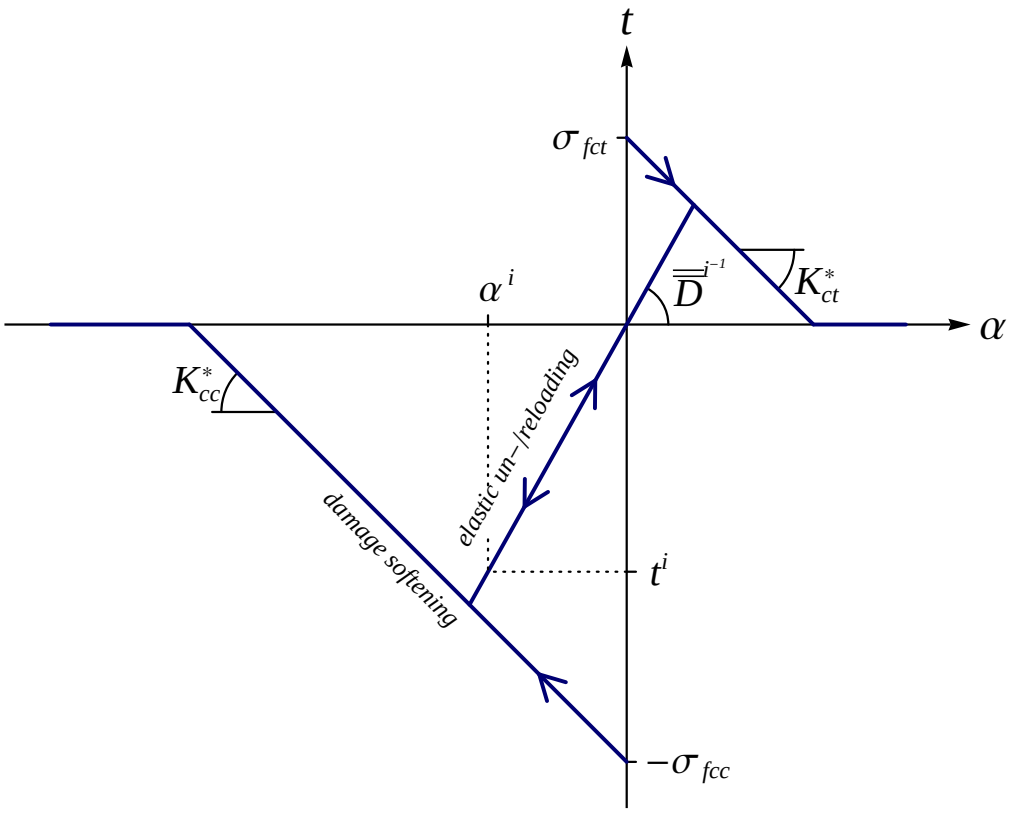

Figure 4.11: *Traction - displacement jump* diagram for discontinuity in concrete layer.
Slika 4.11: Diagram *napetost - skok v pomiku* za nezveznost v sloju betona.

$$\bar{\bar{\phi}}^i\left(t^i,\bar{\bar{q}}^i\right)=\left|t^i\right|-\left(\sigma_{fc}-\bar{\bar{q}}^i\right),\quad \sigma_{fc}=\begin{cases}\sigma_{fcc} & \text{for compression}\\ \sigma_{fct} & \text{for tension}\end{cases} \tag{4.56}$$

Failure function $\bar{\bar{\phi}}^i$ prescribes the admissible values of traction t^i at the discontinuity of a concrete layer. Failure stress of concrete $\sigma_{fc}>0$ indicates the occurrence of the discontinuity and is defined separately for tension and compression. Stress-like softening variable $\bar{\bar{q}}^i$ handles the damage threshold evolution and is described by an exponential function.

$$\bar{\bar{q}}^i=\sigma_{fc}\left(1-e^{K_c\bar{\bar{\xi}}^i}\right),\quad K_c=\begin{cases}K_{cc}=-\dfrac{\sigma_{fcc}}{2G_{fcc}} & \text{for compression}\\ K_{ct}=-\dfrac{\sigma_{fct}}{2G_{fct}} & \text{for tension}\end{cases} \tag{4.57}$$

Here $\bar{\bar{\xi}}^i$ is a displacement-like softening variable with initial value set to zero, and $K_c<0$ is a constant softening modulus of concrete with units m^{-1} and separate values for compression and tension. These are determined by the fracture energies per cross-section unit G_{fcc} and G_{fct} for concrete in compression and tension, respectively. The fracture energy has units kJm^{-2} and can be determined by different tests. Evolution in pseudo-time of internal softening variables $\bar{\bar{D}}^i$ and $\bar{\bar{\xi}}^i$ is defined by evolution equations (4.58).

$$\dot{\bar{\bar{D}}}^i = \frac{\dot{\bar{\bar{\gamma}}}^i \; sign\left(t^i\right)}{t^i}, \quad \dot{\bar{\bar{\xi}}}^i = \dot{\bar{\bar{\gamma}}}^i \tag{4.58}$$

The dot designates the derivative with respect to pseudo-time and $\dot{\bar{\bar{\gamma}}}^i$ is damage multiplier. The loading/unloading conditions and consistency condition (4.59) also apply.

$$\dot{\bar{\bar{\gamma}}}^i \geq 0, \quad \bar{\bar{\phi}}^i \leq 0, \quad \dot{\bar{\bar{\gamma}}}^i \bar{\bar{\phi}}^i = 0, \quad \dot{\bar{\bar{\gamma}}}^i \dot{\bar{\bar{\phi}}}^i = 0 \tag{4.59}$$

A closer inspection of equations (4.55)-(4.59) reveals that the damage loading path of $t^i - \alpha^i$ diagram, corresponding to condition $\bar{\bar{\phi}}^i = 0$, is a straight line, see appendix B. This suggests a possibility of simplifying the equations.

Each point of the damage loading path is determined by its ordinate t^i and the slope $\bar{\bar{D}}^{i^{-1}}$ of the unloading line, which connects the point to the origin. Abscissa α^i is computed from equation (4.55). Evolution equations (4.58) dictate the change of $\bar{\bar{D}}^i$ and $\bar{\bar{\xi}}^i$, the latter defining t^i through equations (4.56), (4.57) and (4.59). Both $\bar{\bar{D}}^i$ and t^i change non-linearly with respect to $\bar{\bar{\gamma}}^i = \dot{\bar{\bar{\gamma}}}^i \Delta t$ (Δt being pseudo-time step), the first one because of non-linear evolution equation (4.58), and the second due to exponential softening law (4.57). However, it is shown in appendix B that the two non-linearities neutralize each other, yielding a linear relation between t^i and α^i.

The damage loading path can also be constructed by defining coordinates α^i and t^i. If they both change linearly with respect to some new variable, the diagram will be a straight line. We introduce a new displacement-like variable $\bar{\bar{\xi}}^{i*}$ and the softening law takes a linear form.

$$\bar{\bar{\xi}}^{i*} = -\frac{1}{K_c}\left(1 - e^{K_c \bar{\bar{\xi}}^i}\right), \quad \bar{\bar{q}}^i = \sigma_{fc}\left(1 - e^{K_c \bar{\bar{\xi}}^i}\right) = -K_c \sigma_{fc} \bar{\bar{\xi}}^{i*} = -K_c^* \bar{\bar{\xi}}^{i*} \tag{4.60}$$

The expression for $\bar{\bar{q}}^i$ in (4.60) holds for $\bar{\bar{\xi}}^i < \infty$, or equivalently $\bar{\bar{\xi}}^{i*} < -1/K_c$. After that $\bar{\bar{q}}^i$ would become greater than the failure stress of concrete σ_{fc}, which is not acceptable. Physically, it means that the carrying capacity cannot drop below zero.

$$\bar{\bar{q}}^i = \min\left\{-K_c^* \bar{\bar{\xi}}^{i*}, \sigma_{fc}\right\}, \quad K_c^* = K_c \, \sigma_{fc} \tag{4.61}$$

Then, the introduction of a new damage multiplier $\bar{\bar{\gamma}}^{i*}$ allows us to write a new set of linear evolution equations for α^i and $\bar{\bar{\xi}}^{i*}$. See appendix B for details.

$$\bar{\bar{\gamma}}^{i*} = -\frac{1}{K_c}\left(1 - e^{K_c \bar{\bar{\gamma}}^i}\right), \quad \dot{\alpha}^i = \dot{\bar{\bar{\gamma}}}^{i*} sign\left(t^i\right), \quad \dot{\bar{\bar{\xi}}}^{i*} = \dot{\bar{\bar{\gamma}}}^{i*} \tag{4.62}$$

The new softening law (4.61) and evolution equations (4.62), due to their linear form, simplify the computational procedure significantly. But there is another advantage over the original equations. As the original damage multiplier $\bar{\bar{\gamma}}^i$ approaches infinity, the traction t^i approaches zero and the displacement jump α^i approaches $-sign\left(t^i\right)/K_c$. No matter how much we increase the multiplier, α^i cannot pass that value. For an individual bar, such limitation is logical, as the complete loss of carrying capacity implies singularity of the problem and a further increase of the discontinuity is meaningless. However, if a layer of a beam loses all carrying capacity, the beam as a whole still possesses stiffness. The broken layer just follows the rest of the beam without resistance. It is

therefore necessary to allow α^i to grow past the point of failure. When the new damage multiplier $\bar{\bar{\gamma}}^{i*}$ reaches the value $-1/K_c$, the original multiplier is pushed to infinity and the old evolution equations (4.58) get out of scope. The new evolution equations (4.62), however, withstand further increase of $\bar{\bar{\gamma}}^{i*}$. As the latter approaches infinity, so does α^i (in absolute value). Once past the failure point the traction t^i remains zero. The relation $t-\alpha$ at the discontinuity is described by equation (4.63).

$$t^i = \begin{cases} \bar{\bar{D}}^{i^{-1}} \alpha^i; & \dot{\bar{\bar{\gamma}}}^{i*} = 0 \\ \sigma_{fc}\, sign\left(\alpha^i\right) + \sigma_{fc} K_c \alpha^i; & \dot{\bar{\bar{\gamma}}}^{i*} > 0,\ \bar{\bar{q}}^i < \sigma_{fc} \\ 0; & \dot{\bar{\bar{\gamma}}}^{i*} > 0,\ \bar{\bar{q}}^i = \sigma_{fc} \end{cases} \tag{4.63}$$

The first expression represents the elastic unloading path, the second one the damage loading path until the traction drops to zero, and the third one the damage loading path further on. The tangent moduli are obtained by a simple differentiation of (4.63).

$$\frac{\partial t^i}{\partial \alpha^i} = \begin{cases} \bar{\bar{D}}^{i^{-1}}; & \dot{\bar{\bar{\gamma}}}^{i*} = 0 \\ K_c^* = \sigma_{fc} K_c; & \dot{\bar{\bar{\gamma}}}^{i*} > 0,\ \bar{\bar{q}}^i < \sigma_{fc} \\ 0; & \dot{\bar{\bar{\gamma}}}^{i*} > 0,\ \bar{\bar{q}}^i = \sigma_{fc} \end{cases} \tag{4.64}$$

4.2.5.4 Bulk of reinforcement layer

Behavior of the bulk of a layer of reinforcement is described by 1D elasto-plasticity model with isotropic hardening. It is symmetrical in tension and compression. Response of the material is linear elastic until yield stress is reached. If loading increases, plastic deformations occur and grow continuously over the layer. Elasticity limit is raised as well. Unloading is elastic and follows a line, parallel to the first loading path. When the stress drops to zero, plastic deformations remain in the layer (Fig. 4.12). Behavior of steel is mathematically described by the following equations, which can be derived by using the principle of maximum plastic dissipation [73].

Stress σ^i is computed from equation (4.65), which represents the elastic loading path and elastic unloading or reloading path of the $\sigma^i - \bar{\varepsilon}^i$ diagram.

$$\sigma^i = E_s\left(\bar{\varepsilon}^i - \bar{\varepsilon}_p^i\right), \quad \varepsilon^i = \breve{\mathbf{B}}^i \mathbf{d} + G^i \alpha^i = \overbrace{\breve{\mathbf{B}}^i \mathbf{d} + \bar{G}^i \alpha^i}^{\bar{\varepsilon}^i} + \bar{\bar{G}}^i \alpha^i \tag{4.65}$$

Here E_s is the elastic modulus of steel, $\bar{\varepsilon}_p^i$ plastic strain, and $\bar{\varepsilon}^i$ the continuous part of axial strain in the i-th layer, composed of the regular strain and the continuous part of the additional strain. Before the appearance of the discontinuity the additional strain is zero. The plastic loading path of the $\sigma^i - \bar{\varepsilon}^i$ diagram is determined indirectly by the rest of the equations in this section.

$$\bar{\phi}^i\left(\sigma^i, \bar{q}^i\right) = \left|\sigma^i\right| - \left(\sigma_y - \bar{q}^i\right) \tag{4.66}$$

Yield function $\bar{\phi}^i$ prescribes the admissible axial stress in the layer. Yield stress $\sigma_y > 0$ is the absolute value of the stress, at which the first plastic deformation occurs. Stress-like hardening variable $\bar{q}^i$ controls yield threshold evolution.

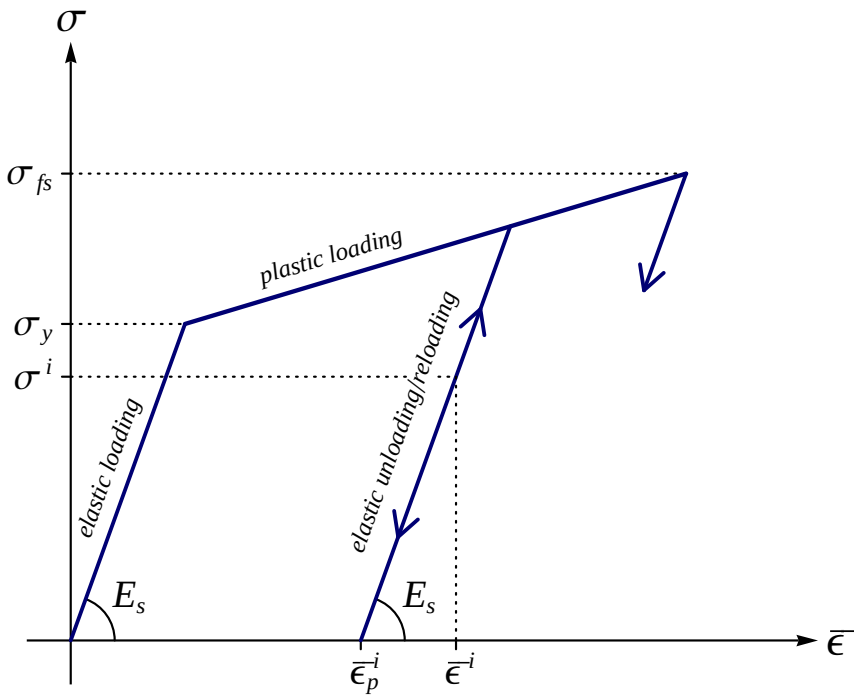

Figure 4.12: *Stress - strain* diagram for bulk of reinforcement layer.
Slika 4.12: Diagram *napetost - deformacija* za sloj armature.

$$\bar{q}^i = -H_s \bar{\xi}^i \tag{4.67}$$

Equation (4.67) describes the linear isotropic hardening of the material. Here $H_s > 0$ is a constant hardening modulus of steel and $\bar{\xi}^i$ is a strain-like hardening variable with the initial value zero. Evolution in pseudo-time of internal hardening variables for plasticity, $\bar{\varepsilon}_p^i$ and $\bar{\xi}^i$, is prescribed by evolution equations (4.68).

$$\dot{\bar{\varepsilon}}_p^i = \dot{\bar{\gamma}}^i sign\left(\sigma^i\right), \quad \dot{\bar{\xi}}^i = \dot{\bar{\gamma}}^i \tag{4.68}$$

The dot designates the derivative with respect to pseudo-time and $\dot{\bar{\gamma}}^i$ is plastic multiplier. The loading/unloading conditions and consistency condition (4.69) apply as well.

$$\dot{\bar{\gamma}}^i \geq 0, \quad \bar{\phi}^i \leq 0, \quad \dot{\bar{\gamma}}^i \bar{\phi}^i = 0, \quad \dot{\bar{\gamma}}^i \dot{\bar{\phi}}^i = 0 \tag{4.69}$$

Tangent moduli of the $\sigma^i - \bar{\varepsilon}^i$ diagram are determined by the described equations. In elastic response, the plastic multiplier is equal to zero. As a consequence, internal variables are constant and the tangent modulus is simply computed by differentiating the expression (4.65) for σ^i with respect to $\bar{\varepsilon}^i$.

$$\dot{\bar{\gamma}}^i = 0 \quad \Rightarrow \quad \bar{\varepsilon}_p^i = \text{const.}, \quad \frac{\partial \sigma^i}{\partial \bar{\varepsilon}^i} = E_s \tag{4.70}$$

In plastic loading, the plastic strain $\bar{\varepsilon}_p^i$ is not constant. It depends on the plastic multiplier $\dot{\bar{\gamma}}^i > 0$ and consequently on the strain $\bar{\varepsilon}^i$. The tangent modulus can be computed from pseudo-time derivatives of stress and strain. It

follows from the last two equations in (4.69) that $\bar{\phi}^i = 0$ and $\dot{\bar{\phi}}^i = 0$. We can express σ^i from equation (4.66) and differentiate it over pseudo-time.

$$\sigma^i = \left(\sigma_y - \bar{q}^i\right) sign\left(\sigma^i\right) = \left(\sigma_y + H_s\bar{\xi}^i\right) sign\left(\sigma^i\right), \quad \dot{\sigma}^i = H_s\dot{\bar{\gamma}}^i sign\left(\sigma^i\right) \tag{4.71}$$

We can replace the stress σ^i with expression (4.65) and differentiate the modified equation over pseudo-time again. Evolution equations (4.68) are utilized in the procedure.

$$\begin{aligned} E_s\left(\bar{\varepsilon}^i - \bar{\varepsilon}_p^i\right) &= \left(\sigma_y + H_s\bar{\xi}^i\right) sign\left(\sigma^i\right) \\ E_s\left(\dot{\bar{\varepsilon}}^i - \dot{\bar{\varepsilon}}_p^i\right) &= H_s\dot{\bar{\xi}}^i sign\left(\sigma^i\right) \qquad / \dot{\bar{\varepsilon}}_p^i = \dot{\bar{\gamma}}^i sign\left(\sigma^i\right),\ \dot{\bar{\xi}}^i = \dot{\bar{\gamma}}^i \\ E_s\dot{\bar{\varepsilon}}^i - E_s\dot{\bar{\gamma}}^i sign\left(\sigma^i\right) &= H_s\dot{\bar{\gamma}}^i sign\left(\sigma^i\right) \\ \dot{\bar{\varepsilon}}^i &= \frac{E_s + H_s}{E_s}\dot{\bar{\gamma}}^i sign\left(\sigma^i\right) \end{aligned} \tag{4.72}$$

Pseudo-time derivatives $\dot{\sigma}^i$ and $\dot{\bar{\varepsilon}}^i$, defined in (4.71) and (4.72), are divided to produce the plastic tangent modulus.

$$\frac{\partial\sigma^i}{\partial\bar{\varepsilon}^i} = \frac{\dot{\sigma}^i}{\dot{\bar{\varepsilon}}^i} = \frac{E_s H_s}{E_s + H_s} \tag{4.73}$$

The elastic and plastic tangent moduli are gathered below. The first expression represents the slope of the elastic loading and unloading path, while the second one represents the slope of the plastic loading path in the $\sigma^i - \bar{\varepsilon}^i$ diagram.

$$\frac{\partial\sigma^i}{\partial\bar{\varepsilon}^i} = \begin{cases} E_s; & \dot{\bar{\gamma}}^i = 0 \\ \dfrac{E_s H_s}{E_s + H_s}; & \dot{\bar{\gamma}}^i > 0 \end{cases} \tag{4.74}$$

4.2.5.5 Discontinuity in reinforcement layer

Behavior of the discontinuity in a layer of reinforcement is described by a plastic softening law, which connects the traction at the discontinuity to the displacement jump (Fig. 4.13). At introduction of the discontinuity the displacement jump is zero and the traction is equal to the failure stress of steel. A further increase of the imposed displacements of the layer reduces the carrying capacity. The traction at the discontinuity decreases and the displacement jump increases. This is referred to as plastic softening. The displacement jump behaves analogously to plastic strain in the continuous model, i.e. it stays the same if the loading is decreased. The traction at the discontinuity in the unloading phase changes in accordance with the stress in the bulk, so that the equilibrium (4.40) is satisfied. When traction (in absolute value) reaches the carrying capacity again, the plastic loading continues and the displacement jump changes accordingly to the sign of traction. It decreases in compression and increases in tension, regardless of its own size and sign. The mathematical description of such behavior is condensed in the following equations, which can be derived by the principle of maximum plastic dissipation [73].

$$\bar{\bar{\phi}}^i\left(t^i, \bar{\bar{q}}^i\right) = \left|t^i\right| - \left(\sigma_{fs} - \bar{\bar{q}}^i\right) \tag{4.75}$$

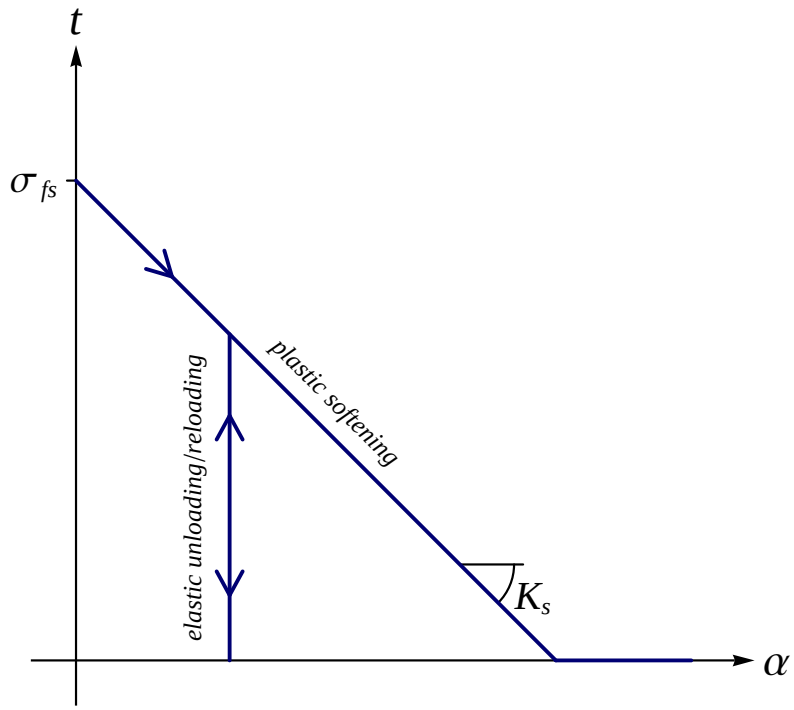

Figure 4.13: *Traction - displacement jump* diagram for discontinuity in reinforcement layer.
Slika 4.13: Diagram *napetost - skok v pomiku* za nezveznost v sloju armature.

Failure function $\bar{\bar{\phi}}^i$ defines the admissible values of traction t^i at the discontinuity of a reinforcement layer. Failure stress of steel $\sigma_{fs} > 0$ is the absolute value of the stress, at which the discontinuity first appears. The stress-like softening variable $\bar{\bar{q}}^i$ manages the softening threshold evolution.

$$\bar{\bar{q}}^i = \min\left\{-K_s\bar{\bar{\xi}}^i, \sigma_{fs}\right\}, \quad K_s = -\frac{\sigma_{fs}^2}{2G_{fs}} \tag{4.76}$$

The linear softening law is described by equation (4.76), where $\bar{\bar{\xi}}^i$ is a displacement-like softening variable with initial value zero, and $K_s > 0$ is a constant softening modulus of concrete with units kNm^{-3}. Fracture energy per cross-section unit of steel G_{fs} represents the area between the horizontal axis and the softening line in the $t-\alpha$ diagram. It has units kJm^{-2} and can be determined from a uniaxial tension test. Evolution in pseudo-time of internal softening variables α^i and $\bar{\bar{\xi}}^i$ is defined by evolution equations (4.77).

$$\dot{\alpha}^i = \dot{\bar{\bar{\gamma}}}^i sign\left(t^i\right), \quad \dot{\bar{\bar{\xi}}}^i = \dot{\bar{\bar{\gamma}}}^i \tag{4.77}$$

The dot designates the derivative with respect to pseudo-time and $\dot{\bar{\bar{\gamma}}}^i$ is plastic softening multiplier. The loading/unloading conditions and consistency condition (4.78) also apply.

$$\dot{\bar{\bar{\gamma}}}^i \geq 0, \quad \bar{\bar{\phi}}^i \leq 0, \quad \dot{\bar{\bar{\gamma}}}^i \bar{\bar{\phi}}^i = 0, \quad \dot{\bar{\bar{\gamma}}}^i \dot{\bar{\bar{\phi}}}^i = 0 \tag{4.78}$$

The equation of the plastic softening loading path of $t^i - \alpha^i$ diagram is not unique. It depends on the loading history. If the softening process alternates between both load signs, the loading path is translated sideways (left or

right). The slope, however, is not affected and can be determined from the pseudo-time derivatives of t^i and α^i. In softening process, when $\dot{\bar{\bar{\gamma}}}^i > 0$, the failure function $\dot{\bar{\bar{\phi}}}^i = 0$. Expression for t^i is then determined by (4.75) and (4.76).

$$t^i = \left(\sigma_{fs} - \bar{\bar{q}}^i\right) sign\left(t^i\right) = \begin{cases} \left(\sigma_{fs} + K_s \bar{\bar{\xi}}^i\right) sign\left(t^i\right); & \bar{\bar{q}}^i < \sigma_{fs} \\ 0; & \bar{\bar{q}}^i = \sigma_{fs} \end{cases} \tag{4.79}$$

The derivative is obtained in accordance with evolution equation (4.77) for $\dot{\bar{\bar{\xi}}}^i$.

$$\dot{t}^i = \begin{cases} K_s \dot{\bar{\bar{\xi}}}^i sign\left(t^i\right) = K_s \dot{\bar{\bar{\gamma}}}^i sign\left(t^i\right); & \bar{\bar{q}}^i < \sigma_{fs} \\ 0; & \bar{\bar{q}}^i = \sigma_{fs} \end{cases} \tag{4.80}$$

The slope of the plastic softening loading path, defined as the derivative of t^i over α^i, is computed by dividing the pseudo-time derivatives (4.80) and (4.77) of both quantities.

$$\frac{\partial t^i}{\partial \alpha^i} = \frac{\dot{t}^i}{\dot{\alpha}^i} = \begin{cases} \text{not defined}; & \dot{\bar{\bar{\gamma}}}^i = 0 \\ K_s; & \dot{\bar{\bar{\gamma}}}^i > 0,\ \bar{\bar{q}}^i < \sigma_{fs} \\ 0; & \dot{\bar{\bar{\gamma}}}^i > 0,\ \bar{\bar{q}}^i = \sigma_{fs} \end{cases} \tag{4.81}$$

A third option was added in equation (4.81). It corresponds to elastic unloading path with $\dot{\bar{\bar{\gamma}}}^i = 0$. It follows from evolution equations (4.77) that $\dot{\alpha}^i = 0$ in such case. And since the failure function $\dot{\bar{\bar{\phi}}}^i$ is no longer required to be zero, the traction t^i cannot be computed as in (4.79). It changes in accordance with equation (4.40) which represents the equilibrium between the bulk and the discontinuity. The fraction in (4.81) is not defined, but it is not required in the computational procedure anyway.

4.3 Computational procedure

Response of a structure, discretized by a mesh of n_{FE} above derived finite elements, is computed at discrete pseudo-time points $\tau_0,\ \tau_1,\ \ldots\ ,\ \tau_n,\ \tau_{n+1},\ \ldots\ ,\ T$ by solving at each pseudo-time point nonlinear equations (4.82) for current values of nodal displacements/rotations.

$$\begin{aligned} &\mathbf{f}^{\text{int,str}} - \mathbf{f}^{\text{ext,str}} = \mathbf{0} \\ &\forall e \in \{1,2,\ldots,n_{FE}\},\ \forall i \in \left\{1,2,\ldots,n_{CL}^{(e)}\right\}: \quad h^{(e),i} = 0 \end{aligned} \tag{4.82}$$

Here, $n_{CL}^{(e)}$ is the number of cracked layers in element (e). At a particular pseudo-time point τ_{n+1}, the solution is searched iteratively by the Newton-Raphson method. Each iteration, denoted by k, consists of two subsequent phases: (A) computation of internal variables, corresponding to the current iterative values of nodal displacements/rotations, in order to compute the stress in accordance with given material laws; (B) solution of linearized equations (4.82) in order to update the iterative values of nodal displacements/rotations. When one phase of the computation is completed, the results are used immediately in the next one.

For a pseudo-time point τ_{n+1}, the computational problem related to a generic element (e) and material layer i can be stated as:

$$\text{given} \quad \mathbf{d}_n^{(e)} \quad \text{and} \quad \begin{cases} \bar{D}_n^{(e),i}, \bar{\xi}_n^{(e),i}, \bar{\bar{D}}_n^{(e),i}, \bar{\bar{\xi}}_n^{(e),i} \\ \bar{\varepsilon}_{p,n}^{(e),i}, \bar{\xi}_n^{(e),i}, \alpha_n^{(e),i}, \bar{\bar{\xi}}_n^{(e),i} \end{cases} \quad \text{find} \quad \mathbf{d}_{n+1}^{(e)} \quad \text{and} \quad \begin{cases} \bar{D}_{n+1}^{(e),i}, \bar{\xi}_{n+1}^{(e),i}, \bar{\bar{D}}_{n+1}^{(e),i}, \bar{\bar{\xi}}_{n+1}^{(e),i} \\ \bar{\varepsilon}_{p,n+1}^{(e),i}, \bar{\xi}_{n+1}^{(e),i}, \alpha_{n+1}^{(e),i}, \bar{\bar{\xi}}_{n+1}^{(e),i} \end{cases}$$

Note that superscript (e) was omitted in section 4.2.5 for the above internal variables. The subscript n and $n+1$ denote the values at pseudo-times τ_n and τ_{n+1}, respectively.

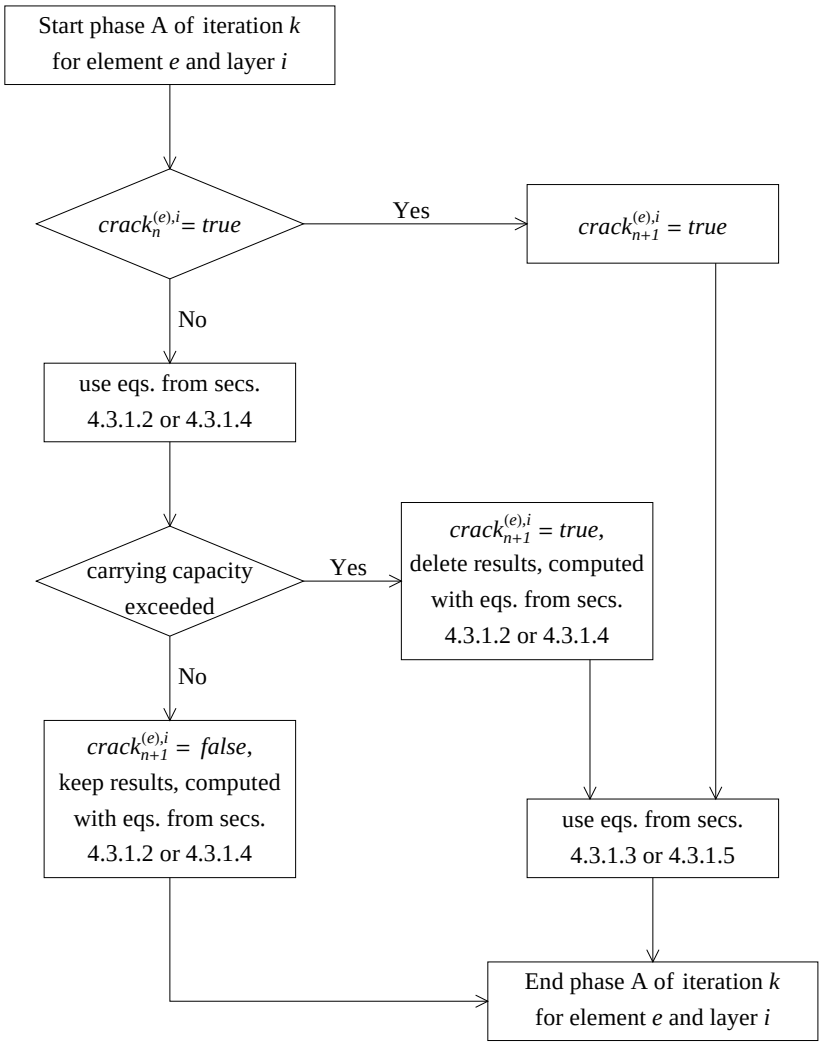

Figure 4.14: Algorithm for phase (A) of k-th iteration for i-th layer of finite element (e).
Slika 4.14: Algoritem za fazo (A) k-te iteracije za i-ti sloj končnega elementa (e).

4.3.1 Computation of internal variables

In this section we will present computations of phase (A). The internal variables for i-th layer of element (e) at pseudo-time point τ_{n+1} will be computed for the k-th iteration, while the nodal displacements/rotations are fixed at the values from the previous iteration $\mathbf{d}_{n+1}^{(e),(k-1)}$. Since every internal variable is connected to a single layer of a

single finite element, the computations are local, i.e. they are performed independently for each element and each layer. The condition of the discontinuity is known by the following flag.

$$crack^{(e),i} = \begin{cases} false & \dots \quad \text{no discontinuity in layer } i \\ true & \dots \quad \text{discontinuity in layer } i \end{cases} \tag{4.83}$$

The algorithm in Fig. 4.14 is applied. If there was no discontinuity in the layer in the previous pseudo-time step, we begin with equations for the hardening phase of material, described in sections 4.3.1.2 for concrete and 4.3.1.4 for steel. We must do so even if the previous iteration of the current step indicated occurrence of the discontinuity, because that was not a converged result. We check if the carrying capacity of the layer is exceeded. If not, we keep the obtained results, otherwise we discard them and use equations for the softening phase of material, described in sections 4.3.1.3 for concrete and 4.3.1.5 for steel. If the discontinuity already existed in the previous pseudo-time step, it must also exist in the current step, therefore we follow the procedure from sections 4.3.1.3 or 4.3.1.5.

For the sake of clarity we will omit in the rest of this section the superscript (e), denoting the finite element, and the superscript i, denoting the layer.

4.3.1.1 Shear response

Computation of the shear response is straightforward. Shear strain is computed according to equation (4.7) with the current values of the nodal displacements. Shear stress is then calculated from (4.43).

$$\gamma_{n+1}^{(k)} = \breve{\mathbf{B}}^* \mathbf{d}_{n+1}^{(k-1)}, \qquad \tau_{n+1}^{i,(k)} = c\mu^i \gamma_{n+1}^{(k)}, \qquad \left.\frac{\partial \tau^i}{\partial \gamma}\right|_{n+1}^{(k)} = c\mu^i \tag{4.84}$$

4.3.1.2 Bulk of concrete layer

This section describes the computational procedure for the hardening phase of a concrete layer. The discontinuity has not yet occurred and the displacement jump is zero. The computation is started by assuming an elastic step, which means that hardening internal variables do not change, but keep the values from the previous step. Trial value of stress is computed according to (4.45), with $\alpha_{n+1}^{(k)} = 0$.

$$\bar{D}_{n+1}^{(k),trial} = \bar{D}_n, \quad \bar{\xi}_{n+1}^{(k),trial} = \bar{\xi}_n, \quad \sigma_{n+1}^{(k),trial} = \bar{D}_{n+1}^{(k),trial^{-1}} \bar{\varepsilon}\left(\mathbf{d}_{n+1}^{(k-1)}, \alpha_{n+1}^{(k)}\right) \tag{4.85}$$

The trial damage function $\bar{\phi}_{n+1}^{(k),trial}$ is computed in accordance with equations (4.46) and (4.47).

$$\bar{\phi}_{n+1}^{(k),trial} = \left|\sigma_{n+1}^{(k),trial}\right| - \left(\sigma_d - \bar{q}_{n+1}^{(k),trial}\right), \quad \bar{q}_{n+1}^{(k),trial} = -H_c \bar{\xi}_{n+1}^{(k),trial} = -H_c \bar{\xi}_n \tag{4.86}$$

The trial solution is accepted if the trial damage function is not positive.

$$\bar{\phi}_{n+1}^{(k),trial} \leq 0 \quad \Rightarrow \quad \bar{D}_{n+1}^{(k)} = \bar{D}_{n+1}^{(k),trial}, \quad \bar{\xi}_{n+1}^{(k)} = \bar{\xi}_{n+1}^{(k),trial}, \quad \sigma_{n+1}^{(k)} = \sigma_{n+1}^{(k),trial} \tag{4.87}$$

Otherwise, the internal variables have to be corrected and the stress recomputed. Incremental form of evolution equations (4.48) is applied, where $\bar{\gamma}_{n+1}^{(k)} = \dot{\bar{\gamma}}_{n+1}^{(k)} (\tau_{n+1} - \tau_n) > 0$. The use of $sign\left(\sigma_{n+1}^{(k)}\right) = sign\left(\sigma_{n+1}^{(k),trial}\right)$ is justified in appendix A.

$$\bar{\phi}_{n+1}^{(k),trial} > 0 \quad \Rightarrow \quad \bar{D}_{n+1}^{(k)} = \bar{D}_n + \bar{\gamma}_{n+1}^{(k)} \frac{sign\left(\sigma_{n+1}^{(k),trial}\right)}{\sigma_{n+1}^{(k)}}, \quad \bar{\xi}_{n+1}^{(k)} = \bar{\xi}_n + \bar{\gamma}_{n+1}^{(k)} \tag{4.88}$$

By using equations (4.88), the stress $\sigma_{n+1}^{(k)}$ and the stress-like hardening variable $\bar{q}_{n+1}^{(k)}$ can be expressed with their trial values and the damage multiplier $\bar{\gamma}_{n+1}^{(k)}$.

$$\begin{aligned}
\sigma_{n+1}^{(k)} &= \bar{D}_{n+1}^{(k)^{-1}} \bar{\varepsilon}\left(\mathbf{d}_{n+1}^{(k-1)}, \alpha_{n+1}^{(k)}\right) \\
\bar{D}_{n+1}^{(k)} \sigma_{n+1}^{(k)} &= \bar{\varepsilon}\left(\mathbf{d}_{n+1}^{(k-1)}, \alpha_{n+1}^{(k)}\right) = \bar{D}_{n+1}^{(k),trial} \sigma_{n+1}^{(k),trial} \\
\left(\bar{D}_n + \bar{\gamma}_{n+1}^{(k)} \frac{sign\left(\sigma_{n+1}^{(k),trial}\right)}{\sigma_{n+1}^{(k)}}\right) \sigma_{n+1}^{(k)} &= \bar{D}_n \sigma_{n+1}^{(k),trial} \\
\bar{D}_n \sigma_{n+1}^{(k)} + \bar{\gamma}_{n+1}^{(k)} sign\left(\sigma_{n+1}^{(k),trial}\right) &= \bar{D}_n \sigma_{n+1}^{(k),trial} \\
\sigma_{n+1}^{(k)} &= \sigma_{n+1}^{(k),trial} - \bar{D}_n^{-1} \bar{\gamma}_{n+1}^{(k)} sign\left(\sigma_{n+1}^{(k),trial}\right)
\end{aligned} \tag{4.89}$$

$$\bar{q}_{n+1}^{(k)} = -H_c \bar{\xi}_{n+1}^{(k)} = -H_c \left(\bar{\xi}_n + \bar{\gamma}_{n+1}^{(k)}\right) = \bar{q}_{n+1}^{(k),trial} - H_c \bar{\gamma}_{n+1}^{(k)} \tag{4.90}$$

Equations (4.89) and (4.90) are used to express the damage function $\bar{\phi}_{n+1}^{(k)}$ as a function of damage multiplier $\bar{\gamma}_{n+1}^{(k)}$, which is then computed from requirement $\bar{\phi}_{n+1}^{(k)} = 0$, coming from loading/unloading conditions (4.49).

$$\begin{aligned}
\bar{\phi}_{n+1}^{(k)} &= \left|\sigma_{n+1}^{(k)}\right| - \left(\sigma_d - \bar{q}_{n+1}^{(k)}\right) = \left|\sigma_{n+1}^{(k),trial}\right| - \bar{D}_n^{-1} \bar{\gamma}_{n+1}^{(k)} - \left(\sigma_d - \bar{q}_{n+1}^{(k),trial}\right) - H_c \bar{\gamma}_{n+1}^{(k)} = \\
&= \bar{\phi}_{n+1}^{(k),trial} - \left(\bar{D}_n^{-1} + H_c\right) \bar{\gamma}_{n+1}^{(k)}
\end{aligned} \tag{4.91}$$

$$\bar{\phi}_{n+1}^{(k)} = 0 \quad \Rightarrow \quad \bar{\gamma}_{n+1}^{(k)} = \frac{\bar{\phi}_{n+1}^{(k),trial}}{\bar{D}_n^{-1} + H_c}$$

Consistent tangent modulus is computed as the derivative of stress over strain. Stress takes the trial value from (4.85) if damage multiplier $\bar{\gamma}_{n+1}^{(k)}$ is zero, and the value from (4.89) if $\bar{\gamma}_{n+1}^{(k)}$ is positive. In the second case, equations (4.91), (4.86) and (4.85) are used to express the stress as a function of strain.

$$\left.\frac{\partial \sigma}{\partial \bar{\varepsilon}}\right|_{n+1}^{(k)} = \begin{cases} \bar{D}_n^{-1}; & \bar{\gamma}_{n+1}^{(k)} = 0 \\ \dfrac{\bar{D}_n^{-1} H_c}{\bar{D}_n^{-1} + H_c}; & \bar{\gamma}_{n+1}^{(k)} > 0 \end{cases} \tag{4.92}$$

The hardening internal variables, stress and tangent modulus have been determined under assumption, that the carrying capacity is not exceeded, which remains to be verified. If indeed the carrying capacity is not reached, the results are accepted. In the opposite case, the results are discarded and computed again, taking into account the newly appeared discontinuity.

First, the potential value of traction at the discontinuity $t_{n+1}^{(k),pot}$ is computed according to equation (4.40). Failure function $\bar{\bar{\phi}}_{n+1}^{(k),pot}$ is then evaluated with the stress-like softening variable $\bar{\bar{q}}_{n+1}^{(k),pot}$ equal to zero, because there has been no reduction of carrying capacity in previous steps.

$$t_{n+1}^{(k),pot} = -\int_L \bar{G}\sigma_{n+1}^{(k)} dx = \sigma_{n+1}^{(k)}, \quad \bar{\bar{\phi}}_{n+1}^{(k),pot} = \left| t_{n+1}^{(k),pot} \right| - \left(\sigma_{fc} - \bar{\bar{q}}_{n+1}^{(k),pot} \right), \quad \bar{\bar{q}}_{n+1}^{(k),pot} = 0 \tag{4.93}$$

The discontinuity flag is set to $true$ if the failure function is positive, and to $false$ otherwise. Note that the value of the flag is not final, until the converged state is reached. It can change in following iterations.

$$\begin{aligned} \bar{\bar{\phi}}_{n+1}^{(k),pot} \leq 0 \quad &\Rightarrow \quad crack_{n+1}^{(e),i} = false \\ \bar{\bar{\phi}}_{n+1}^{(k),pot} > 0 \quad &\Rightarrow \quad crack_{n+1}^{(e),i} = true \end{aligned} \tag{4.94}$$

If the carrying capacity is exceeded ($\bar{\bar{\phi}}_{n+1}^{(k),pot} > 0$), the above computed values of internal variables, stress and tangent modulus are discarded for this iteration and computed anew as described in section 4.3.1.3.

4.3.1.3 Discontinuity in concrete layer

Here we describe the computational procedure for the softening phase of the concrete layer. The procedure is used if the current value of discontinuity flag $crack_{n+1}^{(e),i} = true$. This is a consequence of either an existing discontinuity in the previous step ($crack_n^{(e),i} = true$), or exceeded ultimate stress in this iteration, as written in equation (4.94). In both cases, the hardening internal variables take the last converged values, i.e. the values from the last step.

$$\bar{D}_{n+1}^{(k)} = \bar{D}_n, \quad \bar{\xi}_{n+1}^{(k)} = \bar{\xi}_n \tag{4.95}$$

The computation is started by assuming an elastic step, which implies no change in the softening internal variables in this iteration. We use the displacement-like softening variable $\bar{\bar{\xi}}^*$, introduced in equation (4.60).

$$\bar{\bar{D}}_{n+1}^{(k),trial} = \bar{\bar{D}}_n, \quad \bar{\bar{\xi}}_{n+1}^{*(k),trial} = \bar{\bar{\xi}}_n^* \tag{4.96}$$

The trial value of traction at the discontinuity is defined by equation (4.97). Derivation of the expression is shown in appendix C. According to equation (4.40) it is equal to the trial stress. The trial value of displacement jump is computed from equation (4.55).

$$t_{n+1}^{(k),trial} = \sigma_{n+1}^{(k),trial} = \frac{\breve{\mathbf{B}}\mathbf{d}_{n+1}^{(k-1)}}{\bar{D}_n - \bar{G}\bar{\bar{D}}_n}, \quad \alpha_{n+1}^{(k),trial} = \bar{\bar{D}}_n t_{n+1}^{(k),trial} \tag{4.97}$$

Next, the trial value of failure function $\bar{\bar{\phi}}_{n+1}^{(k),trial}$ is computed, using expression (4.61) for the stress-like softening variable $\bar{\bar{q}}_{n+1}^{(k),trial}$.

$$\bar{\bar{\phi}}_{n+1}^{(k),trial} = \left| t_{n+1}^{(k),trial} \right| - \left(\sigma_{fc} - \bar{\bar{q}}_{n+1}^{(k),trial} \right), \quad \bar{\bar{q}}_{n+1}^{(k),trial} = \min\left\{ -K_c^* \bar{\bar{\xi}}_{n+1}^{*(k),trial}, \sigma_{fc} \right\} = \bar{\bar{q}}_n \tag{4.98}$$

If $\bar{\bar{\phi}}_{n+1}^{(k),trial} \leq 0$, the trial solution is accepted.

$$\begin{aligned} &\bar{\bar{D}}_{n+1}^{(k)} = \bar{\bar{D}}_{n+1}^{(k),trial}, \quad \bar{\bar{\xi}}_{n+1}^{*(k)} = \bar{\bar{\xi}}_{n+1}^{*(k),trial}, \quad \alpha_{n+1}^{(k)} = \alpha_{n+1}^{(k),trial} \\ &t_{n+1}^{(k)} = t_{n+1}^{(k),trial}, \quad \sigma_{n+1}^{(k)} = \sigma_{n+1}^{(k),trial} \end{aligned} \tag{4.99}$$

If $\bar{\bar{\phi}}_{n+1}^{(k),trial} > 0$, the assumed trial values are not admissible. We have to compute the softening damage multiplier $\bar{\bar{\gamma}}_{n+1}^{*(k)} = \dot{\bar{\bar{\gamma}}}_{n+1}^{*(k)}(\tau_{n+1} - \tau_n) > 0$ from equation $\bar{\bar{\phi}}_{n+1}^{(k)} = 0$ in order to compute new values of internal softening variables, see appendix C.

$$\bar{\bar{\gamma}}_{n+1}^{*(k)} = \frac{\bar{\bar{\phi}}_{n+1}^{(k),trial}\left(\bar{D}_n - \bar{G}\bar{\bar{D}}_n\right)}{K_c^* \bar{D}_n - \bar{G}} \tag{4.100}$$

If $\bar{\bar{q}}_{n+1}^{(k)} = -K_c^*\left(\bar{\bar{\xi}}_n^* + \bar{\bar{\gamma}}_{n+1}^{*(k)}\right) < \sigma_{fc}$, the softening internal variables are updated, following the incremental form of evolution equations (4.62).

$$\alpha_{n+1}^{(k)} = \left(\alpha_n^{\max} + \bar{\bar{\gamma}}_{n+1}^{*(k)}\right) sign\left(t_{n+1}^{(k),trial}\right), \;\; \bar{\bar{\xi}}_{n+1}^{*(k)} = \bar{\bar{\xi}}_n^* + \bar{\bar{\gamma}}_{n+1}^{*(k)}, \;\; \bar{\bar{D}}_{n+1}^{(k)} = \frac{\alpha_{n+1}^{(k)}}{t_{n+1}^{(k)}} = \frac{\alpha_n^{\max} + \bar{\bar{\gamma}}_{n+1}^{*(k)}}{\sigma_{fc} + K_c^* \bar{\bar{\xi}}_{n+1}^{*(k)}} \tag{4.101}$$

Here, $\alpha_n^{\max} = \bar{\bar{D}}_n t_n^{\max} = \bar{\bar{D}}_n\left(\sigma_{fc} + K_c^* \bar{\bar{\xi}}_n^*\right)$ is the maximal elastic value of α for the given carrying capacity $t_n^{\max}$ from the last softening step. Traction at the discontinuity and stress in the layer are computed as follows:

$$t_{n+1}^{(k)} = \left(\sigma_{fc} - \bar{\bar{q}}_{n+1}^{(k)}\right) sign\left(t_{n+1}^{(k),trial}\right), \quad \sigma_{n+1}^{(k)} = \bar{D}_n^{-1}\,\bar{\varepsilon}\left(\mathbf{d}_{n+1}^{(k-1)}, \alpha_{n+1}^{(k)}\right) \tag{4.102}$$

If $-K_c^*\left(\bar{\bar{\xi}}_n^* + \bar{\bar{\gamma}}_{n+1}^{*(k)}\right) > \sigma_{fc} = \bar{\bar{q}}_{n+1}^{(k)}$, material has lost all carrying capacity and traction at the discontinuity becomes zero.

$$t_{n+1}^{(k)} = \sigma_{n+1}^{(k)} = \bar{D}_n^{-1}\left(\breve{\mathbf{B}}\mathbf{d}_{n+1}^{(k-1)} + \bar{G}\,\alpha_{n+1}^{(k)}\right) = 0 \tag{4.103}$$

From above equation we can compute the displacement jump and the compliance at the discontinuity.

$$\alpha_{n+1}^{(k)} = -\frac{\breve{\mathbf{B}}\mathbf{d}_{n+1}^{(k-1)}}{\bar{G}}, \quad \bar{\bar{D}}_{n+1}^{(k)} = \frac{\alpha_{n+1}^{(k)}}{t_{n+1}^{(k)}} = \infty \tag{4.104}$$

The tangent modulus is computed as the derivative of traction at the discontinuity over the displacement jump. If $\bar{\bar{\gamma}}_{n+1}^{*(k)} = 0$, their relation is described by equation (4.97). If $\bar{\bar{\gamma}}_{n+1}^{*(k)} > 0$ and $\bar{\bar{q}}_{n+1}^{(k)} = -K_c^*\left(\bar{\bar{\xi}}_n^* + \bar{\bar{\gamma}}_{n+1}^{*(k)}\right) < \sigma_{fc}$, traction takes the value from (4.102). The first of equations (4.101) is used to express the traction as a function of displacement jump. If $\bar{\bar{\gamma}}_{n+1}^{*(k)} > 0$ and $\bar{\bar{q}}_{n+1}^{(k)} = \sigma_{fc}$, traction is constantly zero.

$$\left.\frac{\partial t}{\partial \alpha}\right|_{n+1}^{(k)} = \begin{cases} \bar{\bar{D}}_n^{-1}; & \bar{\bar{\gamma}}_{n+1}^{*(k)} = 0 \\ K_c^* = \sigma_{fc} K_c; & \bar{\bar{\gamma}}_{n+1}^{*(k)} > 0,\ \bar{\bar{q}}_{n+1}^{(k)} < \sigma_{fc} \\ 0; & \bar{\bar{\gamma}}_{n+1}^{*(k)} > 0,\ \bar{\bar{q}}_{n+1}^{(k)} = \sigma_{fc} \end{cases} \tag{4.105}$$

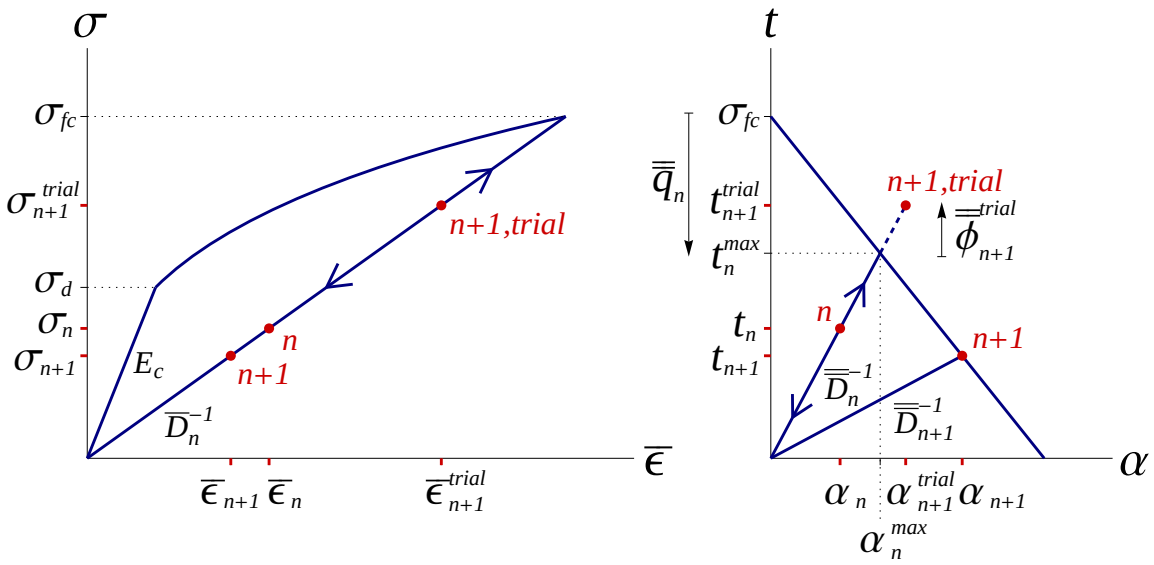

Figure 4.15: Stress in the bulk (left) and traction at the discontinuity (right) of a concrete layer: value from the previous step (n), and trial and final values from the current step $(n+1)$.
Slika 4.15: Napetost v sloju (levo) in v nezveznosti sloja betona (desno): vrednost iz prejšnjega koraka (n) ter testna in končna vrednost iz trenutnega koraka $(n+1)$.

The discontinuity flag is set to $crack_{n+1}^{(e),i} = true$.

4.3.1.4 Bulk of reinforcement layer

The computational procedure for the hardening phase of the reinforcement layer is described next. There is no discontinuity in the layer and the displacement jump is zero. First, we assume elastic behavior, meaning that hardening internal variables keep the values from the previous step. Stress is computed in accordance with equation (4.65), where $\alpha_{n+1}^{(k)} = 0$.

$$\bar{\varepsilon}_{p,n+1}^{(k),trial} = \bar{\varepsilon}_{p,n},\ \bar{\xi}_{n+1}^{(k),trial} = \bar{\xi}_n, \quad \sigma_{n+1}^{(k),trial} = E_s\left(\bar{\varepsilon}\left(\mathbf{d}_{n+1}^{(k-1)}, \alpha_{n+1}^{(k)}\right) - \bar{\varepsilon}_{p,n+1}^{(k),trial}\right) \tag{4.106}$$

Trial yield function $\bar{\phi}_{n+1}^{(k),trial}$ is computed, as defined in (4.66) and (4.67).

$$\bar{\phi}_{n+1}^{(k),trial} = \left|\sigma_{n+1}^{(k),trial}\right| - \left(\sigma_y - \bar{q}_{n+1}^{(k),trial}\right), \quad \bar{q}_{n+1}^{(k),trial} = -H_s\bar{\xi}_{n+1}^{(k),trial} = -H_s\bar{\xi}_n \tag{4.107}$$

The trial solution is accepted if the trial yield function is negative or zero.

$$\bar{\phi}_{n+1}^{(k),trial} \leq 0 \quad \Rightarrow \quad \bar{\varepsilon}_{p,n+1}^{(k)} = \bar{\varepsilon}_{p,n+1}^{(k),trial}, \quad \bar{\xi}_{n+1}^{(k)} = \bar{\xi}_{n+1}^{(k),trial}, \quad \sigma_{n+1}^{(k)} = \sigma_{n+1}^{(k),trial} \tag{4.108}$$

If the trial yield function is positive, the internal variables must be corrected, according to incremental form of evolution equations (4.68), where $\bar{\gamma}_{n+1}^{(k)} = \dot{\bar{\gamma}}_{n+1}^{(k)}\left(\tau_{n+1} - \tau_n\right) > 0$. It is shown in appendix A that $sign\left(\sigma_{n+1}^{(k)}\right) =$

$sign\left(\sigma_{n+1}^{(k),trial}\right)$.

$$\bar{\phi}_{n+1}^{(k),trial} > 0 \quad \Rightarrow \quad \bar{\varepsilon}_{p,n+1}^{(k)} = \bar{\varepsilon}_{p,n} + \bar{\gamma}_{n+1}^{(k)} sign\left(\sigma_{n+1}^{(k),trial}\right), \quad \bar{\xi}_{n+1}^{(k)} = \bar{\xi}_n + \bar{\gamma}_{n+1}^{(k)} \tag{4.109}$$

By exploiting equations (4.109), the stress $\sigma_{n+1}^{(k)}$ and the stress-like hardening variable $\bar{q}_{n+1}^{(k)}$ can be expressed with their trial values and the damage multiplier $\bar{\gamma}_{n+1}^{(k)}$.

$$\begin{aligned}
\sigma_{n+1}^{(k)} &= E_s\left(\bar{\varepsilon}\left(\mathbf{d}_{n+1}^{(k-1)}, \alpha_{n+1}^{(k)}\right) - \bar{\varepsilon}_{p,n+1}^{(k)}\right) = \\
&= E_s\left(\bar{\varepsilon}\left(\mathbf{d}_{n+1}^{(k-1)}, \alpha_{n+1}^{(k)}\right) - \bar{\varepsilon}_{p,n}\right) - E_s\bar{\gamma}_{n+1}^{(k)} sign\left(\sigma_{n+1}^{(k),trial}\right) = \\
&= \sigma_{n+1}^{(k),trial} - E_s\bar{\gamma}_{n+1}^{(k)} sign\left(\sigma_{n+1}^{(k),trial}\right)
\end{aligned} \tag{4.110}$$

$$\bar{q}_{n+1}^{(k)} = -H_s\bar{\xi}_{n+1}^{(k)} = -H_s\left(\bar{\xi}_n + \bar{\gamma}_{n+1}^{(k)}\right) = \bar{q}_{n+1}^{(k),trial} - H_s\bar{\gamma}_{n+1}^{(k)} \tag{4.111}$$

Yield function $\bar{\phi}_{n+1}^{(k)}$ is expressed as a function of plastic multiplier $\bar{\gamma}_{n+1}^{(k)}$ by employing equations (4.110) and (4.111). Value of the plastic multiplier is computed from requirement $\bar{\phi}_{n+1}^{(k)} = 0$.

$$\begin{aligned}
\bar{\phi}_{n+1}^{(k)} &= \left|\sigma_{n+1}^{(k)}\right| - \left(\sigma_y - \bar{q}_{n+1}^{(k)}\right) = \left|\sigma_{n+1}^{(k),trial}\right| - E_s\bar{\gamma}_{n+1}^{(k)} - \left(\sigma_y - \bar{q}_{n+1}^{(k),trial}\right) - H_s\bar{\gamma}_{n+1}^{(k)} = \\
&= \bar{\phi}_{n+1}^{(k),trial} - \left(E_s + H_s\right)\bar{\gamma}_{n+1}^{(k)} \\
\bar{\phi}_{n+1}^{(k)} &= 0 \quad \Rightarrow \quad \bar{\gamma}_{n+1}^{(k)} = \frac{\bar{\phi}_{n+1}^{(k),trial}}{E_s + H_s}
\end{aligned} \tag{4.112}$$

Consistent tangent modulus is computed as the derivative of stress over strain. Stress takes the trial value from equation (4.106) if plastic multiplier $\bar{\gamma}_{n+1}^{(k)}$ is zero, and the value from (4.110) if $\bar{\gamma}_{n+1}^{(k)}$ is positive. In the second case, equations (4.112), (4.107) and (4.106) are used to express the stress as a function of strain.

$$\left.\frac{\partial\sigma}{\partial\bar{\varepsilon}}\right|_{n+1}^{(k)} = \begin{cases} E_s; & \bar{\gamma}_{n+1}^{(k)} = 0 \\ \dfrac{E_s H_s}{E_s + H_s}; & \bar{\gamma}_{n+1}^{(k)} > 0 \end{cases} \tag{4.113}$$

The hardening internal variables, stress in the layer and the tangent modulus have been calculated under assumption that the ultimate stress is not exceeded. This still requires verification. If the assumption is confirmed, the above results are accepted. Otherwise, they are discarded and recomputed with the presence of the discontinuity, see Fig. 4.14.

Potential value of traction at the discontinuity $t_{n+1}^{(k),pot}$ is computed from equation (4.40). Then the failure function $\bar{\bar{\phi}}_{n+1}^{(k),pot}$ is evaluated with the stress-like softening variable equal to zero, as there has been no reduction of carrying capacity in previous steps.

$$t_{n+1}^{(k),pot} = -\int_L \bar{G}\sigma_{n+1}^{(k)} dx, \quad \bar{\bar{\phi}}_{n+1}^{(k),pot} = \left|t_{n+1}^{(k),pot}\right| - \left(\sigma_{fs} - \bar{\bar{q}}_{n+1}^{(k),pot}\right), \quad \bar{\bar{q}}_{n+1}^{(k),pot} = 0 \tag{4.114}$$

We set the value of the discontinuity flag to $true$ if the failure function is positive, and to $false$ otherwise. The value is not final, however, until the converged state is reached. It can change in following iterations.

$$\begin{aligned} \bar{\bar{\phi}}_{n+1}^{(k),pot} \leq 0 \quad &\Rightarrow \quad crack_{n+1}^{(e),i} = false \\ \bar{\bar{\phi}}_{n+1}^{(k),pot} > 0 \quad &\Rightarrow \quad crack_{n+1}^{(e),i} = true \end{aligned} \tag{4.115}$$

If the carrying capacity is exceeded, the above computed values of internal hardening variables, stress in the layer and traction at the discontinuity are discarded and computed again, as explained in the following section.

4.3.1.5 Discontinuity in reinforcement layer

This section describes the computational procedure for the softening phase of the reinforcement layer. It is applied if the current value of the discontinuity flag $crack_{n+1}^{(e),i} = true$, which happens if the discontinuity already existed in the previous step, or if the carrying capacity of the layer was exceeded in this iteration, see equation (4.115) and Fig. 4.14. In any case, the hardening internal variables take the values from the previous step, which are the last converged results. The error of such choice is negligible for small pseudo-time step.

$$\bar{\varepsilon}_{p,n+1}^{(k)} = \bar{\varepsilon}_{p,n}, \quad \bar{\xi}_{n+1}^{(k)} = \bar{\xi}_n \tag{4.116}$$

We start by assuming a trial solution, keeping the softening internal variables at the values from the previous step. Stress in the layer and traction at the discontinuity are computed according to equations (4.65) and (4.40), respectively.

$$\begin{aligned} &\alpha_{n+1}^{(k),trial} = \alpha_n, \quad \bar{\bar{\xi}}_{n+1}^{(k),trial} = \bar{\bar{\xi}}_n \\ &\sigma_{n+1}^{(k),trial} = E_s \left(\bar{\varepsilon} \left(\mathbf{d}_{n+1}^{(k-1)}, \alpha_{n+1}^{(k),trial} \right) - \bar{\varepsilon}_{p,n} \right), \quad t_{n+1}^{(k),trial} = \sigma_{n+1}^{(k),trial} \end{aligned} \tag{4.117}$$

The trial value of failure function $\bar{\bar{\phi}}_{n+1}^{(k),trial}$ is calculated, respecting equations (4.75) and (4.76).

$$\bar{\bar{\phi}}_{n+1}^{(k),trial} = \left| t_{n+1}^{(k),trial} \right| - \left(\sigma_{fs} - \bar{\bar{q}}_{n+1}^{(k),trial} \right), \quad \bar{\bar{q}}_{n+1}^{(k),trial} = \min \left\{ -K_s \bar{\bar{\xi}}_{n+1}^{(k),trial}, \sigma_{fs} \right\} = \bar{\bar{q}}_n \tag{4.118}$$

If $\bar{\bar{\phi}}_{n+1}^{(k),trial} \leq 0$, the trial solution is accepted.

$$\alpha_{n+1}^{(k)} = \alpha_{n+1}^{(k),trial}, \quad \bar{\bar{\xi}}_{n+1}^{(k)} = \bar{\bar{\xi}}_{n+1}^{(k),trial}, \quad \sigma_{n+1}^{(k)} = \sigma_{n+1}^{(k),trial}, \quad t_{n+1}^{(k)} = t_{n+1}^{(k),trial} \tag{4.119}$$

If $\bar{\bar{\phi}}_{n+1}^{(k),trial} > 0$, the assumed solution is not admissible. The softening internal variables are updated according to the incremental form of evolution equations (4.77), where $\bar{\bar{\gamma}}_{n+1}^{(k)} = \dot{\bar{\bar{\gamma}}}_{n+1}^{(k)} (\tau_{n+1} - \tau_n) > 0$. It is shown in appendix A that $sign \left(t_{n+1}^{(k)} \right) = sign \left(t_{n+1}^{(k),trial} \right)$.

$$\alpha_{n+1}^{(k)} = \alpha_n + \bar{\bar{\gamma}}_{n+1}^{(k)} sign \left(t_{n+1}^{(k),trial} \right), \quad \bar{\bar{\xi}}_{n+1}^{(k)} = \bar{\bar{\xi}}_n + \bar{\bar{\gamma}}_{n+1}^{(k)} \tag{4.120}$$

By using equations (4.120), the traction at the discontinuity $t_{n+1}^{(k)}$ and the stress-like softening variable $\bar{\bar{q}}_{n+1}^{(k)}$ are expressed with their trial values and the softening multiplier $\bar{\bar{\gamma}}_{n+1}^{(k)}$.

$$\begin{aligned} t_{n+1}^{(k)} &= \sigma_{n+1}^{(k)} = E_s \left(\check{\mathbf{B}}\mathbf{d}_{n+1}^{(k-1)} + \bar{G}\alpha_{n+1}^{(k)} - \bar{\varepsilon}_{p,n} \right) = \\ &= E_s \left(\check{\mathbf{B}}\mathbf{d}_{n+1}^{(k-1)} + \bar{G}\alpha_n - \bar{\varepsilon}_{p,n} \right) + E_s \bar{G} \bar{\bar{\gamma}}_{n+1}^{(k)} sign\left(t_{n+1}^{(k),trial} \right) = \\ &= t_{n+1}^{(k),trial} + E_s \bar{G} \bar{\bar{\gamma}}_{n+1}^{(k)} sign\left(t_{n+1}^{(k),trial} \right) \end{aligned} \tag{4.121}$$

$$\bar{\bar{q}}_{n+1}^{(k)} = \begin{cases} \bar{\bar{q}}_{n+1}^{A} = \bar{\bar{q}}_{n+1}^{(k),trial} - K_s \bar{\bar{\gamma}}_{n+1}^{(k)}; & -K_s \left(\bar{\bar{\xi}}_n + \bar{\bar{\gamma}}_{n+1}^{A} \right) < \sigma_{fs} \\ \bar{\bar{q}}_{n+1}^{B} = \sigma_{fs}; & -K_s \left(\bar{\bar{\xi}}_n + \bar{\bar{\gamma}}_{n+1}^{A} \right) > \sigma_{fs} \end{cases} \tag{4.122}$$

Obtained expressions are inserted in equation $\bar{\bar{\phi}}_{n+1}^{(k)} = 0$, coming from loading/unloading conditions (4.78).

$$\bar{\bar{\phi}}_{n+1}^{(k)} = \left| t_{n+1}^{(k)} \right| - \left(\sigma_{fs} - \bar{\bar{q}}_{n+1}^{(k)} \right) = 0 \quad \Leftrightarrow \quad t_{n+1}^{(k)} = \left(\sigma_{fs} - \bar{\bar{q}}_{n+1}^{(k)} \right) sign\left(t_{n+1}^{(k),trial} \right) \tag{4.123}$$

After a short derivation we get two expressions for $\bar{\bar{\gamma}}_{n+1}^{(k)}$, depending on the expression, used for $\bar{\bar{q}}_{n+1}^{(k)}$.

$$\bar{\bar{\gamma}}_{n+1}^{(k)} = \begin{cases} \bar{\bar{\gamma}}_{n+1}^{A} = \dfrac{\bar{\bar{\phi}}_{n+1}^{(k),trial}}{-\bar{G}E_s + K_s}; & -K_s \left(\bar{\bar{\xi}}_n + \bar{\bar{\gamma}}_{n+1}^{A} \right) < \sigma_{fs} \\ \bar{\bar{\gamma}}_{n+1}^{B} = \dfrac{\left| t_{n+1}^{(k),trial} \right|}{-\bar{G}E_s}; & -K_s \left(\bar{\bar{\xi}}_n + \bar{\bar{\gamma}}_{n+1}^{A} \right) \geq \sigma_{fs} \end{cases} \tag{4.124}$$

The tangent modulus is computed as the derivative of traction at the discontinuity over the displacement jump. If $\bar{\bar{\gamma}}_{n+1}^{(k)} > 0$, traction takes the value from (4.123). Equations (4.122) and (4.120) are used to express the traction as a function of displacement jump. If $\bar{\bar{\gamma}}_{n+1}^{(k)} = 0$, the displacement jump remains constant, while the traction changes to satisfy the local equilibrium with stress in the layer. The tangent modulus cannot be determined, but it is not required in further computation.

$$\left. \frac{\partial t}{\partial \alpha} \right|_{n+1}^{(k)} = \begin{cases} \text{not defined}; & \bar{\bar{\gamma}}_{n+1}^{(k)} = 0 \\ K_s; & \bar{\bar{\gamma}}_{n+1}^{(k)} > 0,\ \bar{\bar{q}}_{n+1}^{(k)} < \sigma_{fs} \\ 0; & \bar{\bar{\gamma}}_{n+1}^{(k)} > 0,\ \bar{\bar{q}}_{n+1}^{(k)} = \sigma_{fs} \end{cases} \tag{4.125}$$

The discontinuity flag is set to $crack_{n+1}^{(e),i} = true$.

4.3.2 Computation of nodal degrees of freedom

In this section we will describe the computations of phase (B) of k-th iteration, mentioned in the introduction of section 4.3. In this phase, a linearized form of equilibrium equations (4.82) is solved to provide the k-th update of the nodal displacements/rotations at pseudo-time point τ_{n+1}. The computation is performed with known values of internal variables for each layer of each finite element - $\bar{D}_{n+1}^{(e),i,(k)}$, $\bar{\xi}_{n+1}^{(e),i,(k)}$, $\bar{\bar{D}}_{n+1}^{(e),i,(k)}$, $\bar{\bar{\xi}}_{n+1}^{(e),i,(k)}$ for a concrete

layer, and $\bar{\varepsilon}_{p,n+1}^{(e),i,(k)}$, $\bar{\xi}_{n+1}^{(e),i,(k)}$, $\alpha_{n+1}^{(e),i,(k)}$, $\bar{\bar{\xi}}_{n+1}^{(e),i,(k)}$ for a layer of reinforcement - freshly updated in preceding phase (A) of the same iteration. Since the nodal degrees of freedom are generally common to several finite elements, the equations of phase (B) must be handled on structural (global) level. Hence, they are also referred to as global equations.

The first of equations (4.82) would be sufficient for calculating the new values of generalized displacements $\mathbf{d}_{n+1}^{(e),(k)}$, if all displacement jumps $\alpha_{n+1}^{(e),i,(k)}$ were fixed at the values, computed in phase (A). To improve convergence, however, it is useful to update the displacement jumps as well. For that purpose, the second of equations (4.82) are engaged. Actually, they have once already been satisfied by using expression (4.40) for the traction at the discontinuity, but that equality held for the displacements from the previous iteration $\mathbf{d}_{n+1}^{(e),(k-1)}$. Updating the displacements would disrupt the equilibrium between the traction at the discontinuity and the stress in the layer, unless the displacement jumps are updated as well. Solving the whole system of equations (4.82) therefore promises a more accurate solution.

4.3.2.1 Linearization of equilibrium equations

The first of equations (4.82) ensures the equilibrium of the structure, i.e. of its each and every node. It is linearized around the current values of nodal degrees of freedom of the structure $\mathbf{d}_{n+1}^{\text{str},(k-1)}$.

$$\underbrace{\frac{\partial \mathbf{f}_{n+1}^{\text{int,str},(k)}}{\partial \mathbf{d}_{n+1}^{\text{str},(k-1)}}}_{\mathbf{K}_{n+1}^{\text{str},(k)}} \Delta\mathbf{d}_{n+1}^{\text{str},(k)} = \mathbf{f}_{n+1}^{\text{ext,str}} - \mathbf{f}_{n+1}^{\text{int,str},(k)}, \qquad \frac{\partial \mathbf{f}_{n+1}^{\text{ext,str}}}{\partial \mathbf{d}_{n+1}^{\text{str},(k-1)}} = \mathbf{0} \tag{4.126}$$

The derivative on the left side of the equation is designated with $\mathbf{K}_{n+1}^{\text{str},(k)}$ and named the tangent stiffness matrix of the structure. $\Delta\mathbf{d}_{n+1}^{\text{str},(k)}$ is the sought update of the nodal displacements in this iteration. The vector of external forces $\mathbf{f}_{n+1}^{\text{ext,str}}$ represents the loading, which is defined in advance for each pseudo-time point τ_{n+1} and is independent of the nodal displacements. The vector of internal forces $\mathbf{f}_{n+1}^{\text{int,str},(k)}$ is computed from contributions of individual finite elements, according to equation (4.25). Matrices $\mathbf{P}^{(e)}$ and $\mathbf{R}^{(e)}$ are constant.

$$\begin{aligned}
\mathbf{f}_{n+1}^{\text{int,str},(k)} &= \sum_{e=1}^{n_{FE}} {\mathbf{P}^{(e)}}^T {\mathbf{R}^{(e)}}^{-1} \mathbf{f}_{n+1}^{\text{int},(e),(k)} \\
\mathbf{K}_{n+1}^{\text{str},(k)} &= \frac{\partial \mathbf{f}_{n+1}^{\text{int,str},(k)}}{\partial \mathbf{d}_{n+1}^{\text{str},(k-1)}} = \sum_{e=1}^{n_{FE}} {\mathbf{P}^{(e)}}^T {\mathbf{R}^{(e)}}^{-1} \frac{\partial \mathbf{f}_{n+1}^{\text{int},(e),(k)}}{\partial \mathbf{d}_{n+1}^{\text{str},(k-1)}}
\end{aligned} \tag{4.127}$$

Let us recall the relation (4.18) between the vector of nodal displacements of a finite element $\mathbf{d}_{n+1}^{(e),(k-1)}$ and the vector of nodal displacements of the structure $\mathbf{d}_{n+1}^{\text{str},(k-1)}$. The derivative of one over the other will prove useful.

$$\mathbf{d}_{n+1}^{(e),(k-1)} = \mathbf{R}^{(e)}\mathbf{P}^{(e)}\mathbf{d}_{n+1}^{\text{str},(k-1)} \quad \Rightarrow \quad \frac{\partial \mathbf{d}_{n+1}^{(e),(k-1)}}{\partial \mathbf{d}_{n+1}^{\text{str},(k-1)}} = \mathbf{R}^{(e)}\mathbf{P}^{(e)} \tag{4.128}$$

Internal forces $\mathbf{f}_{n+1}^{\text{int},(e),(k)}$ of finite element (e) are defined in equation (4.34) as a sum of contributions of n_L layers. Contributions $\mathbf{f}_{n+1}^{\text{int},(e),i,(k)}$ of the $n_{CL}^{(e)}$ cracked layers are functions of nodal displacements $\mathbf{d}_{n+1}^{(e),(k-1)}$ and displacement jumps $\alpha_{n+1}^{(e),i,(k)}$, while the contributions of the remaining (non-cracked) layers depend solely on the

nodal displacements. For the sake of clarity it is assumed that the cracked layers are numbered with consecutive numbers from 1 to $n_{CL}^{(e)}$.

$$\mathbf{f}_{n+1}^{\text{int},(e),(k)} = \sum_{i=1}^{n_L} \mathbf{f}_{n+1}^{\text{int},(e),i,(k)} = \sum_{i=1}^{n_{CL}^{(e)}} \mathbf{f}_{n+1}^{\text{int},(e),i,(k)} \left(\mathbf{d}_{n+1}^{(e),(k-1)}, \alpha_{n+1}^{(e),i,(k)} \right) + \sum_{i=n_{CL}^{(e)}+1}^{n_L} \mathbf{f}_{n+1}^{\text{int},(e),i,(k)} \left(\mathbf{d}_{n+1}^{(e),(k-1)} \right) \tag{4.129}$$

The derivative of $\mathbf{f}_{n+1}^{\text{int},(e),(k)}$ over $\mathbf{d}_{n+1}^{\text{str},(k-1)}$, which appears in expression (4.127), is developed as follows:

$$\frac{\partial \mathbf{f}_{n+1}^{\text{int},(e),(k)}}{\partial \mathbf{d}_{n+1}^{\text{str},(k-1)}} = \sum_{i=1}^{n_{CL}^{(e)}} \left(\underbrace{\frac{\partial \mathbf{f}_{n+1}^{\text{int},(e),i,(k)}}{\partial \mathbf{d}_{n+1}^{(e),(k-1)}}}_{\mathbf{K}_{n+1}^{fd,(e),i,(k)}} + \underbrace{\frac{\partial \mathbf{f}_{n+1}^{\text{int},(e),i,(k)}}{\partial \alpha_{n+1}^{(e),i,(k)}}}_{\mathbf{K}_{n+1}^{f\alpha,(e),i,(k)}} \frac{\partial \alpha_{n+1}^{(e),i,(k)}}{\partial \mathbf{d}_{n+1}^{(e),(k-1)}} \right) \overbrace{\frac{\partial \mathbf{d}_{n+1}^{(e),(k-1)}}{\partial \mathbf{d}_{n+1}^{\text{str},(k-1)}}}^{\mathbf{R}^{(e)}\mathbf{P}^{(e)}} + \sum_{i=n_{CL}^{(e)}+1}^{n_L} \overbrace{\frac{\partial \mathbf{f}_{n+1}^{\text{int},(e),i,(k)}}{\partial \mathbf{d}_{n+1}^{(e),(k-1)}}}^{\mathbf{K}_{n+1}^{fd,(e),i,(k)}} \overbrace{\frac{\partial \mathbf{d}_{n+1}^{(e),(k-1)}}{\partial \mathbf{d}_{n+1}^{\text{str},(k-1)}}}^{\mathbf{R}^{(e)}\mathbf{P}^{(e)}} \tag{4.130}$$

The derivatives of $\mathbf{f}_{n+1}^{\text{int},(e),i,(k)}$, marked with $\mathbf{K}_{n+1}^{fd,(e),i,(k)}$ and $\mathbf{K}_{n+1}^{f\alpha,(e),i,(k)}$, can be computed and the last term of both sums has been defined in (4.128). The only unknown term $\partial \alpha_{n+1}^{(e),i,(k)} / \partial \mathbf{d}_{n+1}^{(e),(k-1)}$ is determined by the second of equilibrium equations (4.82), which is linearized and solved locally, i.e. independently for each finite element and layer. This can be done because $h_{n+1}^{(e),i,(k)}$ depends on the nodal displacements of a single finite element and on the displacement jump of a single layer.

$$\begin{aligned} &\underbrace{\frac{\partial h_{n+1}^{(e),i,(k)}}{\partial \mathbf{d}_{n+1}^{(e),(k-1)}}}_{\mathbf{K}_{n+1}^{hd,(e),i,(k)}} \Delta \mathbf{d}_{n+1}^{(e),(k)} + \underbrace{\frac{\partial h_{n+1}^{(e),i,(k)}}{\partial \alpha_{n+1}^{(e),i,(k)}}}_{K_{n+1}^{h\alpha,(e),i,(k)}} \Delta \alpha_{n+1}^{(e),i,(k)} = -h_{n+1}^{(e),i,(k)} = 0 \quad \Rightarrow \\ &\Rightarrow \quad \Delta \alpha_{n+1}^{(e),i,(k)} = \underbrace{-\left(K_{n+1}^{h\alpha,(e),i,(k)} \right)^{-1} \mathbf{K}_{n+1}^{hd,(e),i,(k)}}_{\partial \alpha_{n+1}^{(e),i,(k)} / \partial \mathbf{d}_{n+1}^{(e),(k-1)}} \Delta \mathbf{d}_{n+1}^{(e),(k)} \end{aligned} \tag{4.131}$$

Note that each $h_{n+1}^{(e),i,(k)}$, computed by (4.39), evaluates to zero because the traction at the discontinuity $t_{n+1}^{(e),i,(k)}$ has been computed by expression (4.40). The derivatives, designated with $K_{n+1}^{hd,(e),i,(k)}$ and $K_{n+1}^{h\alpha,(e),i,(k)}$ can be easily calculated. Equation (4.131) defines the relation between the increment of nodal displacements $\Delta \mathbf{d}_{n+1}^{(e),(k)}$ and the increment of displacement jump $\Delta \alpha_{n+1}^{(e),i,(k)}$ in the i-th layer of the finite element. Since we are dealing with linearized equations, the derivative $\partial \alpha_{n+1}^{(e),i,(k)} / \partial \mathbf{d}_{n+1}^{(e),(k-1)}$ is equal to the ratio of the increments.

$$\frac{\partial \alpha_{n+1}^{(e),i,(k)}}{\partial \mathbf{d}_{n+1}^{(e),(k-1)}} = -\left(K_{n+1}^{h\alpha,(e),i,(k)} \right)^{-1} \mathbf{K}_{n+1}^{hd,(e),i,(k)} \tag{4.132}$$

We can rewrite expression (4.130), now being able to compute all its components.

$$\frac{\partial \mathbf{f}^{\text{int},(e),(k)}_{n+1}}{\partial \mathbf{d}^{\text{str},(k-1)}_{n+1}} = \sum_{i=1}^{n_{CL}^{(e)}} \underbrace{\left(\mathbf{K}^{fd,(e),i,(k)}_{n+1} - \mathbf{K}^{f\alpha,(e),i,(k)}_{n+1} \left(K^{h\alpha,(e),i,(k)}_{n+1} \right)^{-1} \mathbf{K}^{hd,(e),i,(k)}_{n+1} \right)}_{\hat{\mathbf{K}}^{(e),i,(k)}_{n+1}} \mathbf{R}^{(e)} \mathbf{P}^{(e)} + \\ + \sum_{i=n_{CL}^{(e)}+1}^{n_L} \mathbf{K}^{fd,(e),i,(k)}_{n+1} \mathbf{R}^{(e)} \mathbf{P}^{(e)} \tag{4.133}$$

The expression in parenthesis, marked with $\hat{\mathbf{K}}^{(e),i,(k)}_{n+1}$, is the contribution of a cracked layer to the tangent stiffness matrix of finite element $\mathbf{K}^{fd,(e),i,(k)}_{n+1}$ is the contribution of an non-cracked layer. Finally, we can assemble the tangent stiffness matrix of the structure by inserting (4.133) into (4.127).

$$\mathbf{K}^{\text{str},(k)}_{n+1} = \sum_{e=1}^{n_{FE}} \mathbf{P}^{(e)^T} \mathbf{R}^{(e)^{-1}} \underbrace{\left(\sum_{i=1}^{n_{CL}^{(e)}} \hat{\mathbf{K}}^{(e),i,(k)}_{n+1} + \sum_{i=n_{CL}^{(e)}+1}^{n_L} \mathbf{K}^{fd,(e),i,(k)}_{n+1} \right)}_{\mathbf{K}^{(e),(k)}_{n+1}} \mathbf{R}^{(e)} \mathbf{P}^{(e)} \tag{4.134}$$

Here $\mathbf{K}^{(e),(k)}_{n+1}$ is the (symmetric) tangent stiffness matrix of finite element (e).

4.3.2.2 Components of internal forces and stiffness matrix

Contribution $\mathbf{f}^{\text{int},(e),i,(k)}_{n+1}$ of i-th layer to internal forces of element (e) is computed according to equation (4.34), where stress takes the values computed in phase (A) of this iteration. In order to determine the components of the stiffness matrix, $h^{(e),i,(k)}_{n+1}$ must be written as well. It is computed in accordance with (4.39) and (4.40).

$$\mathbf{f}^{\text{int},(e),i,(k)}_{n+1} = \left(\breve{\mathbf{B}}^{i^T} \sigma^{(e),i,(k)}_{n+1} + \breve{\mathbf{B}}^{*^T} \tau^{(e),i,(k)}_{n+1} \right) A^i L, \quad h^{(e),i,(k)}_{n+1} = A^i \left(-\sigma^{(e),i,(k)}_{n+1} + t^{(e),i,(k)}_{n+1} \right) \tag{4.135}$$

To obtain layer components of the element stiffness matrix, expressions (4.135) are differentiated over nodal degrees of freedom and over displacement jumps.

$$\begin{aligned}
\mathbf{K}^{fd,(e),i,(k)}_{n+1} &= \frac{\partial \mathbf{f}^{\text{int},(e),i,(k)}_{n+1}}{\partial \mathbf{d}^{(e),(k-1)}_{n+1}} = \left(\breve{\mathbf{B}}^{i^T} \left. \frac{\partial \sigma}{\partial \bar{\varepsilon}} \right|^{(e),i,(k)}_{n+1} \underbrace{\breve{\mathbf{B}}^{i}}_{\partial \bar{\varepsilon}/\partial \mathbf{d}} + \breve{\mathbf{B}}^{*^T} \left. \frac{\partial \tau}{\partial \gamma} \right|^{(e),i,(k)}_{n+1} \underbrace{\breve{\mathbf{B}}^{*}}_{\partial \gamma/\partial \mathbf{d}} \right) A^i L \\
\mathbf{K}^{f\alpha,(e),i,(k)}_{n+1} &= \frac{\partial \mathbf{f}^{\text{int},(e),i,(k)}_{n+1}}{\partial \alpha^{(e),i,(k)}_{n+1}} = \left(\breve{\mathbf{B}}^{i^T} \left. \frac{\partial \sigma}{\partial \bar{\varepsilon}} \right|^{(e),i,(k)}_{n+1} \underbrace{\bar{G}^{i}}_{\partial \bar{\varepsilon}/\partial \alpha} \right) A^i L \\
\mathbf{K}^{hd,(e),i,(k)}_{n+1} &= \frac{\partial h^{(e),i,(k)}_{n+1}}{\partial \mathbf{d}^{(e),(k-1)}_{n+1}} = \left(- \left. \frac{\partial \sigma}{\partial \bar{\varepsilon}} \right|^{(e),i,(k)}_{n+1} \underbrace{\breve{\mathbf{B}}^{i}}_{\partial \bar{\varepsilon}/\partial \mathbf{d}} \right) A^i \\
K^{h\alpha,(e),i,(k)}_{n+1} &= \frac{\partial h^{(e),i,(k)}_{n+1}}{\partial \alpha^{(e),i,(k)}_{n+1}} = \left(- \left. \frac{\partial \sigma}{\partial \bar{\varepsilon}} \right|^{(e),i,(k)}_{n+1} \underbrace{\bar{G}^{i}}_{\partial \bar{\varepsilon}/\partial \alpha} + \left. \frac{\partial t}{\partial \alpha} \right|^{(e),i,(k)}_{n+1} \right) A^i
\end{aligned} \tag{4.136}$$

The tangent modulus $(\partial\tau/\partial\gamma\,)_{n+1}^{(e),i,(k)}$ for shear is defined by equation (4.84). The tangent moduli $(\partial\sigma/\partial\bar{\varepsilon}\,)_{n+1}^{(e),i,(k)}$ and $(\partial t/\partial\alpha\,)_{n+1}^{(e),i,(k)}$ are defined by equations (4.92) and (4.105) for concrete, and by equations (4.113) and (4.125) for reinforcement.

The only exception is the elastic step in a cracked layer of reinforcement (when $\bar{\bar{\gamma}}_{n+1}^{(k)} = 0$). The derivative $(\partial t/\partial\alpha\,)_{n+1}^{(e),i,(k)}$ is not defined in that case, neither is it required. Although $\alpha_{n+1}^{(e),i,(k)}$ appears in the expression for internal forces, it appears as a constant, and $\mathbf{f}_{n+1}^{\text{int},(e),i,(k)}$ is function of nodal displacements $\mathbf{d}_{n+1}^{\text{str},(k-1)}$ alone. The component $\mathbf{K}_{n+1}^{f\alpha,(e),i,(k)}$ from equation (4.130) is therefore zero for that layer, and the contribution of the layer to the element tangent stiffness matrix consists solely of the part $\mathbf{K}_{n+1}^{fd,(e),i,(k)}$, the same as for a non-cracked layer.

$$\alpha_{n+1}^{(e),i,(k)} = \text{const.} \;\Rightarrow\; \mathbf{f}_{n+1}^{\text{int},(e),i,(k)} = \mathbf{f}_{n+1}^{\text{int},(e),i,(k)}\left(\mathbf{d}_{n+1}^{\text{str},(k-1)}\right) \;\Rightarrow\; \begin{cases} \mathbf{K}_{n+1}^{f\alpha,(e),i,(k)} = \mathbf{0} \\ \hat{\mathbf{K}}_{n+1}^{(e),i,(k)} = \mathbf{K}_{n+1}^{fd,(e),i,(k)} \end{cases} \tag{4.137}$$

4.3.2.3 Solution of global equations

The system of global equilibrium equations (4.126) is rewritten in a clearer form.

$$\mathbf{K}_{n+1}^{\text{str},(k)}\Delta\mathbf{d}_{n+1}^{\text{str},(k)} = \Delta\mathbf{f}_{n+1}^{\text{str},(k)}, \qquad \Delta\mathbf{f}_{n+1}^{\text{str},(k)} = \mathbf{f}_{n+1}^{\text{ext,str}} - \mathbf{f}_{n+1}^{\text{int,str},(k)} \tag{4.138}$$

The external forces are an input to the analysis, internal forces are defined by equations (4.127), (4.129) and (4.135), and the tangent stiffness matrix of the structure is defined by (4.134) and (4.136). Finally, we can compute the increments and update the nodal displacements of the structure.

$$\Delta\mathbf{d}_{n+1}^{\text{str},(k)} = \left(\mathbf{K}_{n+1}^{\text{str},(k)}\right)^{-1}\Delta\mathbf{f}_{n+1}^{\text{str},(k)}, \qquad \mathbf{d}_{n+1}^{\text{str},(k)} = \mathbf{d}_{n+1}^{\text{str},(k-1)} + \Delta\mathbf{d}_{n+1}^{\text{str},(k)} \tag{4.139}$$

The updates of the displacement jumps could be computed from (4.131), but there is no benefit from that because they will be recomputed anyway in phase (A) of the next iteration.

The iterations at pseudo-time τ_{n+1} are repeated until the tolerance requirements are met.

$$\left\|\Delta\mathbf{f}_{n+1}^{\text{str},(k)}\right\| < tol, \quad \left\|\Delta\mathbf{d}_{n+1}^{\text{str},(k)}\right\| < tol \tag{4.140}$$

When the converged solution is found, we proceed to the next pseudo-time step.

4.4 Numerical examples

In this section we present a set of numerical examples to assess the ability of the derived element to simulate failure of reinforced concrete beams and frames. The element has been programmed in AceGen [68] implemented into the finite element program AceFEM [69].

4.4.1 One element tension and compression tests

We analyze a beam in Fig. 4.16, clamped at one end and subjected to prescribed axial displacement u at the other end. Corresponding reaction F is computed. With this test, we check response of concrete, steel and reinforced

beams in tension and compression. The chosen values of some material parameters may be unrealistic, but they were chosen in order to clearly present the behavior of models used for concrete and steel.

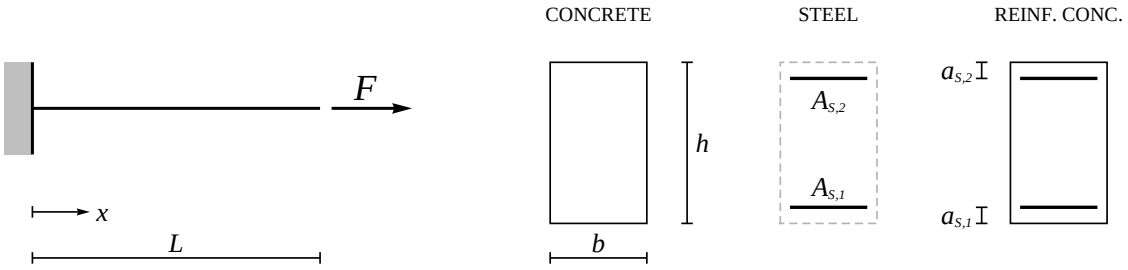

Figure 4.16: Beam in pure tension/compression: geometry.
Slika 4.16: Nosilec v čistem nategu/tlaku: geometrija.

4.4.1.1 Concrete beam

Concrete beam of rectangular cross-section is modeled with one element with two layers. The imposed axial displacement produces either tension or compression. The geometry and the material data are: beam length is $L = 2.5$m, cross-section width is $b = 0.2$m, cross-section height is $h = 0.5$m, elastic modulus is $E_c = 4 \times 10^7 \text{kNm}^{-2}$, elasticity limit in compression is $\sigma_{dc} = 40820 \text{kNm}^{-2}$, limit strength in compression is $\sigma_{fcc} = 44902 \text{kNm}^{-2}$, hardening modulus in compression is $H_{cc} = 2 \times 10^6 \text{kNm}^{-2}$, softening modulus in compression is $K^*_{cc} = -5.2 \times 10^6 \text{kNm}^{-3}$, limit strength in tension is $\sigma_{fct} = 4000 \text{kNm}^{-2}$, and softening modulus in tension is $K^*_{ct} = -8 \times 10^6 \text{kNm}^{-3}$. By setting $\sigma_{dt} > \sigma_{fct}$ we assume no damage of the bulk in tension before crack formation.

The diagrams in Fig. 4.17 show computed elasto-damage relations between the end force F and the end displacement u when the beam is either in tension or compression. The left image represents the tensile response, which is linear elastic, followed by linear softening. Unloading lines return toward the origin, which is typical for a damage model. The right image shows the response in compression. Initial elastic part is followed by damage hardening, which is not linear (although not far from it for this particular data). The softening line is linear. Unloading, both from hardening and softening, returns linearly toward the origin.

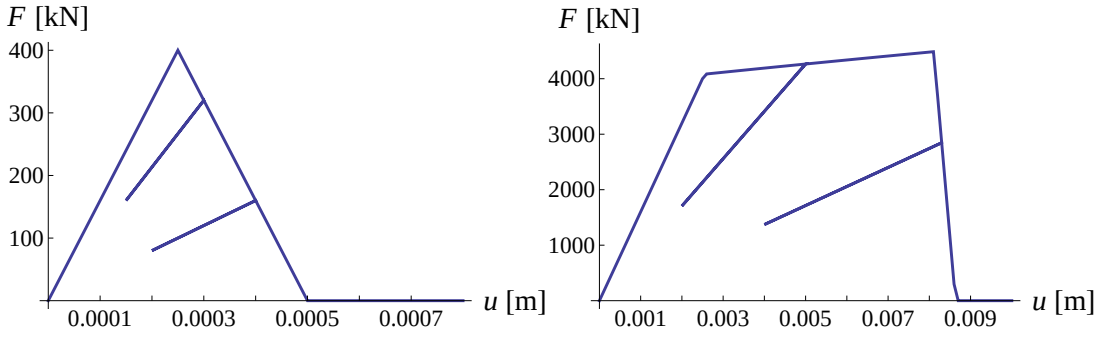

Figure 4.17: *Axial force - displacement* diagrams for concrete beam in pure tension (left) and pure compression (right).
Slika 4.17: Diagram *osna sila - pomik* za betonski nosilec v čistem nategu (levo) in čistem tlaku (desno).

Response is characterized by the following facts: (i) single strain-like internal variable $\bar{\bar{\xi}}^i_c$ controls softening both in tension and compression, (ii) current values of compliance moduli ($\bar{D}^i$ and $\bar{\bar{D}}^i$) are transferred from compression

to tension and vice versa, (iii) once softening is activated, the hardening variables $\bar{D}^i$ and $\bar{\xi}_c^i$ remain unchanged. Of course, the elasto-damage concrete material model can be carefully designed to comply with specific experimental results, however, this is beyond the scope of this work. The results in Fig. 4.18 and Fig. 4.19 illustrate that the present elasto-damage material model is able to describe well enough the common cases of alternating load sign, although it has not been designed for cyclic loading.

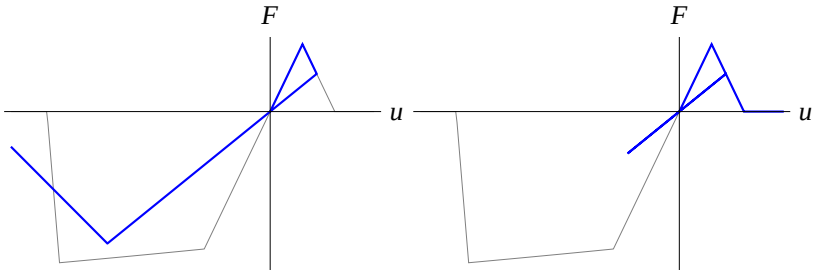

Figure 4.18: Axially loaded concrete beam: switching from softening in tension to compression (left) and back to tension (right).
Slika 4.18: Osno obremenjen betonski nosilec: prehod iz mehčanja v nategu v tlak (levo) in nazaj v nateg (desno).

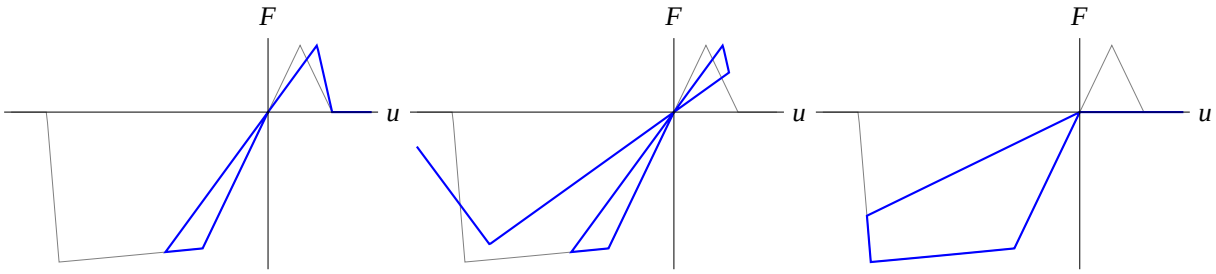

Figure 4.19: Axially loaded concrete beam: switching from hardening in compression to tension (left) and back to compression (middle). Switching from softening in compression to tension (right).
Slika 4.19: Osno obremenjen betonski nosilec: prehod iz utrjevanja v tlaku v nateg (levo) in nazaj v tlak (sredina). Prehod iz mehčanja v tlaku v nateg (desno).

Behavior of implemented model for a beam switching from tension to compression (or from compression to tension) is shown in Fig. 4.18 and Fig. 4.19. On these figures, the light-gray line represents $F-u$ curves for monotonically increasing tensile and compressive forces. The used data is the same as the above, except for $\sigma_{fct} = 2 \times 10^4 \text{kNm}^{-2}$. Fig. 4.18 (left) shows transition from softening in tension to softening in compression. This situation is very uncommon in non-cyclic loading. It may happen that a layer that was in tension softening becomes compressed (e.g. when the neutral axis of the element shifts), however, the compressive stress would normally be far away from the compressive strength. The case, shown in Fig. 4.18 (right), is far more common. Fig. 4.19 shows transition from compression to tension. For example, Fig. 4.19 (right) presents path from compression softening to tension: since σ_{fct} is much lower than σ_{fcc}, the carrying capacity in tension is lost due to $\bar{\xi}_c^i$ accumulated in compression.

4.4.1.2 Steel beam

Steel beam is modeled with one element with two layers. The following data is used: beam length is $L = 2.5\text{m}$, cross-sections of both layers are $A_{s,1} = A_{s,2} = 0.001\text{m}^2$, distances of layer axes from the beam axis are $h/2 - a_{s,1} = h/2 - a_{s,2} = 0.21\text{m}$ ($a_{s,1} = a_{s,2} = 0.04\text{m}$), elastic modulus is $E_s = 2 \times 10^8 \text{kNm}^{-2}$, elasticity limit is $\sigma_y = 4 \times 10^5 \text{kNm}^{-2}$, failure strength is $\sigma_{fs} = 5 \times 10^5 \text{kNm}^{-2}$, hardening modulus is $H_s = 10^7 \text{kNm}^{-2}$, and softening modulus is $K_s = -5 \times 10^7 \text{kNm}^{-3}$.

Diagram in Fig. 4.20 shows elasto-plastic relation between the end force F and the end displacement u in tension. The initial linear elastic response is followed by linear plastic hardening and linear plastic softening with unloading lines, parallel to the initial loading line. Response of the beam in compression is identical.

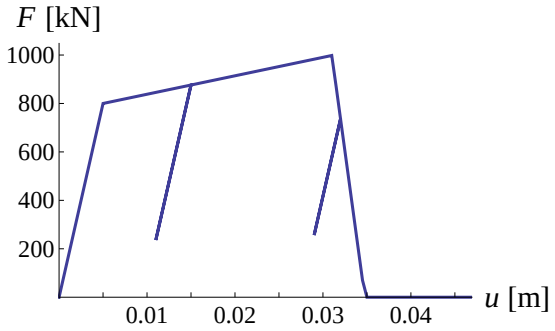

Figure 4.20: *Axial force - displacement* diagram for steel beam (layer) in pure tension.
Slika 4.20: Diagram *osna sila - pomik* za jekleni nosilec (sloj) v čistem nategu.

The diagrams in Fig. 4.21 show response of the beam when loading switches from tension to compression. The light grey lines represent the response of a monotonically loaded beam. The left image is characteristic for isotropic hardening - material yields in compression at the same (absolute) value of F, at which unloading started in tension. If loading is still increased in compression, as shown in the middle image of Fig. 4.21, softening occurs at the same force F as in monotonic loading, but at a smaller displacement u, due to accumulation of plastic deformations in both tension and compression. Change of load sign in softening, Fig. 4.21 (right), produces an equivalent response - unloading is parallel to the elastic loading, and softening in compression begins at the same (absolute) value of F, at which unloading started in tension.

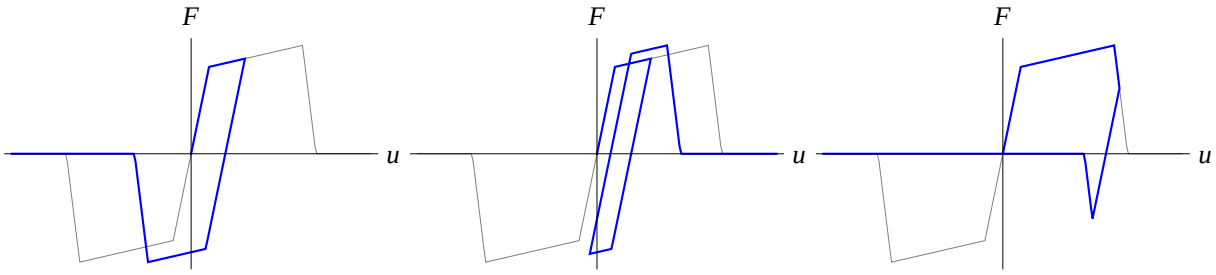

Figure 4.21: Axially loaded steel beam: switching from hardening in tension to compression (left) and back to tension (middle). Switching from softening in tension to compression (right).
Slika 4.21: Osno obremenjen jekleni nosilec: prehod iz utrjevanja v nategu v tlak (levo) in nazaj v nateg (sredina). Prehod iz mehčanja v nategu v tlak (desno).

4.4.1.3 Reinforced concrete beam

Reinforced concrete beam is composed from the two previously presented beams, see Fig. 4.16. Geometry and material properties are listed in sections 4.4.1.1 and 4.4.1.2. The beam is modeled with one finite element with ten concrete layers and two layers of reinforcement. Diagrams in Fig. 4.22 display the responses of the beam under tensile and compressive load. In tension (left image), the first peak represents the point when concrete enters the softening phase and the force F begins to drop. When the concrete breaks completely, the whole load is taken by the two reinforcement layers, which are still elastic. Force F starts rising again. Hereafter, the diagram is equal to the response of the steel beam in Fig. 4.20.

The diagram in Fig. 4.22 (right) shows the response of the beam in compression. After the initial elastic part, the stiffness of the beam drops around $F = 4500$kN due to micro-cracking of concrete, and again at approximately $F = 5000$kN due to yielding of reinforcement. The peak of the diagram marks the moment when concrete begins to soften. Force F drops suddenly, until concrete loses all carrying capacity and only the reinforcement remains to take the load. From now on, the diagram is the same as in Fig. 4.20. The unloading lines return toward the origin, until reinforcement enters hardening phase and first plastic deformations occur. The slope of the unloading lines (axial stiffness of the element) keeps decreasing until the stress in concrete drops to zero. Afterwards it remains constant and only plastic deformations increase. Like in tension, the diagram is a superposition of diagrams of concrete (Fig. 4.17) and steel (Fig. 4.20).

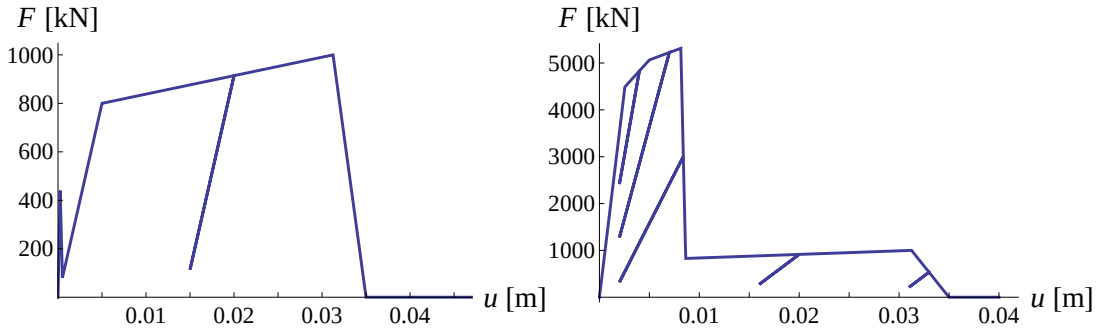

Figure 4.22: *Axial force - displacement* diagrams for reinforced concrete beam in pure tension (left) and pure compression (right).

Slika 4.22: Diagram *osna sila - pomik* za armiranobetonski nosilec v čistem nategu (levo) in čistem tlaku (desno).

4.4.2 Cantilever beam under end moment

We analyze a reinforced concrete cantilever beam with rectangular cross-section under end moment, shown in Fig. 4.23. The load is applied by imposing the rotation at the free end of the beam. The length of the beam is $L = 1$m, the width and the height of the cross-section are $b = 0.3$m and $h = 0.4$m. Bottom and top reinforcements are $A_{s,1} = A_{s,2} = 0.001256\text{m}^2$ and they are positioned at $a_1 = a_2 = 0.05$m from the edges of the concrete cross-section. Material properties of concrete are: elasticity modulus $E_c = 3.3 \times 10^7\text{kNm}^{-2}$, elasticity limit $\sigma_{dc} = 15200\text{kNm}^{-2}$, ultimate stress in compression $\sigma_{fcc} = 38000\text{kNm}^{-2}$, ultimate stress in tension $\sigma_{fct} = 1815\text{kNm}^{-2}$, hardening modulus in compression $H_{cc} = 3.32 \times 10^7\text{kNm}^{-2}$, softening modulus in compression $K^*_{cc} = -5 \times 10^6\text{kNm}^{-3}$ and softening modulus in tension $K^*_{ct} = -10^6\text{kNm}^{-3}$. Material properties of steel are: elasticity modulus $E_s = 2 \times 10^8\text{kNm}^{-2}$, yield stress $\sigma_y = 4 \times 10^5\text{kNm}^{-2}$, ultimate stress $\sigma_{fs} = 5 \times 10^5\text{kNm}^{-2}$, hardening modulus $H_s = 2.665 \times 10^6\text{kNm}^{-2}$ and softening modulus $K_s = -5 \times 10^7\text{kNm}^{-3}$.

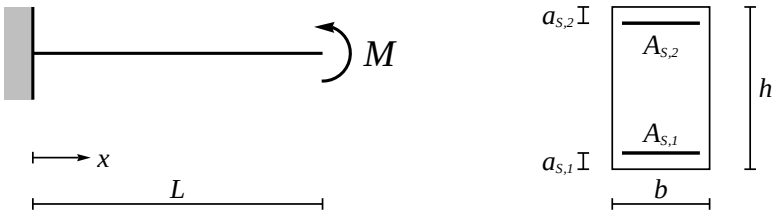

Figure 4.23: Cantilever beam under end moment: geometry.
Slika 4.23: Konzola, obremenjena z momentom: geometrija.

4.4.2.1 Mesh of equal finite elements

The beam is modeled with a mesh of identical finite elements, each consisting of 10 concrete layers and 2 layers of reinforcement. Fig. 4.24 (left) displays the relation of moment M versus rotation θ at the end of the beam for different meshes. The diagram can be divided into three parts. In part 1, most of the beam is still elastic, except for some concrete layers that crack in tension, slightly decreasing the stiffness of the element. Part 2 is characterized by yielding of tensile reinforcement, which causes a plateau in the response curve. More concrete layers break in tension and micro-cracking occurs in concrete in compression. The resistance of the beam increases until the tensile reinforcement begins to soften, which marks the beginning of part 3 of the response curve. Hereafter, the moment drops toward zero. Softening of concrete in compression does not occur at all.

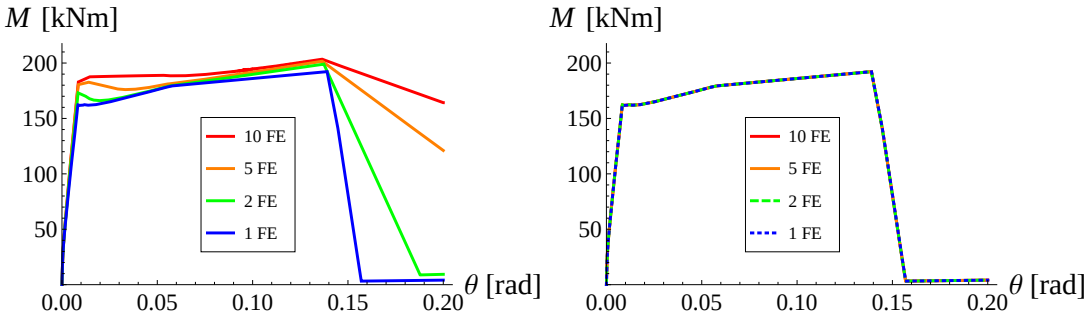

Figure 4.24: *Moment - rotation* diagrams for cantilever beam under end moment: original softening moduli (left), softening moduli modified according to length of FE (right).
Slika 4.24: Diagram *moment - zasuk* za konzolo, obteženo z momentom: originalni moduli mehčanja (levo), moduli mehčanja prirejeni glede na dolžino KE (desno).

Fig. 4.24 (left) shows that part 3 of the diagram depends on the mesh. The slope of the softening line decreases with increasing number of finite elements. This is caused by simultaneous appearance of multiple smaller discontinuities in finer meshes, as opposed to one big discontinuity in a mesh with a single FE. The traction at the discontinuity decreases with the increase of its size. It is therefore understandable that, at the same value of imposed end rotation θ, a coarser mesh produces a lower moment M. The mesh dependency is also present in the first two parts of the diagram, where the concrete layers crack in tension. In part 1, the slower decrease of traction at the discontinuity in finer meshes manifests in a higher yield moment. In part 2, the effect is more evident because the force in plastified tensile reinforcement changes very slowly, and the different tractions in tensile concrete layers have a greater influence.

If the softening moduli of steel and concrete are modified according to the length of FE (i.e. multiplied with the number of FE in the mesh), the results are the same for all meshes, Fig. 4.24 (right). However, this is not a proper

solution of the problem because it interferes with the constitutive law at the discontinuity, which is a material property and should not be affected by the choice of a mesh.

4.4.2.2 Weaker reinforcement in one of the finite elements

The mesh dependency problem, described above, resembles the situation, encountered with the stress resultant Euler-Bernoulli element with embedded discontinuity in rotation in chapter 2. There, the problem is solved by weakening one element of the mesh. When the weak element starts to soften, the other elements have to unload to satisfy the equilibrium and can never reach their failure moments. We will apply the same principle to the multi-layer element.

Since the softening of the beam in part 3 of the $M-\theta$ diagram is caused by failure of tensile reinforcement, it is enough to create a weakness in reinforcement. Ultimate stress σ_{fs} is slightly increased in all but one finite element of the mesh to preserve the original value in the weak element. When the ultimate stress is reached in the weakest reinforcement layer, the moment in that element begins to decrease. The remaining elements in the mesh have to unload to preserve equilibrium and reinforcement in those elements cannot reach the (increased) ultimate stress. This leads to mesh independent part 3 of the diagrams in Fig. 4.25 (left). Such solution is only possible, if failure of the cross-section is caused by softening of reinforcement.

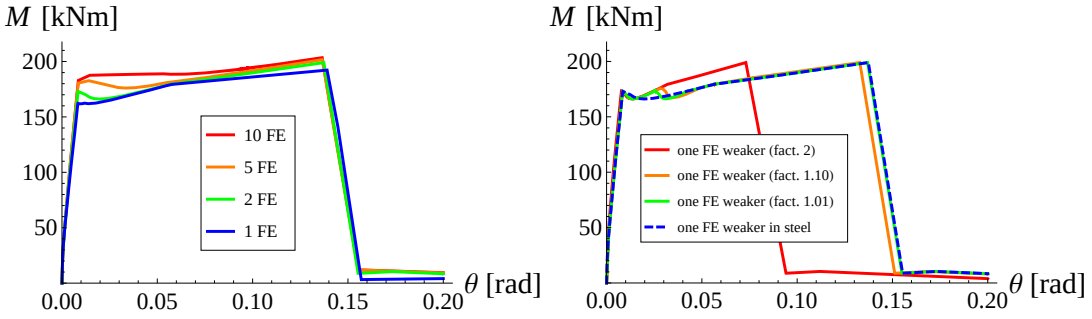

Figure 4.25: *Moment - rotation* diagrams for cantilever beam under end moment: weaker reinforcement in one of the finite elements (left), weaker concrete and reinforcement in one of the elements (right).
Slika 4.25: Diagram *moment - zasuk* za konzolo, obteženo z momentom: malce šibkejša armatura v enem od končnih elementov (levo), šibkejša armatura in beton v enem od elementov (desno).

Mesh dependency in the first two parts of the response cannot be avoided in this manner, because it is created by simultaneous occurrence of multiple discontinuities in concrete in tension. One would assume that weakening concrete in one of the elements would solve the problem, but it turns out differently. Concrete layer in the weak element enters the softening phase sooner than in the remaining elements, but the moment in that element continues to grow along with the force in tensile reinforcement. The moment in the rest of the finite elements grows accordingly, and just a little later the concrete begins to soften there as well.

Fig. 4.25 (right) shows $M-\theta$ diagrams of a beam, modeled with two finite elements, one of them weaker. In the strong element, failure stresses of steel σ_{fs} and concrete in tension σ_{fct} are increased by different factors. The diagrams are compared to response of a beam, where weakness is only created in reinforcement. The factor is irrelevant in case of steel - the increased σ_{fs} in the strong element will not be reached, whether it is 1% or 100% higher than original. Situation is different in concrete. If σ_{fct} is increased by 1% or 10%, the intervention has little effect on the response. Concrete layers of the strong element hold on a little longer in tension, but fail soon after the weak ones. If value of σ_{fct} is doubled, the tensile concrete layers become too strong and increase the stiffness of the element considerably.

4.4.3 Cantilever beam under end transversal force

A cantilever beam is subjected to prescribed lateral displacement at the free end, see Fig. 4.26. The length of the beam is $L = 2.5$m, the width and the height of the cross-section $b = 0.2$m and $h = 0.5$m. The tensile and compressive reinforcement are $A_{s,1} = A_{s,2} = 0.001\text{m}^2$ and the distances from the center of the reinforcement layers to the edges of the concrete cross-section are $a_1 = a_2 = 0.04$m. Material properties of concrete are: elasticity modulus $E_c = 4 \times 10^7\text{kNm}^{-2}$, elasticity limit $\sigma_{dc} = 40820\text{kNm}^{-2}$, ultimate stress in compression $\sigma_{fcc} = 44902\text{kNm}^{-2}$, ultimate stress in tension $\sigma_{fct} = 4000\text{kNm}^{-2}$, hardening modulus in compression $H_{cc} = 2 \times 10^6\text{kNm}^{-2}$, softening modulus in compression $K^*_{cc} = -5.2 \times 10^5\text{kNm}^{-3}$ and softening modulus in tension $K^*_{ct} = -8 \times 10^5\text{kNm}^{-3}$. Material properties of steel are: elasticity modulus $E_s = 2 \times 10^8\text{kNm}^{-2}$, yield stress $\sigma_y = 4 \times 10^5\text{kNm}^{-2}$, ultimate stress $\sigma_{fs} = 5 \times 10^5\text{kNm}^{-2}$, hardening modulus $H_s = 10^7\text{kNm}^{-2}$ and softening modulus $K_s = -3 \times 10^7\text{kNm}^{-3}$. The beam is modeled with different meshes of identical finite elements with ten layers of concrete and two layers of reinforcement.

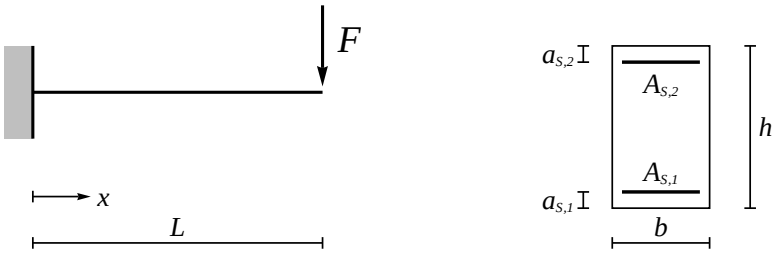

Figure 4.26: Cantilever beam under end transversal force: geometry.
Slika 4.26: Konzola, obremenjena s prečno silo: geometrija.

Moment at the support versus imposed lateral displacement diagrams are presented in Fig. 4.27 (left). The diagram for a single element mesh deviates substantially, because the derived Timoshenko beam element is only able to describe constant stress along the length of each layer. A finer mesh is required for a better approximation of linear stress distribution in the tested beam. Meshes of two or more elements give approximately the same value of the moment at which the tensile reinforcement yields, but the length of the yield plateau only stabilizes for meshes of ten or more elements.

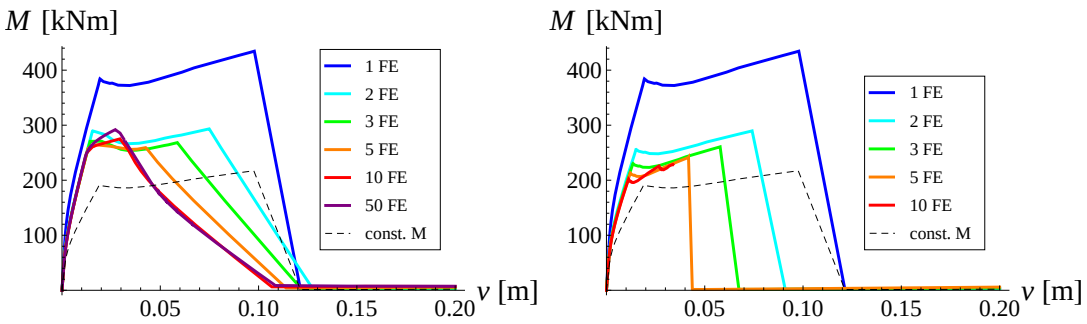

Figure 4.27: *Moment at support - transversal displacement* diagrams for cantilever beam under end transversal force: original softening moduli (left), moduli modified according to length of FE (right).
Slika 4.27: Diagram *moment ob podpori - prečni pomik* za konzolo, obremenjeno s prečno silo: originalni moduli mehčanja (levo), moduli mehčanja prirejeni glede na dolžino KE (desno).

The same beam is analyzed again under a different load. Instead of the force, a moment is applied at the free end, producing a constant moment over the length. This allows us to model the beam with a single finite element and avoid the influence of mesh refinement on the results. Results for the one element mesh are presented as diagram of moment at the support versus lateral displacement at the free end - the black dashed line in Fig. 4.27. Although we cannot expect the curves of different load cases to match, the reinforcement should yield at the same moment. However, comparison in Fig. 4.27 (left) shows that the beam under end force withstands substantially higher moment than the beam under end moment, before yielding.

Analysis of the beam under end force is repeated with a modified set of softening moduli - original values are scaled according to the length of the finite elements (multiplied with the number of FE in the mesh). Results are presented in Fig. 4.27 (right). In these diagrams, the "yield moment" decreases for finer meshes, and for a mesh of ten elements gets very close to the value from the "constant moment" diagram. The ultimate moment is still a little higher. Another change is evident in the right image - the softening parts of the diagrams are more parallel than before and even grow steeper for finer meshes.

Let us take a closer look at what happens inside the finite element. The stress σ^i is constant over the length of each layer. The resulting moment M, computed from equation (4.141), is constant as well.

$$M = \sum_i -y^i \sigma^i A^i \tag{4.141}$$

The internal forces $f^{\theta,int}$, defined by equation (4.33), are different from M, however. After inserting expressions (4.4) for B and B^*, and defining shear force $Q = \sum_i \tau^i A^i$, we obtain the following expressions for nodal moments:

$$\begin{aligned} f^{\text{int}}_{\theta_1} &= \sum_i \left(y^i \frac{1}{L^{(e)}} \sigma^i - \frac{1}{2} \tau^i \right) A^i L^{(e)} = \overbrace{\sum_i y^i \sigma^i A^i}^{-M} - \frac{L^{(e)}}{2} \overbrace{\sum_i \tau^i A^i}^{Q} = - \left(M + \frac{L^{(e)}}{2} Q \right) \\ f^{\text{int}}_{\theta_2} &= \sum_i \left(-y^i \frac{1}{L^{(e)}} \sigma^i - \frac{1}{2} \tau^i \right) A^i L^{(e)} = \overbrace{\sum_i -y^i \sigma^i A^i}^{M} - \frac{L^{(e)}}{2} \overbrace{\sum_i \tau^i A^i}^{Q} = M - \frac{L^{(e)}}{2} Q \end{aligned} \tag{4.142}$$

We can see that the two moments have a different absolute value. The difference $L^{(e)}Q$, where $L^{(e)}$ is the length of the finite element, derives from the shear stress, and it enables the finite element to deal with linear moment in the analyzed structure. Based on equation (4.142), we can characterize M as the average moment in the finite element.

We say that an element yields when the stress in tensile reinforcement reaches the yield value. The matching yield moment M_y is computed from equation (4.141). But when M reaches the yield moment, the corresponding nodal moments $\mathbf{f}^{\theta,int}$ take the values from (4.142), which can differ significantly from M_y, especially in a coarse mesh. The most evident example is the mesh, composed of a single finite element. Since the moment is zero at the free end, the moment at the support is twice as big as the average moment M. When the tensile reinforcement yields, the moment at the support has twice the value of M_y. This is confirmed by comparing the "1FE" and "const. M" diagrams in Fig. 4.27. The yield plateau in the first curve is twice as high as in the second. In the constant moment case, the shear stress is zero and the nodal moments $\mathbf{f}^{\theta,int}$ are equal to the average moment M, which activates plastification. The problems, arising from the described property of Timoshenko beam element, are avoided by using a fine enough mesh, so the nodal moments $f^{\text{int}}_{\theta_1}$ and $f^{\text{int}}_{\theta_2}$ are almost equal.

Refining of the finite element mesh brings about another problem, however. As we have seen in section 4.4.2, shortening the finite elements causes them to soften more slowly. Let us imagine a short section of the tested cantilever beam next to the support, with the tensile reinforcement on the verge of yielding. Concrete in tension

is already in the softening phase by then. If the section is modeled with two finite elements, instead of one, two narrow cracks form in concrete, instead of one wide crack. Since the traction at the discontinuity drops with the growth of the crack, the stress is greater in the short layers. Consequently, the yield moment M_y rises for a finer mesh. This explains why the diagrams in Fig. 4.27 (left) never reach the "const. M" diagram, despite the ever finer mesh.

This phenomenon is confirmed by the diagrams in Fig. 4.27 (right), where the softening moduli are modified according to the length of the finite element. At the same size of the discontinuity, a short layer (of a short element) produces a lower traction than a long one. In the situation, described above, two short layers with two narrow cracks produce the same traction as the long layer with one wide crack. Therefore, the yield moment M_y is not affected by the size of the finite elements. The yield plateau of the diagrams in Fig. 4.27 (right) is too high for coarse meshes because of the linear moments in the beam, but for the mesh of ten elements the yielding begins at almost the same moment, as in the constant moment case.

4.4.4 Simply supported beam

Simply supported beam, loaded by vertical force in the middle of the span, was analyzed in [51]. The length of the beam is $L = 5$m, width and height of the cross-section are $b = 0.2$m and $h = 0.5$m, tensile reinforcement is $A_{s,1} = 0.00161\text{m}^2$, compressive reinforcement is$A_{s,2} = 0.0001\text{m}^2$, distances of axes of tensile and compressive reinforcements from the edges are $a_1 = 0.044$m, and $a_2 = 0.032$m. Material properties of concrete are: elastic modulus $E_c = 37272000\text{kNm}^{-2}$, elasticity limit in compression $\sigma_{dc} = 30600\text{kNm}^{-2}$, failure stress in compression $\sigma_{fcc} = 38300\text{kNm}^{-2}$, hardening modulus in compression $H_{cc} = 9.09 \times 10^6\text{kNm}^{-2}$, softening modulus in compression $K^*_{cc} = -18.165 \times 10^6\text{kNm}^{-3}$, failure stress in tension $\sigma_{fct} = 3727\text{kNm}^{-2}$, softening modulus in tension $K^*_{ct} = -3 \times 10^7\text{kNm}^{-3}$. Material properties of steel are: elastic modulus $E_s = 2 \times 10^8\text{kNm}^{-2}$, yield stress $\sigma_y = 4 \times 10^5\text{kNm}^{-2}$. The above data is the same as in [51]. Since failure stress σ_{fs}, hardening modulus H_s and softening modulus K_s are not given in [51], we choose: $\sigma_{fs} = 5 \times 10^5\text{kNm}^{-2}$, $H_s = 3.3 \times 10^6\text{kNm}^{-2}$, $K_s = -4 \times 10^7\text{kNm}^{-3}$. By taking $\sigma_{dt} > \sigma_{fct}$, we assume that concrete is elastic until the failure stress is reached and a discontinuity appears. Due to the symmetry, only one half of the beam is modeled by using appropriate boundary conditions, see Fig. 4.28. Analysis is performed for meshes of 5, 8, 10 and 16 FE. Each element consists of 20 layers of concrete and 2 layers of reinforcement. Vertical displacement at the position of force F is prescribed and reaction in the same place is computed.

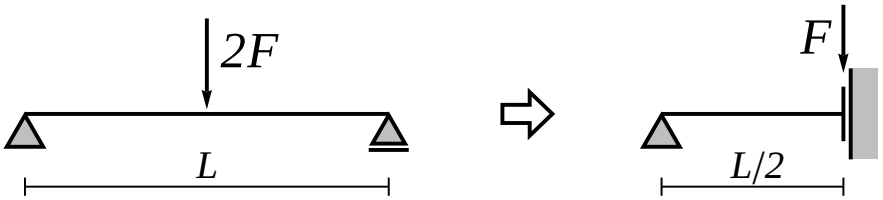

Figure 4.28: Simply supported beam: use of symmetry in computational model.
Slika 4.28: Prostoležeči nosilec: uporaba simetrije v računskem modelu.

Results are presented in Fig. 4.29. They depend only slightly on the number of the elements in the mesh. Comparison with results from [51] reveals that the force-displacement diagrams are similar, except for the shorter yield plateau of present element. Label "stress result." in Fig. 4.29 (right) refers to the stress resultant Timoshenko beam element with embedded strong discontinuity in rotation from [51], while "multi-layer" denotes multi-layer Timoshenko beam element with layer-wise embedded discontinuities in axial displacement and elasto-plastic material models for both concrete and reinforcement from [51].

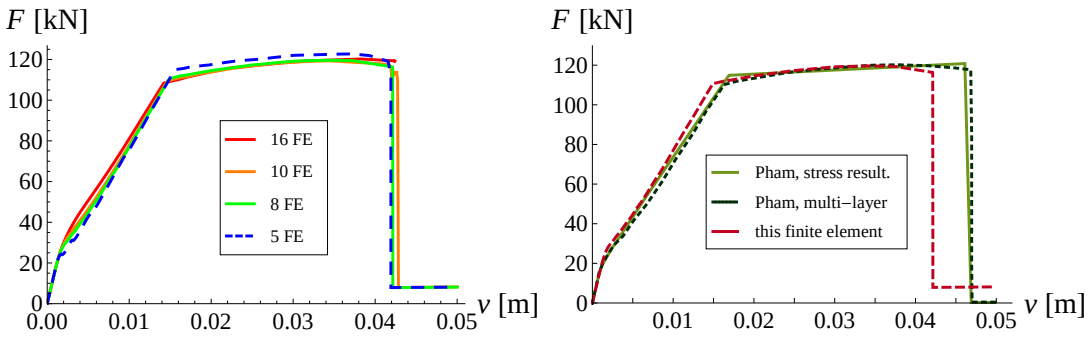

Figure 4.29: *Force - displacement under the force* diagrams for simply supported beam: results for different meshes (left), comparison of results for 8 FE with results of Pham (right).
Slika 4.29: Diagram *sila - pomik pod silo* za prostoležeči nosilec: rezultati za različne mreže končnih elementov (levo), primerjava rezultatov za 8 KE s Phamovimi rezultati (desno).

According to Fig. 4.30 (left), which shows dependence of the results on the number of concrete layers, already ten layers are enough for a proper description of the stress distribution over the height of the beam. Further refinement is not necessary in this case. Fig. 4.30 (right) displays dependence of the results on the hardening modulus of steel. We can see that lower values of H_s lengthen the plateau, while higher values increase the ultimate force F, which is not surprising. The softening modulus K_s does not affect the computation, since the beam collapses due to crushing of concrete in compression, and the reinforcement does not enter the softening phase.

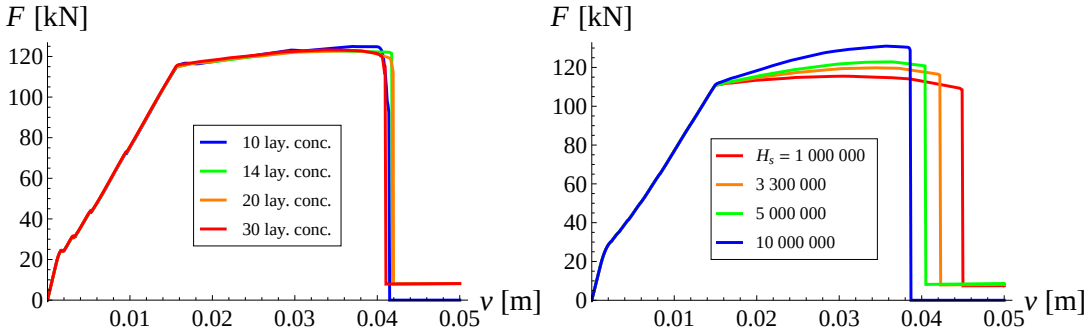

Figure 4.30: *Force - displacement under the force* diagrams for simply supported beam: different number of concrete layers in 5 FE mesh (left), different hardening modulus of steel in 8 FE mesh (right).
Slika 4.30: Diagram *sila - pomik pod silo* za prostoležeči nosilec: različno število slojev betona v mreži s 5 KE (levo), različen modul utrjevanja jekla v mreži z 8 KE (desno).

Fig. 4.31 shows material state at some characteristic stages in the analysis, marked with red dots in the $F - v$ diagram. Results are shown for a mesh of 8 finite elements with 20 concrete layers. It can be seen that the beam collapses due to concrete failure in the middle of the span. The stresses in reinforcements have not yet reached the failure strength. Growth of the discontinuities (cracks) in concrete is shown in Fig. 4.32. The size of the cracks is increased by factor 50. The red color represents the zone of crushing of concrete in compression.

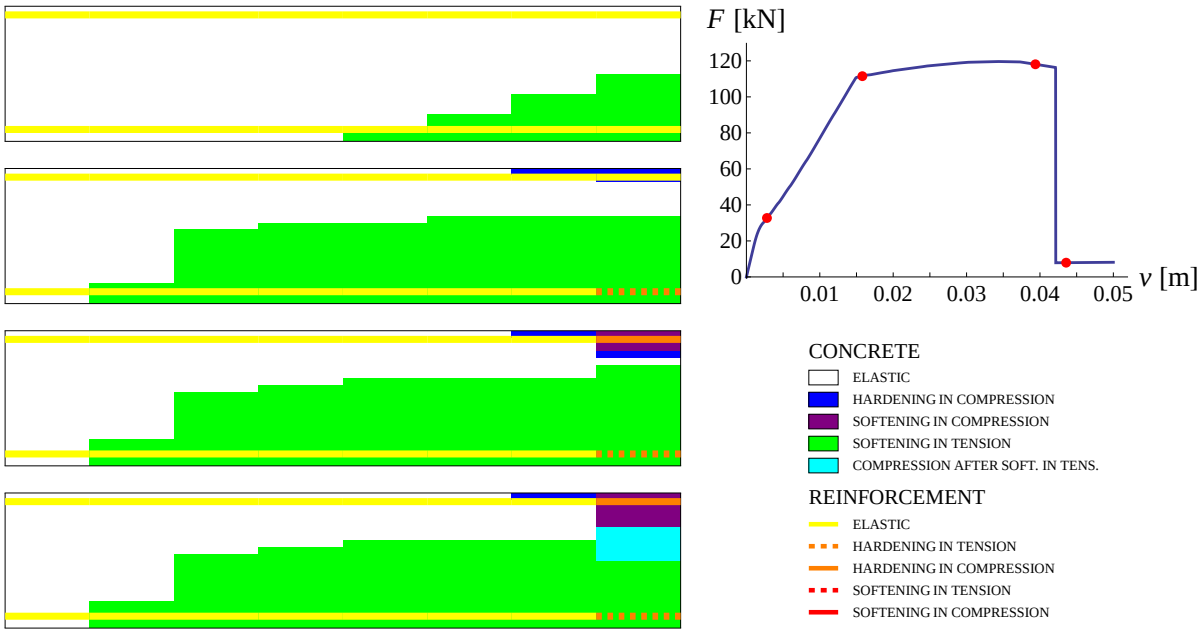

Figure 4.31: Simply supported beam: material state at different stages of analysis (marked with dots).
Slika 4.31: Prostoležeči nosilec: stanje materiala v posameznih fazah analize (označene s pikami).

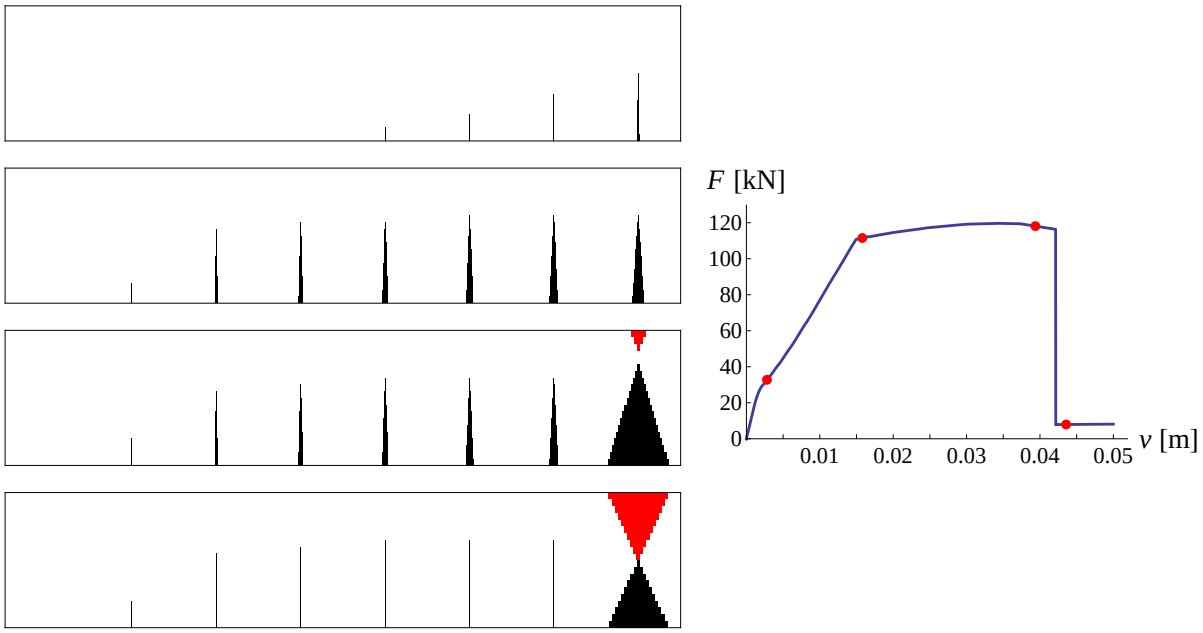

Figure 4.32: Simply supported beam: discontinuities (cracks) at different stages of analysis.
Slika 4.32: Prostoležeči nosilec: nezveznosti (razpoke) v posameznih fazah analize.

4.4.5 Reinforced concrete portal frame

A two-hinge pinned single story frame in Fig. 4.33 was experimentally tested in [75] and numerically analyzed in [76]. The height of the frame is $H = 1.93$m, span is $L = 2.64$m, width and height of rectangular cross-sections of beam and columns are $b = 0.1016$m and $h = 0.1524$m, distances of axes of bottom and top reinforcements from the edges of the cross-section are $a_1 = a_2 = 0.014$m. Bottom and top reinforcements of column and beam are given in Fig. 4.33 (right). The material data for steel is: elastic modulus $E_s = 200000$MPa, yield stress $\sigma_y = 293$MPa, ultimate stress $\sigma_{fs} = 310$MPa, hardening modulus $H_s = 2020$MPa, softening modulus $K_s = -2.5 \times 10^7 \text{kNm}^{-3}$. The material data for concrete is: elastic modulus $E_c = 31500$MPa, elasticity limit in compression $\sigma_{dc} = 0.4\sigma_{fcc} = 14.6$MPa, ultimate stress in compression$\sigma_{fcc} = 36.5$MPa, hardening modulus in compression $H_{cc} = 29000$MPa, softening modulus in compression $K^*_{cc} = -4 \times 10^7 \text{kNm}^{-3}$, ultimate stress in tension $\sigma_{fct} = 0.95$MPa, softening modulus in tension $K^*_{ct} = -1.1 \times 10^7 \text{kNm}^{-3}$. By taking $\sigma_{dt} > \sigma_{fct}$, we assume that concrete is elastic until the failure stress is reached and a discontinuity appears. All the above data, except for the softening moduli K_s, K^*_{cc}, K^*_{ct} and hardening modulus H_{cc}, is adopted from [76]. The frame is loaded symmetrically, with two vertical forces at distance $l_P = 1.09$m from the axis of each column. Thus, we model one half of the frame with appropriate boundary conditions. In analysis, the vertical displacement at location of the force P was imposed. Analysis was performed for different meshes, ranging from 8 to 64 FE for a column, and from 5 to 40 FE for one half of the beam.

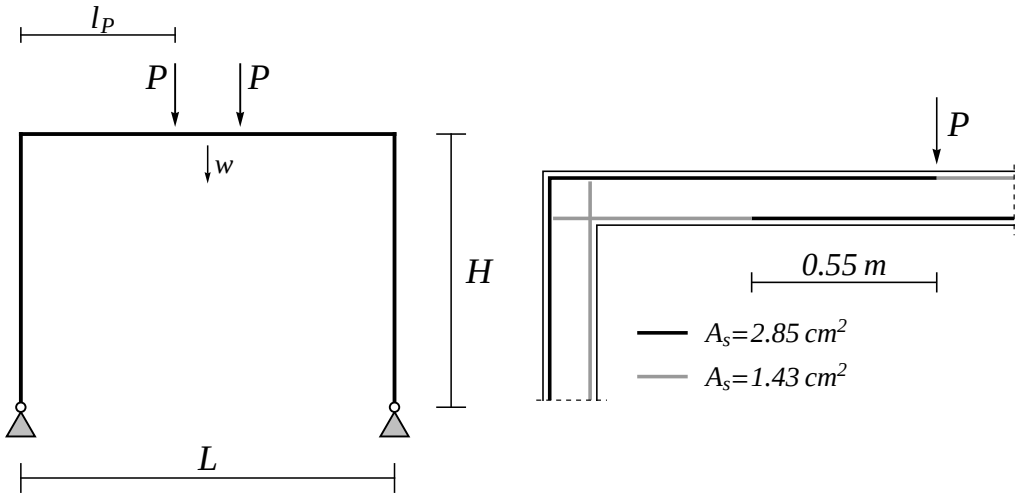

Figure 4.33: Pinned portal frame: geometry, loading pattern and reinforcement.
Slika 4.33: Vrtljivo podprt portalni okvir: geometrija, obtežba in armatura.

Results are presented in Fig. 4.34, where relation between the force P and the vertical displacement in the middle of the frame w is shown. The left image shows the results for the case, in which the material (not geometrical) properties of all finite elements are the same. We can see that the results do not converge, which is caused by the constant moment in the middle section of the span (between the forces P). With refinement of the mesh, more and more discontinuities occur in this part of the beam. This can be solved in a similar way as in section 4.4.2, namely by creating a weaker element. In order to preserve the original material properties in the critical element, we slightly increase the ultimate stress of steel σ_{fs} in all finite elements in the middle section of the span, except for the one adjacent to the force P. Results of the analysis with a weak element are presented in Fig. 4.34 (right).

Comparison of the $P - w$ diagram with experimental results [75] and results, reported in [76] is shown in Fig. 4.35. The moments at the joint of the column and the beam and in the middle of the span are presented in Fig. 4.36.

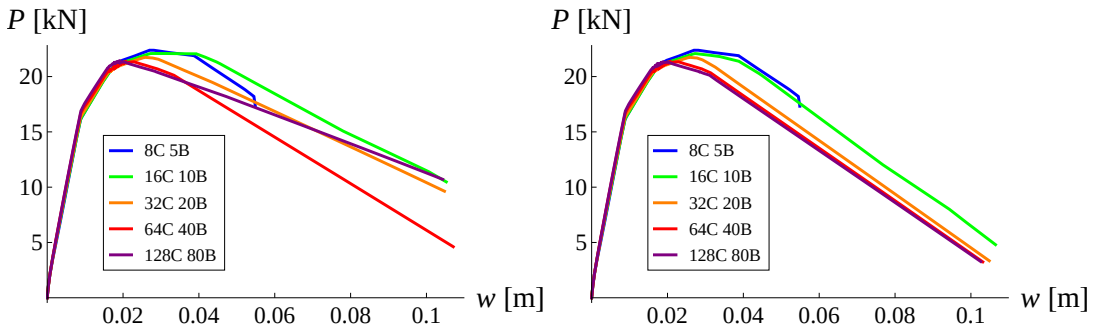

Figure 4.34: $P-w$ diagram: results for different meshes of finite elements if all elements to the right of force P are the same (left) and if reinforcement is weakened in one of them (right).
Slika 4.34: Diagram $P-w$: rezultati za različne mreže končnih elementov, če so vsi elementi desno od sile P enaki (levo) in če je v enem od njih armatura oslabljena (desno).

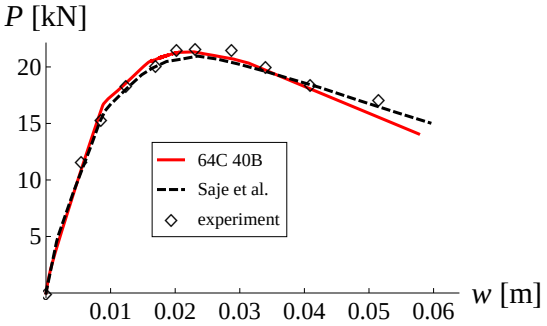

Figure 4.35: $P-w$ diagram: comparison to experiment and results of Saje et al.
Slika 4.35: Diagram $P-w$: primerjava z eksperimentom in z rezultati Saje et al.

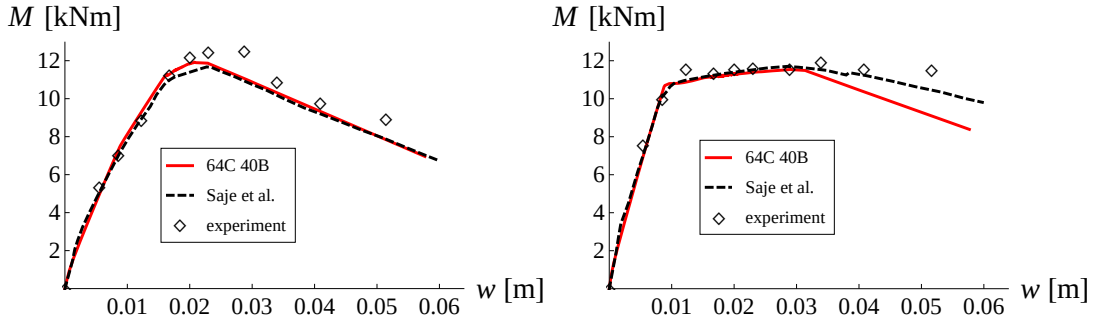

Figure 4.36: Moments at the joint of the beam and the column (left) and in the middle of the span (right): comparison to experiment and results of Saje et al.
Slika 4.36: Moment na stiku stebra in prečke (levo) ter na sredini razpona (desno): primerjava z eksperimentom in z rezultati Saje et al.

Progression of damage, yielding and softening of material is shown in Fig. 4.37, where material state is presented element-wise and layer-wise for different stages of the analysis, performed on the mesh of 32 FE in the column and 20 FE in the half-beam. If we examine the elements near the inflection point of the beam, where the moments are close to zero, we can see transition of some layers from compression to tension and vice versa. This happens due

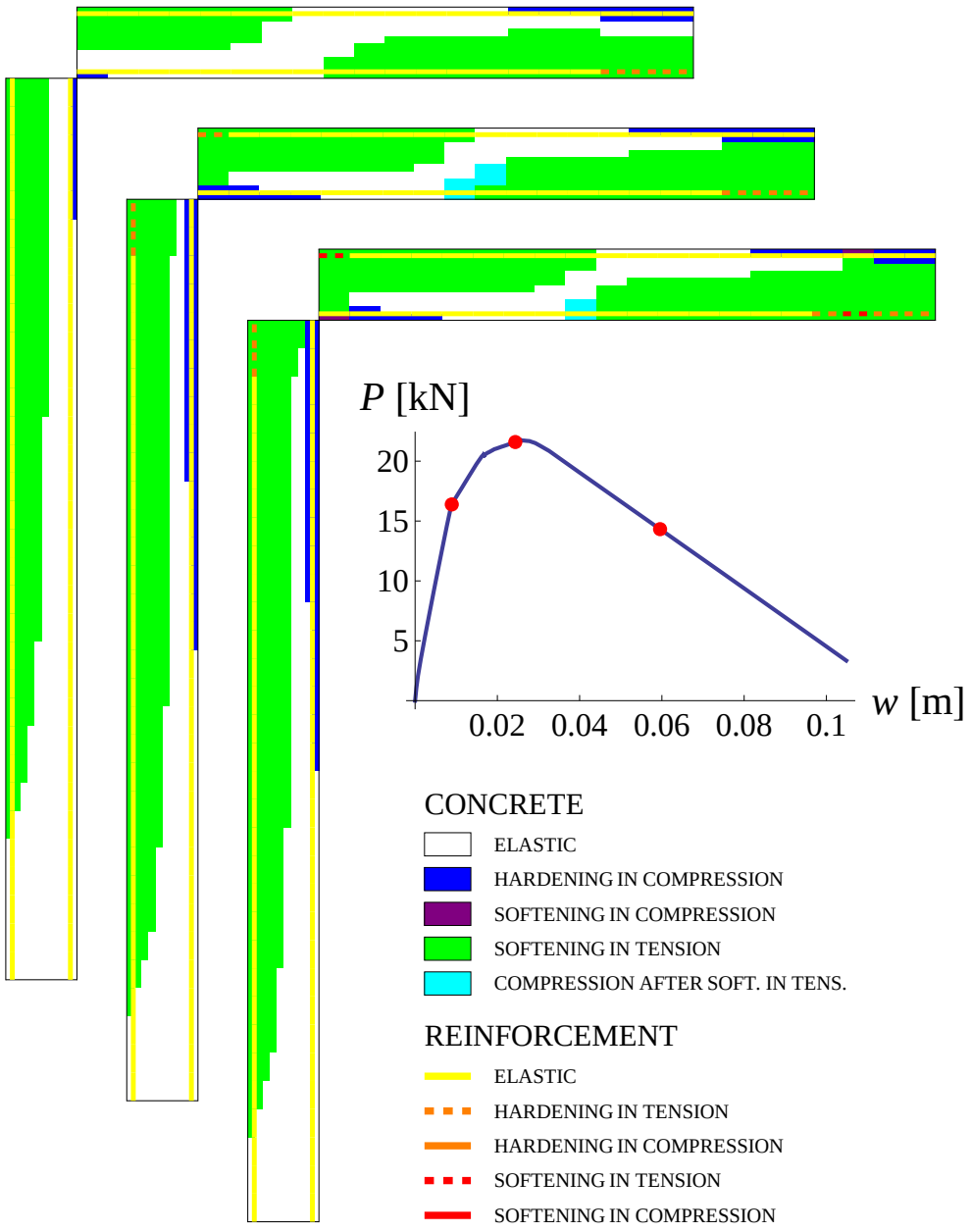

Figure 4.37: Portal frame: material state at different stages of analysis (marked with dots).
Slika 4.37: Portalni okvir: stanje materiala v posameznih fazah analize (označene s pikami).

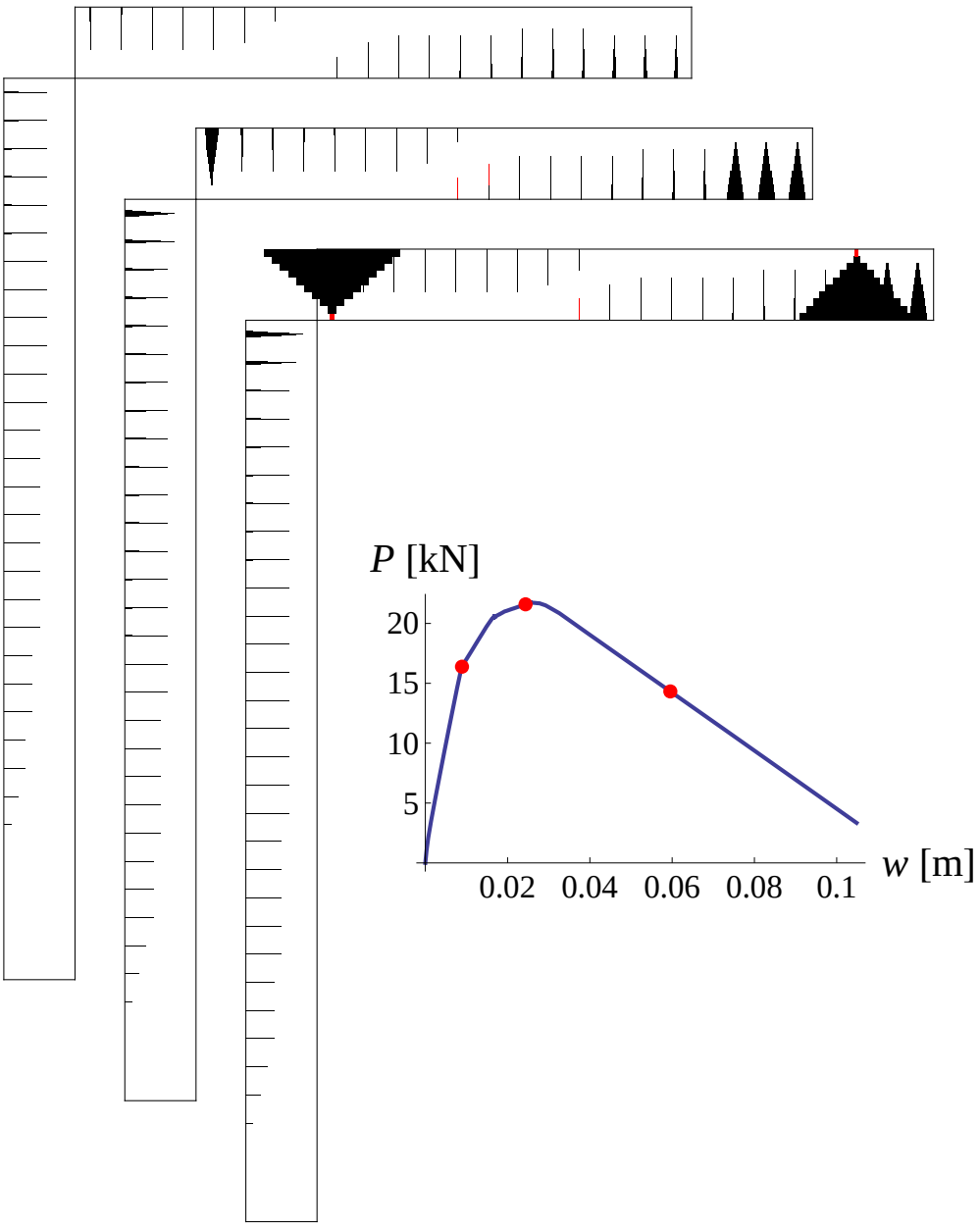

Figure 4.38: Portal frame: discontinuities (cracks) at different stages of analysis (marked with dots).
Slika 4.38: Portalni okvir: nezveznosti (razpoke) v posameznih fazah analize (označene s pikami).

to shifting of the neutral axis and corresponds to the situation in Fig. 4.18 (left). The cyan color designates a layer that has developed a discontinuity in tension and was then loaded in compression. In this case, the compressive stress values are well below σ_{fcc}.

Fig. 4.38 shows the discontinuities in concrete, increased by factor 50, for the phases of the analysis, marked with the red dots. We can see that the greatest part of damage occurs in the middle and at the end of the beam. In the three rightmost elements (to the right of the load P) the cracks grow equally at first. But when the ultimate stress is reached in the tensile reinforcement of the weaker element, the cracks in the remaining elements stop growing. They do not close because of the plastic deformations in steel.

4.4.6 Two story reinforced concrete frame

Two-story reinforced concrete frame in Fig. 4.39 has been experimentally tested in [71]. Numerical analyses were done by Pham et al. [52] and Jukić et al. [74], using stress-resultant Timoshenko and Euler-Bernoulli beam finite elements, respectively, with embedded strong discontinuity in rotation. Analysis with multi-layered Timoshenko beam element with layer-wise embedded discontinuities in axial displacement and elasto-plastic material models for both concrete and reinforcement was also done in [52]. Story height of the frame is $H = 2$m, span is $L = 3.5$m. Beam cross-section data is: width $b = 0.3$m, height $h = 0.4$m, bottom and top reinforcements $A_{s,1} = A_{s,2} = 0.0012\text{m}^2$, distances of reinforcement axes from the edges $a_1 = a_2 = 0.04$m. Column cross-section data is the same, except for $a_1 = a_2 = 0.03$m. Material properties of steel are accommodated from data reported in [71]: elasticity modulus $E_s = 192500$MPa, yield stress $\sigma_y = 418$MPa and ultimate stress $\sigma_{fs} = 596$MPa are taken directly from [71], while the hardening modulus $H_s = 2790$MPa is computed in such way that the ultimate stress is reached at the same strain as in [71], see Fig. 4.40 (left). The softening modulus is not provided in [71]. We choose $K_s = -4 \times 10^7 \text{kNm}^{-3}$. Material properties of concrete are also accommodated from data reported in [71]: ultimate stress in compression $\sigma_{fcc} = 30$MPa is taken directly from [71], elasticity modulus $E_c = 28600$MPa and ultimate stress of concrete in tension $\sigma_{fct} = 1.8$MPa are taken from Fig. 2 in [71]. Elasticity limit $\sigma_{dc} = 8.5$MPa and hardening modulus $H_{cc} = 49000$MPa are computed in such way that the ultimate compressive stress is reached at the same strain as in Fig. 6(a) in [71], see Fig. 4.40 (right). Softening moduli are not provided in [71]. We choose $K^*_{cc} = -2 \times 10^6 \text{kNm}^{-3}$ for compression and $K^*_{ct} = -10^7 \text{kNm}^{-3}$ for tension.

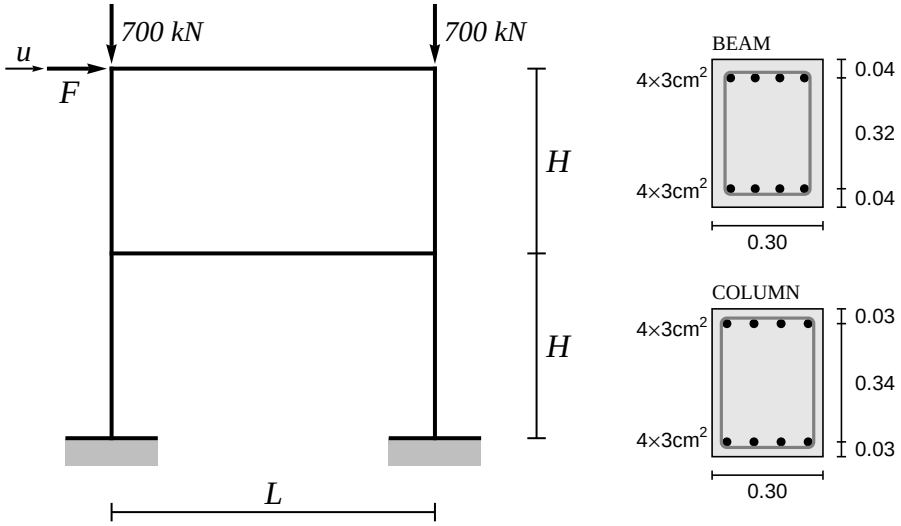

Figure 4.39: Two story frame: geometry, loading pattern and cross-sections.
Slika 4.39: Dvoetažni okvir: geometrija, obtežba in prečni prerezi.

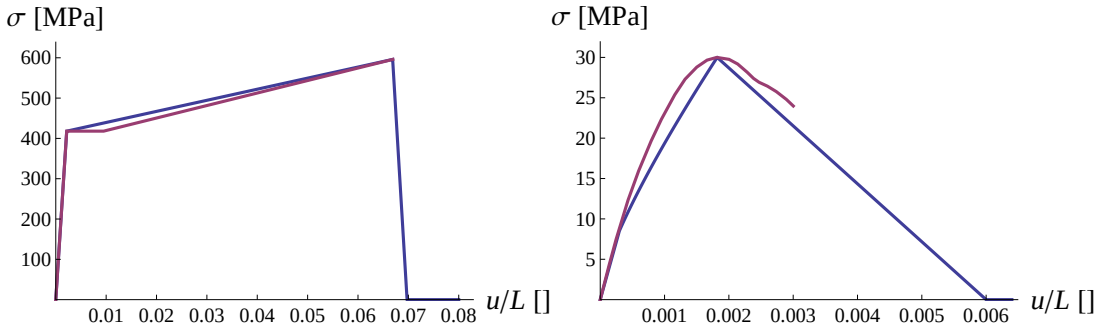

Figure 4.40: *Stress - strain* diagrams for steel (left) and concrete in compression (right) used by Vecchio and Emara, compared to diagrams used in present analysis.

Slika 4.40: Diagrama *napetost - deformacija* za jeklo (levo) in beton v tlaku (desno), ki sta ju uporabila Vecchio in Emara, v primerjavi z diagramoma, uporabljenima v tej analizi.

Remark. *The diagrams in Fig. 4.40 were obtained by modeling steel and concrete beams with one finite element of length* 2.5m *and loading them in pure tension and pure compression, respectively. They show the stress* σ *in the (steel or concrete) beam, depending on the displacement of the free end of the beam, divided by the length of the beam* u/L*. Up to the ultimate stress, the diagrams are identical to* $\sigma - \varepsilon$ *diagrams of steel and concrete.*

The frame is modeled with different meshes of finite elements with ten layers of concrete and two layers of reinforcement. Constant vertical force of 700kN is applied on top of each column, before the frame is pushed horizontally at the top of the second story. Reaction F is computed at location and in direction of the imposed displacement u.

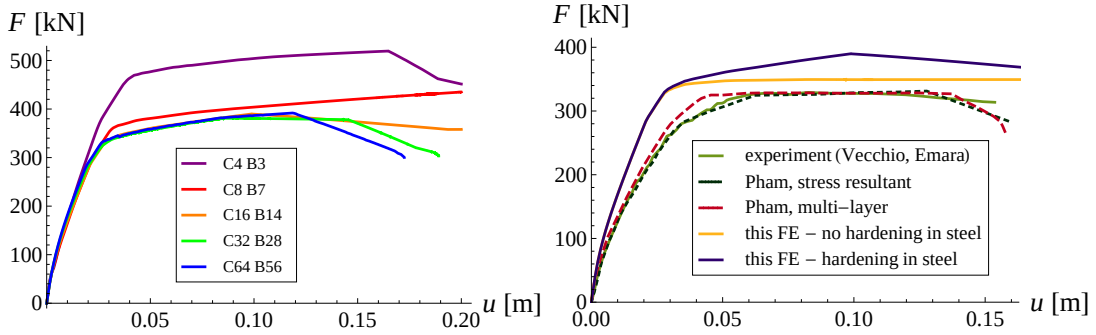

Figure 4.41: Response of two story frame: results for different meshes (left), comparison of results for 16 FE in a column and 14 FE in a beam with experiment and results of Pham (right).

Slika 4.41: Odziv dvoetažnega okvirja: rezultati za različne mreže končnih elementov (levo), primerjava rezultatov za 16 KE v stebru in 14 KE v prečki s Phamovimi rezultati (desno).

Fig. 4.41 (left) shows the results of the analysis, depending on the finite element mesh. The number of the elements ranges from 4 to 64 in columns (from the ground to the top of the frame) and from 3 to 56 in the beam, as indicated in the legend. The greatest deviation occurs for the coarsest mesh because our FE can only describe constant moments over its length. Therefore we need a mesh, fine enough to capture the linear moments in the structural elements. Results for finer meshes match pretty well in the first phase but differ significantly in the softening range. In all cases, the ultimate moment exceeds the experimental results for at least 20%. If no hardening is used for steel, the results are closer to the experiment, although the stiffness remains too big in the first part of the response,

see Fig. 4.41 (right). A case of unloading of the frame is shown in Fig. 4.42. Analysis was performed on a mesh with 16 FE in columns (8 FE in each story) and 14 FE in beams. Apart from the exceeded ultimate moment, a difference occurs in the unloading curves which are straight and a little steeper than experimental. Also, the re-loading follows almost exactly the unloading line.

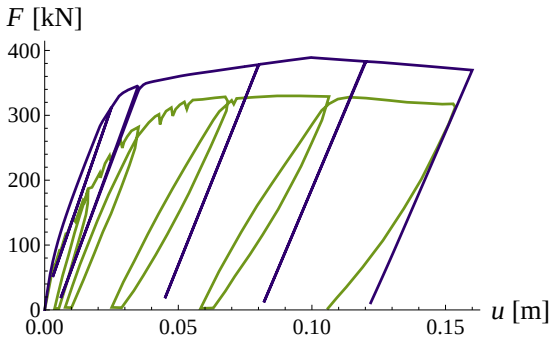

Figure 4.42: Response of two story frame: loading and unloading for a mesh of 16 FE in a column and 14 FE in a beam. Comparison to experiment.

Slika 4.42: Odziv dvoetažnega okvirja: obremenjevanje in razbremenjevanje za mrežo s 16 KE v stebru in s 14 KE v prečki. Primerjava z eksperimentom.

Images in Fig. 4.44 show progression of damage and plasticity in the material at several stages of the frame analysis, performed on a mesh with 16 FE in columns and 14 FE in beams. The stages are marked with red dots in the response of the frame in Fig. 4.43. The legend for Fig. 4.44 is included in Fig. 4.43. Fig. 4.45 shows the discontinuities in concrete, corresponding to the same stages of the analysis. Their sizes are increased by factor 50. The red color represents a discontinuity in compression, (zone of crushing of concrete in compression).

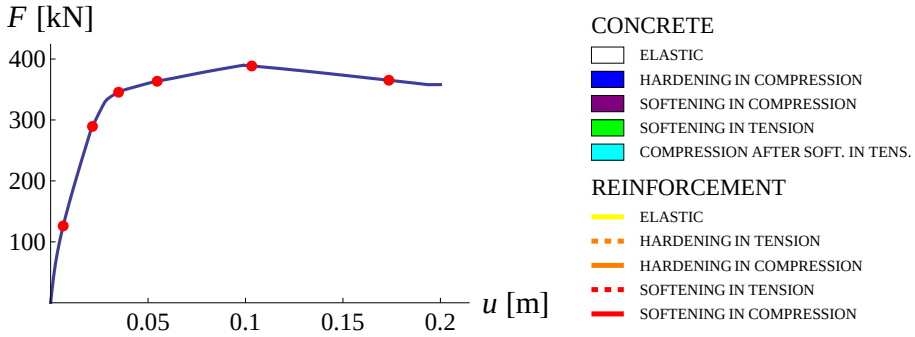

Figure 4.43: Two story frame: stages of analysis, corresponding to images in Figs. 4.44 and 4.45.

Slika 4.43: Dvoetažni okvir: faze analize, ki ustrezajo stanjem materiala na slikah 4.44 in 4.45.

4.5 Concluding remarks

We have presented a planar multi-layer Timoshenko beam finite element, composed of several concrete and steel reinforcement layers. Small deformations are assumed in the beam kinematics. Deformation of an individual layer is computed from axial deformation of the middle axis of the beam and rotation of the cross-section. Contribution of the rotation depends on the distance from the middle axis. A discontinuity in axial displacement is introduced individually into each layer. Axial response of a concrete layer is described with a damage hardening model for the bulk and a damage softening law at the discontinuity. Axial response of a steel layer is described with isotropic

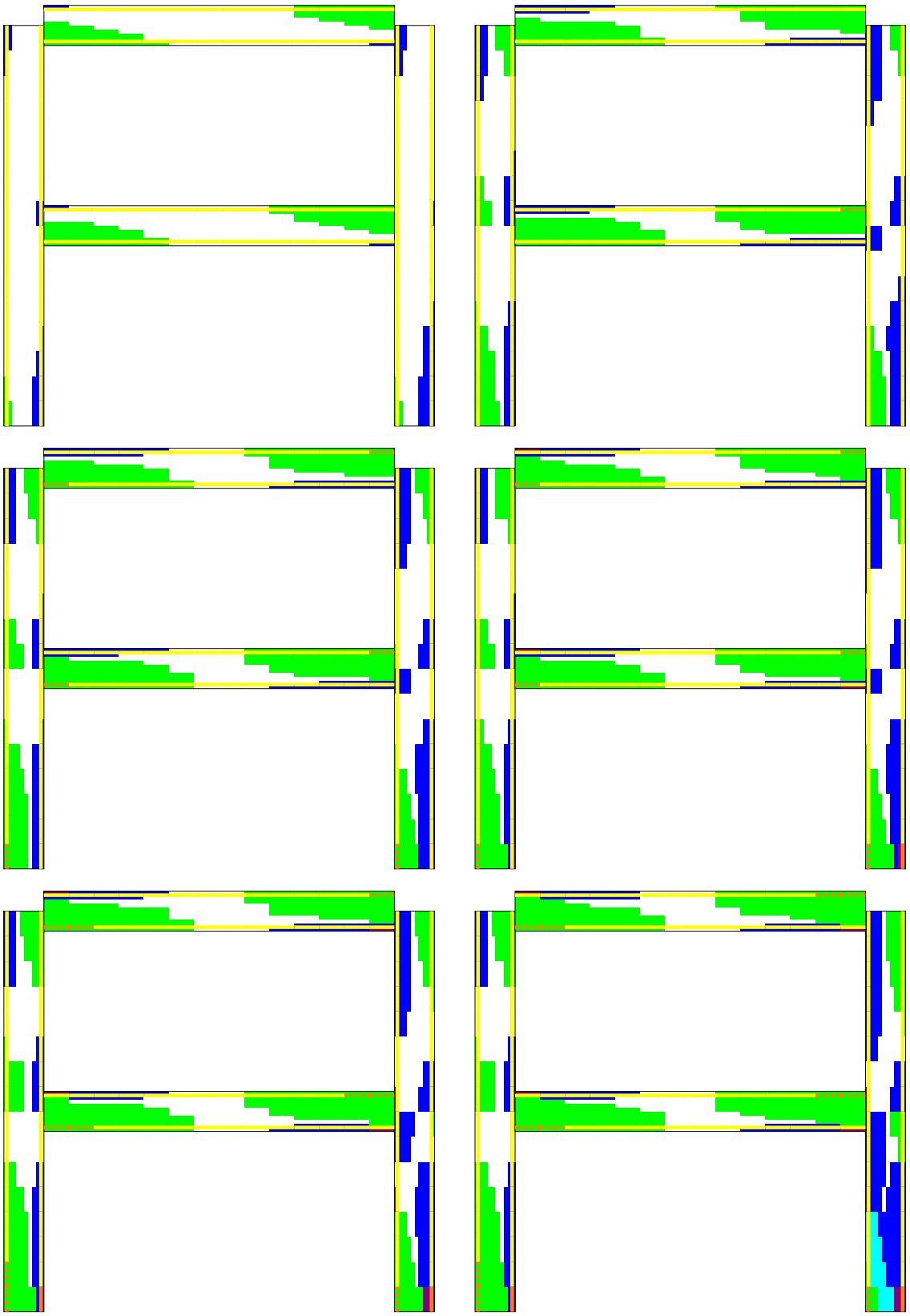

Figure 4.44: Two story frame: material state at different stages of analysis, marked in Fig. 4.43.
Slika 4.44: Dvoetažni okvir: stanje materiala v fazah analize, označenih na sliki 4.43.

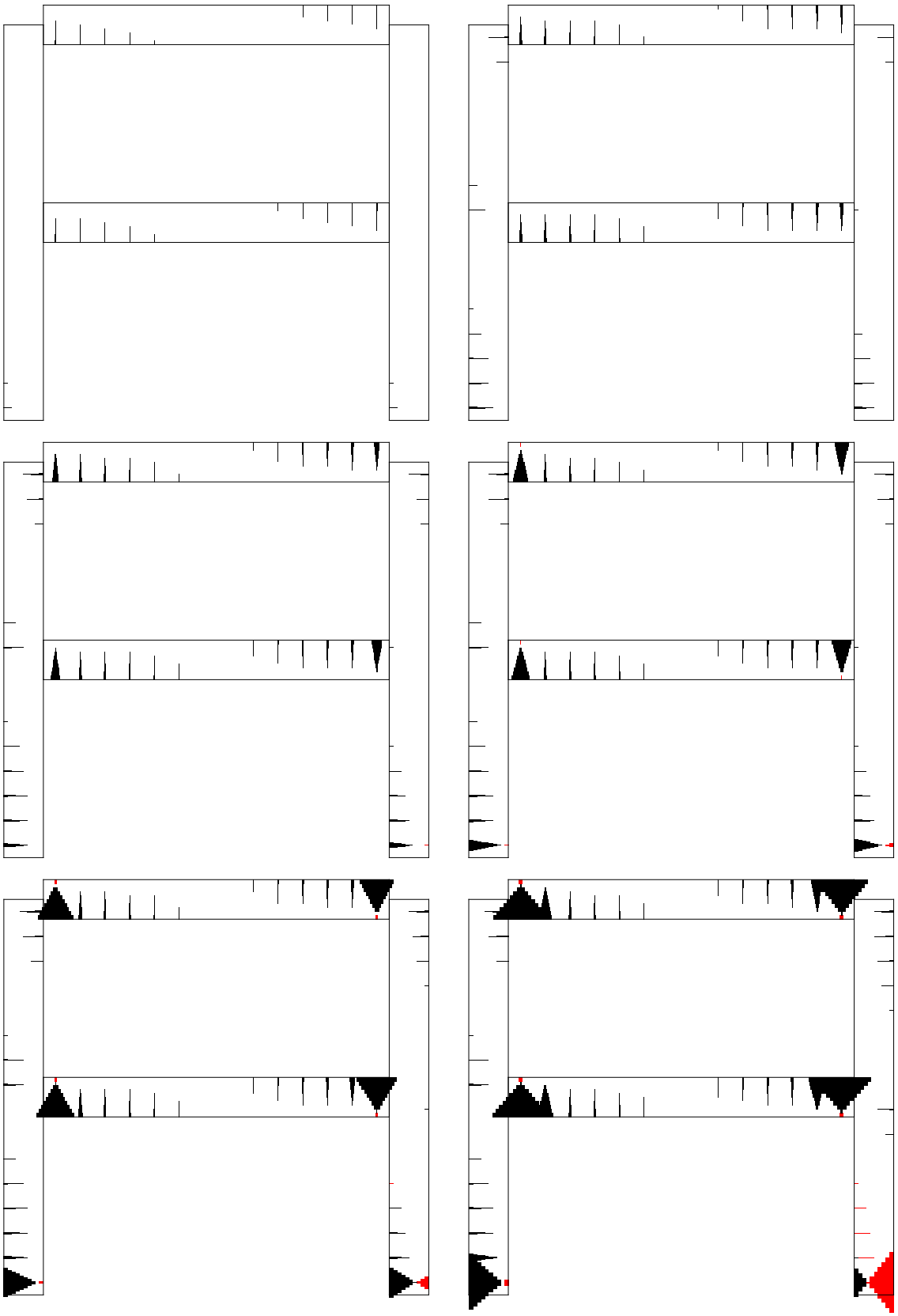

Figure 4.45: Two story frame: discontinuities at different stages of analysis, marked in Fig. 4.43.
Slika 4.45: Dvoetažni okvir: nezveznosti v fazah analize, označenih na sliki 4.43.

hardening plasticity model for the bulk and plastic softening cohesive model at the discontinuity. Shear response is assumed elastic.

The finite element has been derived for analysis of reinforced concrete beams and frames up to complete failure, providing a detailed description of material state over the cross-section. It can also be used for computation of stress-resultant properties of different cross-sections, which are required as an input data in analysis with stress-resultant beam finite elements, such as the one presented in chapter 2. The derived multi-layer element is not intended for cyclic loading. Nevertheless, it can handle minor changes of the load sign, which can occur in some layers due to shifting of the neutral axis even in monotonic loading.

Mesh dependency is observed in the case of cantilever beam under end moment if all finite elements are the same. The reason lies in simultaneous occurrence of multiple discontinuities along the beam. In a fine mesh a large number of small discontinuities are formed, while coarse mesh creates a small number of large discontinuities. Since traction at the discontinuity decreases with its growth, different meshes produce different moment in the beam. The differences are greatest in the last part of the response, when the moment in the beam begins to drop due to softening of tensile reinforcement. This can be solved by slightly weakening reinforcement in one of the elements in the mesh, preventing occurrence of multiple discontinuities in steel along the cantilever beam. If softening of the beam happens due to crushing of concrete in compression, the problem cannot be solved so effectively, since there are multiple critical layers of concrete, as opposed to a single critical layer of tensile reinforcement. Minor deviations appear in the hardening part of the beam response due to cracking of concrete in tension. This cannot be avoided by weakening one of the elements in the mesh because the moment in the beam is still rising and, sooner or later, concrete will crack in the remaining elements as well.

Mesh dependency due to cracking of concrete in tension is more evident in the case of cantilever beam under end transversal force. Since the developed Timoshenko beam finite element can only describe constant state over its length, a fine mesh is required for adequate description of linear moment along the beam. However, shortening of the finite elements increases the number and reduces the size of discontinuities in concrete in tension, resulting in higher traction at the discontinuity and considerably overestimated yield moment of the beam. The same phenomenon is observed in the cantilever beam under end moment, but to a lesser extent.

Another kinematics issue should be addressed. There is no discontinuity (in rotation or axial displacement) on the element level, since the embedded discontinuities in axial displacement are defined locally in each layer. Deformation of the beam axis is always interpolated in the same way as for a regular Timoshenko beam. Even when the element is completely broken, the middle axis is a smooth curve. The bulk of each layer slides along a path, parallel to the middle axis. In a fine mesh, however, this may not be problematic. The critical finite element exhibits a significantly decreased stiffness and greater curvature than neighboring elements, which can be interpreted as a jump in rotation, smeared over the length of the critical element. Still, the global kinematics is not completely accurate.

Several numerical examples and experiments from literature have been modeled with our finite element. Significant deviation is observed in stiffness and ultimate load of the two-story RC frame. However, the shape of the loading and unloading diagram is appropriate. Results of the simply supported beam model and the portal frame model match well the results from the literature. Despite some deficiencies, the finite element allows for quite adequate modeling of reinforced concrete beams and frames, based on axial responses of concrete and steel, which are easily obtained from experiments and are independent of the cross-section geometry.

5 VISCOUS REGULARIZATION OF SOFTENING RESPONSE FOR MULTI-LAYER TIMOSHENKO BEAM FINITE ELEMENT

5.1 Introduction

In this chapter, we upgrade the multi-layer Timoshenko beam finite element, presented in chapter 4, by implementing viscous regularization of the softening response [77]. This method can be used to prevent certain computational problems, such as alternating between equivalent solutions [78]. In present work, we introduce viscous forces at discontinuities to help control their development and prevent (physically) erroneous occurrence of multiple discontinuities in homogeneous stress field.

When several equivalent finite elements develop a discontinuity simultaneously, the viscous regularization favors one of them. The preferred element continues to soften, while the others unload. The selection is based on the rate, at which the discontinuities develop in different elements. The faster a discontinuity grows, the more its growth is encouraged. Eventually, only the "fastest" element develops a discontinuity and the others unload to satisfy the equilibrium.

Introduction of viscous regularization into the finite element slightly modifies the equilibrium equations, while the kinematic and the constitutive equations remain unchanged. This leads to alteration of some expressions, used in the computational procedure. In this chapter, we only derive the equations that differ from the ones in chapter 4.

The outline of the chapter is as follows. In section 5.2, we introduce the viscous forces into the virtual work equation, derived in the previous chapter, which produces modified equilibrium equations. In section 5.3, the modifications to the computation of internal variables are presented. Section 5.4 presents the differences in the global computation of the nodal degrees of freedom. In section 5.5, the newly developed finite element is tested on several numerical examples. Conclusions are given in section 5.6.

5.2 Virtual work equation

We have computed the virtual work of internal forces $G^{\text{int},(e)}$ of the finite element (e) in the previous chapter, see equation (4.31), and we have obtained expression (5.1).

$$G^{\text{int},(e)} = \int_V (\hat{\varepsilon}\sigma + \hat{\gamma}\tau)\, dV = \hat{\mathbf{d}}^{(e)^T} \mathbf{f}^{\text{int},(e)} + \sum_{i=1}^{n_{CL}^{(e)}} \hat{\alpha}^{(e),i} h^{(e),i} \tag{5.1}$$

Here, $\hat{\mathbf{d}}^{(e)}$ and $\mathbf{f}^{\text{int},(e)}$ are virtual nodal displacements and corresponding internal forces of element (e), $\hat{\alpha}^{(e),i}$ is the virtual displacement jump in the i-th layer, and $h^{(e),i}$ is the equivalent of internal force, corresponding to $\hat{\alpha}^{(e),i}$. The number of cracked layers is denoted with $n_{CL}^{(e)}$. We enrich the standard virtual work of internal forces $G^{\text{int},(e)}$ by adding in each discontinuity a viscous term, which depends on the rate of change of the displacement jump $\dot{\alpha}^{(e),i}$ and on viscosity parameter η^i.

$$G_{\text{reg}}^{\text{int},(e)} = G^{\text{int},(e)} + \sum_{i=1}^{n_{CL}^{(e)}} \hat{\alpha}^{(e),i} \underbrace{\eta^i \dot{\alpha}^{(e),i} A^i}_{\text{viscous force}} = \hat{\mathbf{d}}^{(e)^T} \mathbf{f}^{\text{int},(e)} + \sum_{i=1}^{n_{CL}^{(e)}} \hat{\alpha}^{(e),i} \underbrace{\left(h^{(e),i} + \eta^i \dot{\alpha}^{(e),i} A^i \right)}_{h_{\text{reg}}^{(e),i}} \tag{5.2}$$

$$\eta^i = \begin{cases} \eta_c & \text{for concrete} \\ \eta_s & \text{for steel} \end{cases} \qquad \eta_c = \begin{cases} \eta_{cc} & \text{for compression} \\ \eta_{ct} & \text{for tension} \end{cases} \tag{5.3}$$

We refer to the modified expression $G_{\text{reg}}^{\text{int},(e)}$ as the regularized virtual work of internal forces. Expression $\eta^i \dot{\alpha}^{(e),i} A^i$ represents the additional viscous force at the discontinuity in the i-th layer. For the sake of clarity, index (e) is omitted in notations for the viscosity parameter η^i and the cross-section area of the layer A^i. Expression in the parenthesis is further developed by applying equation (4.39) for $h^{(e),i}$.

$$h_{\text{reg}}^{(e),i} = A^i \left(\int_L \bar{G}^i \sigma^i dx + t^i \right) + \eta^i \dot{\alpha}^i A^i = A^i \left(\int_L \bar{G}^i \sigma^i dx + t^i + \eta^i \dot{\alpha}^i \right) \tag{5.4}$$

Here, $\bar{G}^i = -1/L$ is the continuous part of the interpolation function for enhanced strain, σ^i is the stress in the bulk, and t^i is the traction at the discontinuity in the i-th layer. Index (e) is omitted in $\dot{\alpha}^i$ as well.

Equation (5.5) represents the weak equilibrium of the whole structure. Regularized virtual work of internal forces is computed as a sum of contributions from all finite elements, while the virtual work of external forces is calculated as a scalar product of the vector of virtual nodal displacements of the structure $\hat{\mathbf{d}}^{\text{str}}$ and the corresponding vector of external forces $\mathbf{f}^{\text{ext,str}}$. The total number of finite elements in the structure is marked with n_{FE}

$$G_{\text{reg}}^{\text{int}} - G^{\text{ext}} = 0, \qquad G_{\text{reg}}^{\text{int}} = \sum_{e=1}^{n_{FE}} G_{\text{reg}}^{\text{int},(e)}, \qquad G^{\text{ext}} = \hat{\mathbf{d}}^{\text{str}^T} \mathbf{f}^{\text{ext,str}} \tag{5.5}$$

We rearrange equation (5.5) by taking into account the relations between the displacements of the element $\mathbf{d}^{(e)}$ and the displacements of the structure $\mathbf{d}^{\text{str}}$, described in section 4.2.3 of the previous chapter. This brings us to the following system of global equations.

$$\begin{aligned} &\mathbf{f}^{\text{int,str}} - \mathbf{f}^{\text{ext,str}} = \mathbf{0} \\ &\forall e \in \{1,2,\ldots,n_{FE}\},\ \forall i \in \left\{1,2,\ldots,n_{CL}^{(e)}\right\}: \quad h_{\text{reg}}^{(e),i} = 0 \end{aligned} \tag{5.6}$$

The first equation in (5.6) represents the global equilibrium (equilibrium of each node in the structure) and it is exactly the same as before, see equation (4.37). The second equation keeps the previous form, only the expression $h^{(e),i}$ is replaced by $h_{\text{reg}}^{(e),i}$. If expression (5.4) is inserted, the equation can be interpreted as the local equilibrium between the stress in the bulk σ^i and the traction at the discontinuity t^i.

$$h_{\text{reg}}^{(e),i} = 0 \quad \Leftrightarrow \quad t^i = -\int_L \bar{G}^i \sigma^i dx - \eta^i \dot{\alpha}^i = \sigma^i - \eta^i \dot{\alpha}^i \tag{5.7}$$

We notice that σ^i and t^i are no longer equal. They differ for the viscous term $\eta^i \dot{\alpha}^i$. In this aspect, the viscous regularization can be described as a slight alteration of the considered problem by imposing a small imbalance at the discontinuity.

5.3 Computation of internal variables

Introduction of viscosity into the finite element changes some equations in the computational procedure as well. Let us first consider the local phase of the operator-split procedure, in which the internal variables of element (e) are computed for the k-th iteration at the pseudo-time point τ_{n+1}, while the nodal displacements are fixed at the values from the previous iteration $\mathbf{d}_{n+1}^{(e),(k-1)}$. Since each internal variable is associated with a single layer of a single element, the computation is performed separately for each layer i.

For the sake of clarity we will omit in the rest of this section the superscript (e), denoting the finite element, and the superscript i, denoting the layer.

Computations, described in sections 4.3.1.1, 4.3.1.2 and 4.3.1.4 of the previous chapter remain the same as before. They concern the shear response and the hardening axial responses of the bulks of concrete and reinforcement layers, which are described by the original rate independent models. On the other hand, the computations associated with the discontinuities alter. The approach remains the same as in the element without viscosity, but some quantities are evaluated by different expressions.

5.3.1 Discontinuity in concrete layer

Here we describe the computational procedure for the softening phase of the concrete layer. The computation is started by assuming an elastic step, which implies that the softening internal variables $\bar{\bar{D}}$ and $\bar{\bar{\xi}}_n^*$ take the values from the previous step. The same is true for the hardening internal variables $\bar{D}$ and $\bar{\xi}$.

$$\bar{D}_{n+1}^{(k)} = \bar{D}_n, \quad \bar{\xi}_{n+1}^{(k)} = \bar{\xi}_n, \quad \bar{\bar{D}}_{n+1}^{(k),trial} = \bar{\bar{D}}_n, \quad \bar{\bar{\xi}}_{n+1}^{*(k),trial} = \bar{\bar{\xi}}_n^* \tag{5.8}$$

The trial value of traction at the discontinuity is defined by expression (5.9), derived in appendix E. The viscous term is expressed in the incremental form by introducing the pseudo-time increase $\Delta\tau_{n+1} = \tau_{n+1} - \tau_n$ from the previous to the current step. The trial value of displacement jump is evaluated according to equation (4.55).

$$t_{n+1}^{(k),trial} = \frac{\check{\mathbf{B}}\mathbf{d}_{n+1}^{(k-1)} + \bar{D}_n \frac{\eta_c}{\Delta\tau_{n+1}} \alpha_n}{\bar{D}_n - \bar{G}\bar{\bar{D}}_n + \bar{D}_n \frac{\eta_c}{\Delta\tau_{n+1}} \bar{\bar{D}}_n}, \quad \alpha_{n+1}^{(k),trial} = \bar{\bar{D}}_n t_{n+1}^{(k),trial} \tag{5.9}$$

The local equilibrium (5.7) determines the trial value of the stress in the bulk. The rate of change of the displacement jump $\dot{\alpha}_{n+1}^{(k),trial}$ is written in the incremental form, see appendix E for details.

$$\sigma_{n+1}^{(k),trial} = t_{n+1}^{(k),trial} + \frac{\eta_c}{\Delta\tau_{n+1}} \left(\alpha_{n+1}^{(k),trial} - \alpha_n \right) \tag{5.10}$$

The trial value of the failure function $\bar{\bar{\phi}}_{n+1}^{(k),trial}$ is computed in the same way as in the previous chapter.

$$\bar{\bar{\phi}}_{n+1}^{(k),trial} = \left| t_{n+1}^{(k),trial} \right| - \left(\sigma_{fc} - \bar{\bar{q}}_{n+1}^{(k),trial} \right), \quad \bar{\bar{q}}_{n+1}^{(k),trial} = \min \left\{ -K_c^* \bar{\bar{\xi}}_{n+1}^{*(k),trial}, \sigma_{fc} \right\} = \bar{\bar{q}}_n \tag{5.11}$$

If $\bar{\bar{\phi}}_{n+1}^{(k),trial} \leq 0$, the trial solution is accepted.

$$\begin{aligned} &\bar{\bar{D}}_{n+1}^{(k)} = \bar{\bar{D}}_{n+1}^{(k),trial}, \quad \bar{\bar{\xi}}_{n+1}^{*(k)} = \bar{\bar{\xi}}_{n+1}^{*(k),trial}, \quad \alpha_{n+1}^{(k)} = \alpha_{n+1}^{(k),trial} \\ &t_{n+1}^{(k)} = t_{n+1}^{(k),trial}, \quad \sigma_{n+1}^{(k)} = \sigma_{n+1}^{(k),trial} \end{aligned} \tag{5.12}$$

If $\bar{\bar{\phi}}_{n+1}^{(k),trial} > 0$, the assumed trial values are inadmissible. We have to compute the softening damage multiplier $\bar{\bar{\gamma}}_{n+1}^{*(k)}$ from equation $\bar{\bar{\phi}}_{n+1}^{(k)} = 0$ in order to compute the new values of internal softening variables, see appendix E.

$$\bar{\bar{\gamma}}_{n+1}^{*(k)} = \frac{\bar{\bar{\phi}}_{n+1}^{(k),trial}\left(\bar{D}_n - \bar{G}\bar{\bar{D}}_n + \bar{D}_n \frac{\eta_c}{\Delta\tau_{n+1}}\bar{\bar{D}}_n\right)}{K_c^* \bar{D}_n - \bar{G} + \bar{D}_n \frac{\eta_c}{\Delta\tau_{n+1}}} \tag{5.13}$$

If $\bar{\bar{q}}_{n+1}^{(k)} = -K_c^*\left(\bar{\bar{\xi}}_n^* + \bar{\bar{\gamma}}_{n+1}^{*(k)}\right) < \sigma_{fc}$, the softening internal variables are updated, using the same equations as in chapter 4, except that $\bar{\bar{\gamma}}_{n+1}^{*(k)}$ has a different value.

$$\alpha_{n+1}^{(k)} = \left(\alpha_n^{\max} + \bar{\bar{\gamma}}_{n+1}^{*(k)}\right) sign\left(t_{n+1}^{(k),trial}\right), \;\; \bar{\bar{\xi}}_{n+1}^{*(k)} = \bar{\bar{\xi}}_n^* + \bar{\bar{\gamma}}_{n+1}^{*(k)}, \;\; \bar{\bar{D}}_{n+1}^{(k)} = \frac{\alpha_{n+1}^{(k)}}{t_{n+1}^{(k)}} = \frac{\alpha_n^{\max} + \bar{\bar{\gamma}}_{n+1}^{*(k)}}{\sigma_{fc} + K_c^* \bar{\bar{\xi}}_{n+1}^{*(k)}} \tag{5.14}$$

Here, $\alpha_n^{\max} = \bar{\bar{D}}_n t_n^{\max} = \bar{\bar{D}}_n\left(\sigma_{fc} + K_c^* \bar{\bar{\xi}}_n^*\right)$ is the maximal elastic value of α for the given carrying capacity that was reached in the last softening step. Traction at the discontinuity and stress in the layer are computed as follows.

$$t_{n+1}^{(k)} = \left(\sigma_{fc} - \bar{\bar{q}}_{n+1}^{(k)}\right) sign\left(t_{n+1}^{(k),trial}\right), \quad \sigma_{n+1}^{(k)} = \bar{D}_n^{-1}\,\bar{\varepsilon}\left(\mathbf{d}_{n+1}^{(k-1)}, \alpha_{n+1}^{(k)}\right) \tag{5.15}$$

If $-K_c^*\left(\bar{\bar{\xi}}_n^* + \bar{\bar{\gamma}}_{n+1}^{*(k)}\right) > \sigma_{fc} = \bar{\bar{q}}_{n+1}^{(k)}$, material has lost all carrying capacity and traction at the discontinuity becomes zero. Note that, due to viscosity, the stress in the bulk is not zero.

$$t_{n+1}^{(k)} = \sigma_{n+1}^{(k)} - \frac{\eta_c}{\Delta\tau_{n+1}}\left(\alpha_{n+1}^{(k)} - \alpha_n\right) = 0 \tag{5.16}$$

From equation (5.16) the displacement jump is computed, see appendix E. The compliance at the discontinuity becomes infinite because the traction has dropped to zero.

$$\alpha_{n+1}^{(k)} = -\frac{\check{\mathbf{B}}\mathbf{d}_{n+1}^{(k-1)} + \bar{D}_n^{-1}\frac{\eta_c}{\Delta\tau_{n+1}}\alpha_n}{\bar{G} - \bar{D}_n^{-1}\frac{\eta_c}{\Delta\tau_{n+1}}}, \quad \bar{\bar{D}}_{n+1}^{(k)} = \frac{\alpha_{n+1}^{(k)}}{t_{n+1}^{(k)}} = \infty \tag{5.17}$$

Since the introduction of viscosity does not modify the constitutive relation at the discontinuity, the values of the tangent modulus $\left(\partial t/\partial\alpha\right)_{n+1}^{(k)}$ remain the same as in the previous chapter.

5.3.2 Discontinuity in reinforcement layer

In this section we describe the computational procedure for the softening phase of the reinforcement layer. We start by assuming an elastic trial solution, keeping the softening internal variables α and $\bar{\bar{\xi}}$ at the values from the previous step. The hardening internal variables $\bar{\varepsilon}_p$ and $\bar{\xi}$ take the values from the last step as well.

$$\bar{\varepsilon}_{p,n+1}^{(k)} = \bar{\varepsilon}_{p,n}, \quad \bar{\xi}_{n+1}^{(k)} = \bar{\xi}_n, \quad \alpha_{n+1}^{(k),trial} = \alpha_n, \quad \bar{\bar{\xi}}_{n+1}^{(k),trial} = \bar{\bar{\xi}}_n \tag{5.18}$$

Stress in the layer and traction at the discontinuity are computed according to equations (4.65) and (5.7), respectively.

$$\begin{aligned} \sigma_{n+1}^{(k),trial} &= E_s \left(\bar{\varepsilon} \left(\mathbf{d}_{n+1}^{(k-1)}, \alpha_{n+1}^{(k),trial} \right) - \bar{\varepsilon}_{p,n} \right) \\ t_{n+1}^{(k),trial} &= \sigma_{n+1}^{(k),trial} - \frac{\eta_s}{\Delta\tau_{n+1}} \underbrace{\left(\alpha_{n+1}^{(k),trial} - \alpha_n \right)}_{=0} = \sigma_{n+1}^{(k),trial} \end{aligned} \tag{5.19}$$

The viscous term $\eta\dot{\alpha}$ is written in the incremental form, as defined in appendix E. The difference in the parenthesis is zero because the displacement jump α is fixed in the trial step (5.18). Next, the trial value of failure function $\bar{\bar{\phi}}_{n+1}^{(k),trial}$ is computed in the same way as in the previous chapter.

$$\bar{\bar{\phi}}_{n+1}^{(k),trial} = \left| t_{n+1}^{(k),trial} \right| - \left(\sigma_{fs} - \bar{\bar{q}}_{n+1}^{(k),trial} \right), \quad \bar{\bar{q}}_{n+1}^{(k),trial} = \min \left\{ -K_s \bar{\bar{\xi}}_{n+1}^{(k),trial}, \sigma_{fs} \right\} = \bar{\bar{q}}_n \tag{5.20}$$

If $\bar{\bar{\phi}}_{n+1}^{(k),trial} \leq 0$, the trial solution is accepted.

$$\alpha_{n+1}^{(k)} = \alpha_{n+1}^{(k),trial}, \quad \bar{\bar{\xi}}_{n+1}^{(k)} = \bar{\bar{\xi}}_{n+1}^{(k),trial}, \quad \sigma_{n+1}^{(k)} = \sigma_{n+1}^{(k),trial}, \quad t_{n+1}^{(k)} = t_{n+1}^{(k),trial} \tag{5.21}$$

If $\bar{\bar{\phi}}_{n+1}^{(k),trial} > 0$, the assumed solution is inadmissible. The plastic softening multiplier $\bar{\bar{\gamma}}_{n+1}^{(k)}$ must be computed from $\bar{\bar{\phi}}_{n+1}^{(k)} = 0$, in order to update the softening internal variables. The procedure is shown in appendix E.

$$\bar{\bar{\gamma}}_{n+1}^{(k)} = \begin{cases} \bar{\bar{\gamma}}_{n+1}^{A} = \dfrac{\bar{\bar{\phi}}_{n+1}^{(k),trial}}{-\bar{G}E_s + K_s + \frac{\eta_s}{\Delta\tau_{n+1}}}; & -K_s \left(\bar{\bar{\xi}}_n + \bar{\bar{\gamma}}_{n+1}^{A} \right) < \sigma_{fs} \\ \bar{\bar{\gamma}}_{n+1}^{B} = \dfrac{\left| t_{n+1}^{(k),trial} \right|}{-\bar{G}E_s + \frac{\eta_s}{\Delta\tau_{n+1}}}; & -K_s \left(\bar{\bar{\xi}}_n + \bar{\bar{\gamma}}_{n+1}^{A} \right) > \sigma_{fs} \end{cases} \tag{5.22}$$

The internal variables are updated in the same way as before, except that $\bar{\bar{\gamma}}_{n+1}^{(k)}$ takes a different value.

$$\alpha_{n+1}^{(k)} = \alpha_n + \bar{\bar{\gamma}}_{n+1}^{(k)} sign \left(t_{n+1}^{(k),trial} \right), \quad \bar{\bar{\xi}}_{n+1}^{(k)} = \bar{\bar{\xi}}_n + \bar{\bar{\gamma}}_{n+1}^{(k)} \tag{5.23}$$

The stress in the bulk and the traction at the discontinuity can finally be calculated.

$$\sigma_{n+1}^{(k)} = E_s \left(\bar{\varepsilon} \left(\mathbf{d}_{n+1}^{(k-1)}, \alpha_{n+1}^{(k)} \right) - \bar{\varepsilon}_{p,n} \right), \quad t_{n+1}^{(k)} = \left(\sigma_{fs} - \bar{\bar{q}}_{n+1}^{(k)} \right) sign \left(t_{n+1}^{(k),trial} \right) \tag{5.24}$$

Since the introduction of viscosity does not modify the constitutive relation at the discontinuity, the values of the tangent modulus $\left(\partial t / \partial \alpha \right)_{n+1}^{(k)}$ remain the same as in the previous chapter.

5.4 Computation of nodal degrees of freedom

Let us now consider the global phase of the operator-split procedure. Here, the linearized form of global equilibrium equations (5.6) is solved to provide the update of the nodal displacements in the k-th iteration at pseudo-time point τ_{n+1}, while the internal variables are fixed at the values, calculated in the local phase of the same iteration.

Introduction of the viscous regularization hardly affects the global phase of the computation. The equilibrium equations are linearized in exactly the same way as in section 4.3.2.1 of the previous chapter. The only difference is that the quantity $h_{n+1}^{(e),i,(k)}$ is replaced by $h_{\text{reg},n+1}^{(e),i,(k)}$, which depends on $\dot{\alpha}_{n+1}^{(e),i,(k)}$ as well.

$$h_{\text{reg},n+1}^{(e),i,(k)}\left(\mathbf{d}_{n+1}^{(e),(k-1)},\alpha_{n+1}^{(e),i,(k)},\dot{\alpha}_{n+1}^{(e),i,(k)}\right)=h_{n+1}^{(e),i,(k)}\left(\mathbf{d}_{n+1}^{(e),(k-1)},\alpha_{n+1}^{(e),i,(k)}\right)+\eta^i\dot{\alpha}_{n+1}^{(e),i,(k)}A^i \tag{5.25}$$

The pseudo-time derivative $\dot{\alpha}_{n+1}^{(e),i,(k)}$ is expressed in the incremental form as a function of displacement jump $\alpha_{n+1}^{(e),i,(k)}$, as defined in appendix E.

$$\dot{\alpha}_{n+1}^{(e),i,(k)}=\frac{\alpha_{n+1}^{(e),i,(k)}-\alpha_n^{(e),i}}{\Delta\tau_{n+1}},\qquad \frac{\partial\dot{\alpha}_{n+1}^{(e),i,(k)}}{\partial\alpha_{n+1}^{(e),i,(k)}}=\frac{1}{\Delta\tau_{n+1}} \tag{5.26}$$

The stiffness matrix $\mathbf{K}_{n+1}^{(e),(k)}$ of finite element (e), defined in equation (4.134), is computed by the same expression. The term $\hat{\mathbf{K}}_{n+1}^{(e),i,(k)}$ is defined in equation (4.133).

$$\mathbf{K}_{n+1}^{(e),(k)}=\sum_{i=1}^{n_{CL}^{(e)}}\left(\mathbf{K}_{n+1}^{fd,(e),i,(k)}-\mathbf{K}_{n+1}^{f\alpha,(e),i,(k)}\left(K_{n+1}^{h\alpha,(e),i,(k)}\right)^{-1}\mathbf{K}_{n+1}^{hd,(e),i,(k)}\right)+\sum_{i=n_{CL}^{(e)}+1}^{n_L}\mathbf{K}_{n+1}^{fd,(e),i,(k)} \tag{5.27}$$

However, the components must be computed in accordance with the modified equilibrium equations (5.6). The difference arises with the components $\mathbf{K}_{n+1}^{hd,(e),i,(k)}$ and $K_{n+1}^{h\alpha,(e),i,(k)}$, which are now defined as derivatives of $h_{\text{reg},n+1}^{(e),i,(k)}$ over the nodal displacements of the element $\mathbf{d}_{n+1}^{(e),(k-1)}$ and the displacement jump in the i-th layer $\alpha_{n+1}^{(e),i,(k)}$, respectively.

$$\mathbf{K}_{n+1}^{hd,(e),i,(k)}=\frac{\partial h_{\text{reg},n+1}^{(e),i,(k)}}{\partial\mathbf{d}_{n+1}^{(e),(k-1)}}=\frac{\partial h_{n+1}^{(e),i,(k)}}{\partial\mathbf{d}_{n+1}^{(e),(k-1)}}+\underbrace{\frac{\partial\dot{\alpha}_{n+1}^{(e),i,(k)}}{\partial\mathbf{d}_{n+1}^{(e),(k-1)}}}_{=0}\eta^iA^i=\frac{\partial h_{n+1}^{(e),i,(k)}}{\partial\mathbf{d}_{n+1}^{(e),(k-1)}} \tag{5.28}$$

The additional viscous term in (5.25) does not depend on the nodal displacements, so $\mathbf{K}_{n+1}^{hd,(e),i,(k)}$ is computed in exactly the same way as in chapter 4. The only modified term of the stiffness matrix is therefore $K_{n+1}^{h\alpha,(e),i,(k)}$.

$$K_{n+1}^{h\alpha,(e),i,(k)}=\frac{\partial h_{\text{reg},n+1}^{(e),i,(k)}}{\partial\alpha_{n+1}^{(e),i,(k)}}=\frac{\partial h_{n+1}^{(e),i,(k)}}{\partial\alpha_{n+1}^{(e),i,(k)}}+\underbrace{\frac{\partial\dot{\alpha}_{n+1}^{(e),i,(k)}}{\partial\alpha_{n+1}^{(e),i,(k)}}}_{=1/\Delta\tau_{n+1}}\eta^iA^i=\frac{\partial h_{n+1}^{(e),i,(k)}}{\partial\alpha_{n+1}^{(e),i,(k)}}+\frac{\eta^i}{\Delta\tau_{n+1}}A^i \tag{5.29}$$

Let us rewrite the components of the element stiffness matrix, defined in equation (4.136), taking into account the corrected term (5.29).

$$
\begin{aligned}
\mathbf{K}_{n+1}^{fd,(e),i,(k)} &= \frac{\partial \mathbf{f}_{n+1}^{\text{int},(e),i,(k)}}{\partial \mathbf{d}_{n+1}^{(e),(k-1)}} = \left(\breve{\mathbf{B}}^{i\,T} \left. \frac{\partial \sigma}{\partial \bar{\varepsilon}} \right|_{n+1}^{(e),i,(k)} \underbrace{\breve{\mathbf{B}}^{i}}_{\partial \bar{\varepsilon}/\partial \mathbf{d}} + \breve{\mathbf{B}}^{*\,T} \left. \frac{\partial \tau}{\partial \gamma} \right|_{n+1}^{(e),i,(k)} \underbrace{\breve{\mathbf{B}}^{*}}_{\partial \gamma/\partial \mathbf{d}} \right) A^i L \\
\mathbf{K}_{n+1}^{f\alpha,(e),i,(k)} &= \frac{\partial \mathbf{f}_{n+1}^{\text{int},(e),i,(k)}}{\partial \alpha_{n+1}^{(e),i,(k)}} = \left(\breve{\mathbf{B}}^{i\,T} \left. \frac{\partial \sigma}{\partial \bar{\varepsilon}} \right|_{n+1}^{(e),i,(k)} \underbrace{\bar{G}^{i}}_{\partial \bar{\varepsilon}/\partial \alpha} \right) A^i L \\
\mathbf{K}_{n+1}^{hd,(e),i,(k)} &= \frac{\partial h_{\text{reg},n+1}^{(e),i,(k)}}{\partial \mathbf{d}_{n+1}^{(e),(k-1)}} = \left(- \left. \frac{\partial \sigma}{\partial \bar{\varepsilon}} \right|_{n+1}^{(e),i,(k)} \underbrace{\breve{\mathbf{B}}^{i}}_{\partial \bar{\varepsilon}/\partial \mathbf{d}} \right) A^i \\
K_{n+1}^{h\alpha,(e),i,(k)} &= \frac{\partial h_{\text{reg},n+1}^{(e),i,(k)}}{\partial \alpha_{n+1}^{(e),i,(k)}} = \left(- \left. \frac{\partial \sigma}{\partial \bar{\varepsilon}} \right|_{n+1}^{(e),i,(k)} \underbrace{\bar{G}^{i}}_{\partial \bar{\varepsilon}/\partial \alpha} + \left. \frac{\partial t}{\partial \alpha} \right|_{n+1}^{(e),i,(k)} \right) A^i + \frac{\eta^i}{\Delta \tau_{n+1}} A^i
\end{aligned}
\tag{5.30}
$$

As we have already mentioned in previous sections, introduction of viscosity does not affect the constitutive equations, so the tangent moduli in equations (5.30) stay unchanged. The remaining operations of the global computation are performed identically to the previous chapter.

Remark. *Even though the internal forces of the finite element are computed by exactly the same equations, they evaluate to a (slightly) different value than in the case without viscosity. This is due to the modified computation of stress in the local phase of the operator-split procedure.*

5.5 Numerical examples

Performance of the modified multi-layer Timoshenko beam element is tested on basic numerical examples – pure tension/compression and pure bending. The computer code of the element has been implemented in the finite element program AceFEM [69].

5.5.1 One element tension and compression tests

In this section we consider a beam clamped at one end. At the free end, axial displacement is imposed to produce either pure tension or pure compression. The beam is modeled with a single finite element, therefore no benefits of viscous regularization are expected. The purpose of this test is to examine the influence of viscosity on the results.

5.5.1.1 Concrete beam

We consider the concrete beam of rectangular cross-section, described in section 4.4.1.1 of the previous chapter. We model it with one finite element with two layers. The geometry and the material data are: beam length is $L = 2.5\text{m}$, cross-section width is $b = 0.2\text{m}$, cross-section height is $h = 0.5\text{m}$, elastic modulus is $E_c = 4 \times 10^7 \text{kNm}^{-2}$, elasticity limit in compression is $\sigma_{dc} = 40820\text{kNm}^{-2}$, limit strength in compression is $\sigma_{fcc} = 44902\text{kNm}^{-2}$, hardening modulus in compression is $H_{cc} = 2 \times 10^6 \text{kNm}^{-2}$, softening modulus in compression is $K_{cc}^{*} = -5.2 \times 10^6 \text{kNm}^{-3}$, limit strength in tension is $\sigma_{fct} = 4000\text{kNm}^{-2}$, and softening modulus in tension is $K_{ct}^{*} = -8 \times 10^6 \text{kNm}^{-3}$. By setting $\sigma_{dt} > \sigma_{fct}$ we assume no damage of the bulk in tension before crack formation. The additional viscosity parameters for concrete in compression and tension are marked with η_{cc} and η_{ct}, respectively. They have units $\left[\text{kNm}^{-3}\text{s}\right]$.

We impose the axial displacement u at the free end of the beam and compute the resulting axial force F for different values of the viscosity parameters η_{cc} and η_{ct}. Since the model is rate dependent, the loading speed must be prescribed. We impose a unit displacement in a unit of pseudo-time (meter/second).

Remark. *The chosen loading speed* $1\mathrm{m}/\mathrm{s}$ *is not realistic, but that is not important, because we are dealing with pseudo-time. Here, viscosity is not used as a material model, but as a computational aid. In this view, it could be called pseudo-viscosity. Identical results would be computed if the loading speed was changed e.g. to* $1\mathrm{m}/\mathrm{h}$ *and the units (only units, not the numbers) of the viscosity parameters were changed from* $\mathrm{kNm}^{-3}\mathrm{s}$ *to* $\mathrm{kNm}^{-3}\mathrm{h}$.

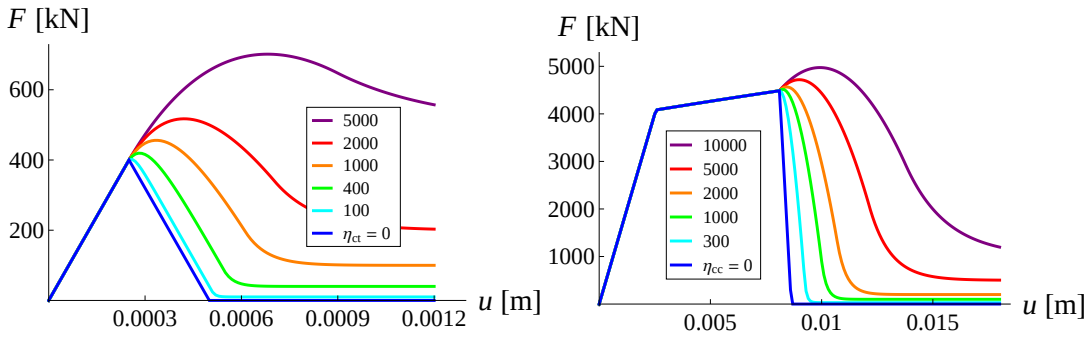

Figure 5.1: *Axial force - displacement* diagrams for concrete beam in pure tension (left) and pure compression (right) for different values of viscosity parameter.

Slika 5.1: Diagram *osna sila - pomik* za betonski nosilec v čistem nategu (levo) in čistem tlaku (desno) za različne vrednosti viskoznega parametra.

The results are presented in Fig. 5.1. If values of the viscosity parameters are zero, the diagrams are identical to those in figure 4.17. With increasing values of η_{cc} and η_{ct}, the results begin to deviate from the original (correct) response. The deviation occurs in the softening range, caused by the imbalance between the stress in the bulk σ and the traction at the discontinuity t. For great values of η, the computed response exceeds considerably the original ultimate force, the softening line is shifted to the right, and the stress in the bulk is non-zero, even when the discontinuity fails completely. Of course, such values of viscosity parameter are too big for realistic analysis, and are applied here for illustration purpose only. For sufficiently small η, the error is negligible.

5.5.1.2 Steel beam

We analyze the steel beam, presented in section 4.4.1.2 of the previous chapter. We model it with one element with two layers. The material and the geometrical data is: beam length is $L = 2.5\mathrm{m}$, cross-sections of both layers are $A_{s,1} = A_{s,2} = 0.001\mathrm{m}^2$, distances of layer axes from the beam middle axis are $h/2 - a_{s,1} = h/2 - a_{s,2} = 0.21\mathrm{m}$ ($a_{s,1} = a_{s,2} = 0.04\mathrm{m}$), elastic modulus is $E_s = 2 \times 10^8 \mathrm{kNm}^{-2}$, elasticity limit is $\sigma_y = 4 \times 10^5 \mathrm{kNm}^{-2}$, failure strength is $\sigma_{fs} = 5 \times 10^5 \mathrm{kNm}^{-2}$, hardening modulus is $H_s = 10^7 \mathrm{kNm}^{-2}$, and softening modulus is $K_s = -5 \times 10^7 \mathrm{kNm}^{-3}$. The additional viscosity parameter with units $\left[\mathrm{kNm}^{-3}\mathrm{s}\right]$ is marked with η_s.

We impose the axial displacement u at the free end of the beam and compute the resulting axial force F for different values of η_s. We impose a unit displacement in a unit of pseudo-time (meter/second).

Results of the analysis are presented in Fig. 5.2. We observe a similar behavior as in concrete in compression, see Fig. 5.1 (right). The elasto-plastic hardening response is not affected, since the viscosity only takes effect when a discontinuity appears. In the softening range the force F rises above the original ultimate force, it drops at higher value of the imposed displacement u, and finishes at a permanent non-zero value. When the value of η_s approaches zero, these effects vanish and the diagram eventually matches the one in figure 4.20.

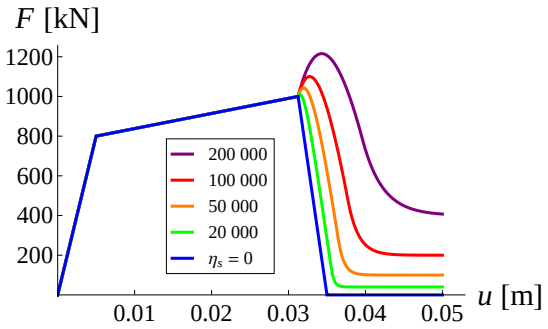

Figure 5.2: *Axial force - displacement* diagram for steel beam (layer) in pure tension for different values of viscosity parameter.

Slika 5.2: Diagram *osna sila - pomik* za jekleni nosilec (sloj) v čistem nategu za različne vrednosti viskoznega parametra.

5.5.2 Tension and compression tests on a mesh of several elements

We repeat the above described uniaxial tests, now modeling the beams with several identical finite elements. We demonstrate the mesh dependency of original results (without viscosity) and examine how they are affected by introduction of viscosity.

5.5.2.1 Concrete beam in compression

In this example we analyze a concrete beam in pure compression. The geometrical and the material properties are listed in section 5.5.1.1. The beam is modeled with different number of identical finite elements, each consisting of two concrete layers. The axial displacement u of the free end of the beam is imposed at a rate of one meter per one pseudo-second, and the axial force F is computed. At first, the viscous regularization is excluded by setting the parameter η_{cc} to zero. Results for this case are shown in Fig. 5.3. We observe the typical mesh dependent response in the softening phase, caused by simultaneous occurrence of multiple discontinuities in the beam. The mesh dependency can be cured by slightly weakening one of the finite elements, as presented in previous chapters. Thus only the weak element softens and the response diagrams match the "1FE" curve for all meshes.

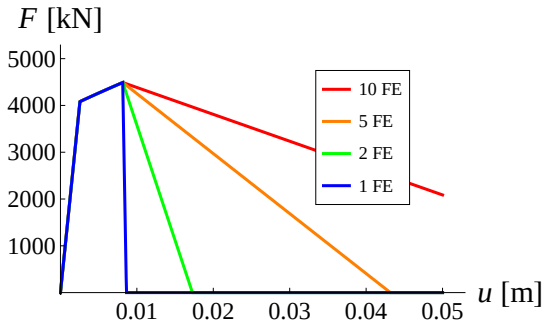

Figure 5.3: *Axial force - displacement* diagram for concrete beam in pure compression for different meshes of finite elements - without viscosity.

Slika 5.3: Diagram *osna sila - pomik* za betonski nosilec v čistem tlaku za različne mreže končnih elementov - brez viskoznosti.

In this analysis, however, we keep all finite elements the same, and introduce viscous regularization. We perform the analysis on a mesh of 5 identical elements. The results for different values of viscosity parameter η_{cc} are presented in Fig. 5.4. For values of the parameter up to $\eta_{cc} \approx 130\text{kNm}^{-3}\text{s}$, the computed response matches the "5FE" curve from Fig. 5.3. With further increase of η_{cc}, the results approach the correct response, Fig. 5.4 (left). The best results are obtained for $\eta_{cc} \approx 260\text{kNm}^{-3}\text{s}$. If the viscosity parameter is still increased, the results worsen again, Fig. 5.4 (right), and we already observe the unwanted side effects, namely the exceeded ultimate force and non-zero force after the complete failure of the beam. Signs of the side effects can be seen in the left image, as well. The softening line of the curve $\eta_{cc} = 260\text{kNm}^{-3}\text{s}$ is not as steep as the correct "1FE" curve in Fig. 5.3. It resembles the curve $\eta_{cc} = 300\text{kNm}^{-3}\text{s}$ in Fig. 5.1 (right).

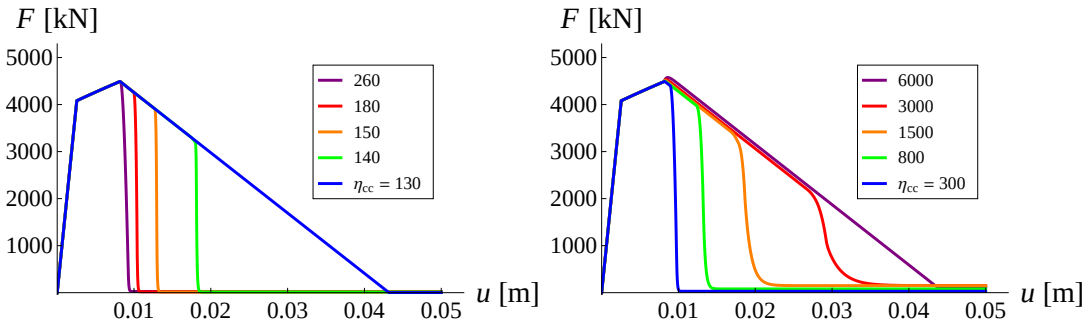

Figure 5.4: *Axial force - displacement* diagram for concrete beam in pure compression for different values of viscosity parameter (5 FE mesh).

Slika 5.4: Diagram *osna sila - pomik* za betonski nosilec v čistem tlaku za različne vrednosti viskoznega parametra (mreža s 5 KE).

In the softening phase, the regularized diagram follows the original curve for a while, until the slope changes suddenly and the force F decreases rapidly. This sudden change of slope coincides with the moment when viscosity causes one of the finite elements to become "preferred". Only the "preferred" element continues to soften, while the others unload elastically. The mechanism of this phenomenon briefly described next.

Let us consider two finite elements from the mesh, and denote them with A and B. If, due to numerical error, one of them develops a displacement jump α at a slightly faster rate than the other $\dot{\alpha}^A > \dot{\alpha}^B$, this results in a slightly higher value of the viscous stress $\eta\dot{\alpha}^A > \eta\dot{\alpha}^B$. Since the bulk stress σ has to be the same in all elements to preserve equilibrium $\sigma^A = \sigma^B$, it follows that $t^A < t^B$, which further increases α^A and $\dot{\alpha}^A$. Of course, numerical errors affect the equality $\sigma^A = \sigma^B$ as well, but the general idea still holds. Fast advancement of a discontinuity further stimulates its growth, while slow advancement inhibits its development. When enough of these micro errors accumulate, one of the elements breaks out, i.e. increases the displacement jump so fast that the others cannot follow. The remaining elements must unload elastically to preserve equilibrium.

5.5.2.2 Steel beam

We consider a steel beam in pure tension. The material and the geometrical properties are listed in section 5.5.1.2. The axial displacement u of the free end of the beam is imposed at a rate of one meter per one pseudo-second and the resulting axial force F is computed. Fig. 5.5 shows the results for different finite element meshes, if no viscous regularization is used. This is achieved by setting the viscosity parameter η_s to zero. We can see the typical mesh dependent response, caused by simultaneous softening of all finite elements. If one of the elements were slightly weakened, the results of all meshes would match the correct "1FE" curve.

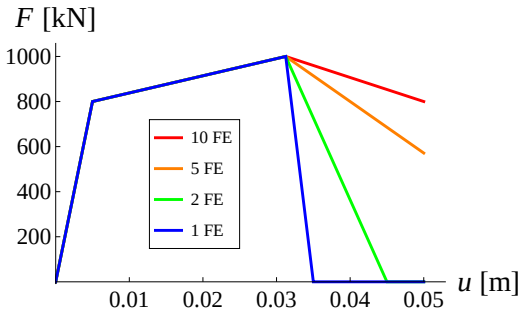

Figure 5.5: *Axial force - displacement* diagram for steel beam (layer) in pure tension for different meshes of finite elements - without viscosity.

Slika 5.5: Diagram *osna sila - pomik* za jekleni nosilec (sloj) v čistem nategu za različne mreže končnih elementov - brez viskoznosti.

The influence of viscous regularization is tested on the mesh of 5 identical elements. Results of the analysis for different values of the viscosity parameter are shown in Fig. 5.6. Some resemblance to Fig. 5.4 is observed, namely the computed response approaches the correct curve "1FE" from Fig. 5.5, when η_s is increased up to $\eta_s \approx 13000\text{kNm}^{-3}\text{s}$. If the parameter is still increased, the results worsen again. The correct curve is never quite reached. Nevertheless the diagram computed with $\eta_s = 13000\text{kNm}^{-3}\text{s}$ is much better than the non-regularized diagram "5FE" in Fig. 5.5.

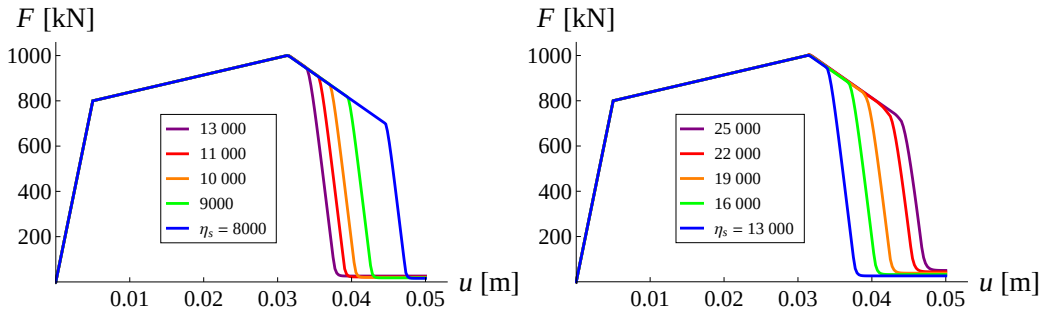

Figure 5.6: *Axial force - displacement* diagram for steel beam (layer) in pure tension for different values of viscosity parameter (5 FE mesh).

Slika 5.6: Diagram *osna sila - pomik* za jekleni nosilec v čistem nategu za različne vrednosti viskoznega parametra (mreža s 5 KE).

5.5.3 Cantilever beam under end moment

In this example we consider a cantilever beam of rectangular cross-section, already analyzed in section 4.4.2 of the previous chapter. The length of the beam is $L = 1\text{m}$, the width and height of the cross-section are $b = 0.3\text{m}$ and $h = 0.4\text{m}$. Bottom and top reinforcements are $A_{s,1} = A_{s,2} = 0.001256\text{m}^2$ and they are positioned at $a_1 = a_2 = 0.05\text{m}$ from the edges of the concrete cross-section. Material properties of concrete are: elasticity modulus $E_c = 3.3 \times 10^7\text{kNm}^{-2}$, elasticity limit $\sigma_{dc} = 15200\text{kNm}^{-2}$, ultimate stress in compression $\sigma_{fcc} = 38000\text{kNm}^{-2}$, ultimate stress in tension $\sigma_{fct} = 1815\text{kNm}^{-2}$, hardening modulus in compression $H_{cc} = 3.32 \times 10^7\text{kNm}^{-2}$, softening modulus in compression $K^*_{cc} = -5 \times 10^6\text{kNm}^{-3}$ and softening modulus in tension $K^*_{ct} = -10^6\text{kNm}^{-3}$. Material properties of steel are: elasticity modulus $E_s = 2 \times 10^8\text{kNm}^{-2}$, yield stress $\sigma_y = 4 \times 10^5\text{kNm}^{-2}$, ultimate stress $\sigma_{fs} = 5 \times 10^5\text{kNm}^{-2}$, hardening modulus $H_s = 2.665 \times 10^6\text{kNm}^{-2}$ and softening modulus $K_s = -5 \times 10^7\text{kNm}^{-3}$.

We impose the rotation θ at the free end of the beam at a rate of one radian per one pseudo-second and calculate the corresponding moment M. The beam is modeled with different number of equal finite elements, each consisting of ten concrete layers and two reinforcement layers. Fig. 5.7 shows the results of the analysis for different meshes, if no viscous regularization is applied. This is achieved by assigning zero value to viscosity parameters η_s, η_{cc} and η_{ct}. As observed already in the previous chapter, the model exhibits mesh dependent response, most evident in the last phase of the analysis, when the beam as a whole begins to soften, due to softening of tensile reinforcement. In chapter 4 the problem was treated by slightly weakening the reinforcement in one of the finite elements. The intervention cured the major mesh dependency in the last part of the diagram, but the lesser deviations in the yield plateau, caused by softening of concrete in tension, remain unsolved.

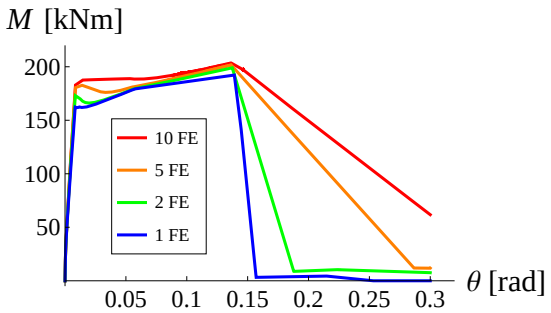

Figure 5.7: *Moment - rotation* diagram for cantilever beam under end moment for different meshes of finite elements - without viscosity.

Slika 5.7: Diagram *moment - zasuk* za konzolo, obteženo z momentom, za različne mreže končnih elementov - brez viskoznosti.

Here, we deal with the mesh dependency problem in a different way. The finite elements are kept identical, but the viscous regularization of the softening response is introduced. The influence of viscosity is examined on the 5 FE mesh. The results of the analysis for different values of viscosity parameter of steel η_s are presented in Fig. 5.8. The viscosity parameters of concrete η_{cc} and η_{ct} were zero in this computation. Similarly to examples in section 5.5.2, the results improve while the viscosity parameter increases up to $\eta_s \approx 5000\text{kNm}^{-3}\text{s}$. If the parameter is further increased, the beneficial effect of viscosity fades and the unwanted side effects occur.

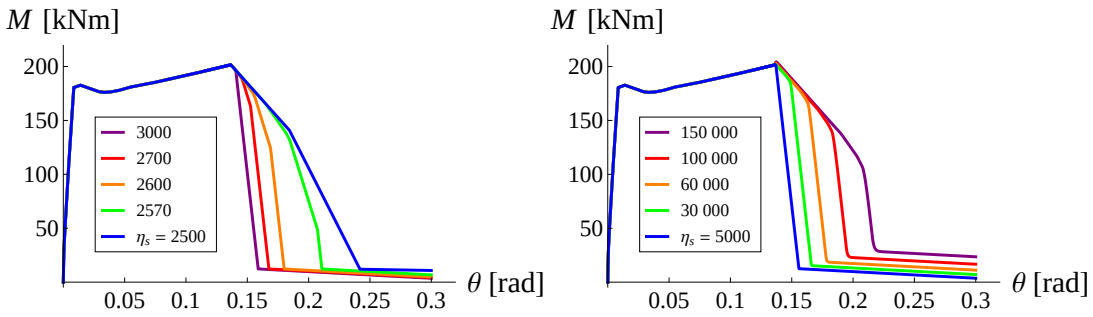

Figure 5.8: *Moment - rotation* diagram for cantilever beam under end moment for different values of viscosity parameter (5 FE mesh).

Slika 5.8: Diagram *moment - zasuk* za konzolo, obteženo z momentom, za različne vrednosti viskoznega parametra (mreža s 5 KE).

The major mesh dependency in the softening part of the $M-\theta$ diagram in Fig. 5.7 can be prevented by viscous regularization of the softening response of steel. However, the minor mesh dependency in the yield plateau of the beam cannot be cured. Even if viscosity is introduced into tensile softening of concrete and one of the tensile concrete layers becomes "preferred", the others cannot elastically unload. Their deformation is dictated by the rest of the cross-section, which is still gaining strength as a whole.

5.6 Concluding remarks

We have presented in this chapter an upgrade for the multi-layer Timoshenko beam finite element with layer-wise embedded discontinuities in axial displacement, so as to include viscous regularization of the softening response. This is achieved by introducing at each discontinuity a viscous force, depending on the rate of change of the displacement jump and on the additional viscosity parameter η.

The viscosity is implemented by adding the viscous force in the virtual work equation, which results in a modified local equilibrium between the stress in the bulk of the layer and the traction at the discontinuity. The two quantities are no longer equal, but differ for the value of the viscous force (stress). The global equilibrium equations remain the same. Kinematic and constitutive equations are not affected either. The computational procedure is only slightly modified. New expressions for softening multiplier, traction at the discontinuity and displacement jump, which are required in the local computation of internal variables, are provided. The global computation of the nodal degrees of freedom remains unchanged, except for an additional viscous term in the element stiffness matrix. Due to the rate dependent nature of the regularization method, specification of the loading speed is required in the analysis.

Influence of viscosity is examined on single element tension/compression tests of concrete and steel beams. Large values of the viscosity parameter substantially increase the ultimate load, shift the softening line to the right, and enforce non-zero axial force in a fully softened beam. These undesired effects are a consequence of an excessive imbalance between the bulk stress and the traction at the discontinuity. The effects are negligible for sufficiently small values of η.

Tension/compression tests of concrete and steel beams, modeled with several identical finite elements, show that applying viscous regularization can prevent mesh dependency in the softening response of the beam. Effectiveness of the method depends on the value of viscosity parameter η. Results approach the correct diagram, if η is increased up to a certain value. A further increase reduces the beneficial effects of viscosity and amplifies the unwanted side effects. The optimal value of the parameter is not unique. It depends e.g. on the chosen load (time) increment (without changing the loading speed).

The last numerical example considers pure bending of a reinforced concrete beam, modeled with a mesh of equal finite elements. It exhibits major mesh dependency in the softening range, caused by softening of tensile reinforcement, and minor mesh dependency in the yield plateau, caused by softening of concrete in tension. The former can be prevented by viscous regularization, similarly to the uniaxial tests. The latter, however, cannot be avoided, because the tensile concrete layers cannot deform freely. Their deformation is dictated by the rest of the cross-section, which is still gaining strength in that moment.

The viscous regularization requires only minor changes of the existing multi-layer Timoshenko beam finite element and is therefore fairly simple to implement. The method can prevent mesh dependency in the softening response of a structural element, but its efficiency depends on the viscosity parameter. For the considered numerical examples, the same can be achieved by weakening one of the elements, which is simpler and independent of any parameter.

6 CONCLUSIONS

The aim of the dissertation was to develop finite elements capable of modeling localized failure in reinforced concrete, for numerical analysis of reinforced concrete beams and frames up to complete collapse. The localized failure was modeled in accordance with the embedded strong discontinuity approach, in which a discontinuity in displacement (or rotation) is incorporated into the finite element, resulting in discontinuous displacement (or rotation) field.

We have derived a stress-resultant Euler-Bernoulli beam finite element with embedded discontinuity in rotation, based on small deformation kinematics, elastoplastic model with bilinear hardening for the bulk of the element, and rigid plastic linear softening model for the discontinuity.

- Despite its simplicity, the finite element is capable of describing the major phenomena in reinforced concrete beam behavior - reduction of stiffness due to cracking of concrete, yielding of reinforcement and localized failure of the beam.
- The finite element allows for analysis of reinforced concrete beams and frames up to complete failure, which provides information not only about the ultimate load, but also about ductility and post-peak response of the structure.
- The obtained results compare reasonably well to other results available in literature and to experimental results.
- The finite element provides mesh independent softening response of the modeled structure.
- Moment vs. curvature diagram for the bulk and moment vs. rotational jump diagram for the discontinuity are required as an input for the analysis. They can be determined from an experiment or computed with a more refined finite element.
- The finite element could be further upgraded by implementing a coupled damage-plasticity model for the bulk or by including a discontinuity in axial displacements, but for the common reinforced concrete structures, improvement of the results should not be substantial.

We have derived a multi-layer Euler-Bernoulli beam finite element with layer-wise embedded discontinuities in axial displacement, based on small deformation kinematics. The reinforced concrete beam is divided into concrete and reinforcement layers, and a jump in axial displacement is introduced separately into each of them. Behavior of a concrete layer is controlled by an elasto-damage hardening law in the bulk and by a rigid damage softening law at the discontinuity. Behavior of a steel layer is controlled by an elastoplastic hardening law in the bulk and by a rigid plastic softening law at the discontinuity.

- The finite element was intended for detailed analysis of reinforced concrete beams and frames, and for computation of stress-resultant properties, required as an input in the stress-resultant analysis. However, the element does not perform as expected. Several issues have been identified.
- The interpolation function for enhanced layer strain has been derived on an isolated layer, under assumption that it can deform freely. This is not true because the layer is bound to other layers through common nodal displacements. Consequently, the additional stress caused by enhanced kinematics cannot redistribute correctly. The stress is only controlled at the discontinuity, where it has to be equal to the traction at the discontinuity and therefore has to decrease with increasing displacement jump. Elsewhere in the layer, the stress may even grow above the ultimate stress.

- Equilibrium is only required on the finite element level, but not for each individual layer. We have seen an example of a beam in pure tension, where stress was linear (not constant) over the length of each layer. If a layer were singled out, it would not be in equilibrium, but the finite element as a whole is in balance because the imbalances of individual layers neutralize each other.
- The displacement jumps of individual layers are independent of each other. In a specific case of a cantilever beam in pure tension, the values of displacement jumps changed linearly over the height of the beam (negative on the bottom edge, positive on the top edge and zero in the middle), resulting in a non-zero lateral displacement of the free end of the beam, without disrupting equilibrium (the internal shear forces and internal moments were zero).
- There is no discontinuity (in rotation) on the element level. The middle axis of the beam always deforms according to standard Euler-Bernoulli kinematics and is therefore smooth, even if the beam is completely broken. The bulk of each layer slides along a path, parallel to the middle axis. This may not be problematic if a fine mesh is used, since the broken finite element exhibits a greater curvature than the neighboring elements, which can be interpreted as a discontinuity smeared over the whole element.
- Mesh dependency has been observed in numerical tests, most clearly in the case of a cantilever beam under end moment. Due to constant stress state over the length of the beam, discontinuities appear simultaneously in all finite elements of the mesh. At the same imposed rotation of the free end of the beam, a fine mesh produces a great number of small discontinuities and a coarse mesh produces a small number of great discontinuities. According to the softening material law, the traction at the discontinuity drops with its increasing size. Therefore, the fine mesh produces a greater moment then the coarse mesh at the same value of imposed rotation. The greatest deviations appear when the beam as a whole enters the softening phase, which usually happens due to softening of tensile reinforcement. This can be cured by slightly weakening reinforcement in one of the finite elements and thus preventing multiple discontinuities. If the beam fails due to crushing of concrete in compression, the problem cannot be solved so effectively. Also, the (lesser) mesh dependency due to cracking of concrete in tension cannot be avoided.
- Considering all the deficiencies, the considered multi-layer Euler-Bernoulli beam finite element cannot be recommended for general use. The only viable application is in case of constant strain/stress state over the length of the beam, which can occur either in pure tension/compression or in pure bending. In case of bending, mesh dependency cannot be completely avoided.

We have derived a multi-layer Timoshenko beam finite element with layer-wise embedded discontinuities in axial displacement, based on small deformation kinematics. The reinforced concrete beam is divided into concrete and reinforcement layers, and a jump in axial displacement is introduced separately into each of them. Behavior of a concrete layer is controlled by an elasto-damage hardening law in the bulk and by a rigid damage softening law at the discontinuity. Behavior of a steel layer is controlled by an elastoplastic hardening law in the bulk and by a rigid plastic softening law at the discontinuity. Shear response is assumed elastic.

- The finite element allows for detailed analysis of reinforced concrete beams and frames up to complete failure, which provides information not only about the ultimate load, but also about ductility and post-peak response of the structure. A detailed description of material state (progression of damage, plasticity and localized failures) is provided at any stage of the analysis.
- The finite element is not intended for cyclic loading. Nevertheless, it can handle minor changes of the load sign, which can occur due to shifting of the neutral axis even in monotonic loading.
- Two material laws are required for each material - stress vs. strain for the bulk of the layer and traction vs. displacement jump for the discontinuity. They can be determined from tension/compression tests. This makes the finite element appropriate for computation of stress-resultant (material-geometrical) properties of beams, required as an input in the analysis with a stress-resultant finite element.

- Mesh dependency has been observed in numerical tests, most clearly in the case of a cantilever beam under end moment. Due to constant stress state over the length of the beam, discontinuities appear simultaneously in all finite elements of the mesh. At the same imposed rotation of the free end of the beam, a fine mesh produces a great number of small discontinuities and a coarse mesh produces a small number of great discontinuities. According to the softening material law, the traction at the discontinuity drops with its increasing size. Therefore, the fine mesh produces a greater moment then the coarse mesh at the same value of imposed rotation. The greatest deviations appear when the beam as a whole enters the softening phase, which usually happens due to softening of tensile reinforcement. This can be cured by slightly weakening reinforcement in one of the finite elements and thus preventing multiple discontinuities. If the beam fails due to crushing of concrete in compression, the problem cannot be solved so effectively. Also, the mesh dependency due to cracking of concrete in tension cannot be avoided.
- Mesh dependency due to cracking of concrete in tension is more evident in the case of a cantilever beam under end transversal force. Since the finite element can only describe constant state over the length, a fine mesh is required for adequate description of the linear moment. However, shortening of the finite elements increases the number and reduces the size of discontinuities, resulting in a higher traction in tensile concrete and considerably overestimated yield moment of the beam.
- There is no discontinuity (in rotation) on the element level. The middle axis of the beam always deforms according to standard Euler-Bernoulli kinematics and is therefore smooth, even if the beam is completely broken. The bulk of each layer slides along a path, parallel to the middle axis. This may not be problematic if a fine mesh is used, since the broken finite element exhibits a greater curvature than the neighboring elements, which can be interpreted as a discontinuity smeared over the whole element.
- Performance of the finite element has been tested on several numerical examples. In some cases, the computed results compare well to other results available in literature and to experimental results. In some cases, however, the difference was considerable.
- Before the finite element is put to general use, the mesh dependency, caused by softening of concrete in tension, should be examined carefully. In the specific case of a cantilever under end force, the influence was substantial. However, in some more complex structures, the mesh dependency was less noticeable.
- The finite element could be modified so as to allow cyclic loading. For that purpose, separate sets of softening internal variables should be introduced. However, softening responses in tension and compression are not independent, neither is their relation trivial to describe.

We have upgraded the multi-layer Timoshenko beam finite element, so as to include viscous regularization of the softening response. This is performed by introducing at each discontinuity a viscous force, depending on the rate of change of the displacement jump and an additional viscosity parameter. The viscous forces are added in the virtual work equation, resulting in slightly modified equilibrium equations and consequent minor alterations of the computational procedure.

- Viscous regularization is relatively simple to implement, as it only requires minor changes of the existing multi-layer Timoshenko beam finite element.
- Great values of the viscosity parameter can corrupt the results of the analysis by increasing the ultimate load, shifting the softening line (delaying the softening) and producing a non-zero stress state in a beam with a fully softened discontinuity. The effects are negligible for sufficiently small values of the parameter.
- Viscous regularization can prevent mesh dependent softening response of a beam, caused by physically erroneous occurrence of multiple discontinuities in a homogeneous stress field. However, effectiveness of the regularization depends on the value of the viscosity parameter. The optimal value is not unique, as it depends e.g. on the chosen load (time) increment.

- Mesh dependency, caused by softening of concrete in tension when the beam as a whole is still gaining strength, cannot be prevented by this method because the softening concrete layers cannot deform freely. Their deformation is dictated by the rest of the cross-section.

RAZŠIRJENI POVZETEK

V gradbeništvu se uporablja mnogo materialov, ki ob določeni obremenitvi lokalno odpovejo. Za lokalizirano porušitev je značilno, da je večji del deformacij zgoščenih na relativno majhnih območjih v okolici kritičnih mest konstrukcije. Z njihovim naraščanjem se napetosti v materialu zmanjšujejo, čemur pravimo mehčanje materiala. Pravilen opis tega pojava je bistvenega pomena v porušni analizi konstrukcij.

V disertaciji se osredotočimo na armiranobetonske nosilce in okvirje, ki so ena prevladujočih konstrukcijskih oblik pri nas in po svetu. V armiranem betonu se lokalizirana porušitev pojavi kot posledica pokanja betona v nategu in krušenja v tlaku, tečenja armature, medsebojnega zdrsa obeh komponent in njune lokalne odpovedi. Te lokalizirane poškodbe materiala, ki jih opazimo npr. na vrhu in na dnu stebrov stavb, poškodovanih v potresih, običajno opišemo s plastičnim členkom. V klasični analizi mejne nosilnosti moment v posameznem členku ohranja isto vrednost, medtem ko se z naraščanjem obremenitve oblikujejo novi členki drugod po konstrukciji. Tak pristop omejuje natančnost določene mejne nosilnosti ter preprečuje analizo duktilnosti konstrukcije in njenega post-kritičnega obnašanja. V statično nedoločenih konstrukcijah porušitev posameznega kritičnega elementa še ne ogrozi celotne konstrukcije, zato je za njeno natančno analizo potrebno poznati tudi odziv elementa v mehčanju.

V zadnjem času smo priča znatnemu napredku na področju modeliranja mehčanja v numerični analizi konstrukcij, vendar precej problemov še vedno ostaja odprtih. Pregled zgodovinskega razvoja in trenutnega stanja na tem področju najdemo npr. v [12–14]. V prvih modelih je bilo mehčanje materiala opisano lokalno, s padajočo krivuljo v diagramu napetost-deformacija. Pristop je sicer enostaven, vendar ga pestijo številne težave, ki jih lahko opredelimo kot matematične, fizikalne in numerične. Z matematičnega vidika postanejo parcialne diferencialne enačbe robnega problema slabo pogojene zaradi negativnega elastičnega modula v območju mehčanja [12, 15, 16]. V konstrukcijskem elementu, diskretiziranem z mrežo končnih elementov, odpove le kritični element. Ker je sipanje energije vezano na prostornino materiala, kjer poteka mehčanje, se količina disipirane energije z zgoščevanjem mreže končnih elementov približuje vrednosti nič. V limitni situaciji to pomeni porušitev brez disipacije energije, kar fizikalno ni sprejemljivo. Z vidika numeričnega modeliranja tak pristop očitno vodi do izrazite odvisnosti rezultatov od izbrane diskretizacije [17, 18].

Za rešitev opisanih težav je bilo predlaganih več pristopov. Nekaj zgodnejših je predstavljenih v [19]. Zelo enostavni so t.i. "crack-band" modeli [20–22], v katerih je lokalizirana porušitev razmazana na celoten končni element in porušitev brez disipacije energije preprečena z omejitvijo minimalne velikosti elementov. Ker je volumen, v katerem se material mehča, še vedno odvisen od diskretizacije, je potrebno vrednost modula mehčanja prilagoditi izbrani mreži. Sorodno rešitev predstavljajo modeli, pri katerih je znotraj elementa predpisan pas fiksne širine (materialna karakteristika), v katerem se material mehča [23, 24]. Omenjene metode ne rešijo matematične plati problema.

Kot alternativa je bilo predstavljenih več ne-lokalnih metod [19,25–27], pri katerih je napetost v neki točki funkcija povprečne (ne-lokalne) deformacije v nekem končnem volumnu okoli te točke. Bolj splošno je napetost v posamezni točki funkcija celotnega deformacijskega polja, pri čemer je vplivno območje določeno z utežnimi funkcijami. Z matematičnega vidika ne-lokalne metode popolnoma regularizirajo obravnavani problem [12]. Zelo sorodna je gradientna metoda [28, 29], pri kateri za opis napetosti v neki točki poleg vrednosti deformacij uporabimo tudi njihov gradient v tisti točki. Uporabimo lahko tudi gradiente višjega reda [30].

Predlaganih je bilo še več pristopov, kot sta na primer model Cosseratovega kontinuuma [31, 32], ki poleg translatornega pomika upošteva tudi lokalno rotacijo posameznega delca (točke) materiala, in viskoplastična regularizacija [33], ki obravnava problem kot časovno odvisen. Skupno vsem naštetim metodam je, da se lotevajo opisa lokalizirane porušitve in mehčanja na nivoju materiala. Končni elementi so zasnovani tako, da čim natančneje

opišejo obnašanje materiala na mikro nivoju, vključno s samodejnim generiranjem nezveznosti na kritičnih mestih, in tako zagotovijo primeren odziv konstrukcijskega elementa na makro nivoju.

Pri razvoju končnih elementov za uporabo v potresnem inženirstvu se pogosto uporablja popolnoma drugačen pristop. Numerična analiza velikih konstrukcij pod kompleksno obtežbo, lahko kaj hitro postane računsko prezahtevna in časovno potratna, zato so končni elementi zasnovani na najenostavnejši način, ki še zagotavlja primeren makro-odziv konstrukcijskega elementa. Obnašanje armiranobetonskih stebrov, ki izkazujejo lokalizirane poškodbe na dnu in na vrhu, lahko zadovoljivo opišemo z zelo enostavnim "lumped plasticity" modelom [34, 35], pri katerem so vse neelastične deformacije združene v plastičnih členkih ničelne dolžine na obeh koncih elementa, medtem ko se vmesni del obnaša elastično. To seveda ne ustreza dejanskemu stanju materiala, kljub temu pa model zajame vse bistvene lastnosti odziva stebra.

Diskretni pristop, uporabljen v "lumped plasticity" in sorodnih modelih je alternativa predhodno predstavljenim zveznim modelom. Obe strani imata svoje prednosti in slabosti. Glavna prednost modelov razmazane nezveznosti je, da so razviti na mikro nivoju, zato so sposobni opisati katerikoli košček materiala, ne glede na velikost in položaj v konstrukciji, nezveznost pa generirajo samodejno. Slaba stran je ta, da zahtevajo precej gosto mrežo končnih elementov v območju nezveznosti, kar je lahko problematično pri analizi večjih konstrukcij [12, 36]. Nekateri imajo tudi težave z blokiranjem [13, 36]. Pomembna prednost diskretnega pristopa je, da se izogne težavam z velikostjo območja mehčanja, tako da ga skrči v točko in vpelje lokalni disipativni mehanizem. Poleg tega so elementi sposobni opisati nezveznosti v pomikih in zasukih, kar omogoča opis konstrukcije z dokaj grobo mrežo končnih elementov. Glavna slabost je ta, da se nezveznosti lahko pojavijo le na predhodno določenih lokacijah.

V zadnjem času se je v modeliranju lokalizirane porušitve uveljavil nov pristop, katerega glavna značilnost je vključitev nezveznih deformacij ali pomikov v standardne končne elemente. Skoke v deformacijskem polju imenujemo tudi šibke nezveznosti, skoke v polju pomikov pa močne nezveznosti. V skladu z metodo vgrajene močne nezveznosti, ki jo uporabimo tudi v tej disertaciji, je bilo razvitih mnogo različnih modelov, npr. [39–48]. Za nas je posebej zanimiva aplikacija metode na linijske končne elemente [49–54]. Vsem modelom je skupno, da končni volumen lokaliziranih deformacij, ki je predstavljal območje disipiranja energije pri modelih razmazane nezveznosti, nadomestijo z nezveznostjo v pomikih in s pripadajočim lokalnim disipativnim mehanizmom. To dosežejo z vpeljavo dodatnih, nezveznih interpolacijskih funkcij. Vsaka oblikovna funkcija je povezana z dodatnim parametrom, ki predstavlja velikost nezveznosti. Z vpeljavo kohezivnega materialnega zakona mehčanja, ki skok v pomiku poveže s konjugirano silo v nezveznosti, se oblikuje lokalni disipativni mehanizem. Dodatne enačbe za nove parametre so zapisane v obliki lokalnega ravnotežja med napetostmi po elementu in silo (ali napetostjo) v nezveznosti [1, 14].

Metoda vgrajene močne nezveznosti združuje dobre lastnosti tako diskretnih, kot zveznih metod. Disipacija energije ob porušitvi je vezana na nezveznost, ki nima volumna, zato zgoščevanje mreže končnih elementov ne vpliva na velikost območja mehčanja in na količino disipirane energije. S tem sta preprečeni odvisnost rezultatov od diskretizacije in fizikalno nerealna porušitev brez disipacije energije. Tudi z matematičnega vidika je problem mejnih vrednosti dobro pogojen, kar pomeni, da pristop uspešno reši na začetku predstavljene fizikalne, numerične in matematične težave. Izboljšana kinematika omogoča korekten opis nezveznega polja pomikov v bližini nezveznosti, kar omogoča razvoj končnih elementov, ki nimajo težav z blokiranjem. Dodatne interpolacijske oblike so namreč zasnovane tako, da omogočajo opis breznapetostnega stanja v elementu v primeru popolnoma zmehčane nezveznosti [14]. Poleg tega vgraditev lokalne kinematike, ki opisuje porušitev materiala na mikro nivoju, v materialni makro-model popolnoma ustreza več-nivojski naravi obravnavnega fizikalnega problema [1, 12, 14, 36, 40] in omogoča modeliranje nezveznosti z relativno grobo mrežo končnih elementov. Ker je vsak posamezen element sposoben opisa nezveznosti, ni potrebe po vnaprejšnjem določanju njene lokacije. Nastane samodejno in napreduje po konstrukciji brez spreminjanja osnovne mreže končnih elementov. Zaradi naštetih lastnosti je metoda primerna tudi za analizo večjih konstrukcij.

Glede na način implementacije nezveznosti ločimo dva glavna pristopa – *extended finite element method* (X-FEM) [39,40,42,57–59] in *embedded discontinuity finite element method* (ED-FEM) [41,60–63]. Pri X-FEM metodah so dodatni parametri, ki se nanašajo na nezvezne interpolacijske funkcije, vezani na vozlišča mreže končnih elementov in se jih obravnava kot globalne neznanke. Pri ED-FEM metodah pa so dodatni parametri na posamezen končni element in se jih obravnava kot lokalne (elementu lastne) neznanke. Prednosti in slabosti obeh pristopov so predstavljene v več študijah [14,64]. Glavna prednost ED-FEM je v tem, da lahko dodatne neznanke izločimo iz globalnih enačb s statično kondenzacijo na nivoju elementa, medtem ko pri X-FEM vsaka nova nezveznost razširi globalni sistem enačb. V disertaciji sledimo ED-FEM pristopu.

Naloga temelji predvsem na predhodnem delu naše raziskovalne skupine, zlasti na linijskih končnih elementih, ki so jih razvili Dujc et al. [54] in Pham et al. [52]. V prvem članku je predstavljen končni element na nivoju rezultant napetosti za Euler-Bernoullijev nosilec, ki ima vgrajeni nezveznosti v zasuku in v osnem pomiku in je namenjen analizi metalnih nosilcev in okvirjev. V drugem članku je opisan končni element na nivoju rezultant napetosti za Timošenkov nosilec, ki ima vgrajeno nezveznost v zasuku in je namenjen analizi armiranobetonskih konstrukcij. Prvi cilj disertacije je združiti oba koncepta in razviti podoben končni element, ki temelji na Euler-Bernoullijevi kinematiki in uporablja materialne zakone, primerne za modeliranje armiranega betona. Naslednji cilj je razširiti ta koncept na večslojni model nosilca, podobno kot v [51]. Bolj konkretno lahko naše cilje opredelimo kot:

- razviti raven končni element na nivoju rezultant napetosti za ravninski Euler-Bernoullijev nosilec z vgrajeno nezveznostjo v zasuku, namenjen enostavni robustni in učinkoviti porušni analizi armiranobetonskih nosilcev in okvirjev,
- razviti raven večslojni končni element za ravninski Euler-Bernoullijev nosilec, ki ima po slojih vgrajene nezveznosti v osnem pomiku, namenjen detajlni porušni analizi armiranobetonskih nosilcev in okvirjev ter računu rezultantnih (materialno-geometrijskih) lastnosti prerezov, potrebnih pri analizi z rezultantnimi končnimi elementi,
- razviti raven večslojni končni element za ravninski Timošenkov nosilec, ki ima po slojih vgrajene nezveznosti v osnem pomiku, namenjen detajlni porušni analizi armiranobetonskih nosilcev in okvirjev ter računu rezultantnih (materialno-geometrijskih) lastnosti prerezov, potrebnih pri analizi z rezultantnimi končnimi elementi,
- nadgraditi večslojni element za Timošenkov nosilec z viskozno regularizacijo odziva v mehčanju.

KONČNI ELEMENT NA NIVOJU REZULTANT NAPETOSTI ZA EULER-BERNOULLIJEV NOSILEC Z VGRAJENO NEZVEZNOSTJO V ZASUKU

V poglavju 2 razvijemo končni element na nivoju rezultant napetosti z vgrajeno nezveznostjo v zasuku za ravninski Euler-Bernoullijev nosilec. Element je namenjen za enostavno, robustno in učinkovito numerično analizo armiranobetonskih nosilcev in okvirjev do popolne porušitve. Element omogoča samodejno generiranje plastičnih členkov z mehčanjem, ki predstavljajo lokalizirano porušitev materiala na kritičnih mestih v konstrukciji. Element temelji na dveh podobnih končnih elementih, predstavljenih v [54] in [52]. V prvem članku je izpeljan končni element za Euler-Bernoullijev nosilec z vgrajenima nezveznostma v zasuku in osnem pomiku za analizo metalnih nosilcev in okvirjev. V drugem članku je predstavljen element za Timošenkov nosilec z vgrajeno nezveznostjo v zasuku, v katerem je uporabljen konstitutivni zakon z bilinearnim utrjevanjem, ki omogoča natančnejši opis nelinearnega obnašanja nosilca zaradi razpokanja betona in tečenja armature. Element je zato primeren za analizo armiranobetonskih konstrukcij, vendar zaradi izbrane kinematike omogoča le opis konstantnega momenta. Tu razvijemo končni element, ki združuje lastnosti obeh navedenih elementov - konstitutivni zakon, primeren za armirani beton, in kinematiko, ki omogoča opis linearnih momentov vzdolž elementa.

Končni element temelji na teoriji majhnih deformacij. Vsebuje vgrajeno nezveznost v zasuku (skok v zasuku), ki se pojavi na kritičnem mestu v elementu, ko je presežena mejna nosilnost. Obnašanje materiala je opisano z elastoplastičnim materialnim zakonom z bilinearnim izotropnim utrjevanjem, obnašanje nezveznosti (plastičnega členka) pa z materialnim zakonom linearnega mehčanja.

Kinematika

Ravninski Euler-Bernoullijev nosilec modeliramo z ravnim dvovozliščnim končnim elementom. Vsako vozlišče ime tri prostostne stopnje, dva pomika in zasuk. V primeru prekoračene nosilnosti se pojavi nezveznost v zasukih pri koordinati x_d in aktivira se dodatna (lokalna) prostostna stopnja - skok v zasuku α. Osni pomik $u(x)$ interpoliramo med vozliščne osne pomike $\mathbf{u}$ s standardnimi linearnimi oblikovnimi funkcijami $\mathbf{N}^u(x)$. Osno deformacijo $\varepsilon(x)$ izračunamo kot odvod osnega pomika.

$$u(x) = \mathbf{N}^u(x)\,\mathbf{u}, \quad \varepsilon(x) = \frac{\partial u}{\partial x} = \mathbf{B}^u(x)\,\mathbf{u}$$

Prečni pomik $v(x)$ interpoliramo med vozliščne prečne pomike $\mathbf{v}$ in zasuke $\boldsymbol{\theta}$ s Hermitovimi polinomi $\mathbf{N}^v(x)$ in $\mathbf{N}^\theta(x)$. Standardni interpolaciji dodamo člen $v^{add}(x,x_d)$, ki opisuje dodatne pomike zaradi skoka v zasuku. Odvod interpolacijske funkcije $\hat{M}(x,x_d)$ ima enotski skok pri x_d, vozliščne vrednosti funkcije in njenega odvoda pa so enake nič.

$$v(x,x_d) = \mathbf{N}^v(x)\,\mathbf{v} + \mathbf{N}^\theta(x)\,\boldsymbol{\theta} + \overbrace{\hat{M}(x,x_d)\,\alpha}^{v^{add}}$$

Ukrivljenost $\kappa(x,x_d)$ izračunamo kot drugi odvod prečnega pomika.

$$\kappa(x,x_d) = \frac{\partial^2 v}{\partial x^2} = \overbrace{\mathbf{B}^v(x)\,\mathbf{v} + \mathbf{B}^\theta(x)\,\boldsymbol{\theta}}^{\tilde{\bar{\kappa}}} + \overbrace{G(x,x_d)\,\alpha}^{\kappa^{add}}$$

Operator $G(x,x_d)$ je drugi odvod interpolacijske funkcije $\hat{M}(x,x_d)$. Zaradi nezveznosti prvega odvoda $\hat{M}'$ je G sestavljen iz zveznega dela $\bar{G}$ in Dirac-delta funkcije, ki ima neskončno vrednost na mestu nezveznosti in vrednost nič drugje. Izraz za $\bar{G}$ izpeljemo iz zahteve, da mora biti v primeru popolne izgube nosilnosti končni element sposoben opisati breznapetostno stanje v nosilcu. V tem primeru se element deformira kot kinematična veriga dveh togih teles.

$$G = \hat{M}'' = \bar{G} + \bar{\bar{G}}, \qquad \bar{G} = -\frac{1 + 3\left(1 - \frac{2x_d}{L}\right)\left(1 - \frac{2x}{L}\right)}{L}, \qquad \bar{\bar{G}} = \delta_{x_d} = \begin{cases} \infty; & x = x_d \\ 0; & \text{sicer} \end{cases}$$

Interpolacijo osne deformacije in standardnega dela ukrivljenosti lahko zapišemo tudi krajše.

$$\varepsilon = \begin{bmatrix} \mathbf{B}^u & \mathbf{0} & \mathbf{0} \end{bmatrix} \mathbf{d} = \breve{\mathbf{B}}^\varepsilon \mathbf{d}, \quad \tilde{\bar{\kappa}} = \begin{bmatrix} \mathbf{0} & \mathbf{B}^v & \mathbf{B}^\theta \end{bmatrix} \mathbf{d} = \breve{\mathbf{B}}^\kappa \mathbf{d}, \quad \mathbf{d}^T = \left\{ \mathbf{u}^T, \mathbf{v}^T, \boldsymbol{\theta}^T \right\}$$

Princip virtualnega dela

Virtualno osno deformacijo $\hat{\varepsilon}$ in virtualno ukrivljenost $\hat{\kappa}$ interpoliramo na enak način kot pravi količini, med virtualne vozliščne pomike $\hat{\mathbf{u}}$, $\hat{\mathbf{v}}$ in $\hat{\boldsymbol{\theta}}$ ter virtualni skok v zasuku $\hat{\alpha}$. To pripelje do dodatnega člena v izrazu za virtualno delo notranjih sil $G^{\text{int},(e)}$ elementa (e).

$$\hat{\varepsilon} = \mathbf{B}^u \hat{\mathbf{u}}, \quad \hat{\kappa} = \mathbf{B}^v \hat{\mathbf{v}} + \mathbf{B}^\theta \hat{\boldsymbol{\theta}} + \underbrace{G\hat{\alpha}}_{\hat{\kappa}^{add}}, \quad G^{\text{int},(e)} = \int_L (\hat{\varepsilon} N + \hat{\kappa} M)\, dx = \underbrace{\hat{\mathbf{d}}^{(e)^T} \mathbf{f}^{\text{int},(e)}}_{\text{standardno}} + \underbrace{\hat{\alpha}^{(e)} h^{(e)}}_{\text{dodatno}}$$

Vektor posplošenih virtualnih pomikov $\hat{\mathbf{d}}^{(e)}$ združuje vse virtualne prostostne stopnje elementa (e), vektor $\mathbf{f}^{\text{int},(e)}$ pa ustrezno urejene notranje sile. Količina $h^{(e)}$ ustreza virtualnemu skoku v zasuku $\hat{\alpha}^{(e)}$.

$$\hat{\mathbf{d}}^{(e)^T} = \left\{ \hat{\mathbf{u}}^T, \hat{\mathbf{v}}^T, \hat{\boldsymbol{\theta}}^T \right\}, \quad \mathbf{f}^{\text{int},(e)} = \int_L \breve{\mathbf{B}}^{\varepsilon^T} N dx + \int_L \breve{\mathbf{B}}^{\kappa^T} M dx, \quad h^{(e)} = \int_L G M dx$$

Z upoštevanjem prej izpeljanega izraza za operator G in pravila za integriranje Dirac-delta funkcije razvijemo izraz za $h^{(e)}$. Moment $M(x)$ je funkcija koordinate x. Njeno vrednost na mestu nezveznosti $M|_{x_d}$ označimo s t in definiramo kot moment v nezveznosti, ki je konjugirana količina skoku v zasuku α.

$$\int_L g(x)\, \delta_{x_d} dx = g(x_d), \quad h^{(e)} = \int_L \left(\bar{G} + \delta_{x_d}\right) M dx = \int_L \bar{G} M dx + M|_{x_d} = \int_L \bar{G} M dx + t$$

Iz principa virtualnega dela $G^{\text{int}} - G^{\text{ext}} = 0$ izpeljemo ravnotežne enačbe konstrukcije. Poleg klasičnega globalnega ravnotežja zunanjih in notranjih sil dobimo dodatno ravnotežno enačbo za vsak element, v katerem je bila nosilnost prekoračena in se je oblikovala nezveznost v zasukih.

$$\mathop{\mathsf{A}}_{e=1}^{n_{FE}} \left[\mathbf{f}^{\text{int},(e)} - \mathbf{f}^{\text{ext},(e)} \right] = \mathbf{0}, \qquad \forall e \in \{1, 2, \ldots, n_\alpha\} : \;\; h^{(e)} = 0$$

Tu je A tako imenovani "assembly" operator, n_{FE} število končnih elementov v celotni konstrukciji, n_α pa število končnih elementov z aktivirano nezveznostjo. Pomen dodatne enačbe se razjasni, če vanjo vstavimo izpeljani izraz za $h^{(e)}$. Ugotovimo, da predstavlja ravnotežje med momentom v nezveznosti t in momenti po elementu M v šibki (integralski) obliki. Ker se nanaša le na posamezen končni element, ji pravimo tudi enačba lokalnega ravnotežja.

$$h^{(e)} = 0 \quad \Leftrightarrow \quad t = -\int_L \bar{G} M dx$$

Materialni modeli

Predpostavimo, da je osna sila ves čas elastična $N = EA\varepsilon$. Za upogibni odziv nosilca uporabimo elastoplastični model z bilinearnim utrjevanjem. Po doseženi meji elastičnosti togost nekoliko pade zaradi poškodb v betonu, bistven padec togosti pa se zgodi zaradi tečenja natezne armature. Krivulja razbremenjevanja ima elastični naklon. Osnovne enačbe materialnega modela so izpeljane iz termodinamike (princip maksimalne plastične disipacije), glej npr. [73]. Moment izračunamo iz elastične ukrivljenosti, ki je razlika med skupno ukrivljenostjo $\bar{\kappa}$ in plastično ukrivljenostjo $\bar{\kappa}_p$. V izrazu za skupno ukrivljenost nastopa tudi prispevek zaradi skoka v zasuku α.

$$M = EI\,(\bar{\kappa} - \bar{\kappa}_p)\,, \quad \bar{\kappa} = \mathbf{B}^v\mathbf{v} + \mathbf{B}^\theta\boldsymbol{\theta} + \bar{G}\alpha$$

Funkcija tečenja $\bar{\phi}$ nadzira prehod iz elastičnega v plastično obnašanje in obratno. Konstanta $M_c > 0$ predstavlja absolutno vrednost momenta, pri katerem se prvič pojavijo neelastične deformacije. Momentu podobna količina $\bar{q} \leq 0$ predstavlja spremembo meje elastičnosti zaradi utrjevanja materiala in je bilinearna funkcija ukrivljenosti podobne spremenljivke $\bar{\xi}$.

$$\bar{\phi}\,(M, \bar{q}) = |M| - (M_c - \bar{q})\,, \quad \bar{q} = \bar{q}\left(\bar{\xi}\right)$$

Potrebujemo še evolucijski enačbi za notranji spremenljivki $\bar{\kappa}_p$ in $\bar{\xi}$ ter Kuhn-Tuckerjeve pogoje obremenjevanja in razbremenjevanja. Tu je $\dot{\gamma}$ plastični množitelj, ki izhaja iz izpeljave enačb s principom maksimalne plastične disipacije.

$$\dot{\bar{\kappa}}_p = \dot{\gamma}\, sign\,(M)\,, \quad \dot{\bar{\xi}} = \dot{\gamma}, \qquad \dot{\gamma} \geq 0, \quad \bar{\phi} \leq 0, \quad \dot{\gamma}\,\bar{\phi} = 0, \quad \dot{\gamma}\,\dot{\bar{\phi}} = 0$$

Podobne enačbe določajo togo-plastičen materialni model, ki povezuje moment v nezveznosti t in skok v zasuku α. Po doseženi meji nosilnosti $M_u > 0$ se začne moment t linearno zmanjševati z naraščanjem α, dokler ne pade na nič (ob tem mu morajo slediti tudi momenti po elementu M). V primeru razbremenjevanja vrednost α miruje.

$$\bar{\bar{\phi}}\,(t, \bar{\bar{q}}) = |t| - (M_u - \bar{\bar{q}})\,, \quad \bar{\bar{q}} = \bar{\bar{q}}\left(\bar{\bar{\xi}}\right)$$

Funkcija $\bar{\bar{\phi}}$ nadzira prehod iz elastičnega obnašanja v mehčanje in obratno. Momentu podobna količina $\bar{\bar{q}} \in [0, M_u]$ predstavlja zmanjšanje nosilnosti zaradi mehčanja materiala in je linearna funkcija zasuku podobne spremenljivke $\bar{\bar{\xi}}$. Materialni model zaokrožimo z evolucijskima enačbama za notranji spremenljivki α in $\bar{\bar{\xi}}$ ter s pogoji obremenjevanja in razbremenjevanja, kjer je $\dot{\bar{\bar{\gamma}}}$ plastični množitelj mehčanja, ki izhaja iz izpeljave enačb s principom maksimalne plastične disipacije.

$$\dot{\alpha} = \dot{\bar{\bar{\gamma}}}\, sign\,(t)\,, \quad \dot{\bar{\bar{\xi}}} = \dot{\bar{\bar{\gamma}}}, \qquad \dot{\bar{\bar{\gamma}}} \geq 0, \quad \bar{\bar{\phi}} \leq 0, \quad \dot{\bar{\bar{\gamma}}}\,\bar{\bar{\phi}} = 0, \quad \dot{\bar{\bar{\gamma}}}\,\dot{\bar{\bar{\phi}}} = 0$$

Računski postopek

Odziv konstrukcije izračunamo tako, da pri posameznih psevdo-časih, ki predstavljajo postopno nanašanje obtežbe, rešimo sistem ravnotežnih enačb, pri čemer moramo zadostiti tudi kinematičnim in konstitutivnim enačbam. Ker so enačbe izrazito nelinearne, jih v vsakem psevdo-časovnem koraku $n+1$ linearizirамo in rešujemo iterativno. Vsaka Newtonova iteracija k sestoji iz faze (A), v kateri zamrznemo trenutne vrednosti vozliščnih pomikov in posodobimo vrednosti notranjih spremenljivk, in faze (B), v kateri zamrznemo pravkar izračunane vrednosti notranjih spremenljivk in izračunamo nove prirastke vozliščnih pomikov.

$$\text{Pri znanih } \left\{\mathbf{d}_n^{(e)};\quad \bar{\kappa}_{p,n}^{(e)},\, \bar{\xi}_n^{(e)},\, \alpha_n^{(e)},\, \bar{\bar{\xi}}_n^{(e)}\right\} \quad \text{iščemo } \left\{\mathbf{d}_{n+1}^{(e)};\quad \bar{\kappa}_{p,n+1}^{(e)},\, \bar{\xi}_{n+1}^{(e)},\, \alpha_{n+1}^{(e)},\, \bar{\bar{\xi}}_{n+1}^{(e)}\right\}.$$

Faza (A) je lokalnega značaja, in jo izvajamo na nivoju končnega elementa. Pri zamrznjenih vrednostih pomikov $\mathbf{d}_{n+1}^{(e),(k-1)}$ iz prejšnje iteracije iščemo pripadajoče iterativne vrednosti notranjih spremenljivk in momentov, ki jih potrebujemo za račun v fazi (B). Dokler element ne doseže meje nosilnosti, sta notranji spremenljivki mehčanja α in $\bar{\bar{\xi}}$ enaki nič in iščemo samo notranji spremenljivki utrjevanja $\bar{\kappa}$ in $\bar{\xi}$. Ko se nezveznost enkrat aktivira, se $\bar{\kappa}$ in $\bar{\xi}$ ne spreminjata več, računamo pa α in $\bar{\bar{\xi}}$. V vsakem primeru je postopek enak. Najprej predpostavimo elastičen testni korak, kar pomeni, da notranje spremenljivke obdržijo vrednosti iz prejšnjega koraka. Izračunamo testni vrednosti momenta in funkcije tečenja. Če je le-ta negativna, je bila predpostavka pravilna in obdržimo testne rezultate. V nasprotnem primeru notranje spremenljivke posodobimo skladno z evolucijskimi enačbami in pogoji obremenjevanja in razbremenjevanja. Izračunamo končno vrednost momenta, ki ga potrebujemo za izračun notranjih sil končnega elementa.

$$\mathbf{K}_{n+1}^{\text{str},(k)}\Delta\mathbf{d}_{n+1}^{\text{str},(k)} = \Delta\mathbf{f}_{n+1}^{\text{str},(k)}, \quad \mathbf{K}_{n+1}^{\text{str},(k)} = \mathop{\mathsf{A}}_{e=1}^{n_{FE}}\left[\mathbf{K}_{n+1}^{(e),(k)}\right], \quad \Delta\mathbf{f}_{n+1}^{\text{str},(k)} = \mathop{\mathsf{A}}_{e=1}^{n_{FE}}\left[\mathbf{f}_{n+1}^{\text{ext},(e)} - \mathbf{f}_{n+1}^{\text{int},(e),(k)}\right]$$

V fazi (B) rešimo zgornji linearizirani sistem ravnotežnih enačb, v katerem iščemo prirastke pomikov konstrukcije $\Delta\mathbf{d}_{n+1}^{\text{str},(k)}$. Operator A sestavi prispevke posameznih elementov v togostno matriko $\mathbf{K}_{n+1}^{\text{str},(k)}$ in rezidual $\Delta\mathbf{f}_{n+1}^{\text{str},(k)}$ celotne konstrukcije. Togostne matrike posameznih elementov izračunamo z naslednjima izrazoma.

$$\begin{aligned}
&e \in \{1,2,\ldots,n_{P\alpha}\}: && \mathbf{K}_{n+1}^{(e),(k)} = \mathbf{K}_{n+1}^{fd,(e),(k)} - \mathbf{K}_{n+1}^{f\alpha,(e),(k)}\left(K_{n+1}^{h\alpha,(e),(k)}\right)^{-1}\mathbf{K}_{n+1}^{hd,(e),(k)}\\
&e \in \{n_{P\alpha}+1,\ldots,n_{FE}\}: && \mathbf{K}_{n+1}^{(e),(k)} = \mathbf{K}_{n+1}^{fd,(e),(k)}
\end{aligned}$$

Tu je n_{FE} število vseh končnih elementov v konstrukciji, $n_{P\alpha}$ pa število elementov, ki so že prekoračili nosilnost in so trenutno v plastičnem koraku mehčanja. Pri elementih, ki so že vstopili v mehčanje opazimo dodaten člen, ki nastopi zaradi izločitve spremenljivk $\alpha_{n+1}^{(e),(k)}$ iz globalnega sistema enačb s kondenzacijo lokalnih ravnotežnih enačb $h_{n+1}^{(e),(k)} = 0$. Pri elementih, ki so že aktivirali nezveznost, vendar se trenutno elastično razbremenjujejo ($\Delta\alpha = 0$), je dodatni člen enak nič. Posamezni členi togostne matrike končnega elementa so definirani s spodnjimi enačbami.

$$\begin{aligned}
\mathbf{K}_{n+1}^{fd,(e),(k)} &= \frac{\partial\mathbf{f}_{n+1}^{\text{int},(e),(k)}}{\partial\mathbf{d}_{n+1}^{(e),(k-1)}}, \qquad \mathbf{K}_{n+1}^{f\alpha,(e),(k)} = \frac{\partial\mathbf{f}_{n+1}^{\text{int},(e),(k)}}{\partial\alpha_{n+1}^{(e),(k)}}\\
\mathbf{K}_{n+1}^{hd,(e),(k)} &= \frac{\partial h_{n+1}^{(e),(k)}}{\partial\mathbf{d}_{n+1}^{(e),(k-1)}}, \qquad K_{n+1}^{h\alpha,(e),(k)} = \frac{\partial h_{n+1}^{(e),(k)}}{\partial\alpha_{n+1}^{(e),(k)}}
\end{aligned}$$

Ko izračunamo prirastke pomikov in posodobimo vrednosti prostostnih stopenj, vstopimo v naslednjo iteracijo.

$$\Delta\mathbf{d}_{n+1}^{\text{str},(k)} = \left(\mathbf{K}_{n+1}^{\text{str},(k)}\right)^{-1}\Delta\mathbf{f}_{n+1}^{\text{str},(k)}, \qquad \mathbf{d}_{n+1}^{\text{str},(k)} = \mathbf{d}_{n+1}^{\text{str},(k-1)} + \Delta\mathbf{d}_{n+1}^{\text{str},(k)}$$

Iteriranje ponavljamo, dokler ne dosežemo zahtevane konvergence $\left\|\Delta\mathbf{f}_{n+1}^{\text{str},(k)}\right\| < tol$, $\left\|\Delta\mathbf{d}_{n+1}^{\text{str},(k)}\right\| < tol$, nato stopimo v naslednji psevdo-časovni korak.

VEČSLOJNI KONČNI ELEMENT ZA EULER-BERNOULLIJEV NOSILEC S PO SLOJIH VGRAJENIMI NEZVEZNOSTMI V OSNEM POMIKU

V poglavju 3 razvijemo večslojni končni element za Euler-Bernoullijev nosilec, ki ima vgrajene nezveznosti v osnem pomiku po posameznih slojih. Element je namenjen za detajlno analizo armiranobetonskih okvirjev in

nosilcev do popolne izgube nosilnosti. Poleg samodejnega pozicioniranja območij lokaliziranih deformacij (plastičnih členkov) večslojna zasnova končnega elementa ponuja vpogled v širjenje poškodb materiala in napredovanje razpok po višini elementa. Za razliko od rezultantnega končnega elementa, predstavljenega v poglavju 2, so materialne karakteristike elementa ločene od geometrijskih. Z znanimi materialnimi lastnostmi (napetost - deformacije), lahko za poljuben prerez izračunamo upogibni odziv (moment - ukrivljenost), ki ga potrebujemo kot vhodni podatek pri analizi z rezultantnim končnim elementom.

Večslojni končni element je zasnovan na teoriji majhnih deformacij. Razdeljen je na več slojev betona in armature, ki jih obravnavamo ločeno, kot posebno vrsto palic (z linearnim potekom napetosti po dolžini). Vsak sloj ima vgrajeno nezveznost v osnem pomiku, ki se razvija neodvisno od drugih slojev. Osni odziv betonskega sloja je opisan z modelom poškodovanosti z utrjevanjem zvezno po sloju in z modelom poškodovanosti v mehčanju za nezveznost. Osni odziv sloja armature je opisan z elastoplastičnim modelom z utrjevanjem materiala zvezno po sloju in s plastičnim modelom mehčanja na mestu nezveznosti.

Kinematika

Obravnavamo raven končni element s tremi vozlišči za ravninski Euler-Bernoullijev nosilec. Končni vozlišči imata po tri prostostne stopnje - dva pomika in zasuk. Dodatno vozlišče na sredini elementa ima le eno prostostno stopnjo - osni pomik, katerega namen je dvigniti red interpolacije osnega pomika in s tem zagotoviti kompatibilnost prispevkov upogibnega in osnega odziva k osnim deformacijam. Osni pomik $\tilde{u}(x)$ srednje osi nosilca interpoliramo med vozliščne osne pomike $\mathbf{u}$ s kvadratičnimi interpolacijskimi funkcijami $\mathbf{N}^u(x)$.

$$\tilde{u}(x) = \mathbf{N}^u(x)\,\mathbf{u}, \quad \mathbf{N}^u(x) = \left\{1 - \frac{3x}{L} + \frac{2x^2}{L^2}, -\frac{x}{L} + \frac{2x^2}{L^2}, \frac{4x}{L} - \frac{4x^2}{L^2}\right\}, \quad \mathbf{u} = \{u_1, u_2, u_3\}^T$$

Prečni pomik $\tilde{v}(x)$ srednje osi interpoliramo med vozliščne prečne pomike $\mathbf{v}$ in zasuke $\boldsymbol{\theta}$ s Hermitovimi polinomi $\mathbf{N}^v(x)$ in $\mathbf{N}^\theta(x)$, zasuk $\tilde{\theta}(x)$ pa izračunamo kot odvod prečnega pomika.

$$\tilde{v}(x) = \mathbf{N}^v(x)\,\mathbf{v} + \mathbf{N}^\theta(x)\,\boldsymbol{\theta}, \qquad \tilde{\theta}(x) = \frac{\partial \tilde{v}}{\partial x} = \frac{\partial \mathbf{N}^v}{\partial x}\mathbf{v} + \frac{\partial \mathbf{N}^\theta}{\partial x}\boldsymbol{\theta}$$

Nosilec razdelimo po višini na poljubno število slojev. Za dovolj fino razdelitev lahko predpostavimo konstantno napetostno stanje po debelini sloja. Osni pomik $u^i(x)$ i-tega sloja izračunamo v njegovi srednji osi, oddaljeni za y^i od srednje osi nosilca.

$$u^i\left(x, x_d^i\right) = \overbrace{\tilde{u}(x) - y^i\tilde{\theta}(x)}^{\tilde{u}^i} + \overbrace{M^i\left(x, x_d^i\right)\alpha^i}^{u^{i,add}}$$

Sprva pomik opišemo le s standardnim delom $\tilde{u}^i(x)$, ki ga sestavljata prispevka zaradi osnega pomika in zaradi zasuka srednje osi nosilca. Ko napetosti v sloju presežejo mejo nosilnosti, se na kritičnem mestu (pri koordinati x_d^i) oblikuje nezveznost v osnem pomiku. Dodatni osni pomik $u^{i,add}\left(x, x_d^i\right)$ zaradi nezveznosti je opisan z velikostjo skoka v pomiku α^i in z oblikovno funkcijo $M^i\left(x, x_d^i\right)$. Osno deformacijo sloja $\varepsilon^i\left(x, x_d^i\right)$ izračunamo kot prvi odvod osnega pomika.

$$\varepsilon^i\left(x, x_d^i\right) = \frac{\partial u^i}{\partial x} = \overbrace{\mathbf{B}^u(x)\,\mathbf{u} - y^i\left(\mathbf{B}^v(x)\,\mathbf{v} + \mathbf{B}^\theta(x)\,\boldsymbol{\theta}\right)}^{\tilde{\varepsilon}^i} + \overbrace{G_R^i\left(x, x_d^i\right)\alpha^i}^{\varepsilon^{i,add}}$$

Zaradi dodatnega vozlišča na sredini elementa in kvadratične interpolacije osnega pomika so vsi členi v standardnem delu osne deformacije $\tilde{\bar{\varepsilon}}^i$ linearno odvisni od x. Interpolacijske funkcije $\mathbf{B}^u$ so namreč prvi odvod kvadratičnih funkcij $\mathbf{N}^u$, funkcije $\mathbf{B}^v$ in $\mathbf{B}^\theta$ pa drugi odvod kubičnih Hermitovih polinomov $\mathbf{N}^v$ in $\mathbf{N}^\theta$. Operator G_R^i je odvod interpolacijske funkcije M^i in ga bomo opisali v nadaljevanju. Indeks R se nanaša na prave (oz. realne) deformacije. Dodatni del $\varepsilon^{i,add}$ se aktivira le v slojih, kjer je bila presežena nosilnost in se je oblikovala razpoka.

$$\mathbf{B}^u(x) = \frac{\partial \mathbf{N}^u(x)}{\partial x}, \qquad \mathbf{B}^v(x) = \frac{\partial^2 \mathbf{N}^v(x)}{\partial x^2}, \qquad \mathbf{B}^\theta(x) = \frac{\partial^2 \mathbf{N}^\theta(x)}{\partial x^2}$$

Standardni del osne deformacije i-tega sloja lahko zapišemo tudi krajše.

$$\tilde{\bar{\varepsilon}}^i = \begin{bmatrix} \mathbf{B}^u & -y^i\mathbf{B}^v & -y^i\mathbf{B}^\theta \end{bmatrix} \mathbf{d} = \check{\mathbf{B}}^i \mathbf{d}, \qquad \mathbf{d}^T = \left\{ \mathbf{u}^T, \mathbf{v}^T, \boldsymbol{\theta}^T \right\}$$

Za pomoč pri določanju oblikovne funkcije $M^i\left(x, x_d^i\right)$, ki opisuje dodatne osne pomike zaradi pojava nezveznosti v sloju, definiramo "vozliščne pomike sloja" $\mathbf{u}^i = \left\{u_1^i, u_2^i, u_3^i\right\}^T$ kot vrednosti standardnega pomika $\tilde{u}^i(x)$ na mestih vozlišč končnega elementa.

$$\mathbf{u}^i = \left\{ \tilde{u}^i\big|_{x=0}, \tilde{u}^i\big|_{x=L}, \tilde{u}^i\big|_{x=L/2} \right\}^T = \left\{ u_1 - y^i\theta_1, u_2 - y^i\theta_2, u_3 - y^i\left(-\frac{3(v_1-v_2)}{2L} - \frac{\theta_1+\theta_2}{4}\right) \right\}^T$$

Ker je pomik $\tilde{u}^i$ kvadratičen, lahko njegovo interpolacijo opišemo s kvadratičnimi interpolacijskimi funkcijami $\mathbf{N}^u$ za osne pomike in z vozliščnimi pomiki sloja. Nato mu prištejemo dodatni pomik zaradi nastanka nezveznosti.

$$\tilde{u}^i(x) = \tilde{u}(x) - y^i\tilde{\theta}(x) = \mathbf{N}^u(x)\,\mathbf{u}^i, \qquad u^i\left(x, x_d^i\right) = \tilde{u}^i(x) + M^i\left(x, x_d^i\right)\alpha^i$$

Da bi celotni pomik sloja u^i ohranil vozliščne vrednosti $\mathbf{u}^i$, mora imeti funkcija M^i v vozliščih (pri $x = 0$, L in $L/2$) vrednost nič, za opis nezveznosti pa potrebuje enotski skok pri koordinati x_d^i. Tem pogojem najlaže zadostimo tako, da za M^i uporabimo Heaviside-ovo funkcijo $H_{x_d^i}$, od katere odštejemo interpolacijske funkcije N_j^u tistih vozlišč j, pri katerih je $x > x_d^i$.

$$H_{x_d^i} = \begin{cases} 0; & x < x_d^i \\ 1; & x \geq x_d^i \end{cases} \qquad M^i = \begin{cases} H_{x_d^i} - (N_2^u + N_3^u); & 0 < x_d^i < L/2 \\ H_{x_d^i} - N_2^u; & L/2 < x_d^i < L \end{cases}$$

Če upoštevamo, da je odvod Heaviside-ove funkcije Dirac-delta, lahko zapišemo izraz za operator G_R^i.

$$\frac{\partial H_{x_d^i}}{\partial x} = \delta_{x_d^i} = \begin{cases} \infty; & x = x_d^i \\ 0; & \text{sicer} \end{cases} \qquad G_R^i = \frac{\partial M^i}{\partial x} = \begin{cases} \delta_{x_d^i} - (B_2^u + B_3^u); & 0 < x_d^i < L/2 \\ \delta_{x_d^i} - B_2^u; & L/2 < x_d^i < L \end{cases}$$

V primeru konstantnih deformacij vzdolž sloja (v primeru čistega upogiba ali čistega natega/tlaka) zgornji izraz za G_R^i ni primeren, saj je linearen. Za ta primer izpeljemo M^i in G_R^i z naslednjim razmislekom. Konstantne deformacije ustrezajo linearnemu poteku pomikov, ki jih lahko interpoliramo med dva vozliščna pomika (namesto treh) z linearnimi oblikovnimi funkcijami $\mathbf{N}^{u*}$.

$$\tilde{u}^i(x) = \mathbf{N}^{u*}(x)\,\mathbf{u}^{i*}, \qquad \mathbf{N}^{u*}(x) = \{N_1^{u*}, N_2^{u*}\} = \left\{1 - \frac{x}{L}, \frac{x}{L}\right\}, \qquad \mathbf{u}^{i*} = \left\{u_1^i, u_2^i\right\}^T$$

Oblikovni funkciji M^i in G_R^i dobimo na enak način kot prej.

$$M^i = H_{x_d^i} - N_2^{u*} = H_{x_d^i} - \frac{x}{L}, \qquad G_R^i = \frac{\partial M^i}{\partial x} = \delta_{x_d^i} - \frac{1}{L}$$

Glede na linearen potek osnih deformacij po posameznem sloju se nezveznost lahko pojavi v enem od končnih vozlišč. V posebnem primeru, ko so deformacije sloja konstantne po dolžini nezveznost postavimo v sredino elementa. Zgornje izraze za operator G_R^i torej lahko združimo v naslednjem zapisu.

$$G_R^i\left(x, x_d^i\right) = \bar{G}_R^i + \bar{\bar{G}}_R^i, \quad \bar{\bar{G}}_R^i = \delta_{x_d^i}, \quad \bar{G}_R^i = \begin{cases} -\dfrac{1}{L}; & x_d^i = L/2 \\ -\dfrac{1}{L}\left(3 - \dfrac{4x}{L}\right); & x_d^i = 0 \\ \dfrac{1}{L}\left(1 - \dfrac{4x}{L}\right); & x_d^i = L \end{cases}$$

Lokacijo nezveznosti določimo glede na vrednosti napetosti v sloju v trenutku, ko je dosežena meja nosilnosti. V sloju armature jo postavimo na mesto največje napetosti po absolutni vrednosti, saj je obnašanje jekla simetrično v tlaku in nategu. V primeru konstantnega napetostnega stanja nezveznost postavimo v sredino sloja.

$$\begin{array}{lcll} \sigma_1 = \sigma_2 = \sigma_3 & \Rightarrow & x_d^i = L/2 & \\ |\sigma_1| > |\sigma_2| & \Rightarrow & x_d^i = 0 & \text{kjer je} \\ |\sigma_1| < |\sigma_2| & \Rightarrow & x_d^i = L & \end{array} \qquad \begin{array}{l} \sigma_1 = \sigma|_{x=0} \\ \sigma_2 = \sigma|_{x=L} \\ \sigma_3 = \sigma|_{x=L/2} \end{array}$$

Pri betonu je lociranje razpoke manj enostavno, saj moramo upoštevati različni nosilnosti betona v tlaku σ_{fcc} in nategu σ_{fct}. Če je več kot polovica sloja v nategu $\sigma_3 \geq 0$, se pojavi nezveznost v nategu na bolj tegnjenem koncu sloja. Če je ves sloj v tlaku, se pojavi tlačna nezveznost na bolj tlačenem koncu. V vmesni situaciji primerjamo nosilnosti betona v tlaku in nategu, da ugotovimo, katera obremenitev je bolj kritična.

$$\begin{array}{l} \sigma_1 = \sigma_2 = \sigma_3 \;\Rightarrow\; x_d^i = L/2 \\ \sigma_1 > \sigma_2 \;\Rightarrow\; \begin{cases} \sigma_3 \geq 0 \;\Rightarrow\; x_d^i = 0 \\ \sigma_3 < 0 \;\Rightarrow\; \begin{cases} \sigma_1 \leq 0 \;\Rightarrow\; x_d^i = L \\ \sigma_1 > 0 \;\Rightarrow\; \begin{cases} |\sigma_2/\sigma_1| \leq (\sigma_{fcc}/\sigma_{fct}) \;\Rightarrow\; x_d^i = 0 \\ |\sigma_2/\sigma_1| > (\sigma_{fcc}/\sigma_{fct}) \;\Rightarrow\; x_d^i = L \end{cases} \end{cases} \end{cases} \\ \sigma_1 < \sigma_2 \;\Rightarrow\; \text{analogno kot pri } \sigma_1 > \sigma_2 \end{array}$$

Princip virtualnega dela

Virtualno osno deformacijo $\hat{\varepsilon}^i$ v i-tem sloju interpoliramo na enak način kot pravo deformacijo, le da operator G_R^i zamenjamo z operatorjem G_V^i, kar nam omogoča prilagodljivo interpolacijo virtualne količine. Tako kot pri

pravi deformaciji, dodatni del $\hat{\varepsilon}^{i,add}$ nastopa le v $n_{CL}^{(e)}$ slojih, ki so presegli mejo nosilnosti in aktivirali nezveznost. Izboljšana interpolacija virtualne deformacije prinese dodaten člen v virtualno delo notranjih sil $G^{\text{int},(e)}$.

$$\hat{\varepsilon}^i = \check{\mathbf{B}}^i \hat{\mathbf{d}} + \underbrace{G_V^i \hat{\alpha}^i}_{\hat{\varepsilon}^{i,add}}, \qquad G^{\text{int},(e)} = \int_V \hat{\varepsilon} \sigma dV = \int_L \sum_i \hat{\varepsilon}^i \sigma^i A^i dx = \underbrace{\hat{\mathbf{d}}^{(e)^T} \mathbf{f}^{\text{int},(e)}}_{\text{standardno}} + \underbrace{\sum_{i=1}^{n_{CL}^{(e)}} \hat{\alpha}^{(e),i} h^{(e),i}}_{\text{dodatno}}$$

Vektor posplošenih virtualnih pomikov $\hat{\mathbf{d}}^{(e)}$ združuje vse virtualne prostostne stopnje elementa (e), vektor $\mathbf{f}^{\text{int},(e)}$ pa ustrezno urejene notranje sile. Izračunamo jih kot vsoto prispevkov posameznih slojev $\mathbf{f}^{\text{int},(e),i}$. Količina $h^{(e),i}$ je ekvivalent notranje sile, ki ustreza virtualnemu skoku v osnem pomiku $\hat{\alpha}^{(e),i}$.

$$\hat{\mathbf{d}}^{(e)^T} = \left\{ \hat{\mathbf{u}}^T, \hat{\mathbf{v}}^T, \hat{\boldsymbol{\theta}}^T \right\}, \qquad \mathbf{f}^{\text{int},(e)} = \sum_{i=1}^{n_L} \underbrace{A^i \int_L \check{\mathbf{B}}^{i^T} \sigma^i dx}_{\mathbf{f}^{\text{int},(e),i}}, \qquad h^{(e),i} = \int_L G_V^i \sigma^i A^i dx$$

Za operator G_V^i obdržimo obliko operatorja G_R^i. Zapišemo ga kot vsoto zveznega dela $\bar{G}_V^i$ in Dirac-delta funkcije.

$$G_V^i = \bar{G}_V^i + \delta_{x_d^i}, \quad \int_L g(x)\, \delta_{x_d^i} dx = g\left(x_d^i\right)$$

Z upoštevanjem pravila za integriranje Dirac-delta funkcije razvijemo izraz za $h^{(e),i}$. Napetost v sloju σ^i je funkcija koordinate x. Njeno vrednost na mestu nezveznosti $\sigma^i\big|_{x_d^i}$ označimo s t^i in definiramo kot napetost v nezveznosti, ki je konjugirana količina skoka v osnem pomiku α^i.

$$h^{(e),i} = \int_L \left(\bar{G}_V^i + \delta_{x_d^i} \right) \sigma^i A^i dx = A^i \int_L \bar{G}_V^i \sigma^i dx + A^i \, \sigma^i\big|_{x_d^i} = A^i \left(\int_L \bar{G}_V^i \sigma^i dx + t^i \right)$$

Iz principa virtualnega dela $G^{\text{int}} - G^{\text{ext}} = 0$ izpeljemo ravnotežne enačbe konstrukcije. Poleg standardne enačbe globalnega ravnotežja zunanjih in notranjih sil dobimo dodatno ravnotežno enačbo za vsak sloj vsakega elementa, v katerem je bila presežena meja nosilnosti in se je v njem pojavila nezveznost.

$$\mathop{\mathsf{A}}_{e=1}^{n_{FE}} \left[\mathbf{f}^{\text{int},(e)} - \mathbf{f}^{\text{ext},(e)} \right] = \mathbf{0}, \qquad \forall e \in \{1,2,\ldots,n_{FE}\}, \; \forall i \in \left\{ 1,2,\ldots,n_{CL}^{(e)} \right\} : \; h^{(e),i} = 0$$

Tu je A "assembly" operator, n_{FE} število končnih elementov v konstrukciji, $n_{CL}^{(e)}$ pa število slojev z aktivirano nezveznostjo v končnem elementu (e). Če v dodatno enačbo vstavimo zgoraj izpeljani izraz za $h^{(e),i}$, jo lahko jasneje interpretiramo. Predstavlja ravnotežje med napetostmi po sloju σ^i in napetostjo v nezveznosti t^i posameznega sloja v šibki (integralski) obliki. Ker se nanaša le na posamezen sloj, jo imenujemo tudi enačba lokalnega ravnotežja.

$$h^{(e),i} = 0 \quad \Leftrightarrow \quad t^i = -\int_L \bar{G}_V^i \sigma^i dx$$

Zvezni del operatorja G_V^i, označen z $\bar{G}_V^i$, izpeljemo na tak način, da ohranimo fizikalni pomen napetosti v nezveznosti, ki smo jo definirali kot $t^i = \sigma^i\big|_{x_d^i}$. Če se držimo spodnje enačbe, zgornji izraz za t^i vedno zavzame vrednost funkcije $\sigma^i\left(x = x_d^i\right)$ za poljubno linearno funkcijo σ^i.

$$G_V^i\left(x, x_d^i\right) = \bar{G}_V^i + \bar{\bar{G}}_V^i, \quad \bar{\bar{G}}_V^i = \delta_{x_d^i}, \quad \bar{G}_V^i = \begin{cases} -\dfrac{1}{L}; & x_d^i = L/2 \\ -\dfrac{2}{L}\left(2 - \dfrac{3x}{L}\right); & x_d^i = 0 \\ \dfrac{2}{L}\left(1 - \dfrac{3x}{L}\right); & x_d^i = L \end{cases}$$

Če bi namesto tega uporabili kar izraze, ki smo jih izpeljali za $\bar{G}_R^i$, bi npr. v primeru $x_d^i = 0$ za t^i dobili vrednost $t^i = \sigma^i\big|_{L/6} \neq \sigma^i\big|_{x_d^i=0}$.

Materialni modeli

Lastnosti materiala opišemo s po dvema konstitutivnima zakonoma za vsak sloj. Prvi opisuje zvezo med napetostjo in deformacijo po sloju, drugi pa zvezo med napetostjo v nezveznosti in skokom v osnem pomiku. Za betonski sloj uporabimo model poškodovanosti z utrjevanjem. Osni odziv je sprva linearno elastičen. Ko dosežemo mejo elastičnosti, se začnejo zvezno po materialu pojavljati mikro poškodbe, kar se odraža v zmanjšani togosti. Ob razbremenjevanju se deformacije zmanjšujejo premo sorazmerno z napetostjo - črta razbremenjevanja se vrača proti izhodišču diagrama. Osnovne enačbe modela so izpeljane iz zakonov termodinamike, glej npr. [73].

$$\sigma^i = \bar{D}^{i^{-1}}\bar{\varepsilon}^i, \qquad \bar{D}^i \in \left[E_c^{-1}, \infty\right), \qquad \bar{\varepsilon}^i = \check{\mathbf{B}}^i\mathbf{d} + \bar{G}_R^i\alpha^i$$

Tu je $\bar{D}^i$ podajnost sloja, ki je na začetku enaka inverzni vrednosti elastičnega modula E_c in narašča s pojavom mikro poškodb. Funkcija poškodovanosti $\bar{\phi}^i$ nadzira prehajanje iz elastičnega obnašanja v poškodovanost in obratno. Konstanta $\sigma_d > 0$ predstavlja absolutno vrednost napetosti, pri kateri se prvič pojavijo mikro razpoke v nategu oz. mikro drobljenje materiala v tlaku. Napetosti podobna količina $\bar{q}^i \leq 0$ predstavlja povečanje meje elastičnosti zaradi utrjevanja materiala. Odvisna je od deformaciji podobne spremenljivke $\bar{\xi}^i$ in modula utrjevanja $H_c > 0$. Vrednosti konstant σ_d in H_c določimo posebej za tlak in nateg.

$$\bar{\phi}^i\left(\sigma^i, \bar{q}^i\right) = \left|\sigma^i\right| - \left(\sigma_d - \bar{q}^i\right), \qquad \bar{q}^i = -H_c\bar{\xi}^i$$

Materialni model obsega še evolucijski enačbi za notranji spremenljivki $\bar{D}^i$ in $\bar{\xi}^i$ ter pogoje obremenjevanja in razbremenjevanja. Tu je $\dot{\bar{\gamma}}^i$ Lagrangev množitelj, ki izhaja iz izpeljave enačb po principu maksimalne disipacije energije.

$$\dot{\bar{D}}^i = \frac{\dot{\bar{\gamma}}^i sign\left(\sigma^i\right)}{\sigma^i}, \quad \dot{\bar{\xi}}^i = \dot{\bar{\gamma}}^i, \qquad \dot{\bar{\gamma}}^i \geq 0, \quad \bar{\phi}^i \leq 0, \quad \dot{\bar{\gamma}}^i\bar{\phi}^i = 0, \quad \dot{\bar{\gamma}}^i\dot{\bar{\phi}}^i = 0$$

Obnašanje nezveznosti v betonskem sloju opišemo z modelom mehčanja, ki povezuje spremenljivki t^i in α^i. Skok v osnem pomiku je enak nič, dokler ne dosežemo meje nosilnosti. Od tu dalje se t^i zmanjšuje z naraščanjem α^i, dokler ne pade na vrednost nič (zaradi enačbe lokalnega ravnotežja mu sledijo tudi napetosti v sloju σ^i).

Ob razbremenjevanju skok v pomiku α^i linearno pada proti nič (razpoka se zapira), kar ustreza značaju betona. Materialni model nezveznosti je definiran z naslednjim kompletom enačb.

$$t^i = \bar{\bar{D}}^{i^{-1}} \alpha^i, \quad \bar{\bar{D}}^i \in [0,\infty), \quad \bar{\bar{\phi}}^i\left(t^i,\bar{\bar{q}}^i\right) = \left|t^i\right| - \left(\sigma_{fc} - \bar{\bar{q}}^i\right), \quad \bar{\bar{q}}^i = \sigma_{fc}\left(1 - e^{K_c \bar{\bar{\xi}}^i}\right)$$

Tu je $\bar{\bar{D}}^i$ podajnost nezveznosti, $\bar{\bar{\phi}}^i$ je funkcija mehčanja, ki nadzoruje prehod iz elastičnega obnašanja v mehčanje in obratno, $\sigma_{fc} > 0$ je absolutna vrednost napetosti, pri kateri se aktivira nezveznost, $\bar{\bar{q}}^i \in [0, \sigma_{fc})$ je napetosti podobna spremenljivka, ki opisuje zmanjšanje nosilnosti zaradi mehčanja materiala, in je odvisna od pomiku podobne spremenljivke $\bar{\bar{\xi}}^i$ in modula mehčanja $K_c < 0$. Vrednosti konstant σ_{fc} in K_c sta različni za tlak in nateg. Opis modela zaključimo z evolucijskima enačbama za notranji spremenljivki $\dot{\bar{\bar{D}}}^i$ in $\dot{\bar{\bar{\xi}}}^i$ ter s pogoji obremenjevanja in razbremenjevanja, v katerih je $\dot{\bar{\bar{\gamma}}}^i$ Lagrangev množitelj, ki izvira iz termodinamične izpeljave enačb.

$$\dot{\bar{\bar{D}}}^i = \frac{\dot{\bar{\bar{\gamma}}}^i \; sign\left(t^i\right)}{t^i}, \quad \dot{\bar{\bar{\xi}}}^i = \dot{\bar{\bar{\gamma}}}^i, \qquad \dot{\bar{\bar{\gamma}}}^i \geq 0, \quad \bar{\bar{\phi}}^i \leq 0, \quad \dot{\bar{\bar{\gamma}}}^i \bar{\bar{\phi}}^i = 0, \quad \dot{\bar{\bar{\gamma}}}^i \dot{\bar{\bar{\phi}}}^i = 0$$

Za izbrani zakon mehčanja (enačba za $\bar{\bar{q}}^i$) se izkaže, da je zveza med t^i in α^i linearna. Reševanje enačb lahko poenostavimo tako, da vpeljemo novo spremenljivko $\bar{\bar{\xi}}^{i*}$. Enačba za $\bar{\bar{q}}^i$ tako dobi linearno obliko.

$$\bar{\bar{\xi}}^{i*} = -\frac{1}{K_c}\left(1 - e^{K_c \bar{\bar{\xi}}^i}\right), \qquad \bar{\bar{q}}^i = \sigma_{fc}\left(1 - e^{K_c \bar{\bar{\xi}}^i}\right) = -K_c \sigma_{fc} \bar{\bar{\xi}}^{i*} = -K_c^* \bar{\bar{\xi}}^{i*}$$

V izvirnem zapisu se je količina $\bar{\bar{q}}^i$ asimptotično približevala vrednosti σ_{fc}, ko je $\bar{\bar{\xi}}^i$ naraščal prek vseh meja. Posledično betonski sloj nikoli ni mogel popolnoma izgubiti nosilnosti , velikost nezveznosti α^i pa je bila navzgor omejena. V novem, linearnem zapisu $\bar{\bar{q}}^i$ doseže vrednost σ_{fc} pri neki končni vrednosti nadomestne spremenljivke $\bar{\bar{\xi}}^{i*}$. Ob njenem nadaljnjem naraščanju količina $\bar{\bar{q}}^i$ ohranja isto vrednost (nosilnost sloja je enaka nič).

$$\bar{\bar{q}}^i = \min\left\{-K_c^* \bar{\bar{\xi}}^{i*}, \sigma_{fc}\right\}, \qquad K_c^* = K_c \, \sigma_{fc}$$

Ustrezno prilagodimo tudi evolucijski enačbi, ki ju izrazimo z nadomestnim Lagrangevim množiteljem $\dot{\bar{\bar{\gamma}}}^{i*}$. To omogoča, da skok v pomiku α^i narašča tudi po tem, ko je sloj popolnoma izgubil nosilnost. Za obravnavo samostojnega betonskega sloja to sicer ne bi imelo pomena, saj bi ob popolni izgubi nosilnosti postal nestabilen. Za sloj, ki predstavlja le del nosilca, pa je zmožnost prostega spreminjanja α^i potrebna, zato da porušeni sloj ne ovira deformiranja preostalih slojev.

$$\bar{\bar{\gamma}}^{i*} = -\frac{1}{K_c}\left(1 - e^{K_c \bar{\bar{\gamma}}^i}\right), \qquad \dot{\alpha}^i = \dot{\bar{\bar{\gamma}}}^{i*} sign\left(t^i\right), \qquad \dot{\bar{\bar{\xi}}}^{i*} = \dot{\bar{\bar{\gamma}}}^{i*}$$

Obnašanje sloja armature opišemo z elastoplastičnim materialnim modelom z linearnim izotropnim utrjevanjem, katerega osnovne enačbe so izpeljane iz zakonov termodinamike [73]. Napetost v sloju izračunamo iz elastične deformacije, ki je razlika med skupno deformacijo $\bar{\varepsilon}^i$ in plastično deformacijo $\bar{\varepsilon}_p^i$.

$$\sigma^i = E_s\left(\bar{\varepsilon}^i - \bar{\varepsilon}_p^i\right), \qquad \bar{\varepsilon}^i = \check{\mathbf{B}}^i \mathbf{d} + \bar{G}_R^i \alpha^i$$

Funkcija tečenja $\bar{\phi}^i$ kontrolira prehod iz elastičnega v plastično obnašanje in obratno. Tu je $\sigma_y > 0$ napetost na meji tečenja, $\bar{q}^i < 0$ pa napetosti podobna količina, ki predstavlja povišanje meje elastičnosti zaradi utrjevanja materiala. Odvisna je od modula utrjevanja $H_s > 0$ in oddeformaciji podobne spremenljivke $\bar{\xi}^i$.

$$\bar{\phi}^i\left(\sigma^i, \bar{q}^i\right) = \left|\sigma^i\right| - \left(\sigma_y - \bar{q}^i\right), \qquad \bar{q}^i = -H_s \bar{\xi}^i$$

Potrebujemo še evolucijski enačbi za notranji spremenljivki utrjevanja $\bar{\varepsilon}_p^i$ in $\bar{\xi}^i$ ter pogoje obremenjevanja in razbremenjevanja. Tu je $\dot{\bar{\gamma}}^i$ plastični množitelj, ki izhaja iz izpeljave enačb s principom maksimalne plastične disipacije.

$$\dot{\bar{\varepsilon}}_p^i = \dot{\bar{\gamma}}^i sign\left(\sigma^i\right), \quad \dot{\bar{\xi}}^i = \dot{\bar{\gamma}}^i, \qquad \dot{\bar{\gamma}}^i \geq 0, \quad \bar{\phi}^i \leq 0, \quad \dot{\bar{\gamma}}^i \bar{\phi}^i = 0, \quad \dot{\bar{\gamma}}^i \dot{\bar{\phi}}^i = 0$$

Obnašanje nezveznosti v sloju armature opišemo s togo-plastičnim modelom mehčanja. Do prekoračitve meje nosilnosti σ_{fs} je skok v osnem pomiku α^i enak nič. Nato se ob povečevanju α^i napetost v nezveznosti t^i linearno zmanjšuje, dokler ne doseže vrednosti nič. V primeru razbremenjevanja se vrednost α^i ne spreminja.

$$\bar{\bar{\phi}}^i\left(t^i, \bar{\bar{q}}^i\right) = \left|t^i\right| - \left(\sigma_{fs} - \bar{\bar{q}}^i\right), \qquad \bar{\bar{q}}^i = \min\left\{-K_s \bar{\bar{\xi}}^i, \sigma_{fs}\right\}$$

Funkcija $\bar{\bar{\phi}}^i$ nadzira prehajanje med elastičnim obnašanjem in mehčanjem. Napetosti podobna količina $\bar{\bar{q}}^i \in [0, \sigma_{fs}]$ predstavlja zmanjšanje nosilnosti zaradi mehčanja materiala. Odvisna je od pomiku podobne spremenljivke $\bar{\bar{\xi}}^i$ in modula mehčanja $K_s < 0$. Potrebujemo še evolucijski enačbi za notranji spremenljivki mehčanja α^i in $\bar{\bar{\xi}}^i$ ter pogoje obremenjevanja in razbremenjevanja. Tu je $\dot{\bar{\bar{\gamma}}}^i$ plastični množitelj, ki izhaja iz izpeljave enačb po principu maksimalne disipacije energije.

$$\dot{\alpha}^i = \dot{\bar{\bar{\gamma}}}^i sign\left(t^i\right), \quad \dot{\bar{\bar{\xi}}}^i = \dot{\bar{\bar{\gamma}}}^i, \qquad \dot{\bar{\bar{\gamma}}}^i \geq 0, \quad \bar{\bar{\phi}}^i \leq 0, \quad \dot{\bar{\bar{\gamma}}}^i \bar{\bar{\phi}}^i = 0, \quad \dot{\bar{\bar{\gamma}}}^i \dot{\bar{\bar{\phi}}}^i = 0$$

Računski postopek

Konstrukcijo obremenjujemo v psevdo-časovnih korakih. V vsakem koraku rešimo sistem ravnotežnih enačb, pri čemer mora biti zadoščeno tudi kinematičnim in konstitutivnim enačbam. Ker so enačbe nelinearne, jih linearizirамo in rešujemo iterativno po Newtonovi metodi. Vsaka iteracija k je sestavljena iz dveh faz. V fazi (A) zamrznemo trenutne vrednosti vozliščnih pomikov in posodobimo vrednosti notranjih spremenljivk, v fazi (B) pa zamrznemo izračunane vrednosti notranjih spremenljivk in izračunamo nove vozliščne pomike.

$$\text{Pri znanih } \mathbf{d}_n^{(e)} \text{ in } \begin{cases} \bar{D}_n^{(e),i}, \bar{\xi}_n^{(e),i}, \bar{\bar{D}}_n^{(e),i}, \bar{\bar{\xi}}_n^{(e),i} \\ \bar{\varepsilon}_{p,n}^{(e),i}, \bar{\xi}_n^{(e),i}, \alpha_n^{(e),i}, \bar{\bar{\xi}}_n^{(e),i} \end{cases} \text{ iščemo } \mathbf{d}_{n+1}^{(e)} \text{ in } \begin{cases} \bar{D}_{n+1}^{(e),i}, \bar{\xi}_{n+1}^{(e),i}, \bar{\bar{D}}_{n+1}^{(e),i}, \bar{\bar{\xi}}_{n+1}^{(e),i} \\ \bar{\varepsilon}_{p,n+1}^{(e),i}, \bar{\xi}_{n+1}^{(e),i}, \alpha_{n+1}^{(e),i}, \bar{\bar{\xi}}_{n+1}^{(e),i} \end{cases}.$$

Fazo (A) izvajamo na nivoju posameznega sloja končnega elementa. Pri fiksiranih vrednostih pomikov $\mathbf{d}_{n+1}^{(e),(k-1)}$ iz prejšnje iteracije iščemo pripadajoče vrednosti notranjih spremenljivk in napetosti po sloju, ki jih potrebujemo za račun v fazi (B). Dokler sloj ne preseže meje nosilnosti, sta notranji spremenljivki mehčanja ($\bar{\bar{D}}^i$ in $\bar{\bar{\xi}}^i$ za beton oz. α^i in $\bar{\bar{\xi}}^i$ za jeklo) enaki nič in računamo samo vrednosti spremenljivk utrjevanja ($\bar{D}^i$ in $\bar{\xi}^i$ za beton oz. $\bar{\varepsilon}_p^i$ in $\bar{\xi}^i$ za jeklo). Ko se nezveznost aktivira, se spremenljivke utrjevanja ne spreminjajo več in iščemo samo spremenljivke

mehčanja. V vsakem primeru je postopek enak. Predpostavimo elastičen testni korak, kar pomeni, da notranje spremenljivke ohranijo vrednosti iz prejšnjega koraka, nato izračunamo testni vrednosti napetosti v sloju funkcije tečenja. Če je slednja negativna, je bila predpostavka pravilna in obdržimo testno rešitev. V nasprotnem primeru posodobimo notranje spremenljivke skladno z evolucijskimi enačbami, pri čemer moramo zadostiti tudi pogojem obremenjevanja in razbremenjevanja. Izračunamo končno vrednost napetosti, ki jo potrebujemo za izračun notranjih sil končnega elementa (prispevek tega sloja).

$$\mathbf{K}_{n+1}^{\text{str},(k)}\Delta\mathbf{d}_{n+1}^{\text{str},(k)}=\Delta\mathbf{f}_{n+1}^{\text{str},(k)},\quad \mathbf{K}_{n+1}^{\text{str},(k)}=\mathop{\mathsf{A}}_{e=1}^{n_{FE}}\left[\mathbf{K}_{n+1}^{(e),(k)}\right],\quad \Delta\mathbf{f}_{n+1}^{\text{str},(k)}=\mathop{\mathsf{A}}_{e=1}^{n_{FE}}\left[\mathbf{f}_{n+1}^{\text{ext},(e)}-\mathbf{f}_{n+1}^{\text{int},(e),(k)}\right]$$

V fazi (B) rešimo linearizirani sistem ravnotežnih enačb, v katerem so neznanke prirastki pomikov konstrukcije $\Delta\mathbf{d}_{n+1}^{\text{str},(k)}$. Operator A sestavi prispevke posameznih elementov v togostno matriko $\mathbf{K}_{n+1}^{\text{str},(k)}$ in rezidual $\Delta\mathbf{f}_{n+1}^{\text{str},(k)}$ celotne konstrukcije. Togostne matrike in notranje sile posameznih elementov izračunamo kot vsoto prispevkov posameznih slojev.

$$\mathbf{K}_{n+1}^{(e),(k)}=\sum_i\mathbf{K}_{n+1}^{(e),i,(k)},\qquad \mathbf{f}_{n+1}^{\text{int},(e),(k)}=\sum_i\mathbf{f}_{n+1}^{\text{int},(e),i,(k)}$$

Prispevke $\mathbf{K}_{n+1}^{(e),i,(k)}$ posameznih slojev k togostni matriki elementa izračunamo z naslednjima izrazoma.

$$\begin{aligned}
&i\in\left\{1,2,\ldots,n_{CL}^{(e)}\right\}: && \mathbf{K}_{n+1}^{(e),i,(k)}=\mathbf{K}_{n+1}^{fd,(e),i,(k)}-\mathbf{K}_{n+1}^{f\alpha,(e),i,(k)}\left(K_{n+1}^{h\alpha,(e),i,(k)}\right)^{-1}\mathbf{K}_{n+1}^{hd,(e),i,(k)}\\
&i\in\left\{n_{CL}^{(e)}+1,\ldots,n_L\right\}: && \mathbf{K}_{n+1}^{(e),i,(k)}=\mathbf{K}_{n+1}^{fd,(e),i,(k)}
\end{aligned}$$

Tu je n_L število slojev v končnih elementih, $n_{CL}^{(e)}$ število slojev v elementu (e), ki so prekoračili mejo nosilnost. Dodatni člen v prvem izrazu je posledica izločitve neznank $\alpha_{n+1}^{(e),i,(k)}$ iz globalnega sistema enačb s kondenzacijo lokalnih ravnotežnih enačb $h_{n+1}^{(e),i,(k)}=0$. Opomba: v slojih armature, ki so že aktivirali nezveznost, vendar se trenutno elastično razbremenjujejo ($\Delta\alpha^i=0$), je dodatni člen zaradi kondenzacije enak nič.

$$\begin{aligned}
\mathbf{K}_{n+1}^{fd,(e),i,(k)}&=\frac{\partial\mathbf{f}_{n+1}^{\text{int},(e),i,(k)}}{\partial\mathbf{d}_{n+1}^{(e),(k-1)}}, && \mathbf{K}_{n+1}^{f\alpha,(e),i,(k)}=\frac{\partial\mathbf{f}_{n+1}^{\text{int},(e),i,(k)}}{\partial\alpha_{n+1}^{(e),i,(k)}}\\
\mathbf{K}_{n+1}^{hd,(e),i,(k)}&=\frac{\partial h_{n+1}^{(e),i,(k)}}{\partial\mathbf{d}_{n+1}^{(e),(k-1)}}, && K_{n+1}^{h\alpha,(e),i,(k)}=\frac{\partial h_{n+1}^{(e),i,(k)}}{\partial\alpha_{n+1}^{(e),i,(k)}}
\end{aligned}$$

V zgornjih enačbah so definirane vse komponente, potrebne za izračun $\mathbf{K}_{n+1}^{(e),i,(k)}$. Ko izračunamo nove vrednosti vozliščnih pomikov konstrukcije, jih zamrznemo in vstopimo v fazo (A) naslednje iteracije.

$$\Delta\mathbf{d}_{n+1}^{\text{str},(k)}=\left(\mathbf{K}_{n+1}^{\text{str},(k)}\right)^{-1}\Delta\mathbf{f}_{n+1}^{\text{str},(k)},\qquad \mathbf{d}_{n+1}^{\text{str},(k)}=\mathbf{d}_{n+1}^{\text{str},(k-1)}+\Delta\mathbf{d}_{n+1}^{\text{str},(k)}$$

Z iteriranjem nadaljujemo, dokler ne dosežemo zahtevane konvergence $\left\|\Delta\mathbf{f}_{n+1}^{\text{str},(k)}\right\|<tol$, $\left\|\Delta\mathbf{d}_{n+1}^{\text{str},(k)}\right\|<tol$, potem stopimo v naslednji psevdo-časovni korak.

VEČSLOJNI KONČNI ELEMENT ZA TIMOŠENKOV NOSILEC S PO SLOJIH VGRAJENIMI NEZVEZNOSTMI V OSNEM POMIKU

V poglavju 4 izpeljemo večslojni končni element za Timošenkov nosilec, ki ima vgrajene nezveznosti v osnem pomiku po posameznih slojih. Element omogoča detajlno porušno analizo armiranobetonskih nosilcev in okvirjev s samodejno identifikacijo kritičnih mest v konstrukciji, na katerih pride do lokaliziranih deformacij (plastičnih členkov). Večslojna zasnova elementa omogoča pregled nad nastankom in razvojem poškodb materiala v posameznih slojih ter nad napredovanjem nezveznosti (razpok) po višini nosilca. Materialne karakteristike elementa so definirane ločeno od geometrijskih in jih je moč določiti z enostavnimi tlačnimi ali nateznimi testi betona in jekla. Večslojni element lahko zato uporabimo za izračun rezultantnih materialno-geometrijskih lastnosti (diagram moment-ukrivljenost), ki so značilne za posamezen prerez in jih potrebujemo kot vhodni podatek pri analizi z enostavnejšimi, rezultantnimi končnimi elementi. V primerjavi z večslojnim elementom za Euler-Bernoullijev nosilec, je tu izpeljani element enostavnejši, saj je napetostno stanje konstantno po njegovi dolžini. To se odraža v preprostejši aplikaciji in odsotnosti nekaterih težav, ki spremljajo element iz prejšnjega poglavja.

Večslojni končni element je zasnovan na teoriji majhnih deformacij. Razdeljen je na več slojev betona in armature, ki jih obravnavamo ločeno, kot palice. Vsak sloj ima vgrajeno nezveznost v osnem pomiku, ki se razvija neodvisno od drugih slojev. Osni odziv betonskega sloja je opisan z modelom poškodovanosti z utrjevanjem zvezno po sloju in z modelom poškodovanosti v mehčanju za nezveznost. Osni odziv sloja armature je opisan z elastoplastičnim modelom z utrjevanjem materiala zvezno po sloju in s plastičnim modelom mehčanja na mestu nezveznosti. Predpostavimo linearno elastičen strižni odziv.

Kinematika

Obravnavamo raven dvovozliščni končni element za ravninski Timošenkov nosilec. Vsako vozlišče ima tri prostostne stopnje - dva pomika in zasuk. Osni pomik $\tilde{u}(x)$ srednje osi nosilca interpoliramo med vozliščna osna pomika $\mathbf{u}$ z linearnimi interpolacijskimi funkcijami $\mathbf{N}(x)$. Enako interpoliramo zasuk $\tilde{\theta}(x)$ med vozliščna zasuka $\boldsymbol{\theta}$.

$$\tilde{u}(x) = \mathbf{N}(x)\,\mathbf{u}, \qquad \tilde{\theta}(x) = \mathbf{N}(x)\,\boldsymbol{\theta}, \qquad \mathbf{N}(x) = \{N_1, N_2\} = \left\{1 - \frac{x}{L}, \frac{x}{L}\right\}$$

Linearna interpolacija prečnega pomika $\tilde{v}(x)$ srednje osi nosilca bi privedla do strižnega blokiranja končnega elementa, čemur se izognemo z dodatno kvadratično interpolacijsko funkcijo $N_3(x)$. Parameter v_3 določimo tako, da je končni element sposoben opisati napetostno stanje brez strižnih napetosti v primeru konstantnega momenta.

$$\tilde{v}(x) = \mathbf{N}(x)\,\mathbf{v} + N_3(x)\,v_3, \qquad N_3(x) = \frac{4(L-x)\,x}{L^2}, \qquad v_3 = \frac{L}{8}(\theta_1 - \theta_2)$$

Strižno deformacijo γ izračunamo s spodnjo enačbo. Opazimo, da je konstantna tako po dolžini, kot tudi po višini končnega elementa.

$$\gamma = \frac{\partial \tilde{v}}{\partial x} - \tilde{\theta} = \mathbf{B}\mathbf{v} + \mathbf{B}^*\boldsymbol{\theta}, \quad \mathbf{B} = \{B_1, B_2\} = \left\{-\frac{1}{L}, \frac{1}{L}\right\}, \quad \mathbf{B}^* = \{B^*, B^*\} = \left\{-\frac{1}{2}, -\frac{1}{2}\right\}$$

Nosilec razdelimo na poljubno število slojev po višini. Za dovolj fino razdelitev lahko predpostavimo konstantno napetostno stanje po debelini posameznega sloja. Osni pomik $u^i(x)$ i-tega sloja izračunamo v njegovi srednji osi, ki je za y^i oddaljena od srednje osi nosilca.

$$u^i\left(x,x_d^i\right)=\overbrace{\tilde{u}\left(x\right)-y^i\tilde{\theta}\left(x\right)}^{\tilde{u}^i}+\overbrace{M^i\left(x,x_d^i\right)\alpha^i}^{u^{i,add}}$$

Na začetku pomik opišemo le s standardnim delom $\tilde{u}^i\left(x\right)$ zaradi osnega pomika in zasuka srednje osi nosilca. Ko napetost v sloju prekorači mejo nosilnosti, se v sloju (pri koordinati x_d^i) pojavi nezveznost v osnem pomiku. Dodatni osni pomik $u^{i,add}\left(x,x_d^i\right)$ zaradi nezveznosti opišemo z interpolacijsko funkcijo $M^i\left(x,x_d^i\right)$ in z velikostjo skoka v pomiku α^i. Osno deformacijo i-tega sloja izračunamo kot odvod osnega pomika.

$$\varepsilon^i\left(x,x_d^i\right)=\frac{\partial u^i}{\partial x}=\overbrace{\mathbf{Bu}-y^i\mathbf{B}\boldsymbol{\theta}}^{\tilde{\bar{\varepsilon}}^i}+\overbrace{G^i\left(x,x_d^i\right)\alpha^i}^{\varepsilon^{i,add}}$$

Standardni del osne deformacije $\tilde{\bar{\varepsilon}}^i$ je konstanten po posameznem sloju. Operator G^i je odvod oblikovne funkcije M^i in ga bomo opisali v nadaljevanju. Standardno osno deformacijo $\tilde{\bar{\varepsilon}}^i$ in strižno deformacijo γ lahko zapišemo tudi krajše.

$$\tilde{\bar{\varepsilon}}^i=\begin{bmatrix}\mathbf{B} & \mathbf{0} & -y^i\mathbf{B}\end{bmatrix}\mathbf{d}=\check{\mathbf{B}}^i\mathbf{d},\qquad \gamma=\begin{bmatrix}\mathbf{0} & \mathbf{B} & \mathbf{B}^*\end{bmatrix}\mathbf{d}=\check{\mathbf{B}}^*\mathbf{d},\qquad \mathbf{d}^T=\left\{\mathbf{u}^T,\mathbf{v}^T,\boldsymbol{\theta}^T\right\}$$

Za pomoč pri izpeljavi funkcije M^i definiramo "vozliščne pomike sloja" $\mathbf{u}^i=\left\{u_1^i,u_2^i\right\}^T$ kot vrednosti standardnega pomika sloja $\tilde{u}^i\left(x\right)$ v vozliščih končnega elementa.

$$\mathbf{u}^i=\left\{\left.\tilde{u}^i\right|_{x=0},\left.\tilde{u}^i\right|_{x=L}\right\}^T=\left\{u_1-y^i\theta_1,u_2-y^i\theta_2\right\}^T$$

Ker je pomik $\tilde{u}^i$ linearen, lahko njegovo interpolacijo zapišemo tudi drugače - z linearnimi interpolacijskimi funkcijami $\mathbf{N}\left(x\right)$ in vozliščnimi pomiki sloja. Prištejemo mu dodatni pomik zaradi nezveznosti $u^{i,add}$.

$$\tilde{u}^i\left(x\right)=\tilde{u}\left(x\right)-y^i\tilde{\theta}\left(x\right)=\mathbf{N}\left(x\right)\mathbf{u}^i,\qquad u^i\left(x,x_d^i\right)=\tilde{u}^i\left(x\right)+M^i\left(x,x_d^i\right)\alpha^i$$

Da bi celotni pomik sloja u^i ohranil vozliščne vrednosti $\mathbf{u}^i$, mora imeti funkcija M^i v vozliščih (pri $x=0$ in L) vrednost nič, za opis nezveznosti pa potrebuje enotski skok pri koordinati x_d^i. Pogojem najlaže zadostimo tako, da za M^i uporabimo Heaviside-ovo funkcijo $H_{x_d^i}$, od katere odštejemo interpolacijsko funkcijo N_2.

$$M^i\left(x,x_d^i\right)\alpha^i=H_{x_d^i}\left(x,x_d^i\right)-N_2\left(x\right)$$

Upoštevamo, da je odvod Heaviside-ove funkcije Dirac-delta (obe funkciji sta definirani v prejšnjem razdelku), in zapišemo izraz za operator G^i.

$$G^i\left(x,x_d^i\right)=\frac{\partial}{\partial x}M^i\left(x,x_d^i\right)=\bar{G}^i+\bar{\bar{G}}^i,\quad \bar{\bar{G}}^i=\delta_{x_d^i},\quad \bar{G}^i=-B_2=-\frac{1}{L}$$

Glede na konstantno napetostno stanje vzdolž sloja, se lahko nezveznost pojavi kjerkoli. Brez izgube splošnosti jo lahko postavimo v sredino sloja $x_d^i=L/2$.

Princip virtualnega dela

Virtualno osno deformacijo $\hat{\varepsilon}^i$ i-tega sloja in virtualno strižno deformacijo $\hat{\gamma}$ interpoliramo na enak način kot pravi količini. Dodatni del virtualne deformacije $\hat{\varepsilon}^{i,add}$ nastopa le v slojih, kjer je napetost presegla mejo nosilnosti in se je oblikovala nezveznost v pomiku. Izboljšana interpolacija prinese dodaten člen v virtualnem delu notranjih sil $G^{\text{int},(e)}$ elementa (e).

$$\hat{\varepsilon}^i = \check{\mathbf{B}}^i\hat{\mathbf{d}} + \underbrace{G^i\hat{\alpha}^i}_{\hat{\varepsilon}^{i,add}}, \qquad \hat{\gamma} = \check{\mathbf{B}}^*\hat{\mathbf{d}}, \qquad G^{\text{int},(e)} = \int_V (\hat{\varepsilon}\sigma + \hat{\gamma}\tau)\, dV = \underbrace{\hat{\mathbf{d}}^{(e)^T}\mathbf{f}^{\text{int},(e)}}_{\text{standardno}} + \underbrace{\sum_{i=1}^{n_{CL}^{(e)}} \hat{\alpha}^{(e),i} h^{(e),i}}_{\text{dodatno}}$$

Vektor $\hat{\mathbf{d}}^{(e)}$ združuje vse virtualne prostostne stopnje elementa (e), vektor $\mathbf{f}^{\text{int},(e)}$ pa ustrezno urejene notranje sile. Izračunamo jih kot vsoto prispevkov posameznih slojev $\mathbf{f}^{\text{int},(e),i}$. Količina $h^{(e),i}$ je ekvivalent notranje sile, ki ustreza virtualnemu skoku v osnem pomiku $\hat{\alpha}^{(e),i}$.

$$\hat{\mathbf{d}}^{(e)^T} = \left\{\hat{\mathbf{u}}^T, \hat{\mathbf{v}}^T, \hat{\boldsymbol{\theta}}^T\right\}, \qquad \mathbf{f}^{\text{int},(e)} = \sum_{i=1}^{n_L} \underbrace{\left(\check{\mathbf{B}}^{i^T}\sigma^i + \check{\mathbf{B}}^{*^T}\tau^i\right) A^i L}_{\mathbf{f}^{\text{int},(e),i}}, \qquad h^{(e),i} = \int_L G^i\sigma^i A^i dx$$

Z upoštevanjem prej izpeljanega izraza za operator G^i in pravila za integriranje Dirac-delta funkcije (zapisano v prejšnjem razdelku) razvijemo izraz za $h^{(e),i}$. Vrednost napetosti na mestu nezveznosti $\sigma^i\big|_{x_d^i}$ označimo s t^i in definiramo kot napetost v nezveznosti, ki je konjugirana količina skoka v osnem pomiku α^i.

$$h^{(e),i} = \int_L \left(\bar{G}^i + \delta_{x_d^i}\right)\sigma^i A^i dx = A^i \int_L \bar{G}^i\sigma^i dx + A^i\,\sigma^i\big|_{x_d^i} = A^i\left(\int_L \bar{G}^i\sigma^i dx + t^i\right)$$

Princip virtualnega dela $G^{\text{int}} - G^{\text{ext}} = 0$ nas pripelje do ravnotežnih enačb konstrukcije. Poleg standardnega globalnega ravnotežja notranjih in zunanjih sil dobimo dodatno ravnotežno enačbo za vsak sloj posameznega elementa, v katerem je bila prekoračena meja nosilnosti in se je v njem pojavila nezveznost.

$$\mathop{\mathsf{A}}_{e=1}^{n_{FE}} \left[\mathbf{f}^{\text{int},(e)} - \mathbf{f}^{\text{ext},(e)}\right] = \mathbf{0}, \qquad \forall e \in \{1,2,\ldots,n_{FE}\},\ \forall i \in \left\{1,2,\ldots,n_{CL}^{(e)}\right\}:\ \ h^{(e),i} = 0$$

Tu je A "assembly" operator, n_{FE} število končnih elementov v konstrukciji, $n_{CL}^{(e)}$ pa število slojev z aktivirano nezveznostjo v končnem elementu (e). Dodatno enačbo lahko jasneje interpretiramo, če vanjo vstavimo prej izpeljana izraza za $h^{(e),i}$ in $\bar{G}^i$. Vidimo, da zahteva enakost napetosti v sloju σ^i in napetosti v nezveznosti t^i. Ker se nanaša le na posamezen sloj, jo imenujemo enačba lokalnega ravnotežja.

$$h^{(e),i} = 0 \quad \Leftrightarrow \quad t^i = -\int_L \bar{G}^i\sigma^i dx = \sigma^i$$

Materialni modeli

Predpostavimo linearno elastičen strižni odziv, ki ga opišemo s spodnjo enačbo, v kateri je c strižni korekcijski faktor za pravokotni prerez, μ^i pa strižni modul betonskega ali jeklenega sloja, ki ga izračunamo iz ustreznega

elastičnega modula in Poissonovega količnika.

$$\tau^i = c\mu^i\gamma, \qquad c = 5/6, \qquad \mu^i = \frac{E^i}{2\,(1+\nu^i)}$$

Osni odziv sloja opišemo popolnoma enako kot pri večslojnem elementu za Euler-Bernoullijev nosilec v prejšnjem razdelku, torej z dvema materialnima zakonoma za betonski sloj in z dvema za sloj armature.

Računski postopek

Računski algoritem je enak tistemu pri Euler-Bernoullijevem nosilcu v prejšnjem razdelku, le da se za račun notranjih spremenljivk, napetosti, notranjih sil itd. uporabljajo malce drugačni (enostavnejši) izrazi. Poleg tega se pri Timošenkovem nosilcu ni potrebno ukvarjati z določanjem lokacije nezveznosti.

NADGRADNJA VEČSLOJNEGA KONČNEGA ELEMENTA ZA TIMOŠENKOV NOSILEC Z VISKOZNO REGULARIZACIJO ODZIVA V MEHČANJU

V poglavju 5 nadgradimo večslojni končni element za Timošenkov nosilec iz prejšnjega poglavja z viskozno regularizacijo odziva v mehčanju. Pri tej metodi vpeljemo dodatno viskozno silo v nezveznosti, katere namen je preprečiti hkraten pojav več nezveznosti v homogenem napetostnem polju. Če se nezveznost pojavi v več končnih elementih hkrati, viskozna regularizacija da prednost enemu izmed njih. Izbrani element se mehča naprej, ostali pa se elastično razbremenjujejo. Izbira prednostnega elementa se izvede na podlagi hitrosti napredovanja nezveznosti. Hitreje kot nezveznost raste, bolj se njena rast vzpodbuja, tako da v končni fazi samo "najhitrejši" element razvije nezveznost. Z vpeljavo viskozne sile malenkostno spremenimo ravnotežne enačbe, medtem ko kinematične in konstitutivne enačbe ostanejo nespremenjene. Posledično se rahlo spremenijo določeni izrazi, ki jih uporabljamo v računskem postopku.

Princip virtualnega dela

V večslojnem elementu vpeljemo viskozne sile v vsak sloj posebej in jih upoštevamo pri računu virtualnega dela notranjih sil elementa (e). Izrazu $G^{\text{int},(e)}$, ki smo ga izpeljali v poglavju 4, prištejemo dodaten člen zaradi viskoznih sil, ki delujejo na virtualnih skokih v pomiku $\hat{\alpha}^{(e),i}$ in katerih velikost je odvisna od hitrosti naraščanja (pravega) skoka v pomiku $\dot{\alpha}^{(e),i}$ in od viskoznega parametra η^i posameznega sloja.

$$G^{\text{int},(e)}_{\text{reg}} = G^{\text{int},(e)} + \sum_{i=1}^{n^{(e)}_{CL}} \hat{\alpha}^{(e),i} \underbrace{\eta^i \dot{\alpha}^{(e),i} A^i}_{\text{viskozna sila}} = \hat{\mathbf{d}}^{(e)^T} \mathbf{f}^{\text{int},(e)} + \sum_{i=1}^{n^{(e)}_{CL}} \hat{\alpha}^{(e),i} \underbrace{\left(h^{(e),i} + \eta^i \dot{\alpha}^{(e),i} A^i \right)}_{h^{(e),i}_{\text{reg}}}$$

Dobljeni izraz $G^{\text{int},(e)}_{\text{reg}}$ imenujemo regularizirano virtualno delo notranjih sil. Spremenjeni izraz ob virtualnem skoku v osnem pomiku $\hat{\alpha}^{(e),i}$ označimo s $h^{(e),i}_{\text{reg}}$. Dodatno ga lahko razvijemo, če upoštevamo znani izraz za $h^{(e),i}$.

$$h^{(e),i}_{\text{reg}} = A^i \left(\int_L \bar{G}^i \sigma^i dx + t^i \right) + \eta^i \dot{\alpha}^i A^i = A^i \left(\int_L \bar{G}^i \sigma^i dx + t^i + \eta^i \dot{\alpha}^i \right)$$

Tu je $\bar{G}^i = -1/L$ oblikovna funkcija za interpoliranje dodatnih napetosti zaradi nezveznosti, σ^i je napetost v sloju, t^i napetost v nezveznosti in A^i prerez i-tega sloja. Iz principa virtualnega dela $G^{\text{int}}_{\text{reg}} - G^{\text{ext}} = 0$ izpeljemo ravnotežne enačbe konstrukcije.

$$\mathop{\mathsf{A}}_{e=1}^{n_{FE}} \left[\mathbf{f}^{\text{int},(e)} - \mathbf{f}^{\text{ext},(e)}\right] = \mathbf{0}, \qquad \forall e \in \{1,2,\ldots,n_{FE}\}\,,\ \forall i \in \left\{1,2,\ldots,n_{CL}^{(e)}\right\}:\ \ h_{\text{reg}}^{(e),i} = 0$$

Enačbe globalnega ravnotežja konstrukcije so popolnoma enake kot pri elementu brez viskozne regularizacije, enačbe lokalnega ravnotežja pa obdržijo isto obliko, le izraz $h^{(e),i}$ je nadomeščen s $h_{\text{reg}}^{(e),i}$. Če razvijemo lokalno ravnotežno enačbo i-tega sloja, opazimo, da σ^i in t^i nista več enaka. Z vpeljavo viskozne sile torej v sloj vnesemo (majhno) neravnotežje med napetostmi v sloju in v nezveznosti.

$$h_{\text{reg}}^{(e),i} = 0 \quad \Leftrightarrow \quad t^i = -\int_L \bar{G}^i \sigma^i dx - \eta^i \dot{\alpha}^i = \sigma^i - \eta^i \dot{\alpha}^i$$

Račun notranjih spremenljivk

Vsiljeno neravnotežje v sloju se odraža v nekoliko spremenjenih izrazih, ki jih uporabljamo pri računu notranjih spremenljivk v fazi (A) posamezne iteracije. V betonskem sloju se izraz za testno vrednost napetosti v nezveznosti $t_{n+1}^{(k),trial}$ spremeni na naslednji način.

$$t_{n+1}^{(k),trial} = \frac{\check{\mathbf{B}}\mathbf{d}_{n+1}^{(k-1)}}{\bar{D}_n - \bar{G}\bar{\bar{D}}_n} \qquad \rightarrow \qquad t_{n+1}^{(k),trial} = \frac{\check{\mathbf{B}}\mathbf{d}_{n+1}^{(k-1)} + \bar{D}_n \frac{\eta}{\Delta\tau_{n+1}} \alpha_n}{\bar{D}_n - \bar{G}\bar{\bar{D}}_n + \bar{D}_n \frac{\eta}{\Delta\tau_{n+1}} \bar{\bar{D}}_n}$$

Tu je $\Delta\tau_{n+1} = \tau_{n+1} - \tau_n$ prirastek psevdo-časa, ki izhaja iz zapisa psevdo-časovnega odvoda $\dot{\alpha}^{(e),i}$ v inkrementalni obliki. Podobno se spremenita izraz za $\bar{\bar{\gamma}}_{n+1}^{*(k)}$, s katerim posodobimo vrednosti notranjih spremenljivk v primeru prekoračene nosilnosti (ko je $\bar{\bar{\phi}}_{n+1}^{(k),trial} > 0$), in izraz za skok v pomiku v primeru popolne izgube nosilnosti (ko je $t_{n+1}^{(k)} = 0$).

$$\bar{\bar{\gamma}}_{n+1}^{*(k)} = \frac{\bar{\bar{\phi}}_{n+1}^{(k),trial}\left(\bar{D}_n - \bar{G}\bar{\bar{D}}_n + \bar{D}_n \frac{\eta}{\Delta\tau_{n+1}} \bar{\bar{D}}_n\right)}{K_c^* \bar{D}_n - \bar{G} + \bar{D}_n \frac{\eta}{\Delta\tau_{n+1}}}, \qquad \alpha_{n+1}^{(k)} = -\frac{\check{\mathbf{B}}\mathbf{d}_{n+1}^{(k-1)} + \bar{D}_n^{-1} \frac{\eta}{\Delta\tau_{n+1}} \alpha_n}{\bar{G} - \bar{D}_n^{-1} \frac{\eta}{\Delta\tau_{n+1}}}$$

V sloju armature dobita izraza za $\bar{\bar{\gamma}}_{n+1}^{(k)}$, s katerima posodobimo vrednosti notranjih spremenljivk (v primeru, da je $\bar{\bar{\phi}}_{n+1}^{(k),trial} > 0$), naslednjo obliko.

$$\bar{\bar{\gamma}}_{n+1}^{(k)} = \begin{cases} \bar{\bar{\gamma}}_{n+1}^{A} = \dfrac{\bar{\bar{\phi}}_{n+1}^{(k),trial}}{-\bar{G}E_s + K_s + \frac{\eta}{\Delta\tau_{n+1}}}; & -K_s\left(\bar{\bar{\xi}}_n + \bar{\bar{\gamma}}_{n+1}^{A}\right) < \sigma_{fs} \\ \bar{\bar{\gamma}}_{n+1}^{B} = \dfrac{\left|t_{n+1}^{(k),trial}\right|}{-\bar{G}E_s + \frac{\eta}{\Delta\tau_{n+1}}}; & -K_s\left(\bar{\bar{\xi}}_n + \bar{\bar{\gamma}}_{n+1}^{A}\right) > \sigma_{fs} \end{cases}$$

Vsi navedeni izrazi prevzamejo prvotno obliko (kot v končnem elementu brez viskoznosti), če vanje vstavimo vrednost viskoznega parametra $\eta = 0$. Opomba: v izrazih sta opuščena indeksa (e) in i.

Račun vozliščnih pomikov

Pri reševanju ravnotežnih enačb moramo upoštevati, da je $h_{\text{reg}}^{(e),i}$ odvisen ne le od vozliščnih pomikov elementa $\mathbf{d}^{(e)}$ in skoka v osnem pomiku i-tega sloja $\alpha^{(e),i}$, temveč tudi od njegovega psevdo-časovnega odvoda $\dot{\alpha}^{(e),i}$.

$$h_{\text{reg},n+1}^{(e),i,(k)}\left(\mathbf{d}_{n+1}^{(e),(k-1)},\alpha_{n+1}^{(e),i,(k)},\dot{\alpha}_{n+1}^{(e),i,(k)}\right)=h_{n+1}^{(e),i,(k)}\left(\mathbf{d}_{n+1}^{(e),(k-1)},\alpha_{n+1}^{(e),i,(k)}\right)+\eta^i\dot{\alpha}_{n+1}^{(e),i,(k)}A^i$$

Odvod $\dot{\alpha}^{(e),i}$ zapišemo v inkrementalni obliki, kjer je $\alpha_{n+1}^{(e),i,(k)}$ trenutna vrednost skoka, $\alpha_n^{(e),i}$ vrednost iz prejšnjega koraka in $\Delta\tau_{n+1}=\tau_{n+1}-\tau_n$ prirastek psevdo-časa od prejšnjega do trenutnega koraka. Izračunamo lahko tudi odvod $\partial\dot{\alpha}_{n+1}^{(e),i,(k)}/\partial\alpha_{n+1}^{(e),i,(k)}$, ki ga potrebujemo pri računu togostne matrike elementa.

$$\dot{\alpha}_{n+1}^{(e),i,(k)}=\frac{\alpha_{n+1}^{(e),i,(k)}-\alpha_n^{(e),i}}{\Delta\tau_{n+1}},\qquad\frac{\partial\dot{\alpha}_{n+1}^{(e),i,(k)}}{\partial\alpha_{n+1}^{(e),i,(k)}}=\frac{1}{\Delta\tau_{n+1}}$$

Togostna matrika elementa je določena z enakim izrazom kot prej, le pri računu posameznih komponent moramo upoštevati odvisnost izrazov od $\dot{\alpha}^{(e),i}$.

$$\mathbf{K}_{n+1}^{(e),(k)}=\sum_{i=1}^{n_{CL}^{(e)}}\left(\mathbf{K}_{n+1}^{fd,(e),i,(k)}-\mathbf{K}_{n+1}^{f\alpha,(e),i,(k)}\left(K_{n+1}^{h\alpha,(e),i,(k)}\right)^{-1}\mathbf{K}_{n+1}^{hd,(e),i,(k)}\right)+\sum_{i=n_{CL}^{(e)}+1}^{n_L}\mathbf{K}_{n+1}^{fd,(e),i,(k)}$$

Komponenti $\mathbf{K}_{n+1}^{fd,(e),i,(k)}$ in $\mathbf{K}_{n+1}^{f\alpha,(e),i,(k)}$ ostaneta nespremenjeni, saj so izrazi za notranje sile $\mathbf{f}_{n+1}^{\text{int},(e),i,(k)}$ enaki kot pri elementu brez viskoznosti. Komponenti $\mathbf{K}_{n+1}^{hd,(e),i,(k)}$ in $K_{n+1}^{h\alpha,(e),i,(k)}$ pa sta sedaj definirani kot odvoda $h_{\text{reg}}^{(e),i}$, namesto $h^{(e),i}$.

$$\mathbf{K}_{n+1}^{fd,(e),i,(k)}=\frac{\partial\mathbf{f}_{n+1}^{\text{int},(e),i,(k)}}{\partial\mathbf{d}_{n+1}^{(e),(k-1)}},\qquad\mathbf{K}_{n+1}^{f\alpha,(e),i,(k)}=\frac{\partial\mathbf{f}_{n+1}^{\text{int},(e),i,(k)}}{\partial\alpha_{n+1}^{(e),i,(k)}}$$

$$\mathbf{K}_{n+1}^{hd,(e),i,(k)}=\frac{\partial h_{\text{reg},n+1}^{(e),i,(k)}}{\partial\mathbf{d}_{n+1}^{(e),(k-1)}},\qquad K_{n+1}^{h\alpha,(e),i,(k)}=\frac{\partial h_{\text{reg},n+1}^{(e),i,(k)}}{\partial\alpha_{n+1}^{(e),i,(k)}}$$

Izkaže se, da je tudi komponenta $\mathbf{K}_{n+1}^{hd,(e),i,(k)}$ enaka kot prej, saj psevdo-časovni odvod $\dot{\alpha}^{(e),i}$ ni funkcija vozliščnih pomikov $\mathbf{d}^{(e)}$.

$$\mathbf{K}_{n+1}^{hd,(e),i,(k)}=\frac{\partial h_{\text{reg},n+1}^{(e),i,(k)}}{\partial\mathbf{d}_{n+1}^{(e),(k-1)}}=\overbrace{\frac{\partial h_{n+1}^{(e),i,(k)}}{\partial\mathbf{d}_{n+1}^{(e),(k-1)}}}^{\text{od prej}}+\overbrace{\underbrace{\frac{\partial\dot{\alpha}_{n+1}^{(e),i,(k)}}{\partial\mathbf{d}_{n+1}^{(e),(k-1)}}}_{=0}\eta^iA^i}^{\text{dodatno}}=\frac{\partial h_{n+1}^{(e),i,(k)}}{\partial\mathbf{d}_{n+1}^{(e),(k-1)}}$$

Spremeni se torej samo komponenta $K_{n+1}^{h\alpha,(e),i,(k)}$.

$$K_{n+1}^{h\alpha,(e),i,(k)} = \frac{\partial h_{\text{reg},n+1}^{(e),i,(k)}}{\partial \alpha_{n+1}^{(e),i,(k)}} = \overbrace{\frac{\partial h_{n+1}^{(e),i,(k)}}{\partial \alpha_{n+1}^{(e),i,(k)}}}^{\text{od prej}} + \overbrace{\underbrace{\frac{\partial \dot{\alpha}_{n+1}^{(e),i,(k)}}{\partial \alpha_{n+1}^{(e),i,(k)}}}_{=1/\Delta\tau_{n+1}} \eta^i A^i}^{\text{dodatno}} = \frac{\partial h_{n+1}^{(e),i,(k)}}{\partial \alpha_{n+1}^{(e),i,(k)}} + \frac{\eta^i}{\Delta\tau_{n+1}} A^i$$

Združevanje togostnih matrik in rezidualov posameznih elementov v togostno matriko in rezidual celotne konstrukcije izvedemo enako kot prej. Nato izračunamo prirastke vozliščnih pomikov in stopimo v naslednjo iteracijo. Ko dosežemo zahtevano konvergenco rezultatov, nadaljujemo z analizo pri naslednjem psevdo-časovnem koraku.

ZAKLJUČKI

Cilj doktorske naloge je bil razviti končne elemente, sposobne verodostojnega modeliranja lokaliziranih porušitev v armiranem betonu, za numerično analizo armiranobetonskih nosilcev in okvirjev do popolne porušitve. Za modeliranje lokalizirane porušitve smo uporabili metodo vgrajene nezveznosti, pri kateri se interpolacijo pomikov v standardnem končnem elementu nadgradi z nezvezno funkcijo, ki omogoča opis skoka v pomiku znotraj elementa.

Izpeljali smo končni element na nivoju rezultant napetosti z vgrajeno nezveznostjo v zasuku za ravninski Euler-Bernoullijev nosilec. Element temelji na teoriji majhnih deformacij, elastoplastičnem materialnem modelu z bilinearnim utrjevanjem in zakonu linearnega plastičnega mehčanja v nezveznosti.

- Kljub enostavnosti je končni element sposoben opisati vse bistvene značilnosti odziva armiranobetonskih nosilcev - razpokanje betona, tečenje armature in lokalizirano porušitev nosilca.
- Končni element omogoča analizo konstrukcij do popolne izgube nosilnosti, zato lahko poleg mejne nosilnosti analiziramo tudi duktilnost in post-kritično obnašanje konstrukcije.
- Rezultati numeričnih primerov se razmeroma dobro ujemajo z drugimi rezultati, dostopnimi v literaturi, in z eksperimentalnimi rezultati.
- Končni element zagotavlja odziv v mehčanju, neodvisen od mreže končnih elementov.
- Kot vhodni podatek potrebujemo diagram moment - ukrivljenost in diagram moment v nezveznosti - skok v zasuku. Lahko ju določimo z eksperimentom ali izračunamo z natančnejšim končnim elementom.
- Element bi lahko nadgradili z mešanim materialnim modelom, ki bi poleg plastičnih deformacij znal opisati tudi zmanjšano togost betonskega prereza zaradi mikro-razpok, ali z vpeljavo skoka v osnem pomiku, vendar za običajne armiranobetonske nosilce ni pričakovati bistveno drugačni rezultatov.

Izpeljali smo večslojni končni element za Euler-Bernoullijev nosilec, ki ima po slojih vgrajene nezveznosti v osnem pomiku. Zasnovan je na teoriji majhnih deformacij. Nosilec razdelimo na več slojev betona in armature. Obnašanje betonskega sloja je opisano z modelom poškodovanosti z utrjevanjem zvezno po sloju in z modelom mehčanja v nezveznosti. Sloj armature je opisan z elastoplastičnim modelom z linearnim utrjevanjem zvezno po sloju in z modelom plastičnega linearnega mehčanja v nezveznosti.

- Končni element je bil namenjen za natančno analizo armiranobetonskih okvirjev in nosilcev ter za račun rezultantnih (materialno-geometrijskih) karakteristik poljubnih armiranobetonskih prerezov, potrebnih pri analizi z rezultantnimi končnim elementi, vendar element ne deluje, kot je bilo zamišljeno. Našli smo več nepravilnosti.

- Interpolacijsko funkcijo za dodatne napetosti zaradi nezveznosti smo izpeljali na izoliranem sloju ob predpostavki, da se lahko prosto deformira. To ne drži, saj je sloj povezan z ostalimi sloji preko vozliščnih pomikov. Posledično se dodatne napetosti, ki so posledica nezveznosti, ne morejo pravilno razporediti. Napetost v sloju nadziramo samo na mestu nezveznosti, kjer mora biti enaka napetosti v razpoki, torej pada z rastjo nezveznosti. Drugod po sloju lahko napetosti celo presežejo mejo nosilnosti.

- Ravnotežje se zagotavlja samo na nivoju končnega elementa, ne pa tudi na nivoju posameznega sloja. V disertaciji smo predstavili numerični primer armiranobetonskega nosilca v čistem nategu, v katerem se je napetost spreminjala linearno (!) po dolžini posameznega sloja. Če bi posamezen sloj osamili, ne bi bil v ravnotežju, nosilec kot celota pa je, saj se neravnotežja posameznih slojev medsebojno izničijo.

- Skoki v osnem pomiku v posameznih slojih so popolnoma neodvisni med seboj. V enem od numeričnih primerov nosilca (s simetričnim prerezom) v čistem nategu smo opazili linearno spreminjanje velikosti nezveznosti po višini nosilca (negativna na spodnjem robu, pozitivna na zgornjem robu in nič v sredini). Kot posledica se je pojavil prečni pomik prostega konca nosilca brez kakršne koli prečne obtežbe.

- V kinematiki na nivoju elementa ni nezveznosti (v zasuku). Srednja os elementa se vedno deformira skladno s standardno Euler-Bernoullijevo kinematiko, torej je gladka, tudi če nosilec izgubi vso nosilnost. Vsak sloj zdrsne po tirnici, ki je vzporedna s srednjo osjo elementa. To ne bi smelo povzročati večjih težav, če uporabimo dovolj fino mrežo končnih elementov. Poškodovani končni element ima namreč povečano ukrivljenost v primerjavi s sosednjimi elementi, kar lahko interpretiramo kot skok v zasuku, razmazan na celoten element.

- Opazili smo odvisnost rezultatov od mreže končnih elementov, ki je bila najlepše vidna v primeru konzole v čistem upogibu. Zaradi konstantnega napetostnega stanja vzdolž nosilca se nezveznosti pojavijo hkrati v vseh končnih elementih. Ob isti vrednosti vsiljenega zasuka na prostem koncu konzole v fini mreži nastane večje število manjših nezveznosti, v grobi mreži pa manjše število večjih nezveznosti. Skladno z zakonom mehčanja, napetost v nezveznosti pada z naraščanjem njene velikosti. Ob istem vsiljenem zasuku torej s fino mrežo izračunamo večji moment kot z grobo. Do največjih odstopanj pride v zadnjem delu odziva, ko se element kot celota začne mehčati, običajno zaradi odpovedi natezne armature. Težavo rešimo tako, da malce oslabimo armaturo v enem od končnih elementov, s čimer preprečimo hkratno odpove armature v vseh elementih. Če konzola odpove zaradi drobljenja betona v tlaku, problema ne moremo rešiti tako elegantno. Poleg tega se ne moremo izogniti (manjši) odvisnosti od diskretizacije zaradi mehčanja betona v nategu, preden element kot celota doseže mejno nosilnost.

- Glede na naštete pomanjkljivosti obravnavanega večslojnega elementa za Euler-Bernoullijev nosilec ne moremo priporočiti za splošno uporabo. Edina sprejemljiva aplikacija elementa je za primere s konstantnim napetostnim stanjem vzdolž nosilca (čisti upogib ali čisti tlak/nateg). Ob tem je treba poskrbeti za pravilno lociranje nezveznosti znotraj elementa. V primeru čistega upogiba se ne moremo popolnoma izogniti odvisnosti od diskretizacije.

Izpeljali smo večslojni končni element za Timošenkov nosilec, ki ima po slojih vgrajene nezveznosti v osnem pomiku. Zasnovan je na teoriji majhnih deformacij. Nosilec razdelimo na več slojev betona in armature. Obnašanje betonskega sloja je opisano z modelom poškodovanosti z utrjevanjem zvezno po sloju in z modelom mehčanja v nezveznosti. Sloj armature je opisan z elastoplastičnim modelom z linearnim utrjevanjem zvezno po sloju in z modelom plastičnega linearnega mehčanja v nezveznosti.

- Končni element omogoča detajlno analizo armiranobetonskih nosilcev in okvirjev do popolne porušitve, zaradi česar lahko poleg določitve mejne nosilnosti konstrukcije določimo tudi njeno duktilnost in analiziramo njeno post-kritično obnašanje. V vsaki fazi analize je na voljo podroben opis stanja materiala v konstrukciji (širjenje poškodovanosti betona, plastificiranja jekla in lokalizirane odpovedi obeh materialov).

- Končni element ni namenjen cikličnemu obremenjevanju, vendar kljub temu prenese manjše spremembe predznaka napetosti, ki se v nekaterih slojih lahko pojavi zaradi premika nevtralne osi tudi pri monotonem obremenjevanju.
- Potrebujemo dva materialna zakona za vsak material - zvezo med napetostmi in deformacijami po sloju ter zvezo med napetostjo in skokom v pomiku v nezveznosti. Lahko jih določimo z nateznim/tlačnim preizkusom. Zaradi tega je element primeren za računanje rezultantnih (materialno-geometrijskih) karakteristik poljubnih armiranobetonskih prerezov, potrebnih pri analizi z rezultantnimi končnim elementi.
- Pri numeričnih primerih smo opazili odvisnost rezultatov od mreže končnih elementov, ki je bila najlepše vidna pri konzoli v čistem upogibu. Zaradi konstantnega napetostnega stanja vzdolž konzole se nezveznosti pojavijo v vseh končnih elementih hkrati. Ob isti vrednosti vsiljenega zasuka na prostem koncu konzole v fini mreži nastane večje število manjših nezveznosti, v grobi mreži pa manjše število večjih nezveznosti. Skladno z zakonom mehčanja, napetost v nezveznosti pada z naraščanjem njene velikosti. Ob istem vsiljenem zasuku torej s fino mrežo izračunamo večji moment kot z grobo. Do največjih odstopanj pride v zadnjem delu odziva, ko se element kot celota začne mehčati, običajno zaradi odpovedi natezne armature. Težavo rešimo tako, da malce oslabimo armaturo v enem od končnih elementov, s čimer preprečimo hkratno odpove armature v vseh elementih. Če konzola odpove zaradi drobljenja betona v tlaku, problema ne moremo rešiti tako elegantno. Poleg tega se ne moremo izogniti (manjši) odvisnosti od diskretizacije zaradi mehčanja betona v nategu, preden element kot celota doseže mejno nosilnost.
- Odvisnost rezultatov od diskretizacije zaradi mehčanja betona v nategu je bila bolj očitna v primeru konzole s prečno silo na prostem koncu. Ker je element sposoben opisati samo konstantno napetostno stanje po svoji dolžini, je za zadovoljiv opis linearnega momenta potrebna precej fina mreža končnih elementov. Drobljenje mreže poveča število in zmanjša velikost razpok ter tako povzroči večje napetosti v tegnjenem betonu. Posledica tega je občutno precenjena vrednost momenta na meji tečenja.
- V kinematiki na nivoju elementa ni nezveznosti (v zasuku). Srednja os elementa se vedno deformira skladno s standardno Euler-Bernoullijevo kinematiko, torej je gladka, tudi če nosilec izgubi vso nosilnost. Vsak sloj zdrsne po tirnici, ki je vzporedna s srednjo osjo elementa. To ne bi smelo povzročati večjih težav, če uporabimo dovolj fino mrežo končnih elementov. Poškodovani končni element ima namreč povečano ukrivljenost v primerjavi s sosednjimi elementi, kar lahko interpretiramo kot skok v zasuku, razmazan na celoten element.
- Končni element smo testirali na več numeričnih primerih. V nekaterih primerih so se rezultati analize dobro ujemali z drugimi rezultati, dostopnimi v literaturi, in z rezultati eksperimentov. V nekaterih primerih pa je prišlo do večjih odstopanj.
- Preden lahko element priporočimo za splošno rabo, je treba natančno preučiti težave z odvisnostjo rezultatov od mreže končnih elementov, ki jo povzroči mehčanje betona v nategu. V primeru konzole z linearnim potekom momentov je bil vpliv pojava občuten, medtem ko v nekaterih kompleksnejših primerih odstopanje ni bilo tako opazno. Morda je vredno razmisliti o drugačnem materialnem modelu za beton v nategu (npr. princip razmazane nezveznosti, zanemarjena nosilnost betona v nategu, ipd.).
- Končni element bi lahko nadgradili, tako da bi dovoljeval ciklično nanašanje obtežbe. V ta namen bi morali vpeljati ločena kompleta notranjih spremenljivk za beton v tlaku in nategu, vendar to ni enostavna naloga. Tlačni in natezni odziv betona namreč nista neodvisna, njuna povezava pa ni čisto preprosta.

Večslojni končni element za Timošenkov nosilec smo nadgradili, tako da vključuje viskozno regularizacijo odziva v mehčanju. V nezveznost vsakega posameznega sloja smo vpeljali dodatno viskozno silo, odvisno hitrosti povečevanja nezveznosti in dodatnega viskoznega parametra. Dodatne sile smo upoštevali v zapisu virtualnega dela, kar je pripeljalo do rahlo spremenjenega sistema ravnotežnih enačb in posledično do manjših sprememb v računskem postopku.

- Vpeljava viskozne regularizacije je dokaj enostavna, saj zahteva le manjše spremembe obstoječega večslojnega elementa za Timošenkov nosilec.
- Velike vrednosti viskoznega parametra lahko vplivajo na pravilnost rezultatov. Povečajo lahko mejno nosilnost, zamaknejo krivuljo mehčanja (zakasnitev mehčanja) in povzročijo neničelno napetostno stanje v elementu, tudi ko napetost v razpoki pade na vrednost nič. Za majhne vrednosti viskoznega parametra so ti vplivi zanemarljivi.
- Viskozna regularizacija lahko prepreči odvisnost rezultatov od mreže končnih elementov, ki jo povzroči (fizikalno nepravilen) hkraten pojav več nezveznosti v homogenem napetostnem polju, vendar je učinkovitost metode odvisna od vrednosti viskoznega parametra. Optimalna vrednost parametra ni enolična, saj je npr. odvisna od izbrane velikosti obtežnega (časovnega) koraka.
- Z viskozno regularizacijo ne moremo preprečiti odvisnosti rezultatov od mreže končnih elementov, ki jo povzroči mehčanje betona v nategu, ko element kot celota še pridobiva nosilnost. Sloji betona se namreč ne morejo prosto deformirati, ker preostali del prereza diktira njihovo obnašanje.

BIBLIOGRAPHY

[1] Armero, F. 1999. Large-scale modeling of localized dissipative mechanisms in a local continuum: applications to the numerical simulation of strain localization in rate-dependent inelastic solids. Mechanics of Cohesive-frictional Materials 4, 2: 101–131.

[2] Lubliner, J. 1990. Plasticity theory. New York, MacMillan: 495 p.

[3] Moy, S. S. J. 1996. Plastic methods for steel and concrete structures. London, MacMillan: 271 p.

[4] Nielsen, M. P. 1984. Limit analysis and concrete plasticity. Englewood Cliffs, Prentice Hall: 420 p.

[5] De Borst, R., Bicanic, N., Mang, H., Meschke, G. (editors). 1998. Computational modelling of concrete structures: Proceedings of EURO-C 1998, Badgastain, Austria, March-April 1998. Rotterdam, Balkema: 1022 p.

[6] Bicanic, N., De Borst, R., Mang, H., Meschke, G. (editors). 2011. Computational modelling of concrete structures: Proceedings of EURO-C 2010, Schladming, Austria, March 2010. Leiden, CRC Press/Balkema: 836 p.

[7] Dolsek, M. 2010. Development of computing environment for the seismic performance assessment of reinforced concrete frames by using simplified nonlinear models. Bulletin of Earthquake Engineering 8, 6: 1309–1329.

[8] Fajfar, P., Dolsek, M., Marusic, D., Stratan, A. 2006. Pre- and post-test mathematical modelling of a plan-asymmetric reinforced concrete frame building. Earthquake Engineering and Structural Dynamics 35, 11: 1359–1379.

[9] Markovic, M., Saje, M., Planinc, I., Bratina, S. 2012. On strain softening in finite element analysis of RC planar frames subjected to fire. Engineering Structures 45: 349–361.

[10] Markovic, M., Krauberger, N., Saje, M., Planinc, I., Bratina, S. 2013. Non-linear analysis of pre-tensioned concrete planar beams. Engineering Structures 46: 279–293.

[11] Bratina, S., Saje, M., Planinc, I. 2004. On materially and geometrically non-linear analysis of reinforced concrete planar frames. International Journal of Solids and Structures 41, 24–25: 7181–7207.

[12] Mosler, J. 2004. On the modeling of highly localized deformations induced by material failure: The strong discontinuity approach. Archives of Computational Methods in Engineering 11, 4: 389–446.

[13] Jirasek, M. 2000. Comparative study on finite elements with embedded discontinuities. Computer Methods in Applied Mechanics and Engineering 188, 1–3: 307–330.

[14] Linder, C., Armero, F. 2007. Finite elements with embedded strong discontinuities for the modeling of failure in solids. International Journal for Numerical Methods in Engineering 72, 12: 1391–1433.

[15] Bazant, Z. P. 1976. Instability ductility and size effect in strain - softening concrete. Journal of the Engineering Mechanics Division 102, 2: 331–344.

[16] Hill, R. 1958. A general theory of uniqueness and stability in elastic-plastic solids. Journal of the Mechanics and Physics of Solids 6, 3: 236–249.

[17] Tvergaard, V., Needleman, A., Lo, K. K. 1981. Flow localization in the plane-strain tensile test. Journal of the Mechanics and Physics of Solids 29, 2: 115–142.

[18] De Borst, R. 2001. Some recent issues in computational failure mechanics. Internationl Journal for Numerical Methods in Engineering 52, 1–2: 63–95.

[19] Pijaudier-Cabot, G., Bazant, Z. P. 1987. Nonlocal damage theory. Journal of Engineering Mechanics 113, 10: 1512–1533.

[20] Bazant, Z. P., Oh, B. H. 1983. Crack band theory for fracture of concrete. Materials and Structures 16, 3: 155–177.

[21] Rots, J. G., Nauta, P., Kuster, G. M. A., Blaauwendraad, J. 1985. Smeared Crack Approach and Fracture Localization in Concrete. HERON 30, 1: 1–48.

[22] Bicanic, N., Pramono, E., Sture, S., Willam, K. J. 1985. On numerical prediction of concrete fracture localizations. In: Proceedings of NUMETA '85, Swansea, UK, January 1985. Rotterdam, Balkema: p. 385-392.

[23] Pietruszczak, S., Mroz, Z. 1981. Finite element analysis of deformation of strain-softening materials. International Journal for Numerical Methods in Engineering 17, 3: 327–334.

[24] Oliver, J. 1989. A consistent characteristic length for smeared cracking models. International Journal for Numerical Methods in Engineering 28, 2: 461–474.

[25] Eringen, A. C. 1981. On nonlocal plasticity. International Journal of Engineering Science 19, 12: 1461–1474.

[26] Eringen, A. C. 1983. Theories of nonlocal plasticity. International Journal of Engineering Science 21, 7: 741–751.

[27] Bazant, Z. P., Belytschko, T. B., Chang, T. P. 1984. Continuum theory for strain-softening. Journal of Engineering Mechanics 110, 12: 1666–1692.

[28] Aifantis, E. C. 1984. On the microstructural origin of certain inelastic models. Journal of Engineering Materials and Technology 106, 4: 326–330.

[29] De Borst, R., Muhlhaus, H. B. 1992. Gradient-dependent plasticity: Formulation and algorithmic aspects. International Journal for Numerical Methods in Engineering 35, 3: 521–539.

[30] Coleman, B. D., Hodgdon, M. L. 1985. On shear bands in ductile materials. Archive for Rational Mechanics and Analysis 90, 3: 219–247.

[31] De Borst, R., Sluys, L. J. 1991. Localization in a Cosserat continuum under static and dynamic loading conditions. Computer Methods in Applied Mechanics and Engineering 90, 1–3: 805–827.

[32] De Borst, R. 1991. Simulation of strain localization: A reappraisal of the Cosserat continuum. Engineering Computations 8, 4: 317–332.

[33] Needleman, A. 1988. Material rate dependence and mesh sensitivity in localization problems. Computer Methods in Applied Mechanics and Engineering 67, 1: 69–85.

[34] Ricles, J. M., Yang, Y. S., Priestley, M. J. N. 1998. Modeling nonductile R/C columns for seismic analysis of bridges. Journal of Structural Engineering 124, 4: 415–425.

[35] Ricles, J. M., Popov, E. P. 1994. Inelastic link element for EBF seismic analysis. Journal of Structural Engineering 120, 2: 441–463.

[36] Wells, G. N., Sluys, L. J. 2000. Application of embedded discontinuities for softening solids. Engineering Fracture Mechanics 65, 2–3: 263–281.

[37] Belytschko, T., Fish, J., Engelmann, B. E. 1988. A finite element with embedded localization zones. Computer Methods in Applied Mechanics and Engineering 70, 1: 59–89.

[38] Sluys, L., Berends, A. 1998. Discontinuous failure analysis for mode-I and mode-II localization problems. International Journal of Solids and Structures 35, 31–32: 4257–4274.

[39] Simo, J., Oliver, J., Armero, F. 1993. An analysis of strong discontinuities induced by strain-softening in rate-independent inelastic solids. Computational Mechanics 12, 5: 277–296.

[40] Garikipati, K., Hughes, T. J. R. 1998. A study of strain localization in a multiple scale framework – The one-dimensional problem. Computer Methods in Applied Mechanics and Engineering 159, 3: 193–222.

[41] Moes, N., Dolbow, J., Belytschko, T. 1999. A finite element method for crack growth without remeshing. International Journal for Numerical Methods in Engineering 46, 1: 131–150.

[42] Dvorkin, E. N., Cuitino, A. M., Gioia, G. 1990. Finite elements with displacement interpolated embedded localization lines insensitive to mesh size and distortions. International Journal for Numerical Methods in Engineering 30, 3: 541–564.

[43] Klisinski, M., Runesson, K., Sture, S. 1991. Finite element with inner softening band. Journal of Engineering Mechanics 117, 3: 575–587.

[44] Larsson, R., Runesson, K. 1996. Element-embedded localization band based on regularized displacement discontinuity. Journal of Engineering Mechanics 122, 5: 402–411.

[45] Oliver, J., Linero, D., Huespe, A., Manzoli, O. 2008. Two-dimensional modeling of material failure in reinforced concrete by means of a continuum strong discontinuity approach. Computer Methods in Applied Mechanics and Engineering 197, 5: 332–348.

[46] Dujc, J., Brank, B., Ibrahimbegovic, A., Brancherie, D. 2010. An embedded crack model for failure analysis of concrete solids. Computers and Concrete 7, 4: 331–346.

[47] Brancherie, D., Ibrahimbegovic, A. 2009. Novel anisotropic continuum-discrete damage model capable of representing localized failure of massive structures: Part I: theoretical formulation and numerical implementation. Engineering Computations 26, 1–2: 100–127.

[48] Ibrahimbegovic, A., Brancherie, D. 2003. Combined hardening and softening constitutive model of plasticity: precursor to shear slip line failure. Computational Mechanics 31, 1–2: 88–100.

[49] Armero, F., Ehrlich, D. 2006. Numerical modeling of softening hinges in thin Euler-Bernoulli beams. Computers and Structures 84, 10–11: 641–656.

[50] Ehrlich, D., Armero, F. 2005. Finite element methods for the analysis of softening plastic hinges in beams and frames. Computational Mechanics 35, 4: 237–264.

[51] Pham, B. H. 2009. Stress-resultant models for optimal design of reinforced-concrete frames. Doctoral thesis. Cachan, Ecole Normale Superieure de Cachan: 101 p.

[52] Pham, B. H., Davenne, L., Brancherie, D., Ibrahimbegovic, A. 2010. Stress resultant model for ultimate load design of reinforced-concrete frames: combined axial force and bending moment. Computers and Concrete 7, 4: 303–315.

[53] Wackerfuss, J. 2008. Efficient finite element formulation for the analysis of localized failure in beam structures. International Journal for Numerical Methods in Engineering 73, 9: 1217–1250.

[54] Dujc, J., Brank, B., Ibrahimbegovic, A. 2010. Multi-scale computational model for failure analysis of metal frames that includes softening and local buckling. Computer Methods in Applied Mechanics and Engineering 199, 21–22: 1371–1385.

[55] Jelenic, G., Sculac, P., Skec, L. 2012. Plain- and reinforced-concrete planar beam finite elements with embedded transversal cracking. In: Proceedings of ECCOMAS 2012, Vienna, Austria, September 2012.

[56] Skec, L., Jelenic, G. 2013. Analysis of a geometrically exact multi-layer beam with a rigid interlayer connection. Acta Mechanica. DOI: 10.1007/s00707-013-0972-5 .

[57] Oliver, J. 1996. Modelling strong discontinuities in solid mechanics via strain softening constitutive equations. Part 1: Fundamentals. International Journal for Numerical Methods in Engineering 39, 21: 3575–3600.

[58] Oliver, J. 1996. Modelling strong discontinuities in solid mechanics via strain softening constitutive equations. Part 2: Numerical simulation. International Journal for Numerical Methods in Engineering 39, 21: 3601–3623.

[59] Armero, F., Garikipati, K. 1996. An analysis of strong discontinuities in multiplicative finite strain plasticity and their relation with the numerical simulation of strain localization in solids. International Journal of Solids and Structures 33, 20–22: 2863–2885.

[60] Belytschko, T., Black, T. 1999. Elastic crack growth in finite elements with minimal remeshing. International Journal for Numerical Methods in Engineering 45, 5: 601–620.

[61] Wells, G. N., Sluys, L. J. 2001. A new method for modelling cohesive cracks using finite elements. International Journal for Numerical Methods in Engineering 50, 12: 2667–2682.

[62] Hansbo, A., Hansbo, P. 2004. A finite element method for the simulation of strong and weak discontinuities in solid mechanics. Computer Methods in Applied Mechanics and Engineering 193, 33–35: 3523–3540.

[63] Mariani, S., Perego, U. 2003. Extended finite element method for quasi-brittle fracture. International Journal for Numerical Methods in Engineering 58, 1: 103–126.

[64] Oliver, J., Huespe, A. E., Sanchez, P. J. 2006. A comparative study on finite elements for capturing strong discontinuities: E-FEM vs X-FEM. Computer Methods in Applied Mechanics and Engineering 195, 37–40: 4732–4752.

[65] Dujc, J. 2010. Finite element analysis of limit load and localized failure of structures. Doctoral thesis. Ljubljana, University of Ljubljana, Faculty of Civil and Geodetic Engineering: 211 p.

[66] Dujc, J., Brank, B., Ibrahimbegovic, A. 2010. Quadrilateral finite element with embedded strong discontinuity for failure analysis of solids. Computer Modeling in Engineering and Sciences 69, 3: 223–259.

[67] Dujc, J., Brank, B., Ibrahimbegovic, A. 2013. Stress-hybrid quadrilateral finite element with embedded strong discontinuity for failure analysis of plane stress solids. International Journal for Numerical Methods in Engineering 94, 12: 1075–1098.

[68] AceGen. <http://www.fgg.uni-lj.si/Symech>.

[69] AceFEM. <http://www.fgg.uni-lj.si/Symech>.

[70] Lane, G. E. 1972. Behavior of reinforced concrete beams under combined axial and lateral loading. Air force weapons laboratory. Kirtland air force base. New Mexico, AFWL-TR-76-130.

[71] Vecchio, F. J., Emara, M. B. 1992. Shear deformations in reinforced concrete frames. ACI Structural Journal 89, 1: 46–56.

[72] OpenSees. <http://opensees.berkeley.edu>.

[73] Ibrahimbegovic, A. 2009. Nonlinear solid mechanics: Theoretical formulations and finite element solution methods. Dordrecht, Springer: 574 p.

[74] Jukic, M., Brank, B., Ibrahimbegovic, A. 2013. Embedded discontinuity finite element formulation for failure analysis of planar reinforced concrete beams and frames. Engineering Structures 50: 115–125.

[75] Cranston, W. B. 1965. Tests on reinforced concrete frames, 1: Pinned portal frames. Technical report TRA/392, Cement and concrete association, London, England.

[76] Saje, M., Planinc, I., Bratina, S. 2005. Large displacements and instability of beam-like structural systems. In: Engineering structures under extreme conditions: Multi-physics and multi-scale computer models in nonlinear analysis and optimal design. Amsterdam, IOS Press: p. 329-350.

[77] Oliver, J., Huespe, A. E. 2004. Theoretical and computational issues in modelling material failure in strong discontinuity scenarios. Computer Methods in Applied Mechanics and Engineering 193, 27–29: 2987–3014.

[78] Li, L., Brancherie, D., Favergeon, J., Roelandt, J. M. 2010. Numerical approach for the description of different fracture modes for Zr/ZrO2 system - deterministic and probabilistic aspects. Surface and Coatings Technology 205, 5: 1475–1480.

LIST OF APPENDICES

APPENDIX A: EQUAL SIGNS OF TRIAL AND FINAL VALUES OF VARIABLES

We show in this appendix that the signs of trial and final values of certain variables, appearing in computational procedure, are equal. We demonstrate this equality for the moment in the bulk of the element M and the moment at the softening hinge t of the stress resultant finite element, and for the stress in the bulk of the layer σ and the traction at the discontinuity t of the multi-layer finite elements.

STRESS RESULTANT FINITE ELEMENT

Moment in the bulk of the element

Here we show that $sign\left(M_{n+1}^{trial}\right) = sign\left(M_{n+1}\right)$. Index k, referring to the Newton iteration, is omitted. Behavior of the bulk of the element is described by plasticity model with bilinear isotropic hardening, for which the following equations hold.

$$M_{n+1}^{trial} = EI\left(\bar{\kappa}_{n+1} - \bar{\kappa}_{p,n}\right), \quad \bar{\phi}_{n+1}^{trial} = \left|M_{n+1}^{trial}\right| - \left(M_c - \bar{q}_n\right) \tag{A.1}$$

If trial value of yield function $\bar{\phi}_{n+1}^{trial}$ is positive, internal variables are corrected to satisfy $\bar{\phi}_{n+1} = 0$. We can also write the updated value of the moment M_{n+1} and connect it to the trial value M_{n+1}^{trial}.

$$\begin{aligned} \bar{\kappa}_{p,n+1} &= \bar{\kappa}_{p,n} + \bar{\gamma}_{n+1} sign\left(M_{n+1}\right), \quad \bar{\xi}_{n+1} = \bar{\xi}_n + \bar{\gamma}_{n+1} \\ M_{n+1} &= EI\left(\bar{\kappa}_{n+1} - \bar{\kappa}_{p,n+1}\right) = EI\left(\bar{\kappa}_{n+1} - \bar{\kappa}_{p,n} - \bar{\gamma}_{n+1} sign\left(M_{n+1}\right)\right) = \\ &= M_{n+1}^{trial} - EI\bar{\gamma}_{n+1} sign\left(M_{n+1}\right) \end{aligned} \tag{A.2}$$

Above expressions are inserted into equation $\bar{\phi}_{n+1} = 0$. We consider both options for the hardening variable $\bar{q}$.

$$\bar{q}_{n+1} = \begin{cases} -H_1 \bar{\xi}_{n+1}; & \bar{\xi}_{n+1} \le \bar{\xi}_{\Delta H} \\ -\left(M_y - M_c\right) - H_2\left(\bar{\xi}_{n+1} - \bar{\xi}_{\Delta H}\right); & \bar{\xi}_{n+1} > \bar{\xi}_{\Delta H} \end{cases} \tag{A.3}$$

When $\bar{\xi}_{n+1} \le \bar{\xi}_{\Delta H}$, we obtain:

$$\begin{aligned} \bar{\phi}_{n+1} &= \left|M_{n+1}\right| - \left(M_c - \bar{q}_{n+1}\right) = \\ &= \left(M_{n+1}^{trial} - EI\bar{\gamma}_{n+1} sign\left(M_{n+1}\right)\right) sign\left(M_{n+1}\right) - \left(M_c + H_1 \bar{\xi}_{n+1}\right) = \\ &= M_{n+1}^{trial} sign\left(M_{n+1}\right) - EI\bar{\gamma}_{n+1} - \left(M_c + H_1 \bar{\xi}_{n+1}\right) = 0 \end{aligned} \tag{A.4}$$

It follows that:

$$M_{n+1}^{trial} sign\left(M_{n+1}\right) = \underbrace{EI\bar{\gamma}_{n+1}}_{>0} + \underbrace{M_c}_{>0} + \underbrace{H_1 \bar{\xi}_{n+1}}_{>0} > 0 \quad \Rightarrow \quad sign\left(M_{n+1}^{trial}\right) = sign\left(M_{n+1}\right) \tag{A.5}$$

When $\bar{\xi}_{n+1} > \bar{\xi}_{\Delta H}$, we get:

$$\begin{aligned}\bar{\phi}_{n+1} &= |M_{n+1}| - (M_c - \bar{q}_{n+1}) = \\ &= \left(M_{n+1}^{trial} - EI\bar{\gamma}_{n+1} sign\left(M_{n+1}\right)\right) sign\left(M_{n+1}\right) - \left(M_c + (M_y - M_c) + H_2\left(\bar{\xi}_{n+1} - \bar{\xi}_{\Delta H}\right)\right) = \\ &= M_{n+1}^{trial} sign\left(M_{n+1}\right) - EI\bar{\gamma}_{n+1} - \left(M_y + H_2\left(\bar{\xi}_{n+1} - \bar{\xi}_{\Delta H}\right)\right) = 0\end{aligned} \tag{A.6}$$

Again, it follows that:

$$M_{n+1}^{trial} sign\left(M_{n+1}\right) = \underbrace{EI\bar{\gamma}_{n+1}}_{>0} + \underbrace{M_y}_{>0} + \underbrace{H_2\left(\bar{\xi}_{n+1} - \bar{\xi}_{\Delta H}\right)}_{>0} > 0 \quad \Rightarrow \quad sign\left(M_{n+1}^{trial}\right) = sign\left(M_{n+1}\right) \tag{A.7}$$

Moment in the softening hinge

Similarly, we can show that $sign\left(t_{n+1}^{trial}\right) = sign\left(t_{n+1}\right)$. For the softening hinge it holds:

$$t_{n+1}^{trial} = M_{n+1}^{trial}\big|_{x_d} = \left[EI\bar{\kappa}_{n+1} + \bar{G}\alpha_n - \bar{\kappa}_{p,n}\right]_{x=x_d}, \quad \bar{\bar{\phi}}_{n+1}^{trial} = \left|t_{n+1}^{trial}\right| - (M_u - \bar{\bar{q}}_n) \tag{A.8}$$

If $\bar{\bar{\phi}}_{n+1}^{trial}$ is positive, internal variables are corrected. Let us write the expression for the traction at the discontinuity t_{n+1} and express it with the trial value t_{n+1}^{trial}.

$$\begin{aligned}&\alpha_{n+1} = \alpha_n + \bar{\bar{\gamma}}_{n+1} sign\left(t_{n+1}\right), \quad \bar{\bar{\xi}}_{n+1} = \bar{\bar{\xi}}_n + \bar{\bar{\gamma}}_{n+1} \\ &t_{n+1} = M_{n+1}|_{x_d} = EI\left[\bar{\kappa}_{n+1} + \bar{G}\alpha_{n+1} - \bar{\kappa}_{p,n}\right]_{x=x_d} = t_{n+1}^{trial} + EI\,\bar{G}\big|_{x_d}\bar{\bar{\gamma}}_{n+1} sign\left(t_{n+1}\right)\end{aligned} \tag{A.9}$$

Above expressions are inserted into equation $\bar{\bar{\phi}}_{n+1} = 0$.

$$\begin{aligned}\bar{\bar{\phi}}_{n+1} &= |t_{n+1}| - (M_u - \bar{\bar{q}}_{n+1}) = \\ &= \left(t_{n+1}^{trial} + EI\,\bar{G}\big|_{x_d}\bar{\bar{\gamma}}_{n+1} sign\left(t_{n+1}\right)\right) sign\left(t_{n+1}\right) - (M_u - \bar{\bar{q}}_{n+1}) = \\ &= t_{n+1}^{trial} sign\left(t_{n+1}\right) + EI\,\bar{G}\big|_{x_d}\bar{\bar{\gamma}}_{n+1} - (M_u - \bar{\bar{q}}_{n+1}) = 0\end{aligned} \tag{A.10}$$

It follows that:

$$t_{n+1}^{trial} sign\left(t_{n+1}\right) = \underbrace{-EI\,\bar{G}\big|_{x_d}\bar{\bar{\gamma}}_{n+1}}_{>0} + \underbrace{(M_u - \bar{\bar{q}}_{n+1})}_{\geq 0} > 0 \quad \Rightarrow \quad sign\left(t_{n+1}^{trial}\right) = sign\left(t_{n+1}\right) \tag{A.11}$$

MULTI-LAYER FINITE ELEMENTS

Stress in the bulk of a reinforcement layer

We show in this section that $sign\left(\sigma_{n+1}^{trial}\right) = sign\left(\sigma_{n+1}\right)$. Indices i and k, referring to a certain layer and the Newton iteration, are omitted. The bulk of a reinforcement layer is described by plasticity model with isotropic hardening, for which the following equations hold.

$$\sigma_{n+1}^{trial} = E_s\left(\bar{\varepsilon}_{n+1} - \bar{\varepsilon}_{p,n}\right), \quad \bar{\phi}_{n+1}^{trial} = \left|\sigma_{n+1}^{trial}\right| - \left(\sigma_y - \bar{q}_n\right) \tag{A.12}$$

If trial value of yield function $\bar{\phi}_{n+1}^{trial}$ is positive, internal variables are corrected to satisfy $\bar{\phi}_{n+1} = 0$. We write the expression for the final value of stress σ_{n+1} and connect it to the trial value σ_{n+1}^{trial}.

$$\begin{aligned}
\bar{\varepsilon}_{p,n+1} &= \bar{\varepsilon}_{p,n} + \bar{\gamma}_{n+1} sign\left(\sigma_{n+1}\right), \quad \bar{\xi}_{n+1} = \bar{\xi}_n + \bar{\gamma}_{n+1} \\
\sigma_{n+1} &= E_s\left(\bar{\varepsilon}_{n+1} - \bar{\varepsilon}_{p,n+1}\right) = E_s\left(\bar{\varepsilon}_{n+1} - \bar{\varepsilon}_{p,n} - \bar{\gamma}_{n+1} sign\left(\sigma_{n+1}\right)\right) = \\
&= \sigma_{n+1}^{trial} - E_s \bar{\gamma}_{n+1} sign\left(\sigma_{n+1}\right)
\end{aligned} \tag{A.13}$$

Above expressions are inserted into equation $\bar{\phi}_{n+1} = 0$.

$$\begin{aligned}
&\bar{\phi}_{n+1} = \left|\sigma_{n+1}\right| - \left(\sigma_y - \bar{q}_{n+1}\right) = \\
&= \left(\sigma_{n+1}^{trial} - E_s \bar{\gamma}_{n+1} sign\left(\sigma_{n+1}\right)\right) sign\left(\sigma_{n+1}\right) - \left(\sigma_y + H_s \bar{\xi}_{n+1}\right) = \\
&= \sigma_{n+1}^{trial} sign\left(\sigma_{n+1}\right) - E_s \bar{\gamma}_{n+1} - \left(\sigma_y + H_s \bar{\xi}_{n+1}\right) = 0
\end{aligned} \tag{A.14}$$

It follows that:

$$\sigma_{n+1}^{trial} sign\left(\sigma_{n+1}\right) = \underbrace{E_s \bar{\gamma}_{n+1}}_{>0} + \underbrace{\sigma_y}_{>0} + \underbrace{H_s \bar{\xi}_{n+1}}_{>0} > 0 \quad \Rightarrow \quad sign\left(\sigma_{n+1}^{trial}\right) = sign\left(\sigma_{n+1}\right) \tag{A.15}$$

Stress in the bulk of a concrete layer

We use a similar procedure for the bulk of a concrete layer. First, we write expressions for the trial values of stress and damage function.

$$\sigma_{n+1}^{trial} = \bar{D}_n^{-1} \bar{\varepsilon}_{n+1} \quad \Leftrightarrow \quad \bar{D}_n \sigma_{n+1}^{trial} = \bar{\varepsilon}_{n+1}, \qquad \bar{\phi}_{n+1}^{trial} = \left|\sigma_{n+1}^{trial}\right| - \left(\sigma_d - \bar{q}_n\right) \tag{A.16}$$

Just like before, internal variables are corrected if the trial value of yield function $\bar{\phi}_{n+1}^{trial}$ is positive. We express the final stress σ_{n+1} with the trial value σ_{n+1}^{trial} and insert it into equation $\bar{\phi}_{n+1} = 0$.

$$\begin{aligned}
&\sigma_{n+1} = \bar{D}_{n+1}^{-1} \bar{\varepsilon}_{n+1} = \bar{D}_{n+1}^{-1} \bar{D}_n \sigma_{n+1}^{trial} \\
&\bar{\phi}_{n+1} = \left|\sigma_{n+1}\right| - \left(\sigma_d - \bar{q}_{n+1}\right) = \bar{D}_{n+1}^{-1} \bar{D}_n \sigma_{n+1}^{trial} sign\left(\sigma_{n+1}\right) - \left(\sigma_d + H_c \bar{\xi}_{n+1}\right) = 0
\end{aligned} \tag{A.17}$$

From here, we can conclude:

$$\sigma_{n+1}^{trial} sign\left(\sigma_{n+1}\right) = \underbrace{\bar{D}_{n+1}}_{>0} \underbrace{\bar{D}_n^{-1}}_{>0} \underbrace{\left(\sigma_d + H_c \bar{\xi}_{n+1}\right)}_{>0} > 0 \quad \Rightarrow \quad sign\left(\sigma_{n+1}^{trial}\right) = sign\left(\sigma_{n+1}\right) \tag{A.18}$$

Traction at the discontinuity of a reinforcement layer

This section refers to the Timoshenko beam element. The only difference in the procedure for the Euler-Bernoulli beam element is that the traction at the discontinuity is equal to the stress evaluated at the location of the discontinuity $t = \sigma|_{x_d}$, instead of just $t = \sigma$. As a consequence, certain quantities are evaluated at x_d, in the same way as for the stress resultant element above. This does not affect the procedure, nor the results.

We show in this section that $sign\left(t_{n+1}^{trial}\right) = sign\left(t_{n+1}\right)$. For the discontinuity in a layer of reinforcement it holds:

$$t_{n+1}^{trial} = \sigma_{n+1}^{trial} = E_s\left(\bar{\tilde{\varepsilon}}_{n+1} + \bar{G}\alpha_n - \bar{\varepsilon}_{p,n}\right), \quad \bar{\bar{\phi}}_{n+1}^{trial} = \left|t_{n+1}^{trial}\right| - (\sigma_{fs} - \bar{\bar{q}}_n) \tag{A.19}$$

If $\bar{\bar{\phi}}_{n+1}^{trial}$ is positive, internal variables are corrected. We express the final value of traction at the discontinuity t_{n+1} with the trial value t_{n+1}^{trial}.

$$\begin{aligned} &\alpha_{n+1} = \alpha_n + \bar{\bar{\gamma}}_{n+1} sign\left(t_{n+1}\right), \quad \bar{\bar{\xi}}_{n+1} = \bar{\bar{\xi}}_n + \bar{\bar{\gamma}}_{n+1} \\ &t_{n+1} = \sigma_{n+1} = E_s\left(\bar{\tilde{\varepsilon}}_{n+1} + \bar{G}\alpha_{n+1} - \bar{\varepsilon}_{p,n}\right) = t_{n+1}^{trial} + E_s\bar{G}\bar{\bar{\gamma}}_{n+1} sign\left(t_{n+1}\right) \end{aligned} \tag{A.20}$$

Above expressions are inserted into equation $\bar{\bar{\phi}}_{n+1} = 0$.

$$\begin{aligned} &\bar{\bar{\phi}}_{n+1} = |t_{n+1}| - (\sigma_{fs} - \bar{\bar{q}}_{n+1}) = \\ &= \left(t_{n+1}^{trial} + E_s\bar{G}\bar{\bar{\gamma}}_{n+1} sign\left(t_{n+1}\right)\right) sign\left(t_{n+1}\right) - (\sigma_{fs} - \bar{\bar{q}}_{n+1}) = \\ &= t_{n+1}^{trial} sign\left(t_{n+1}\right) + E_s\bar{G}\bar{\bar{\gamma}}_{n+1} - (\sigma_{fs} - \bar{\bar{q}}_{n+1}) = 0 \end{aligned} \tag{A.21}$$

It follows that:

$$t_{n+1}^{trial} sign\left(t_{n+1}\right) = \underbrace{-E_s\bar{G}\bar{\bar{\gamma}}_{n+1}}_{>0} + \underbrace{(\sigma_{fs} - \bar{\bar{q}}_{n+1})}_{\geq 0} > 0 \quad \Rightarrow \quad sign\left(t_{n+1}^{trial}\right) = sign\left(t_{n+1}\right) \tag{A.22}$$

Traction at the discontinuity of a concrete layer

This section refers to the Timoshenko beam element. The only difference in the procedure for the Euler-Bernoulli beam element is that the traction at the discontinuity is equal to the stress evaluated at the location of the discontinuity $t = \sigma|_{x_d}$, instead of just $t = \sigma$. As a consequence, certain quantities are evaluated at x_d, in the same way as for the stress resultant element above. This does not affect the procedure, nor the results.

First, we write the expression for the trial value of traction at the discontinuity t_{n+1}^{trial}. In this expression appears the displacement jump α_{n+1}^{trial}, which is directly dependent on t_{n+1}^{trial}. Therefore, we have to rearrange the equation to express the trial value of traction with known quantities.

$$t_{n+1}^{trial} = \sigma_{n+1}^{trial} = \bar{D}_n^{-1}\left(\bar{\tilde{\varepsilon}}_{n+1} + \bar{G}\alpha_{n+1}^{trial}\right), \quad \alpha_{n+1}^{trial} = \bar{\bar{D}}_n t_{n+1}^{trial} \tag{A.23}$$

$$\begin{aligned} t_{n+1}^{trial} &= \bar{D}_n^{-1}\left(\bar{\tilde{\varepsilon}}_{n+1} + \bar{G}\bar{\bar{D}}_n t_{n+1}^{trial}\right) \\ \bar{D}_n t_{n+1}^{trial} &= \bar{\tilde{\varepsilon}}_{n+1} + \bar{G}\bar{\bar{D}}_n t_{n+1}^{trial} \\ t_{n+1}^{trial}\left(\bar{D}_n - \bar{G}\bar{\bar{D}}_n\right) &= \bar{\tilde{\varepsilon}}_{n+1} \end{aligned} \tag{A.24}$$

From here we can conclude:

$$t_{n+1}^{trial} = \underbrace{\left(\bar{D}_n - \bar{G}\bar{\bar{D}}_n\right)}_{>0}^{-1}\bar{\tilde{\varepsilon}}_{n+1} \quad \Rightarrow \quad sign\left(t_{n+1}^{trial}\right) = sign\left(\bar{\tilde{\varepsilon}}_{n+1}\right) \tag{A.25}$$

Exactly the same operation is performed on t_{n+1}, only α_{n+1}^{trial} and $\bar{\bar{D}}_n$ are replaced by α_{n+1} and $\bar{\bar{D}}_{n+1}$.

$$t_{n+1} = \sigma_{n+1} = \bar{D}_n^{-1}\left(\bar{\tilde{\varepsilon}}_{n+1} + \bar{G}\alpha_{n+1}\right), \quad \alpha_{n+1} = \bar{\bar{D}}_{n+1} t_{n+1} \tag{A.26}$$

We come to an equivalent conclusion:

$$t_{n+1} = \underbrace{\left(\bar{D}_n - \bar{G}\bar{\bar{D}}_{n+1}\right)}_{>0}^{-1}\bar{\tilde{\varepsilon}}_{n+1} \quad \Rightarrow \quad sign\left(t_{n+1}\right) = sign\left(\bar{\tilde{\varepsilon}}_{n+1}\right) \tag{A.27}$$

From (A.25) and (A.27) it is obvious that:

$$sign\left(t_{n+1}^{trial}\right) = sign\left(t_{n+1}\right) \tag{A.28}$$

Since $\bar{\bar{D}}_{n+1}$ is positive, we can also conclude from the second of equations (A.26):

$$sign\left(\alpha_{n+1}\right) = sign\left(t_{n+1}\right) \tag{A.29}$$

APPENDIX B: LINEAR RELATION BETWEEN t AND α IN CONCRETE LAYER

In this appendix we take a closer look at the relation between the traction t^i and the displacement jump α^i at the discontinuity of the i-th concrete layer. Index i is omitted in the following equations.

We are interested in the case when the layer is in softening and still possesses some carrying capacity, that is when $\bar{\bar{q}} < \sigma_{fc}$. The following equations then hold.

$$\bar{\bar{q}} = \sigma_{fc}\left(1 - e^{K_c \bar{\bar{\xi}}}\right), \quad \dot{\bar{\bar{q}}} = -K_c\,\sigma_{fc}\,e^{K_c \bar{\bar{\xi}}}\,\dot{\bar{\bar{\xi}}} = -K_c\,\sigma_{fc}\,e^{K_c \bar{\bar{\xi}}}\,\dot{\bar{\bar{\gamma}}} \tag{B.1}$$

The first of the following evolution equations was already used in the above expression.

$$\dot{\bar{\bar{\xi}}} = \dot{\bar{\bar{\gamma}}}, \quad \dot{\bar{\bar{D}}} = \frac{\dot{\bar{\bar{\gamma}}}}{t}\,sign\,(t) \tag{B.2}$$

Displacement jump α and its pseudo-time derivative are computed as follows.

$$\alpha = \bar{\bar{D}}t, \quad \dot{\alpha} = \dot{\bar{\bar{D}}}t + \bar{\bar{D}}\dot{t} \tag{B.3}$$

Since we are considering a softening step, rather than elastic unloading, the failure function $\bar{\bar{\phi}}$ must be zero. We use this requirement to write the expressions for traction t and its pseudo-time derivative.

$$\bar{\bar{\phi}} = |t| - (\sigma_{fc} - \bar{\bar{q}}) = 0 \quad \Rightarrow \quad t = (\sigma_{fc} - \bar{\bar{q}})\,sign\,(t)\,, \quad \dot{t} = -\dot{\bar{\bar{q}}}\,sign(t) \tag{B.4}$$

We can now further develop the pseudo-time derivative $\dot{\alpha}$ by utilizing expressions (B.2), (B.4) and (B.1).

$$\begin{aligned} &\dot{\alpha} = t\frac{\dot{\bar{\bar{\gamma}}}}{t}sign\,(t) - \bar{\bar{D}}\dot{\bar{\bar{q}}}\,sign(t) = \dot{\bar{\bar{\gamma}}}\,sign\,(t) + \bar{\bar{D}}K_c\,\sigma_{fc}\,e^{K_c \bar{\bar{\xi}}}\,\dot{\bar{\bar{\gamma}}}\,sign(t) \\ &\dot{\alpha}\,sign(t) = \dot{\bar{\bar{\gamma}}}\left(1 + \bar{\bar{D}}K_c\,\sigma_{fc}\,e^{K_c \bar{\bar{\xi}}}\right) \end{aligned} \tag{B.5}$$

We introduce a new variable $\mathtt{A}$.

$$\mathtt{A} = \frac{\dot{\alpha}\,sign(t)}{\dot{\bar{\bar{q}}}} = \frac{\dot{\bar{\bar{\gamma}}}\left(1 + \bar{\bar{D}}K_c\,\sigma_{fc}\,e^{K_c \bar{\bar{\xi}}}\right)}{-K_c\,\sigma_{fc}\,e^{K_c \bar{\bar{\xi}}}\,\dot{\bar{\bar{\gamma}}}} = -\frac{1}{\sigma_{fc}}\left(\frac{1}{K_c}e^{-K_c \bar{\bar{\xi}}} + \sigma_{fc}\bar{\bar{D}}\right) \tag{B.6}$$

Pseudo-time derivative $\dot{\mathtt{A}}$ is computed by utilizing the evolution equations (B.2). Expressions for $\bar{\bar{q}}$ and t from (B.1) and (B.4) are also used.

$$\begin{aligned}\dot{\mathtt{A}} &= -\frac{1}{\sigma_{fc}}\left(\frac{-K_c\dot{\bar{\xi}}}{K_c}e^{-K_c\bar{\xi}}+\sigma_{fc}\frac{\dot{\bar{\gamma}}}{t}sign\,(t)\right)=\frac{\dot{\bar{\gamma}}}{\sigma_{fc}}\left(e^{-K_c\bar{\xi}}-\frac{\sigma_{fc}}{t\,sign\,(t)}\right)= \\ &= \frac{\dot{\bar{\gamma}}}{\sigma_{fc}}\left(e^{-K_c\bar{\xi}}-\frac{\sigma_{fc}}{\sigma_{fc}-\bar{\bar{q}}}\right)=\frac{\dot{\bar{\gamma}}}{\sigma_{fc}}\left(e^{-K_c\bar{\xi}}-\frac{\sigma_{fc}}{\sigma_{fc}-\sigma_{fc}\left(1-e^{K_c\bar{\xi}}\right)}\right)= \\ &= \frac{\dot{\bar{\gamma}}}{\sigma_{fc}}\left(e^{-K_c\bar{\xi}}-e^{-K_c\bar{\xi}}\right)=0\end{aligned} \tag{B.7}$$

We observe that $\mathtt{A}$ is constant in pseudo-time, since its derivative $\dot{\mathtt{A}}$ is equal to zero. The value of $\mathtt{A}$ can be determined at any particular point in pseudo-time but the obvious choice is the moment when softening begins (denoted with index 0). Then, the values of certain variables are known: $\bar{\bar{\xi}}_0=0$, $\bar{\bar{D}}_0=0$, and consequently $\alpha_0=0$, $\bar{\bar{q}}_0=0$. Time derivatives $\dot{\bar{\bar{q}}}$ and $\dot{\alpha}$ evaluate to:

$$\dot{\bar{\bar{q}}}_0=-K_c\,\sigma_{fc}\dot{\bar{\bar{\gamma}}},\quad \dot{\alpha}_0=\dot{\bar{\bar{\gamma}}}\,sign(t) \tag{B.8}$$

$$\frac{\Delta\alpha}{\Delta\bar{\bar{q}}}=\frac{\partial\alpha}{\partial\bar{\bar{q}}}=\frac{\dot{\alpha}}{\dot{\bar{\bar{q}}}}=\frac{\dot{\alpha}_0}{\dot{\bar{\bar{q}}}_0}=-\frac{sign(t)}{K_c\,\sigma_{fc}} \tag{B.9}$$

For evolution equations (B.2) and the chosen exponential softening law (B.1), the increments $\Delta\alpha$ and $\Delta\bar{\bar{q}}$ are linearly dependent.

Exactly the same behavior would be obtained by employing another set of evolution equations and softening law.

$$\dot{\bar{\bar{\xi}}}^*=\dot{\bar{\bar{\gamma}}}^*,\quad \dot{\alpha}=\dot{\bar{\bar{\gamma}}}^*sign\,(t)\,,\quad \bar{\bar{q}}=-K_c^*\bar{\bar{\xi}}^*,\quad K_c^*=K_c\,\sigma_{fc} \tag{B.10}$$

Variables $\bar{\bar{\xi}}^*$ and $\bar{\bar{\gamma}}^*$ are denoted with $*$ to be distinguished from the original variables.

$$\frac{\Delta\alpha}{\Delta\bar{\bar{q}}}=\frac{\partial\alpha}{\partial\bar{\bar{q}}}=\frac{\dot{\alpha}}{\dot{\bar{\bar{q}}}}=\frac{\dot{\bar{\bar{\gamma}}}^*sign\,(t)}{-K_c^*\dot{\bar{\bar{\gamma}}}^*}=-\frac{sign(t)}{K_c^*} \tag{B.11}$$

By taking into account the initial conditions ($\alpha^i=0$, $t^i=\sigma_{fc}\,sign\left(\alpha^i\right)$), we can finally write t^i as a function of α^i

$$t^i=\sigma_{fc}\,sign\left(\alpha^i\right)+\sigma_{fc}\,K_c\,\alpha^i \tag{B.12}$$

Remark. (B.10) *are not actual evolution equations and softening law. This is merely an aid which allows for considerable simplification of the computational procedure. Due to linear form of all equations, an explicit analytical expression can be easily obtained for $\bar{\bar{\gamma}}^*$, as opposed to $\bar{\bar{\gamma}}$. Indeed, the calculated value of $\bar{\bar{\gamma}}^*$ in a certain step is different than the value of $\bar{\bar{\gamma}}$, but the corresponding values of α and $\bar{\bar{q}}$ are correct. Of course, this procedure is only applicable in case of the particular softening law, chosen in* (B.1).

APPENDIX C: EXPRESSIONS FOR t_{n+1}^{trial} AND $\bar{\bar{\gamma}}_{n+1}^{*}$ IN CONCRETE LAYER

In this appendix we derive the expressions for the trial value of traction t_{n+1}^{trial} at the discontinuity of a concrete layer and for the damage softening multiplier $\bar{\bar{\gamma}}_{n+1}^{*}$. Both variables are used in the computational procedure, described in section 4.3.1.3 of chapter 4 and in section 3.3.1.2 of chapter 3.

MULTI-LAYER TIMOSHENKO BEAM FINITE ELEMENT

Trial value of traction at the discontinuity of concrete layer

Once a discontinuity occurs in a concrete layer, the hardening internal variables are frozen. From then on, we always use $\bar{D}_n$ for the bulk compliance. In a trial step, the behavior of the discontinuity is assumed to be elastic, which means that the discontinuity compliance $\bar{\bar{D}}$ and displacement-like variable $\bar{\bar{\xi}}^{*}$ that controls the reduction of carrying capacity, keep the values from the previous step. The size of the discontinuity is proportional to the traction at the discontinuity.

$$\bar{\bar{D}}_{n+1}^{trial} = \bar{\bar{D}}_n, \quad \bar{\bar{\xi}}_{n+1}^{*,trial} = \bar{\bar{\xi}}_n^{*}, \quad \alpha_{n+1}^{trial} = \bar{\bar{D}}_n t_{n+1}^{trial} \tag{C.1}$$

The trial value of stress in the bulk is defined by equation (4.45).

$$\sigma_{n+1}^{trial} = \bar{D}_n^{-1}\left(\check{\mathbf{B}}\mathbf{d}_{n+1} + \bar{G}\alpha_{n+1}^{trial}\right) \tag{C.2}$$

We multiply equation (C.2) by $\bar{D}_n$ and then use the expression (C.1) for α_{n+1}^{trial}. We also take into account the equality of traction at the discontinuity and stress in the bulk (4.40).

$$\bar{D}_n\sigma_{n+1}^{trial} = \check{\mathbf{B}}\mathbf{d}_{n+1} + \bar{G}\bar{\bar{D}}_n t_{n+1}^{trial} = \check{\mathbf{B}}\mathbf{d}_{n+1} + \bar{G}\bar{\bar{D}}_n\sigma_{n+1}^{trial} \tag{C.3}$$

The trial values of traction at the discontinuity and stress in the bulk can easily be obtained from (C.3).

$$t_{n+1}^{trial} = \sigma_{n+1}^{trial} = \frac{\check{\mathbf{B}}\mathbf{d}_{n+1}}{\bar{D}_n - \bar{G}\bar{\bar{D}}_n} \tag{C.4}$$

Damage softening multiplier for concrete layer

The trial failure function is computed from (4.56), where $\bar{\bar{q}}\left(\bar{\bar{\xi}}_{n+1}^{*,trial}\right)$ is defined by (4.61).

$$\bar{\bar{\phi}}_{n+1}^{trial} = \left|t_{n+1}^{trial}\right| - \left(\sigma_{fc} + K_c^{*}\bar{\bar{\xi}}_{n+1}^{*,trial}\right) \tag{C.5}$$

If $\bar{\bar{\phi}}_{n+1}^{trial} < 0$, the assumption about elastic behavior was correct and the trial values are confirmed as final. Otherwise the internal variables have to be corrected. The incremental form of evolution equations in (4.62) reads as follows.

$$\alpha_{n+1} = \left(\alpha_n^{\max} + \bar{\bar{\gamma}}_{n+1}^*\right) sign\left(t_{n+1}\right), \quad \bar{\bar{\xi}}_{n+1}^* = \bar{\bar{\xi}}_n^* + \bar{\bar{\gamma}}_{n+1}^* \tag{C.6}$$

Here $\alpha_n^{\max} = \bar{\bar{D}}_n t_n^{\max} = \bar{\bar{D}}_n \left(\sigma_{fc} + K_c^* \bar{\bar{\xi}}_n^*\right)$ is the maximal elastic value of α for the given carrying capacity, that was reached in the last softening step, see figure 4.15. If $|\alpha| < \alpha_n^{\max}$ or equivalently $|t| < t_n^{\max}$, behavior of the discontinuity is elastic. The failure function from (C.5) can now be rewritten, using the updated values of internal variables (C.6).

$$\bar{\bar{\phi}}_{n+1} = |t_{n+1}| - \left(\sigma_{fc} + K_c^* \bar{\bar{\xi}}_{n+1}^*\right), \quad t_{n+1} = \sigma_{n+1} = \bar{D}_n^{-1}\left(\breve{\mathbf{B}}\mathbf{d}_{n+1} + \bar{G}\alpha_{n+1}\right) \tag{C.7}$$

We express all unknown variables with the softening multiplier $\bar{\bar{\gamma}}_{n+1}^*$, which remains the only unknown, and equal the obtained expression for $\bar{\bar{\phi}}_{n+1}$ to zero as required by loading/unloading conditions (4.59).

$$\begin{aligned}
&\bar{\bar{\phi}}_{n+1} = \bar{D}_n^{-1}\left(\breve{\mathbf{B}}\mathbf{d}_{n+1} + \bar{G}\alpha_{n+1}\right) sign\left(t_{n+1}\right) - \left(\sigma_{fc} + K_c^* \bar{\bar{\xi}}_{n+1}^*\right) = \\
&= \bar{D}_n^{-1}\left(\breve{\mathbf{B}}\mathbf{d}_{n+1} + \bar{G}\underbrace{\left(\bar{\bar{D}}_n\left(\sigma_{fc} + K_c^* \bar{\bar{\xi}}_n^*\right) + \bar{\bar{\gamma}}_{n+1}^*\right) sign\left(t_{n+1}\right)}_{\alpha_{n+1}}\right) sign\left(t_{n+1}\right) - \left(\sigma_{fc} + K_c^*\left(\bar{\bar{\xi}}_n^* + \bar{\bar{\gamma}}_{n+1}^*\right)\right) = \\
&= \bar{D}_n^{-1}\left(\breve{\mathbf{B}}\mathbf{d}_{n+1} sign\left(t_{n+1}\right) + \bar{G}\bar{\bar{D}}_n\left(\sigma_{fc} + K_c^* \bar{\bar{\xi}}_n^*\right) + \bar{G}\bar{\bar{\gamma}}_{n+1}^*\right) - \left(\sigma_{fc} + K_c^* \bar{\bar{\xi}}_n^*\right) - K_c^* \bar{\bar{\gamma}}_{n+1}^* = 0
\end{aligned} \tag{C.8}$$

The two parts of the equation, containing $\bar{\bar{\gamma}}_{n+1}^*$, are put to the right side of the equation, which is then multiplied by $\bar{D}_n$ and divided by $\left(\bar{D}_n - \bar{G}\bar{\bar{D}}_n\right)$:

$$\begin{aligned}
\bar{D}_n^{-1}\left(\breve{\mathbf{B}}\mathbf{d}_{n+1} sign\left(t_{n+1}\right) + \bar{G}\bar{\bar{D}}_n\left(\sigma_{fc} + K_c^* \bar{\bar{\xi}}_n^*\right)\right) - \left(\sigma_{fc} + K_c^* \bar{\bar{\xi}}_n^*\right) &= K_c^* \bar{\bar{\gamma}}_{n+1}^* - \bar{D}_n^{-1}\bar{G}\bar{\bar{\gamma}}_{n+1}^* \\
\breve{\mathbf{B}}\mathbf{d}_{n+1} sign\left(t_{n+1}\right) + \bar{G}\bar{\bar{D}}_n\left(\sigma_{fc} + K_c^* \bar{\bar{\xi}}_n^*\right) - \bar{D}_n\left(\sigma_{fc} + K_c^* \bar{\bar{\xi}}_n^*\right) &= \left(K_c^* \bar{D}_n - \bar{G}\right)\bar{\bar{\gamma}}_{n+1}^* \\
\breve{\mathbf{B}}\mathbf{d}_{n+1} sign\left(t_{n+1}\right) + \left(\bar{G}\bar{\bar{D}}_n - \bar{D}_n\right)\left(\sigma_{fc} + K_c^* \bar{\bar{\xi}}_n^*\right) &= \left(K_c^* \bar{D}_n - \bar{G}\right)\bar{\bar{\gamma}}_{n+1}^* \\
\underbrace{\underbrace{\frac{\breve{\mathbf{B}}\mathbf{d}_{n+1}}{\bar{D}_n - \bar{G}\bar{\bar{D}}_n}}_{t_{n+1}^{trial}} sign\left(t_{n+1}\right) - \left(\sigma_{fc} + K_c^* \bar{\bar{\xi}}_n^*\right)}_{\bar{\bar{\phi}}_{n+1}^{trial}} &= \frac{K_c^* \bar{D}_n - \bar{G}}{\bar{D}_n - \bar{G}\bar{\bar{D}}_n}\bar{\bar{\gamma}}_{n+1}^*
\end{aligned} \tag{C.9}$$

Finally, we can write the expression for $\bar{\bar{\gamma}}_{n+1}^*$.

$$\bar{\bar{\gamma}}_{n+1}^* = \frac{\bar{\bar{\phi}}_{n+1}^{trial}\left(\bar{D}_n - \bar{G}\bar{\bar{D}}_n\right)}{K_c^* \bar{D}_n - \bar{G}} \tag{C.10}$$

MULTI-LAYER EULER-BERNOULLI BEAM FINITE ELEMENT

Derivation of expressions for t_{n+1}^{trial} and $\bar{\bar{\gamma}}_{n+1}^{*}$ for the Euler-Bernoulli beam is performed in the same way as for the Timoshenko beam element.The only difference is that stress in no longer constant over the layer and the traction at the discontinuity is equal to the stress, evaluated at the location of the discontinuity $t = \sigma|_{x_d}$, instead of just $t = \sigma$. Some other non-constant quantities are evaluated at x_d as well, which reflects in the resulting expressions.

$$t_{n+1}^{trial} = \left[\frac{\breve{\mathbf{B}}\mathbf{d}_{n+1}}{\bar{D}_n - \bar{G}_R \bar{\bar{D}}_n} \right]_{x=x_d}, \qquad \bar{\bar{\gamma}}_{n+1}^{*} = \left[\frac{\bar{\bar{\phi}}_{n+1}^{trial} \left(\bar{D}_n - \bar{G}_R \bar{\bar{D}}_n \right)}{K_c^* \bar{D}_n - \bar{G}_R} \right]_{x=x_d} \tag{C.11}$$

APPENDIX D: INFLUENCE OF x_d^i ON COMPUTATION OF INTERNAL FORCES

In this appendix we demonstrate how the location of the discontinuity x_d^i in a layer affects the computation in case of constant strain/stress, resulting in incorrect response of the finite element. The problem was encountered in pure tension/compression numerical examples in section 3.4.1 and pure bending numerical examples in section 3.4.2.

Pure tension or pure compression

Here, we examine the reasons for the incorrect response of the reinforced concrete beam, computed in section 3.4.1.3. According to section 3.2.4.1, in case of constant stress the discontinuity is placed in the middle of the layer and the constant operator $\bar{G}_R^i$ is chosen from (3.46). The strain in the bulk is computed, as shown in equation (3.54). Interpolation functions $\breve{\mathbf{B}}^i$ are defined by (3.7) and (3.8).

$$\bar{\varepsilon}^i = \breve{\mathbf{B}}^i \mathbf{d} + \bar{G}_R^i \alpha^i = C_1 x + C_2, \quad C_1, C_2 = \text{const.} \tag{D.1}$$

If the strain is to remain constant over the layer, which is required for the equilibrium, the linear part of expression (D.1) must be zero. Since $\bar{G}_R^i$ is constant, it makes no contribution to the constant C_1. For a single-layer finite element, the coordinate y^i is zero and we can conclude

$$C_1 = \frac{4}{L^2}\left(u_1 + u_2 - 2u_3\right) = 0 \quad \Rightarrow \quad u_3 = \frac{u_1 + u_2}{2} \tag{D.2}$$

Expression (D.2) for u_3 is inserted in (D.1) to obtain

$$\bar{\varepsilon}^i = \frac{1}{L}\left(u_2 - u_1 - \alpha^i\right) \tag{D.3}$$

The jump in displacements can be computed from equation (3.35), which reduces to $t^i = \sigma^i$ for the constant $\bar{G}_V^i$. In case of monotonic softening, $\alpha^i = \bar{\bar{\xi}}^{*i}$. For concrete one gets

$$t^i = \left(\sigma_{fc} + K_c^* \bar{\bar{\xi}}^{*i}\right) sign\left(t^i\right), \quad \sigma^i = \bar{D}^{i^{-1}} \bar{\varepsilon}^i \quad \Rightarrow \quad \alpha^i = \frac{u_2 - u_1 - \bar{D}^i L\, \sigma_{fc}\, sign\left(t^i\right)}{1 + \bar{D}^i L K_c^*\, sign\left(t^i\right)} \tag{D.4}$$

For a steel layer, the only difference would be in the constitutive equation for σ^i, leading to a slightly different expression for α^i. These equations have been developed for a single-layer finite element and a constant operator $\bar{G}_R^i$, but they also hold for each layer of a multi-layer element if the transversal displacements **v** and rotations $\boldsymbol{\theta}$ of the nodes are zero, as in pure tension/compression. Such tests were modeled in section 3.4.1.4. Since expression for α^i depends on material parameters, the displacement jumps are different in concrete and reinforcement.

A different scenario unfolds in sections 3.4.1.1, 3.4.1.2 and 3.4.1.3, however. Despite the linear stress in a layer, the algorithm detects even the smallest difference between the values at both ends of the finite element, arising from the numerical procedure. The discontinuity is positioned at the "critical" node and one of the linear operators

$\bar{G}_R^i$ is chosen from (3.46). The constant C_1 from (D.1) is now affected by $\bar{G}_R^i$, but it still has to be zero to provide constant strain over the layer.

$$C_1 = \frac{4}{L^2}\left(u_1 + u_2 - 2u_3 - \alpha^i\right) = 0 \quad \Rightarrow \quad u_3 = \frac{u_1 + u_2 - \alpha^i}{2} \tag{D.5}$$

Inserting expression (D.5) for u_3 into (D.1) returns exactly the equation (D.3). The strain is therefore computed in the same manner as in the case with constant $\bar{G}_R^i$. However, the displacement u_3 is no longer independent of α^i, which means that the middle node has to move out of the middle of the element to preserve the equilibrium. By itself, this is not problematic. In a single-layer finite element or an element composed of equal layers, like the beams in sections 3.4.1.1 and 3.4.1.2, all displacement jumps α^i are equal and require the same u_3 to "balance" them. An issue arises in a finite element, composed of different layers, like the reinforced concrete beam in section 3.4.1.3. Since the displacement jumps are different in steel and concrete, they would each require a different middle node displacement u_3 (computed from (D.5)), which is not possible. A constant strain state is therefore not possible in such case!

Nevertheless, equilibrium is achievable. For any u_3, different from the value in (D.5), stress is linear over the length of the layer. Contributions of the layer to the internal forces are computed as integrals of the stress, and the components are different at both ends of the layer $f_{u_1}^{\text{int},(e),i} \neq -f_{u_2}^{\text{int},(e),i}$, see Fig. 3.26. The layer by itself is out of balance, but equilibrium of the finite element is satisfied by finding the exact value of u_3, at which the imbalance of internal forces in steel and the imbalance of the internal forces in concrete neutralize each other, see Fig. 3.27, where $f_{u_1}^{\text{int},(e)} = -f_{u_2}^{\text{int},(e)}$. This is possible, because the equilibrium is only required on the element level, and not on the layer level. Of course, this solution is incorrect, see the comparison in Fig. 3.28.

$$f_{u_1}^{\text{int},(e),i} \neq -f_{u_2}^{\text{int},(e),i} \quad \rightarrow \quad \underbrace{\sum_i f_{u_1}^{\text{int},(e),i}}_{f_{u_1}^{\text{int},(e)}} = -\underbrace{\sum_i f_{u_2}^{\text{int},(e),i}}_{f_{u_2}^{\text{int},(e)}} \tag{D.6}$$

Remark. *Fig. 3.26 and Fig. 3.27 only show the contributions of the i-th layer to the axial internal forces at the end nodes. Contributions to the axial internal force at the middle node and contributions to transversal forces and moments exist also, but their resultants are zero on the element level.*

Pure tension or pure compression, non-zero transversal displacement

Another incorrect solution of equilibrium equations exists. So far, we have assumed that the transversal displacements $\mathbf{v}$ and rotations $\boldsymbol{\theta}$ of the nodes are zero, but this is never explicitly requested. The degrees of freedom change so as to satisfy the equilibrium equations and it turns out that equilibrium is also possible in pure tension or pure compression if transversal displacement at the free end of the beam is different from zero. Such situation arises in a beam with symmetrical cross-section, if the layer discontinuities are positioned at $x = 0$ in the bottom half of the beam ($y^i < 0$) and at $x = L$ in the top half of the beam ($y^i > 0$), or vice versa. In the particular example from section 3.4.1.5, the only difference from section 3.4.1.3 was the reversed orientation of the local axis x, which sufficed for a slightly different numerical evaluations of stress in the layers and different positioning of the discontinuities. Results in Fig. 3.31 and Fig. 3.32 state that the transversal displacement at the end of the beam increases with the loading (imposed axial displacement), while the rotation, shear force and moment remain zero. Although physically not sensible, these results are mathematically possible which is easily verified.

Let us inspect two symmetrically positioned concrete layers of a beam in pure tension. We will show that their contributions to internal shear forces and moments neutralize each other. Quantities, related to the layer above

the neutral axis, are denoted with $+$, and the quantities, related to the layer below the neutral axis, with $-$. The elasticity limit is defined higher than the failure stress so there is no damage in the bulk of the layer ($\bar{D}^i = E_c^{-1}$). Strain and stress in the layers are computed according to equation (3.54), with zero values for nodal rotations $\boldsymbol{\theta}$. The operator $\bar{G}_R^i$ takes the appropriate value from (3.46), depending on the location of the discontinuity. We choose $x_d = 0$ for $y^{i-} < 0$, and $x_d = L$ for $y^{i+} > 0$.

$$\sigma^i = E_c \bar{\varepsilon}^i, \quad \bar{\varepsilon}^{i+} = \breve{\mathbf{B}}^i \mathbf{d} + \bar{G}_R^{i+} \alpha^{i+}, \quad \bar{\varepsilon}^{i-} = \breve{\mathbf{B}}^i \mathbf{d} + \bar{G}_R^{i-} \alpha^{i-} \tag{D.7}$$

Contributions of the two layers to shear force $f_{v_1}^{\text{int},(e)}$ in node 1 are defined in equation (3.28). Symmetry of the layers is taken into account: $-y^{i-} = y^{i+} = y^i$ and $A^{i-} = A^{i+} = A^i$.

$$\begin{aligned} f_{v_1}^{\text{int},(e),i+} &= -\int_L B_1^v \, y^{i+} \sigma^{i+} A^{i+} dx = -\int_L B_1^v \, y^i \sigma^{i+} A^i dx \\ f_{v_1}^{\text{int},(e),i-} &= -\int_L B_1^v \, y^{i-} \sigma^{i-} A^{i-} dx = \int_L B_1^v \, y^i \sigma^{i-} A^i dx \end{aligned} \tag{D.8}$$

After some straightforward manipulation we obtain the expression for their sum. Procedure is repeated for the remaining shear force $f_{v_2}^{\text{int},(e)}$ and moments $f_{\theta_1}^{\text{int},(e)}$ and $f_{\theta_2}^{\text{int},(e)}$.

$$\begin{aligned} f_{v_1}^{\text{int},(e),i+} + f_{v_1}^{\text{int},(e),i-} &= \frac{4 A^i E_c \, y^i \left(6 y^i \left(v_1 - v_2\right) + L \left(\alpha^{i-} + \alpha^{i+}\right)\right)}{L^3} \\ f_{v_2}^{\text{int},(e),i+} + f_{v_2}^{\text{int},(e),i-} &= -\frac{4 A^i E_c \, y^i \left(6 y^i \left(v_1 - v_2\right) + L \left(\alpha^{i-} + \alpha^{i+}\right)\right)}{L^3} \\ f_{\theta_1}^{\text{int},(e),i+} + f_{\theta_1}^{\text{int},(e),i-} &= \frac{A^i E_c \, y^i \left(12 y^i \left(v_1 - v_2\right) + L \left(3\alpha^{i-} + \alpha^{i+}\right)\right)}{L^2} \\ f_{\theta_2}^{\text{int},(e),i+} + f_{\theta_2}^{\text{int},(e),i-} &= \frac{A^i E_c \, y^i \left(12 y^i \left(v_1 - v_2\right) + L \left(\alpha^{i-} + 3\alpha^{i+}\right)\right)}{L^2} \end{aligned} \tag{D.9}$$

If the displacement jumps α^{i-} and α^{i+} take the value from (D.10), all four expressions in (D.9) are zero. Since the beam has a symmetrical cross-section, all layers can be arranged into symmetrical pairs and their contributions to internal shear forces and moments neutralize each other.

$$\alpha^{i-} = \alpha^{i+} = -\frac{3\left(v_1 - v_2\right) y^i}{L} \quad \Rightarrow \quad f_{v_1}^{\text{int},(e)} = f_{v_2}^{\text{int},(e)} = f_{\theta_1}^{\text{int},(e)} = f_{\theta_2}^{\text{int},(e)} = 0 \tag{D.10}$$

Therefore, the results from section 3.4.1.5 do not contradict the equations, used in our finite element. Equilibrium of a beam in "pure tension" (with imposed axial displacement) is indeed possible, even if transversal displacement at the free end is not zero. The solution is incorrect, but mathematically possible. One of the reasons for existence of such solution is the absence of any regulation to correlate the displacement jumps in different layers. Each α^i is free to follow equation (D.10). Since the expression depends on the distance of the layer from the middle axis, the sizes of the discontinuities grow linearly from the middle toward the edge of the beam, which is not physically reasonable.

Pure bending

Here, we examine the effect of incorrect automatic positioning of the discontinuity in case of pure bending, when only one layer of concrete exceeds the ultimate tensile stress. Such situation was encountered in sections 3.4.2.1

and 3.4.2.2. The first discontinuity appears in the bottom layer of concrete in tension. The rest of the element is still elastic at that point. Even though the stress is constant over the layer when the ultimate stress is reached, the discontinuity is placed at either of the two end nodes, rather than in the middle of the element, due to numerical error. One of the linear functions from (3.46) is chosen for operator $\bar{G}_R^i$. We can see from Fig. 3.13 that the additional strain in the bulk $\bar{G}_R^i \alpha^i$ is negative at the discontinuity and positive at the other end of the layer, which means that the stress is decreased at x_d^i and increased at the opposite end. Of course, this is not the converged state, but even when equilibrium is reached, the stress in the layer is not physically logical. At the discontinuity, the value of σ^i is equal to the traction t^i and smaller than the ultimate tensile stress σ_{fct}, which is correct. On the other end, however, the value of σ^i is higher than σ_{fct}. This happens because $\bar{G}_R^i$ was derived on an isolated layer. If the layer was a self standing three-node bar, as assumed for the derivation, it would deform in such way that the stress in it would be constant and equal to t^i. In truth, the layer is bound to the remaining layers through common nodal displacements and cannot deform freely. The imbalance, produced by additional strain, is not neutralized within the cracked layer, but on the level of the finite element. The cracked layer makes only a part of the "required deformation" and the stress at the non-cracked end of the layer remains too high. Eventually, the traction at the discontinuity t^i and the value of stress σ^i at the discontinuity x_d^i would drop to zero, but at the opposite end of the layer the stress would stay positive. The layer would contribute to internal forces, computed as an integral of σ^i over the length of the element, even when it is supposed to be completely broken.

Almost constant strain/stress state in a layer

In all previous cases, described in this appendix, the stress in the layer was constant at the moment when the carrying capacity was reached. The algorithm wrongly positioned the discontinuity at one of the end nodes, due to numerical error. However, the problem was avoided by manually imposing the location of the discontinuity at the middle of the element.

This trick cannot be used if the stress state in the layer is linear. In that case, the discontinuity must be placed at the location of highest stress. If the stress is almost constant (but not quite), for instance in a cantilever beam, loaded with a great axial force and very small transversal force at the free end, the situation is virtually identical to the one described above, only without the remedy. Incorrect computation cannot be avoided here. We conclude that, for a general stress state, the operator $\bar{G}_R^i$, derived in section 3.2.4.1, is inappropriate.

APPENDIX E: EXPRESSIONS FOR t_{n+1}^{trial}, $\bar{\bar{\gamma}}_{n+1}^{*}$, α_{n+1} AND $\bar{\bar{\gamma}}_{n+1}$ IN VISCOSITY

In this appendix we derive expressions, required for the computation of softening internal variables in multi-layer Timoshenko beam finite element with viscous regularization of softening response, presented in chapter 5. Expressions for the trial value of traction at the discontinuity t_{n+1}^{trial}, the damage softening multiplier $\bar{\bar{\gamma}}_{n+1}^{*}$ and the displacement jump α_{n+1} are required in the computation of internal variables of a concrete layer, while the expressions for plastic softening multiplier $\bar{\bar{\gamma}}_{n+1}$ is required in the computation of internal variables of a reinforcement layer.

Discontinuity in concrete layer when $\bar{\bar{q}} < \sigma_{fc}$

Here, we derive the expressions for the trial value of traction at the discontinuity $t_{n+1}^{(k),trial}$ and the damage softening multiplier $\bar{\bar{\gamma}}_{n+1}^{*(k)}$, which are used in the computation of internal variables in a concrete layer in section 5.3.1. The following derivation is valid while $\bar{\bar{q}} < \sigma_{fc}$, i.e. until the traction at the discontinuity drops to zero and the discontinuity compliance $\bar{\bar{D}}$ becomes infinite.

Once a discontinuity occurs in the layer, the bulk internal variables are frozen. Therefore, the value $\bar{D}_n$ is used as the bulk compliance. In the trial step, the behavior of the discontinuity is assumed to be elastic, which means that the discontinuity compliance $\bar{\bar{D}}$ and displacement-like softening variable $\bar{\bar{\xi}}^{*}$ that controls the reduction of carrying capacity, keep the values from the previous step. The size of the discontinuity is computed in accordance with equation (4.55).

$$\bar{\bar{D}}_{n+1}^{(k),trial} = \bar{\bar{D}}_n, \quad \bar{\bar{\xi}}_{n+1}^{*(k),trial} = \bar{\bar{\xi}}_n^{*}, \quad \alpha_{n+1}^{(k),trial} = \bar{\bar{D}}_n\, t_{n+1}^{(k),trial} \tag{E.1}$$

The trial value of stress in the bulk is defined by equation (4.45).

$$\sigma_{n+1}^{(k),trial} = \bar{D}_n^{-1}\left(\check{\mathbf{B}}\mathbf{d}_{n+1}^{(k-1)} + \bar{G}\alpha_{n+1}^{(k),trial}\right) \tag{E.2}$$

Relation between t_{n+1}^{trial} and σ_{n+1}^{trial} is described in equation (5.7). It depends on the pseudo-time derivative $\dot{\alpha}$, which is here defined in incremental form, as the difference between the current value of α and the value from the previous step, divided by the corresponding increase of time $\Delta\tau_{n+1} = \tau_{n+1} - \tau_n$.

$$\dot{\alpha}_{n+1}^{(k)} = \frac{\alpha_{n+1}^{(k)} - \alpha_n}{\Delta\tau_{n+1}}, \quad \dot{\alpha}_{n+1}^{(k),trial} = \frac{\alpha_{n+1}^{(k),trial} - \alpha_n}{\Delta\tau_{n+1}} \tag{E.3}$$

Equation (5.7) can now be rewritten.

$$t_{n+1}^{(k),trial} = \sigma_{n+1}^{(k),trial} - \frac{\eta}{\Delta\tau_{n+1}}\left(\alpha_{n+1}^{(k),trial} - \alpha_n\right) \tag{E.4}$$

After using the expression (E.1) for $\alpha_{n+1}^{(k),trial}$ in equation (E.4) we can express $\sigma_{n+1}^{(k),trial}$ with $t_{n+1}^{(k),trial}$.

$$\sigma_{n+1}^{(k),trial} = t_{n+1}^{(k),trial} + \frac{\eta}{\Delta\tau_{n+1}}\left(\alpha_{n+1}^{(k),trial} - \alpha_n\right) = t_{n+1}^{(k),trial} + \frac{\eta}{\Delta\tau_{n+1}}\bar{\bar{D}}_n\, t_{n+1}^{(k),trial} - \frac{\eta}{\Delta\tau_{n+1}}\alpha_n \tag{E.5}$$

We multiply equation (E.2) with $\bar{D}_n$ and substitute $\sigma_{n+1}^{(k),trial}$ with (E.5) and $\alpha_{n+1}^{(k),trial}$ with (E.1).

$$\bar{D}_n\left(t_{n+1}^{(k),trial} + \frac{\eta}{\Delta\tau_{n+1}}\bar{\bar{D}}_n\, t_{n+1}^{(k),trial} - \frac{\eta}{\Delta\tau_{n+1}}\alpha_n\right) = \breve{\mathbf{Bd}}_{n+1}^{(k-1)} + \bar{G}\bar{\bar{D}}_n\, t_{n+1}^{(k),trial} \tag{E.6}$$

After some straightforward manipulation, the trial value of traction at the discontinuity is obtained from (E.6).

$$t_{n+1}^{(k),trial} = \frac{\breve{\mathbf{Bd}}_{n+1}^{(k-1)} + \bar{D}_n \frac{\eta}{\Delta\tau_{n+1}}\alpha_n}{\bar{D}_n - \bar{G}\bar{\bar{D}}_n + \bar{D}_n \frac{\eta}{\Delta\tau_{n+1}}\bar{\bar{D}}_n} \tag{E.7}$$

Next, the trial value of failure function is computed from (4.56), where $\bar{\bar{q}}\left(\bar{\bar{\xi}}_{n+1}^{*(k),trial}\right)$ is defined by (4.61).

$$\bar{\bar{\phi}}_{n+1}^{(k),trial} = \left|t_{n+1}^{(k),trial}\right| - \left(\sigma_{fc} + K_c^* \bar{\bar{\xi}}_{n+1}^{*(k),trial}\right) \tag{E.8}$$

If $\bar{\bar{\phi}}_{n+1}^{(k),trial} < 0$, the assumption about elastic behavior was correct and the trial values are confirmed as final. Otherwise the internal variables have to be corrected. The incremental form of evolution equations (4.62) reads as follows.

$$\alpha_{n+1}^{(k)} = \left(\alpha_n^{\max} + \bar{\bar{\gamma}}_{n+1}^{*(k)}\right) sign\left(t_{n+1}^{(k)}\right), \quad \bar{\bar{\xi}}_{n+1}^{*(k)} = \bar{\bar{\xi}}_n^* + \bar{\bar{\gamma}}_{n+1}^{*(k)} \tag{E.9}$$

where $\alpha_n^{\max} = \bar{\bar{D}}_n t_n^{\max} = \bar{\bar{D}}_n\left(\sigma_{fc} + K_c^* \bar{\bar{\xi}}_n^*\right)$ is the maximal elastic value of α for the given carrying capacity, that was reached in the last softening step. If $|\alpha| < \alpha_n^{\max}$, or equivalently $|t| < t_n^{\max}$, behavior of the discontinuity is elastic. The failure function is now written, using the updated values of internal variables (E.9).

$$\begin{aligned} \bar{\bar{\phi}}_{n+1}^{(k)} &= \left|t_{n+1}^{(k)}\right| - \left(\sigma_{fc} + K_c^* \bar{\bar{\xi}}_{n+1}^{*(k)}\right) \\ t_{n+1}^{(k)} &= \sigma_{n+1}^{(k)} - \frac{\eta}{\Delta\tau_{n+1}}\left(\alpha_{n+1}^{(k)} - \alpha_n\right), \quad \sigma_{n+1}^{(k)} = \bar{D}_n^{-1}\left(\breve{\mathbf{Bd}}_{n+1}^{(k-1)} + \bar{G}\alpha_{n+1}^{(k)}\right) \end{aligned} \tag{E.10}$$

We express all unknown variables with the softening multiplier $\bar{\bar{\gamma}}_{n+1}^{*(k)}$, which remains the only unknown, and equal the obtained expression for $\bar{\bar{\phi}}_{n+1}^{(k)}$ to zero as required by loading/unloading conditions (4.59).

$$\begin{aligned} \bar{\bar{\phi}}_{n+1}^{(k)} &= \left(\bar{D}_n^{-1}\left(\breve{\mathbf{Bd}}_{n+1}^{(k-1)} + \bar{G}\alpha_{n+1}^{(k)}\right) - \frac{\eta}{\Delta\tau_{n+1}}\left(\alpha_{n+1}^{(k)} - \alpha_n\right)\right) sign\left(t_{n+1}^{(k)}\right) - \left(\sigma_{fc} + K_c^* \bar{\bar{\xi}}_{n+1}^{*(k)}\right) = \\ &= \bar{D}_n^{-1}\left(\breve{\mathbf{Bd}}_{n+1}^{(k-1)} + \left(\bar{G} - \bar{D}_n \frac{\eta}{\Delta\tau_{n+1}}\right)\alpha_{n+1}^{(k)} + \bar{D}_n \frac{\eta}{\Delta\tau_{n+1}}\alpha_n\right) sign\left(t_{n+1}^{(k)}\right) - \left(\sigma_{fc} + K_c^* \bar{\bar{\xi}}_{n+1}^{*(k)}\right) = \\ &= \bar{D}_n^{-1}\left(\breve{\mathbf{Bd}}_{n+1}^{(k-1)} + \left(\bar{G} - \bar{D}_n \frac{\eta}{\Delta\tau_{n+1}}\right)\underbrace{\left(\bar{\bar{D}}_n\left(\sigma_{fc} + K_c^* \bar{\bar{\xi}}_n^*\right) + \bar{\bar{\gamma}}_{n+1}^{*(k)}\right) sign\left(t_{n+1}^{(k)}\right)}_{\alpha_{n+1}^{(k)}} + \bar{D}_n \frac{\eta}{\Delta\tau_{n+1}}\alpha_n\right) sign\left(t_{n+1}^{(k)}\right) - \left(\sigma_{fc} + K_c^*\left(\bar{\bar{\xi}}_n^* + \bar{\bar{\gamma}}_{n+1}^{*(k)}\right)\right) = \\ &= \bar{D}_n^{-1}\left(\left(\breve{\mathbf{Bd}}_{n+1}^{(k-1)} + \bar{D}_n \frac{\eta}{\Delta\tau_{n+1}}\alpha_n\right) sign\left(t_{n+1}^{(k)}\right) + \left(\bar{G} - \bar{D}_n \frac{\eta}{\Delta\tau_{n+1}}\right)\bar{\bar{D}}_n\left(\sigma_{fc} + K_c^* \bar{\bar{\xi}}_n^*\right) + \left(\bar{G} - \bar{D}_n \frac{\eta}{\Delta\tau_{n+1}}\right)\bar{\bar{\gamma}}_{n+1}^{*(k)}\right) - \left(\sigma_{fc} + K_c^* \bar{\bar{\xi}}_n^*\right) - K_c^* \bar{\bar{\gamma}}_{n+1}^{*(k)} = 0 \end{aligned} \tag{E.11}$$

The two parts of the equation, which contain $\bar{\bar{\gamma}}^{*(k)}_{n+1}$, are put to the right side of the equation, which is then multiplied by $\bar{D}_n$ and divided by $\left(\bar{D}_n - \bar{G}\bar{\bar{D}}_n + \bar{D}_n \frac{\eta}{\Delta\tau_{n+1}}\bar{\bar{D}}_n\right)$:

$$
\begin{aligned}
\bar{D}_n^{-1}\left(\left(\breve{\mathbf{B}}\mathbf{d}^{(k-1)}_{n+1} + \bar{D}_n\frac{\eta}{\Delta\tau_{n+1}}\alpha_n\right) sign\left(t^{(k)}_{n+1}\right) + \left(\bar{G} - \bar{D}_n\frac{\eta}{\Delta\tau_{n+1}}\right)\bar{\bar{D}}_n\left(\sigma_{fc} + K_c^*\bar{\bar{\xi}}^*_n\right)\right) - \left(\sigma_{fc} + K_c^*\bar{\bar{\xi}}^*_n\right) = K_c^*\bar{\bar{\gamma}}^{*(k)}_{n+1} - \bar{D}_n^{-1}\left(\bar{G} - \bar{D}_n\frac{\eta}{\Delta\tau_{n+1}}\right)\bar{\bar{\gamma}}^{*(k)}_{n+1} \\
\left(\breve{\mathbf{B}}\mathbf{d}^{(k-1)}_{n+1} + \bar{D}_n\frac{\eta}{\Delta\tau_{n+1}}\alpha_n\right) sign\left(t^{(k)}_{n+1}\right) + \left(\bar{G} - \bar{D}_n\frac{\eta}{\Delta\tau_{n+1}}\right)\bar{\bar{D}}_n\left(\sigma_{fc} + K_c^*\bar{\bar{\xi}}^*_n\right) - \bar{D}_n\left(\sigma_{fc} + K_c^*\bar{\bar{\xi}}^*_n\right) = K_c^*\bar{D}_n\bar{\bar{\gamma}}^{*(k)}_{n+1} - \left(\bar{G} - \bar{D}_n\frac{\eta}{\Delta\tau_{n+1}}\right)\bar{\bar{\gamma}}^{*(k)}_{n+1} \\
\left(\breve{\mathbf{B}}\mathbf{d}^{(k-1)}_{n+1} + \bar{D}_n\frac{\eta}{\Delta\tau_{n+1}}\alpha_n\right) sign\left(t^{(k)}_{n+1}\right) + \left(\left(\bar{G} - \bar{D}_n\frac{\eta}{\Delta\tau_{n+1}}\right)\bar{\bar{D}}_n - \bar{D}_n\right)\left(\sigma_{fc} + K_c^*\bar{\bar{\xi}}^*_n\right) = \left(K_c^*\bar{D}_n - \bar{G} + \bar{D}_n\frac{\eta}{\Delta\tau_{n+1}}\right)\bar{\bar{\gamma}}^{*(k)}_{n+1} \\
\underbrace{\underbrace{\frac{\breve{\mathbf{B}}\mathbf{d}^{(k-1)}_{n+1} + \bar{D}_n\frac{\eta}{\Delta\tau_{n+1}}\alpha_n}{\bar{D}_n - \bar{G}\bar{\bar{D}}_n + \bar{D}_n\frac{\eta}{\Delta\tau_{n+1}}\bar{\bar{D}}_n}}_{t^{(k),trial}_{n+1}} sign\left(t^{(k)}_{n+1}\right) - \left(\sigma_{fc} + K_c^*\bar{\bar{\xi}}^*_n\right)}_{\bar{\bar{\phi}}^{(k),trial}_{n+1}} = \frac{K_c^*\bar{D}_n - \bar{G} + \bar{D}_n\frac{\eta}{\Delta\tau_{n+1}}}{\bar{D}_n - \bar{G}\bar{\bar{D}}_n + \bar{D}_n\frac{\eta}{\Delta\tau_{n+1}}\bar{\bar{D}}_n}\bar{\bar{\gamma}}^{*(k)}_{n+1}
\end{aligned}
\tag{E.12}
$$

Finally, we can write the expression for $\bar{\bar{\gamma}}^{*(k)}_{n+1}$.

$$
\bar{\bar{\gamma}}^{*(k)}_{n+1} = \frac{\bar{\bar{\phi}}^{(k),trial}_{n+1}\left(\bar{D}_n - \bar{G}\bar{\bar{D}}_n + \bar{D}_n\frac{\eta}{\Delta\tau_{n+1}}\bar{\bar{D}}_n\right)}{K_c\bar{D}_n - \bar{G} + \bar{D}_n\frac{\eta}{\Delta\tau_{n+1}}}
\tag{E.13}
$$

Discontinuity in concrete layer when $\bar{\bar{q}} = \sigma_{fc}$

Here we consider the situation, when the concrete layer loses all carrying capacity. When the stress-like softening variable reaches the value $\bar{\bar{q}} = \sigma_{fc}$, the traction at the discontinuity t drops to zero (at a non-zero displacement jump α) and the discontinuity compliance $\bar{\bar{D}}$ becomes infinite, so the above derivation does not apply any more. Instead, the displacement jump $\alpha^{(k)}_{n+1}$ is computed from equation $t^{(k)}_{n+1} = 0$.

We start by inserting expressions (5.15) for $\sigma^{(k)}_{n+1}$ and (E.3) for $\dot{\alpha}^{(k)}_{n+1}$ into equation (5.7).

$$
t^{(k)}_{n+1} = \sigma^{(k)}_{n+1} - \eta\,\dot{\alpha}^{(k)}_{n+1} = \bar{D}_n^{-1}\left(\breve{\mathbf{B}}\mathbf{d}^{(k-1)}_{n+1} + \bar{G}\alpha^{(k)}_{n+1}\right) - \frac{\eta}{\Delta\tau_{n+1}}\left(\alpha^{(k)}_{n+1} - \alpha_n\right)
\tag{E.14}
$$

The obtained expression for $t^{(k)}_{n+1}$ is equaled to zero. The equation is then multiplied with $\bar{D}_n$ and rearranged to collect the terms containing $\alpha^{(k)}_{n+1}$.

$$
\begin{aligned}
\bar{D}_n^{-1}\left(\breve{\mathbf{B}}\mathbf{d}^{(k-1)}_{n+1} + \bar{G}\alpha^{(k)}_{n+1}\right) - \frac{\eta}{\Delta\tau_{n+1}}\left(\alpha^{(k)}_{n+1} - \alpha_n\right) &= 0 \\
\breve{\mathbf{B}}\mathbf{d}^{(k-1)}_{n+1} + \bar{G}\alpha^{(k)}_{n+1} - \bar{D}_n\frac{\eta}{\Delta\tau_{n+1}}\alpha^{(k)}_{n+1} + \bar{D}_n\frac{\eta}{\Delta\tau_{n+1}}\alpha_n &= 0 \\
\left(\bar{G} - \bar{D}_n\frac{\eta}{\Delta\tau_{n+1}}\right)\alpha^{(k)}_{n+1} &= -\left(\breve{\mathbf{B}}\mathbf{d}^{(k-1)}_{n+1} + \bar{D}_n\frac{\eta}{\Delta\tau_{n+1}}\alpha_n\right)
\end{aligned}
\tag{E.15}
$$

We can now write the expression for the displacement jump $\alpha^{(k)}_{n+1}$.

$$
\alpha^{(k)}_{n+1} = -\frac{\breve{\mathbf{B}}\mathbf{d}^{(k-1)}_{n+1} + \bar{D}_n\frac{\eta}{\Delta\tau_{n+1}}\alpha_n}{\bar{G} - \bar{D}_n\frac{\eta}{\Delta\tau_{n+1}}}
\tag{E.16}
$$

Discontinuity in reinforcement layer when $\bar{\bar{q}} < \sigma_{fs}$

In this section we derive the expression for the plastic softening multiplier $\bar{\bar{\gamma}}^{(k)}_{n+1}$, required for the computation of internal variables in the reinforcement layer in section 5.3.2 of chapter 5, in case that the layer still possesses some carrying capacity, i.e. $\bar{\bar{q}} < \sigma_{fs}$.

We begin by expressing the traction at the discontinuity $t^{(k)}_{n+1}$ with its trial value $t^{(k),trial}_{n+1}$. To achieve this, we insert expressions (5.24) for $\sigma^{(k)}_{n+1}$ and (E.3) for $\dot{\alpha}^{(k)}_{n+1}$ into equation (5.7).

$$t^{(k)}_{n+1} = \sigma^{(k)}_{n+1} - \eta\,\dot{\alpha}^{(k)}_{n+1} = E_s\left(\breve{\mathbf{B}}\mathbf{d}^{(k-1)}_{n+1} + \bar{G}\alpha^{(k)}_{n+1} - \bar{\varepsilon}_{p,n}\right) - \frac{\eta}{\Delta\tau_{n+1}}\left(\alpha^{(k)}_{n+1} - \alpha_n\right) \tag{E.17}$$

The displacement jump is expressed with the softening multiplier by using the evolution equation (5.23). The applied equality $sign\left(t^{(k)}_{n+1}\right)$=$sign\left(t^{(k),trial}_{n+1}\right)$ is justified in appendix A.

$$\begin{aligned} t^{(k)}_{n+1} &= E_s\left(\breve{\mathbf{B}}\mathbf{d}^{(k-1)}_{n+1} + \bar{G}\left(\alpha_n + \bar{\bar{\gamma}}^{(k)}_{n+1}\,sign\left(t^{(k)}_{n+1}\right)\right) - \bar{\varepsilon}_{p,n}\right) - \frac{\eta}{\Delta\tau_{n+1}}\left(\alpha_n + \bar{\bar{\gamma}}^{(k)}_{n+1} sign\left(t^{(k)}_{n+1}\right) - \alpha_n\right) = \\ &= \underbrace{E_s\left(\breve{\mathbf{B}}\mathbf{d}^{(k-1)}_{n+1} + \bar{G}\alpha_n - \bar{\varepsilon}_{p,n}\right)}_{=\sigma^{(k),trial}_{n+1} = t^{(k),trial}_{n+1}} + E_s\bar{G}\,\bar{\bar{\gamma}}^{(k)}_{n+1}\,sign\left(t^{(k)}_{n+1}\right) - \frac{\eta}{\Delta\tau_{n+1}}\,\bar{\bar{\gamma}}^{(k)}_{n+1}\,sign\left(t^{(k)}_{n+1}\right) = \\ &= t^{(k),trial}_{n+1} + \left(E_s\bar{G} - \frac{\eta}{\Delta\tau_{n+1}}\right)\bar{\bar{\gamma}}^{(k)}_{n+1}\,sign\left(t^{(k)}_{n+1}\right) \end{aligned} \tag{E.18}$$

Equation (5.19) has been applied as well, stating that the trial values of traction at the discontinuity and the stress in the bulk are equal. The stress-like softening variable $\bar{\bar{q}}$ is determined by equation (4.76). We are considering the case when $\bar{\bar{q}} < \sigma_{fs}$. This value is designated with $\bar{\bar{q}}^A_{n+1}$.

$$\bar{\bar{q}}^{(k)}_{n+1} = -K_s\bar{\bar{\xi}}^{(k)}_{n+1} = -K_s\left(\bar{\bar{\xi}}_n + \bar{\bar{\gamma}}^{(k)}_{n+1}\right) = \bar{\bar{q}}^{(k),trial}_{n+1} - K_s\bar{\bar{\gamma}}^{(k)}_{n+1} \quad \rightarrow \quad \bar{\bar{q}}^A_{n+1} \tag{E.19}$$

Expressions (E.18) and (E.19) are inserted in the failure function $\bar{\bar{\phi}}^{(k)}_{n+1}$, determined by equation (4.75). The obtained expression has to be zero to fulfill the loading/unloading conditions (4.78).

$$\bar{\bar{\phi}}^{(k)}_{n+1} = \left|t^{(k)}_{n+1}\right| - \left(\sigma_{fs} - \bar{\bar{q}}^{(k)}_{n+1}\right) = 0 \tag{E.20}$$

$$\begin{aligned} \left(t^{(k),trial}_{n+1} + \left(E_s\bar{G} - \frac{\eta}{\Delta\tau_{n+1}}\right)\bar{\bar{\gamma}}^{(k)}_{n+1} sign\left(t^{(k)}_{n+1}\right)\right) sign\left(t^{(k)}_{n+1}\right) - \left(\sigma_{fs} - \bar{\bar{q}}^{(k),trial}_{n+1} + K_s\bar{\bar{\gamma}}^{(k)}_{n+1}\right) = 0 \\ t^{(k),trial}_{n+1} sign\left(t^{(k)}_{n+1}\right) + \left(E_s\bar{G} - \frac{\eta}{\Delta\tau_{n+1}}\right)\bar{\bar{\gamma}}^{(k)}_{n+1} - \left(\sigma_{fs} - \bar{\bar{q}}^{(k),trial}_{n+1}\right) - K_s\bar{\bar{\gamma}}^{(k)}_{n+1} = 0 \\ \underbrace{\left|t^{(k),trial}_{n+1}\right| - \left(\sigma_{fs} - \bar{\bar{q}}^{(k),trial}_{n+1}\right)}_{\bar{\bar{\phi}}^{(k),trial}_{n+1}} - \left(K_s - E_s\bar{G} + \frac{\eta}{\Delta\tau_{n+1}}\right)\bar{\bar{\gamma}}^{(k)}_{n+1} = 0 \end{aligned} \tag{E.21}$$

From (E.21), the expression for the plastic softening multiplier $\bar{\bar{\gamma}}^{(k)}_{n+1}$ is obtained. It is denoted with $\bar{\bar{\gamma}}^A_{n+1}$ to associate it with the stress-like softening variable $\bar{\bar{q}}^A_{n+1} < \sigma_{fs}$.

$$\bar{\bar{\gamma}}^{A}_{n+1} = \frac{\bar{\bar{\phi}}^{(k),trial}_{n+1}}{-\bar{G}E_s + K_s + \frac{\eta}{\Delta\tau_{n+1}}} \tag{E.22}$$

We have derived expression (E.22) under assumption that $\bar{\bar{q}} < \sigma_{fs}$, which has to be verified. $\bar{\bar{q}}^{A}_{n+1}$ has to be computed from equation (E.19), using expression (E.22) for $\bar{\bar{\gamma}}^{(k)}_{n+1}$. If the calculated value is indeed smaller than σ_{fs}, the assumption was correct. Otherwise, the carrying capacity at the discontinuity has dropped to zero and $\bar{\bar{q}} = \sigma_{fs}$.

Discontinuity in reinforcement layer when $\bar{\bar{q}} = \sigma_{fs}$

In this section we derive the expression for the plastic softening multiplier $\bar{\bar{\gamma}}^{(k)}_{n+1}$ for the case when the layer has lost all carrying capacity at the discontinuity (the stress in the bulk may be different from zero). The stress-like softening variable is denoted with $\bar{\bar{q}}^{B}_{n+1} = \sigma_{fs}$ in order to be distinguished from $\bar{\bar{q}}^{A}_{n+1} < \sigma_{fs}$ above.

By inserting $\bar{\bar{q}}^{B}_{n+1}$ in equation (E.20), we conclude that $t^{(k)}_{n+1} = 0$. Expression (E.18) for the traction at the discontinuity is equaled to zero. The equality $sign\left(t^{(k)}_{n+1}\right)$=$sign\left(t^{(k),trial}_{n+1}\right)$ is applied again.

$$\begin{aligned} t^{(k),trial}_{n+1} + \left(E_s\bar{G} - \frac{\eta}{\Delta\tau_{n+1}}\right)\bar{\bar{\gamma}}^{(k)}_{n+1} sign\left(t^{(k)}_{n+1}\right) = 0 \\ t^{(k),trial}_{n+1} sign\left(t^{(k),trial}_{n+1}\right) + \left(E_s\bar{G} - \frac{\eta}{\Delta\tau_{n+1}}\right)\bar{\bar{\gamma}}^{(k)}_{n+1} = 0 \end{aligned} \tag{E.23}$$

Expression for $\bar{\bar{\gamma}}^{(k)}_{n+1}$ is acquired from (E.23). It is marked with $\bar{\bar{\gamma}}^{B}_{n+1}$ to be associated with $\bar{\bar{q}}^{B}_{n+1} = \sigma_{fs}$.

$$\bar{\bar{\gamma}}^{B}_{n+1} = \frac{\left|t^{(k),trial}_{n+1}\right|}{-\bar{G}E_s + \frac{\eta}{\Delta\tau_{n+1}}} \tag{E.24}$$

During the computational procedure in section 5.3.2, $\bar{\bar{\gamma}}^{(k)}_{n+1}$ is first evaluated according to equation (E.22), then the stress-like variable is computed according to (E.19): $\bar{\bar{q}}^{A}_{n+1} = -K_s\left(\bar{\bar{\xi}}_n + \bar{\bar{\gamma}}^{A}_{n+1}\right)$. If the value is indeed $\bar{\bar{q}}^{A}_{n+1} < \sigma_{fs}$, the value $\bar{\bar{\gamma}}^{A}_{n+1}$ is stored. Otherwise the value $\bar{\bar{\gamma}}^{B}_{n+1}$ from (E.24) is taken.